Realizing superconducting spin qubits

Pita-Vidal, Marta

DOI
10.4233/uuid:1314fbd5-794a-47d7-8bc6-ed73a84d8a6d

Publication date
2023

Document Version
Final published version

Citation (APA)
Pita-Vidal, M. (2023). *Realizing superconducting spin qubits*. [Dissertation (TU Delft), Delft University of Technology]. https://doi.org/10.4233/uuid:1314fbd5-794a-47d7-8bc6-ed73a84d8a6d

REALIZING SUPERCONDUCTING SPIN QUBITS

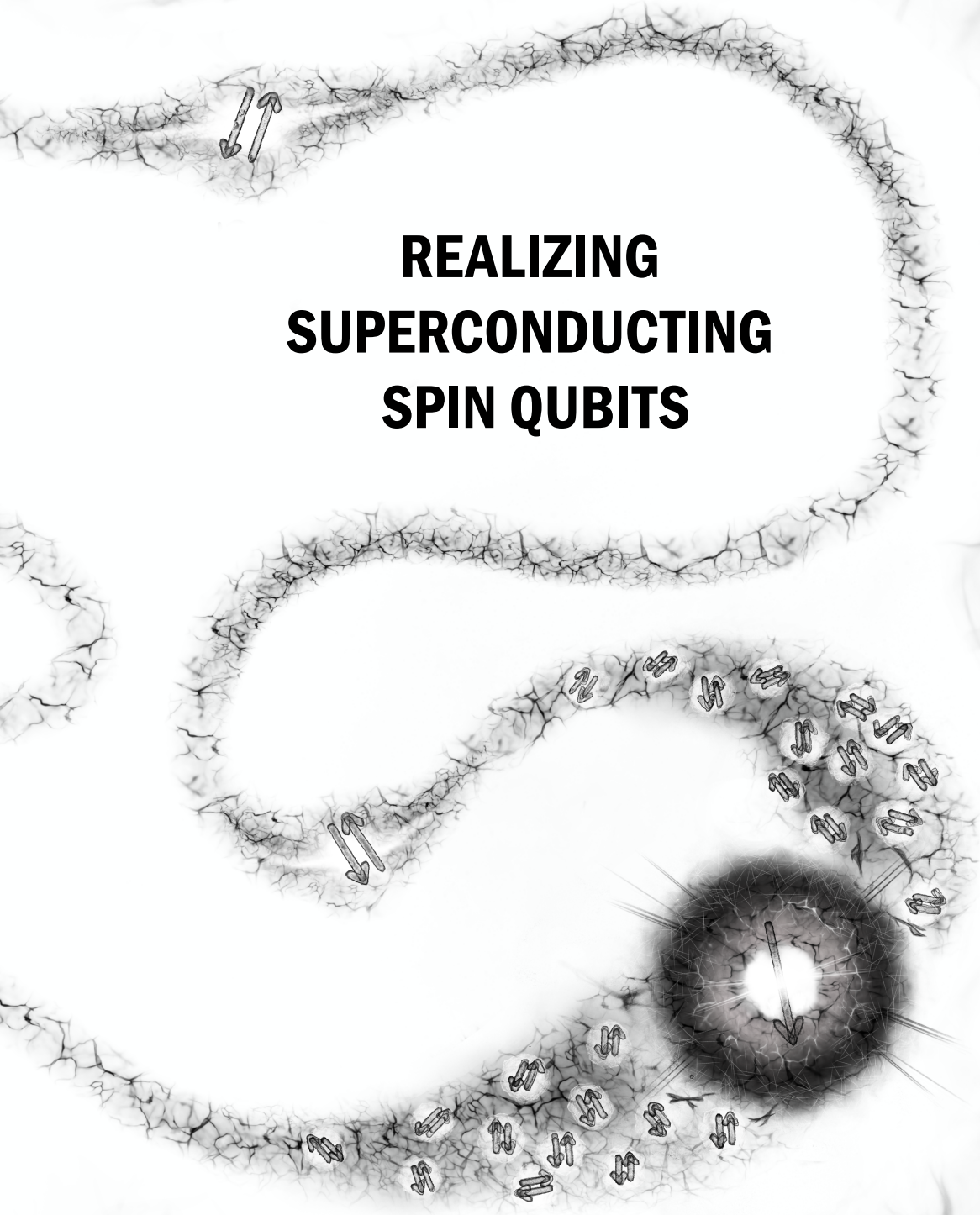

Marta Pita-Vidal

REALIZING SUPERCONDUCTING SPIN QUBITS

Dissertation

for the purpose of obtaining the degree of doctor
at Delft University of Technology,
by the authority of the Rector Magnificus prof. dr. ir. T. H. J. J. van der Hagen,
chair of the Board of Doctorates,
to be defended publicly on
Monday 11, December 2023 at 15:00 o'clock

by

Marta PITA-VIDAL

Master of Science in Applied Physics,
Delft University of Technology, Delft, The Netherlands,
born in Ferrol, Spain.

This dissertation has been approved by the promotors.

Composition of the doctoral committee:

Rector Magnificus	chairperson
Prof. dr. ir. L. P. Kouwenhoven,	Delft University of Technology, promotor
Dr. C. K. Andersen,	Delft University of Technology, promotor
Independent members:	
Prof. dr. B. M. Terhal	Technische Universiteit Delft
Prof. dr. P. Jarillo-Herrero	Massachusetts Institute of Technology
Prof. dr. P. Scarlino	École polytechnique fédérale de Lausanne
Dr. R. Aguado	Consejo Superior de Investigaciones Científicas
Prof. dr. L. DiCarlo	Technische Universiteit Delft, reserve member

Cover: Artistic impression of two inductively coupled superconducting spin qubits.
By Manuela Pita Vidal.
manupitart@gmail.com @manupitart

Casimir PhD Series, Delft-Leiden 2023-38

ISBN 978-90-8593-584-1

An electronic version of this dissertation is available at
http://repository.tudelft.nl/.

CONTENTS

SUMMARY

Josephson junctions implemented in semiconducting nanowires proximitized by a superconductor exhibit intricate physics arising from the interplay of electron-electron interactions, superconductivity, spin-orbit coupling, and the Zeeman effect. This thesis explores these phenomena through a series of experiments conducted using circuit quantum electrodynamics techniques.

After establishing the fundamental theoretical concepts and experimental methodologies, we introduce a crucial element for probing our devices with microwaves: magnetic field-compatible resonators. We then describe various experiments conducted over the past years in which superconducting resonators and other circuits are used to explore the physics of nanowire Josephson junctions.

In an initial experiment, we develop a magnetic-field-resilient fluxonium circuit that incorporates an InAs semiconducting nanowire at its core. We show that the device's spectrum is highly dependent on both the electrostatic gate voltage and the magnetic field strength, allowing us to detect signatures of non-conventional phenomena in semiconducting Josephson junctions.

The bulk of this thesis revolves around a second set of experiments, where a quantum dot is electrostatically defined within the nanowire Josephson junction. This time, we use a transmon circuit to investigate singlet-doublet ground state transitions and their dynamics. The two spinful doublet states of the junction define a novel type of qubit with intriguing properties: a superconducting (or Andreev) spin qubit (ASQ). Thus, we then shift our focus to the doublet states and explore their magnetic field dependence with transmon spectroscopy. Subsequently, we turn to directly investigating the spin-flip transition and the coherence properties of the two spin states. We find that the intrinsic coupling between the spin state and the supercurrent through the junction enables strong coupling between the ASQ and the transmon qubit in which it is embedded.

In a final experiment, we connect two such Andreev spin qubits in parallel and investigate their supercurrent-mediated longitudinal coupling. We find that the qubits are strongly coupled and their coupling strength can be switched on and off by adjusting the magnetic flux. Notably, given that the spins are placed micrometers apart, this mechanism enables interaction between distant spins. Building on these promising characteristics, we end by introducing a proposal that outlines our vision for scaling up ASQs. The proposed architecture, where multiple ASQs are connected in parallel, enables the selective coupling of any pair of qubits in the system, regardless of their spatial separation, through flux control.

This thesis concludes by outlining potential future experiments that could be conducted with devices and techniques similar to those investigated here.

SAMENVATTING

Josephson-juncties geïmplementeerd in halfgeleidende nanodraden die genaderd worden door een supergeleider vertonen complexe fysica voortkomend uit de wisselwerking van elektron-elektron interacties, supergeleiding, spin-baan koppeling en het Zeeman-effect. Deze scriptie verkent deze verschijnselen door middel van een reeks experimenten uitgevoerd met circuit quantum elektrodynamica technieken.

Na het vaststellen van de fundamentele theoretische concepten en experimentele methodologieën, introduceren we een cruciaal element voor het onderzoeken van onze apparaten met microgolven: magnetisch veld-compatibele resonatoren. Vervolgens beschrijven we verschillende experimenten die in de afgelopen jaren zijn uitgevoerd, waarbij supergeleidende resonatoren en andere circuits worden gebruikt om de fysica van nanodraad Josephson-juncties te verkennen.

In een eerste experiment ontwikkelen we een magnetisch veld-resistent fluxonium-circuit dat een InAs halfgeleidende nanodraad in zijn kern bevat. We tonen aan dat het spectrum van het apparaat sterk afhankelijk is van zowel elektrostatische gate-spanning als magnetische veldsterkte, wat ons in staat stelt om handtekeningen van niet-conventio nele verschijnselen in halfgeleidende Josephson-juncties te detecteren.

Het grootste deel van deze scriptie draait om een tweede reeks experimenten, waarin een kwantumdot elektrostatisch wordt gedefinieerd binnen de nanodraad Josephson-junctie. Deze keer gebruiken we een transmon-circuit om overgangen van singlet-dublet grondtoestanden en hun dynamiek te onderzoeken. De twee dubbele spinvolle staten van de junctie definiëren een nieuw type qubit met intrigerende eigenschappen: een supergeleidende (of Andreev) spin qubit (ASQ). Daarom verschuiven we vervolgens onze focus naar de dublettoestanden en verkennen hun magnetische veldafhankelijkheid met transmon-spectroscopie. Daarna richten we ons rechtstreeks op de spin-flip-overgang en de coherentie-eigenschappen van de twee spintoestanden. We vinden dat de intrinsieke koppeling tussen de spintoestand en de superstroom door de junctie een sterke koppeling mogelijk maakt tussen de ASQ en de transmon qubit waarin deze is ingebed.

In een laatste experiment verbinden we twee van dergelijke Andreev-spin qubits parallel en onderzoeken hun superstroom-gemedieerde longitudinale koppeling. We vinden dat de qubits sterk gekoppeld zijn en dat hun koppelingssterkte aan en uit kan worden gezet door het magnetische flux aan te passen. Opmerkelijk is dat, gezien het feit dat de spins micrometers uit elkaar liggen, dit mechanisme interactie tussen verre spins mogelijk maakt. Voortbouwend op deze veelbelovende kenmerken, sluiten we af door een voorstel te introduceren dat onze visie voor het opschalen van ASQ's schetst. De voorgestelde architectuur, waarbij meerdere ASQ's parallel zijn verbonden, maakt de selectieve koppeling van elk paar qubits in het systeem mogelijk, ongeacht hun ruimtelijke scheiding, door fluxcontrole.

Deze scriptie wordt afgesloten met een overzicht van mogelijke toekomstige experimenten die zouden kunnen worden uitgevoerd met apparaten en technieken vergelijkbaar met die hier onderzocht.

RESUMEN

Las uniones de Josephson implementadas en nanohílos semiconductores proximizados por superconductores exhiben una física compleja que surge de la interacción entre la superconductividad, el acoplamiento espín-órbita, las interacciones electrón-electrón, y el efecto Zeeman. Esta tesis explora estos fenómenos a través de una serie de experimentos llevados a cabo con técnicas de electrodinámica cuántica de circuitos.

Tras establecer los conceptos teóricos fundamentales y los métodos experimentales, introducimos un elemento crucial para sondear los dispositivos con microondas: los resonadores compatibles con campos magnéticos. Después, describimos experimentos realizados durante los últimos años en los que usamos resonadores superconductores y otros circuitos para explorar la física de las uniones de Josephson en nanohílos.

En un primer experimento, desarrollamos un circuito tipo fluxónium resistente al campo magnético que incorpora un nanohílo de InAs. Demostramos que su espectro depende en gran medida tanto del voltaje en la puerta electrostática como de la intensidad del campo magnético, lo que nos permite detectar características de fenómenos no convencionales en uniones de Josephson semiconductoras.

La mayor parte de esta tesis gira en torno a un un segundo conjunto de experimentos, en los que definimos un punto cuántico de forma electrostática dentro de la unión de Josephson. En este caso, utilizamos un circuito tipo transmon para investigar las transiciones singlete-doblete del estado fundamental y su dinámica. Los dos dobletes de la unión, con espín opuesto, definen un nuevo tipo de cúbit con propiedades intrigantes: un cúbit de espín superconductor (o de Andreev) (ASQ, por sus siglas en inglés). Por lo tanto, pasamos a centrar nuestra atención en los estados dobletes y exploramos su dependencia del campo magnético usando espectroscopía de transmon. Posteriormente, pasamos a investigar, de forma directa, la transición de inversión de espín y las propiedades de coherencia de los dos estados de espín. Descubrimos que el acoplamiento intrínseco entre el estado de espín y la supercorriente a través de la unión permite un acoplamiento fuerte entre el ASQ y el cúbit tipo transmon en el que se encuentra.

En un último experimento, conectamos dos de estos ASQ en paralelo e investigamos su acoplamiento longitudinal mediado por supercorriente. Descubrimos que los cúbits están acoplados fuertemente y que su fuerza de acoplamiento se puede activar o desactivar ajustando el flujo magnético. En particular, dado que los espines están situados a micrómetros de distancia, este mecanismo permite la interacción entre espines distantes. Basándonos en estas prometedoras características, concluimos presentando una propuesta que esboza nuestra visión para escalar los ASQ. La arquitectura propuesta, en la que múltiples ASQ están conectados en paralelo, permite el acoplamiento selectivo de cualquier par de cúbits en el sistema, independientemente de su distancia, a través del control de flujo magnético.

Esta tesis concluye describiendo posibles experimentos que podrían llevarse a cabo con técnicas y dispositivos similares a los investigados aquí.

1

INTRODUCTION

Prefiero caminar con una duda que con un mal axioma.

Javier Krahe

1

1.1. THE SYMBIOSIS OF SCIENCE AND TECHNOLOGY

There is a deep connection between fundamental scientific research and the development of new technologies. Advances in our scientific understanding often catalyze pioneering technological developments. Conversely, these technological breakthroughs frequently open doors to fresh scientific discoveries by enabling researchers to investigate previously unexplored dimensions of the universe. The field of experimental physics research stands as a great example of this interdependence. Consider, for instance, the monumental impact of the physics of semiconductors in modern technology. The comprehension of semiconductor properties led not only to the development of the transistor, revolutionizing computing and electronics, but also to the development of photovoltaic cells that harness solar energy to generate electricity and to the majority of display technologies used in consumer electronics. Similarly, the understanding of the principles of quantum mechanics supports technologies like lasers (Mainan, 1960) and magnetic resonance imaging (MRI) machines (Lauterbur, 1973; Mansfield and Maudsley, 1977). Additionally, the comprehension of general relativity underlies the accuracy of the global positioning system (GPS), while the understanding of the physics of elementary particle physics facilitated the obtention of clean energy through nuclear fission. Conversely, the development of novel technologies often triggers the revelation of new scientific insights, and countless historical examples are proof of this. The development of cryogenics (Kamerlingh Onnes, 1908) enabled the discovery of superconductivity (Kamerlingh Onnes, 1911), the construction of particle accelerators allowed us to explore the fundamental nature of matter and advanced space telescopes enabled cosmologists to study the universe's evolution and structure.

The experiments documented in this thesis, while modest in comparison to the expansive physics literature, illustrate the intrinsic symbiosis between science and technology. Here, we explore various condensed matter physics phenomena in hybrid superconducting-semiconducting devices. These experiments become feasible due to various tools that grant access to the extreme conditions wherein these phenomena manifest. Cryogenic refrigerators, sustaining millikelvin temperatures for periods of several months, enable the investigation of low-energy scale phenomena. Electron beam lithography tools, with an accuracy down to tens of nanometers, facilitate the fabrication of devices with dimensions comparable to the phenomena under scrutiny. Superconducting coil magnets generate magnetic fields on the order of Teslas, needed for observing specific effects researched in this thesis. Additionally, high-quality microwave sources yield pulses with nanosecond-scale timing precision, enabling the exploration of quantum coherent effects occurring at rapid time scales.

These tools empower us to deepen our understanding of fundamental effects. We focus on the physics of Josephson junctions implemented in InAs nanowires, which serve as a playground for probing the interplay of diverse, and sometimes competing, energy scales. In particular, we look at phenomena arising from the interplay of spin-orbit interaction, superconductivity, the electron-electron interaction and the Zeeman effect. These effects, together, yield outcomes such as the non-monotonicity of the junction's Josephson energy as a function of the magnetic field. Furthermore, they can lead to energy-phase relations that deviate from those of a typical tunnel junction. In this the-

sis, we investigate some of these deviations, encompassing the presence of channels with non-zero transmission, a π phase shift resulting in a π-junction, and the anomalous Josephson effect. Moreover, we research the junction phase maps resulting from the competition between its charging energy and the superconductivity from the leads and look at how different phases result in different switching rates for the quasiparticle parity in the junction.

Furthermore, the journey from scientific exploration to technological application comes full circle. The insights gained in the first half of this thesis offer a fresh perspective for the development of a new qubit – the fundamental unit of information of a quantum computer. We find that the spinful states of a quantum dot Josephson junction can be used to encode the state of a so-called "superconducting spin qubit". With the knowledge built in the preceding experiments, we demonstrate a prototype of a superconducting spin qubit, demonstrating its coherent coupling to both a superconducting transmon qubit and a remote superconducting spin qubit. This achievement contributes to the progress towards realizing a spin-based quantum computer, as it facilitates long-distance spin-spin coupling. Additionally, it establishes a way of interconnecting two of the major qubit platforms: superconducting qubits and spin qubits.

As the physics community starts to produce promising quantum simulation outcomes with quantum processors, it is reasonable to anticipate that quantum computers could yet enable the discovery of new physics in the future. This observation underscores, once more, the profound collaborative nature between science and technology. It becomes evident that the development of technology and the pursuit of scientific understanding are not isolated endeavors. The results presented in this thesis are a testament to the unending cycle of advancement driven by the synergy between them.

1.2. THESIS STRUCTURE

In **Chapter 2**, we start by delving into the fundamental theoretical concepts behind the experiments performed in this thesis. The chapter commences with a discussion of the physics governing Josephson junctions implemented in Al/InAs nanowires. We subsequently zoom into the use of these junctions as superconducting spin qubits. Additionally, we introduce two superconducting circuit examples: the fluxonium and the transmon. Finally, we briefly discuss the physics of qubit-qubit coupling, differentiating between transverse and longitudinal coupling mechanisms.

The methodologies used to conduct the experiments presented in this thesis are introduced in **Chapter 3**. Here, we embark on a discussion of the design and simulation procedures used for superconducting chip design. Subsequently, we describe the most relevant nanofabrication techniques and details of the measurement setup.

Before diving into the core of the experimental results, **Chapter 4** offers a concise exposition of the various characterization measurements performed on lumped element resonators (see Fig. 1.1(a)). We focus on describing various design considerations that render these resonators resilient to large magnetic fields.

The first of the five experiments documented in this thesis is presented in **Chapter 5**. Here, we investigate a fluxonium circuit wherein the Josephson junction is implemented using an InAs nanowire (see Fig. 1.1(b)). We show spectroscopy data of the device over a wide range of junction gate voltages and under the application of a magnetic field.

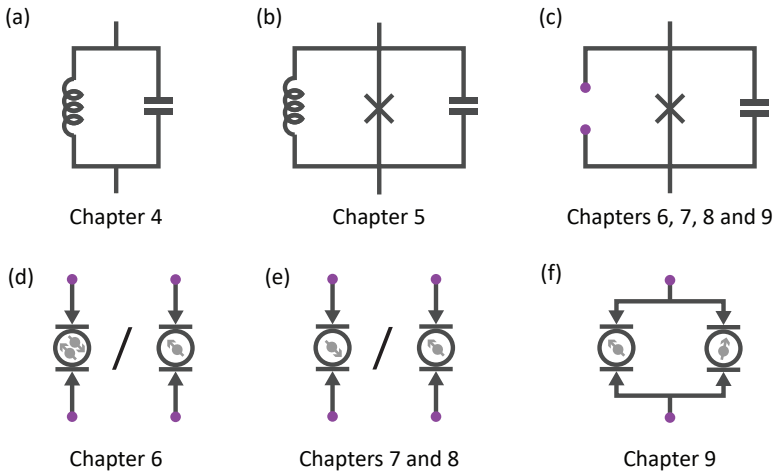

Figure 1.1: **Circuit models of devices investigated in this thesis** (a) Lumped element resonator composed of an inductor and a capacitor connected in parallel. (b) Fluxonium circuit composed of an inductor, a capacitor and a Josephson junction connected in parallel. (c) Transmon circuit composed of a capacitor, a Josephson junction and an extra element connected in parallel. Depending on the chapter, the extra element is either a quantum dot Josephson junction in either a singlet or doublet state (d), a quantum dot Josephson junction in either a spin-up or a spin-down state (e), or two quantum dot Josepshon junctions connected in parallel (f).

Additionally, we explore the use of this device as a sensor for different properties of the Josephson junction and exemplify it by discussing signatures of the anomalous Josephson effect and of the presence of highly transparent junction channels.

In the next four chapters, we instead use a transmon circuit to sensitively probe the inductance-phase relationship of quantum dot Josephson junctions (see Fig. 1.1(c)). By doing so, we exploit the higher energy and time resolution of circuit quantum electrodynamics compared to conventional transport techniques. In **Chapter 6**, we focus on resolving transitions between the singlet and doublet junction ground states (Fig. 1.1(d)) as a function of different control parameters. We find that the measured transition boundaries are in good agreement with those predicted by a single-impurity Anderson model with superconducting leads. We additionally investigate the lifetimes of the junction states in different parameter regimes.

Subsequently, in **Chapter 7** we set the quantum dot junction to an odd-parity ground state, where spin-orbit interaction induces an energy-splitting between the two possible spin states (see Fig. 1.1(e)). We see that the energy-phase relation of the junction, and in turn its current-phase relation, strongly depend on the spin state. By applying an external magnetic field oriented along varying directions, we infer the spin direction and gain insights into the anomalous Josephson effect. We also determine the minimal extensions to the single impurity Anderson model that are required to mimic the experimental data. Moreover, we directly drive the spin-flip transition using a microwave tone, gaining access to not only the inductance, but also the energy of the junction states. By performing two-tone spectroscopy, we investigate the dependence of the spin-flip transition frequency on the magnetic field.

The coherent properties of the two spin states are investigated in a follow-up experiment performed in the same device and presented in **Chapter 8**. We find that the two spin states define a charging energy-protected superconducting spin qubit which can be rapidly manipulated with all-electric signals. Furthermore, we study the strong coherent coupling between the superconducting spin qubit and the transmon qubit into which it is embedded.

In **Chapter 9**, we connect two superconducting spin qubits in parallel, as shown in Fig. 1.1(f). We demonstrate that, as the spin of each qubit is intrinsically coupled to the supercurrent through it, the two qubits become inductively coupled. We show that the coupling is of the longitudinal type and that it can attain the strong coupling regime. Moreover, we demonstrate that the coupling strength can be tuned via both an electrostatic gate voltage and a magnetic flux.

Subsequently, we elaborate on the prospects of this supercurrent-mediated coupling to scale up superconducting spin qubits. In **Chapter 10** we propose an architecture where multiple superconducting spin qubits are connected in parallel, resulting in all-to-all selective coupling between them.

We conclude in **Chapter 11** by reflecting on the challenges and open avenues of research found in the preceding chapters. We additionally propose potential future experiments that could be performed with devices similar to those investigated here.

B = 0

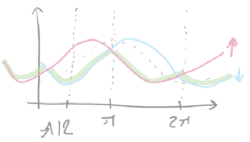

B = 15mT

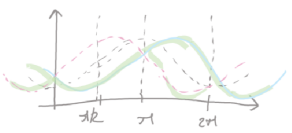

B = 40 mT

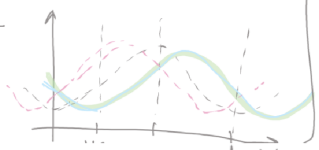

P_{11} — Not looking at this freq

P_{01} — Two-tone at this freq — Rate J

P_{10} — Third tone at this freq — Rate K

P_{00}

- Situation A (only 2-tone)
  - 50% P_{01}
  - 50% P_{00} → Signal 50%
- Situation B (also 3rd tone)
  - $K(P_{10}-P_{00}) + J(P_{01}-P_{00}) = 0$
  - $K(P_{00}-P_{10}) = 0 \Rightarrow P_{00} = P_{10}$
  - $J(P_{00}-P_{01}) = 0 \Rightarrow P_{01} = P_{00}$
  - → 33% each
  - Signal 33%
- Situation C (only 3rd tone)
  - 50% P_{00}, 50% P_{10} (background)
  - Signal 17%

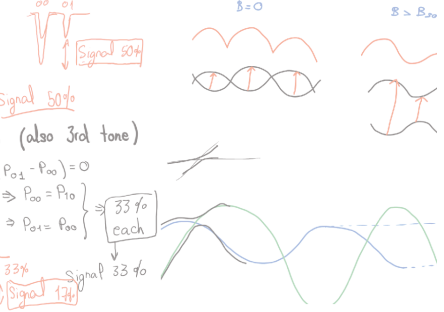

branch and then switch to the top one when th up spin goes up

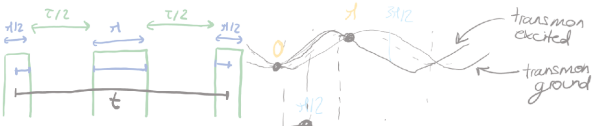

$t = \frac{\pi}{4} + \frac{\tau}{2} + \pi + \frac{\tau}{2} + \frac{\pi}{4} = \tau + 3\frac{\pi}{2}$

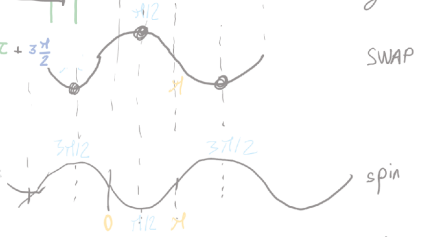

$E_{Jn}^{\cos} \cos(n\phi)\,|N\rangle = E_{Jn}^{\cos} \frac{1}{2}(e^{in\phi} + e^{-in\phi})\,|N\rangle =$

since $\cos(n\phi) = \cos(-n\phi)$ then $E_{Jn}^{\cos} = E_{J(-n)}^{\cos}$

$= E_{Jn}^{\cos} \frac{1}{2}(|N+n\rangle + |N-n\rangle)$

$E_{Jn}^{\sin} \sin(n\phi)\,|N\rangle = E_{Jn}^{\sin} \frac{1}{2i}(e^{in\phi} - e^{-in\phi})\,|N\rangle =$

since $\sin(n\phi) = \sin(-n\phi)$ then $E_{Jn}^{\sin} = -E_{J(-n)}^{\sin}$

$= -i\,E_{Jn}^{\sin} \frac{1}{2}(|N+n\rangle - |N-n\rangle)$

$\sum_n \left[E_{Jn}^{\cos}\cos(n\phi) + E_{Jn}^{\sin}\sin(n\phi)\right]|N\rangle = \sum_n \frac{E_{Jn}^{\cos} - iE_{Jn}^{\sin}}{2}|N+n\rangle + \frac{E_{Jn}^{\cos} + iE_{Jn}^{\sin}}{2}|N-$

$\frac{E_{Jn}^{\cos} + iE_{J,-n}^{\sin}}{2}|N-$

$\frac{E_{Jn}^{\cos} - iE_{J,n}^{\sin}}{2}|N-n$

$|N+n\rangle + |N-n\rangle$

$|N\rangle\langle N-n| = |N'+n\rangle\langle N'|$

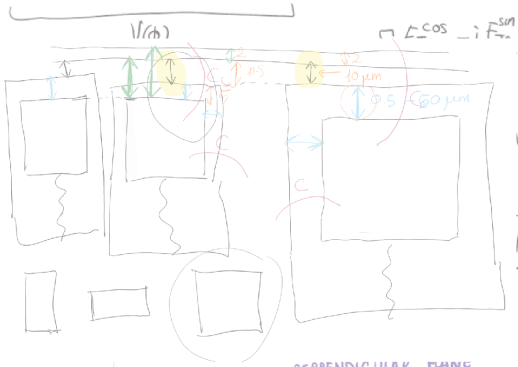

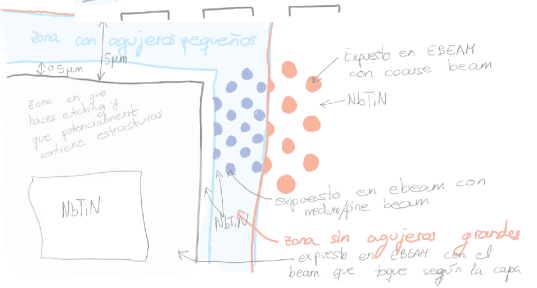

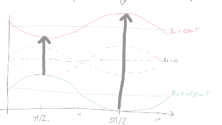

PERPENDICULAR PLANE defined by two vectors, one living on the YZ plane and another on the XZ plane

$\vec{V}_1 = (\theta_1 = 165,\ \varphi = 90)$

$\vec{V}_2 = (\theta = \theta_2,\ \varphi = 0)$

$\vec{V}_1 = (0, \sin\theta_1, \cos\theta_1)$

$\vec{V}_2 = (\sin\theta_2, 0, \cos\theta_2)$

angle between $\vec{V}_1$ and $\vec{V}_2$

VECTOR PERPENDICULAR TO THAT PLANE (∞ along BSO)

$\vec{V}_{SO} = \vec{V}_1 \times \vec{V}_2 =$

$= \begin{vmatrix} \vec{i} & \vec{j} & \vec{k} \\ 0 & s\theta_1 & c\theta_1 \\ s\theta_2 & 0 & c\theta_2 \end{vmatrix} =$

$= (s\theta_1 c\theta_2,\ s\theta_2 c\theta_1,\ s\theta_2 s\theta_1)$

$= (s\theta_{SO}\cos\varphi_{SO},\ \sin\theta$

$\theta_{SO} = \arccos\left(-\sin(\theta_1)\cdot\sin(\theta_2)\right)/s$

$\sin(\theta_1)\cdot\cos(\theta_2)$ /

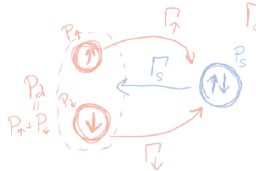

When $E_s = E_\downarrow = E_\uparrow = E_\downarrow$

$\Gamma_\uparrow = \Gamma_\downarrow = \Gamma_s$

$\Gamma_d = 2\Gamma_s$

$\Gamma_d = \Gamma_\uparrow + \Gamma_\downarrow$

$\dot{\Gamma}_\uparrow = \frac{1}{2}P_s\Gamma_s - P_\uparrow\Gamma_\uparrow = 0 \Rightarrow \frac{1}{2}P_s = P_\uparrow$

$\dot{\Gamma}_\downarrow = \frac{1}{2}P_s\Gamma_s - P_\downarrow\Gamma_\downarrow = 0 \Rightarrow \frac{1}{2}P_s = P_\downarrow$

$P_s = P_d$

$\dot{\Gamma}_2 = P_\uparrow\Gamma_\uparrow + P_\downarrow\Gamma_\downarrow - P_s\Gamma_s = 0$

$\sqrt{\ell(1-\cos(2\phi))E_s^2 - 4E_sE_x\sin\phi + E_x^2} =$

$= \sqrt{4E_s^2\sin^2\phi - 4E_sE_x\sin\phi + \ell}$

$= \sqrt{(2E_s\sin\phi - E_x)^2} = 2E_s$

FWHM $= 2\sqrt{2\ln 2}\,\sigma = 6$

$L = 6\sigma = \frac{6}{2\sqrt{2\ln 2}}$

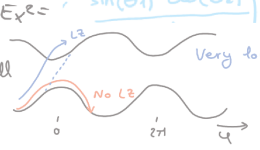

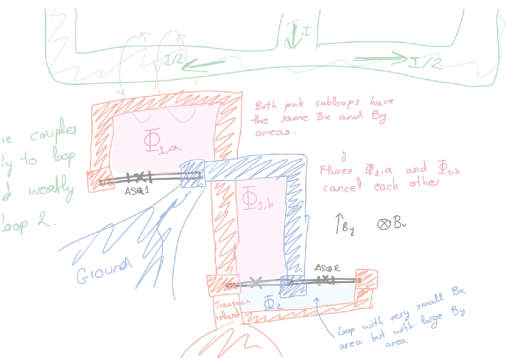

2

THEORETICAL BACKGROUND

This provides an introduction to the major concepts of the field on a level somewhere between "Donald Duck" and the "Americal Journal of Physics".

Richard D. Mattuck

Our experimental results capitalize on the advancements made in two active areas of research within condensed matter physics: superconductor-proximitized semiconducting nanowires and circuit quantum electrodynamics. In this chapter, we provide a concise overview of the fundamental theoretical concepts of these two fields. Without diving into details, we start by reviewing some key aspects of the physics of nanowire-based Josephson junctions, which will bear significant relevance in subsequent chapters. Emphasis is placed on the recent use of InAs Josephson junctions to implement superconducting spin qubits. Then, we switch gears and discuss two examples of superconducting circuits that will hold substantial importance in the next chapters: the transmon and the fluxonium. We end by reviewing basic aspects of the physics related to qubit-qubit coupling.

2.1. JOSEPHSON JUNCTIONS

The physics of Josephson junctions is remarkably diverse and has been subject of investigation for decades. The purpose of this chapter is not to provide a mathematical derivation of junction physics from first principles. Instead, our starting point assumes that the fundamental properties of tunneling superconducting-isolating-superconducting (SIS) Josephson junction are known and we focus on examining how these properties evolve when more exotic elements are introduced. The junction observables will, in this chapter, be described from a phenomenological perspective.

In the following sections, we discuss the effects of changing the central material from an insulator (I) to a semiconductor (N), leading to the formation of an SNS Josephson junction (Golubov et al., 2004). Furthermore, we describe the consequences of incorporating spin-orbit interaction and a Zeeman field, which give rise to new experimental observables. Then, we introduce an additional ingredient to the junction: charging energy. A system involving significant charging energy can be modeled by replacing the central part of the junction with a quantum dot (QD) that is tunnel-coupled to the superconducting leads, resulting in an SQDS junction. We present the key findings predicted by one of the simplest model for describing this system: a single impurity Anderson model (SIAM). Finally, we describe novel features that emerge when new elements, such as spin-orbit coupling and multiple levels, are added to the SIAM.

Our primary focus is on a crucial experimental observable of Josephson junctions, namely their energy-phase relation, denoted as $U(\phi)$, where ϕ denotes the phase drop across the junction (Golubov et al., 2004). This quantity can be accessed experimentally with the devices presented in later chapters[1] (Sec. 2.3). The most simple energy-phase relation is the celebrated sinusoidal relation of tunnel SIS junctions (Josephson, 1962). Although, at the microscopic level, this relation is determined by the transmission of multiple conduction channels with small transparencies (Willsch et al., 2023), this complexity can be macroscopically condensed into a single effective parameter: the Josephson energy E_J. The energy-phase relation takes the form

$$U_{SIS}(\phi) = -E_J \cos(\phi) + E_J \tag{2.1}$$

Two other junction properties, the supercurrent flowing across it, $I(\phi)$, and its inductance, $L(\phi)$, can be obtained from the first and second derivatives of the energy-phase relation, respectively (Martinis and Osborne, 2004). As the number of Cooper pairs that have gone through the junction is the quantum conjugate variable to the phase ϕ, we have that

$$I(\phi) = \frac{2\pi}{\Phi_0} \frac{\partial U(\phi)}{\partial \phi}, \tag{2.2}$$

where $\Phi_0 = h/2e$ is the magnetic flux quantum, with h being the Planck constant and e denoting the absolute value of the electron charge. Eq. 2.2 will be of particular relevance in Chapter 9, as it will be used for calculating the supercurrent-mediated coupling between two superconducting spin qubits. Similarly, for the Josephson inductance, we

[1] For most experiments in this thesis, we will actually be sensitive to the inductance-phase relation instead, which is inversely proportional to the second derivative of the energy-phase relation.

have

$$\frac{1}{L(\phi)} = \frac{4\pi^2}{\Phi_0^2}\frac{\partial^2 U(\phi)}{\partial\phi^2}. \tag{2.3}$$

For the case of a tunnel SIS junction, the supercurrent corresponding to the energy of Eq. 2.1 is sinusoidal and vanishes at $\phi = 0$:

$$I_{\mathrm{SIS}}(\phi) = I_{\mathrm{J}}\sin(\phi), \tag{2.4}$$

where $I_{\mathrm{J}} = \frac{2\pi}{\Phi_0}E_{\mathrm{J}}$ is the critical current. The inductance of a tunnel junction becomes

$$L_{\mathrm{SIS}}(\phi) = \frac{L_{\mathrm{J}}}{\cos(\phi)}, \tag{2.5}$$

with $L_{\mathrm{J}} = \frac{\Phi_0^2}{4\pi^2}/E_{\mathrm{J}}$. Eq. 2.5 will again be of particular relevance in Chapter 9, as the inductance of a coupling SIS Josephson junction will mediate the coupling between two superconducting spin qubits and determine their coupling strength. Superconducting tunnel junctions will moreover find use in other chapters (Chapters 6, 7 and 8) as reference junctions that determine the average frequency of transmon circuits (see Sec. 2.3).

2.1.1. SEMICONDUCTING JOSEPHSON JUNCTIONS

All Josephson junctions present in the devices investigated in this thesis are constructed using indium arsenide (InAs) nanowires that are partially covered by a thin layer of aluminum (Al), which induces superconductivity (Krogstrup et al., 2015). These junctions consist of two outer proximitized leads with a central region of bare InAs in between, as illustrated in Fig. 2.1(a). We refer to these superconducting-semiconducting-superconducting junctions as SNS junctions.

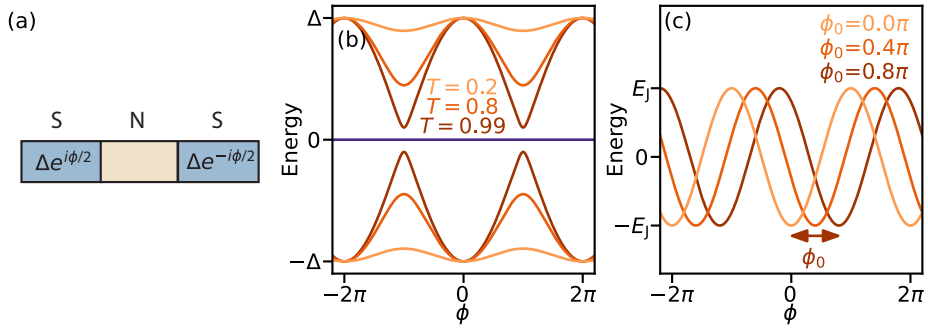

Figure 2.1: **SNS Josephson junction.** (a) Diagram of an SNS junction where a central semiconducting part (yellow) is surrounded by two superconducting leads (blue) with superconducting gap Δ and phase-offset ϕ between them. (b) Energy-phase relation on an Andreev level with different occupations. The ground and doubly excited states are shown in orange for various values of the channel transparency, T (Eq. 2.6). The states occupied by a single quasiparticle are shown in purple. The ground-state branch corresponds to Eq. 2.7 for the case $N = 1$. (c) Energy-phase relation showing the anomalous Josephson effect for different values of ϕ_0, for the case of a low transparency junction.

SHORT-JUNCITON LIMIT

The energy-phase relation of these junctions can deviate significantly from the simple sinusoidal dependence of superconducting tunnel junctions when highly transmissive Andreev bound states (ABSs) are present[2]. Andreev bound states are subgap states that are spatially localized at the junction. They are formed due to interference between Andreev-reflected (Andreev, 1964) electrons and holes at the central part of the junction, which results in standing waves with quantized energy. Depending on their occupation, Andreev bound states can assume four different fermionic configurations (Bretheau, 2013; Bretheau et al., 2013). The first of these configurations is the ground state, with energy $-E_{\mathrm{ABS}}(\phi)$ with respect to the Fermi energy[3]. In the short junction limit, i.e. when the length of the junction is much shorter than the superconductor coherence length, $E_{\mathrm{ABS}}(\phi)$ is given by (Beenakker, 1991)

$$E_{\mathrm{ABS}}(\phi) = \Delta\sqrt{1 - T\sin^2(\phi/2)}. \tag{2.6}$$

Here, Δ denotes the induced gap on the proximitized sections of the nanowire and T is the transmission probability (or transparency) of the ABS. The ABS can also be in one of two odd quasiparticle configurations which, at zero magnetic field and in the absence of spin-orbit interaction, are spin-degenerate, with 0 energy with respect to the Fermi level, and thus not dispersing with phase (see purple line in Fig. 2.1(b)). Finally, the doubly occupied excited state, assuming a non-interacting model, is energetically $2E_{\mathrm{ABS}}(\phi)$ above the ground state and thus has energy $+E_{\mathrm{ABS}}(\phi)$. The energies of the four possible fermionic configurations are shown in Fig. 2.1(b) for different values of T.

An SNS junction typically contains several ABSs, each serving as a transmission channel through the junction, that contribute to its total energy-phase relation, $U_{\mathrm{SNS}}(\phi)$. For a short junction with N Andreev levels with transmission probabilities T_i, and when all levels are in their ground state, the total energy-phase relation can be expressed as follows[4]:

$$U_{\mathrm{SNS}}(\phi) = -\Delta\sum_{i=1}^{N}\sqrt{1 - T_i\sin^2(\phi/2)}. \tag{2.7}$$

In the limit of low tranparencies, $T_i \to 0$, this relation converges to a sinusoidal form (Eq. 2.1) with $E_{\mathrm{J}} = \Delta\sum_{i=1}^{N} T_i/4$. Supercurrent and current-voltage characteristic measurements in semiconducting nanowires have shown that this model describes them more accurately than a sinusoidal relation (Goffman et al., 2017; Hart et al., 2019; Spanton et al., 2017). The defining feature of SNS junctions is that the transparencies, T_i, are strongly influenced by the electrostatic environment, and can thus be tuned using a gate voltage. At very negative gate voltage values, the transparency of all channels is zero, resulting in a closed or pinched-off junction. As the gate voltage increases, the transparencies undergo non-monotonic fluctuations due to mesoscopic effects until they eventually stabilize in the open junction regime (de Lange et al., 2015; Goffman et al., 2017; Hart

[2] Note that highly transmissive ABSs are not exclusively a property of SNS junctions and that they can also be present in other weak links as in point contact junctions (Bretheau, 2013; Bretheau et al., 2013).

[3] Note that the total energy of the many-body ground state is determined by the sum of $-E_{\mathrm{ABS}}(\phi)$ plus the energy of the continuum of states below the Fermi energy. Here, we ignore the continuum, as we are only interested in the phase-dependence of the energy and the continuum energy is phase-independent in the short junction limit (Beenakker, 1991).

[4] Again, we ignore the phase-independent contribution of the continuum of states below the Fermi energy.

et al., 2019; Larsen et al., 2015; Spanton et al., 2017; van Woerkom et al., 2017; Zuo et al., 2017).

When an applied magnetic field is taken into account, additional effects become apparent. Firstly, the presence of a magnetic field leads to a reduction of the gap on the parent superconductor (Tinkham and Gordon, 1996) and, consequently, of the induced gap, Δ, and the effective E_J^{eff} (defined as $E_J^{\text{eff}} = \left(\max\{U_{\text{SNS}}(\phi)\} - \min\{U_{\text{SNS}}(\phi)\}\right)/2$). If interference occurs among the channels of the junction, this decrease can happen in a non-monotonic way (Zuo et al., 2017). Moreover, the interplay between the magnetic field, spin-orbit interaction and the presence of multiple junction channels can result in the anomalous Josephson effect (Szombati et al., 2016). The anomalous Josephson effect is characterized by a ϕ_0-shift of the energy-phase relation, resulting in a non-zero supercurrent at $\phi = 0$ (see Fig. 2.1(c)).

In Chapter 5, we employ a fluxonium circuit, which will be introduced in Sec. 2.3, to investigate the energy-phase relation of an SNS junction in the presence of a magnetic field. Our study explores the non-monotonic evolution of the effective E_J with gate and magnetic field. The experiments also reveal signatures of highly transparent channels and of the anomalous Josephson effect.

Numerous other effects on SNS Josephson junctions have been extensively investigated, extending beyond the scope of this thesis. Recent experiments, for instance, have used microwave spectroscopy to investigate junctions that go beyond the short-junction limit, hosting multiple subgap manifolds. For more detailed information, see Refs. (Tosi et al., 2018; Wesdorp et al., 2022). Moreover, intriguing phenomena are expected to arise when the superconducting leads undergo a transition into a topological regime, leading to the manifestation of the 4π-Josephson effect. For a review on these topological junctions, see (Kitaev, 2001; Prada et al., 2020). Although this physics is not investigated in this thesis, the experiments discussed here could be extended to detect signatures of topological Josephson junctions, as elaborated in Chapter 11.

2.1.2. QUANTUM DOT JOSEPHSON JUNCTIONS

We now shift our focus to considering electron-electron interactions at the junction. Unlike in Sec. 2.1.1, where the energy of a double-occupied junction is simply the sum of the energies of individual quasiparticles, this scenario introduces an additional term known as the charging energy, U. The charging energy arises from Coulomb repulsion between electrons and affects the energy of the doubly-occupied state. To capture this behavior, the central region of the junction is typically described by a quantum dot that is tunnel-coupled to the two superconducting leads. In this situation, the charging energy discourages double occupancy of the junction, while the superconducting pairing from the leads favors double occupancy. The interplay between these two competing energy scales is governed by the coupling strength between the central part of the junction and the leads.

SINGLE-IMPURITY ANDERSON MODEL WITH SUPERCONDUCTING LEADS

A well-researched minimal model to investigate this system is the single-impurity Anderson model (SIAM) with superconducting leads. In this model, the quantum dot is described by a single energy level, denoted by ϵ, and charging energy, denoted by U. The

dot is tunnel-coupled to two superconducting leads, characterized by a superconducting gap, Δ, and a phase difference, ϕ, between them. The coupling between the quantum dot and the leads is determined by two tunneling rates Γ_L and Γ_R (Fig. 2.2(a)). Further details about the model description can be found in Sec. 6.8 of Chapter 6. For a review of the vast experimental research on quantum dot Josephson junctions, see Ref. (Martín-Rodero and Levy Yeyati, 2011).

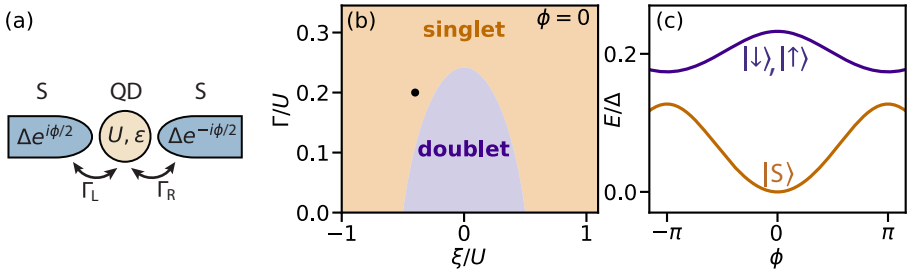

Figure 2.2: **Quantum dot Josephson junction described by the single-impurity Anderson model (SIAM) with superconducting leads.** (a) Diagram of the SIAM of an SQDS junction where a quantum dot with charging energy U and level ϵ (yellow) is tunnel coupled, with tunnel rates Γ_L and Γ_R, to two superconducting leads (blue). (b) Phase diagram indicating the regions for which the SQDS junction has a singlet ground state (orange) and a doublet ground state (purple). $\Gamma = \Gamma_L + \Gamma_R$ and $\xi = \epsilon + U/2$. The results are obtained by the numerical renormalization group (NRG) method (see Ref. (Žitko, 2021)) for $U = 5\Delta$. (c) Energy-phase relation of the singlet (orange) and doublet (purple) states of the SQDS junction at the $(\xi/U, \Gamma/U) = (-0.4, 0.2)$ point indicated with a black marker in (b), where the singlet is the ground state.

The SIAM with superconducting leads provides a simple yet accurate description of quantum dot junctions in various scenarios, as demonstrated in Chapter 6. The model enables the prediction of the parameter dependence of the energy of the different junction states, which can be either singlets ($|S\rangle$, with even quasiparticle occupancy and total spin 1) or degenerate doublets ($\{|\uparrow\rangle$ and $|\downarrow\rangle\}$, with odd quasiparticle occupancy and total spin 1/2). Thus, by solving the SIAM, one can reconstruct phase maps depicting the singlet or doublet ground state versus the different control parameters, as well as the energy-phase relation for each state. In the limit $\Delta \gg U, \Gamma_i$, the model can be mapped onto an analytically solvable single site problem with proximitized ABSs which is thus referred to as the superconducting atomic limit (Meng et al., 2009; Tanaka et al., 2007). However, this analytically solvable limit does not apply to the junctions investigated in this thesis (Chapters 6, 7, 8 and 9), where $U \gtrsim 10\Delta$ and Γ is in the range $0.02U - 0.2U$. Nonetheless, the system can be fully solved numerically using the powerful numerical renormalization group (NRG) method (Bulla et al., 2008). Results of NRG calculations for a large range of model parameters can be found in Ref. (Žitko, 2021) and are used in Chapter 6 to fit the experimental data.

One example of a phase diagram, obtained by NRG calculations, versus two of the model parameters is presented in Fig. 2.2(b), where we introduce the quantity $\Gamma = \Gamma_L + \Gamma_R$. At $\Gamma = 0$, the quantum dot is fully decoupled from the leads and exhibits the expected behavior of an isolated single-level quantum dot. In this situation, singlet-doublet ground state transitions occur when the energy of the doublet state, ϵ, coincides with either that of an empty singlet state, 0, or with that of the two-particle single state $2\epsilon + U$. As these

crossings occur at $\epsilon = 0$ and at $\epsilon = -U$, it is common to introduce $\xi = \epsilon + U/2$, which becomes 0 at the symmetry point. As Γ increases, however, the interaction with the leads favors singlet pairing, leading to a reduction in the ξ region where the system has a doublet ground state. The dependence of the system's ground state on these and other model parameters is discussed and experimentally investigated in Chapter 6, where we build on previous results that investigate such transitions with either Josephson supercurrent measurements (Delagrange et al., 2015, 2016, 2018; Jørgensen et al., 2007; van Dam et al., 2006) or measuring tunneling spectroscopy (Chang et al., 2013; Deacon et al., 2010; Lee et al., 2014, 2017; Pikulin et al., 2019; Valentini et al., 2021).

For the experiments performed in this thesis, an important feature predicted by the SIAM is the qualitative difference between the energy-phase relations of the junction states with different occupancy. As shown in Fig. 2.2(c) for the case where the ground state is a singlet $|S\rangle$, the energy-phase relation of the singlet exhibits a minimum at $\phi = 0$, in analogy to the case for an SNS junction described in previous sections. However, the energy-phase relation of the doublet states displays a minimum at $\phi = \pi$, commonly referred to as π-junction behavior. The origin of this π-shift, in terms of cotunneling sequences through the quantum dot level, is discussed in detail in Ref. (van Dam et al., 2006). In Chapter 6, we use the distinct energy-phase relations of the singlet and doublet junction states to discern between the two using a transmon circuit, which will be introduced in Sec. 2.3. These measurements enable us to map out the dependence of the singlet and doublet ground states on different experimental parameters that control Γ_R, Γ_R, ϕ, ξ and the Zeeman energy.

EXTENSIONS TO THE SIAM WITH SUPERCONDUCTING LEADS

Real quantum dot junction devices can exhibit properties that go beyond the scope of the SIAM with superconducting leads, which considers only a single quantum dot level with degenerate doublet states at zero magnetic field. Deviations from this model can occur when the junction materials possess a strong spin-orbit interaction (SOI) or when multiple quantum dot levels are present. In particular, the combination of these two factors can lead to a breaking of the spin degeneracy of the two doublet states $\{|\uparrow\rangle, |\downarrow\rangle\}$ away from $\phi = 0, \pi$, even in the absence of a magnetic field, as shown in Ref. (Padurariu and Nazarov, 2010). Furthermore, in such situations, some of the conclusions drawn from the single-impurity Anderson model with superconducting leads no longer hold. For instance, the 0- or π-junction behavior of the junction is no longer solely determined by the parity of its quasiparticle occupancy.

A phenomenological model that captures the energy-phase relation of the two spinful doublet states is discussed in Ref. (Padurariu and Nazarov, 2010). In the limit of weak tunneling rate between the quantum dot and the superconducting leads, the energies of the spin states can be described by the following equation:

$$U(\phi) = E_0 \cos\left(\phi\right) - E_{SO}\vec{\sigma}\cdot\vec{n}\sin\left(\phi\right) + \frac{1}{2}\vec{E}_Z\cdot\vec{\sigma}. \tag{2.8}$$

Here, $\vec{\sigma} = (\sigma_x, \sigma_y, \sigma_z)$ represents the vector of Pauli matrices, $\vec{n}$ is a unit vector along the spin-polarization direction set by the spin-orbit interaction in the absence of an applied magnetic field, and E_{SO} and E_0 are the spin-dependent and spin-independent Cooper pair tunneling rates across the quantum dot junction, respectively.

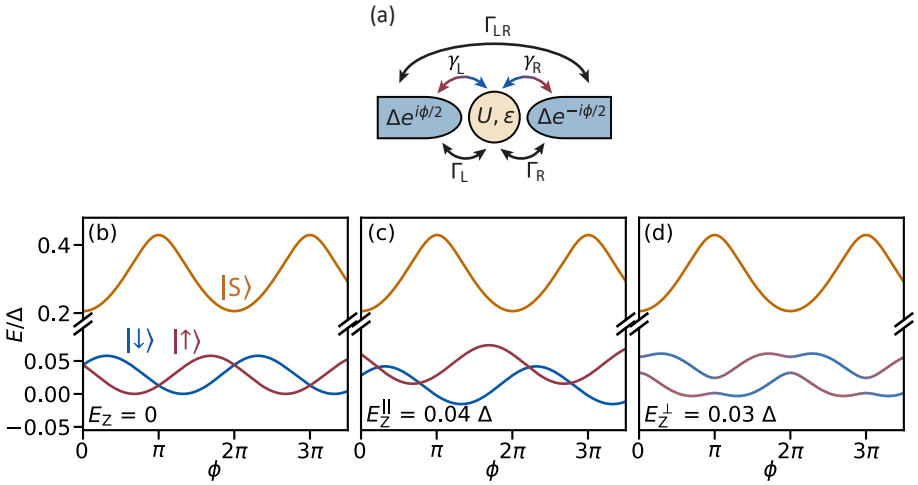

Figure 2.3: **Quantum dot Josephson junctions with multiple levels and spin-orbit interaction.** (a) Diagram of an SQDS junction with multiple quantum dot levels, modeled by a direct lead-lead tunneling rate Γ_{LR}, and with spin-orbit interaction, modeled by spin-flipping tunneling rates $\gamma_{L,R}$. (b) Energy-phase relation of the singlet (orange), spin-up (blue) and spin-down (red) states of the SQDS junction for a situation in which the doublets are the lowest energy states. Model parameters are $U = 10\Delta$, $\epsilon = -U/2$, $\Gamma_L = \Gamma_R = 2\Delta$, $\gamma_L = \gamma_R = 4\Delta$ and $\Gamma_{LR} = \Delta$. (c) Same as (b) but under the application of a Zeeman field $E_Z^{\parallel} = 0.04\Delta$ along $\vec{n}$. (d) Same as (b) but under the application of a Zeeman field $E_Z^{\perp} = 0.03\Delta$ in the direction perpendicular to $\vec{n}$. A blend of blue and red indicates mixing of the $|\downarrow\rangle$ and $|\uparrow\rangle$ states.

Alternatively, these features can be modeled at a microscopic level. For instance, Ref. (Padurariu and Nazarov, 2010) introduced spin-orbit interaction into the microscopic model by incorporating a spin-dependent term in the tunneling rates between the leads and the quantum dot. In Chapter 7, we instead modify the SIAM and introduce spin-flipping tunneling rates to account for the spin-orbit interaction. Additionally, to accommodate the presence of multiple levels, we introduce a tunneling rate directly between the two superconducting leads that circumvents the quantum dot level of interest, as illustrated in Fig. 2.3(a). We demonstrate that both terms are necessary to break the degeneracy of the doublet states at zero magnetic field. Fig. 2.3(b) shows the energies of the singlet and doublet junction states obtained by solving the modified SIAM using NRG calculations.

According to the theoretical prediction from Eq. 2.8 and the modified SIAM, the effect of an external magnetic field varies depending on its direction relative to $\vec{n}$. When a parallel field is applied, the two spin states experience a ϕ-independent Zeeman energy splitting, as depicted in Fig. 2.3(c). As the energy separation between the spin states increases, one of them becomes unoccupied, and the overall energy-phase relation of the junction becomes solely determined by its ground state. Since the energy-phase relation of each spin branch is offset from $\phi = 0$, this once again gives rise to the anomalous Josephson effect. In contrast, when a perpendicular magnetic field is introduced, the spin states become hybridized, leading to alterations in the shape of the energy-phase relation, as illustrated in Fig. 2.3(d).

2.2. SUPERCONDUCTING SPIN QUBITS

Josephson junctions featuring spin-split states, as the ones presented in the preceding section, lay the foundation for implementing superconducting (or Andreev) spin qubits (ASQs) (Chtchelkatchev and Nazarov, 2003; Padurariu and Nazarov, 2010). These qubits exhibit shared properties both with semiconducting spin qubits (Burkard et al., 2023; Hanson et al., 2007; Koppens et al., 2006; Loss and DiVincenzo, 1998) and superconducting qubits (Blais et al., 2021; Girvin, 2016; Koch et al., 2007; Krantz et al., 2019; Manucharyan et al., 2009). In an ASQ, the qubit's state is encoded in the spin degree of freedom of a fermionic quasiparticle, as for other types of semiconducting spin qubits. In this case, however, the quasiparticle is situated in a bound state of a Josephson junction. In the presence of spin-orbit interaction, the dispersion of the junction's energy-phase relation is spin-state-dependent, which, in combination with Eq. 2.2, leads to the defining feature of ASQs: the supercurrent flowing through the junction depends on the qubit state. This relation between the qubit state and a macroscopic circuit variable is characteristic of other superconducting qubits, like the transmon or the fluxonium (see Sec. 2.3). Thus, this spin-supercurrent coupling could be exploited, similarly to how it is done in the superconducting qubit community, to use circuit quantum electrodynamics techniques for qubit-qubit interactions and reading out of spin qubits.

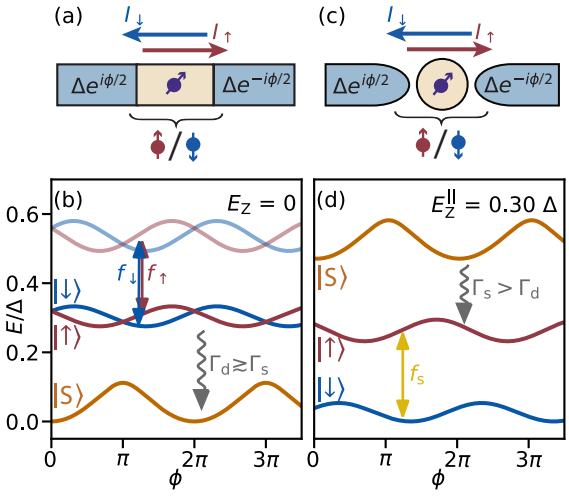

Figure 2.4: **Superconducting spin qubits.** (a) Schematic diagram of a superconducting spin qubit implemented in a long SNS Josephson junction for which an Andreev level is occupied by a single spinful quasiparticle. (b) Eigenenergies of the singlet ground state (orange), the excited $|\uparrow\rangle$ and $|\downarrow\rangle$ doublet states that form the qubit (dark blue and red) and the two spin states of a higher energy manifold (light blue and red). The double-headed arrows indicate (virtual) transitions used for qubit manipulation (Hays et al., 2021). (c) and (d) Same as (a) and (b) but for an SQDS junction instead of a long SNS junction and under the application of a parallel Zeeman field $E_Z^{\parallel}$. The double-headed arrow indicates the spin-flip transition. The oscillating arrows in (b) and (d) indicate spontaneous emission.

Two implementations of superconducting spin qubits in semiconducting nanowire junctions are depicted in Fig. 2.4. The first, proposed by Chtchelkatchev and Nazarov

in 2003 (Chtchelkatchev and Nazarov, 2003), was experimentally realized by Hays *et al.* in 2021 (Hays, 2021; Hays et al., 2021) using an Al/InAs nanowire. As illustrated in Fig. 2.4(a), this approach leverages two spin-split doublet states of a long[5] semiconducting Josephson junction as the qubit's basis. In its experimental implementation, the ASQ was incorporated into the inductor of a lumped element resonator. By doing so, the intrinsic spin-supercurrent coupling of the superconducting spin qubit could be exploited to monitor the spin state of the qubit using circuit quantum electrodynamics techniques and enabled single-shot quantum non-demolition spin readout (Hays et al., 2020). The operation of this first ASQ implementation occurred at a vanishing magnetic field. Spin manipulation was accomplished using a Raman scheme involving an energetically higher bound state of the SNS junction (Hays et al., 2020) by simultaneously driving equally detuned transitions between the $|\downarrow\rangle$ and $|\uparrow\rangle$ qubit states and a virtual level, as illustrated in Fig. 2.4(b). For details on the microwave investigation of higher energy manifolds in long SNS junctions, see Refs. (Tosi et al., 2018; Wesdorp and *et al.*, 2023b; Wesdorp et al., 2022).

This first ASQ implementation based on a long SNS junction, however, presents a fundamental challenge: the ground state of the system is a singlet, making the two qubit states an excited manifold (see Fig. 2.4(b)). Decay from the qubit states to the ground state, consequently, leads to leakage and constrains the qubit's coherence times. The singlet and doublet switching rates, $\Gamma_{s,d}$, in such system were characterized by Hays *et al.* in Ref. (Hays et al., 2018), Ref. (Hays et al., 2020) and Ref. (Hays et al., 2021), where the parity lifetime $1/(\Gamma_d + \Gamma_s)$ was found to be of 160 µs, 31 µs and 22 µs, respectively. In all cases, the singlet and doublet switching rates were found to be of the same order of magnitude. The spin lifetime was fount to be 51 µs or 17 µs, respectively for Ref. (Hays et al., 2020) and Ref. (Hays et al., 2021).

An alternative approach to implementing ASQs in semiconducting nanowires, suggested by Padurariu and Nazarov (Padurariu and Nazarov, 2010), involves exploiting a quantum dot's charging energy within the Josephson junction. This method enables the operation of the ASQ in a regime where the qubit states are the lowest energy states of the system (see Figs. 2.4(c) and (d)). As discussed in the previous section, such SQDS junction can be tuned into a regime where the doublet states constitute the lowest energy manifold of the system.

In this thesis, we investigate this second ASQ implementation. As explored in Chapters 6 and 8, following Ref. (Padurariu and Nazarov, 2010) allows for a notable increase in the doublet lifetime up to the order of 1 to 10 milliseconds. Furthermore, Chapter 8 shows that the application of a magnetic field not only increases the qubit frequency due to the Zeeman effect, but, in combination with spin-orbit interaction, also allows for direct driving of the spin-flip transition, as indicated by the yellow arrow in Fig. 2.4(d).

2.3. SUPERCONDUCTING CIRCUITS

Throughout this thesis, our investigation of the physics of nanowire-based Josephson junctions will be conducted using superconducting circuits integrated within a circuit quantum electrodynamics (cQED) architecture (Blais et al., 2004; Girvin, 2016). Over the

[5] Longer or comparable to the superconducting coherence length.

past two decades, significant progress has been made in understanding and exploring the behavior of superconducting circuits based on SIS Josephson junctions. Many aspects of these circuits have been thoroughly investigated and are now well-established. In this section, we provide a concise summary of the key aspects of superconducting circuit physics that are relevant to the subsequent chapters.

The field of qubits utilizing Josephson junctions emerged in the late 1990s and early 2000s with pioneering experiments involving charge qubits (Nakamura et al., 1999), phase qubits (Martinis et al., 2002) and flux qubits (Chiorescu et al., 2003; van der Wal et al., 2000). Following the proposal by Yale for a cQED architecture to address, couple and read out these qubits (Blais et al., 2004; Girvin, 2016), significant advancements were made. First, superconducting qubits were coherently coupled to harmonic electromagnetic modes (Chiorescu et al., 2004; Wallraff et al., 2004). Then, the transmon qubit, renowned for its robustness, was introduced (Koch et al., 2007), and shortly thereafter, the first implementation of a fluxonium qubit was realized (Manucharyan et al., 2009). Progress continued at a remarkable pace, including notable achievements such as the coupling of two qubits via a coplanar waveguide transmission line (Majer et al., 2007; Sillanpää et al., 2007), the successful implementation of single and multiple qubit gates (Blais et al., 2007; Ding et al., 2023), and experimental demonstrations of simple quantum algorithms (DiCarlo et al., 2009). These and many other initial achievements sparked a rapid expansion of the field, with a growing number of industrial and academic players currently contributing to the development of superconducting qubits. Emphasis has diversified and the state-of-the-art focuses on, among other topics, realizing error correction and operations on logical qubits (Google Quantum AI, 2023; Krinner et al., 2022), demonstrating the beyond-classical performance of quantum processors (Arute et al., 2019; Google Quantum AI, 2023b; Wu et al., 2021), or finding practical applications of quantum computing before reaching fault tolerance (Daley et al., 2022; Kim et al., 2023).

Superconducting circuits are composed of capacitors, inductors and Josephson junctions, as well as distributed elements such as coplanar waveguides. A capacitor with capacitance C can be characterized by its charging energy, E_c, which represents the energy required to imbalance the charge across it by e (the absolute value of the electron charge). It is given by

$$E_c = \frac{e^2}{2C}. \tag{2.9}$$

On the other hand, an inductor with inductance L is characterized by its inductive energy E_L, this is the energy required to bias it with superconducting phase 2π,

$$E_L = \frac{\Phi_0^2}{4\pi^2 L}. \tag{2.10}$$

When capacitors and inductors are combined, they form harmonic circuits with equidistant energy levels. The inclusion of Josephson junctions introduces nonlinearity into the system's Hamiltonian, leading to an anharmonic distribution of eigenenergies. This nonlinearity is crucial for implementing superconducting qubits as it enables transitions between the two lowest energy levels, $|g\rangle$ and $|e\rangle$, which can be selectively manipulated independent of other transitions. Thus, Josephson junctions play a vital role in the construction of superconducting qubits.

The simplest Josephson junction-based circuits consist of two superconducting nodes connected in parallel by at least a capacitor and a Josephson junction. Their degrees of freedom are the gauge-invariant superconducting phase difference across the junction ϕ and its conjugated reduced charge variable n, the number of excess Cooper pairs across the capacitor:

$$n = -i\hbar\frac{\partial}{\partial\phi}, \qquad \phi = i\hbar\frac{\partial}{\partial n}. \tag{2.11}$$

Such circuits can be classified into two big groups, depending on the topology of the space where ϕ and n are defined.

When the nodes on both sides of the junction are isolated from each other, at least one node can be considered as a floating island, while the other can act as another floating island or a superconducting reservoir. In this case, the phase difference, ϕ, is only defined modulo 2π since all physical properties of the junction are periodic with a period of 2π, as discussed in the previous section. The conjugate charge variable, n, representing the number of Cooper pairs occupying the island, must therefore be an integer. A circuit model for this configuration is shown in Fig. 2.5(a), where the two separate pieces of superconductor (purple and red) are coupled via a Josephson junction and a coupling capacitor.

The situation changes when both sides of the junction are shunted by a piece of superconductor with finite inductance (as depicted in Fig. 2.7(a)). In this case, ϕ is defined over the entire real axis, as two ϕ values differing by 2π are no longer physically equivalent (Devoret, 2021; Koch et al., 2009). Furthermore, the number operator n now has a continuous spectrum due to the ability to continuously displace the Cooper-pair condensate towards one side of the junction.

In the following subsections, we will delve into these two topologically distinct classes of qubits, focusing exclusively on the circuit configurations and parameter regimes relevant to the subsequent chapters. These are the fluxonium and transmon circuits.

2.3.1. TRANSMON

A transmon circuit comprises a superconducting island with charging energy E_c connected to a superconducting reservoir through a Josephson junction with an energy-phase relation $U_J(\phi)$ (Fig. 2.5(a)). The circuit's Hamiltonian, denoted as H_t, can be expressed in terms of the phase drop across the Josephson junction, ϕ, and its conjugate charge, n, by combining the Coulomb and Josephson energy contributions (Bouchiat et al., 1998; Shnirman et al., 1997), as

$$H_t = 4E_c(n - n_g)^2 + U_J(\phi). \tag{2.12}$$

In the above equation, n_g represents an offset charge on the island expressed in units of the Cooper pair charge ($2e$). The factor of 4 multiplying the charging energy arises from the fact that n is expressed in units of the Cooper pair charge, and the energy cost of transferring a Cooper pair through the junction is 4 times larger than for transferring a single electron.

When the charging energy, E_c, is much larger than E_J, the circuit operates in the Cooper pair box regime. In this regime, the system's eigenstates are characterized by

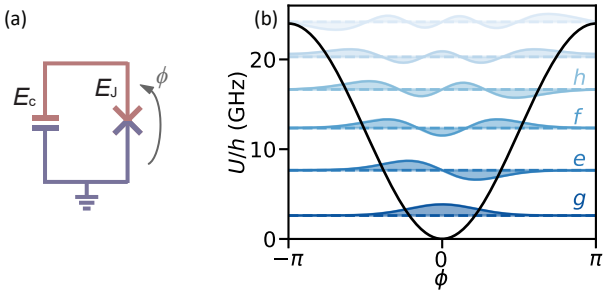

Figure 2.5: **Transmon circuit.** (a) Circuit model. The transmon is composed of a Josephson junction shunted by a capacitor, which are characterized by the energies E_J and E_c, respectively. (b) Sinusoidal junction potential with $E_J/h = 9.0$ GHz (black) versus the phase difference across the junction, ϕ. The real parts of the eigenstates wavefunction for $E_c/h = 0.2$ GHz and $n_g = 0$ are shown with continuous lines and offset from zero by their eigenenergies, which are indicated with color-matching dashed horizontal lines.

a well-defined number of Cooper pairs on the island n (Nakamura et al., 1999; Shnirman et al., 1997). The qubit transitions in this regime exhibit strong anharmonicity and are highly sensitive to the offset charge n_g. However, for the purposes of this thesis, the circuit shown in Fig. 2.5(a) is used to perform spectroscopy of junctions with varying energy-phase relations. In such applications, a strong dependence on n_g would introduce complexity to the obtained spectra. Therefore, we instead operate the circuit in the transmon regime (Koch et al., 2007), where $E_J/E_c \gg 1$. In this regime, the increased Josephson energy causes mixing of the number states, resulting in a circuit spectrum that is independent of the offset charge and resembles that of a slightly anharmonic oscillator, as depicted in Fig. 2.5(b). The presence of nonlinear inductance in the Josephson junction introduces an anharmonicity that lowers the energy of higher excited states[6], enabling individual addressing of the first transition $g \leftrightarrow e$.

TRANSMON AS AN INDUCTANCE SENSOR

In this thesis, transmon circuits primarily serve as sensors of the inductance-phase relation, $L_{J,\text{test}}(\delta)$, of various Josephson junctions. This is particularly the case in Chapters 6 and 7, where we use a transmon to investigate the inductance-phase relations of the singlet/doublet and the spin-up/spin-down states of a quantum dot Josephson junction, respectively.

Fig. 2.6 illustrates the use of a transmon circuit in the transmon regime, $E_J/E_c \gg 1$, as a sensor for the inductance of a given inductive element. The technique involves connecting the inductive element —with energy-phase relation $U_{J,\text{test}}(\delta)$ and inductance-phase relation $L_{J,\text{test}}(\delta)$— in parallel with the transmon's SIS reference Josephson junction, which possesses a Josephson energy E_J (see Fig. 2.6(a)). This configuration forms a superconducting quantum interference device (SQUID) with an external flux Φ_{ext} threaded through it.

When $U_{J,t}(\delta) \ll E_J$, the phase drop across the reference junction is near zero, $\phi \sim 0$, and the phase drop across the secondary inductive element, δ, is determined by the external flux: $\delta \simeq \varphi_{\text{ext}} = \frac{2\pi}{\Phi_0}\Phi_{\text{ext}}$. In this situation, the reference junction sets a reference

[6] In the limit of $E_J/E_c \gg 1$, the energy of the $g \leftrightarrow e$ transition is E_c higher than that of the $e \leftrightarrow f$ transition.

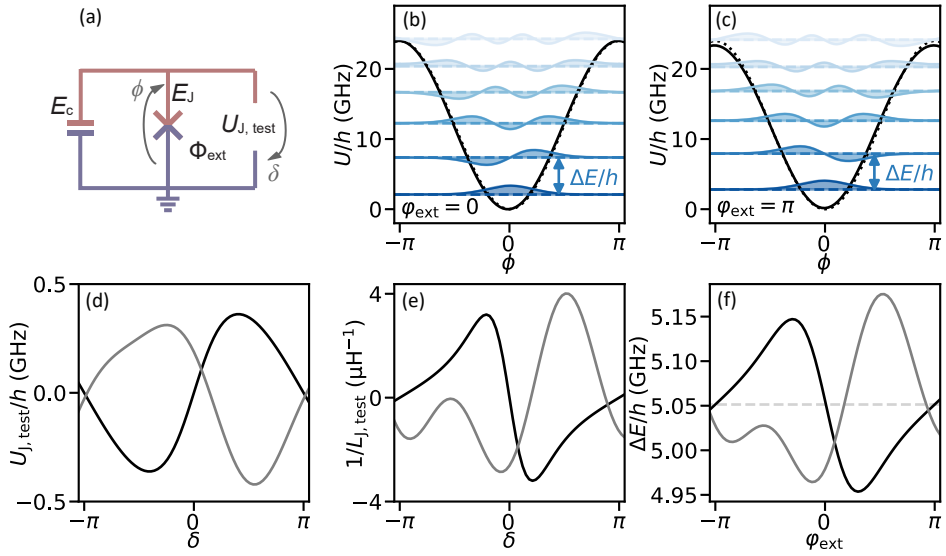

Figure 2.6: **Transmon circuit as an inductance sensor.** (a) Circuit model of a transmon with an asymmetric SQUID. The reference junction has a sinusoidal energy-phase relation with Josephson energy E_J and the inductive element under test has an energy-phase relation $U_{J,test}(\delta)$. (b) Total transmon potential given the $U_{J,test}(\delta)$ potential shown with a black line in (d), as a function of the phase difference across the reference junction, ϕ, and at $\varphi_{ext} = 0$. The real parts of the eigenstates wavefunctions are shown with continuous blue lines and offset from zero by their eigenenergies, which are indicated with color-matching dashed horizontal lines. The dotted line indicates the transmon potential in the absence of $U_{J,test}(\delta)$. (c) Same as (b) but at $\varphi_{ext} = \pi$. The dotted line potential is the same as in (b) and the continuous line potential and eigenenergies are slightly different due to the change in flux. (d) Two examples of energy-phase relations $U_{J,test}(\delta)$ of the inductive element under test. (e) Inductances corresponding to the energy-phase relations in (d) (see Eq. 2.3). (f) Frequency of the $g \leftrightarrow e$ transmon transition versus φ_{ext} for the two potentials in (d). For all panels, the values of E_J and E_c are the same as in Fig. 2.5.

transmon transition frequency, indicated with a dashed line in Fig. 2.6(f). The crucial point exploited in Chapters 6 and 7 is that deviations from this reference frequency are dictated by $L_{J,test}(\delta)$, consequently mapping the transmon transition frequency spectrum versus external flux to the inductance-phase relation of the element under test.

In Fig. 2.6(d) we provide two arbitrary examples of $U_{J,test}(\delta)$, selected for comparative purposes, though they do not necessarily represent real junctions' energy-phase relations. As Figs. 2.6(b) and (c) illustrate, for $U_{J,test}(\delta) \ll E_J$, the $U_{J,test}$ potential only minimally alters the overall transmon potential, $U(\phi) = -E_J \sin(\phi) + E_J + U_{J,test}(\phi - \varphi_{ext})$, and results in nearly identical transmon eigenenergies. Fig. 2.6(b) and (c) correspond to $\varphi_{ext} = 0$ and $\varphi_{ext} = \pi$, respectively. In both cases, the lowest energy states have wavefunctions that are centered around $\phi = 0$ and thus have eigenenergies that are mostly determined by the potential curvature at $\phi = 0$. As this potential curvature is affected by $\frac{\partial^2 U_{J,test}}{\partial \delta^2}(\varphi_{ext}) \propto \frac{1}{L_{J,test}(\varphi_{ext})}$, the transmon frequency deviations from the reference setpoint consequently mimic the shape of the inverse of the inductance of the element under test (compare Fig. 2.6(e) and (f)). This transmon property is used in Chapters 6 and 7 to ac-

cess the inductance of quantum dot Josephson junctions.

2.3.2. FLUXONIUM

A fluxonium circuit, as shown in Fig. 2.7(a), comprises a Josephson junction shunted by an inductor with an inductive energy E_L and a capacitor with a charging energy E_c. The energy spectrum of the fluxonium can be controlled by the external flux, Φ_{ext}, through the loop formed by the Josephson junction and the inductor. This enforces the sum of phase drops across the junction and inductor to equal Φ_{ext}. The circuit's Hamiltonian, H_f, can be expressed as (Manucharyan et al., 2009)

$$H_f = 4E_c n^2 + \frac{1}{2}E_L\phi^2 + U_J(\phi - \varphi_{ext}). \tag{2.13}$$

Here, $\varphi_{ext} = 2\pi\frac{\Phi_{ext}}{\Phi_0}$ represents the reduced flux associated with Φ_{ext}, where Φ_0 denotes the superconducting magnetic flux quantum.

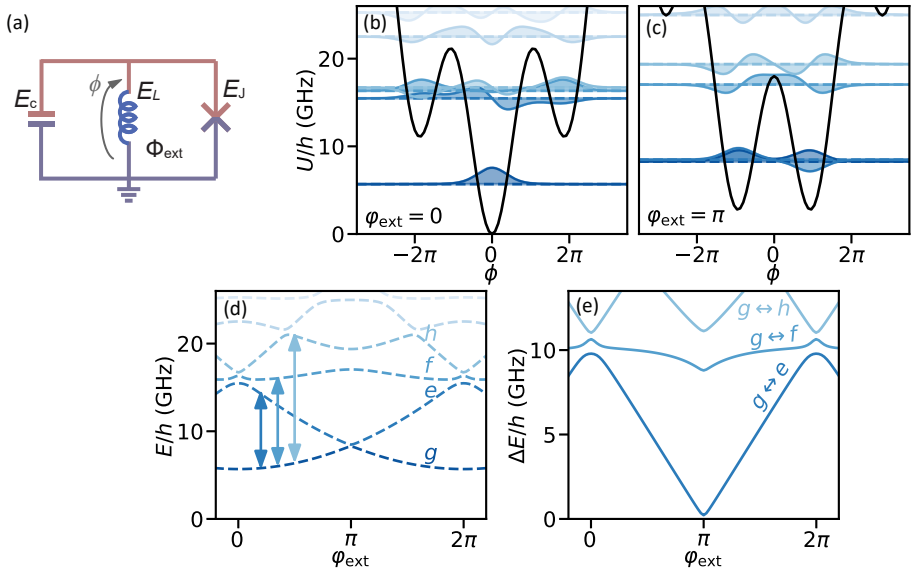

Figure 2.7: **Fluxonium circuit.** (a) Circuit model. The fluxonium is composed of a Josephson junction shunted by an inductor and a capacitor, which are characterized by the energies E_J, E_L, and E_c, respectively. The loop formed by the inductor and the junction is threaded by an external magnetic flux, Φ_{ext}. (b) Fluxonium potential with $E_L/h = 0.6$ GHz and $E_J/h = 9.0$ GHz (black) versus the phase difference across the inductor, ϕ, at $\varphi_{ext} = 0$. The real parts of the eigenstates wavefunction for $E_c/h = 2.0$ GHz are shown with continuous lines and offset from zero by their eigenenergies, which are indicated with color-matching dashed horizontal lines. (c) Same as (b) but at $\varphi_{ext} = \pi$. (d) Flux-dependence of the fluxonium energy spectrum for the same parameters as in panels (b) and (c). Different lines indicate the energies of the different eigenstates. Blue arrows indicate transitions involving the ground state. (e) Frequencies of different transitions between the ground state and the next states in energy, as a function of the external flux. Each transition is color-coded based on its higher energy state.

The ϕ and n variables can be regarded as analogous to position and momentum,

respectively. With this interpretation, the two ϕ-dependent terms in Eq. 2.14 constitute a potential energy defined across the entire real axis:

$$U(\phi) = \frac{1}{2}E_L\phi^2 + U_J(\phi - \varphi_{ext}). \tag{2.14}$$

Figs. 2.7(b) and (c) illustrate the shape of $U(\phi)$ near its minimum, assuming a sinusoidal energy-phase relation for the junction ($U_J(\phi) = U_{SIS}(\phi)$, as given by Eq. 2.1), at two values of the external flux through the loop, $\varphi_{ext} = 0$ and π. The E_L term contributes to a parabolic background centered at $\phi = 0$, while the junction's potential $U_J(\phi)$ introduces a periodic modulation on top of it, which becomes more pronounced with increasing E_J. The charging energy E_c can be regarded as the kinetic energy that, together with the potential $U(\phi)$, determines the fluxonium eigenstates.

Of particular relevance to Chapter 5 is the so-called fluxonium regime of this circuit, proposed by Manucharyan *et al.* in 2009. In the fluxonium regime, the inductor possesses a large inductance that reduces its inductive energy E_L, making it less susceptible to flux noise than in other regimes. Fig. 2.7(d) showcases the φ_{ext}-dependence of the energies of the lowest states of a fluxonium circuit. The spectrum of transitions originating from the ground state $|g\rangle$, which can be accessed experimentally, is depicted in Fig. 2.7(e). In Chapter 5, we investigate variations in the fluxonium spectrum as the effective Josephson energy E_J of a semiconducting junction varies with gate voltage and magnetic field, as well as when the junction potential U_J deviates from that of a sinusoidal SIS junction.

2.4. QUBIT-QUBIT COUPLING

In this thesis, we investigate two instances of qubit-qubit coupling. First, in Chapter 8, we investigate the interaction between a transmon and a superconducting spin qubit. Then, in Chapter 9, we characterize the coupling between two superconducting spin qubits. The qubit-qubit coupling can take different forms depending on the degrees of freedom from each qubit that interact with each other. In this section, we briefly present two relevant types of qubit-qubit interaction.

We consider the ideal case where each qubit is a perfect two-level system. In this situation, we can write the Hamiltonian of the uncoupled qubit i, where $i \in \{1,2\}$, as $H_i = \frac{E_i}{2}\sigma_i^z$. Here, E_i is the energy difference between the two levels of qubit i, $|0_i\rangle$ and $|1_i\rangle$, and σ_i^z is the z Pauli matrix of qubit i. We use the convention $\sigma_i^z|0_i\rangle = -|0_i\rangle$ and $\sigma_i^z|1_i\rangle = +|1_i\rangle$. The total Hamiltonian of the coupled qubit-qubit system can be written, in its most general form, as

$$H = \frac{E_1}{2}\sigma_1^z + \frac{E_2}{2}\sigma_2^z + H_c. \tag{2.15}$$

The last term couples the variables of both individual qubits. Depending on the form of H_c, the coupled qubit-qubit system can behave in different ways. Below, we explore two examples, those of transverse coupling and longitudinal (or Ising, or ZZ) coupling (Krantz et al., 2019; Richer and DiVincenzo, 2016; Richer et al., 2017).

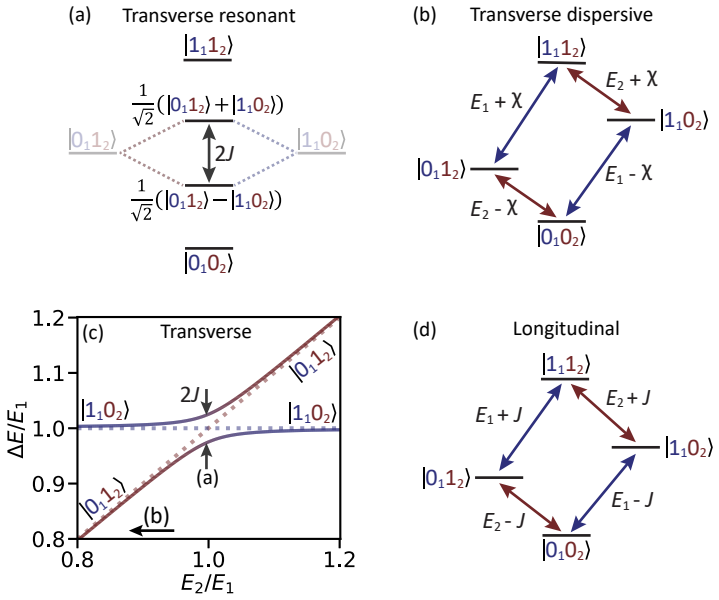

Figure 2.8: **Transverse and longitudinal coupling.** (a) Energy diagram of a transversely coupled qubit-qubit system when the two qubits are resonant (where $E_1 = E_2$, see Eq. 2.18). (b) Same as (a) but for a transversely coupled system in the dispersive regime (where $E_1 - E_2 \gg |J|$, see Eq. 2.17). (c) Transition spectrum of a transversely coupled qubit-qubit system as E_2 is varied from $E_2 < E_1$ to $E_2 > E_1$. The continuous lines indicate the energy difference between the ground state and the two lowest excited states. The line color indicates whether the excited state is $|1_1 0_2\rangle$ (purple), $|0_1 1_2\rangle$ (maroon) or a superposition of the two (mixed color). The situations shown in (a) and (b) correspond, respectively, to the $E_2/E_1 = 1$ case and the $|E_1 - E_2| >> J$ limit, as indicated. $J = 0.02E_1$. (d) Energy diagram of a longitudinally coupled qubit-qubit system (see Eq. 2.21). For (a), (b) and (d), the energy levels are indicated with horizontal black lines labeled by the corresponding eigenstates. The transitions between them are indicated with diagonal double-headed arrows, labeled by their energy. Purple and maroon arrows indicate the transitions of qubits 1 and 2, respectively.

2.4.1. TRANSVERSE COUPLING

The most common type of qubit-qubit coupling in modern implementations of superconducting qubits is transverse coupling. Transverse coupling is simple to implement by, for instance, capacitively coupling transmon qubits to each other, either directly or via an intermediate cavity (Majer et al., 2007). The transverse coupling Hamiltonian can be expressed in the eigenbasis of $H_1 \otimes H_2$ as

$$H_c = J\sigma_1^x \sigma_2^x, \tag{2.16}$$

where J denotes the transverse coupling energy. In the basis $\{|1_1 1_2\rangle, |1_1 0_2\rangle, |0_1 1_2\rangle, |0_1 0_2\rangle\}$, the transverse coupling Hamiltonian has non-zero matrix elements only at the off-diagonal positions:

$$H = \begin{pmatrix} \frac{E_1}{2} + \frac{E_2}{2} & 0 & 0 & J \\ 0 & \frac{E_1}{2} - \frac{E_2}{2} & J & 0 \\ 0 & J & -\frac{E_1}{2} + \frac{E_2}{2} & 0 \\ J & 0 & 0 & -\frac{E_1}{2} - \frac{E_2}{2} \end{pmatrix}. \tag{2.17}$$

The behavior of the system depends on the relative values of the qubit energies, E_i, and the coupling energy, J. The energy level diagram for a transversely coupled system is shown in Figs. 2.8(a) and (b) for the resonant case ($E_1 = E_2$) and the detuned (or dispersive) limit ($|E_1 - E_2| \gg |J|$), respectively.

The **resonant regime** of transverse coupling is particularly useful to implement various types of two-qubit gates. To first order in J, the total system Hamiltonian in the resonant regime, $E_1 - E_2 = 0$, is given by

$$H_{\text{resonance}} = \begin{pmatrix} \frac{E_1}{2} + \frac{E_2}{2} & 0 & 0 & 0 \\ 0 & 0 & J & 0 \\ 0 & J & 0 & 0 \\ 0 & 0 & 0 & -\frac{E_1}{2} - \frac{E_2}{2} \end{pmatrix}, \tag{2.18}$$

where, on basis of $E_i \gg |J|$, we have applied the rotating wave approximation to ignore the terms proportional to $\sigma_1^+\sigma_2^+$ and $\sigma_1^-\sigma_2^-$, which represent double excitation and double de-excitation processes, respectively[7]. Here, $\sigma_i^+ = (\sigma_i^x + i\sigma_i^y)/2 = |1_i\rangle\langle 0_i|$ and $\sigma_i^- = (\sigma_i^x - i\sigma_i^y)/2 = |0_i\rangle\langle 1_i|$.

The energy level diagram in resonance is shown in Fig. 2.8(a). When the qubit frequencies are similar, $|E_1 - E_2| \sim |J|$, the $|1_1 0_2\rangle$ and $|0_1 1_2\rangle$ states hybridize. At exact resonance, when $E_1 = E_2$, the two states hybridize fully and the system eigenstates become $\{|1_1 1_2\rangle, \frac{1}{\sqrt{2}}(|1_1 0_2\rangle + |0_1 1_2\rangle), \frac{1}{\sqrt{2}}(|1_1 0_2\rangle - |0_1 1_2\rangle), |0_1 0_2\rangle\}$. Spectroscopically, the hybridization of the two qubits results in an avoided crossing when their transition energies cross (see Fig. 2.8(c)). In this regime, if the system is initialized in the $|1_1 0_2\rangle$ or $|0_1 1_2\rangle$ states, these states undergo vacuum Rabi oscillations in the time domain. After turning the interaction on, the qubits exchange states at a rate determined by J. This enables the direct implementation of an iSWAP gate by activating the coupling for an amount of time $t = h/(2J)$ (Majer et al., 2007). Alternatively, by setting $t = h/(4J)$, one can implement a $\sqrt{i\text{SWAP}}$ gate, which is useful for generating Bell states. While simple, this way of implementing two-qubit gates puts a big constraint on the qubit energies, as they are required to be equal during the realization of the gate. This, in turn, leads to frequency-crowding challenges when designing large-scale quantum devices.

In the **dispersive limit**, the two qubits are mostly uncoupled and the eigenstates of the system, to first order in J/Δ, are the original eigenstates of the individual qubits. Here, $\Delta = |E_1 - E_2|$ represents the qubit-qubit detuning. Their eigenenergies are modified by a dispersive shift $\chi = J^2/\Delta$ (see Fig. 2.8(b)). After applying the rotating wave approximation and considering terms up to first order in J/Δ, the transverse coupling Hamiltonian becomes

$$H_{\text{c,dispersive}} = \chi\sigma_1^z\sigma_2^z. \tag{2.19}$$

DISPERSIVE READOUT

The dispersive limit of a qubit transversely coupled to a cavity is commonly used for qubit state readout (Blais et al., 2004; Wallraff et al., 2004). Asymptotically, this becomes a longitudinal interaction (see Sec. 2.4.2), enabling qubit state readout by detecting shifts

[7] Note that the energies of the $|0_1 0_2\rangle$ and $|1_1 1_2\rangle$ states get a Bloch-Siegert shift of $J^2/(E_1 + E_2)$, as in the dispersive limit.

in the resonator frequency without energy exchange between the two systems. Such interaction can be used to implement quasi quantum non-demolition (QND) readout. This dispersive readout, however, suffers from a few disadvantages. First, it is only non-demolition in a perturbative sense and, to second order in J/Δ, it leads to the Purcell effect, where the qubit can relax by emitting a resonator photon (Houck et al., 2008). Second, the speed of dispersive readout is limited by the fact that the dispersive shift is only a weak second-order effect, which decreases as the qubit-resonator detuning increases, putting a constraint on the energy difference between resonator and qubit. Finally, a high photon population in the cavity during measurement can induce qubit transitions (Blais et al., 2004). This, in turn, imposes a limit on the number of photons that can be used for readout and, consequently, on how fast dispersive readout can be performed.

2.4.2. LONGITUDINAL COUPLING

Although not as common as transverse coupling, longitudinal coupling is arguably the most conceptually simple type of qubit-qubit coupling. It is naturally found between J-coupled nuclear magnetic resonance (NMR) qubits implemented in nuclear spins (Gershenfeld and Chuang, 1997; Jones, 2004; Vandersypen and Chuang, 2005), and can be readily obtained by inductively coupling flux qubits (Plantenberg et al., 2007) or, as we discuss in Chapter 9, by inductively coupling superconducting spin qubits (Chtchelkatchev and Nazarov, 2003; Padurariu and Nazarov, 2010). Longitudinal interactions can moreover be engineered between other types of qubits by incorporating coupling elements, as was demonstrated for transmon qubits (Collodo et al., 2020; Xu et al., 2020).

As before, we can express the longitudinal coupling Hamiltonian in the eigenbasis of the individual systems as

$$H_{\mathrm{c}} = \frac{J}{2}\sigma_1^z\sigma_2^z, \tag{2.20}$$

where J denotes the longitudinal coupling energy. In this case, the coupling axis is the same as the qubit quantization axis σ_i^z, and thus the eigenstates of the coupled system are the same as those of the uncoupled system. However, the presence of H_{c} renormalizes the system eigenenergies, resulting in qubit transition energies that depend on the state of the other qubit. The total Hamiltonian of the coupled system, exactly diagonal, can be written in the uncoupled basis $\{|1_1 1_2\rangle, |1_1 0_2\rangle, |0_1 1_2\rangle, |0_1 0_2\rangle\}$ as

$$H = \begin{pmatrix} \frac{E_1}{2}+\frac{E_2}{2}+\frac{J}{2} & 0 & 0 & 0 \\ 0 & \frac{E_1}{2}-\frac{E_2}{2}-\frac{J}{2} & 0 & 0 \\ 0 & 0 & -\frac{E_1}{2}+\frac{E_2}{2}-\frac{J}{2} & 0 \\ 0 & 0 & 0 & -\frac{E_1}{2}-\frac{E_2}{2}+\frac{J}{2} \end{pmatrix}. \tag{2.21}$$

The resulting energy levels are shown in Fig. 2.8(d). As depicted, the transition of qubit 1 ($|0_1\rangle \leftrightarrow |1_1\rangle$) can have two different energies: $E_1 - J$ or $E_1 + J$, depending on the state of qubit 2 being $|0_2\rangle$ or $|1_2\rangle$, respectively. Similarly, the transition energy of qubit 2 depends on the state of qubit 1.

In contrast to transverse coupling, longitudinal coupling does not impose any constraints on the qubit frequencies for implementing a two-qubit gate, as the coupling strength is independent of the qubit detuning. When two qubits interact longitudinally

with a fixed coupling strength, two-qubit gates can be readily implemented by selectively pulsing different transitions (Chuang et al., 1998; Gershenfeld and Chuang, 1997; Linden et al., 1998; Orlando et al., 1999; Padurariu and Nazarov, 2010; Plantenberg et al., 2007). In particular, controlled rotations can be performed on one qubit, controlled by the state of the other, by driving the corresponding frequency. On the other hand, performing arbitrary single-qubit rotations in this scenario is not trivial, as the frequency of the target qubit depends on state of the other qubit. Suggested schemes for realizing single-qubit operations under the presence of longitudinal coupling involve combining the corresponding 0- and 1-controlled operations (Plantenberg et al., 2007) or using more intricate two-axes multi-pulse gate schemes (Long et al., 2021). By combining conditional rotations with single-qubit rotations, other two-qubit gates such as the CPHASE or the CNOT gates can be implemented, as discussed in Refs. (Padurariu and Nazarov, 2010; Plantenberg et al., 2007).

While it enables the simple implementation of proof-of-principle two-qubit gates, always-on longitudinal coupling can lead to challenges, as it results in the unwanted evolution of the system when no gate is needed. Approaches to address this issue have primarily relied on incorporating sequences of refocusing π-pulses to compensate for the continuously evolving phases (Jones and Knill, 1999; Vandersypen et al., 2001). While simple to apply in small systems, such approaches would lead to issues when scaled up to systems containing a large number of coupled qubits. Selectively driving qubit subarrays has been suggested as an alternative scheme to overcome this challenge (Le et al., 2023).

When it comes to scaling up longitudinally-coupled multi-qubit systems, the complexity can be significantly reduced by employing qubits with switchable longitudinal coupling strength (Bøttcher et al., 2022; Collodo et al., 2020; Hime et al., 2006; Xu et al., 2020). This allows the system to be fully decoupled while idling. As demonstrated in Refs. (Collodo et al., 2020; Long et al., 2021; Ma et al., 2023; Xu et al., 2020), a tunable longitudinal interaction can be used to implement a CPHASE gate with an arbitrary conditional phase by pulsing the coupling. In particular, by applying a pulse on the J control parameter for a duration of $t = h/(4J)$, a CZ gate can be realized. In Chapter 9 we demonstrate how, by inductively coupling superconducting spin qubits (Chtchelkatchev and Nazarov, 2003; Padurariu and Nazarov, 2010), we can realize strong switchable longitudinal coupling between them. This feature highlights the potential of superconducting spin qubits as a promising platform for implementing fast two-qubit gates.

LONGITUDINAL READOUT

Another area where longitudinal coupling offers advantages compared to transverse coupling is resonator-based qubit readout. When a qubit is longitudinally coupled to a readout cavity, it does not suffer from the Purcell effect, as the two systems can interact without energy exchange. This enables a pure quantum non-demolition readout (and not an approximate one like in the dispersive limit of transverse coupling) (Bøttcher et al., 2022; Didier et al., 2015; Richer et al., 2017). Moreover, longitudinal readout does not put any constraints on the relative difference between qubit and resonator, as their coupling strength does not depend on the detuning. Finally, longitudinal readout can in principle be performed even for a large number of resonator photons without the complications that it entails in the case of dispersive readout.

3

EXPERIMENTAL METHODS

This chapter is authored by Jaap J. Wesdorp and Marta Pita-Vidal and adapted to fit each thesis.

3.1. SUPERCONDUCTING CHIP DESIGN

In this thesis, we use superconducting circuits to probe physics with radio-frequency (RF) microwave signals. The advantage of using superconducting circuits as a tool to probe condensed matter is that it allows to design for high sensitivity to the device under test and high energy resolution. This, unfortunately, comes with a drawback: the circuit design becomes more challenging. Thus, the lead time to go from an experimental idea towards starting the fabrication is often much longer than with conventional DC-transport techniques. Additionally, all time spent on optimizing and designing the circuit is time not spent on studying the underlying physics. For this purpose, we have tried to optimize the workflow in our team to allow for the least possible time lost in the design and fabrication[1], which is summarized in Fig. 3.1.

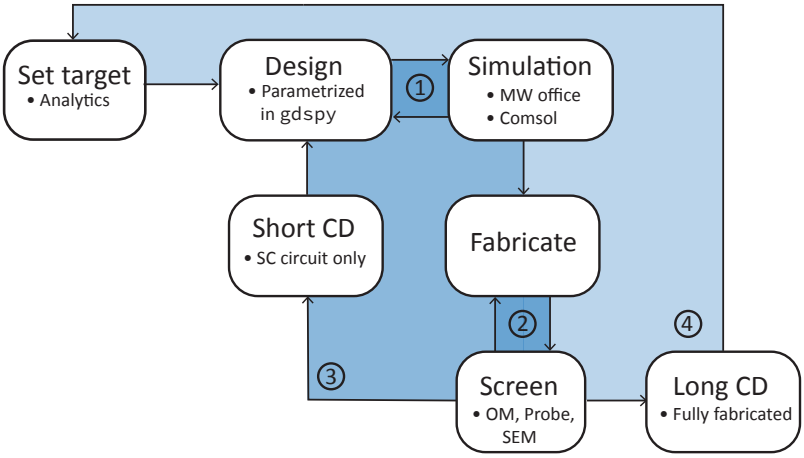

Figure 3.1: **Device creation process.** Each block describes a process, with arrows indicating the step evolution. At some points, arrows point towards steps that have already been performed and create feedback loops (indicated with a colored background). The numbers identify each feedback loop. For example, loop 1 is the iterative process where the output of the design is simulated and subsequently modified to converge towards the target parameters. Detailed explanations for the steps and acronyms can be found in the main text.

The first step of every project is to **set the target**. Guided by a wish-list of on-chip components, this step consists on performing analytical calculations of the desired couplings and frequencies and translating them to physical capacitances, inductances and shapes. This is followed by implementing the chip **design**, which is done in *Python* using the *gdspy* package. The design step results in a .gds file –a standard integrated circuit (IC) fabrication file format– and consists of layers of 2-dimensional patterns, each representing an e-beam lithography patterning step. The design philosophy is that, by defining the chip design in *Python*, each chip element can be parameterized. This allows for fast adaptations without requiring a complete overhaul of all other parts of the design. This involves a higher initial effort on the design side compared to using graphical drawing

[1] Unfortunately, this is still in general a considerable fraction of the total time spent in a project and improvements the flow are definitely welcome and recommended.

software such as *AutoCAD*, but saves a lot of time in the following iteration steps. Moreover, having programmatic access to the geometry allows to instantly estimate the total inductance of a resonator when changing the design.

We then perform **simulations** of the circuit layer in *Comsol* for calculating capacitances and in *Microwave Office* (MWO) for determining the resonator frequencies and coupling quality factors. This step is made as automated as possible by making the design code output an inverted version of the nanofabrication layers. Moreover, we include only a small ground-plane region around each resonator to limit the simulation time. *Microwave Office* uses a finite element simulation of the microwave response with a 2.5-dimensional method of moments solver, which can efficiently combine layers, such us dielectrics, that do not vary in the x-y plane with circuit layers that do vary. This is especially suited for IC design simulation. The simulations often result in design changes, as indicated by loop 1 in Fig. 3.1. For the *Microwave Office* simulations to be accurate, the dielectric constant of the Si substrate, $\epsilon_r = 11.7$, and the kinetic inductance per square are added as material settings.

When the simulations indicate that the couplings, quality factors and resonance frequencies are as desired, we continue towards the **fabrication** of the chips, of which the precise steps are described in Sec. 3.2. During the fabrication, each step and the final result is **screened** using, for instance, optical microscopy (OM), electrical probing of the NbTiN sheet resistance or scanning electron microscopocy (SEM). This is in turn used as feedback to obtain accurate doses for the sub-micrometer-wide features, such as the inductors and gates. The screening at each fabrication step can provide early warning signs that a step failed and the fabrication should start over, indicated as loop 2 in Fig. 3.1. To increase the fabrication yield when faced with multiple steps, we follow a redundancy strategy. We begin by processing a slightly larger number of chips than required, typically around twice the target count. Rather than performing all nanofabrication steps simultaneously for all chips, we keep a subset designated as "backup chips." For these backup chips, every nanofabrication step lags behind by one step. With this approach, if any of the nanofabrication steps is unsuccessful, which is not rare in academic nanofabrication, the backup chips can continue being processed. This prevents having to restart the process from the initial step.

When a design is new and yet untested, we generally first perform only the fabrication steps involving the superconducting circuit patterning. The resulting chip is then loaded in either a quick-test fridge[2] or a dilution refrigerator for a **short cooldown (CD)**. This only takes a few days of loading and cooling down and can already show whether the circuit behaves as expected. As this is unfortunately often not the case, feedback loop 3 consists on going back to the design phase and updating the circuit design before running this test again. This step also serves as the best feedback on the value of the real kinetic inductance of the devices that should be used in the simulations to target resonator frequencies, as this can typically vary by approximately 10 to 20% (see Appendix C). Finally, the last and the longest loop, number 4, indicates that, after a **long**

[2] We often use the Heliox, a dipstick kindly made available to us from the neighbouring superconducting qubit group of L. DiCarlo. This dipstick includes a sorb with He^{-3} and can reach 300 mK, which is well below the 9 K critical temperature of NbTiN films. Additionally, below 1 K we generally do not see the internal quality factors of the resonators decrease, so this step also allows to determine how well the designed resonators perform.

cooldown (CD), we still find features that can be improved in next design generations or designs of other group members. This serves as a "collective memory" of the group. Examples of these elements include changes in the gate line filter order, resonator shapes and geometry, hole-patterning areas, and asymmetric input ports for the feedline.

3.1.1. DESCRIPTION OF SUPERCONDUCTING CIRCUIT ELEMENTS

In this section, we give an overview of the typical elements used in our superconducting circuits accompanied, when relevant, with simulations.

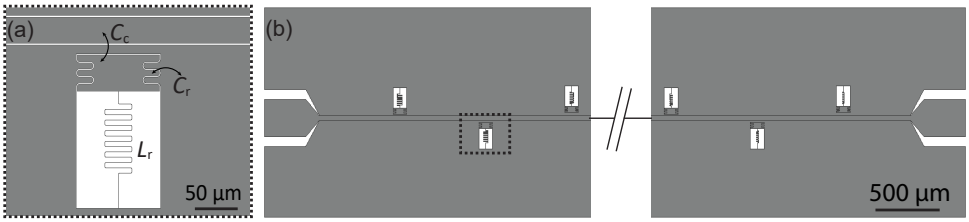

Figure 3.2: **Feedline with multiple devices coupled to it for transmission readout.** (a) Zoom in of example lumped element resonator that is capacitively coupled to the feedline (dashed box in (b)). The capacitance of the resonator is implemented using an in-plane capacitance to ground, C_r, and to the feedline, C_c. The capacitor plate is connected to ground via a thin meandering strip of NbTiN that has a high kinetic inductance, L_r, forming the LC resonance circuit. (b) Left and right sides of a full (7 mm-long) chip with a total of nine resonators (three of them not shown) coupled to it.

THE FEEDLINE

The design of our devices starts with a feedline, an impedance-matched coplanar waveguide with input and output ports, as shown in Fig. 3.2. See Ref. (Pozar, 2012) for an introduction to distributed element microwave components. Since the characteristic impedance of commercially available coaxial cables is 50 Ω, we match the printed-circuit board lines (see Sec. 3.3.2) and the on-chip waveguides to have this same 50 Ω characteristic impedance. This minimizes reflections that arise from impedance mismatches, and thus allows most of the signal sent to our device to reach it. Additionally, due to interference, a not well impedance-matched configuration can have standing waves that appear as resonances in the signal transmitted through the system. The number of devices coupled to a single feedline is generally between two and eight, depending on the size of each device and on the required input lines. This increases the likelihood of obtaining a working device in a single cooldown. When using semiconducting nanowires, the yield is generally not as high as for "pure" superconducting circuits. An additional benefit of this approach is that it leads to (limited) statistics about the reproducibility of the physics observed.

For Chapters 8 and 9, where we perform time-domain coherence experiments, we added an input capacitor to the feedline (see Fig. 3.3). A disadvantages of measuring in transmission with symmetric input and output ports is that around half of the input photons are reflected and go out through the input port (Girvin, 2014). This reduces the signal-to-noise ratio by a factor of two. For spectroscopy experiments, this is not an issue, as one can generally increase the readout power to compensate. However, when

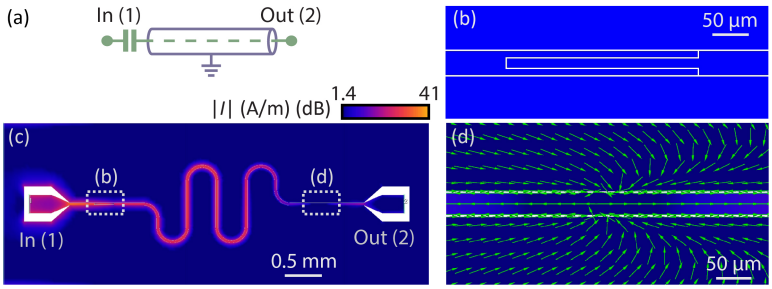

Figure 3.3: **Feedline input capacitor design and simulation of the current distribution.** (a) Circuit diagram of a coplanar-waveguide transmission line with a capacitor at its input port. (b) Design of the input capacitor, the NbTiN regions are denoted in blue. (c) Current magnitude yielded by a microwave simulation performed with Microwave Office. A current node forms at a distance of approximately $l = \lambda/2$ away from the capacitor, where λ denotes the wavelength at the intended resonator frequency. (d) Enlargement of the region where the current node forms. The green arrows indicate the current direction at each point.

interested in single-shot measurements, or photon-number sensitive measurements, improving the signal by a factor of two can be advantageous. This can be achieved by weakly coupling the input port to the feedline. From a quantum optics point of view, the feedline can then be seen as having one very transparent mirror (to the output port) and one very reflective mirror (to the input port). Thus, for an input attenuation of roughly 20 dB, 99% of all photons that enter the feedline, exit through the output line.

Note, however, that, with the inclusion of an input capacitor, the length of the feedline becomes relevant, as standing waves will form due to the boundary condition at the input capacitor (see Fig. 3.3(c)). To maximize the capacitive coupling and prevent asymmetric resonance shapes, each resonator should be placed at a voltage anti-node, whose positions depend on the resonator frequency. Additionally, the required input power for the same amount of microwave power at the resonator rises by about 20 dB.

THE RESONATORS

Throughout this thesis, we use lumped element resonators, consisting of a coplanar capacitance to ground, C_r, and inductance, L_r, set by the film kinetic inductance (see Fig. 3.2(a)). Their design is extensively discussed in Chapter 4.

THE ELECTROSTATIC GATES AND FILTERS

One of the main advantages of using semiconducting components is that their conductivity and inductance can be tuned by applying an electrostatic gate voltage. However, incorporating gate lines in superconducting circuits must be done with care, as they can act as microwave loss channels. For the gates used in this thesis, we generally add on-chip low-pass LC filters that attenuate strongly at the resonance frequency of the resonator. In Chapter 5 we use a planar filter similar to that in Ref. (Mi et al., 2017), with a spiral inductor and an interdigitated capacitor (see Fig. 3.4(a)). Subsequently, inspired by Ref. (Harvey-Collard et al., 2020), we replace the interdigitated capacitor with a parallel plate capacitor to reduce the filter footprint (see Chapters 6, 7 and 8). The parallel-plate capacitors, shown in Fig. 3.5(a), can be implemented without any additional fabrication steps because they are fabricated at the same time as the nanowire contacts

(see Sec. 3.2). Finally, in Chapter 9 we implement forth order LCLC filters, as shown in Fig. 3.4(b-d).

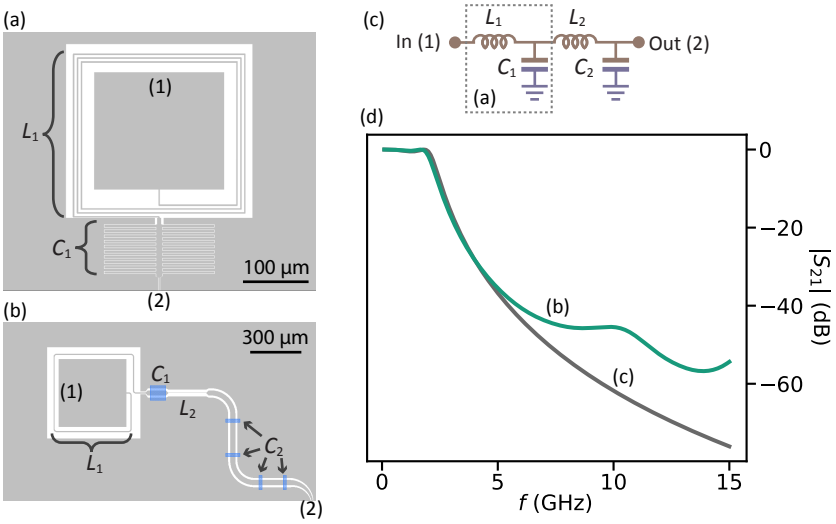

Figure 3.4: **Low-pass filters for the gate lines.** (a) First order low-pass on-chip LC filter, a design which was followed up by (b). (b) Fourth-order LCLC Chebyshev filter, which is simulated using the indicated microwave ports, labeled as (1) and (2), at each end of the gate line section. (c) Circuit diagram of a fourth-order LCLC Chebyshev filter, composed of inductances $L_1 = 5.21\,\text{nH}$ and $L_2 = 6.13\,\text{nH}$ and capacitances $C_1 = 2.45\,\text{pF}$ and $C_2 = 2.08\,\text{pF}$. The equivalent diagram of (a) is indicated with a dashed box (note that the capacitance and inductance values in (a) are different). (d) Simulated transmission from the input to the output port, as a function of frequency, f. The grey and green lines correspond to the circuit in (c) and to the simulation in (b), respectively.

Note that the gate line can also act as a resonator. We thus make its length on-chip as short as possible to keep the self-resonance frequency as high as possible. The distance from the PCB to the gate bondpads is covered with long bond wires. Finally, we design the bondpad size to be large ($200\times200\,\mu\text{m}^2$) to prevent unwanted shorts while wire-bonding ant to facilitate rebonding the device if necessary.

DRIVE LINES

In Chapters 7, 8 and 9, we use one of the gate lines for driving spin-flip transitions. Therefore, these lines do not include on-chip low-pass filtering and are instead formed by a $50\,\Omega$ coplanar waveguide. In this case, as opposed to the DC gate lines, the bondpads are placed as close to the edge of the chip as possible. This minimizes the bond length and, with it, impedance mismatches (Krinner et al., 2022).

ON-CHIP OVERPASSES

Our standard fabrication recipe involves both a dielectric deposition step and a NbTiN deposition step after having defined the base circuit layer. We thus use these existing steps to define bridges that connect the ground plane across the DC lines (see Fig. 3.5(a)). Since these bridges are only separated from the DC line by a dielectric layer of approximately 28 nm, they are not used to connect the ground plane across the feedlines and

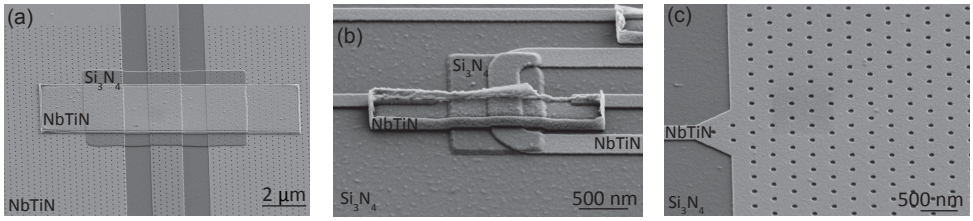

Figure 3.5: **Scanning electron micrographs of various chip elements.** (a) Large NbTiN overpass over a gate line to connect the ground plane on each side. These structures are also used as parallel plate capacitors for the gate line filters. (b) Example of a smaller overpass to connect a gate line across a SQUID loop. (c) Part of the capacitor plate of the resonator, which is patterned with vortex trapping holes in a triangular lattice and with a diameter of approximately 80 nm.

drivelines, as they would drastically change the impedance of these elements. An alternative would be to use air bridges, which have vacuum instead of dielectric and thus a much smaller dielectric constant (Stavenga et al., 2023).

THE FLUX BIAS LINE

For the device in Chapter 9, we use on-chip flux-bias lines to control the flux through the superconducting quantum interference device (SQUID) loops. The SQUID loops that we use are generally small, on the order of several tens of μm^2. Additionally, the flux line is fabricated in the 20 nm thick base layer of NbTiN. Hence, we needed to make sure that the line can sustain a supercurrent that can generate several flux quanta in the loop. Additionally, for compatibility with future experiments, we wanted to allow for the ability of fast-flux pulsing up to approximately 1 GHz. The flux line was therefore designed as a 50 Ω coplanar waveguide which is shorted to ground at its end.

From measurements of their critical current, we found that similar flux lines were resilient to maximally around 3 mA of on-chip current before the narrowest section of the flux line on chip turned normal. Additionally, we found that the line kept around half of its critical current at 1.5 T. To continue being able to drive several flux quanta, the flux line needed to be placed close to the loop (as $B \propto 1/r$, with r being the distance from the flux line).

To mitigate losses through the flux line, which we found to be significant in an earlier design iteration (Wesdorp and *et al.*, 2023b), we implemented an on-chip low-pass LC filter similar to that in the gate lines. The difference is that we could not use the thin inductors to keep the critical current maximal. We therefore implemented the filter by adding a parallel-plate capacitor, as shown in Fig. 3.6. This capacitance, combined with the existing inductance of the transmission line, gives the filter response shown in Fig. 3.6(c) and (d).

3.1.2. CAPACITANCE SIMULATIONS

Besides simulations in *Microwave Office*, we often additionally use *Comsol*, following the approach outlined in Ref. (Friedel, 2017), to simulate coupling capacitances between resonator and feedline, resonator and transmon and between either the resonator or transmon to all other gate- and drive-lines. An example of the simulation performed on

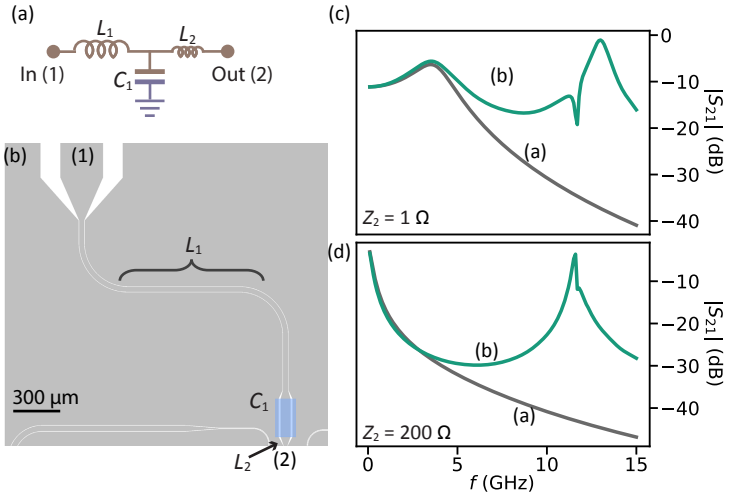

Figure 3.6: **Flux line with a low-pass LC filter.** (a) Circuit diagram of an LC filter, composed of an inductance $L_1 = 1$ nH and a capacitance $C_1 = 22$ pF. An extra inductor segment, with inductance $L_2 = 0.08$ nH, is included at the end of the filter to account for the non-idealities of the real implementation of the flux line. (b) Schematic of the simulated part of the flux line including the input and output microwave ports, labeled as 1 and 2, at each of its ends. (c) and (d) Simulated transmission from the input to the output port, as a function of frequency. The grey lines correspond to the circuit in (a) and the green lines correspond to the circuit in (b). The impedance of the input port is 50 Ω in both cases, while the impedance of the output port is 1 Ω in (c) and 200 Ω in (d).

the device used in Chapter 9 is shown in Fig. 3.7.

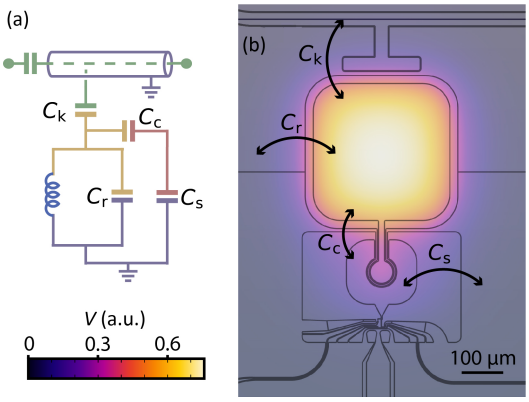

Figure 3.7: **Capacitance simulations.** (a) Circuit model of a feedline (with inner conductor in green) capacitively coupled to a resonator island (yellow) which is in turn capacitively coupled to a transmon island (red). Ground is indicated in purple. (b) Result of an electrostatics simulation performed with *Comsol* showing the potential, V, distribution when a certain charge is applied to the resonator island. This simulation is used to estimate the capacitance between each pair of elements.

3.2. STANDARD NANOFABRICATION

The fabrication process for the InAs/Al nanowire-based devices employed in the experimental sections of this thesis initiates with the preparation of a complete 4-inch wafer. Over this wafer, a layer of NbTiN is deposited before the wafer is diced into smaller chips. As opposed to individual chip preparation, this method allows for higher homogeneity of the film properties across different devices and for more accurate targeting of the kinetic inductance for each device.

Most of the nanofabrication steps undergone by our hybrid devices are visually summarized in Fig. 3.8 and detailed in the following sections. Further comprehensive information regarding the practical aspects of each fabrication step can be found in Appendix D.

3.2.1. WAFER PREPARATION

The wafer preparation steps prior to dicing are shown in Fig. 3.8(a)-(e). We use high resistivity silicon substrates coated with low-pressure chemical vapor deposited (LPCVD) SiN_x[3]. For details on the impact of the LPCVD SiN_x on resonator performance, see Chapter 4. Prior to the deposition of NbTiN, the substrate is cleaned with fuming nitric acid. The exact cleaning steps are outlined in Appendix D.

Subsequently, a thin film of NbTiN is sputtered onto the entire 4-inch wafer, with the film thickness determined by the targeted kinetic inductance of the film. Opting for a thinner film results in a higher kinetic inductance and higher field compatibility. However, excessively thin films can lead to a larger variation of the kinetic inductance across the wafer, hindering accurate kinetic inductance targeting (see Appendix C for typical numbers). To strike a balance, we choose a film thickness of approximately 20 nm for the experiments requiring a modest kinetic inductance in the range of 10 to 15 pH/□. For Chapter 5, we instead require a higher film kinetic inductance of around 40 pH/□ and thus use a thinner film thickness of approximately 9 nm. Details on the temporal stability of the NbTiN sputtering parameters can be found in Appendix B.

In a subsequent step, not shown in Fig. 3.8, we pattern markers across the entire wafer. The markers have a size of 20×20 μm^2 and are used for alignment at the various e-beam lithography steps. When choosing the marker material, various aspects, such as fabrication ease, contrast under the electron beam and compatibility with subsequent nanofabrication steps, must be taken into consideration. One efficient option fabrication-wise would be to define negative-tone[4] markers together with the initial NbTiN dry etching step (see next section). However, given the typically small thickness of our NbTiN layers, this approach could lead to reduced contrast under the e-beam, hampering subsequent alignment steps. Moreover, the patterning of the base etching layer for the different devices presented in this thesis involves several layers that are written with different beams. Such layers must be aligned with each other, which requires alignment markers to be present before performing this first patterning step. An alternative approach, which we used for Chapter 5, is using positive-tone gold markers with high enough thickness, on the order of 100 nm. Gold markers offer nanofabrication bene-

[3] The SiN_x was deposited by Paolo M. Sberna at the Else Kooi Laboratory of the TU Delft.

[4] Negative-tone and positive-tone markers respectively appear darker and brighter than the surrounding material.

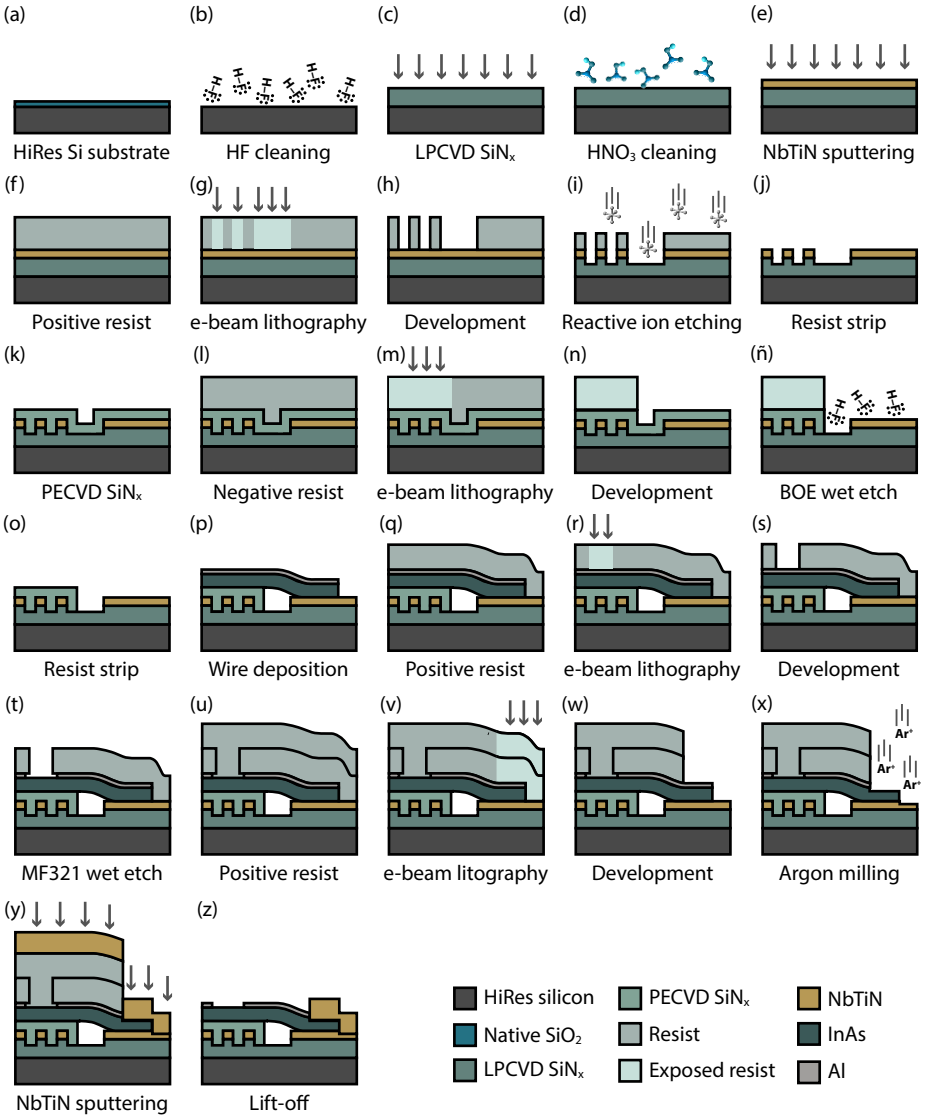

Figure 3.8: **Nanofabrication steps.** Diagrams showing the cross-section view after each of the nanofabrication steps undergone to fabricate a device, starting from a substrate (a) and ending with the depositing the nanowire contacts (z). The marker step and the two dicing steps —one between (e) and (f) and the other after (z)— are not shown.

fits, as they can be deposited at multiple evaporators of the Kavli Nanolab and are very easy to lift off. Moreover, the high gold atomic number translates into enhanced e-beam contrast, thanks to an increased backscattered signal. However, due to potential cross-contamination issues with other materials, gold is prohibited within certain deposition

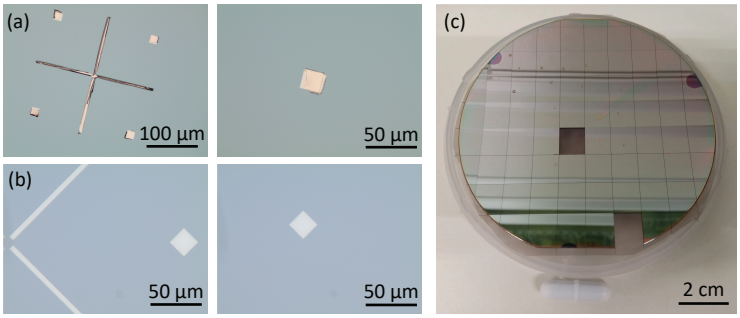

Figure 3.9: **Wafer preparation.** (a) Optical microscope images of ill-defined platinum markers obtained by performing a single evaporation step. (b) Optical microscope images of well-defined platinum markers obtained by performing three subsequent evaporation steps with cooldown times in between. (c) Photograph of a 4-inch wafer covered by dicing resist and diced onto smaller chips.

and etching cleanroom systems. In particular, it is not allowed in the reactive ion etching system used for Chapters 6, 7, 8 and 9 (see Appendix D). For these chapters, we explored different alternative materials. One such option which also has a large atomic number, thus leading to high e-beam contrast, is platinum (Pt). While Pt markers were used for the devices in Chapter 6, we often found that thin films of platinum showed a high surface roughness when deposited on 4-inch wafers, resulting in ill-defined markers. Fig. 3.9(a) and (b) show Pt markers obtained from two different depositions. Despite both Pt evaporation processes using identical parameters, the Pt markers in the first deposition exhibit lift-off imperfections, absent in the second deposition. The only differences lay in that, for the markers in Fig. 3.9(a), the deposition was done over a complete 4-inch wafer and in a continuous manner, while, for those in Fig. 3.9(b), it was performed over half of a 4-inch wafer and in three subsequent deposition steps with 20 min cooldown intervals between them. We hypothesize that the imperfections found in the first deposition may be attributed to either high tensile stress on the films (Afshar et al., 2010) or inadequate thermalization during metal evaporation. To avoid the complications found for Pt marker fabrication, for Chapters 7, 8 and 9 we instead converged to using palladium (Pd) markers. Pd markers have proven simple to fabricate in a reproducible way, show enough e-beam contrast, and are compatible with most nanofabrication tools.

After marker deposition and lift-off, the wafer is coated with dicing resist and diced onto smaller chips of approximately 1×1 mm^2, as shown in Fig. 3.9(c). Subsequently, the chips are reserved and used to fabricate the different devices. The dicing resist is left on each of the chips, serving as a protective layer. The chips are then stored in a cleanroom space until further processing, a period typically spanning from a few days to several months after the wafer's initial preparation.

3.2.2. SUBSTRATE PREPARATION PRIOR TO THE NANOWIRE DEPOSITION

For each individual chip, we maximize the number of nanofabrication steps that are performed before depositing the Al/InAs nanowires. This is done to mitigate potential detrimental effects on the nanowire, which could arise from the different steps. Such effects

can be due to factors such as electrostatic discharge, mechanical stress during e-beam resist application and lift-off, or elevated processing temperatures leading to diffusion of the aluminium shell onto the InAs nanowire core. The steps performed prior to nanowire deposition are schematically depicted in Fig. 3.8(f)-(o) and involve the definition of the NbTiN circuitry by dry etching and the subsequent deposition of the bottom gate dielectric.

The processing of an individual chip begins by removing the dicing resist using an organic solvent (not shown in Fig. 3.8, see Appendix D). Following this, we define all of the NbTiN base layer structures using electron beam (e-beam) lithography. To enhance precision in regions with finer structures, such as gates and narrow inductors, we use an electron beam with a low current and a small spot size. The coarser structures are instead patterned with an electron beam with a higher current and larger spot size, thus reducing the exposition time. Strategically adjusting the current and spot size of the electron beams across different layers results in significant reductions in overall writing time, from multiple hours down to approximately 10 to 20 minutes.

During the base layer definition step, we also pattern holes in the superconducting film (Kroll et al., 2019). The holes configuration, while always distributed in a honeycomb lattice, varies depending on the region of the device and on their function. For the regions of the ground plane near any microwave circuitry structures, as well as for the capacitive transmon and resonator pads and the inner conductor of the feedline and drive lines, we use small holes. These holes serve as pinning sites for magnetic vortices and their specific geometry varies among chapters, with diameters ranging from 70 to 100 nm and inter-hole distances spanning 320 to 550 nm. This minimizes the disruption to the transmon and resonator capacitance, as well as to the impedance of the feedline and drive lines, values which we simulate without accounting for vortex pinning sites. For the wide ground plane regions which are far away from the main structures, we instead use larger holes with a squared shape to allow for magnetic field penetration and reduce the amount of ground plane surface that is exposed to it. These bigger holes have an edge length of 500 nm and an inter-hole spacing between 1.5 and 2.2 µm depending on the chapter, to reduce the total writing time.

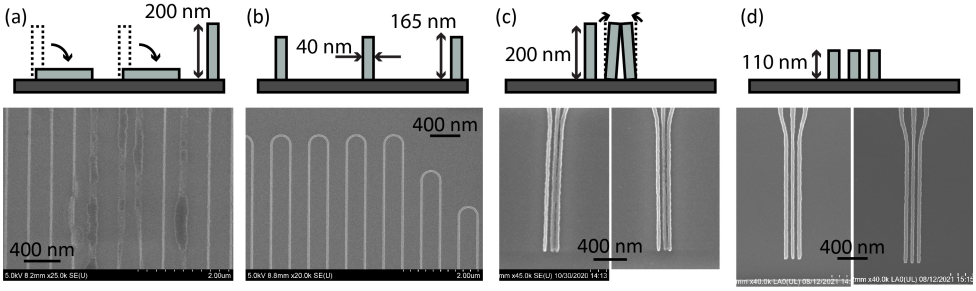

Figure 3.10: **Fine structures optimization.** (a), (b) Scanning electron micrographs (SEMs) of the fluxonium inductors after NbTiN etch for two different resist thicknesses: 200 nm and 165 nm, respectively. (c), (d) SEMs of quantum dot junction bottom gates after NbTiN etch for two different resist thicknesses: 200 nm and 110 nm, respectively. The top panels show schematics of the device cross-section after resist development in each case.

Finally, during the e-beam patterning of the base layer we consider different aspects

to enhance the definition accuracy of the fine structures. Apart from using a small-sized beam with a precisely calibrated dose, we use proximity effect correction (PEC) in the vicinity of narrow gates and inductors. Additionally, for certain devices, we develop using the critical point drying (CPD) method to ensure a more gentle process. Moreover, we found that using too thick resist can lead to undesired outcomes, as exemplified in Fig. 3.10. For Chapter 5 we need to define a meandering inductor with a width of around 35 to 50 nm. When we employ a 200 nm-thick e-beam resist layer (Fig. 3.10(a)), the resist often collapses due to its high aspect ratio after development, resulting in poorly defined inductor shapes. Using instead a resist layer of 165 nm leads to more reproducible and well-defined structures (Fig. 3.10(b)). Similarly, in Chapters 6, 7, 8 and 9 we pattern 40 nm-wide gates spaced roughly 40 nm apart. A 200 nm-thick resist layer often leads to two neighboring gates shorting due to the resist's high aspect ratio, as shown in Fig. 3.10(c). Using 110 nm-thick resist instead leads to better defined gates (Fig. 3.10(d)). Note that the minimum resist thickness that can be used is, in each case, determined by the duration of the NbTiN etching step (Fig. 3.8(i)), during which the resist is etched at a rate of approximately 1.8 nm/s. This constrains the thickness to at least 60 nm for Chapter 5 and at least 100 nm for Chapters 6, 7, 8 and 9. See Appendix D for the exact etch details used for each of the experimental chapters.

For all experiments performed in this thesis, we use a SiN_x layer of approximately 28 nm as the gate dielectric. This dielectric film is first epitaxially grown over the entire chip using plasma-enhanced chemical vapor deposition (PECVD) (see Fig. 3.8(k)). It is subsequently etched so that it only remains over specific regions (see Fig. 3.8(l-o)). To detect potential variations of the PECVD deposition rate over time, an ellipsometry measurement of the film thickness is usually performed on a test chip following each deposition. This measurement determines the deposition time used for the following devices. While performing the experiments detailed in Chapter 5 we confirmed that the gate dielectric layer remains resilient up to a voltage offset of approximately 7 V, after which point the dielectric breaks down. Consequently, to mitigate potential issues arising from excessive voltage offsets and current leakage across the dielectric, the gate voltages are intentionally maintained below 4 V throughout the experiments discussed in the subsequent chapters.

3.2.3. NANOWIRE-SPECIFIC STEPS

The nanowire-related nanofabrication steps, schematically depicted in Fig. 3.8(p)-(z), include the nanowire deposition process, the junction etching and the establishment of electrical contact between the nanowire and the underlying circuitry. Optical images of the device chip before and after each of these steps are shown in Fig. 3.11. The InAs nanowires used in this thesis are grown with the vapor-liquid-solid (VLS) method and have a length of approximately 10 µm. They have a hexagonal cross-section and are covered by epitaxially grown aluminum on two of their facets (Krogstrup et al., 2015).

The transfer from the growth chip to the device chip is performed under an optical microscope using a commercially available tungsten needle attached to a micromanipulator[5]. During the design and fabrication of the device chip, different aspects can be

[5] For Chapter 5 the deposition is performed by Kongyi Li and, for all other chapters, it is performed by Lukas J. Splitthoff.

considered to streamline the nanowire deposition process. As the deposition can be performed with an accuracy of approximately 1 µm in the longitudinal direction, maintaining a short distance between contact pads (7 µm or less) facilitates comfortable nanowire placement. Similarly, wider contact pads result in a broader deposition area, with 2 µm providing adequate space for comfortable nanowire deposition.

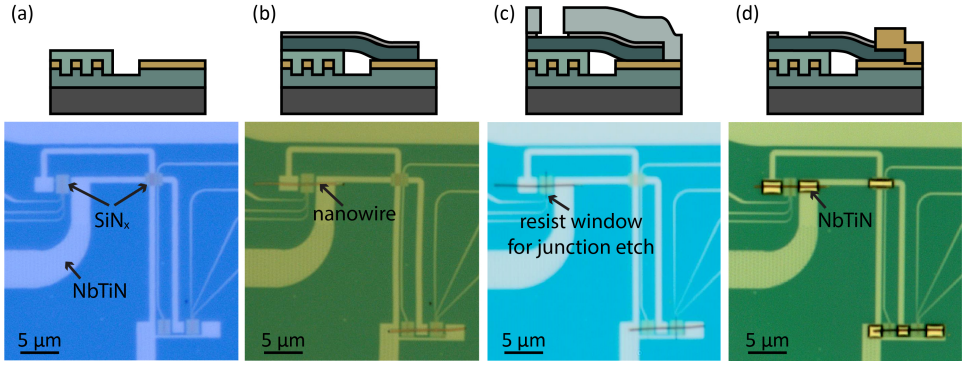

Figure 3.11: **Nanowire-specific nanofabrication steps.** Optical microscope images of the nanowire area. (a) Right after dielectric etch and before nanowire deposition (Fig. 3.8(o)). (b) Right after nanowire deposition (Fig. 3.8(p)). (c) Right after junction etch (Fig. 3.8(t)). (d) Right after contact lift-off (Fig. 3.8(z)). The top panels show schematics of the device cross-section at each step, with the same legend as in Fig. 3.8.

Following the nanowire deposition, the junctions are defined by etching away the aluminium on a nanowire section on top of the pre-patterned gates (see Appendix D). The resist mask used for selectively wet-etching of these aluminium segments can be seen in Fig. 3.11(c). After etching, the e-beam resist that covers the nanowires is not removed, to prevent potential nanowire displacement on the chip surface. Instead, a new layer of resist is applied (Fig. 3.8(u)) and used to pattern the contacts that galvanically connect the nanowire to the underlying circuitry.

The contact fabrication process entails the removal of surface oxides through argon milling (Fig. 3.8(x)), followed by sputtering a 120 nm-thick layer of NbTiN (Fig. 3.8(y)). These two processes are also used to define NbTiN structures in other chip areas, as needed depending on the device. In Chapter 5, such parts are the feedline and fluxline (not used), the top fluxonium capacitor plate, the gate bonding pads, and the gate jumps over the fluxonium inductor. For Chapters 6, 7, 8 and 9, this step is used to create the capacitive parts of the gate line low-pass filters. Finally, in Chapter 9 this step is also used to fabricate the top capacitor plate of the flux line low-pass filter and, as shown in Fig. 3.11(d), the loop twist overjump.

3.2.4. POSTFAB AND FINAL DEVICE CHECKS

The final fabrication steps prior to loading the device into the cryogenic refrigerator, which are not included in Fig. 3.8, comprise dicing, probing and wire-bonding the device to the printed circuit board (PCB).

The chips are diced to match the size of the PCB sample area (see Sec. 3.3.2 for PCB details), which is either 2×7 mm^2 or 6×6 mm^2 depending on the chapter. To prevent

damage to the nanowires due to electrostatic discharge during dicing, the process is only initiated when the dicing water resistivity drops below 1 Ω.

Subsequently, the room temperature resistance of different circuit elements is determined by probing the device using tungsten needles, as shown in Fig. 3.12. Measuring the resistance between the resonator island and the ground plane facilitates estimating the resonator inductance (see Appendix C) and, in turn, its resonance frequency. A similar estimate can be obtained by probing the resistance between input and output feedline ports for the devices without an input capacitor. Similarly, the resistance between the transmon island and ground provides information about the quality of the nanowire contacts. For working devices as those in Chapter 9, resistance measurements ranging from 20 to 200 kΩ are typically observed between the transmon island and ground. Additionally, the resistance between chip lines and ground is probed to identify potential short circuits.

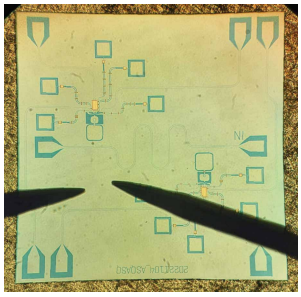

Figure 3.12: **Optical image of a diced chip being probed at the probing station prior to wire-bonding.**

Finally, the chip is mounted onto the printed circuit board and wire-bonded to it using aluminum bonds. We include short bonds along the chip edge that connect the ground plane of the chip to that of the PCB. In addition to establishing a homogeneous ground connection, these bonds serve as a path for heat dissipation away from the chip during cool-down. For each device, the radio-frequency (RF) lines design is realized to position their bonding pads in close proximity to corresponding bonding pads on the PCB. This configuration enables the use of wire bonds that are as short as possible, minimizing the potential for undesirable RF signal reflections resulting from impedance mismatches, as the longer wire-bonds have a large inductance (see Fig. 3.13(a) and (b)). This consideration, however, does not apply to the direct current (DC) lines, whose on-chip length is instead minimized to prevent unwanted line self-resonance. Consequently, the wire bonds arriving at the DC lines' bond pads are relatively longer (see Fig. 3.13(a) and (b)).

Finally, we incorporate on-chip bonds that interconnect different ground plane regions. Such bonds prevent the formation of unwanted resonance modes and result in a more uniform ground reference across the chip, resulting in higher internal quality factors of the resonators. An example of a chip with four resonators that initially had a single on-chip bond is visible in Fig. 3.13(a), black curve in (c). The same device with extra on-chip bonds is shown in Fig. 3.13(b), red curve in (c). As shown, the internal quality factors increase significantly.

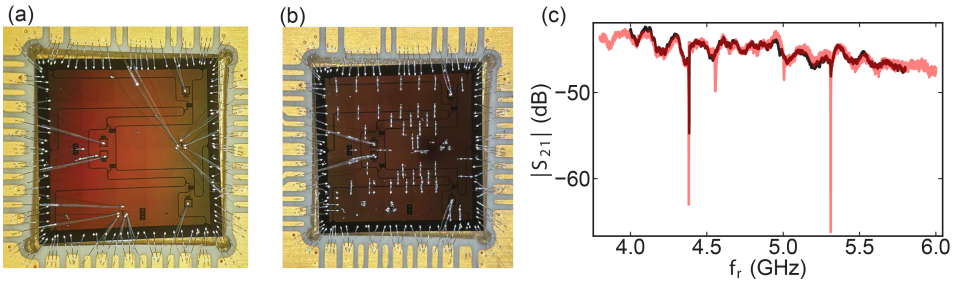

Figure 3.13: **Comparison of spectra with and without on-chip bonds.** (a) Optical microscope image of a chip with four resonators, with only a single on-chip bond. The ground plane was simply-connected on-chip because the resonators are encircled with ground strips. (b) Optical microscope image of the same device after warming up and adding many on-chip bonds. (c) Microwave response through the feedline for the cooldown of the bond configuration of (a) (black) and (b) (red), illustrating the increase in internal quality factor after adding on-chip bonds. The curve without on-chip bonds is offset by 25 dB to account for attenuation and cable changes at the room-temperature equipment between the cooldowns.

3.3. EXPERIMENTAL SETUP

3.3.1. CRYOGENIC SETUP

The experiments presented in this thesis are performed at temperatures of a few tens of mK to suppress thermal excitations, and they involve magnetic fields on the order of 1 T. To achieve these conditions, all experiments are performed using cryogenic dilution refrigerators equipped with vector magnets. An exception is made for fast resonator characterization at zero field, performed while iterating the chip designs, which are carried out using an Oxford Instruments Heliox system, a sorption-based ^{3}He insert. In particular, for Chapter 5 we use a Bluefors XLD refrigerator, nicknamed "QT2". For Chapters 6, 7 and 8, we instead use a Triton 300 refrigerator from Oxford Instruments, nicknamed "K2". Finally, for Chapter 9 we use a different, but almost identical, Triton 300 refrigerator, nicknamed "K1".

A simplified schematic of a Triton 300 system is shown in Fig. 3.14. The inside of the fridge is maintained under high vacuum and separated by the exterior by the outer shield shown in red. Within it, multiple layers of inner shields, each thermally anchored to a different temperature stage, prevent radiation towards the interior of the fridge. The fridge is equipped with a multi-axis vector magnet capable of reaching magnetic fields up to 6 T in the vertical direction and up to 1 T in the horizontal plane. This magnet is thermally anchored to the PT1 plate, which is kept at around 4 K, thus maintaining the superconducting state of the magnet coils. The sample is situated within a cylindrical enclosure known as the puck. The puck is situated at the center of the magnet but is thermally anchored to the lowest temperature stage, referred to as the mixing chamber (MC). The MC can reach a base temperature of 10 to 20 mK.

A bottom-loading mechanism enables sample exchange while maintaining the system's low temperature[6] and vacuum conditions (Batey et al., 2014). The bottom-loading

[6] Note that, during sample exchange, the system is not at base temperature. As the ^{4}He/^{3}He mixture has to be collected during sample exchange, the MC temperature rises to a few Kelvin before and during the process. Right after inserting the new sample, the system temperature reaches a few tens of Kelvin due to the extra

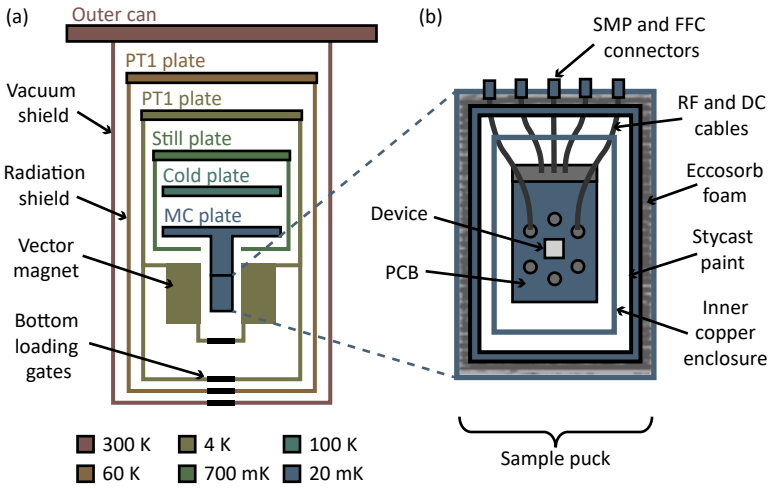

Figure 3.14: **Dilution fridge and sample puck.** (a) Diagram of a dilution refrigerator. Different colors denote different temperature stages. The shields prevent radiation from the outer temperature stages towards the inner ones. The puck (blue rectangle, enlarged in (b)) is thermally anchored to the lowest temperature stage and placed at the center of the vector magnet. The loading gates at the bottom of the fridge (black rectangles) permit inserting the puck into the fridge while keeping the fridge cold and under vacuum. (b) Puck formed by an outer can and various copper enclosure boxes which shield against radiation. The gap between the outer can and the outer enclosure box is filled with Eccosorb foam, which absorbs stray microwave radiation. The outer enclosure box is moreover pained on both sides with a mixture of silicon carbide grains, Stycast and carbon powder (Bargerbos, 2023b).

gates, depicted in black in Fig. 3.14(a), open when pushed upward by the exchange mechanism and allow passage of the puck from the outside to the inside of the fridge, and vice-versa. When the puck is pressed onto the MC stage, its lines are connected to those inside the fridge.

The refrigerators used in this thesis are equipped with both radio-frequency (RF) and direct-current (DC) lines. The precise attenuation, filtering and amplification of each RF line differ based on its intended function, as detailed in the supplementary section of each of the experimental chapters (Krinner et al., 2019). A schematic of the DC lines is shown in Fig. 3.15.

The DC lines, totaling 48 in number, are connected to the room-temperature DC electronics outside of the fridge via two separate Fischer cables, each containing 24 lines. At the higher temperature stages within the fridge, these lines are divided into two distinct bundles of 24 lines each. Successive sections of these bundles are interconnected at each temperature stage using micro-D (Ohmnetics) connectors. In the mixing chamber stage, each line passes through a series of low-pass filters (see Fig. 3.15(b))[7]. Each filter board is thermally anchored to the MC through a large surface to enable efficient heat dissipation. Upon entry into the puck, the two bundles merge into a single group,

heat load.

[7] The design of these filter boards was carried out by Maja Cassidy and Rogier van de Berg from DEMO, the electronics shop of the TU Delft.

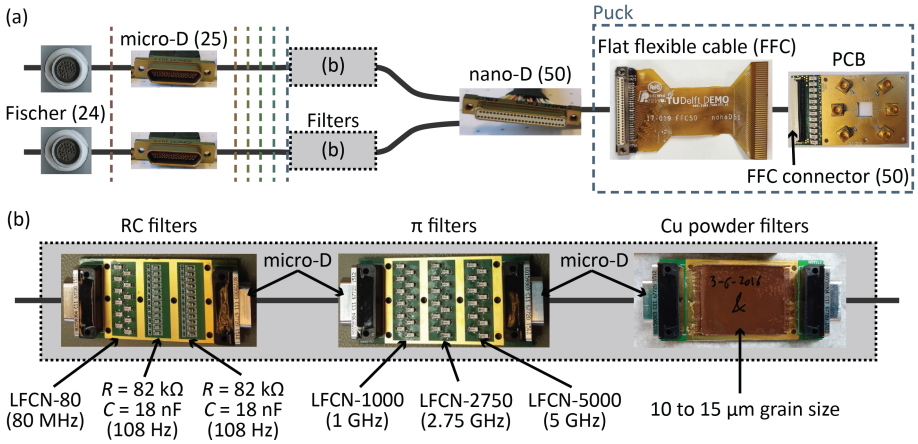

Figure 3.15: **DC cryogenic wiring and filtering.** (a) DC wiring from the top of the fridge (left) to the bottom of the fridge (right). The dashed lines indicate the different temperature stages, with the same legend as in Fig. 3.14. (b) Photographs of the three subsequent filter boards placed on the mixing chamber. The frequencies in the labels denote the 3 dB point of each filter.

soldered to a nano-D (Ohmnetics) connector. Within the puck itself, a nano-D to flat flexible cable (FFC)[8] adapter directly connects the DC lines to the printed circuit board (PCB). On the PCB, each DC line features an additional low-pass filter, as discussed in Sec. 3.3.2. On the PCB, 16 of the lines are directly routed to the sample and 4 other lines are combined with RF lines via bias tees (see Fig. 3.16(d)). The remaining 28 lines are shorted to ground and remain unused.

3.3.2. HYBRID PRINTED CIRCUIT BOARD DETAILS

Throughout this thesis, we used hybrid DC-RF printed circuit boards to route the DC and RF signals from the fridge lines to the chip[9]. The latest version of this hybrid PCB design at the time of writing[10], which was employed in the experiments detailed in Chapter 9, is presented in Fig. 3.16. The hybrid PCB has a total thickness of 705 µm and it is composed of four copper layers separated by insulating layers of different materials and thicknesses, as indicated in Fig. 3.16(b). The board is gold-plated to prevent oxidation of the outer copper layers. Throughout the board, through-hole ground vias (indicated by black circles in Fig. 3.16(e-h) uniformly interconnect the ground reference of all layers. The sample area, with a squared shape, is situated in the central part of the board and is surrounded by bonding pads that permit bonding the chip to different DC and RF PCB lines.

[8] Although similar flexible cables are commercially available, the FFCs used in this thesis were designed in-house and tailored to fit the particular needs of the experiments conducted in this thesis. This was done by Jason Mensingh and by Kees Esser from DEMO, the electronics shop of the TU Delft.

[9] Note that, for the resonator characterization measurements performed at the Heliox, we instead used simpler only-RF PCBs with a circular shape and formed by just two copper layers separated by a single dielectric layer.

[10] This design, adapted by Kees Esser to accommodate a greater number of DC lines and larger chip sizes, is an extension of Maja Cassidy's original concept, and incorporates elements from a variation by Angela Kou. The boards are machined by Fineline.

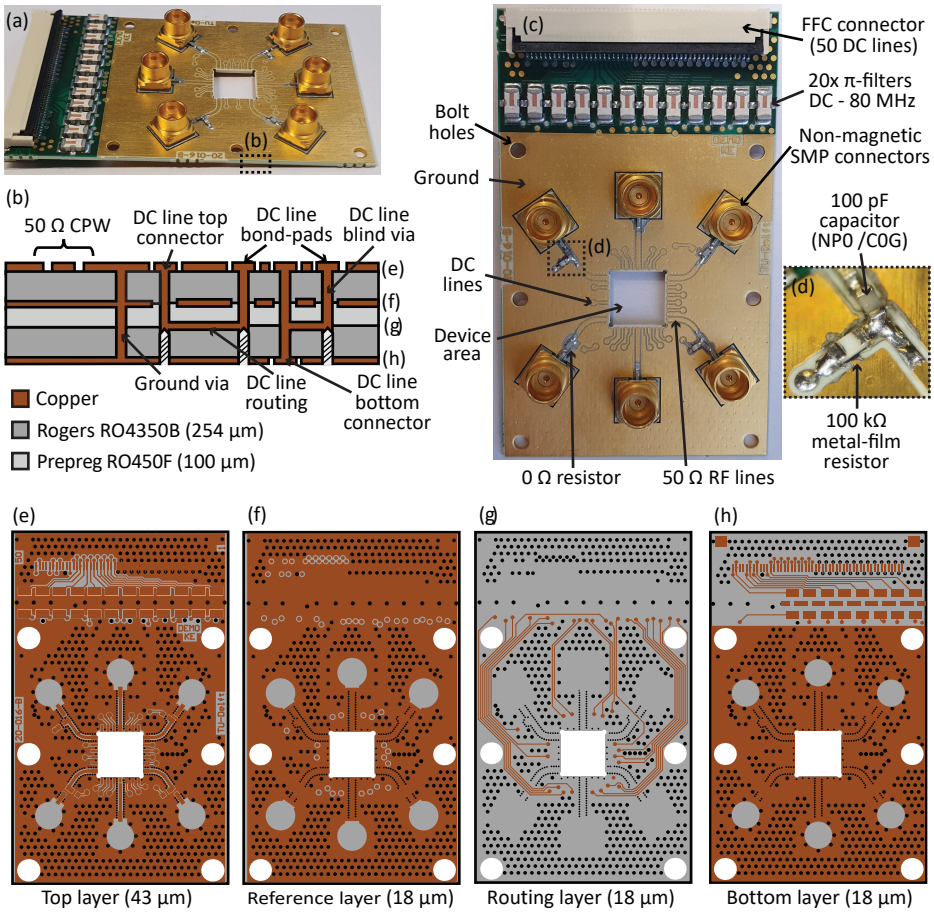

Figure 3.16: **Printed circuit board (PCB) design.** (a) Photograph of the hybrid PCB from an angle. The cross-section is enlarged in (b). (b) Diagram of the PCB cross-section (not to scale) showing four copper layers separated by three insulating layers. Through-hole vias connect all four copper layers together. Blind vias connect only the three topmost layers. Not shown is the gold-plating layer which covers all exposed metallic surfaces. (c) Top view of the PCB showing the different components assembled on the top layer. (d) Enlargement of the bias tee, composed of a resistor and a capacitor. (e-h) Diagrams of each of the four layers.

The 48 fridge DC lines from the fridge reach the board through an FFC connector (see Fig. 3.16(c)). To prevent problems derived from electrostatic discharge during loading and unloading the puck from the fridge, two copies of the FFC connector are placed on the front and back of the PCB, shorted to each other. This arrangement ensures that all lines remain grounded when a shorting strip is connected to one of the FFC connectors while the other one becomes connected or disconnected from the fridge. Among the 48 fridge DC lines, only 20 are used; the rest are shorted to ground. Each of the 20 lines is filtered on the PCB with a low-pass π-filter with a cutoff frequency of 80 MHz. These π-filters are arranged as a capacitance to ground, followed by an inductor, and then an-

other capacitance to ground, resembling the shape of the Greek letter π. Twelve of the π-filters are situated on the top part of the board (visible in Fig. 3.16(a) and (c)). The remaining eight are instead placed on the bottom part (see filter pads in Fig. 3.16(h)). Following the filters, all DC lines are connected to the third layer of the PCB. For the DC lines that come from the top of the PCB, this connection is established via blind vias, while, for the ones that come from the bottom, it is done via through-hole vias, as indicated in Fig. 3.16(b). All DC lines are then routed on the third layer until reaching the sample area, as shown in Fig. 3.16(g). Subsequently, additional blind vias bring the DC lines up to the top PCB layer, where they reach the bond pads situated at the edge of the sample area. All blind vias are machined by Fineline using the back-drilling technique. This method involves a first step where a complete through-hole via is fabricated. Such through-hole via is subsequently selectively drilled to a precise depth using a drill tool with a diameter larger than that of the hole of the original via (see Fig. 3.16(b)). This procedure prevents undesirable antenna and cross-talk effects that could be caused by the unconnected vias parts or stubs, enhancing overall signal integrity.

The RF signals instead reach the board through six non-magnetic Rosenberger subminiature push-on (SMP) connectors, serving as both entry and exit points. From there, the RF lines are routed through the surface of the board until the edge of the sample area. The surface RF lines are implemented with conductor-backed coplanar waveguide (CPW) transmission lines with a 50 Ω impedance and use the second layer as the bottom ground reference (see Fig. 3.16(f)). Out of the six RF lines, two are directly routed to the edge of the sample area and are used as input and output lines for transmission measurements. The remaining four RF lines incorporate pads with 0402 footprints, allowing versatile component integration based on the specific experimental requirements. For instance, in Chapter 9, one of the RF lines is purposed as a flux line by connecting a 0 Ω surface-mounted device (SMD) resistor to it. Another RF line is instead used as a drive line through an electrostatic gate. To combine the DC and RF components of the signal, we mount a bias tee on the line, as shown in Fig. 3.16(d). On the DC part of the bias tee, we connect a 100 kΩ SMD resistor of the thin-film type (Panasonic ERA-2AEB104X), while on the RF part, we connect a 100 pF SMD multilayer ceramic capacitor (MLCC) of type NPO (Kemet C0402C101J5GACTU). These components result in an RC time constant of 10 µs, equivalent to a cutoff frequency of 16 kHz.

3.3.3. DETAILS ON MAGNETIC FIELD CONTROL

One of the key new parameters varied in the experiments presented in this thesis, when compared to other experiments with superconducting circuits, is the global magnetic field. Thus, naturally, we spent some time optimizing the setting of this field. All devices that are shown in this thesis are cooled down in dilution refrigerators with a commercial 6 T-1 T-1 T axis vector magnet. These magnets are generally made by three independent superconducting coils. Each coil is controlled with a separate current source. Typically the coil constants of the 1 T axes are around 60 A/T and these of the 6 T axes are 12-16 A/T. Thus, for using the full field range, one needs a large 100 A rated current source. This range is supported by the commercially available sources that are delivered with the magnets (in our case from mercuryIPS (see Fig. 3.17(b)) and American Magnetics Inc.). Due to the large operation range, the minimum step size of these sources is generally

quite large, for example, the American Magnetics Inc. current source has a quoted programming accuracy of 50 mA and a stability of 25 mA, which corresponds to about 1 mT and 0.5 mT resolution and stability respectively (in reality the resolution and stability are much better). For the mercuryIPS the quoted stability is ±2 mA (33 μT) and minimum step size is 0.15 mA (2 μT).

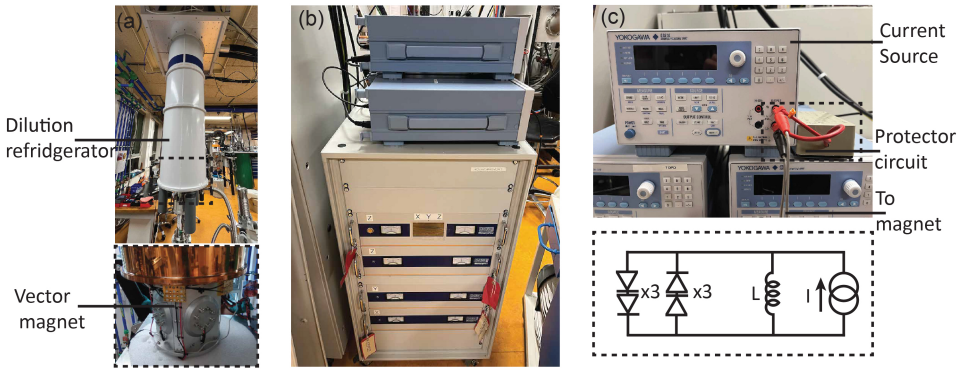

Figure 3.17: **Triton dilution refrigerator with a** 6 T-1 T-1 T **vector magnet and current sources used for magnetic field control.** (a) Top panel: Triton dilution refrigerator with all shields installed and bottom loader. Bottom panel: vector magnet attached to the still shield. The pucl is loaded via the bottom loader in the bore of the magnet. (b) Large (bottom) and small (top) current sources used to control the magnets. (c) Zoom in on the Yokogawa GS610 current source used for fine-stepped field control connected to the magnet leads, together with a diode protection box wired in parallel, as shown in the wiring diagram (bottom panel).

For flux control we only apply fields of a few millitesla. Therefore, we used smaller current sources to control these axes. For example, if one has a 10 μm^2 area SQUID loop, the field required to thread one flux quantum is approximately 200 μT (12 mA). The current sources used were the Yokogawa GS200(GS210), rated up to 200 mA, and the GS610 source measure unit, rated up to 3 A with minimum current step size of 1 μA for < 200 mA, 10 μA for < 3 A (see Fig. 3.17(c)). During an in-house stability test by Raymond (our electronics expert), we found the output current to drift during setting it at 1 A for about one hour (no temperature control applied) by approximately 60 μA (1 μT).

The larger current sources supplied with the magnets have built-in quench protection. To protect the Yokogawa current sources in case of a sudden quench of the magnet, which is not rated for such large inductive loads, we built a small safety box (see Fig. 3.17(c)). The box contains two antiparallel rows of several Schottky diodes in series that all together can be added in parallel with the magnet current loop. The main functionality is that, when a large voltage develops —a rapid change in current during a quench generates a voltage proportional to the inductance of the magnet, which is several Henry—, it allows current to flow through the diodes. As a result, the voltage stops increasing. When the voltage is low, however, no current can flow (otherwise the magnet field setting might be affected). The choice of diodes thus was aimed at having a negligible current at the operation voltages, while being able to handle the full 3 A current in case of a quench.

LOOP DESIGN CONSIDERATIONS FOR PROPER FLUX CONTROL

We found that, even after optimizing the circuit for field compatibility with holes and thin components, small out-of-plane fields of several tens of μT could still cause both large and small flux jumps through the superconducting SQUID loops, hindering the use of flux as a controlled parameter in our initial experiments. However, we found that the vertical offset of the nanowire over the gate and dielectric creates a small vertical loop with an area of around $0.3\,\mu m^2$ for 28 nm SiN_x of gate dielectric. With this design, it is possible to use a magnetic field parallel to the chip plane and perpendicular to the nanowire for flux biasing. As a result, the flux period is several mT per flux quantum. With this configuration, the cross-section of the superconductor area exposed to a magnetic field is proportional to the film thickness (tens of nanometers) instead of the width of the chip (several millimeters), greatly reducing the observed flux jumps. Various sketches of possible loop designs that can be used to exploit this mechanism are shown in Fig. 3.18. Interestingly, it would be possible to design a SQUID without a loop in the vertical direction, as shown in Fig. 3.18)(c), which could allow for compact circuits or loops with small footprints.

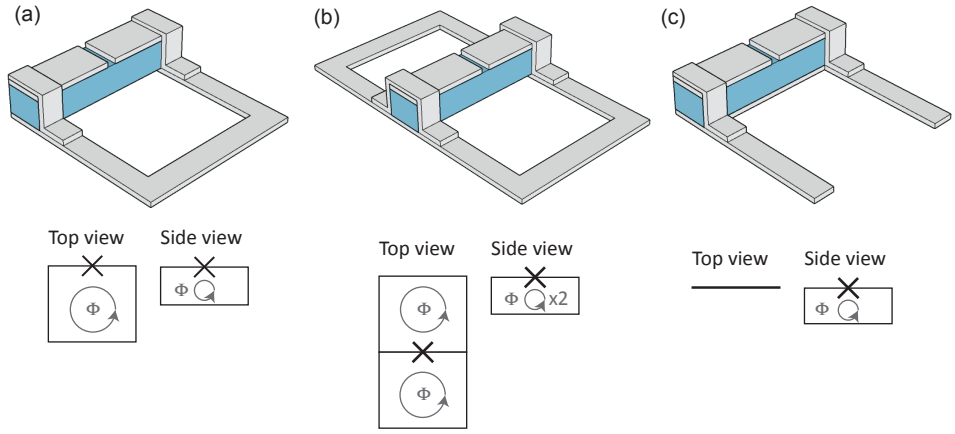

Figure 3.18: **Schematic of vertical loop superconducting quantum interference devices for parallel field flux biasing.** (a) RF-SQUID with a single loop and Josephson junction. The suspension of the junction allows flux biasing using either a parallel or a perpendicular field. (b) Gradiometric RF-SQUID design, which cancels perpendicular flux and amplifies parallel flux by a factor of two. (c) Vertical RF-SQUID loop solely defined by the elevated nanowire. See Ref. (Wesdorp and de Lange, 2020) for more details. A fourth iteration of a loop design is given in Chapter 9 (Fig. 9.9), where the loop is twisted (Pita-Vidal et al., 2023).

In Chapter 5 we use a gradiometric design (see Fig. 3.18(b)). In this design, the total flux is proportional to the area difference between the two loops. By designing the areas to be equal (up to the accuracy of the nanowire placement), one can become nearly insensitive to a global out-of-plane magnetic field. One of the advantages of this design is that each of the individual loops can still be large, simplifying the design of large loop inductances and allowing the use of on-chip flux lines in combination with a global magnet, as we do in Chapter 9.

FLUX JUMPS DUE TO ON-CHIP WIREBONDS

Even while using the in-plane magnetic field for flux control, flux jumps can still occur. We found that the presence of on-chip wire bonds can lead to undesired flux jumps when sweeping the B_y component of the magnetic field (parallel to the chip plane and perpendicular to the nanowires). This phenomenon is attributed to the wire bonds having a cross-sectional area in the B_y direction, as the ones shown in Fig. 3.19(c). As, at zero magnetic fields and cold temperatures, these wire bonds are superconducting, an applied B_y field produces a circulating supercurrent that passes through them and through the chip plane. This circulating supercurrent, in turn, generates an out-of-plane field that affects the flux through the device loop. As the magnitude of B_y is swept, spurious currents are produced in the loop that contains the bond wire, resulting in unwanted flux jumps on the device.

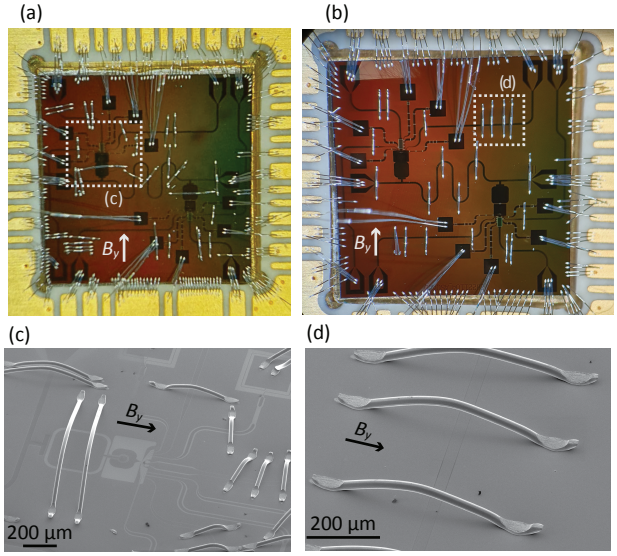

Figure 3.19: **Field-aligned wire-bonding.** (a) Optical microscope image of a chip bonded with an on-chip bond configuration that results in multiple flux jumps when sweeping the B_y on-chip component of the magnetic field. This bonding configuration includes multiple bonds with a y cross-section underneath on-chip bonds that are in the region nearby the nanowire region. (b) Similar to (a) but for an almost identical device for which the on-chip bonds are instead made along the y direction. The length of the side of the chip is 6 mm. (c)-(d) Scanning electron micrographs (SEM) showing enlargements of different wire-bonds. These images correspond to a device almost identical but different from the ones shown in (a)-(b). (c) shows wire bonds with a y cross-section placed over the resonator. (d) show wire bonds without a y cross-section that connected the pieces of ground plane on both sides of the feedline and drive line, respectively.

Throughout this thesis, different strategies are used to mitigate such undesired effect. In Chapter 5, we apply B_z and not B_y to tune the flux, so this effect is not observed. For device A in Chapter 6, the flux jumps are observed in the absence of a magnetic field. To circumvent them, we apply 10 mT and turn the bond wires normal. In this way, supercurrents can not circulate through the bond wire, resolving the issue (see Fig. 6.16 in Chapter 6). This is however not a general solution as, in general, we need to measure

the flux dependence of devices also in the absence of a magnetic field. For this reason, for device B in Chapter 6 and for the device investigated in Chapters 7 and 8, we instead incorporate a ground plane cut that interrupts the ground plane in the vicinity of the device (see Fig. 6.13 in Chapter 6 and Fig. 7.10 in Chapter 7). This cut prevents supercurrents from circulating in ground plane regions nearby the device, again resolving the flux jumps issues. Meanwhile, in Chapter 9 we follow a different strategy. We found that flux jumps are most often observed while sweeping B_y for devices that have wirebonds perpendicular to the B_y direction, as that shown in Fig. 3.19(a, c). However, when the on-chip bonds are instead arranged parallel to the B_y direction (as those in Fig. 3.19(b, d)), we find that the frequency of flux jumps is substantially reduced.

3.3.4. MEASUREMENT AND DATA PROCESSING

As has become the standard in experimental condensed matter physics, we use *Python* to code up measurement, analysis and plotting scripts. In general, our approach to data collection can be summarized in the following statements:

1. A measurement result should be accompanied by sufficient metadata, such that a person who did not perform the measurement can figure out what all instrument settings were.

2. The order in which the measurements were performed should be clear.

3. The intention of the experimenter for taking the measurement should be retrievable.

To adhere to the first point, we use *qcodes* as our measurement framework. For each instrument in the setup, *qcodes* generates a snapshot of its settings that is saved along with each dataset. We extend this feature by creating so-called virtual instruments. These are used to store additional information of interest during our experiment in the snapshot. For example, one such virtual instrument is called Magnet3D and saves all the settings of the field alignment angles used and has additional functions that allow one to sweep various coordinates in the rotated frame of the chip.

To adhere to the second point, *qcodes* stores the data in a *sqlite* database that contains timestamps and incrementing IDs. Together with the *plottr* software package, one can easily inspect the data in chronological order to quickly get a data overview.

The third point is covered by making annotations in the laboratory notebook, for which we use *OneNote*. The idea is that, because all data is saved in the *qcodes* snapshot, one should never have to write down a setting or value in the lab notebook. Thus, *OneNote* is reserved to write down the interpretation and motivation behind the datasets, together with plots of the results.

DATA PROCESSING FOR A MANUSCRIPT

We now describe the typical procedure followed when a collection of data is complete enough to make a manuscript. Recently, a large effort from the university has been directed towards promoting open science, and especially towards open data. Here, open data means that anyone should be able to find the raw data underlying the manuscript, reproduce the figures, inspect the code analysis line-by-line, and, perform their own

analysis on the raw data. All this should be possible on a generic hardware. More formally, the following open data levels are suggested (Akhmerov and Steele, 2019):

1. Level 0: Publication of the processed data files as plotted in the figures in the paper.
2. Level 1: Publication of the raw data, as recorded by our computers, along with software and processing scripts that derive the plotted data from the raw data.

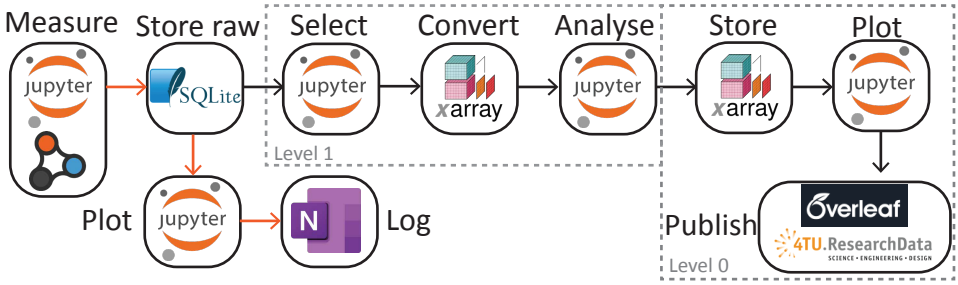

Figure 3.20: **Data processing pipeline.** Two routes are illustrated, with icons representing the specific software or package used for the step. A fast route to go from measurements to logging the data in the lab notebook during day-to-day work (in orange), and a longer route that prepares a selection of the data for publication. Grey boxes indicate steps needed to reach the open data standards as defined in Ref. (Akhmerov and Steele, 2019).

We have generally adhered to level 1 by using the steps shown in Fig. 3.20. First, we select the data of interest and convert it (without processing) to a more generally accessible format *.netcdf* using the *xarray* package. With this format, access to variables in arrays is done by the variable name, such that the analysis code that follows becomes more readable. The selected data is then analysed using a combination of custom-written functions (usually shared within the team with *git* version control) and open-source libraries. The results of this analysis are then stored again using *xarray*, or *pickle* for unsupported formats. Finally, the processed data is plotted (without additional processing) using *Python* and input in the manuscript.

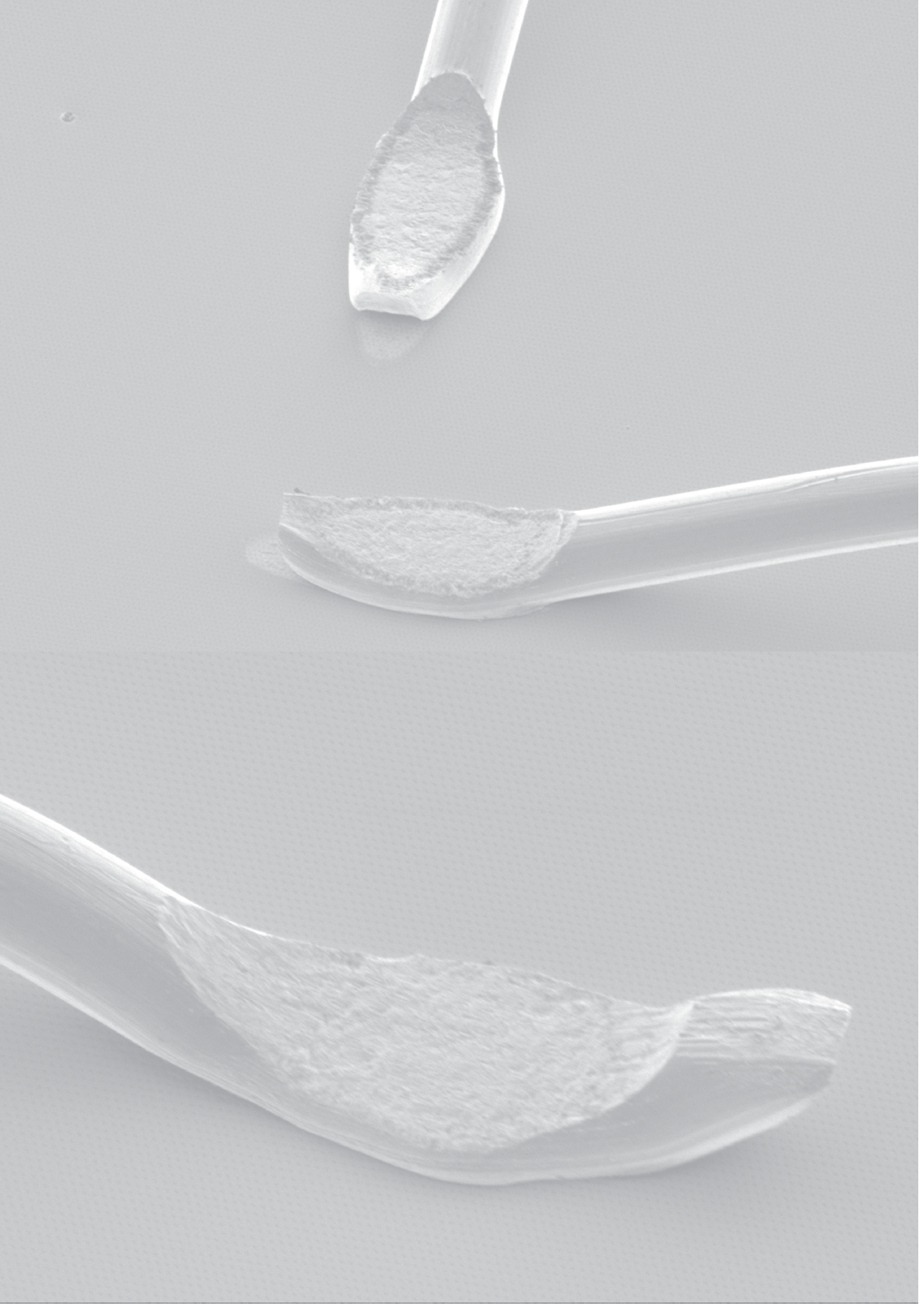

4

LUMPED ELEMENT RESONATORS IN A MAGNETIC FIELD

The results discussed in Sec. 4.2 of this chapter are part of the Master thesis work of David Feldstein i Bofill (2022) (Feldstein i Bofill, 2022).

The resonators used throughout this thesis have a lumped element design. Unlike distributed resonators, such as those based on coplanar waveguides (CPW), lumped element resonators consist of well-separated capacitive and inductive parts. This design choice offers several distinct advantages for our applications:

- **Smaller footprint**. Lumped element resonators typically have a compact size compared to other resonator types. For instance, CPW resonators often require larger dimensions, with lengths typically on the order of a few millimeters, inversely proportional to their frequency. The reduced size of lumped element resonators allows for a more efficient use of chip space. Given the typical non-perfect yields of hybrid cQED nanowire devices, this size advantage becomes especially valuable, as it permits fitting multiple devices within the same chip

- **Magnetic field compatibility**. Lumped element resonators concentrate voltage fluctuations around the capacitive part and current fluctuations around the inductive part. This spatial separation of voltage and current is beneficial for the field compatibility of these devices. When a perpendicular magnetic field is applied, it generates vortices within the superconducting film. The oscillating currents can interact with these vortices, causing undesired resonator losses. In our resonator designs, the inductive part is intentionally designed to be narrow, preventing the formation of vortices within that region and minimizing vortex-related losses. Additionally, we strategically incorporate vortex pinning sites across the capacitive plate to immobilize any vortices that form there, preventing them from migrating into areas with high currents. Together, these factors effectively enhance the resilience of the resonator in the presence of a magnetic field.

- **Straightforward inductive coupling**. The lumped element design enables coupling a readout resonator to a qubit circuit through a mutual inductance. We harness this feature for the fluxonium devices discussed in Chapter 5, where the fluxonium and resonator are coupled through a shared inductor segment.

- **Simplified design process**. Lumped element resonators streamline the design process. First, the capacitive couplings to the feedline and qubit can be determined based on the capacitor geometry. Subsequently, the resonator frequency can be easily selected by adjusting the inductor length, with no impact on the coupling capacitances.

In the subsequent sections, we present various characterization measurements performed on lumped element resonators throughout the past years. These include a comparison of different substrates (Sec. 4.1) and an exploration of the field resilience of different resonator geometries (Sec. 4.2).

4.1. SUBSTRATE COMPARISON

Throughout this thesis, we use various lumped element resonators designs. In all cases, the resonators are placed over a high resistivity silicon substrate covered by a 100 nm-thick low-pressure chemical vapor deposited (LPCVD) SiN_x layer (see Appendix D for details on fabrication).

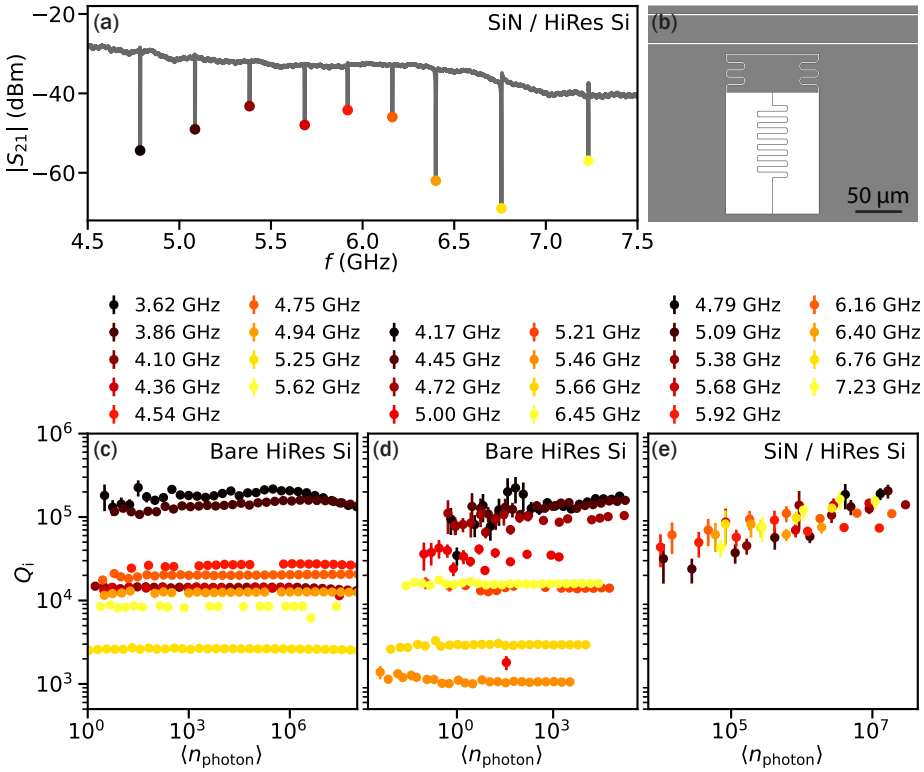

Figure 4.1: **Substrate comparison.** (a) Amplitude of the transmission through the feedline of the chip fabricated on a high resistivity silicon substrate covered by 100 nm of low-pressure chemical vapor deposited (LPCVD) silicon nitride. (b) Design of one of the nine lumped element resonators in the chip, capacitively coupled to the feedline. (c-e) Internal quality factors of the different resonators as a function of the photon number. The markers indicate the values extracted from fits to the measured complex transmission S_{21} and the error bars indicate one-sigma confidence intervals extracted from the fit. Panels (c) and (d) correspond to a high-resistivity silicon substrate and panel (e) to a substrate covered by 100 nm of LPCVD silicon nitride.

The inclusion of the SiN_x layer is due mainly to preventive reasons. Firstly, it acts as a stopping layer for reactive ion etching, as it is etched at a rate one order of magnitude slower than bare silicon (150 nm/min for SiN_x and 1500 nm/min for Si (Li et al., 1995)). To account for potential etch rate variability, we typically over-etch the NbTiN base layer for several seconds. Thus, the absence of a SiN_x stopping layer would result in abrupt topographic steps on the superconducting circuitry that would complicate subsequent steps, like nanowire deposition.

The second reason for employing a SiN_x layer is to prevent potential unwanted current leakage from the electrostatic gates. In some projects, we define electrostatic gate electrodes separated from each other by distances of 30 to 40 nm (Chapters 6, 7, 8 and 9) and from other circuit structures by around 500 nm (Chapter 5). Although our silicon substrates have high resistivity, they still contain some level of doping, limiting their resistivity to the order of 10^4 to 10^5 Ωcm. This could result in leakage currents from the

gates on the order of tens to hundreds of nA when a potential of several volts is applied to them (Splitthoff et al., 2022). Such leakage could become detrimental to the performance of the superconducting circuit elements. The presence of SiN_x prevents this potential complication.

However, the SiN_x layer introduces an extra material interface, which could lead to increased microwave losses. To address this concern, here we investigate whether there are differences in quality factors between resonators fabricated on SiN_x-covered substrates and those directly fabricated on bare HF-cleaned high-resistivity silicon.

To compare the two substrates, we fabricate three chips like the one shown in Fig. 4.1(a), each containing nine lumped element resonators. Two of the chips are fabricated on a bare HF-cleaned silicon substrate and the third is fabricated on a SiN_x-covered substrate. Each resonator (Fig. 4.1(b)) has an identical capacitor pad shape and an inductor width of 300 nm. Their frequencies range between 3.5 and 7.5 GHz and are determined by varying the inductor length (see Fig. 4.1(c)).

As shown in Fig. 4.1(d-f), we find quality factors ranging between 10^4 and 10^5, with some outliers. Although a systematic comparison of the different chips is not possible due to the different photon numbers at which they were measured, we do not find a strong correlation between the resonator performance and the substrate used. We thus conclude that, for our applications, both substrates are similarly suitable in terms of microwave losses and that we are limited by something else than the substrate interfaces. Moreover, subsequent nanofabrication steps typically lower the Q_i of the resonators in hybrid devices investigated in the experimental chapters in this thesis below these values (see Sec. 4.3).

Finally, we also measured the leakage current between NbTiN electrodes placed directly over the bare Si substrates. We found leakage currents of around 70 pA/V for probes separated by 200 nm and of around 40 pA/V for probes separated by 400 nm. These currents would not constitute an issue for the devices investigated in this thesis.

4.2. FIELD RESILIENCE OF LUMPED ELEMENT RESONATORS

In this section, we investigate the effect of various geometric parameters on the resonator performance, measured by its internal quality factor and magnetic field resilience. We focus on reporting on the parameters that we experimentally found to influence the resonator's performance, namely the inductor width, w_r, and the island size, L_r (see Fig. 4.2). For a more detailed report on this study, see Ref. (Feldstein i Bofill, 2022), where Feldstein i Bofill further describes various design, simulation and measurement considerations as well as the investigation of other geometric parameters, like the capacitor corner radius.

The devices investigated here are presented in Fig. 4.2. All circuit elements are placed over an intrinsic silicon substrate covered by 100 nm-thick low-stress PECVD silicon nitride and defined on a 20 nm-thick NbTiN film with a kinetic inductance of $L_k = 11.8$ pH/□ (see Appendix C) . Each measured chip contains ten different resonators (see Fig. 4.2(b)) for which one geometric parameter is fixed and all other design parameters are either kept fixed or minimally varied to keep the frequencies on target. Each resonator is capacitively coupled to a coplanar waveguide with input and output ports denoted by 1 and 2, for transmission measurements (see Fig. 4.2(c)).

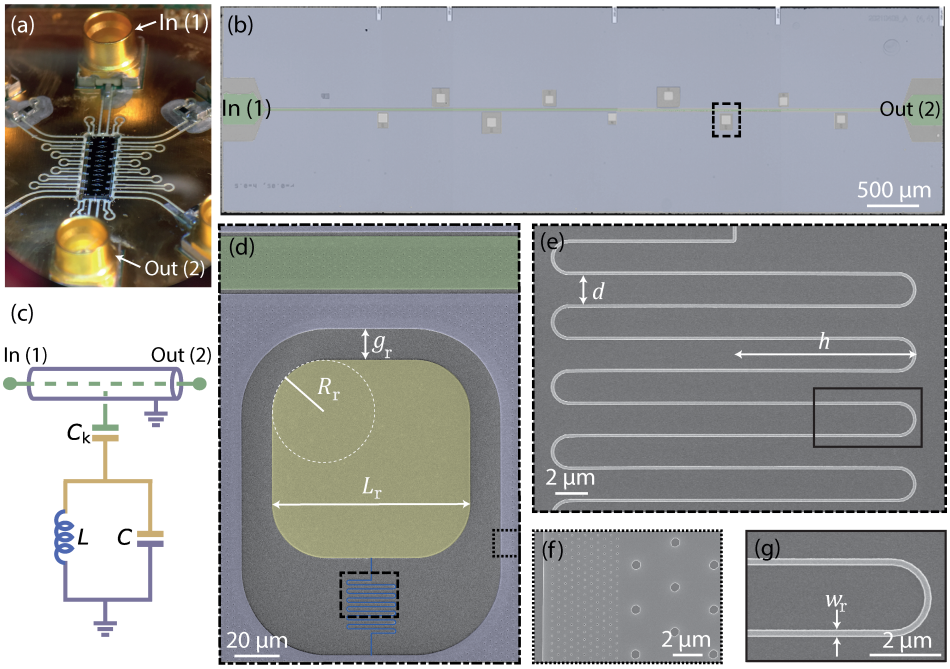

Figure 4.2: **Device overview.** (a) Chip mounted on a printed circuit board (PCB) with SMP connectors for the input and output signals. (b) False-colored optical microscope image of one of the 2x7 mm^2 chips containing ten lumped element resonators coupled to the same transmission line (green). (c) Diagram of the microwave circuit. A coplanar waveguide transmission line (green inner conductor) is capacitively coupled to a grounded LC resonator. The resonator consists of an island (yellow) capacitively and inductively (blue) shunted to ground (purple). (d) False-colored scanning electron microscope (SEM) image of one of the resonators showing the squared resonator island with edge length L_r and corner radius R_r (yellow) and the resonator inductor (blue). (e) SEM enlargement of the meandering resonator inductor. (f) SEM enlargement of the vortex pinning holes on the ground plane. The density of holes is larger in the regions closer to the resonator. (g) SEM enlargement of a turn of the inductor. The inductor width is denoted by w_r.

As shown in Fig. 4.2(d), the capacitive part of the resonator is implemented with a squared island with edge length L_r and corner radius R_r. As we did not observe a clear R_r dependence of the resonator performance (Feldstein i Bofill, 2022), R_r is kept fixed to 0 throughout this section. The gap between resonator island and ground is in turn fixed to be $g_r = 15\,\mu$m and the gap between island and feedline is adapted for each design so that the coupling quality factor is approximately 10^4, to ensure that the extracted internal quality factors and frequencies of different resonators are compared reliably. The inductive part is realized with a narrow meandering stripe of thin NbTiN. The main parameters determining its geometry are the distance between meander turns, d, the half-length of each segment, h, the inductor width, w_r, and the number of turns, N. For our design, we fix $d = 2\,\mu$m so that the turns are as close as possible while avoiding a large reduction of the total inductance due to negative mutual inductance (Stojanović et al., 2004).

The resonators are designed with a symmetric shape. Before measuring the real devices, we confirm their lumped-element character by performing current density simu-

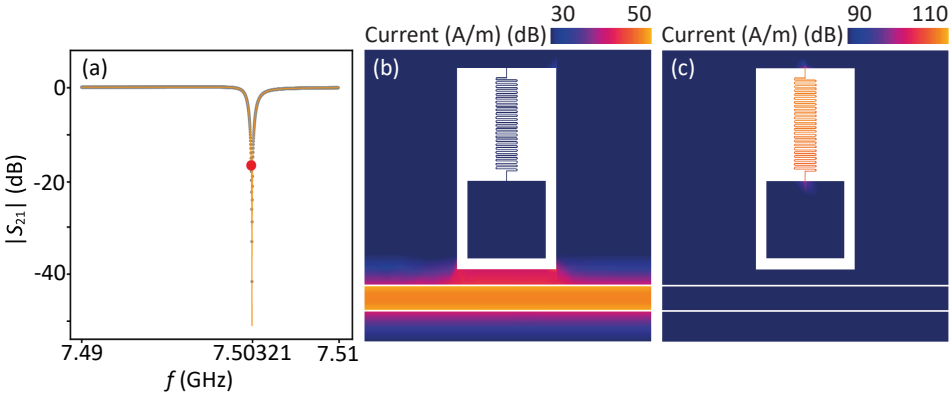

Figure 4.3: **Current distribution on lumped element geometry.** (a) Amplitude of the transmission through the feedline obtained from a Microwave Office simulation (grey markers) of the resonator shown in (b,c), with $N = 25$. The orange line indicates a fit with the diameter correction method (Khalil et al., 2012) from which we extract a resonant frequency $f_r = 7.50321$ GHz, indicated with a red marker. (b) Current distribution at $f = 2$ GHz. (c) Current distribution at the resonance frequency $f = 7.5$ GHz.

lations with Microwave Office (see Chapter 3). The simulation results are presented in Fig. 4.3. We find that, at the resonator resonance frequency, the current is localized in the inductor, as shown in Fig. 4.3(c), and is absent from the capacitive pad. This behavior confirms the separate inductive and capacitive characters of the different parts of the resonator.

In the next sections, we present measurements of three different devices. For two of them (chips A and B), we vary the inductor width, w_r, and, for the third (chip C), we vary the capacitor size, L_r. In chips A and B, w_r ranges over more than an order of magnitude, from 50 nm up to 1 µm. Three examples of such resonators are shown in Fig. 4.4(d-f). For chip C, L_r ranges from 15 µm up to 150 µm, as shown in Fig. 4.4(a-c). In both cases, we compensate for the effect of the parameter variations on the resonance frequency by adapting the number of turns of the inductor, N. We first explore the effect of these parameters on the internal quality factor, Q_i, at zero field and then turn to investigate the in-plane and out-of-plane magnetic field dependencies. We performed identical measurements for a chip on which we vary the edge radius (chip D, see Fig. 4.4(g-i)). However, this parameter did not result in a noticeable influence on the resonator performance. For a complete dataset of chip D, we refer you to Ref. (Feldstein i Bofill, 2022).

4.2.1. QUALITY FACTORS AT ZERO MAGNETIC FIELD

We start by investigating the resonator performance at zero external magnetic field with transmission measurements. For each chip, we identify various resonances (see Fig. 4.5(b)), which we associate to their corresponding resonator by comparison to the simulated response (Fig. 4.5(a)). To extract the resonant frequency, f_r, and quality factors, Q_c and Q_i, of each resonator, we fit them with the diameter correction method (Khalil et al., 2012), as shown in Fig. 4.5(c-e).

For all resonators, the measured coupling quality factors agree with their designed

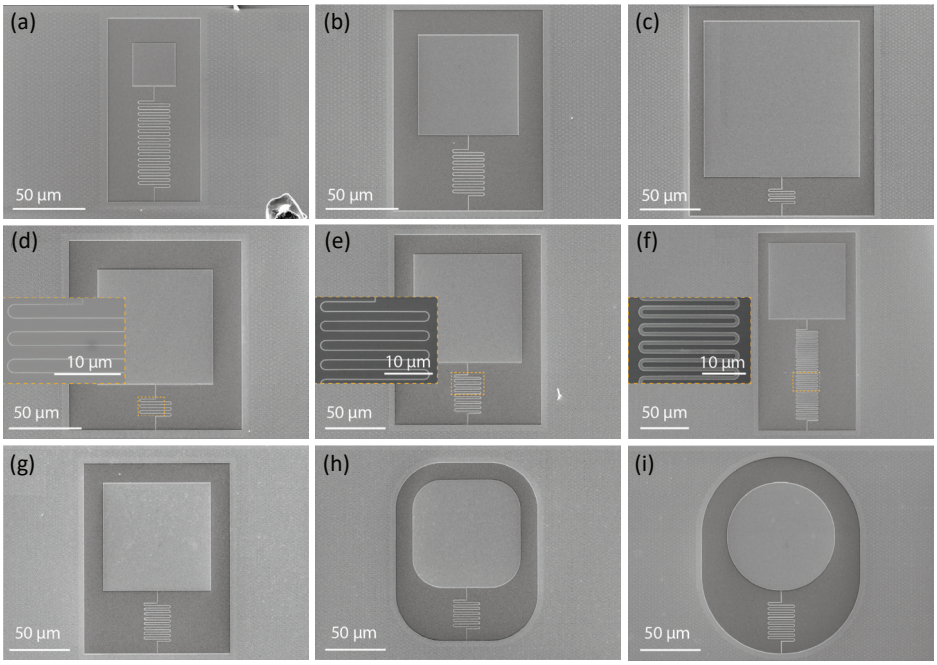

Figure 4.4: **Scanning electron micrographs (SEMs) of resonators with varying geometries.** (a-c) Three variations of capacitor size in chip C: L_r = 30, 70, 130 µm, respectively. (d-f) Three variations of inductor width in chips A and B: w_r = 100, 200, 1000 nm, respectively. (g-i) Three variations of edge radius in chip D: R_r = 0, 25, 45 µm, respectively.

values $Q_c \sim 10^4$ (Feldstein i Bofill, 2022). Moreover, we find internal quality factors in the range of $Q_i = 10^5 - 6 \cdot 10^5$, that don't show a strong correlation with the resonator geometry (Feldstein i Bofill, 2022; Shearrow et al., 2018). The average extracted Q_i does however vary from chip to chip, as expected due to potential variability in the fabrication conditions.

POWER DEPENDENCE OF QUALITY FACTORS

The power dependence of Q_i provides information on the dominant loss mechanisms at play. The results obtained for devices A, B and C are illustrated in Fig. 4.6(a), (b) and (c), respectively. We find that the majority of resonators show an initial increase of Q_i with power, followed by a strong reduction of Q_i as the power is further increased, present for all resonators.

The initial increase in Q_i at low power levels is commonly attributed to losses induced by two-level systems (TLSs) (Martinis et al., 2005; Oliver and Welander, 2013; O'Connell et al., 2008). TLSs are localized low-energy excitations primarily found at material surfaces and interfaces that arise from defects or impurities. They are formed by a charged particle that can tunnel between two spatial states and, at low powers, they thus possess a dipole moment. This dipole moment interacts with the electric field of the resonator, inducing losses. Consequently, TLS losses are associated with the capacitive part of the

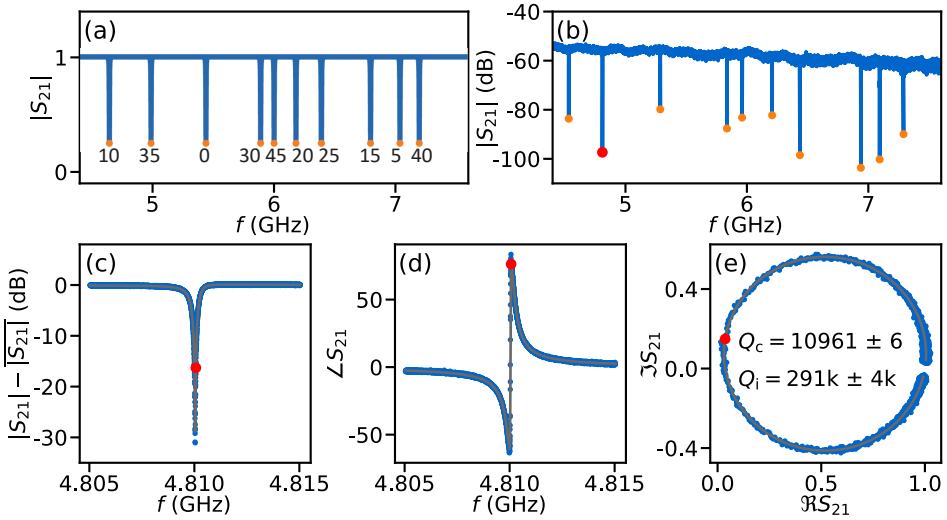

Figure 4.5: **Resonator identification and fitting for chip D.** (a) Amplitude of the simulated transmission through the feedline, obtained using Microwave Office. Each resonance corresponds to a resonator with different R_r, indicated by the labels in µm. (b) Amplitude of the measured transmission through the feedline of chip D. The orange markers in (a) and (b) indicate 10 local minima and identify the resonance frequencies. (c-d) Zoom in on the measured transmission around the resonance at 4.81 GHz. (c) and (d) show the amplitude and phase of the measured signal, respectively, while (e) shows the real and imaginary parts. The grey line is a fit to the complex signal with the diameter correction method (Khalil et al., 2012), from which we extract a resonant frequency, indicated with a red marker, as well as the coupling and internal quality factors, indicated with labels in (e).

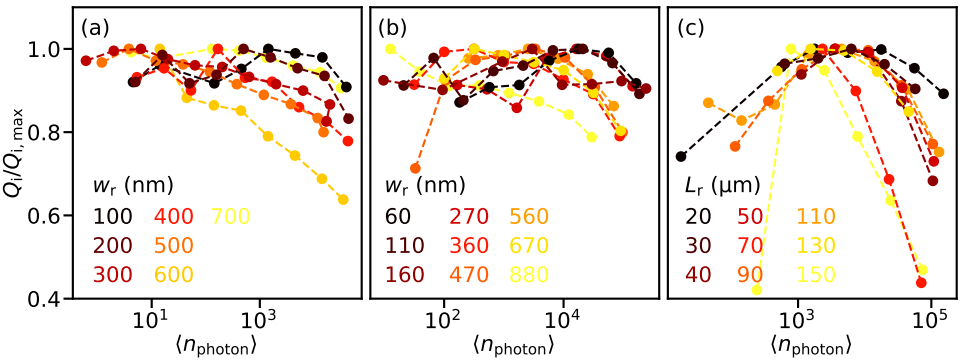

Figure 4.6: **Internal quality factor versus photon number.** Panels (a), (b) and (c) correspond to devices A, B and C, respectively. For each resonator, the maximum measured quality factor, $Q_{i,max}$, is divided out.

resonator and could thus be correlated with the capacitor geometry. However, our observations do not reveal a conclusive correlation between the capacitor size and TLS losses (Fig. 4.6(c)), prompting further measurements to investigate this effect.

One possible mechanism proposed to explain the reduction of Q_i with increasing photon number is microwave-induced Cooper pair breaking (de Visser et al., 2014). Mi-

crowaves can excite quasiparticles above the superconducting gap (de Visser et al., 2012). When these quasiparticles relax, they can emit pair-breaking phonons which produce quasiparticles on the resonator inductor, leading to losses (de Visser et al., 2014; Goldie and Withington, 2012; Martinis, 2021). Our findings suggest that microwave-induced quasiparticle loss may be a dominant mechanism for our resonators.

For chips C and D, we did not observe a clear correlation between the power dependence of Q_i and the resonator geometry (Feldstein i Bofill, 2022). For chips A and B, however, we find a more pronounced reduction of Q_i with power for resonators with wider inductors (Fig. 4.6(a) and (b)). Nonetheless, it is important to note that there are resonators on both chips that deviate from this overall trend, emphasizing the need for further investigation to validate these preliminary results. The larger effect of increased power on wider-inductor resonators aligns with the microwave-induced Cooper pair breaking mechanism, as wider inductors provide a larger area where Cooper pairs can break, making them more susceptible to this form of loss. Consequently, narrow inductor resonators appear more suitable for applications requiring high powers.

4.2.2. MAGNETIC FIELD DEPENDENCE

We now turn to investigating the performance of lumped-element resonators under the presence of a magnetic field, applied either parallel ($B_{||}$, Fig. 4.7) or perpendicular ($B_{\perp}$, Fig. 4.9) to the chip plane (Graaf et al., 2012; Kroll et al., 2019; Müller et al., 2022; Samkharadze et al., 2016; Zollitsch et al., 2019).

MAGNETIC FIELD APPLIED ON THE CHIP PLANE

The $B_{||}$ dependence of the resonators in chips A, B and C is illustrated in Fig. 4.7. We find that the resonators are resilient to a parallel magnetic field, retaining their internal quality factor up to at least 1 T. Unfortunately, higher fields could not be applied due to the presence of magnetic-field-sensitive mu-metal components in the measurement setup.

Additionally, we observe a dip in Q_i within the range of 120 to 260 mT for all resonators. The dip is centered at a different magnetic field for each resonator that scales linearly with its resonance frequency (Feldstein i Bofill, 2022). This behavior is consistent with previous findings in NbTiN thin-film resonators (Graaf et al., 2012; Kroll et al., 2019; Samkharadze et al., 2016; Zollitsch et al., 2019) and has been associated with coupling to an electron spin resonance (ESR) originating at a dangling bond in the substrate material, which leads to increased losses in the cavity. By considering the resonance condition between the resonator and the ESR, $hf_r = g\mu_B B_{min}$, we extract the Landé g-factor associated with the ESR, obtaining $g \sim 2.14$. See Ref. (Feldstein i Bofill, 2022) for detailed information on the extraction of g.

Apart from the ESR feature, we observe a limited magnetic field dependence of Q_i within the investigated range of fields. For most resonators, we find that the point of maximum Q_i does not occur at $B_{||} = 0$. This observation aligns with previous studies (Kroll et al., 2019; Zollitsch et al., 2019), where it has been attributed to either the formation of Abrikosov vortices that act as quasiparticle traps (Kroll et al., 2019) on the film or to the fact that the ESR dip might be limiting the resonator performance even at zero magnetic field (Zollitsch et al., 2019).

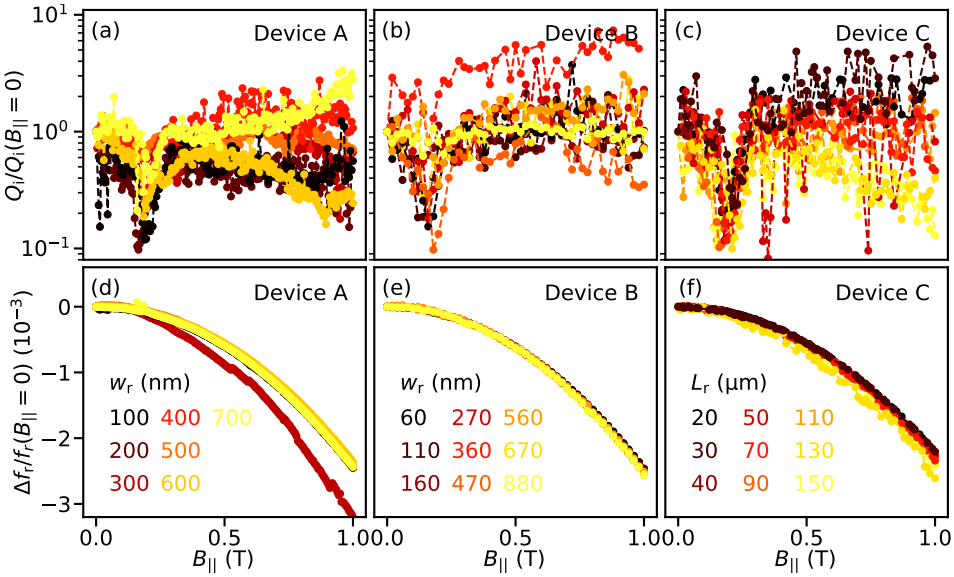

Figure 4.7: **Resonator performance versus magnetic field applied parallel to the chip plane, $B_{||}$.** (a)-(c) Relative internal quality factor Q_i with respect to the quality factor at zero field, $Q_i(B_{||}=0)$, for devices A, B and C, respectively. (d)-(f) Relative resonance frequency shift, Δf_r, with respect to the resonance frequency at zero field $f_r(B_{||}=0)$, for devices A, B and C, respectively. Different colors correspond to different resonator geometries, as indicated. Data taken at $\langle n_{photon}\rangle \sim 5\cdot10^2 - 1\cdot10^3$.

Although not particularly pronounced, for several resonators we also note a slight reduction in Q_i with increasing $B_{||}$ in the range of 0.5 to 1 T. Significantly stronger reductions in Q_i have been previously observed in 250 nm-thick lumped element resonators with inductor widths of a few micrometers (Müller et al., 2022), as well as in 200 nm-thick Nb lumped element resonators with capacitor pads ranging from 10 to 100 µm in size (Graaf et al., 2012). Q_i reductions comparable to the one observed in our case were found for 100 nm-thick coplanar waveguide resonators with widths of around 10 µm (Kroll et al., 2019) (stronger reduction than for this work) and for 50 nm-thick NbN lumped element resonators with 10 µm-wide capacitive part (Zollitsch et al., 2019) (weaker reduction than in this work). In contrast, previous measurements on 7 nm-thick nanowire stripline resonators with widths of 100 to 700 nm exhibited no Q_i reduction with $B_{||}$ up to a field of 6 T (Samkharadze et al., 2016). In summary, the observed reduction in Q_i appears to be more pronounced for thicker superconducting films and in resonators with wider regions. This observation is consistent with our finding of a stronger reduction of Q_i in larger capacitor resonators (indicated by lighter colors in Fig. 4.7(c)), while no clear correlation is found between the in-plane field performance of the resonators and their inductor width (Fig. 4.7(a, b)). Quasiparticle loss (Kroll et al., 2019) has been suggested as a possible mechanism that contributes to this Q_i reduction, as an in-plane magnetic field enhances the generation rate of quasiparticles within the resonator. As larger capacitor resonators contain more Cooper pairs, the number of Cooper pairs broken by $B_{||}$ increases, leading to a higher production of quasiparticles and, consequently, to an

increase in quasiparticle loss.

We now focus on the relative frequency change, $\Delta f_r = f_r(B_{||}) - f_r(B_{||} = 0)$, as a function of $B_{||}$ (see Fig. 4.7(d-f)). As expected, as $B_{||}$ increases, the resonator frequency, f_r, decreases. Moreover, as shown in Fig. 4.8, it does it following a parabolic dependence of the form

$$\frac{\Delta f_r}{f_r(B_{||} = 0)} = -k_{||} B_{||}^2. \tag{4.1}$$

This dependence is expected when the change in frequency originates from a reduction of the film's kinetic inductance. Deviations from a parabolic dependence would be expected to occur at larger fields when vortices become the dominant loss mechanism (Zollitsch et al., 2019). For our resonators, the highly disordered nature of NbTiN and the small cross-sectional width of the inductors make the kinetic inductance the largest contribution to their total inductance. As $B_{||}$ increases, the Cooper pair density, n_s, is reduced, which leads to an increase of the film's kinetic inductance (as $L_k \propto 1/n_s$ (Annunziata et al., 2010)) and in turn to a reduction of the resonator's resonance frequency (as $f_r \propto 1/\sqrt{L_k}$).

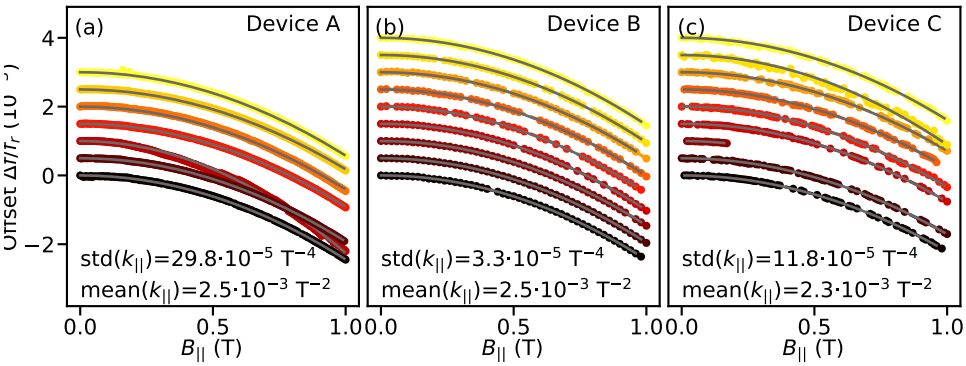

Figure 4.8: **Quadratic fits of relative resonance frequency shift versus $B_{||}$.** (a)-(c) Same data as in Fig. 4.7(d), (e) and (f), respectively, with an offset in the y-axis to reduce overlaps. The grey lines indicate the best fits to the quadratic dependence from Eq. 4.1. The average and standard deviation of the extracted $k_{||}$ are indicated with labels for each chip.

By fitting the relative resonance shift with the quadratic dependence from Eq. 4.1, we extract the coefficient $k_{||}$ (see Fig. 4.8). As detailed by Samkharadze et al. (2016), when the dominant contribution to the total inductance of the resonator inductor is kinetic, $k_{||}$ is given by

$$k_{||} = \frac{\pi}{48} \frac{t^2 e^2 D}{\hbar K_B T_c}, \tag{4.2}$$

where D is the electron diffusion constant in NbTiN, e is the electron charge, t denotes the film thickness, K_B is the Boltzmann constant and $T_c \sim 10\,\mathrm{K}$ (see Appendix C) is the critical temperature of the film. As the film thickness is the same for all resonators, the relative frequency change should be the same independently of the resonator geometry. We find very similar $k_{||}$ for all resonators (see Fig. 4.8), which serves as a consistency check to confirm that the magnetic field is indeed applied in-plane. If we fix $t = 20\,\mathrm{nm}$

to the actual value of the film thickness, we extract $D = 0.52\,\mathrm{cm^2 s^{-1}}$, similar to values obtained in different experiments in the same material: $D = 0.79\,\mathrm{cm^2 s^{-1}}$ by Kroll et al. (2019), $D = 2\,\mathrm{cm^2 s^{-1}}$ by Samkharadze et al. (2016) and $D = 0.47\,\mathrm{cm^2 s^{-1}}$ by Sidorova et al. (2021). Note that, as NbTiN is a highly disordered material, the exact value of D is expected to vary for different films depending on their exact level of disorder, while staying at the same order of magnitude. For a more precise estimation of D based on the out-of-plane magnetic field dependence, see the next section.

MAGNETIC FIELD APPLIED PERPENDICULAR TO THE CHIP PLANE

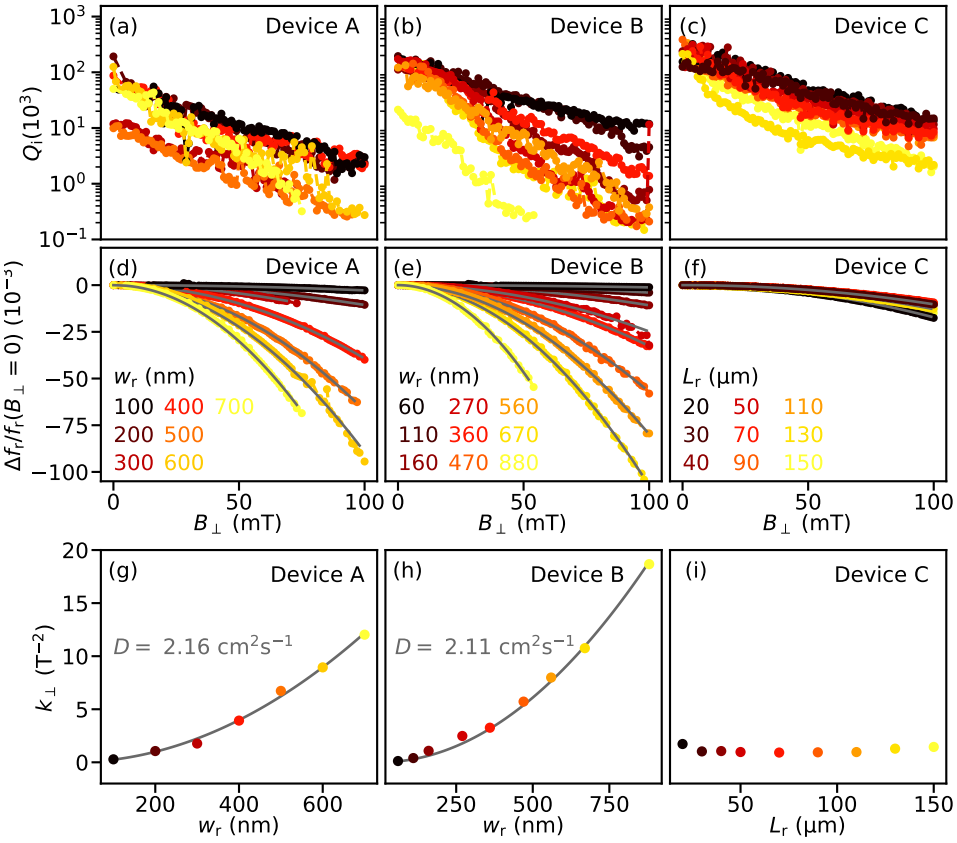

Figure 4.9: **Resonator performance versus magnetic field applied perpendicular to the chip plane, $B_\perp$.** (a)-(c) Internal quality factor, Q_i, for devices A, B and C, respectively. (d)-(f) Relative resonance frequency shift, Δf_r with, respect to the resonance frequency at zero field $f_r(B_\perp = 0)$, for devices A, B and C, respectively. The grey lines indicate the best fits to the quadratic dependence from Eq. 4.3. Different colors correspond to different resonator geometries, as indicated. Data taken at $\langle n_{\mathrm{photon}} \rangle \sim 5 \cdot 10^2 - 1 \cdot 10^3$.

For all resonators, we observe a significant reduction in Q_i, ranging from 1 to 2 orders of magnitude, in the presence of a perpendicular magnetic field $B_\perp = 100\,\mathrm{mT}$. Notably, resonators with wider inductors exhibit a stronger reduction in Q_i (Fig. 4.9(a, b)), as also

observed in Ref. (Samkharadze et al., 2016). Fig. 4.9(c) further reveals that the impact of $B_\perp$ on the quality factor is more pronounced for larger capacitor resonators. Both effects are expected, as a higher surface area leads to an increased formation of vortices on the film, which detrimentally affects the resonator performance.

Next, we explore the dependence of the resonator frequency on $B_\perp$ to extract a more accurate estimation of the film's electron diffusion constant, D. Similarly to the case of a parallel magnetic field, we find a quadratic relationship given by:

$$\frac{\Delta f_\mathrm{r}}{f_\mathrm{r}(B_\perp = 0)} = -k_\perp(w_\mathrm{r}) B_\perp^2. \tag{4.3}$$

However, this time the coefficient $k_\perp$ is not determined by the film thickness but rather by the width of the inductor:

$$k_\perp(w_\mathrm{r}) = \frac{\pi}{48} \frac{w_\mathrm{r}^2 e^2 D}{\hbar K_\mathrm{B} T_\mathrm{c}} \propto w_\mathrm{r}^2. \tag{4.4}$$

Consistent with expectations, the observed frequency change is more pronounced in resonators with wider inductor (Fig. 4.9(d, e)). We extract the values of $k_\perp(w_\mathrm{r})$ by fitting quadratic functions to the $B_\perp$ dependence of the frequency (gray lines in Fig. 4.9(d, e)). Fig. 4.9(g, h) displays the extracted $k_\perp(w_\mathrm{r})$ values. By fitting the extracted $k_\perp(w_\mathrm{r})$ values to Eq. 4.4, we derive electron diffusion constants of $D = 2.16\,\mathrm{cm^2 s^{-1}}$ and $2.11\,\mathrm{cm^2 s^{-1}}$ for devices A and B, respectively (Fig. 4.9(g) and (h)). This number differs from that extracted in the previous section. This misestimation might be due to the effective film thickness of the material being lower than the expected one. Given $D = 2.1\,\mathrm{cm^2 s^{-1}}$, the field dependence found in the previous section would correspond to an effective superconductor thickness of $t_\mathrm{eff} = 9.8\,\mathrm{nm}$. A similar reduction in effective thickness was also reported in previous studies on NbTiN thin films, as discussed in Ref. (Samkharadze et al., 2016). Its origin may be attributed to surface oxidation.

4.3. LUMPED ELEMENT RESONATOR DESIGNS IN THIS THESIS

Throughout this thesis, we varied the lumped element resonator design to suit the specific requirements of each experiment while incorporating insights gained over time. The resonator designs used for the different experimental chapters are shown in Fig. 4.10. All designs include vortex pinning holes on the capacitor plates, as it was shown previously in our group that such pinning holes enhance the resonators' field compatibility (Kroll et al., 2018).

In Chapter 5, we focused on performing two-tone spectroscopy of a fluxonium circuit resilient to magnetic fields up to 1 T. Thus, the main focus was put on achieving a resonator design that (1) enables simple inductive coupling to the fluxonium and that (2) is highly field compatible. Moreover, optimizing the internal quality factor of such resonators was not a priority, as the coherence properties of the fluxonium were not of relevance for the experiments performed in Chapter 5. Therefore, we transitioned from the standard coplanar waveguide resonator design used in previous experiments in our group (Bargerbos et al., 2020; Kroll et al., 2018, 2019; Uilhoorn et al., 2021) to a lumped element configuration, as shown in Fig. 4.10(a). This LC design allowed inductive coupling to the fluxonium by sharing a segment of the inductor between the resonator and

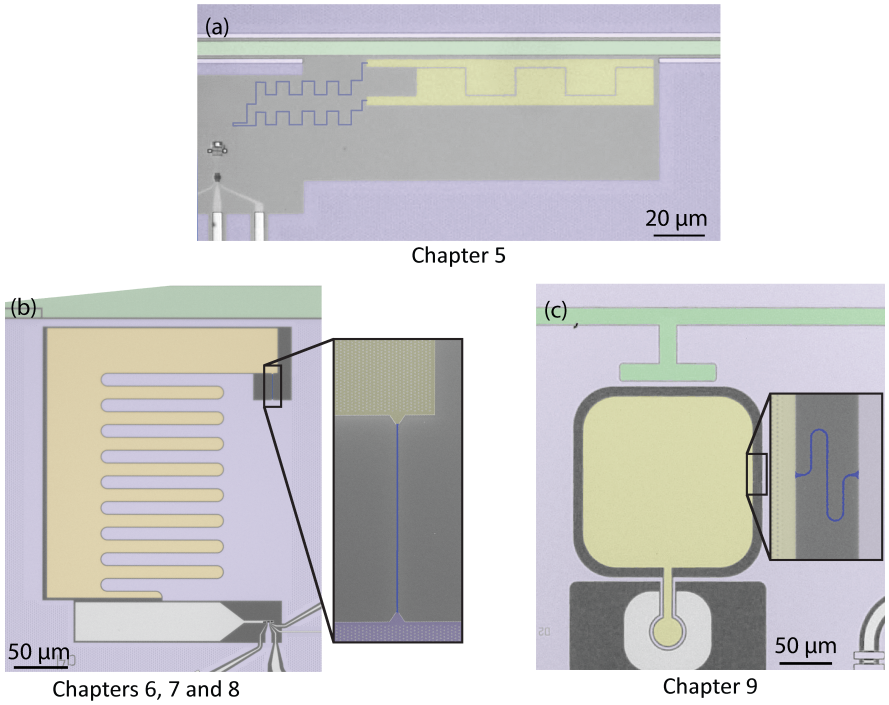

Figure 4.10: **Lumped element resonator designs used throughout this thesis.** False-colored optical images of the lumped element resonator designs used throughout the different chapters. For all panels, the capacitive islands are indicated in yellow and the inductors in blue. Ground and the feedline are colored purple and green, respectively. The insets in (b) and (d) are false-colored scanning electron microscope (SEM) enlargements of the inductors. All inductors are 200 nm-wide.

the fluxonium, as proposed in Ref. (Smith et al., 2016). To optimize for field resilience, we designed the resonator with a small footprint, featuring capacitive regions with an area of approximately 20 µm×20 µm. Additionally, the inductor width was set at 200 nm.

For the experiments presented in Chapters 6, 7, and 8, we made further alterations to the resonator design, as depicted in Fig. 4.10(b). As the maximum magnetic field investigated in these experiments was an order of magnitude lower than in Chapter 5, the requirement for field compatibility became less stringent, allowing for a larger capacitor size. In these cases, the resonator served as the readout for a transmon qubit capacitively coupled to it. To minimize direct transmon-feedline coupling, we adapted the resonator shape, allowing the transmon to be positioned further away from the feedline. The measured internal quality factors for these resonators, after completing all nanowire-related nanofabrication steps (see Appendix D), ranged from slightly below 10^3 to slightly above 10^4.

Lastly, for the experiments presented in Chapter 9, we further adapted the resonator design as shown in Fig. 4.10(c). This design features larger gaps between the resonator island and ground, more rounded corners, a more symmetric overall shape, and complete surrounding of the resonator by the ground plane. The internal quality factors of

these resonators, after completing all nanowire-related nanofabrication steps, ranged from slightly below 10^3 to slightly above $5 \cdot 10^4$.

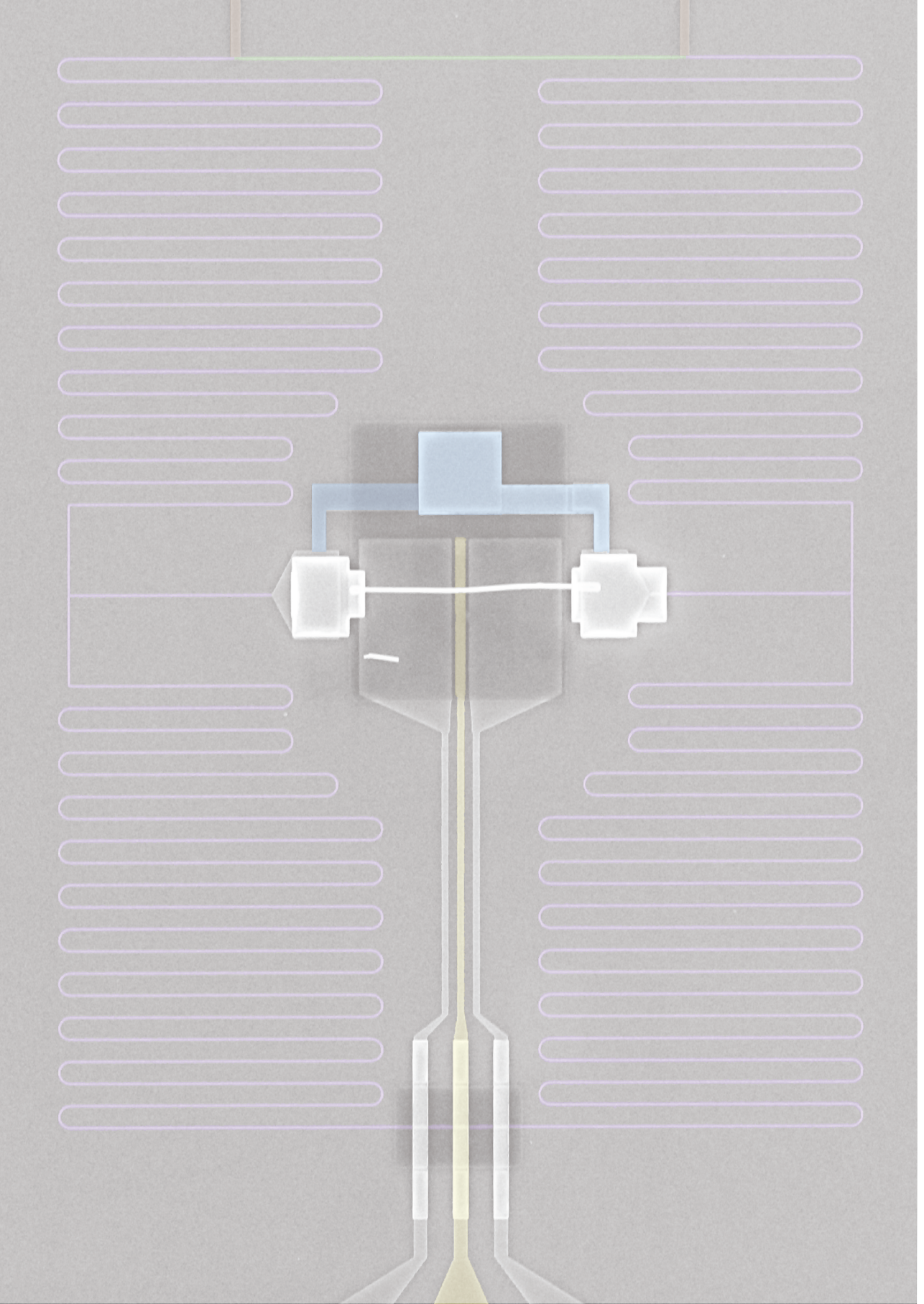

5

A GATE-TUNABLE, FIELD-COMPATIBLE FLUXONIUM

Hybrid superconducting circuits, which integrate non-superconducting elements into a circuit quantum electrodynamics (cQED) architecture, expand the possible applications of cQED. Building hybrid circuits that work in large magnetic fields presents even further possibilities such as the probing of spin-polarized Andreev bound states and the investigation of topological superconductivity. Here we present a magnetic-field compatible hybrid fluxonium with an electrostatically-tuned semiconducting nanowire as its non-linear element. We operate the fluxonium in magnetic fields up to 1 T and use it to observe the φ_0-Josephson effect. This combination of gate-tunability and field-compatibility opens avenues for the control of spin-polarized phenomena using superconducting circuits and enables the use of the fluxonium as a readout device for topological qubits.

The work in this chapter has been published as: **M. Pita-Vidal**, A. Bargerbos, C-K Yang, D. J. van Woerkom, W. Pfaff, N. Haider, P. Krogstrup, L. P. Kouwenhoven, G. de Lange and A. Kou, A gate-tunable field-compatible fluxonium, Phys. Rev. Applied **14**, 064038 (2020).

5.1. INTRODUCTION

Circuit quantum electrodynamics, where photons are coherently coupled to artificial atoms built with superconducting circuits, has enabled the investigation and control of macroscopic quantum-mechanical phenomena in superconductors (Blais et al., 2004; Chiorescu et al., 2004; Wallraff et al., 2004). Recently, hybrid circuits incorporating semiconducting nanowires (de Lange et al., 2015; Hays et al., 2018; Larsen et al., 2015; Luthi et al., 2018) and other electrostatically-gateable elements (Casparis et al., 2018; Kroll et al., 2018; Mi et al., 2017; Wang et al., 2019) into superconducting circuits have broadened the scope of cQED to probing mesoscopic superconductivity (de Lange et al., 2015; Hays et al., 2018, 2020; Larsen et al., 2015). Further extending the capabilities of hybrid circuits to work in magnetic fields presents the intriguing possibility of insights into *topological* superconductivity (Ginossar and Grosfeld, 2014; Hassler et al., 2011; Hyart et al., 2013; Stenger et al., 2019; van Heck et al., 2017; Väyrynen et al., 2015; Yavilberg et al., 2019; Zazunov et al., 2014).

Topological superconductivity, which has garnered much theoretical and experimental interest lately (Kitaev, 2001; Lutchyn et al., 2018; Sarma et al., 2015; Sato and Ando, 2017), results from the interplay between magnetism and superconductivity. In superconductor-proximitized semiconductors exposed to a large magnetic field, emergent quasiparticle states known as Majorana zero modes (MZM) can form. Majorana zero modes are predicted to be robust to local perturbations and could thus serve as long-lived qubits. Several groups have proposed using superconducting circuits to both probe and control MZMs (Hassler et al., 2011; Hyart et al., 2013; Pekker et al., 2013; Stenger et al., 2019; Väyrynen et al., 2015). All of the above-mentioned proposals, however, require the operation of a flux-based superconducting circuit in large magnetic fields.

Additionally, the behavior of superconductor-proximitized semiconductors exposed to a large magnetic field in the trivial phase remains an active field of research. Most experiments investigating the behavior of Andreev bound states (ABS) in a magnetic field have been focused on the magnetic-field dependence of the switching current (Hart et al., 2019; Paajaste et al., 2015; Zuo et al., 2017) with the exceptions of references (van Woerkom et al., 2017) and (Tosi et al., 2018), which performed ABS spectroscopy up to fields of 300 mT and 11 mT respectively. Energies below 20 μeV, which are interesting for high-transparency ABSs and MZMs, were, however, not accessible. A fluxonium that works in high magnetic fields and with semiconducting weak-links would thus be an extremely useful tool both for investigating the magnetic field behavior of ABSs and also for coupling to topological superconductors. First, the fluxonium ground-to-excited state transitions are typically accessible at microwave frequencies over the entire flux range from 0 to π. One therefore gains access to the full energy-phase relations of the junction. Second, the Josephson energy of the junction can be known extremely precisely (to $<$ 0.4 μeV) and over multiple decades, which allows for the mapping of the characteristic energy of the semiconducting weak-link. Finally, the fluxonium is also sensitive to quasiparticle poisoning events in individual ABS in the junction since poisoning of individual ABSs would lead to additional spectral lines. Knowledge of these rates would greatly aid the design of Andreev-based qubits (Hays et al., 2020; Janvier et al., 2015).

Moreover, the unique parameter regime of the fluxonium makes it particularly suited to detecting and controlling MZMs. A switch in the parity of MZMs coupled to the fluxo-

nium circuit corresponds to a switch in the direction of the persistent current flowing in the fluxonium circuit. Parity switches of the MZMs would thus result in the observation of two copies of the fluxonium spectrum (Pekker et al., 2013). In addition, the presence of MZMs coupled to the fluxonium changes the periodicity of its spectrum from 2π to 4π. In these proposals, the linewidth of the fluxonium transition determines the sensitivity with which the fluxonium could determine the presence of MZMs. Beyond its detection capabilities, multiple fluxonium devices coupled to MZMs could also implement braiding operations on the MZMs (Stenger et al., 2019).

Here we have realized a hybrid fluxonium incorporating an Al-proximited nanowire that operates up to 1T. We build upon recent work proximitizing semiconducting nanowires to incorporate a magnetic-field compatible, electrostatically tunable weak-link junction into the fluxonium (Krogstrup et al., 2015). The presented fluxonium device also has a gradiometric design and is composed of NbTiN for further field-compatibility. We demonstrate in-situ gate tunability of the fluxonium Josephson energy over more than a decade. We then operate the fluxonium in fields up to 1 T and map out the dependence of the fluxonium Josephson energy as a function of field. In all regimes of magnetic field and gate voltage, we observe excellent agreement between the data and a theoretical model based on a simple Hamiltonian with a few degrees of freedom. Finally, we also demonstrate the utility of the fluxonium as a probe of mesoscopic superconductivity in magnetic fields by using the measured energy-phase relation of the junction to observe the φ_0-Josephson effect. The ability to observe the fluxonium spectrum over wide ranges in gate voltage and magnetic fields establishes the hybrid fluxonium as a novel superconducting circuit for exploring superconducting phenomena in a magnetic field and as realistic readout platform for MZMs.

5.2. MAGNETIC-FIELD COMPATIBLE MATERIALS AND DESIGN

Building a fluxonium compatible with the application of a magnetic field presents multiple challenges. The first challenge is reaching the fluxonium regime using magnetic-field compatible materials. The fluxonium consists of a Josephson junction with Josephson energy E_J in parallel with a linear superinductor (Manucharyan, 2012), with inductive energy E_L, and a capacitor characterized by the energy E_C, as shown in Fig. 5.1(a). The fluxonium regime ($E_L < E_C < E_\mathrm{J}$) is achieved by shunting the junction with a large inductance. This parameter regime results in the eigenstates of the fluxonium being composed of superpositions of persistent currents in multiple directions (Fig. 5.1(b)). Additionally, the chosen fluxonium parameters result in a spectrum that is observable over the entire range of applied external flux. Superconductor-insulator-superconductor (SIS) Josephson junction arrays, commonly used to implement the fluxonium superinductance (Kalashnikov et al., 2020; Manucharyan, 2012; Manucharyan et al., 2009) can not be used since they are incompatible with large magnetic fields. Recent work on magnetic-field compatible materials with a large kinetic inductance such as granular aluminium (Grünhaupt et al., 2018; Grünhaupt et al., 2019; Maleeva et al., 2018; Rotzinger et al., 2016) and NbTiN (Annunziata et al., 2010; Hazard et al., 2019; Samkharadze et al., 2016) has presented a path to meeting the stringent requirements of the fluxonium superinductance. The magnetic-field compatible fluxonium device is shown in Figs. 5.1(c-f). All circuit elements except for the junction are fabricated using NbTiN, which has

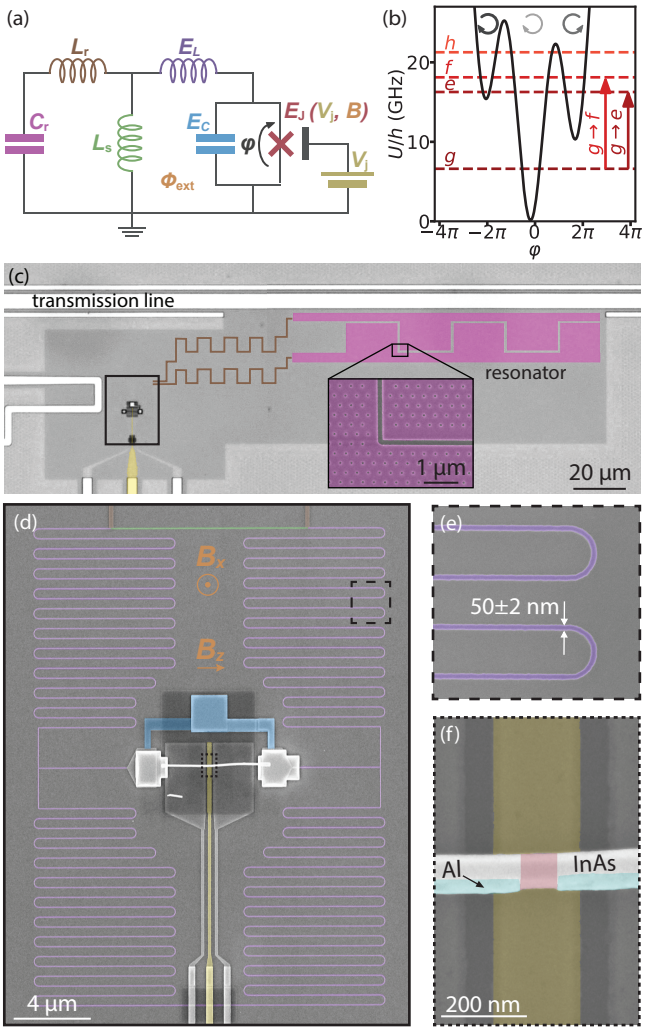

Figure 5.1: Nanowire fluxonium. (a) Circuit model. The fluxonium is composed of a Josephson junction shunted by an inductor and a capacitor, which are characterized by the energies E_J, E_L, and E_C, respectively. The value of E_J depends on the external magnetic field, B_z, and the gate voltage, V_j. An readout resonator (constituted by L_r and C_r) is coupled to the fluxonium via a shared inductance L_s. (b) Potential of the fluxonium (black) versus the phase difference across the junction, φ, at $\varphi_{ext} = 0.2\pi$. The lowest eigenenergies are indicated with dashed horizontal lines. Red arrows indicate transitions starting from the ground state. Circular gray arrows represent the amplitude and direction of the persistent-current states associated with different potential wells. (c) False-colored optical image showing the transmission line and the resonator, with capacitive and inductive elements shaded in pink and brown respectively. Inset, scanning electron microscope (SEM) image of the resonator's capacitive plates. (d) SEM image of a fluxonium lithographically similar to Device A, corresponding to the area indicated by the box in (c). The NbTiN superinductor (purple, enlarged in (e)), the shared inductance section (green), the parallel plate capacitor (blue) and the nanowire junction (red, enlarged in (f)), correspond, respectively, to the E_L, L_s, E_C and E_J elements in (a). The out-of-plane component of B, B_x, tunes the external magnetic flux Φ_{ext}. B_z is the component parallel to the wire.

been demonstrated to have critical fields exceeding 9 T and inductances exceeding 75 pH/□ (Samkharadze et al., 2016). Here we define the fluxonium by etching a 9 nm-thick sputtered NbTiN film, which has a kinetic inductance of 41 pH/□. The superinductance of the fluxonium is made with a 50 nm-wide NbTiN meander (Fig. 5.1(e)) in order to maximize the inductance of the device while minimizing spurious capacitances to ground. This design realizes an inductance of approximately 100 nH. The small width of the meanders additionally suppresses the emergence of lossy vortices due to out-of-plane fields, B_x, up to tens of mT (Stan et al., 2004). We further mitigate the effects of these vortices by introducing vortex-pinning holes (inset, Fig. 5.1(c)) into the capacitor of the fluxonium readout resonator and the ground plane.

In addition to being composed of magnetic-field compatible materials, for use as a detector, the fluxonium must also maintain its narrow linewidth during the application of a magnetic field. The application of a magnetic field precludes the possibility of using the magnetic shielding necessary for limiting flux noise in flux-based superconducting circuits. We address this challenge by building a gradiometric superinductance as shown in Fig. 5.1(d). Equal fluxes through each of the two loops generate equal currents that are canceled at the junction, rendering the fluxonium insensitive to flux noise due to sources larger than the fluxonium device.

Finally, a SIS Josephson junction made of Al and AlOx, which has been used in all previously reported fluxonium devices, can not be used as the E_J element here due to its incompatibility with magnetic field. We build a magnetic-field compatible junction by incorporating a semiconducting InAs nanowire proximitized by an epitaxially-grown 6 nm-thick aluminum layer (Fig. 5.1(f)) (Krogstrup et al., 2015) into the fluxonium. The small thickness of the aluminum shell makes it resilient to magnetic fields along the wire of more than 1 T (Krogstrup et al., 2015). Similar resilience to magnetic fields could also be attained using weak links of disordered superconducting materials, such as indium-oxide (Astafiev et al., 2012) or granular aluminum (Winkel et al., 2020), as the Josephson junction. The nanowire is deterministically deposited on top of the pre-patterned leads of the inductor and capacitor using a micromanipulator. The Josephson junction is then defined by etching away an Al section of approximately 80 nm on top of the junction gate. This small junction, however, does not provide a large enough capacitance to achieve the fluxonium regime for typical E_J values in nanowire junctions. We thus add a parallel plate capacitor (blue in Fig. 5.1(d)) to decrease E_C and achieve its required value for the fluxonium. The fluxonium capacitor consists of two square NbTiN plates sandwiching a 29 nm-thick SiN dielectric. We note that this fluxonium design is flexible enough to incorporate any semiconducting material as its small junction.

5.3. FLUXONIUM SPECTROSCOPY

We first demonstrate that our device behaves as expected for a fluxonium coupled to a readout resonator. Data from two similar fluxonium devices (device A and device B) will be presented in this chapter. We first focus on the behavior of device A. We monitored the transmission amplitude, $|S_{21}|$, at frequencies $f_{\mathrm{r,drive}}$ around the resonator frequency $f_{g0\to g1}$, as a function of the external phase $\varphi_{\mathrm{ext}} = \frac{2e}{\hbar}\Phi_{\mathrm{ext}}$, as shown in the top panel of Fig. 5.2(a). Transitions are labelled as $m_i n_i \to m_e n_e$, where m_i (m_e) and n_i (n_e) are the initial (end) states of the fluxonium and resonator, respectively. The resonator spectrum

is periodic in flux and also exhibits gaps in its visibility, which indicate that the resonator is coupled to the fluxonium. The bottom panel in Fig. 5.2(a) shows the flux dependence of the observed transition frequencies of the fluxonium-resonator system, measured by monitoring the transmission amplitude at $f_{\mathrm{r,drive}} = f_{g0\to g1}$ while the system is driven with a second tone with frequency $f_{\mathrm{f,drive}}$, also via the resonator. Though the gradiometric loops that comprise the fluxonium are designed to be symmetric, the placement of the capacitor and gate lines inside them, together with inevitable imprecision when manually depositing the nanowire, lead to a small imbalance between the effective area of the two gradiometer loops. The imbalance allows us to thread a flux using an out-of-plane magnetic field, B_x. Threading a flux quantum through the gradiometer corresponds to $B_x = 550\,\mu\mathrm{T}$, which is much greater than the $15\,\mu\mathrm{T}$ that would be needed to thread a flux quantum through one of the two symmetric loops. The gradiometric geometry thus reduces the sensitivity of the fluxonium to magnetic field noise larger than the fluxonium loop by more than an order of magnitude.

To fit the spectroscopy data (markers in Fig. 5.2(b)), we diagonalize the Hamiltonian for the coupled fluxonium-resonator system shown in Fig. 5.1(a), $\hat{H}$ (Smith et al., 2016). In the limit $L_\mathrm{f} \gg L_\mathrm{s}, L_\mathrm{r}$ (where $L_\mathrm{f} = \frac{\Phi_0^2}{4\pi^2 E_L}$ and $\Phi_0 = h/2e$),

$$\hat{H} = \frac{2e^2}{C_\mathrm{r}}\hat{n}_\mathrm{r}^2 + \frac{1}{2}\frac{(\Phi_0/2\pi)^2}{(L_\mathrm{r}+L_\mathrm{s})}\hat{\varphi}_\mathrm{r}^2 - \frac{1}{2}\frac{(\Phi_0/2\pi)^2 L_\mathrm{s}}{L_\mathrm{f}(L_\mathrm{r}+L_\mathrm{s})}\hat{\varphi}_\mathrm{r}\hat{\varphi}_\mathrm{f} + \hat{H}_\mathrm{f}, \tag{5.1}$$

where

$$\hat{H}_\mathrm{f} = 4E_C\hat{n}_\mathrm{f}^2 - E_\mathrm{J}(V_\mathrm{j}, B)\cos(\hat{\varphi}_\mathrm{f}) + \frac{1}{2}E_L\left(\hat{\varphi}_\mathrm{f} - \varphi_\mathrm{ext}\right)^2 \tag{5.2}$$

is the Hamiltonian of the uncoupled fluxonium. Here, $\hat{\varphi}_\mathrm{f}$ and $\hat{\varphi}_\mathrm{r}$ are the phase drops across the fluxonium junction and across C_r, respectively, and $\hat{n}_\mathrm{f}$ and $\hat{n}_\mathrm{r}$ are their conjugated charges. We leave all circuit parameters free except for $C_\mathrm{r} = 26\,\mathrm{fF}$, which we extract from electromagnetic simulations. The parameters obtained from the fit are shown in Tab. 5.1 and the fitted transition frequencies are denoted with lines in Fig. 5.2(b). Each state is identified by the closest state in energy for the uncoupled system. In addition to transitions originating from the ground state, $g0$, we also observe transitions for which the initial state is $g1$, with one photon in the resonator (dashed lines). This is due to the continuous drive used to monitor $|S_{21}|$ at $f_{g0\to g1}$, which can populate the resonator. Transitions starting from the first excited fluxonium state, $e0$, around $\varphi_\mathrm{ext} = \pi$ (dotted lines) are also observed. The transition frequency for $g0 \to e0$ goes below 1 GHz near $\varphi_\mathrm{ext} = \pi$. The transitions from $e0$ thus occur due to the expected equilibrium thermal occupation of $e0$ for temperatures of around 20 mK. We find excellent agreement between the experimental data and the fit, with all fit parameters coming to within 5% of the designed circuit parameters except for E_J, which we can only coarsely predict. We have etched a 80 nm-junction to maximize E_J, but the specific values of E_J are determined by the interaction with the electrostatic gate and the microscopic details of the junction.

5.4. ELECTROSTATIC TUNING OF FLUXONIUM PARAMETERS

Mesoscopic phenomena often require fine tuning of the charge carrier density in the semiconductor. We here demonstrate that the spectrum of the fluxonium is measur-

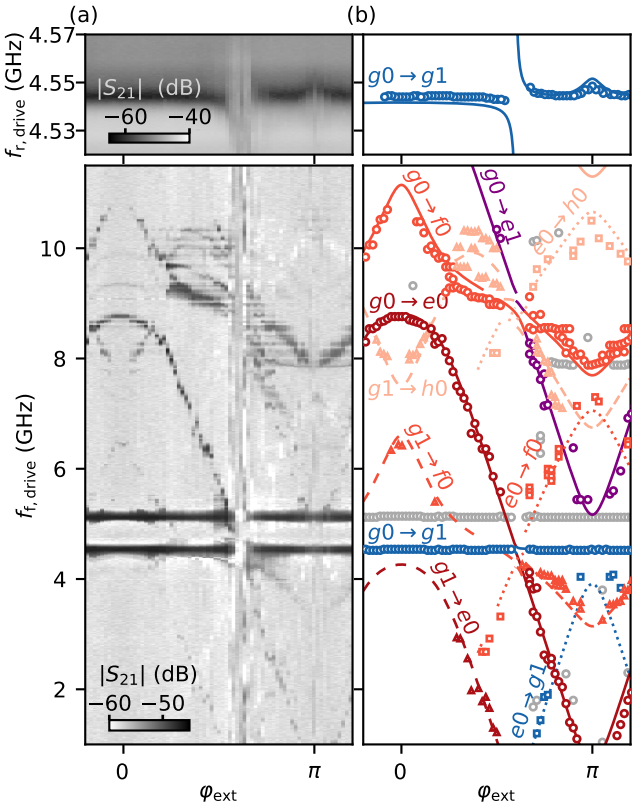

Figure 5.2: Two-tone spectroscopy of device A, at $B_z = 0$. (a) Magnitude of the transmitted readout signal as a function of the external flux and $f_{\mathrm{r,drive}}$ (top) and $f_{\mathrm{f,drive}}$ (bottom), showing the flux modulation of the different transitions. (b) Extrema (maxima and minima) extracted from (a) (markers) and fitted transition frequencies (lines) obtained from the numerical diagonalization of the model Hamiltonian (see Sec. 5.9.1). Gray markers indicate extrema that are not associated with any fluxonium-resonator transitions. A value of $E_{\mathrm{J}}/h = 6.7$ GHz is extracted from the fit.

able over a large range of gate voltages and thus does not limit the possible observable phenomena. We first measure $f_{g0\to g1}$ versus V_{j}. As shown in Fig. 5.3(a), the resonator frequency is constant at low and high voltage values but has non-monotonic fluctuations in an intermediate range, which is consistent with observations in previous experiments on nanowire junctions (de Lange et al., 2015; Larsen et al., 2015; Luthi et al., 2018; van Woerkom et al., 2017), where these fluctuations were attributed to consecutive openings of different junction channels in the nanowire, whose transparencies oscillate with gate. The behavior of the $f_{g0\to g1}$ transition provides insight into the V_{j}-dependence of the fluxonium E_{J}. The value of $f_{g0\to g1}$ can be seen as the bare resonant frequency of the uncoupled resonator plus a dispersive shift caused by the coupling to the fluxonium. The dispersive shift depends on the frequency of all level transitions of the coupled fluxonium-resonator system and is thus different for different values of E_{J}. This change in the dispersive shift leads to the observed changes in the measured resonant

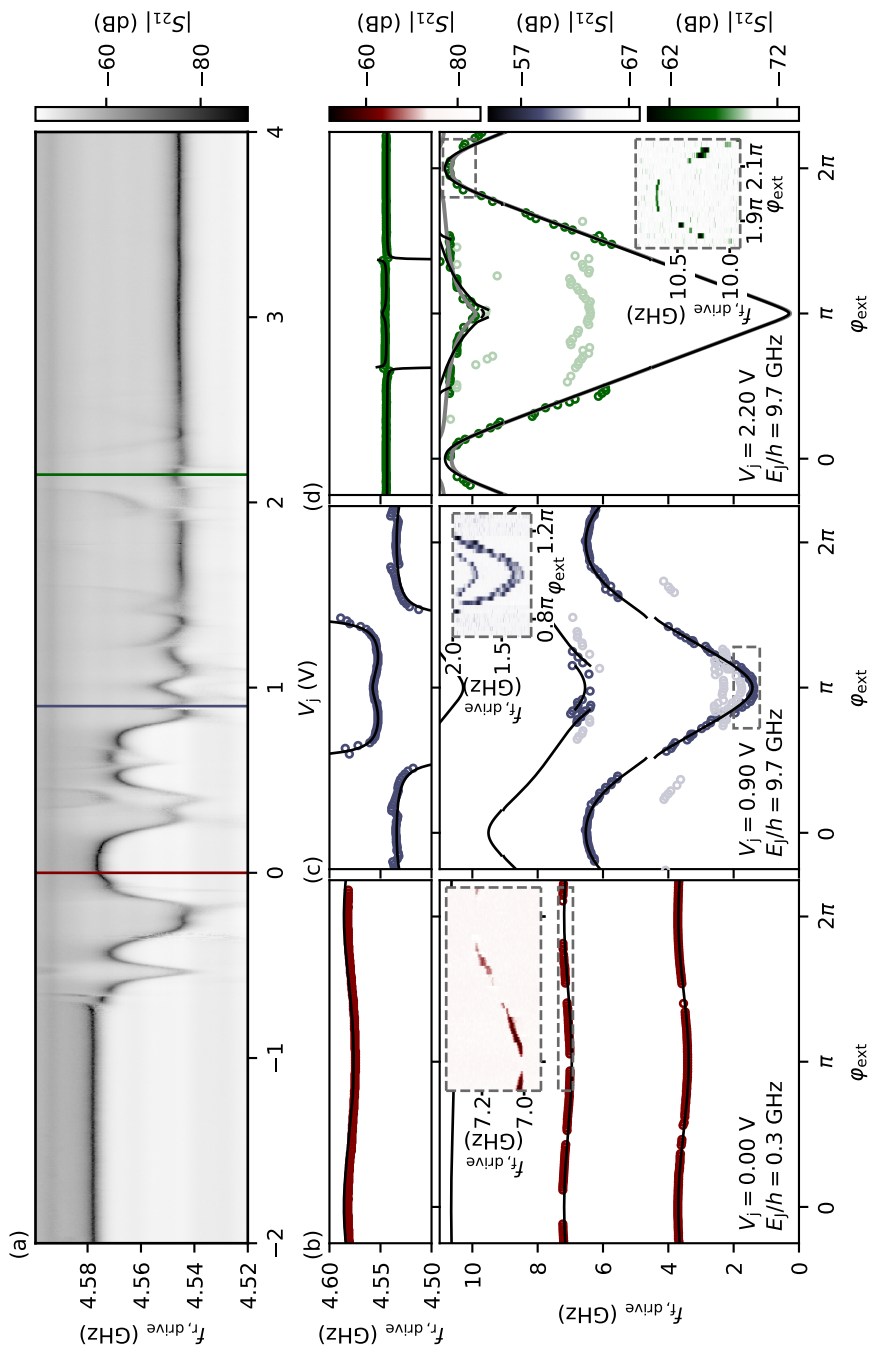

Figure 5.3: Gate tuning of E_J in device A, at $B_z = 0$. (a) Gate dependence of the resonator's resonant frequency, $f_{g0\to g1}$, at $\varphi_{\mathrm{ext}} = 1.25\pi$. (b)-(d), Fluxonium spectra at three different gate points, indicated with vertical lines in (a). The markers correspond to the peaks extracted from the measured resonator (top) and two-tone (bottom) transmission data. The fitted transition frequencies $f_{g0\to e0}$, $f_{g0\to f0}$ and $f_{g0\to h0}$ (black lines) are obtained by fitting the darker markers with Hamiltonian 5.1. The values of E_J/h extracted are 0.2, 3.8 and 9.6 GHz respectively. For (d) the spectrum can be fitted more accurately with a Hamiltonian including one highly transparent channel (grey lines). The insets in (b), (c) and (d) show sections of the measured transmission magnitude. In (b) we observe gaps in visibility at zero and half flux in the $g0 \to f0$ transition.

	Device A	Device B
E_C/h (GHz)	2.35	1.75
E_L/h (GHz)	0.7	1.1
C_r (fF)	26	26
L_r (nH)	47	42
L_s (nH)	8.5	4.6

Table 5.1: Device parameters obtained by fitting spectra in Figs. 5.2, 5.3 and 5.4 and by electromagnetic simulations. h is Planck's constant.

frequency of the resonator.

We now investigate directly the fluxonium spectrum. Figures 5.3(b-d) present spectra taken at three different V_j values (marked by solid lines in Fig. 5.3(a)). Here we use a lower drive power than in Fig. 5.2 to reduce broadening of the spectral lines due to the drive power. Therefore, the main observable transitions start from the ground state, $g0$. For low V_j, we observe a weakly anharmonic spectrum (Fig. 5.3(b)). For large V_j values (Figs. 5.3(c),(d)), however, the flux dependence and the anharmonicity become much stronger. We also note the presence of additional transitions in the spectroscopy data for intermediate and large V_j denoted by the lighter markers in Fig. 5.3(c) and (d). The spectrum at intermediate V_j is taken at a point where the junction is very sensitive to gate voltage; the additional transitions are due to the E_J of the junction fluctuating while the spectroscopy is being performed. At higher V_j, the E_J of the junction is stable as a function of gate but additional transitions due to the presence of the resonator drive are also observed. We fit the data of the three spectra using the same parameters as those used in Fig. 5.2 while only allowing E_J to vary. The fits maintain their accuracy over the whole V_j range. We do note, however, that for large E_J the fit starts to deviate from the data for transitions to higher excited states (Fig. 5.3(d)). This may be due to a non-sinusoidal energy-phase relation of a transparent channel in the junction. A fit using a Hamiltonian including the Andreev potential for a short transparent junction instead of the standard $\cos\varphi$ potential is shown in gray in Fig. 5.3(d). Details of the fit as well as additional fits to the data in Fig. 5.3(b-c) using the Andreev potential in the Hamiltonian can be found in Appendix 5.8.

We have therefore shown that the behavior of a hybrid fluxonium circuit with a semiconducting weak-link can still be predicted and understood using a simple Hamiltonian with a few degrees of freedom. Moreover, we can conclude that E_J is the only circuit parameter affected by large changes in V_j and that it generally increases with V_j. Our results thus show that it is possible to address and observe the state of the system over a large E_J-range encompassing regimes where its eigenstates are of very different character.

5.5. FLUXONIUM BEHAVIOR IN MAGNETIC FIELD

Next, we explore the magnetic field compatibility of the nanowire fluxonium. The magnetic field behavior of the device strongly depends on the microscopic details of the nanowire junction. In order to demonstrate the field compatibility of the fluxonium circuit elements, we here show data from device B, whose parameters were optimized

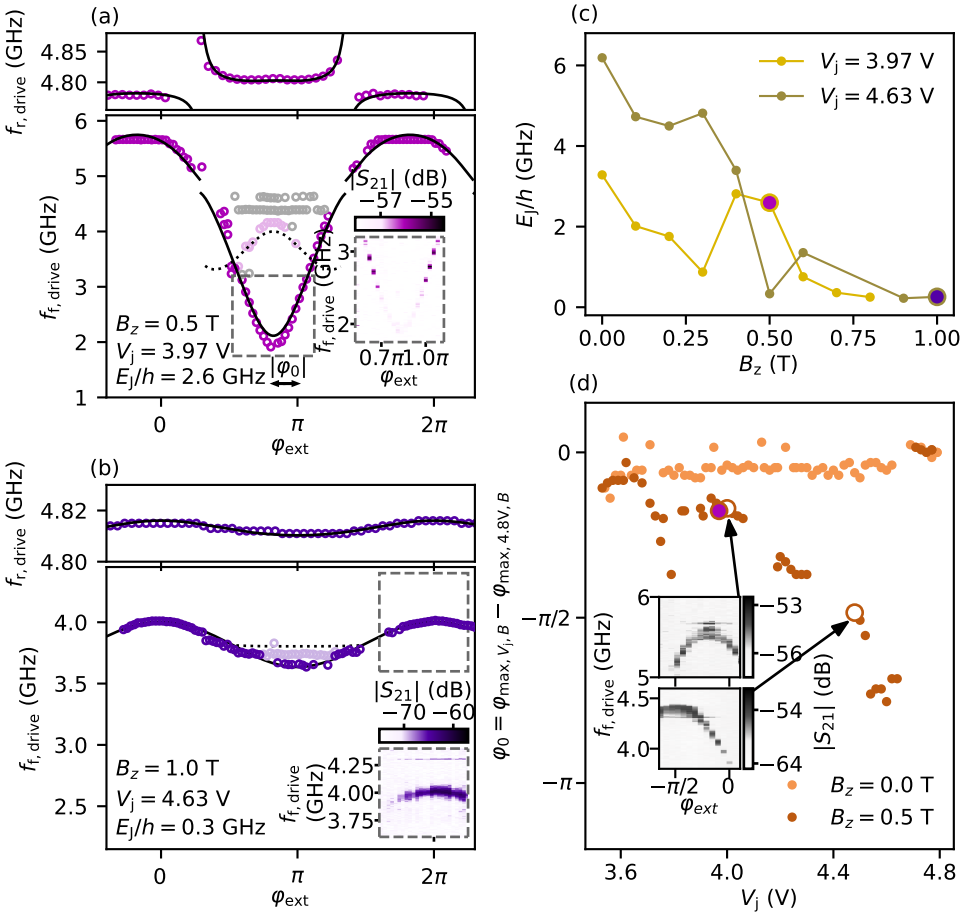

Figure 5.4: Behavior of device B in magnetic field. (a), (b), Fluxonium spectra at two different V_j and B_z points. The E_J value extracted from the fit is lower at higher magnetic field. In (a) we observe a $\varphi_0 = -0.16\pi$ phase shift with respect to a reference φ_{ext} taken at the same field at $V_j = 4.80$ V. (c) E_J versus B_z at two different gate voltage points. E_J decreases non-monotonically with field. (d), φ_0 versus V_j at two different magnetic field points. At $B_z = 0.0$ T, φ_0 stays constant for the whole V_j range. At $B_z = 0.5$ T, however, there is a continuous φ_0 shift that ranges from 0 to $-\pi$. The two insets show the zero-flux spectroscopy feature shifted from zero at two different gate points. In (c) and (d), the points corresponding to the spectra in (a) and (b) are highlighted with matching colors.

for magnetic field compatibility. The magnetic field behavior of device A is provided in Sec. 5.9.4. Spectroscopy measurements at two different V_j and B_z points are shown in Figs. 5.4(a) and (b). We continue to be able to perform spectroscopy on the fluxonium over the full range in φ_{ext} at fields up to 1 T. We do note, however, that at higher magnetic fields, the thermal occupation of the excited state of the fluxonium does increase since we observe transitions from this state even when the $g0 \rightarrow e0$ frequency is above 1 GHz. Importantly, we can still fit the spectroscopy data accurately in this regime, indicating that the fluxonium-resonator Hamiltonian remains valid at high magnetic fields, with E_J being the only parameter largely affected by B_z. Fit parameters for device B are shown in Tab. 5.1.

We finally use the nanowire fluxonium to investigate the behaviour of spin-orbit coupled semiconducting junctions in magnetic field. We perform spectroscopy measurements at gate voltages ranging from 3.5 to 4.8 V and fields ranging from 0 to 1 T. From the spectroscopy, we extract E_J as a function of B_z at two different gate points, which is shown in Fig. 5.4(c). A non-monotonic decrease of E_J with field is observed at both gate points. We expect an overall decrease in E_J versus B_z due to the superconducting gap closing at high magnetic fields. The non-monotonic behaviour of E_J, however, suggests the presence of interference between different modes in the junction (Zuo et al., 2017). Additional in-field E_J data is provided in Sec. 5.9.5. An overall decrease of E_J with B_z is observed for all investigated gate values, while the non-monotonic dependence is often, but not always, observed.

A shifting of the zero-flux point in the spectroscopy of the fluxonium device at high fields can be used to determine the breaking of multiple symmetries in the semiconducting junction (Yokoyama et al., 2014). This phase shift is known as the φ_0-Josephson effect, which occurs when chiral and time-reversal symmetries are both broken in the junction. In InSb- and InAs-based junctions, this symmetry-breaking originates from the interplay between the presence of multiple channels in the junction, spin-orbit coupling, and the Zeeman splitting due to the applied magnetic field (Szombati et al., 2016; van Woerkom et al., 2017; Yokoyama et al., 2014). We observe such a shift in the zero-flux point of the spectroscopy lines as V_j is varied in a B_z-field (indicated by $\varphi_0 = \varphi_{\max,V_j,B} - \varphi_{\max,4.8V,B}$ in Fig. 5.4(a)). The φ_0-shift as a function of V_j is shown, at $B_z = 0$ and at $B_z = 0.5$ T, in Fig. 5.4(d).The φ_0 value at $V_j = 4.80$ V is taken as the $\varphi_0 = 0$ reference at each B_z. The value of φ_0 is thus a relative value at each B_z. At $B_z = 0$ the zero-flux point does not change, while it changes continuously with V_j when a B_z-field is applied. Since the observed phase shift appears as a function of only V_j at fixed magnetic fields, we can exclude trivial effects such as misalignment of the magnetic field. We note that we observe shifts in φ_0 approaching π, which is significantly larger than previously predicted (Yokoyama et al., 2014). Mixing between a large number of spin-split Andreev channels in the junction may lead to the larger observed shifts. Additional φ_0 data as a function of V_j and B_z can be found in the Supplementary Material (Sec. 5.9.5).

5.6. SPECTROSCOPIC LINEWIDTH

For the fluxonium's applications as a detector of field-dependent mesoscopic effects, its spectral lines must be measurable under the magnetic field and electrostatic conditions of interest, but also must maintain a narrow linewidth in all regimes. The spectroscopic

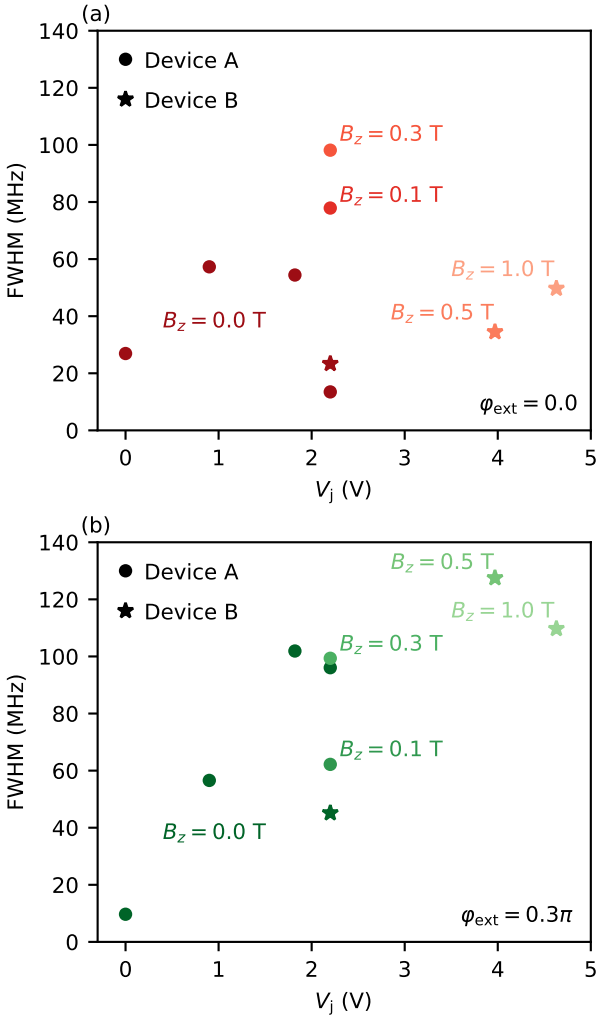

Figure 5.5: Spectroscopic linewidth. Extracted linewidth (full width at half maximum (FWHM)) of the $g \rightarrow e$ transition as a function of V_j for devices A (circular markers) and B (star markers). Different color strengths denote different magnetic fields. The data for device A corresponds to the spectra shown in Fig. 5.3(b,c,d) and Fig. 5.10 in the Supplementary Material (Sec. 5.9.4). The in-field data for device B corresponds to the spectra shown in Fig. 5.4(a,b). The linewidths are extracted in symmetric 0.05π flux windows around $\varphi_{ext} = 0$, which is a sweet spot for the external flux, and $\varphi_{ext} = 0.3\pi$ for (a) and (b), respectively.

linewidth bounds the resolution with which we can resolve the splitting of lines due to, for example, quasiparticle poisoning of highly transparent ABSs or MZMs at the junction.

We have performed a spectroscopic linewidth analysis for devices A and B at different points in external flux (Fig. 5.5): near the flux sweet spot at $\varphi_{ext} = 0$ and also at $\varphi_{ext} = 0.3\pi$. As shown in Fig. 5.5(a), the linewidth of device B stays below 50 MHz up to 1 T at

the $\varphi_{\text{ext}} = 0$. However, the linewidth overall becomes larger, for both devices, at $\varphi_{\text{ext}} = 0.3\pi$ (Fig. 5.5(b)). This behavior is consistent with residual flux noise broadening the linewidth of the fluxonium. Our linewidth analysis indicates that the energy resolution of the fluxonium would, if measuring near $\varphi_{\text{ext}} = 0$, be at most 0.4 μeV in all regimes, which significantly improves upon the resolution that can currently be reached by transport experiments, where the linewidth is limited by thermal broadening (typically ~10 μeV).

We do note that, in our experiment, the fluxonium and resonator parameters were chosen for the greatest visibility over the largest range of E_J and φ_{ext}. Improvements upon the design such as weaker coupling to the readout resonator, smaller asymmetry in the gradiometric superinductance, and materials optimizations such as changing the dielectric of the fluxonium capacitor would lead to significantly narrower linewidths.

5.7. CONCLUSION

In conclusion, we have successfully realized a gate-tunable fluxonium resilient to high magnetic fields. We have combined a gate-controlled junction with magnetic field-compatible materials and a novel gradiometric design to build the hybrid fluxonium. We are able to perform spectroscopy over a large range of gate voltages and in-plane magnetic fields. We have used the fluxonium to investigate the behavior of an InAs Josephson junction in a magnetic field and observed a non-monotonic decrease of the E_J of the junction as well as the φ_0-Josephson effect. The observed φ_0-shift is gate-tunable up to $\varphi_0 = \pi$. One could therefore use this effect to build extremely small, flux-noise insensitive superconducting circuits where the phase difference of the junction could be tuned using a gate-voltage.

The magnetic-field compatible hybrid fluxonium is also now ready to detect the 4π-periodic Josephson effect (Pekker et al., 2013) and measure Majorana parity dynamics. We remark that, while our experiment was performed with similar materials and in similar magnetic fields to previous experiments where transport signatures pointed to the presence of MZMs, we did not observe any signatures of MZMs. Recent theoretical work has suggested that previously observed signatures of MZMs may be due to trivial Andreev bound states (Huang et al., 2018) and has advocated for cleaner materials with stronger spin-orbit coupling proximitized by superconductors with larger energy gaps. Future experiments will thus incorporate InSb nanowires with thinner Al shells as the small junction of the hybrid fluxonium.

The excellent agreement we have demonstrated between data and theory indicate that one can engineer hybrid circuits such that their behavior can continue to be understood even when the circuit is complicated by the interplay of superconductivity, spin-orbit coupling, and magnetism. This opens avenues for using the hybrid fluxonium to explore superconductivity in the presence of a magnetic field as well as reading out and controlling materials platforms that require the application of a large magnetic field. Since it is straightforward to incorporate different materials into the hybrid fluxonium, proposals to probe superconductor-proximitized edge states in a quantum spin Hall insulator (Dolcini et al., 2015; Wu et al., 2018) or field-dependent spin-polarized correlated insulating phases (Cao et al., 2020; Liu et al., 2020) are now possible using our hybrid circuit.

ACKNOWLEDGEMENTS

We thank W. Uilhoorn for fabrication advice. We also thank B. van Heck and A. Antipov for helpful discussions. This research was co-funded by the allowance for Top consortia for Knowledge and Innovation (TKI's) from the Dutch Ministry of Economic Affairs and the Microsoft Quantum initiative.

5.8. APPENDIX: MODELING THE JUNCTION ACCOUNTING FOR HIGHLY TRANSPARENT TRANSMISSION CHANNELS

In Figs. 5.2, 5.3 and 5.4 we fit the spectroscopy data assuming a sinusoidal current-phase relation at the junction, which results in the term $-E_J\cos(\varphi)$ in the Hamiltonian (equation 5.2), which is characteristic of superconductor-insulator-superconductor (SIS) junctions with low transparency channels. A more accurate model for the potential of a semiconducting Josephson junction with N channels with transparencies T_i is (Beenakker, 1991)

$$V_{sJJ}(\varphi) = \Delta \sum_{i=1}^{N} \sqrt{1 - T_i \sin^2(\varphi/2)}, \tag{5.3}$$

where Δ denotes the induced gap on the proximitized sections of the nanowire. When the transparencies of the different channels are low, this dependence converges to a sinusoidal relation with $E_J = \Delta \sum_{i=1}^{N} T_i/4$.

Here, we show fits to the spectroscopy data from Fig. 5.3 using the semiconducting junction potential V_{sJJ} with different number of channels and for various values of Δ. Fig. 5.6 shows fits to the transitions starting from the ground state with the Hamiltonian for the uncoupled fluxonium (equation 5.2) using a sinusoidal potential, a one-channel potential and a two-channel potential. In Fig. 5.7 we show the Δ-sensitivity of the one-channel spectrum, showing the fit accuracy for Δ-values lower and higher than the optimum value. For low and intermediate E_J values the accuracy of the different models is very similar. For high E_J, however, the fits to the high frequency transitions are more accurate when highly transparent channels are included. This points toward the presence of at least one highly transparent channel in the junction. The fit accuracy is however similar when one, two or more channels are considered. We thus can not extract a measure of the number of junction channels by performing fits of the spectroscopic data.

We furthermore observe that the best fit assuming a single channel occurs at $\Delta/h = 26$ GHz. This is smaller than the gap ($\Delta/h = 53$ GHz) typically measured in transport experiments. This discrepancy may be due to the necessity of incorporating excited Andreev states into the fluxonium model or interactions due to an accidental quantum dot in the junction (Bargerbos et al., 2020; Hazard et al., 2019; Kringhøj et al., 2020).

5.9. SUPPLEMENTARY MATERIAL

5.9.1. FITTING PROCEDURE

To find the relative extrema we apply a peak finding algorithm to the raw data. This algorithm first smooths the data in the frequency axis to avoid errors in peak finding due

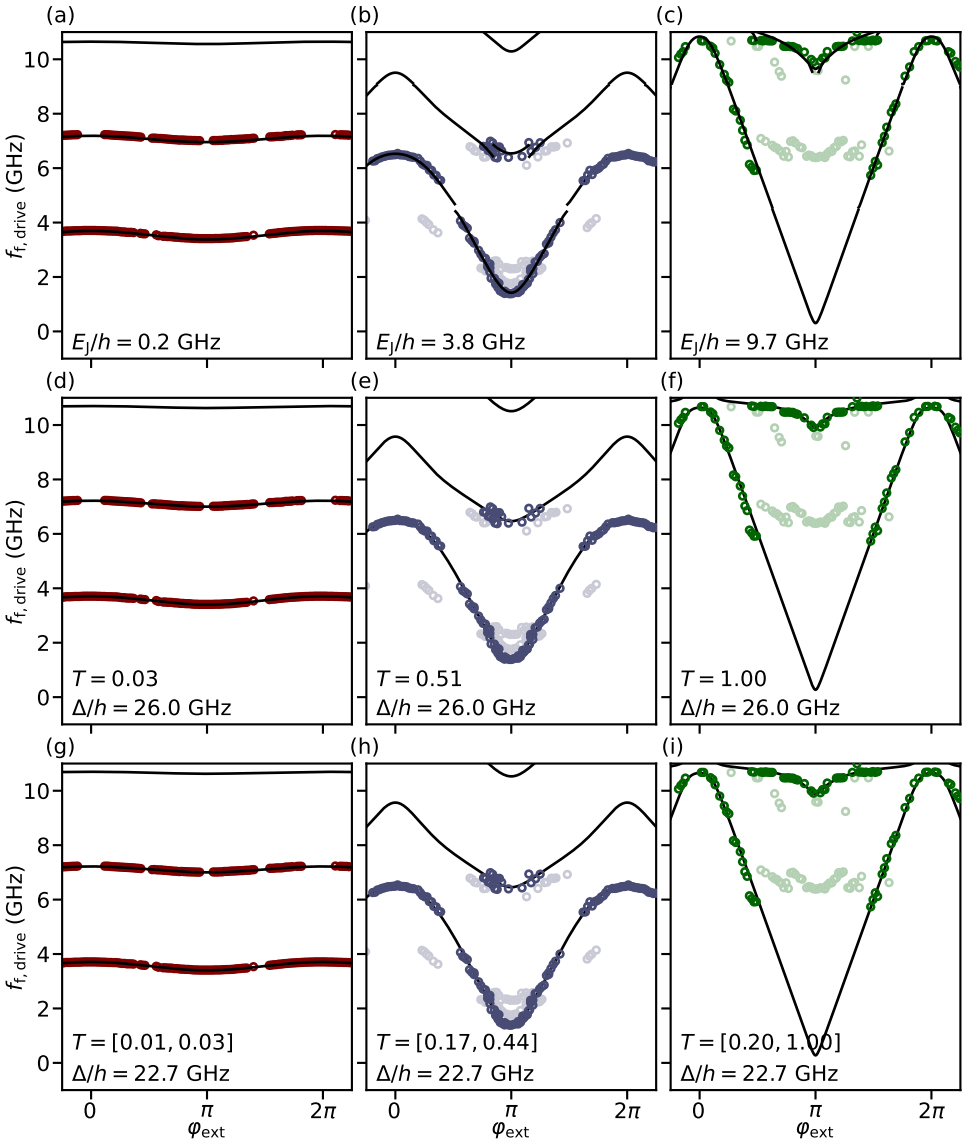

Figure 5.6: Fits using the Andreev potential in the Hamiltonian. Spectroscopy data fit with the uncoupled fluxonium Hamiltonian (equation 5.2) with a sinusoidal potential (first row), with a one-channel potential (second row) and with a two-channel potential (third row). Only the dark markers, corresponding to transitions starting from the ground state, are included in the fit. $E_C/h = 2.35$ GHz and $E_L/h = 0.7$ GHz are obtained for the three different fits. The rest of the fit parameters are indicated in the different panels.

to noise. A minimum peak height is specified.

We fit the extracted data with the Hamiltonian corresponding to the circuit model in Fig. 5.1(a). The fluxonium Hamiltonian, $\hat{H}_{\mathrm{f}}$, and the total Hamiltonian of the coupled

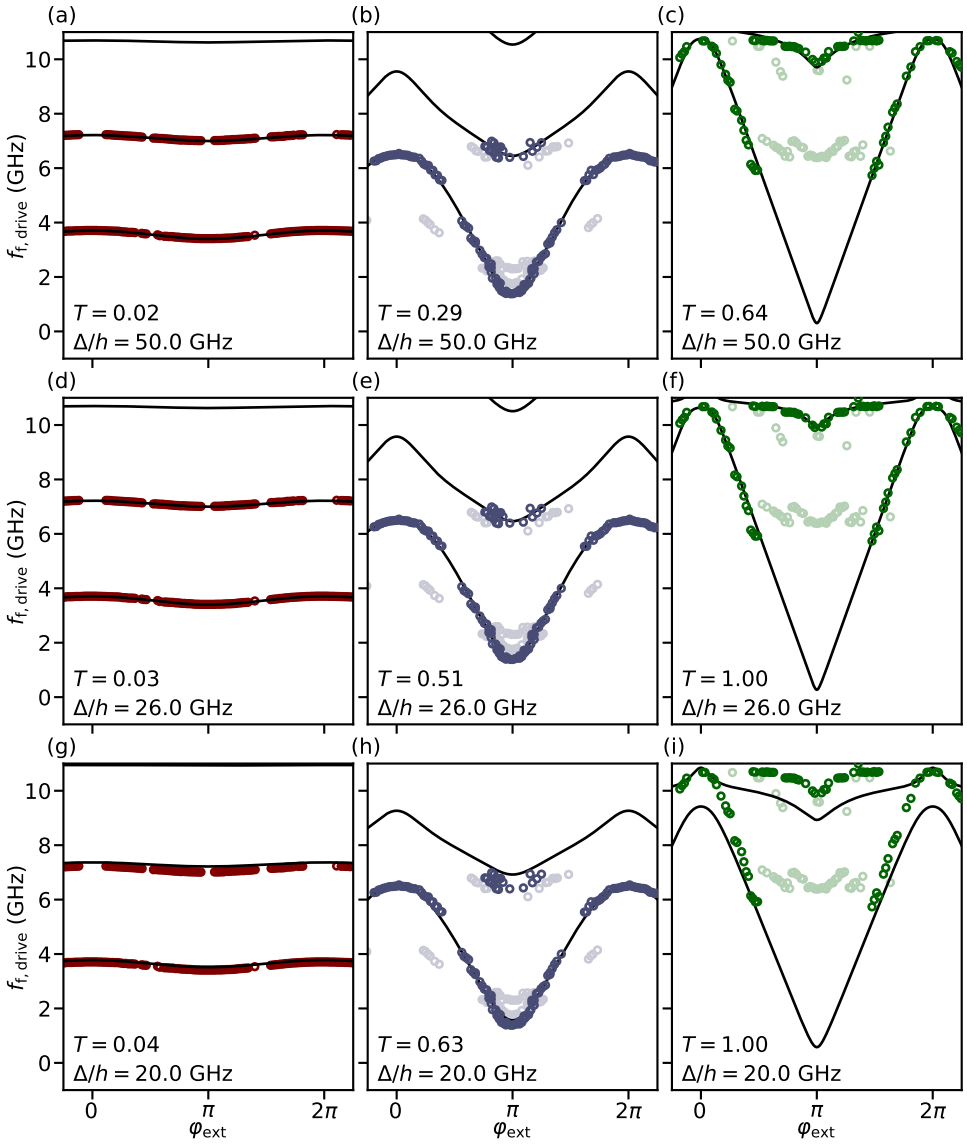

Figure 5.7: Δ-dependence of fits using the Andreev potential in the Hamiltonian. Spectroscopy data fitted with the uncoupled fluxonium Hamiltonian (equation 5.2) with a one-channel potential. In the first and third rows the value of Δ is fixed to $\Delta/h = 50.0$ GHz and $\Delta/h = 20.0$ GHz, respectively. In the second row Δ is left free and $\Delta/h = 26.0$ GHz is obtained as the optimum value. Only the dark markers, corresponding to transitions starting from the ground state, are included in the fit.

readout-fluxonium system, $\hat{H}$, can be written in terms of two degrees of freedom, $\hat{\varphi}_{\mathrm{f}}$ and $\hat{\varphi}_{\mathrm{r}}$ (the phase drops across the fluxonium junction and across C_{r}, respectively), and their conjugated charges, $\hat{n}_{\mathrm{f}}$ and $\hat{n}_{\mathrm{r}}$ (Smith et al., 2016). In the limit $L_{\mathrm{f}} \gg L_{\mathrm{s}}, L_{\mathrm{r}}$ (where

$L_\mathrm{f} = \frac{\Phi_0^2}{4\pi^2 E_L}$ and $\Phi_0 = h/2e$),

$$\hat{H}_\mathrm{f} = 4E_C\hat{n}_\mathrm{f}^2 - E_\mathrm{J}(V_\mathrm{j}, B)\cos(\hat{\varphi}_\mathrm{f}) + \frac{1}{2}E_L\big(\hat{\varphi}_\mathrm{f} - \varphi_\mathrm{ext}\big)^2 \tag{5.4}$$

and

$$\hat{H} = \frac{2e^2}{C_\mathrm{r}}\hat{n}_\mathrm{r}^2 + \frac{1}{2}\frac{(\Phi_0/2\pi)^2}{(L_\mathrm{r}+L_\mathrm{s})}\hat{\varphi}_\mathrm{r}^2 - \frac{1}{2}\frac{(\Phi_0/2\pi)^2 L_\mathrm{s}}{L_\mathrm{f}(L_\mathrm{r}+L_\mathrm{s})}\hat{\varphi}_\mathrm{r}\hat{\varphi}_\mathrm{f} + \hat{H}_\mathrm{f}. \tag{5.5}$$

The first two terms of $\hat{H}$ describe the uncoupled resonator, while the third term accounts for the coupling between resonator and fluxonium.

We diagonalize Hamiltonian 5.5 using the numerical method in Ref. (Smith et al., 2016). All the spectra for the same device are fit simultaneously. The free parameters E_C, E_L, L_r and L_s are common for all spectra corresponding to the same device. The free parameter E_J, however, has a different value for each spectrum.

All markers shown in Figs. 5.2, 5.3 and 5.4 are included in the fits. The marker colors are assigned by association to the different transitions. Gray markers indicate extrema that could not be assigned to any transition included in the fit.

5.9.2. THEORETICAL MODEL FOR THE UNCOUPLED FLUXONIUM

The Hamiltonian for the uncoupled fluxonium, $\hat{H}_\mathrm{f}$, can be written in terms of the phase drop across the junction, $\hat{\varphi}_\mathrm{f}$, and its conjugate charge $\hat{n}_\mathrm{f}$ (Manucharyan et al., 2009; Smith et al., 2016)

$$\hat{H}_\mathrm{f} = 4E_C\hat{n}_\mathrm{f}^2 - E_\mathrm{J}(V_\mathrm{j}, B)\cos(\hat{\varphi}_\mathrm{f}) + \frac{1}{2}E_L\big(\hat{\varphi}_\mathrm{f} - \varphi_\mathrm{ext}\big)^2. \tag{5.6}$$

Each of the terms in $\hat{H}_\mathrm{f}$ results from one of the three characteristic energies of fluxonium: E_C, E_L and E_J. The two conjugate variables in this Hamiltonian, $\hat{\varphi}_\mathrm{f}$ and $\hat{n}_\mathrm{f}$, are analogous to position and momentum, respectively. With this interpretation, the two terms involving $\hat{\varphi}_\mathrm{f}$ constitute a phase-dependent potential

$$V(\varphi) = -E_\mathrm{J}\cos(\varphi) + \frac{1}{2}E_L\big(\varphi - \varphi_\mathrm{ext}\big)^2. \tag{5.7}$$

Fig. 5.8(i) shows the potential at $\varphi_\mathrm{ext} = 0$ for the three E_J values in Fig. 5.3. The E_L term results in a parabolic background, common for the three cases. The E_J adds a periodic modulation on top of it, which becomes more noticeable as E_J increases. E_C can be seen as a mass term and, together with the potential V, determines the eigenstates of fluxonium. The lowest energy eigenstates are labelled g, e, f and h. Their energies at $\varphi_\mathrm{ext} = 0$ are shown as colored lines in Fig. 5.8(i). Fig. 5.8(ii) shows the energy dispersion of the fluxonium with respect to φ_ext. For small E_J values, the variation of φ_ext results in weak oscillations of the eigenenergies, while for large E_J's the φ_ext-dependence is much stronger. In the limit of small E_J the eigenstates are vibrational modes of the harmonic LC oscillator determined by E_L and E_C. Therefore, their energies are evenly spaced with a separation determined by the plasma frequency $\sqrt{8E_C E_L}/h$. In the limit of large E_J the eigenstates become superpositions of persistent currents localized in phase.

Fig. 5.8(iii) shows the transition frequencies between different pairs of eigenstates, which are the quantities that can be addressed experimentally. For simplicity, only the transitions starting from the ground state are shown here. The two-tone spectroscopy data in Figs. 5.2, 5.3 and 5.4 show the measured transition frequencies for the coupled fluxonium-resonator system.

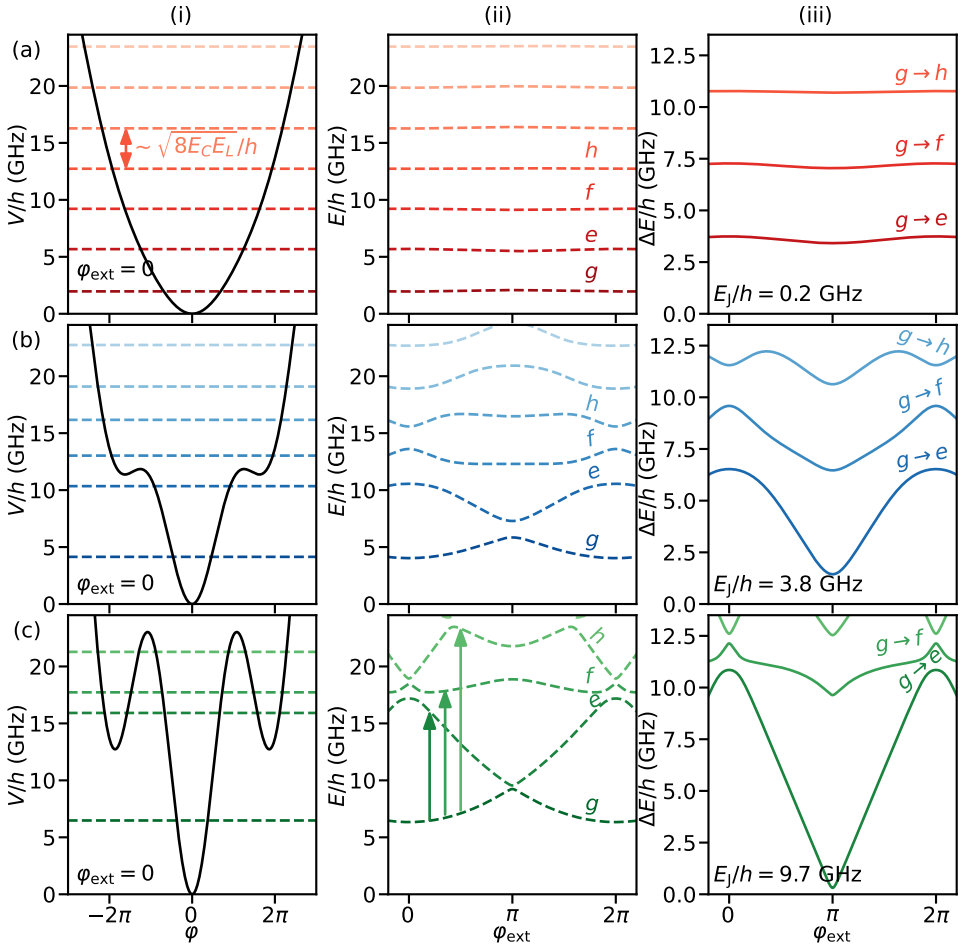

Figure 5.8: Potential, energy spectrum and transition frequencies of the uncoupled fluxonium. Rows (a), (b) and (c) correspond to $E_J/h = 0.2$, 3.8 and 9.6 GHz, respectively, for the model parameters of device A. Column (i) shows the fluxonium potential in equation 5.7, at $\varphi_{ext} = 0$, in black lines. The lowest eigenenergies of Hamiltonian 5.4 at $\varphi_{ext} = 0$ are superimposed as horizontal dashed lines. Column (ii) shows how these energies disperse as φ_{ext} is varied. The solid arrows indicate transitions starting from the ground state, g. The energies of these transitions are plotted in column (iii) as a function of φ_{ext}.

5.9.3. RESONATOR-FLUXONIUM INDUCTIVE COUPLING FOR DEVICE B

The SEM image shown in Fig. 5.1(d) corresponds to a device with design identical to the one of device A, for which the shared inductance is situated on the top part of the fluxonium loop. For device B, however, the shared inductance is placed on a side of the superinductive loop, as shown in Fig. 5.9. We do not expect this difference in design to have had a measurable impact on the measurements of devices A and B.

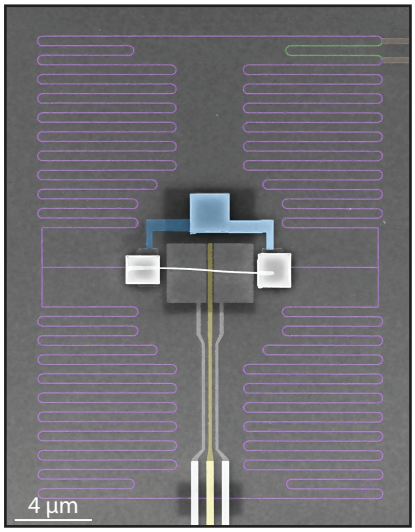

Figure 5.9: False-colored SEM image showing the resonator-fluxonium inductive coupling for a device with design identical to the one of device B. Parts implementing the different circuit elements are shaded with the same colors as in Fig. 5.1.

5.9.4. FIELD DATA FOR DEVICE A

Fig. 5.10 shows the spectroscopy data for device A under in-plane magnetic field, up to 0.3 T. We note the presence of phase-independent lines crossing the fluxonium spectrum at frequencies above 6 GHz at 0.3 T. Beyond 0.3 T, the transition frequencies of the fluxonium came within 1 GHz of the resonator frequency, which resulted in the spectroscopy of the fluxonium becoming unmeasureable.

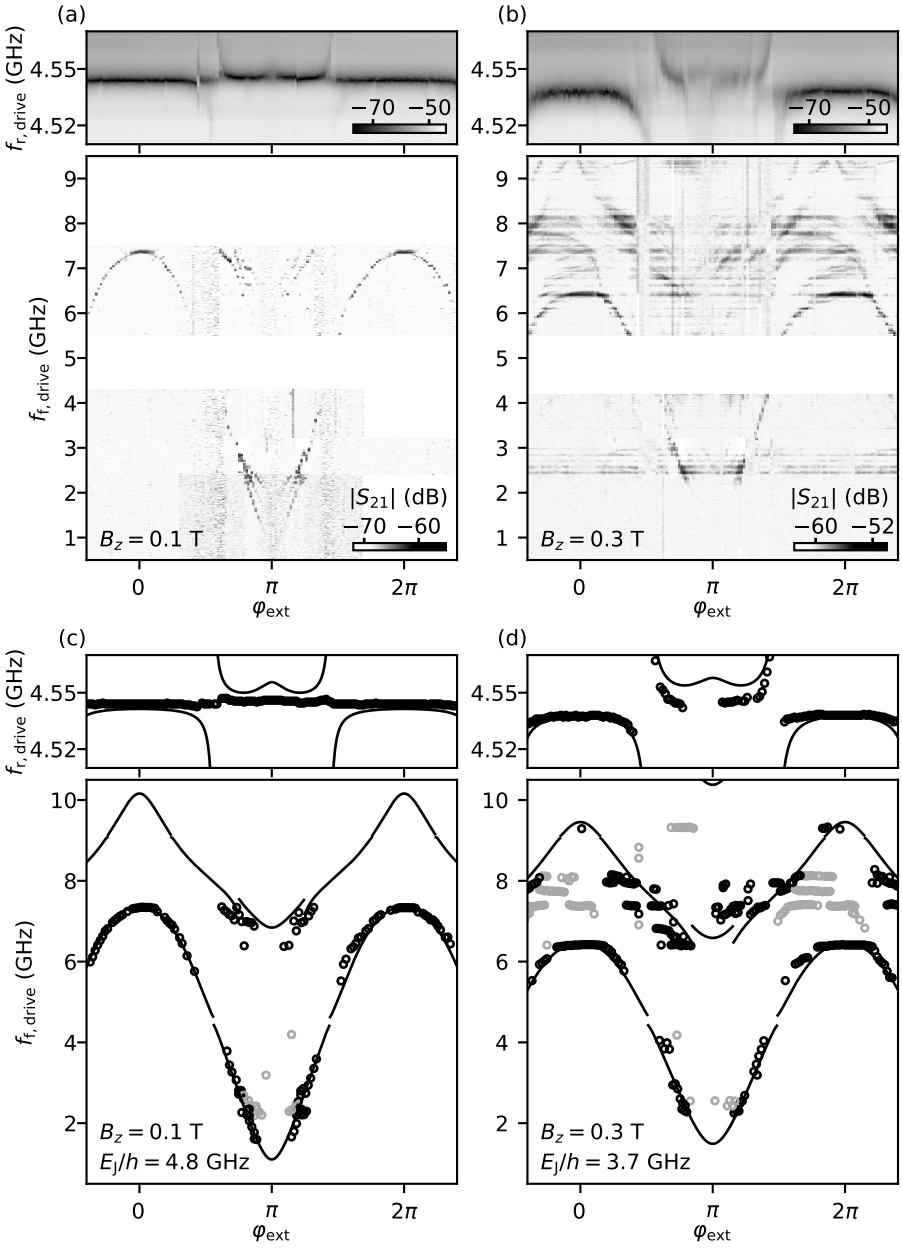

Figure 5.10: Spectroscopy data for device A under in-plane magnetic field. Spectra in (a) and (b) are taken at $B_z = 0.1$ T and 0.3 T, respectively, at the same gate voltage, $V_j = 2.20$ V, as the spectrum in Fig. 5.3(c). (c) and (d) show the extracted peaks (markers) and the fitted transition frequencies (solid lines). The E_J/h values obtained from the fit are 4.8 and 3.7 GHz, respectively.

5.9.5. ADDITIONAL FIELD AND GATE DATA FOR DEVICE B

Fig. 5.11 shows E_J and φ_0 extracted from spectroscopy data at multiple field and gate values, complementing the data shown in Fig. 5.4(c,d). The Josephson energy decreases with B_z for all V_j values (Fig. 5.11(a)) and does so in a non-monotonic way for multiple gate points. We observe the anomalous Josephson effect starting from 0.1 T and becoming stronger for larger values of B_z (Fig. 5.11(b)). Above 0.8 T, E_J is very low for multiple gate voltages, which makes it difficult to observe the φ_0-shift at those points.

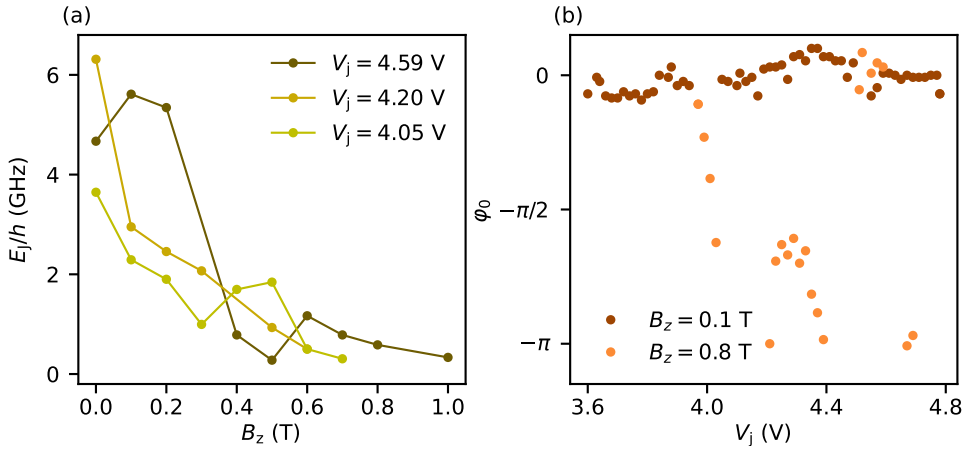

Figure 5.11: Extra data for device B in magnetic field. (a), E_J versus B_z at three different V_j points that complement the data shown in Fig. 5.4(c). (b), φ_0 versus V_j at three different B_z points that complement the data shown in Fig. 5.4(d). $V_j = 4.8$ V is taken as the $\varphi_0 = 0$ reference for $B_z = 0.1$ T and $B_z = 0.3$ T and $V_j = 4.6$ V is taken as the $\varphi_0 = 0$ reference for $B_z = 0.8$ T.

6

SINGLET-DOUBLET TRANSITIONS OF A QUANTUM DOT JOSEPHSON JUNCTION DETECTED IN A TRANSMON CIRCUIT

We realize a hybrid superconductor-semiconductor transmon device in which the Josephson effect is controlled by a gate-defined quantum dot in an InAs/Al nanowire. Microwave spectroscopy of the transmon's transition spectrum allows us to probe the ground state parity of the quantum dot as a function of gate voltages, external magnetic flux, and magnetic field applied parallel to the nanowire. The measured parity phase diagram is in agreement with that predicted by a single-impurity Anderson model with superconducting leads. Through continuous time monitoring of the circuit we furthermore resolve the quasiparticle dynamics of the quantum dot Josephson junction across the phase boundaries. Our results can facilitate the realization of semiconductor-based $0-\pi$ qubits and Andreev qubits.

The work in this chapter has been published as: A. Bargerbos*, **M. Pita-Vidal***, R. Žitko, J. Ávila, L.J. Splitthoff, L. Grünhaupt, J.J. Wesdorp, C.K. Andersen, Y. Liu, P. Krogstrup, L.P. Kouwenhoven, R. Aguado, A. Kou, and B. van Heck, Singlet-doublet transitions of a quantum dot Josephson junction revealed in a transmon circuit, PRX Quantum **3**, 030311 (2022). * Equal contributions.

6.1. INTRODUCTION

Superconducting pairing and charging energy are two fundamental interactions that determine the behavior of mesoscopic devices. Notably, when a quantum dot (QD) is coupled to a superconductor, they compete to determine its ground state. A large charging energy favors single-electron doublet occupancy of the dot and thus a spin-1/2 ground state, while a strong coupling to the superconducting leads favors double occupancy in a singlet configuration with zero spin. A quantum phase transition between the singlet and doublet ground state can occur as system parameters such as the dot energy level and the coupling strength are varied. The latter also controls the nature of the singlet ground state, which can be either of the Bardeen-Cooper-Schrieffer (BCS) type or of the Kondo type. The rich phase diagram of the system, as well as its transport properties, are theoretically well captured by an Anderson model with superconducting leads (Choi et al., 2004; Glazman and Matveev, 1989; Kadlecová et al., 2019; Karrasch et al., 2008; Luitz et al., 2012; Martín-Rodero and Levy Yeyati, 2011; Meden, 2019; Oguri et al., 2004; Tanaka et al., 2007; Yoshioka and Ohashi, 2000).

Quantum dots coupled to superconductors have been studied experimentally over the last two decades. Signatures of the singlet-doublet transition have been detected in tunneling spectroscopy measurements of N-QD-S devices (where N is a normal lead, and S is a superconducting one) via the observation of Fermi-level crossings (Chang et al., 2013; Deacon et al., 2010; Lee et al., 2014, 2017; Li et al., 2017; Pillet et al., 2010, 2013; Valentini et al., 2021; Whiticar et al., 2021). Additionally, they have been detected in switching current measurements of S-QD-S devices via π-phase shifts in the current-phase relation of the resulting quantum dot Josephson junction (Cleuziou et al., 2006; Delagrange et al., 2015, 2018; Eichler et al., 2009; García Corral et al., 2020; Jørgensen et al., 2009; Jørgensen et al., 2007; Kumar et al., 2014; Lee et al., 2012; Maurand et al., 2012; Szombati et al., 2016; van Dam et al., 2006; Whiticar et al., 2021).

Recent experiments (Hays et al., 2020, 2021; Janvier et al., 2015) on Andreev pair and spin qubits (Chtchelkatchev and Nazarov, 2003; Padurariu and Nazarov, 2010; Pavešić and Žitko, 2022; Zazunov et al., 2003) have renewed the interest in quantum dot junctions due to the possibility of tuning the ground state of the system to be in addressable spin states. Knowledge of the phase diagram of the quantum dot junction is also beneficial for realizing proposals for a quantum-dot-based readout of topological qubits (Karzig et al., 2017; Plugge et al., 2017; Smith et al., 2020).

These developments have highlighted the need for a better fundamental understanding of the quantum dot junction and its dynamics, requiring tools which are not limited by the long integration times of low-frequency measurements nor by the invasiveness of transport probes. To address this need, we have embedded a fully controllable quantum dot in a microwave superconducting circuit. This experimental choice is motivated by the success of circuit quantum electrodynamics (QED) techniques in the investigation of mesoscopic effects in Josephson junctions (de Lange et al., 2015; Hays et al., 2018, 2020, 2021; Janvier et al., 2015; Kringhøj et al., 2020; Larsen et al., 2015; Matute-Cañadas et al., 2022; Tosi et al., 2018; Uilhoorn et al., 2021), which stems from its enhanced energy and time resolution compared to low-frequency transport techniques. In this context, the microwave response of a quantum dot junction has attracted recent theoretical (Hermansen et al., 2022; Kurilovich et al., 2021) and experimental (Fatemi et al., 2022)

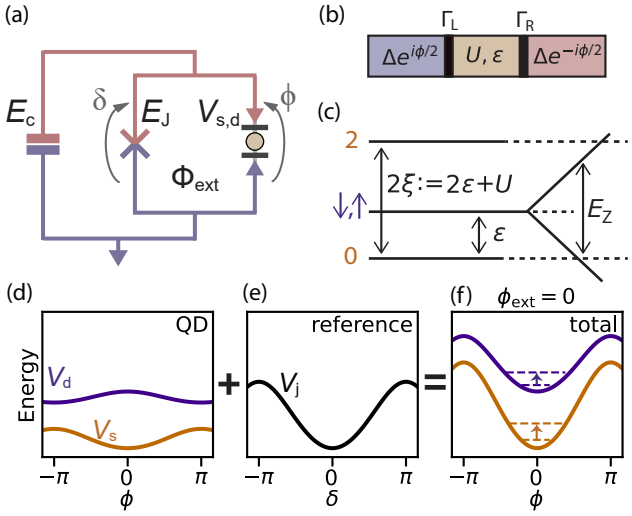

Figure 6.1: (a) Schematic diagram of a quantum dot junction incorporated into a transmon circuit. The transmon island with charging energy E_c is connected to ground by a SQUID formed by the parallel combination of a quantum dot junction and a reference junction. In this panel ϕ and δ denote the superconducting phase difference across the quantum dot and reference junctions respectively. Φ_{ext} is the externally applied magnetic flux through the SQUID loop. (b) Model diagram of the quantum dot junction in the excitation picture. Two s-wave superconductors are connected via tunnel barriers to a single level quantum dot. (c) Level diagram of the quantum dot hosting 0, 1, or 2 electrons when disconnected from the leads ($\Gamma_L = \Gamma_R = 0$). (d) Phase dependence of the Josephson potential of the quantum dot junction in the singlet (orange) and doublet (purple) state. (e) Josephson potential of the reference junction. (f) Josephson potential of the DC SQUID for $\phi_{ext} = (2e/\hbar)\Phi_{ext} = 0$, with the quantum dot junction in the singlet (orange) and doublet (purple) state. The dashed lines represented the two lowest transmon energy levels in each branch of the Josephson potential, with the arrow denoting the resulting transition frequency, which can differ for the two quantum dot junction states (orange and purple arrows for singlet and doublet, respectively).

attention.

The core of our experiment is a transmon circuit formed by an island with charging energy E_c, coupled to ground via a superconducting quantum interference device (SQUID) formed by a parallel combination of a junction with a known Josephson energy E_J and a quantum dot junction (Fig. 6.1(a-c)). The energy-phase relation of the quantum dot junction depends on whether it is in a singlet or doublet state, with a characteristic π-phase shift between the two relations (Fig. 6.1(d)) (Spivak and Kivelson, 1991). The two energy-phase relations of the junctions add up together in the SQUID. Depending on whether the quantum dot junction is in the singlet or doublet state, as well as on the external flux, this results in a higher or lower curvature of the total potential around its minimum with respect to that of the reference junction. Therefore, the two branches of the spectrum give rise to two distinct transition frequencies of the transmon circuit, which can be detected and distinguished via standard circuit QED techniques (Blais et al., 2004). As a result, a transition from a singlet to a doublet state will appear as a discontinuous jump in a measurement of the transmon frequency spectrum.

Using this method, we have detected the singlet-doublet transition and reconstructed

the phase diagram of a quantum dot junction as a function of all experimentally controlled parameters in a single device: the energy level of the dot, the tunnel couplings to the superconducting leads, the superconducting phase difference across the quantum dot junction, and also an external Zeeman field. The measured phase boundaries are in agreement with the single-impurity Anderson model with superconducting leads as calculated via the numerical renormalization group (NRG) (Bulla et al., 2008; Satori et al., 1992; Wilson, 1975; Yoshioka and Ohashi, 2000) methods, and include parameter regimes that have experimentally not been explored before. Finally, we have investigated the rates at which the quantum dot switches between doublet and singlet occupation via real-time monitoring of the transmon circuit, allowing us to determine the switching time-scales of the quantum dot junction parity across the phase transition.

6.2. DEVICE OVERVIEW

The quantum dot junction under investigation is formed in a 10 µm-long epitaxial super conductor-semiconductor nanowire with a 100 nm-wide hexagonal InAs core and a 6 nm-thick Al shell covering two of its facets (Krogstrup et al., 2015). The quantum dot junction is located in a 200 nm-long uncovered section of the nanowire where the Al has been etched away, where it is electrostatically defined by three bottom gate electrodes (Fig. 6.2(d)). As shown in the circuit of Fig. 6.2(a), this quantum dot junction is placed in parallel to a second Josephson junction, hereafter referred to as the "reference junction", to form a SQUID. The reference junction consists of a second 110 nm-long uncovered segment of InAs on the same nanowire as the quantum dot junction. Its Josephson energy E_J can be tuned with a single gate electrode via the field effect.

The SQUID connects a superconducting island to ground, resulting in a transmon circuit (Koch et al., 2007) governed by the Hamiltonian

$$H = -4E_c\partial_\phi^2 + V(\phi), \tag{6.1}$$

where $E_c = e^2/2C_\Sigma$, with C_Σ the total capacitance of the island to ground. The Josephson potential $V(\phi)$ is determined by the phase-dependent energies of the reference junction, $V_j(\delta) = E_J(1-\cos\delta)$, and of the quantum dot junction, $V_{s,d}(\phi)$:

$$V(\phi) = E_J\left[1-\cos(\phi-\phi_{ext})\right] + \begin{cases} V_s(\phi) & \text{singlet} \\ V_d(\phi) & \text{doublet}. \end{cases} \tag{6.2}$$

Here, the phase drops across the quantum dot junction (ϕ) and across the reference junction (δ) are connected according to $\phi-\delta = \phi_{ext}$, where $\phi_{ext} = (2e/\hbar)\Phi_{ext}$ is the phase difference resulting from the externally applied magnetic flux through the SQUID loop, Φ_{ext}.

The presence of the reference junction serves several purposes. First, it allows us to tune the phase difference at the quantum dot junction by changing Φ_{ext} with the B_y component of the magnetic field (see Sec. 6.8). We generally operate the device in a regime where the reference junction has a Josephson energy that is larger than that of the quantum dot by more than an order of magnitude. This ensures that δ is close to zero, while ϕ is close to ϕ_{ext} (Della Rocca et al., 2007). Second, the ability to tune E_J independently of the quantum dot junction ensures that the transition frequencies of the

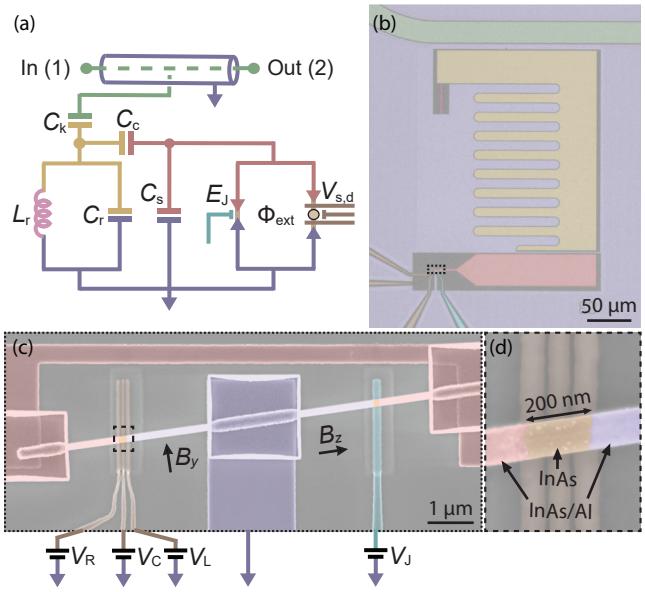

Figure 6.2: **Device overview.** (a) Diagram of the microwave circuit. A coplanar waveguide transmission line (green center conductor) is capacitively coupled to a grounded LC resonator. The resonator consists of an island (yellow) capacitively and inductively (pink) shunted to ground (blue). The resonator is in turn capacitively coupled to a transmon island (red), which is shunted to ground capacitively as well as via two parallel Josephson junctions. (b) False-colored optical microscope image of device A showing the qubit island, the resonator island, the resonator inductor, the transmission line, the electrostatic gates and ground. (c) False-colored scanning electron micrograph (SEM) of the transmon's Josephson junctions, showing the InAs/Al nanowire into which the junctions are defined. The B_y component of the magnetic field is used to tune Φ_{ext}. B_z is the magnetic field component parallel to the nanowire. (d) False-colored SEM of the quantum dot junction in which the quantum dot is gate defined. The three bottom gates have a width and spacing of 40 nm, although this is obfuscated by the dielectric layer placed on top.

transmon circuit remain inside the measurement bandwidth for all parameter regimes of the quantum dot junction. Finally, the Josephson energy of the reference junction is such that $E_J/E_c > 25$, suppressing unwanted sensitivity to fluctuating charges in the environment and justifying the absence of an offset charge in the Hamiltonian of Eq. (6.1) (Koch et al., 2007).

In order to perform microwave spectroscopy measurements, the transmon is capacitively coupled to a readout resonator which is in turn coupled to a transmission line. This allows us to measure the circuit's complex microwave transmission S_{21} through the transmission line's input (1) and output (2) ports.

The experimental implementation of the circuit (Fig. 6.2(b-d)) differs from conventional circuit QED geometries in several ways (Blais et al., 2021), in order to allow the application of magnetic fields in excess of 100 mT. Apart from the Josephson junctions, all circuit elements are made out of field compatible 20 nm-thick NbTiN films (Luthi et al., 2018). We additionally incorporate vortex pinning sites in the ground plane, the transmission line, the resonator island and the transmon island (Kroll et al., 2019). We use a lumped element readout resonator, which has previously been successfully utilized in

flux-sensitive devices up to 1 T, as discussed in Chapter 5. Its capacitance is formed by an interdigitated capacitor to ground, while its inductance is formed by a 200 nm wide NbTiN nanowire, which has a kinetic inductance of 15 pH/□. This design localizes the regions of high current density at the narrow inductor where vortices are less likely to nucleate due to its reduced width (Samkharadze et al., 2016). For the transmon circuit the SQUID loop area is chosen to be small, $\sim 5\mu m^2$, in order to suppress flux noise from misalignment in large parallel magnetic fields. Finally, InAs/Al nanowires, in which both junctions are defined, have been shown to support sizeable Josephson energies in fields in excess of 1 T (Uilhoorn et al., 2021). Further details about device fabrication as well as the cryogenic and room temperature measurement setup can be found in the Supplementary Information of Sec. 6.8.

6.3. ANDERSON MODEL FOR A QUANTUM DOT JUNCTION

As we will show, the quantum dot junction can be described by a single Anderson impurity tunnel-coupled to two superconducting leads. We review its most important properties to facilitate the discussion of the experimental results that follow. In particular, we discuss here the important parameters and concepts that are required to interpret the experimental results, deferring to the Supplementary Information of Sec. 6.8 for a technical description of the Hamiltonian and of the numerical methods used to produce the theoretical results.

The model contains a single-level quantum dot coupled to two superconducting leads via tunnel barriers, schematically depicted in Fig. 6.1(b). The superconducting leads have a pairing gap Δ and a phase difference ϕ, and the barriers are characterized by single-electron tunneling rates Γ_L and Γ_R. The energy diagram for the isolated quantum dot is shown in Fig. 6.1(c). The quantum dot is modeled as an Anderson impurity with single-occupancy energy ϵ, measured with respect to the Fermi level in the leads, and a repulsive Coulomb interaction U, which penalizes the double occupancy of the dot energy level.

The quantum dot is spin-degenerate at zero magnetic field. An external magnetic field B splits the degeneracy by a Zeeman energy $E_Z = g\mu_B B$, where g is the effective g-factor of the level and μ_B is the Bohr magneton. In the experiment we choose the B-field direction to be parallel to the nanowire, since this is the direction that suppresses the superconductivity in the Al nanowire shell the least.

The energy levels of Fig. 6.1(c) are divided in two sectors, corresponding to their fermion parity, or equivalently, to their total spin S. The singlet sector includes the states of even parity: the empty state $|0\rangle$ and the pair state $|2\rangle$. These states have $S = 0$ and are therefore insensitive to the magnetic field B. The doublet sector includes the states of odd parity, $|\uparrow\rangle$ and $|\downarrow\rangle$, which have $S = 1/2$. It is convenient to introduce the energy $\xi = \epsilon + U/2$, corresponding to half of the energy gap in the singlet sector, so that $\xi = 0$ corresponds to the electron-hole symmetry point, where $|0\rangle$ and $|2\rangle$ are degenerate in energy. The ground state of the isolated dot (that is, $\Gamma_L = \Gamma_R = 0$) belongs to the doublet sector for $|\xi| < \frac{1}{2}U$.

A salient feature of the model is that a quantum phase transition between doublet and singlet ground state can occur upon changing several experimentally-tunable parameters. The dot energy level ξ and the coupling strengths $\Gamma_{L,R}$ (all experimentally tun-

able via the bottom electrostatic gates), as well as the superconducting phase difference ϕ and the magnetic field B, all act to shift the relative positions of the potentials V_s and V_d and to cause an energy crossing between the ground states of the two sectors. In the measurements reported in Sec. 6.4 and 6.5, we vary all these parameters and compare the extracted phase boundaries to theory.

For the theoretical comparison we use the NRG method (Žitko and Pruschke, 2009; Wilson, 1975; Žitko, 2021) to compute the lowest-lying eigenvalues in the singlet and doublet spin sectors as a function of the phase difference ϕ[1]. This results in the Josephson potentials $V_s(\phi)$ and $V_d(\phi)$, which are then used as input to the model of Eq. (6.2) to calculate the transmon transition frequencies (see Sec. 6.8). The projection onto the lowest-energy state of the Josephson junction in each sector is enough to capture the salient features of our experiment, although the inclusion of excited Andreev states of the quantum dot junction in the circuit model is theoretically possible (Ávila et al., 2020; Avila et al., 2020b; Keselman et al., 2019; Kurilovich et al., 2021; Zazunov et al., 2003).

Experimentally, the observation of the phase transition is facilitated by the presence of a π-phase shift between $V_s(\phi)$ and $V_d(\phi)$. The phase shift arises because the sequence of single-electron tunneling events that leads to the transport of a Cooper pair between the two leads depends on whether the quantum dot is initially in the singlet or the doublet sector. In particular, if the dot is initially in the doublet state, a permutation of spin-up and spin-down electrons is required in order to complete the tunneling sequence (Spivak and Kivelson, 1991), leading to a π phase shift due to Fermi-Dirac statistics. Thus, while $V_s(\phi)$ has a minimum at $\phi = 0$, as encountered for conventional Josephson junctions, $V_d(\phi)$ has a minimum at $\phi = \pi$ (Fig. 6.1(d)). A quantum dot junction in a doublet state is often denominated as a π-junction, and the singlet-doublet transition is also referred to as the 0-π transition. In the following sections we will use the presence or absence of such a π-phase shift to identify regions with a singlet or a doublet ground state[2].

6.4. TRANSMON SPECTROSCOPY OF THE QUANTUM DOT

To perform spectroscopy of the resonator, we monitor the microwave transmission S_{21} across the transmission line while varying the frequency of a single continuous microwave tone, f_r. This results in a dip with Lorentzian lineshape around the resonance frequency of the lumped-element resonator. Two-tone spectroscopy is subsequently performed by fixing the frequency of this first tone, f_r, at the minimum of the transmission amplitude, $|S_{21}|$, while varying the frequency of a second tone, f_t, also sent through the transmission line. When the second tone matches the frequency of the ground to first excited transmon transition, $f_t = f_{01}$, a peak in $|S_{21}|$ is observed due to the transmon-state-dependent dispersive shift of the resonator (Blais et al., 2004). This gives us access to the transmon

[1] Note that the notion of singlet and doublet sectors, introduced for the isolated quantum dot, extends naturally to the coupled quantum dot, provided that the spin S is now regarded as the total spin of the system, including that of quasi-particles in the reservoirs

[2] Our assumption that regimes with 0-junction and π-junction behaviour correspond to the quantum dot junction being in a singlet or doublet state, respectively, is only valid in the single-level regime, where the level spacing of the quantum dot is significantly larger than Δ and U. In the multi-level regime, where excited states of the quantum dot are involved, the presence or absence of the π offset also depends on the character of the orbital wavefunctions in addition to the fermion parity (van Dam et al., 2006).

transition frequency.

We are interested in the behavior of the device when a single level of the quantum dot provides the dominant contribution to the Josephson effect. To find such a regime, we search for an isolated resonance in the gate dependence of the frequency spectrum. Isolated resonances often occur when the gate voltages controlling the quantum dot are set close to their pinch-off values (see Refs. (Bargerbos et al., 2020; Kringhøj et al., 2020)), here operationally defined as the voltage values below which the quantum dot junction does not contribute appreciably to the transmon's transition frequency. In order to identify the right gate configuration, we perform the following sequence of calibration measurements. First, we characterize the reference junction with the quantum dot pinched-off; second, we explore the sizeable parameter space governed by the three quantum dot gates; third, we identify the relation between B_y and ϕ_{ext} through the transmon frequency's SQUID oscillations and find that 2.2 mT corresponds to one flux quantum through the loop; and finally we define appropriate gate coordinates to account for cross-couplings. These calibration measurements are detailed in the Supplementary Material of Sec. 6.8. As a result of this procedure, the gate voltage of the reference junction V_{J} is fixed such that the transmon frequency when the quantum dot junction is pinched-off is $f_{01}^0 \approx 4.4\,\text{GHz}$. Furthermore, we fix $V_{\text{L}} = 470$ mV and introduce virtual plunger (V_{P}) and right tunnel (V_{T}) gates as a linear combination of V_{C} and V_{R}, such that, in what follows, the single-particle energy level ξ is mostly independent of V_{T}.

We then move on to study the quantum dot junction. We first monitor the resonator frequency for $\phi_{\text{ext}} = 0$ while the plunger gate voltage V_{P} is varied (Fig. 6.3(a)). This reveals a resonant shape which is discontinuously interrupted near its peak at $V_{\text{P}} = 395$ mV, followed by other discontinuous jumps in the resonator frequency. A zoom into the resonance is shown in Fig. 6.3(b) and the corresponding transmon transition frequency, exhibiting the same discontinuity as the resonator, is shown in Fig. 6.3(d). We identify regions in V_{P} where the transmon frequency f_{01} is larger and smaller than the reference frequency f_{01}^0. This hierarchy is reversed upon changing the applied flux to $\phi_{\text{ext}} = \pi$, as shown in Figs. 6.3(c, e).

These observed discontinuities in frequency are a signature of a singlet-doublet transition. The change of the ground state of the quantum dot junction determines a sudden switch in the branch of the Josephson potential of Eq. (6.2) (from V_{s} to V_{d} or vice-versa) and, thus, a sudden change in the transmon frequency. This is illustrated numerically in Figs. 6.3(f-g), which show the expected evolution of the transmon frequencies as a function of the single-particle energy level ξ. Here, the transition occurs as ξ is tuned toward the electron-hole symmetry point $\xi = 0$, where the doublet ground state is energetically favorable.

The occurrence of the singlet-doublet transition requires a change of the fermion parity of the quantum dot junction. In the S-QD-S setup, this is possible in the presence of a population of excited quasiparticles in the superconducting leads, providing the required fermion parity reservoir. The presence of these quasiparticles should further result in a finite occupation of both the singlet and doublet states when their energy difference is small compared to the effective temperature of the quasiparticle bath, namely in the vicinity of the transition. Indeed, upon closer inspection of the data of Figs. 6.3(b-c), both branches of the spectrum are visible in a small frequency window surrounding each

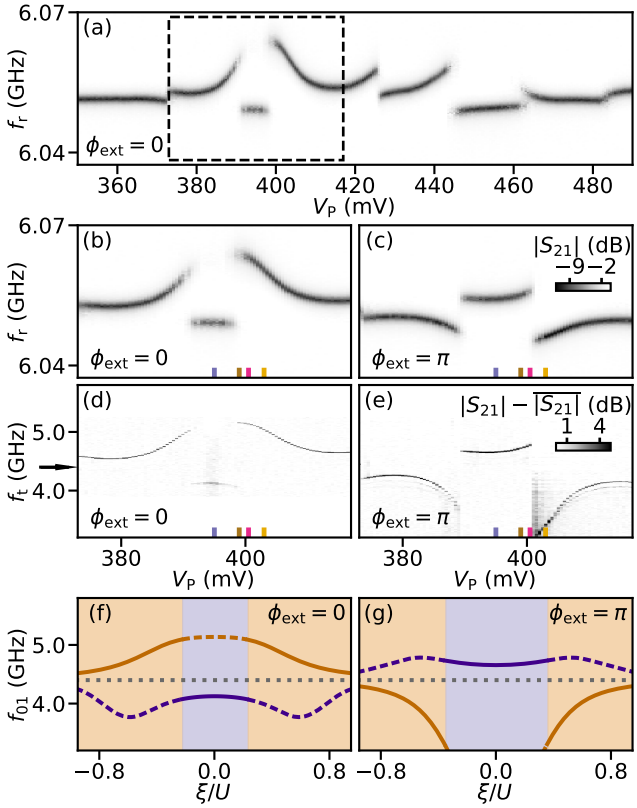

Figure 6.3: **Resonator and transmon spectroscopy.** (a) V_P dependence of single-tone spectroscopy for $\phi_{ext} = 0$, showing the resonator's transition frequency. V_P is a virtual gate voltage defined as a linear combination of V_C and V_R (see text). (b) Zoom-in of (a) in the plunger gate range indicated with dashed lines in (a). (c) Same as (b) but for $\phi_{ext} = \pi$. (d) V_P dependence of two-tone spectroscopy for $\phi_{ext} = 0$, showing the transmon's transition frequency. For each frequency trace, $|S_{21}| - |\overline{S_{21}}|$ is the magnitude of the transmission minus its average. The black arrow indicates f_{01}^0, the transmon frequency set by the reference junction when the quantum dot is pinched off. (e) Same as panel (d) but for $\phi_{ext} = \pi$. For panels (a-e) $V_T = 182$ mV and $V_L = 470$ mV. (f) Theoretical estimates of the singlet (orange), doublet (purple) and reference junction-only (dotted, grey) transmon frequencies as ξ is varied for ϕ_{ext} =0. Solid (dashed) lines indicate which quantum dot occupation corresponds to the ground (excited) state. (g) Same as panel (f) but for $\phi_{ext} = \pi$. For panels (f-g) $\Delta/h = 46$ GHz, $U/\Delta = 12.2$, $\Gamma_L/\Delta = 1.05$ and $\Gamma_R/\Delta = 1.12$. f_t and f_{01} denote, respectively, the frequency of the second tone in two-tone spectroscopy and the first transmon transition frequency (see text).

discontinuous jump. This is because these transition spectra are obtained by averaging over many subsequent frequency sweeps, thus reflecting the occupation statistics of the junction. This feature is further discussed in the next Section.

In Figs. 6.3(d-e), the fact that the frequency shift of the transmon has the opposite sign for the singlet and doublet sectors is a consequence of the π-phase shift in the Josephson potential between the two sectors. For the case $\phi_{ext} = 0$, the singlet potential interferes constructively with the reference junction potential, while the doublet potential interferes destructively, resulting in $f_{01} > f_{01}^0$ for the singlet and $f_{01} < f_{01}^0$ for the

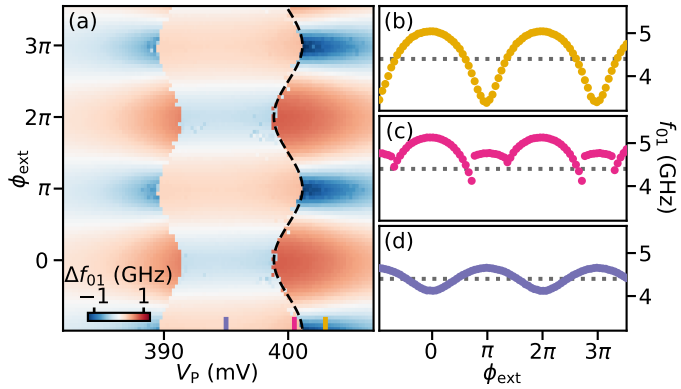

Figure 6.4: **Flux and plunger gate dependence.** (a) Transmon frequency shift with respect to the frequency set by the reference junction, $\Delta f_{01} = f_{01} - f_{01}^0$, versus V_P and ϕ_{ext} as extracted from two-tone spectroscopy. The dashed line is a sinusoidal guide for the eye, denoting the transition boundary in line with the theoretical expectation. (b)-(d) Three linecuts of f_{01} versus ϕ_{ext} at representative V_P values, indicated in panel (a) and Fig. 6.3(b-e). The dotted line indicates f_{01}^0. For all panels $V_T = 182$ mV.

doublet. This behaviour is reversed when $\phi_{ext} = \pi$, and thus serves as a method for identifying the quantum dot junction state.

6.5. SINGLET-DOUBLET TRANSITION BOUNDARIES

Having established a method for identifying singlet and doublet states by transmon spectroscopy, we now experimentally investigate the phase diagrams of the quantum dot junction. We focus on the behaviour around $V_P = 395$ mV and monitor singlet-doublet transitions versus multiple different control parameters.

6.5.1. PLUNGER GATE AND FLUX

We first study the singlet-doublet phase map in V_P and ϕ_{ext} space. Fig. 6.4(a) shows the transmon frequency offset with respect to the frequency set by the reference junction, $\Delta f_{01} = f_{01} - f_{01}^0$, as a function of V_P and ϕ_{ext}. As discussed in the previous Section, positive values of Δf_{01} result from constructive interference between the two junctions, while negative Δf_{01} values result from destructive interference. Going from left to right, three distinct plunger regions can be observed, with a sudden flux offset of exactly π between them (Fig. 6.4(b,d)). We identify the outer two regions as phases with a singlet ground state and the inner region as a doublet ground state. We note that the change in contrast between the two singlet regions suggests that V_P also weakly tunes $\Gamma_{L,R}$ in addition to ξ.

For values of V_P close to the singlet-doublet transition we also observe a sinusoidal dependence of the transition boundary on the external flux, resulting in an enhanced region of doublet occupation around $\phi_{ext} = \pi$ with respect to $\phi_{ext} = 0$. This comes about from interference between tunneling processes involving the two superconducting leads of the quantum dot junction (Delagrange et al., 2015; Oguri et al., 2004), as further discussed in Sec. 6.5.2. At a value of V_P fixed near this boundary one thus also observes a singlet-doublet transition versus the external flux (Fig. 6.4(c)).

In Fig. 6.4 and subsequent figures, the transition boundary between the singlet and doublet phase appears to be sharp and not affected by the thermal broadening typical of transport experiments (Cleuziou et al., 2006; Delagrange et al., 2015, 2018; Jørgensen et al., 2007; Szombati et al., 2016; van Dam et al., 2006). The sharpness is a result of a selective spectroscopy technique. As shown in Fig. 6.23, in the vicinity of a transition two resonant dips appear in single-tone spectroscopy, one for the singlet and one for the doublet. In this circumstance, the center frequency of either dip can be chosen as the readout frequency for the subsequent two-tone spectroscopy measurement. This binary choice selects the transmon transition frequency belonging to the corresponding quantum dot junction state. It is reasonable to assume that the most prominent dip corresponds to the state of the quantum dot junction which is more prominently occupied, and thus lower in energy. If this is the case, the extracted phase boundaries are a close approximation of the zero-temperature phase diagram of the quantum dot junction. We note that when the occupations of singlet and doublet states are almost equally probable, the selective spectroscopy method is affected by selection errors, which leads to the pixelation effects visible in Fig. 6.4 near the phase boundaries. In Sec. 6.6, we will explicitly measure the lifetimes of the quantum dot in the singlet and doublet states, substantiating the latter statements.

6.5.2. TUNNEL GATE

Next, we explore the singlet-doublet transition in plunger and tunnel gate space, where the tunnel gate is expected to control the tunnel rates between the quantum dot and the leads, $\Gamma_{L,R}$. Fig. 6.5(a) shows Δf_{01} versus plunger and tunnel gates at $\phi_{ext} = 0$. The region of doublet occupancy ($\Delta f_{01} < 0$) takes the shape of a dome, similar to the one coarsely seen in flux-insensitive tunneling spectroscopy experiments (Lee et al., 2014, 2017). This shape is in accordance with theoretical expectations for the boundary in the $\xi - \Gamma$ plane. Its physical origin depends on the parameter regime (Kadlecová et al., 2019). For $U \ll \Delta$ it arises due to an increase in induced superconductivity on the dot with increasing values of Γ, favoring BCS-like singlet occupation. For $U \gg \Delta$ it instead comes about from increased anti-ferromagnetic Kondo exchange interactions between the spin on the dot and the quasiparticles in the leads, favoring a Yu-Shiba-Rusinov (YSR)-like singlet occupation. In both regimes the singlets compete with doublets, ultimately determining the transition to a singlet ground state at large enough $\Gamma = \Gamma_L + \Gamma_R$.

We investigate the same plunger and tunnel gate dependence at an external flux $\phi_{ext} = \pi$, see Fig. 6.5(b). We find that the doublet phase is enhanced considerably compared to $\phi_{ext} = 0$, due to the previously mentioned interference between tunneling processes to the superconducting leads. Notably, rather than a dome-like shape, the phase boundary takes a characteristic "chimney" shape that was theoretically predicted (Oguri et al., 2004) but, to our knowledge, not yet confirmed experimentally before these measurements. Unlike the dome, the chimney does not close for any V_T. In an extended gate range, it is seen to connect to another doublet region of the parameter space which was disconnected from the dome of Fig. 6.5(a) at $\phi_{ext} = 0$ (see Sec. 6.8).

The chimney at $\phi_{ext} = \pi$ is much less thoroughly researched than the dome at $\phi_{ext} = 0$. The open questions include that of the exact nature of the doublet states as a function of the U/Δ and Γ/U ratios, and the role of the flux bias (Escribano et al., 2022; Kadlecová

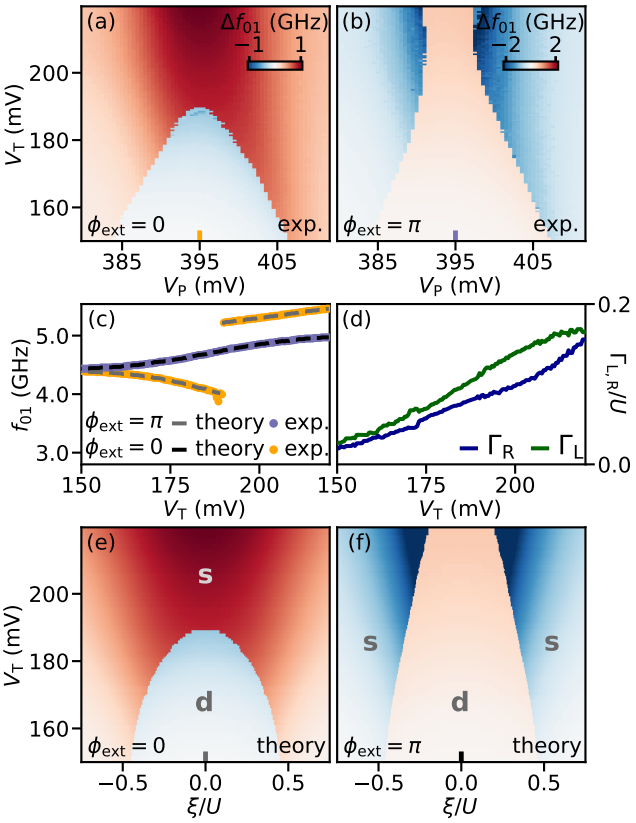

Figure 6.5: **Tunnel gate dependence.** (a) Δf_{01} versus V_P and V_T at $\phi_{ext} = 0$, where V_T is a virtual gate voltage defined as a linear combination of V_C and V_R (see text). The blue region corresponds to a negative supercurrent contribution from the quantum dot junction, while the red region corresponds to a positive contribution. (b) The same measurement as (a) repeated for $\phi_{ext} = \pi$. (c) Linecuts of (a) and (b) at $V_P = 395$ mV overlayed with best-fits based on NRG calculations. (d) Extracted dependence of $\Gamma_{L,R}$ on V_T. (e) Calculated transmon frequencies based on NRG calculations at $\phi_{ext} = 0$ as matched to the measured data, with the V_T axis as given in figure (d). The color bar is shared with panel (a). (f) Same as (e) but for $\phi_{ext} = \pi$, with the same color bar as (b). For the NRG calculations in panels (c-f) we fix $\Delta/h = 46$ GHz and $U/\Delta = 12.2$.

et al., 2017; Kiršanskas et al., 2015; Zalom et al., 2021). In particular, when $U \gg \Delta$, the doublet state for small Γ is a decoupled doublet state with a single local moment in the quantum dot. On the other hand, in the same limit but at large Γ (i.e. in the neck of the chimney), the strong exchange interaction with both superconductors is expected to lead to some mixing with the doublet states that involve one Bogoliubov quasiparticle from each lead (Žitko and Michele, 2017), causing an overscreening of the local moment in the quantum dot. The role of the exchange interaction is more pronounced at $\phi_{ext} = \pi$ also because the anomalous component of the hybridisation (describing the proximity effect) is suppressed due to the cancellation of contributions from the left and right leads (Zalom et al., 2021), where the cancellation is exact when $\Gamma_L = \Gamma_R$. This further stabilizes

the spin-doublet states. The experimental observation of the chimney calls for more thorough theoretical studies of this parameter regime of the model.

We compare the results at both values of external flux to the expected transition frequencies obtained from NRG calculations. We assume that $\xi = 0$ occurs at $V_P = 395\,\text{mV}$ since this is the symmetry point of the experimental data. At this point, by requiring simultaneous agreement between experiment and theory for both values of external flux (Fig. 6.5(c)), we are able to extract several of the model parameters. We find that $\Delta/h = 46\,\text{GHz}$ (190 μeV), close to the bulk value of Al. We furthermore extract $U/\Delta = 12.2$, corresponding to a sizeable charging energy of 2.3 meV. It places the nature of the singlets near $\xi = 0$ in the strongly correlated regime, with a YSR-like character rather than a BCS-like one. By matching values of $\Gamma_{L,R}$ to V_T we then find that Γ/U varies between 0.05 and 0.4, while $\Gamma_R/\Gamma_L \approx 0.75 - 1$ in the range of gates explored (Fig. 6.5(d)). The details of the numerical procedure as well as error estimation can be found in the Supplementary Information (Section I.C), including estimates based on an alternative potential shape for the reference junction (see Sec. 6.8).

The extracted set of parameters is consistent with the observed dome shape at $\phi_{ext} = 0$, as shown in Fig. 6.5(e). Additionally, as a result of the ratio Γ_R/Γ_L remaining close to 1, the extracted parameters also match the observed diverging behaviour at $\phi_{ext} = \pi$ (Fig. 6.5(f)), which was not enforced in the parameter extraction. In these panels we did not map V_P to ξ beyond identifying $V_P = 395\,\text{mV}$ with $\xi = 0$ as a unique mapping could not be constructed due to the unintended dependence of Γ on V_P. We speculate that this causes the remaining discrepancies between the measured and calculated boundaries in the horizontal direction.

6.5.3. MAGNETIC FIELD PARALLEL TO THE NANOWIRE

Finally, we investigate the effect of a magnetic field applied parallel to the nanowire on the phase transition boundaries. Here, we expect a magnetic-field induced singlet-doublet transition to occur (Lee et al., 2014; Valentini et al., 2021; Whiticar et al., 2021). As B_z increases, the doublet sector separates into spin species that are aligned and anti-aligned with respect to the magnetic field, dispersing in opposite energy directions. The singlet ground state energy, on the other hand, is approximately independent of magnetic field. Given an appropriate zero-field energy level configuration, for some B_z value the energy of one of the two doublet states will thus become lower than that of the singlet, and become the ground state instead (see Fig. 6.1(c)).

Such a transition will only occur for specific configurations of V_P and V_T in the experimentally accessible range of magnetic fields. We therefore start by applying $B_z = 200\,\text{mT}$ parallel to the nanowire axis, a sizeable magnetic field, yet one for which the E_J of the reference junction is not yet substantially suppressed (see Sec. 6.8). At this field we investigate the effect on the V_P and V_T phase map. The result, shown in Figs. 6.6(a-b), reveals an expansion of the doublet region for both $\phi_{ext} = 0$ and $\phi_{ext} = \pi$. We can classify different regions in the parameter space by comparing the phase boundaries at $B_z = 10\,\text{mT}$ and $B_z = 200\,\text{mT}$. There are regions in which a singlet ground state remains a singlet ground state, independent of the flux and the magnetic field, as well as regions where a singlet-doublet transition occurs depending on the value of the flux. However, there is also a region that starts off as a singlet ground state and ends up as a doublet ground state at

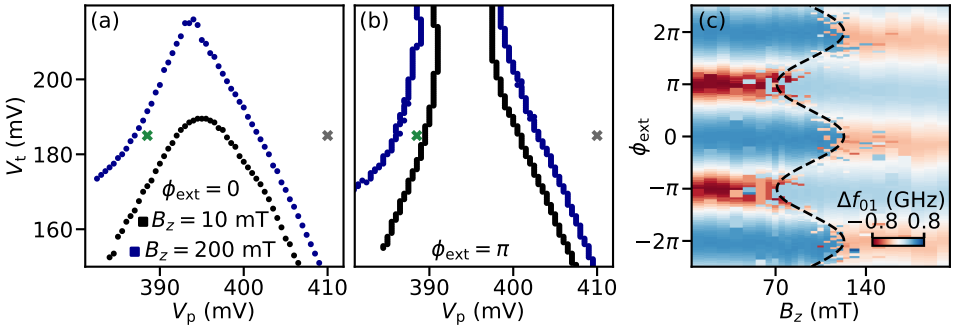

Figure 6.6: **Parallel magnetic field dependence.** (a) Borders between singlet and doublet regions for $B_z = 10$ mT (black) and $B_z = 200$ mT (blue). $\phi_{ext} = 0$ (b) Same as (a) but for $\phi_{ext} = \pi$. The grey marker denotes the gate point used to re-calibrate the flux axis after varying B_z (see Sec. 6.8). (c) Δf_{01} versus B_z and ϕ_{ext}, measured at the gate point indicated in (a) and (b) with a green marker. The sinusoidal dashed line serves as a guide for the eye, in line with the transition boundary expect from theory.

high field, for all values of the flux. Thus, fixing V_P and V_T in this region, we expect to observe a transition with B_z for any value of ϕ_{ext}. A measurement of Δf_{01} versus ϕ_{ext} and B_z (Fig. 6.6(c)) indeed reveals such a transition, occurring at a different magnetic field depending on the external flux value. For details about the data analysis and identification of the flux axis we refer to the Supplementary Information of Sec. 6.8.

6.6. DYNAMICS OF THE SINGLET-DOUBLET TRANSITION

In the preceding sections we made use of selective spectroscopy to reconstruct the phase transition boundaries. We now turn to time-resolved spectroscopy techniques to study the parity dynamics of the quantum dot junction close to the transition, aiming to characterize the lifetimes of singlet (even parity) and doublet (odd parity) states. These methods have previously been used to study quasiparticle dynamics in superconducting qubits (Serniak et al., 2019; Uilhoorn et al., 2021), and recently also applied to a nanowire junction to study the poisoning of Andreev bound states (Hays et al., 2018, 2020; Wesdorp et al., 2023).

To resolve individual switching events we use a second device (device B) with a larger signal-to-noise ratio (SNR) than the device used for the preceding sections (device A), enabling the use of short acquisition times. Device B is nearly identical to device A, except for two features meant to increase the SNR: (1) a stronger coupling between the resonator and the transmission line; (2) an additional capacitor at its input port, which increases the directionality of the outgoing signal (Heinsoo et al., 2018). On device B we perform measurements on microsecond timescales by directly monitoring changes in the outgoing signal at a fixed readout frequency. A continuous measurement of the outgoing microwave field then reveals a random telegraph signal between two different levels, a consequence of the switches in the quantum dot junction parity (Fig. 6.7(a-b)). Owing to the increased temporal resolution of the detection method, even short-lived excited state occupation can now be detected. The characteristic time scales of the telegraph signal reflect the underlying lifetimes of the singlet and doublet states, T_s and T_d,

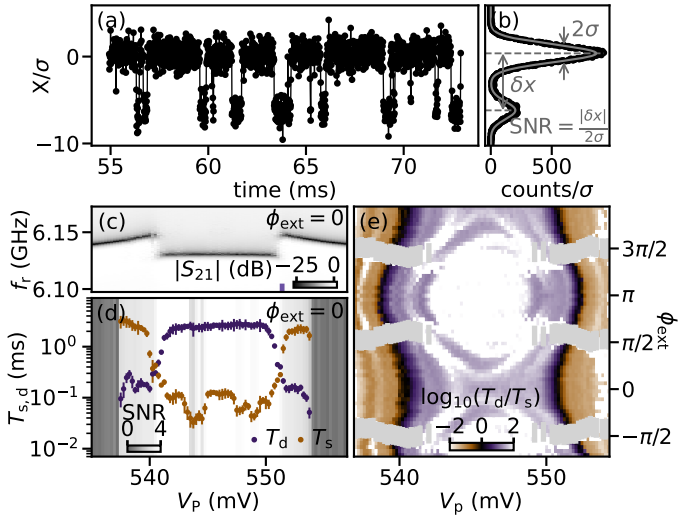

Figure 6.7: **Dependence of parity lifetimes on V_P and ϕ_{ext} for device B.** (a) A 18 ms cut of a continuously measured time trace integrated in time bins of $t_{int} = 11.4\,\mu s$, revealing jumps between two distinct states. X is the common axis onto which the quadratures of the outgoing microwave field are rotated to obtain the highest SNR, which takes a value of 3.3 in this panel. (b) 1D histogram of the response in (a) (black) and the best fit of a double Gaussian line-shape (gray). The separation of their centers δx and their width σ together define the SNR. The ratio of their amplitudes determines the ratio of the lifetimes. For panels (a-b) $V_P = 551.4$ mV and $\phi_{ext} = 0$. (c) V_P dependence of $|S_{21}|$ at $\phi_{ext} = 0$. (d) V_P dependence of the extracted lifetimes at $\phi_{ext} = 0$. Markers indicate the mean while error bars indicate the maximum and minimum values of 10 consecutive 2 s time traces. The SNR is shown in greyscale in the background. For points where SNR < 1, the extracted lifetimes are discarded. (e) 2D map of $\log_{10}(T_d/T_s)$ versus V_P and ϕ_{ext}, extracted from a 2 s time trace for each pixel. White pixels indicate points at which SNR < 1, while grey regions indicate where the resonator frequencies of singlet and doublet states overlap and thus cannot be distinguished.

or equivalently their decay rates, $\Gamma_s = 1/T_s$ and $\Gamma_d = 1/T_d$. These quantities can be extracted via a spectral analysis of the time traces, as described in Sec. 6.8.

To investigate the switching dynamics we tune device B to a regime similar to that of Sec. 6.5.1 studied in device A. By measuring S_{21} with single-tone spectroscopy we once-more find ground state transitions between singlet and doublet as a function of V_P (Fig. 6.7(c)). The discontinuous resonant shape, akin to that of Fig. 6.3(b), is symmetric around $V_P = 546$ mV, which we identify with $\xi = 0$. The singlet and doublet resonant frequencies are simultaneously visible close to the discontinuity at the transition. The time-resolved measurements over the same gate voltage range reveal a smooth but strong evolution of the parity lifetimes with V_P (Fig. 6.7(d)). The hierarchy of lifetimes inverts as V_P is tuned across the phase transition, reflecting the change in the ground state parity. Away from the transition, in either the singlet or doublet phase, we observe the lifetime in the ground state sector to be on the order of several milliseconds, exceeding that of the excited state by more than an order of magnitude. These numbers are very favorable for the implementation of Andreev pair qubits (Janvier et al., 2015) as well as Andreev spin qubits (Hays et al., 2018, 2020, 2021), whose control has so far been limited by microsecond parity lifetimes.

We further explore the evolution of the relative lifetimes versus V_P and ϕ_{ext}. Fig. 6.7(e) shows a two-dimensional map of $\log_{10}(T_d/T_s)$, which is a measure of the lifetime asymmetry. We find behaviour similar to that previously seen in Fig. 6.4, with a sinusoidal boundary of equal rates, indicative of the singlet-doublet transition. Furthermore, we observe a strong polarization of the junction parity inside the doublet phase ($T_d \gg T_s$), where the signal-to-noise ratio (SNR) eventually becomes limited by our ability to resolve the rare and short-lived switches out of the ground state. Additionally, we find a modulation of T_d with flux, with longer lifetimes at $\phi_{ext} = \pi$ (see Sec. 6.8). This flux dependence likely originates from the oscillation of the singlet-doublet energy gap with flux, but might also be indicative of a coherent suppression of the tunneling rates.The polarization of the junction parity also occurs inside the singlet phase, where $T_s \gg T_d$ for V_P values away from the transition (Fig. 6.7(d)).

Strong parity polarization may not be surprising for a system in thermal equilibrium at temperatures below 100 mK, typical of these experiments, corresponding to a thermal energy small compared to the singlet-doublet energy difference away from the transition. However, parity lifetimes in superconducting circuits are seldom determined by thermal fluctuations, but rather by highly energetic non-equilibrium quasiparticles (Glazman and Catelani, 2021). While such non-equilibrium quasiparticles are most likely also present in our device, we believe that their influence is suppressed by the large charging energy of the quantum dot junction.

Finally, we observe a non-monotonic variation of the rate asymmetry inside both the singlet and doublet phase, forming apparent contours of fixed lifetimes (Fig. 6.7(e)). We hypothesize two possible reasons behind this structure in the data: it could be caused by parity pumping mechanisms where the readout tone is resonant with the energy difference between singlet and doublet (Wesdorp et al., 2023), as well as by the spectral density of the non-equilibrium quasiparticles present in the environment (Serniak et al., 2018). Further investigation of the tunnel gate, power, and temperature dependence of the rate asymmetry can be found at the end of 6.8; we leave a more detailed study for future work.

6.7. CONCLUSIONS

We have demonstrated the use of a transmon circuit to sensitively detect the ground state parity of a quantum dot Josephson junction. The transition frequency of the transmon exhibits a discontinuity if the ground state of the device changes from a singlet to a doublet, due to the presence of a π-phase shift in the Josephson potential of the junction. This allowed us to accurately reconstruct the occurrence of the singlet-doublet transition as a function of all control parameters available in a single device, matching them to those expected from NRG calculations of an Anderson impurity model. In particular, we have observed the flux-induced enhancement of the doublet phase, in the form of the striking transformation of a dome-shaped phase boundary at $\phi_{ext} = 0$ into a chimney-shaped phase boundary at $\phi_{ext} = \pi$ (Fig. 6.5).

In future research, this singlet-doublet tuning capability could become beneficial for several applications. First, it can be used to define and control Andreev pair and spin qubits, and to couple them to conventional superconducting qubits. Second, tuning the dot to the doublet phase is a robust way to induce a π phase shift, which could be

exploited to define a hybrid $0-\pi$ qubit that does not rely on the fine-tuning of the applied flux (Larsen et al., 2020). Third, it can facilitate the bottom-up realization of a topological superconductor from a chain of proximitized quantum dots (Fulga et al., 2013; Sau and Sarma, 2012; Stenger et al., 2018). Finally, fast gate or flux-based switching between the 0 and π shift of the dot can also be of interest for applications in Josephson magnetic random access memory (JMRAM) technologies (Dayton et al., 2018).

We have subsequently used continuous time-domain monitoring of the transmon resonant frequency to determine the lifetimes of singlet and doublet states. We find that the time between switching events is strongly enhanced when the quantum dot is tuned away from the phase transition. Since our estimates indicate that $U \gg \Delta$ in our devices, we attribute this effect to the large energy difference associated with charging the quantum dot. These findings are encouraging for Andreev qubits, which benefit from long parity lifetimes, and suggest that large-U quantum dots could be effective as filters for high-energy quasiparticles. However, further work is required to understand the full dependence of parity lifetimes on U.

In this work we have focused on the study of a single-level quantum dot by tuning our junction very close to pinch-off. Looking forward, there is much left to explore in the parameter space of such a device. To begin with, it would be interesting to understand whether the crossover from the BCS-like to the YSR-like singlet has any signature in the microwave response of the system. Second, opening the junction further brings the quantum dot into a multi-level regime, not captured by the single impurity Anderson model, and still largely unexplored. Finally, while we have primarily studied the ground state properties of the quantum dot junction, microwave spectroscopy should allow one to study its excitations, as e.g. recently demonstrated in Refs. (Fatemi et al., 2022; Matute-Cañadas et al., 2022), particularly at $\phi_{\text{ext}} = \pi$.

Further work will also aim at elucidating the role of spin-orbit coupling in the quantum dot junction. It is well known that, when time-reversal invariance is broken, spin-orbit coupling can induce a spin-splitting of energy levels in the doublet sector (Chtchelkatchev and Nazarov, 2003; Padurariu and Nazarov, 2010; Tosi et al., 2018), essential for Andreev spin qubits. While this effect could have been expected to occur in the measurements presented here, it was not detected; we speculate that the level spacing in the dot was too large to result in a significant splitting (Padurariu and Nazarov, 2010).

Important extensions of our work could arise if the hybrid nanowire in our microwave circuit was driven into the Majorana topological phase (Ávila et al., 2020; Avila et al., 2020b; Ginossar and Grosfeld, 2014; Keselman et al., 2019), which is currently challenging because of a large parameter space (Pikulin et al., 2021) and because of demanding disorder requirements (Ahn et al., 2021). Including a quantum dot in a Josephson junction between two topological superconductors could be beneficial for the detection of the 4π Josephson effect: as we have seen, it mitigates quasiparticle poisoning, although it would not resolve (Schulenborg and Flensberg, 2020) the problem of distinguishing Majorana zero modes from trivial zero-energy Andreev bound states (Prada et al., 2020). Finally, the manipulation of quantum dots coupled to superconducting leads is an essential ingredient of scalable proposals for topological quantum computation (Karzig et al., 2017).

DATA AVALABILITY

The data and analysis code that support the findings of this study are openly available in 4TU.ResearchData at https://doi.org/10.4121/c.5801744.

AUTHOR CONTRIBUTIONS

A.B., M.P.V., B.v.H. and A.K. conceived the experiment. Y.L. developed and provided the nanowire materials. A.B., M.P.V., L.S., L.G. and J.J.W prepared the experimental setup and data acquisition tools. L.S. deposited the nanowires. A.B. and M.P.V. designed and fabricated the device, performed the measurements and analysed the data, with continuous feedback from L.S., L.G., J.J.W, C.K.A, A.K. and B.v.H. R.A., J.A., B.v.H. and R.Z. provided theory support during and after the measurements, and formulated the theoretical framework to analyze the experiment. R.Z. performed the NRG calculations. A.B., M.P.V. and B.v.H. wrote the code to compute the circuit energy levels and extract experimental parameters. L.P.K., R.A., A.K. and B.v.H. supervised the work. A.B., M.P.V., R.Z. and B.v.H. wrote the manuscript with feedback from all authors.

6.8. SUPPLEMENTARY INFORMATION

6.8.1. NUMERICAL MODELING

ANDERSON MODEL WITH SUPERCONDUCTING LEADS

As discussed in the main text, we model the quantum dot junction as a single Anderson impurity coupled to two superconducting leads. The Hamiltonian of the model takes the form

$$H = H_{\text{dot}} + H_{\text{leads}} + H_{\text{T}}. \tag{6.3}$$

The first term describes a single-level quantum dot,

$$H_{\text{dot}} = \sum_{\sigma=\uparrow,\downarrow} \epsilon_\sigma d_\sigma^\dagger d_\sigma + U n_\uparrow n_\downarrow . \tag{6.4}$$

Here, $\epsilon_{\uparrow,\downarrow} = \epsilon \pm E_Z/2$ gives the single-particle energies: ϵ is the dot energy level measured with respect to the Fermi level in the leads, and $E_Z = g\mu_B B$ is the Zeeman energy. In the latter, g is the effective g-factor of the level, μ_B is the Bohr magneton, and B is the magnetic field strength. Finally, $U > 0$ is the repulsive Coulomb interaction between the electrons, which disfavors the double occupancy of the impurity, while $n_\sigma = d_\sigma^\dagger d_\sigma$ are number operators for the dot level, with d_σ ($d_\sigma^\dagger$) the electron annihilation (creation) operators.

The many-particle energy levels of Eq. (6.4) are divided in two sectors, corresponding to their fermion parity, or equivalently, to their total spin S. The singlet sector includes the states of even parity, which have $S = 0$: the empty state $|0\rangle$ and the pair state $|2\rangle = d_\uparrow^\dagger d_\downarrow^\dagger |0\rangle$. The doublet sector includes the states of odd parity, which have $S = 1/2$: $|\uparrow\rangle = d_\uparrow^\dagger |0\rangle$ and $|\downarrow\rangle = d_\downarrow^\dagger |0\rangle$. It is convenient to introduce the energy $\xi = \epsilon + U/2$, corresponding to half of the energy gap in the singlet sector, so that $\xi = 0$ corresponds to the electron-hole symmetry point, where $|0\rangle$ and $|2\rangle$ are degenerate in energy. The ground state of H_{dot} belongs to the doublet sector for $|\xi/U| < 1/2$.

The second term in Eq. (6.3) describes two superconducting reservoirs,

$$H_{\text{leads}} = \sum_{i,k} \epsilon_k n_{i,k} + \sum_{i,k} \left(\Delta e^{-i\phi_i} c^\dagger_{i,k\uparrow} c^\dagger_{i,k\downarrow} + \text{h.c.} \right) \tag{6.5}$$

where $i = \text{L,R}$ labels the left and right leads, k labels spin-degenerate single-particle states, $\Delta e^{-i\phi_i}$ is the s-wave pairing potential in each reservoir, and $c_{i,k\sigma}$ ($c^\dagger_{i,k\sigma}$) are the electron annihilation (creation) operators in the leads. The gauge-invariant phase difference between them is $\phi = \phi_\text{L} - \phi_\text{R}$. We assume the reservoirs to have identical gap Δ and density of states ρ; this assumption should be reasonable since in the experiment the two leads are made out of a single hybrid nanowire. We further take the g-factor of the reservoirs to be zero, capturing the magnetic field dependence of the combined system in the effective quantum dot g-factor of Eq. (6.4).

Finally, the third term is the tunneling Hamiltonian coupling the dot and the reservoirs,

$$H_\text{T} = \sum_{i,k,\sigma} \left(t_i c^\dagger_{i,k,\sigma} d_\sigma + \text{h.c.} \right), \tag{6.6}$$

where t_i are the dot-reservoir tunnel coupling strengths, which, for simplicity, we choose to be independent of k and spin. The tunneling rate across each barrier is given by $\Gamma_i = \pi\rho|t_i|^2$. The tunneling terms in H_T break the conservation of the parity and spin in the quantum dot. Nevertheless, the notion of singlet and doublet sectors introduced for the dot Hamiltonian of Eq. (6.4) is inherited by the total Hamiltonian of Eq. (6.3), provided that the spin S is now regarded as the total spin of the system, including that of quasiparticles in the reservoirs. The same holds for parity, which must be redefined as the parity of the total number of electrons in the system.

Over the years, the model of Eq. (6.3) (or immediate extensions of it) has become paradigmatic to describe quantum dots coupled to superconducting leads. It has been studied in different limits and using a variety of numerical methods, often requiring advanced many-body methods such as the numerical renormalization group (NRG) and quantum Monte Carlo for full quantitative descriptions (Meden, 2019). In the present work, we used NRG methods to extract the energies of the singlet and doublet states for any combination of the model parameters. These energies are then incorporated in a DC SQUID transmon Hamiltonian which is used to match the experimental data and extract estimates of the model parameters. These procedures are detailed in the remainder of this Section.

NRG CALCULATION

The NRG method is an iterative procedure for solving quantum impurity problems involving a localized few-level system coupled to a continuum of itinerant electrons (fermionic bath, normal-state or mean-field BCS superconductor). It consists of several steps: 1) discretization of the continuum parts of the Hamiltonian using a geometric-progression mesh with an accumulation point at the Fermi level (the so-called logarithmic discretization), 2) unitary transformation of the resulting discretized Hamiltonian from the star-geometry (impurity coupling to each representative mesh point) to a linear tight-binding chain representation (the so-called Wilson chain), 3) iterative diagonalization in which

the Wilson chain sites are taken into account consecutively (Bulla et al., 2008; Krishna-murthy et al., 1980; Satori et al., 1992; Wilson, 1975; Yoshioka and Ohashi, 2000). The discretization is controlled by the discretization parameter $\Lambda > 1$ which controls the coarseness of the grid. When the discretization is coarse, the results can be improved by twist averaging, which consists of performing the same calculation for several different discretization grids and averaging the results (Bulla et al., 2008; Žitko and Pruschke, 2009). The growth of the Hilbert space is controlled by the truncation parameters which control the number of states retained after each step of the iteration.

The calculations in this work have been performed with the NRG Ljubljana code (Žitko, 2021). Since the main quantities of interest are the ground state energies in each spin sector, very high quality results can be obtained even with coarse discretization ($\Lambda = 8$) and keeping no more than 3000 states (spin multiplets) in the truncation. We have verified that the twist averaging is not required. The BCS gap was chosen to be $\Delta = 0.1D$, where D is the half-bandwidth. The calculations were performed for a problem with symmetric hybridisations, $\Gamma_L = \Gamma_R$. This is sufficient, because the results for an arbitrary coupling asymmetry can be obtained from the following mapping (Kadlecová et al., 2017):

$$\phi_S(\phi, a) = 2\arccos\sqrt{1 - \frac{4a}{(a+1)^2}\sin^2(\phi/2)}, \tag{6.7}$$

where $a = \Gamma_L/\Gamma_R$ is the asymmetry, ϕ is the BCS phase difference in the asymmetric problem, and ϕ_S is the effective BCS phase difference in the effective symmetric problem.

Such calculations were performed for a set of values of the interaction strength U (from very low values $U = 0.1\Delta$ that correspond to ABS-like subgap states, up to $U = 30\Delta$ that correspond to YSR-like subgap states). In every value of U, a grid of ξ and Γ parameters was set up, and a sweep of ϕ between 0 and π (50 points) has been performed for each (ξ, Γ) pair. The ground state energies are obtained as the sum of all energy shifts (Krishna-murthy et al., 1980) performed during the NRG evolution, which has been shown to produce extremely accurate results (Žitko and Pruschke, 2009). Some calculations have also been performed in the presence of a small Zeeman splitting. The results have been collected, documented, and made available on a public repository (Žitko, 2021). The full set of input files and scripts is provided for running the calculations for different parameters or for different Hamiltonians.

Having developed the NRG calculation, we can gain insight into the expected boundaries between singlet and doublet occupation. In Fig. 6.8(a), we show the phase diagram for the symmetric configuration $\Gamma_L = \Gamma_R$ at fixed $\phi = 0$ and $U/\Delta = 5$. In the (ξ, Γ) plane, the phase diagram takes a dome-like shape with the transition value of Γ being the highest at the electron-hole symmetry point $\xi = 0$. At this point, the transition value of Γ diverges if the phase difference between the reservoirs is changed to $\phi = \pi$, because in this case a destructive interference between tunneling events to the left or right occurs. This causes the "dome" in the (ξ, Γ) plane to turn into the "chimney" shown in Fig. 6.8(b).

As mentioned above, at $\Gamma = 0$ the ground state is in the doublet sector for $|\xi/U| < 1/2$. Upon increasing Γ, the Kondo coupling favours the binding of a Bogoliubov quasiparticle in the superconductor to the impurity local moment ("Yu-Shiba-Rusinov" screening), ultimately determining the transition to a singlet ground state at a value Γ_c. The value of Γ_c depends on ξ, ϕ, U and Δ, as well as on the asymmetry between Γ_L and Γ_R. This im-

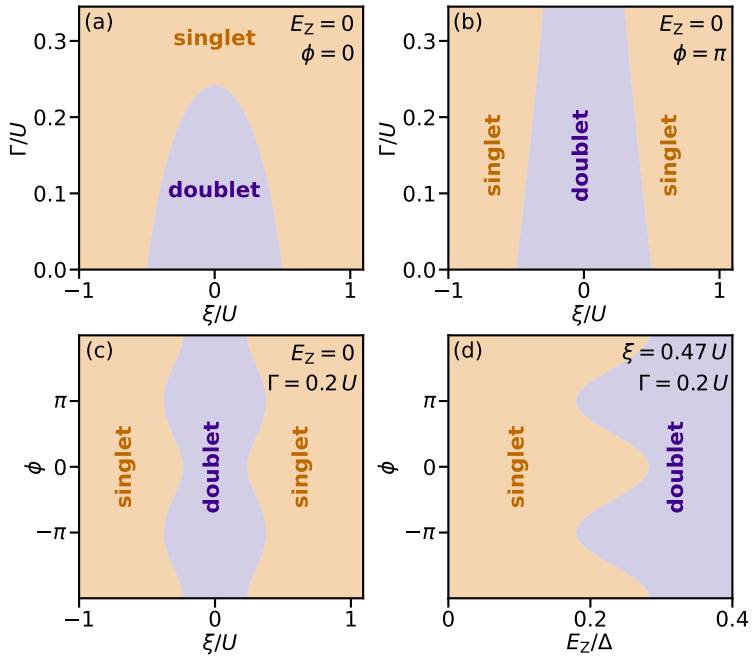

Figure 6.8: **Boundaries between singlet and doublet ground states extracted from NRG calculations.** (a) Boundary in the $\xi - \Gamma$ plane at $\phi = 0$ for $\Gamma_L = \Gamma_R$. (b) Same as (a) for $\phi = \pi$. (c) Boundary in the $\xi - \phi$ plane at $\Gamma = 0.2\,U$. (d) Boundary in the $E_Z - \phi$ plane for $\xi = 0.47\,U$. All panels are for $U/\Delta = 5$.

plies that the singlet-doublet transition can be observed varying any of these parameters individually. Since in the experiment the values of U and Δ are fixed, being determined by the materials and the geometry of the physical device, we focus here on variations in ξ, ϕ, Γ_L and Γ_R.

In Fig. 6.8(c), we show the singlet-doublet transition boundary in the $\xi - \phi$ plane. The interference effect is modulated continuously by the value of the phase difference ϕ, resulting in periodic oscillations of the boundary. The average position of the oscillating boundary is determined by Γ. In Fig. 6.8(d), we show the effect of a Zeeman energy E_Z in the case when the ground state is singlet at $B = 0$. As mentioned in the main text, a singlet-doublet transition is induced at finite E_Z due to the spin-splitting of energy levels in the doublet sector.

TRANSMON DIAGONALIZATION

Having established how to calculate singlet and doublet potentials using the NRG method, we now turn to their inclusion in the Hamiltonian of the transmon circuit [main text Eq. (6.1)]. To numerically solve the Hamiltonian for an arbitrary potential term $V(\phi)$ we make use of the Fourier decomposition (note that the potential can include an external flux ϕ_{ext}):

$$V(\phi) = E_{J,0} + \sum_n E_{J,n}^{\cos} \cos\left(n\phi\right) + \sum_n E_{J,n}^{\sin} \sin\left(n\phi\right) \tag{6.8}$$

with the components

$$E_{\mathrm{J},0} = \frac{1}{2\pi}\int_{-\pi}^{\pi} V(\phi)\,d\phi \tag{6.9a}$$

$$E_{\mathrm{J},n}^{\cos} = \frac{1}{\pi}\int_{-\pi}^{\pi} V(\phi)\cos\left(n\phi\right)d\phi \tag{6.9b}$$

$$E_{\mathrm{J},n}^{\sin} = \frac{1}{\pi}\int_{-\pi}^{\pi} V(\phi)\sin\left(n\phi\right)d\phi \tag{6.9c}$$

where we assume the potential to be a real-valued 2π-periodic function. We can then express the full Hamiltonian in the charge basis as

$$H = 4E_c\hat{N}^2 + E_{\mathrm{J},0} + \sum_n \tfrac{1}{2}E_{\mathrm{J},n}\hat{N}_+^n + \mathrm{h.c.} \tag{6.10}$$

with $E_{\mathrm{J},n} = E_{\mathrm{J},n}^{\cos} - iE_{\mathrm{J},n}^{\sin}$, $\hat{N}$ the charge operator and $\hat{N}_+^n|N\rangle = |N+n\rangle$.

Upon substituting the potential of main text Eq. (6.2) into Eq. (6.10) and diagonalizing the Hamiltonian, we find the eigenvalues and obtain the energy levels of the combined reference junction and quantum dot junction system. Their difference then results in the transmon's transition frequencies. To numerically compute the eigenvalues we truncate the number of charge states and Fourier coefficients to $N = 35$ for all calculations (Koch et al., 2007). We verify that this leads to good convergence for the eigenvalues. We further note that while the presence of the potential offset $E_{\mathrm{J},0}$ does not affect the transmon transition frequencies, its inclusion is crucial: it plays a large role in determining whether the ground state of the combined system corresponds to singlet or doublet occupation for a given set of quantum dot junction parameters.

PARAMETER MATCHING ROUTINE

To match the numerical model to the experimental data we have to overcome several complications. First, the mapping between experimental control parameters and those present in the model is not always trivial. As discussed in the main text, V_{p} appears to not only tune ξ but also $\Gamma_{\mathrm{L,R}}$. In turn V_{t} is constructed in such a way that (to first approximation) it does not tune ξ, but it does act on both tunnel rates simultaneously with different, unknown lever arms. For mapping the magnetic field axis to the Zeeman energy the challenge lies in determination of the effective g-factor of the quantum dot, known to be a strongly gate and angle-dependent quantity (Schroer et al., 2011). Only the flux axis allows for a simpler identification, in particular if one assumes that in the singlet configuration the combined DC SQUID Josephson potential takes its minimal (maximal) values at 0 (π), which should hold for even modest SQUID asymmetry. A separate challenge comes from the large number of parameters of the model: Δ, U, ξ, Γ_{L}, Γ_{R}, and ϕ_{ext}. With 6 potentially correlated parameters to match one has to carefully assess whether the fit is under-determined.

Given these considerations, we identify a specific gate point in the experimental data that could result in a well-constrained situation: the top of the dome shape of Fig. 6.5(a) in the main text. Here we have access to three measured quantities at a known flux ϕ_{ext}: the singlet and doublet qubit frequencies $f_{01}^{\mathrm{s}}(0)$ and $f_{01}^{\mathrm{d}}(0)$ measured at the boundary of the transition, and also the doublet qubit frequency $f_{01}^{\mathrm{d}}(\pi)$. We furthermore know

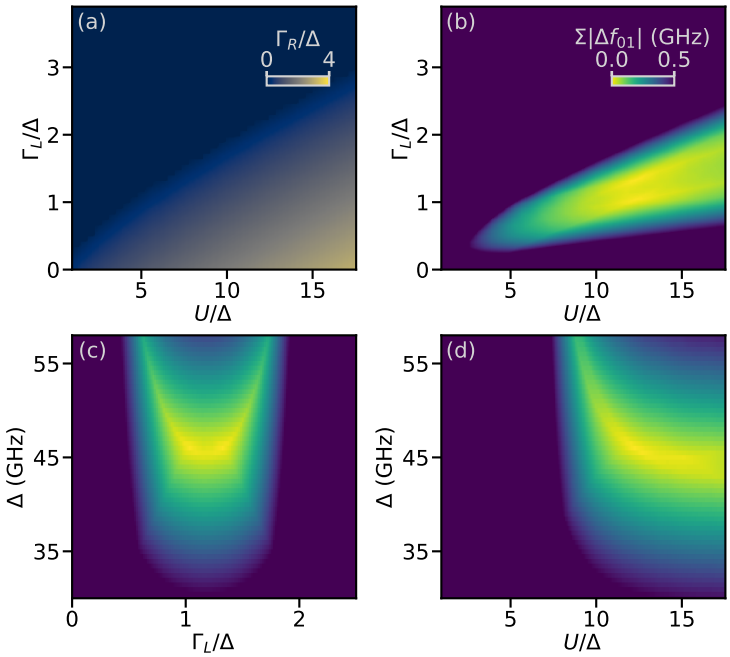

Figure 6.9: **Numerical matching of model parameters** (a) Calculation of the value of Γ_R that leads to a singlet-doublet transition with other model parameters held fixed. Here we fix $\phi_{ext} = 0$ and $\xi = 0$. A value of zero indicates that no such transition occurs. (b) Calculation Eq. (6.11) in the $U - \Gamma_L$ plane evaluated at $\Delta = 46$ GHz. (c) Same as (b) in the $\Delta - \Gamma_L$ plane for $U/\Delta = 12.2$. (d) Same as (b) in the $U - \Delta$ plane for $\Gamma_L/\Delta = 1.19$.

that here $E_s \approx E_d$ for $\phi_{ext} = 0$, since the data lies on the boundary of a singlet-doublet transition versus tunnel gate. Finally, based on the symmetry of the dome shape we identify that this V_P should correspond to $\xi \approx 0$. We can therefore eliminate two of the model parameters (ξ and ϕ_{ext}) and are left to determine Δ, U, Γ_L and Γ_R.

In a first step we tackle the condition of a singlet-doublet transition occurring versus tunnel gate. For each value of Δ, U and Γ_L we numerically diagonalize the Hamiltonian of Eq. (6.10) to determine the lowest energy level of the total circuit for both the singlet and doublet states and find the value of Γ_R for which these energies are equal. For this we use a reference junction potential $V_j = E_J(1 - \cos\phi)$ with $E_J = 12.8$ GHz and $E_c/h = 210$ MHz as determined later in this section. Shown in Fig. 6.9(a), this results in a U-dependent range of Γ_L for which there is indeed a value of Γ_R that leads to a singlet-doublet transition. Outside of this range Γ_L is so large that the ground state is always a singlet.

Having determined these possible values of Γ_R we calculate the three relevant transmon frequencies $f_{01}^s(0)$, $f_{01}^d(0)$, and $f_{01}^d(\pi)$. These are then compared to the measured values, and an optimal solution is sought that minimizes the sum of the absolute difference between calculation and measurement of all three quantities

$$\Sigma|\Delta f_{01}| = |f_{01}^{s,exp.}(0) - f_{01}^{s,calc.}(0)| + |f_{01}^{d,exp.}(0) - f_{01}^{d,calc.}(0)| + |f_{01}^{d,exp.}(\pi) - f_{01}^{d,calc.}(\pi)|. \quad (6.11)$$

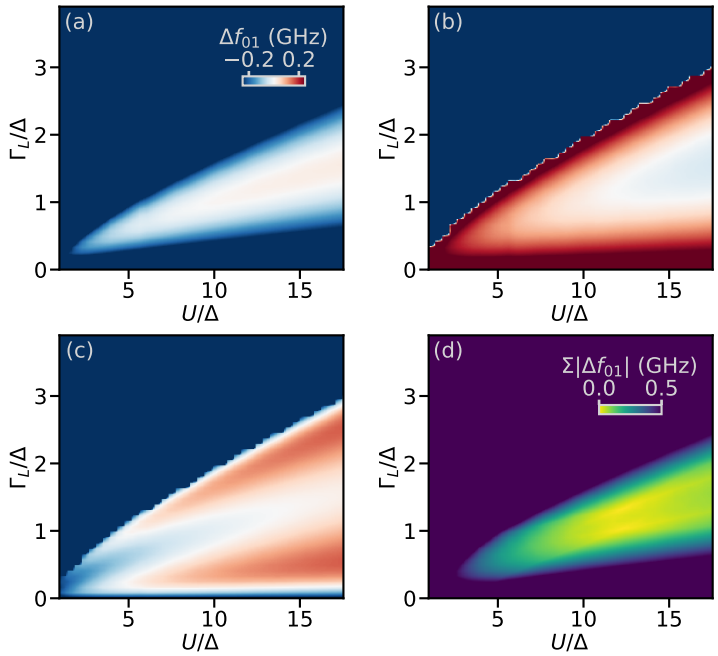

Figure 6.10: **Numerical matching in $\Gamma_L - U$ plane** (a) Difference in the calculated and measured singlet qubit frequency at $\phi_{ext} = 0$ evaluated at $\Delta = 46$ GHz. (b) Same as (a) for the doublet qubit frequency at $\phi_{ext} = 0$. (c) Same as (a) for the doublet qubit frequency at $\phi_{ext} = \pi$. (d) The absolute sum of the differences in panels (a-c).

In Figs. 6.9(b-d) we plot a sample of this three-dimensional optimization, while Fig. 6.10 shows how each panel is constructed from the individual singlet and doublet qubit frequencies. Other than the trivial symmetry between $\Gamma_{L,R}$, it appears that there is indeed a single region of parameters matching our data. At its global minimum we find $\Delta/h = 46$ GHz (190 μeV), $U = 12.2\Delta$, $\Gamma_L = 1.19\Delta$ and $\Gamma_R = 1.47\Delta$, which results in a precise match to the measured qubit frequencies.

Having determined Δ, U, Γ_L, and Γ_R at this single point in gate space, we attempt to match the model to the V_T axis of the data. To do so we fix Δ and U to the determined values and for each value of V_T find the best set of $\Gamma_{L,R}$ to match the data. To determine these two parameters we have two measured quantities: up to the transition we have $f_{01}^{d}(0)$ and $f_{01}^{d}(\pi)$, and after the transition we have $f_{01}^{s}(0)$ and $f_{01}^{d}(\pi)$. This procedure results in good correspondence to the experimental results, as shown in main text Fig. 6.5(c,d). We note that by construction this captures all the granularity and measurement uncertainty of the experimental data, even though the underlying quantities might have been more smooth. A subsequent procedure that attempts to match V_P to ξ did not turn out to be unique, as V_P appears to also act on $\Gamma_{L,R}$. We therefore leave this mapping undetermined.

The uncertainty in the extracted quantities is affected by several factors. The first is the measurement accuracy; we measure the qubit frequency with MHz-scale precision.

Based on numerical evaluation of the model, this precision in qubit frequency should limit the extracted parameter accuracy to several GHz. A more substantial uncertainty comes from the determination of the transmon island charging energy E_c, which is typically determined from the transmon transition anharmonicity $\alpha = f_{12} - f_{01}$. While the anharmonicity can be measured to high precision, a complication arises from the usage of a nanowire based Josephson junction as the reference junction. Up to now we have assumed its potential to take the form $V(\delta) = E_J(1 - \cos\delta)$; that of a conventional superconductor-insulator-superconductor (SIS) tunnel junction governed by many weakly transparent channels. In this case we find that $E_c/h = 210\,\text{MHz}$, resulting in the parameter estimates given above. However, previous work has found that nanowire-based Josephson junctions are better described by several or even a single transport channel, such that $V(\delta) = -\sum_n \Delta\sqrt{1 - T_n \sin^2\delta/2}$. This change in potential shape can lead to a strong reduction in the anharmonicity, and thus an underestimation of E_c when using the SIS potential (Kringhøj et al., 2018). We therefore also match our reference junction dependence to a single transport channel, which is the most extreme case for a reduction in the anharmonicity, finding good agreement with a single transport channel of $T = 0.58$. This in turn leads to an extracted $E_c/h = 306\,\text{MHz}$, resulting in a different set of extracted quantum dot parameters. In particular, we now find $\Delta = 30.5\,\text{GHz}$ and $U = 17.3\Delta$. This value of the induced gap in the InAs-Al nanowire is on the low end of what is typically found in DC transport experiments, which might hint at a reduced proximity effect in the ungated leads (Antipov et al., 2018; Winkler et al., 2019).

Capacitance simulations of the full circuit do not provide an unambiguous answer for which of the two limits is more appropriate, as the circuit was designed to target $E_c/h = 250\,\text{MHz}$ which falls in the center of the estimated range. As it stands we therefore do not have to uniquely determine the experimentally realized E_c and thereby resolve the uncertainty in the extracted quantities. However, future works could make use of additional circuit QED compatible quantum dot probes such as direct DC access (Kringhøj et al., 2020) or dispersive gate-sensing techniques (de Jong et al., 2021) to independently characterize several model parameters and further constrain the matching.

CALCULATED 2D MAPS

Having established how to match the model parameters to the data, we now turn to the reconstruction of the full 2D dependencies measured in the experiment (Fig. 6.11). For the plunger versus tunnel gate dependence, we calculate both the singlet and doublet qubit frequencies for all values of $\Gamma_{L,R}$ encoded by V_T for a range of ξ at both $\phi_{ext} = 0$ and π. We subsequently mask the data according to the ground state of the combined transmon Hamiltonian, and obtain a result that closely approximates the measured data (main text Fig. 6.5). Using the same set of quantum dot junction parameters, we also perform a similar procedure for the 2D map of plunger gate and external flux, resulting good correspondence with main text Fig. 6.4.

STATE POPULATION

We now turn to the singlet and doublet lifetimes determined in device B. For this device we could not identify a measurement point where a unique set of parameters matched the measured data, and can therefore not make a quantitative comparison to the numer-

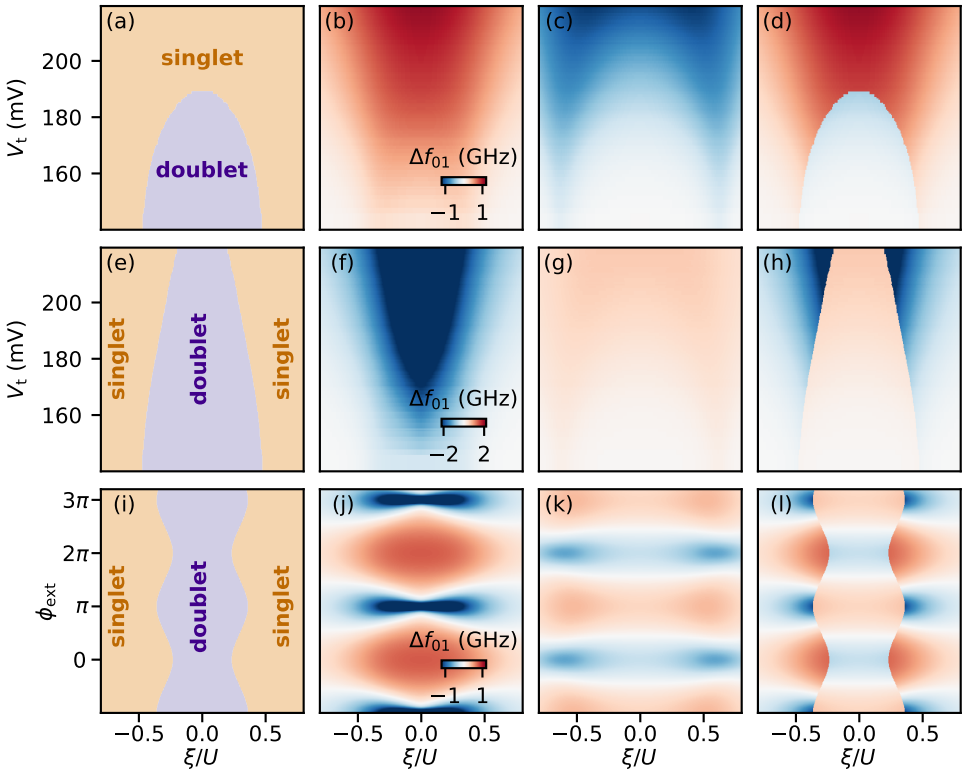

Figure 6.11: **Numerically calculated transmon frequency maps** (a,e,i) Boundaries between singlet and doublet ground states extracted from NRG calculations for $\phi_{ext} = 0$, $\phi_{ext} = \pi$, and $\Gamma_R = 1.23\Gamma_L$ respectively. Panels (b-d), (f-h), (j-l) show how the singlet qubit frequency, the doublet qubit frequency, and the combined result conditioned on the ground state of panels (a,e,i) respectively depend on the parameters. Each row shares the same color map. This leads to saturation of the color map in the panels corresponding to the unconditioned singlet and doublet qubit frequencies, but facilitates comparison to the experimental results. For all panels $U/\Delta = 12.2$ and $\Delta = 46\,\mathrm{GHz}$.

ics. Instead, we attempt to gain some intuition about the obtained results based on the parameters of device A.

In main text Fig. 6.7 we extract $\log_{10}(T_d/T_s)$, the ratio of the lifetimes of singlet and doublet occupation. If the system was in thermal equilibrium with a bath of temperature T, one would naively expect that the relative lifetimes should follow the state populations $P_{s,d}$ as described by a Maxwell-Boltzmann distribution:

$$P_i = \frac{1}{Z} g_i \exp(-E_i/k_B T) \tag{6.12}$$

where g_i is the degeneracy of the state, $E_{s,d}$ are the singlet and doublet energies, and k_B is the Boltzmann constant. We take $Z = 2\exp(-E_d/k_B T) + \exp(-E_s/k_B T)$, where we neglect potential other many-body states which should be unoccupied at the experimentally relevant temperatures. In Fig. 6.12(a) we then plot $\log_{10}(P_d/P_s)$, choosing a

bath temperature of 400 mK. Qualitatively this follows the same trend as observed experimentally, with a sharp boundary at the phase transition and a saturated population imbalance away from that. We stress once-more that this is not a quantitative comparison. However, the need for a temperature far in excess of the refrigerator's base temperature of 20 mK could hint at a non-thermal origin such as non-equilibrium quasiparticles (Glazman and Catelani, 2021).

In the main text we also speculate that non-thermal effects lie at the origin of the experimentally observed contours of fixed lifetime ratio's. We corroborate this in Fig. 6.12(b), where we plot the energy difference between singlet and doublet occupation of the quantum dot junction. This quantity exhibits distinct contours of equal energy difference that qualitatively match those found in the experiment. If the environment has spectral components resonant with these specific energies, one could expect these to modify the dynamics.

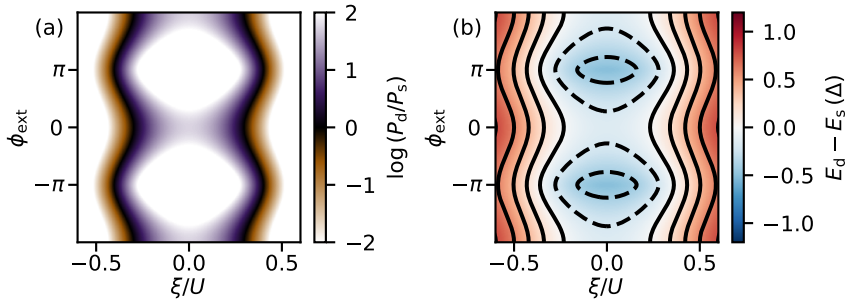

Figure 6.12: **State population versus ξ and ϕ_{ext}** (a) Ratio of the expected state population as calculated from Eq. (6.12) for a temperature of 400 mK. The colormap is saturated to facilitate comparison to main text Fig. 6.7. (b) Difference between doublet and singlet energy. Each contour indicates a boundary of equal energy difference. Parameters are the same as that of Fig. 6.11.

6.8.2. DEVICE AND EXPERIMENTAL SETUP

NANOFABRICATION DETAILS

The device fabrication occurs in several steps using standard nanofabrication techniques, and it is identical for device A and B. The substrate consists of 525 µm-thick high-resistivity silicon, covered in 100 nm of low pressure chemical vapor deposited Si_3N_4. On top of this a 20 nm thick NbTiN film is sputtered, into which the gate electrodes and circuit elements are patterned using an electron-beam lithography mask and SF_6/O_2 reactive ion etching. Subsequently, 30 nm of Si_3N_4 dielectric is deposited on top of the gate electrodes using plasma enhanced chemical vapor deposition and then etched with buffered oxide etchant. The nanowire is then deterministically placed on top of the dielectric using a nanomanipulator and an optical microscope. For this we use an approximately 10 um-long vapour-liquid-solid (VLS) hexagonal InAs nanowire with a diameter of 100 nm and a 6 nm-thick epitaxial Al shell covering two facets (Krogstrup et al., 2015). After placement, two sections of the aluminium shell are removed by wet etching with MF-321 developer. These sections form the quantum dot junction and the reference junc-

tion, with lengths 200 nm and 110 nm respectively. A zoom-in of the the quantum dot junction is shown in Fig. 6.2(d) of the main text. The reference junction is controlled by a single 110 nm-wide electrostatic gate, set at a DC voltage V_J. The quantum dot junction is defined by three 40 nm-wide gates separated from each other by 40 nm, set at DC voltages V_L, V_C and V_R. Note that in Fig. 6.2(d) the gates appear wider (and the gaps between gates appear smaller) than stated due to distortion by the Si_3N_4 layer; the given dimensions are therefore determined from a scanning electron microscopy image taken before the deposition of the dielectric. After the junction etch the nanowire is contacted to the transmon island and to ground by an argon milling step followed by the deposition of 150 nm-thick sputtered NbTiN. Finally, the chip is diced into 2 by 7 millimeters, glued onto a solid copper block with silver epoxy, and connected to a custom-made printed circuit board using aluminium wirebonds.

GENERAL CHIP OVERVIEW

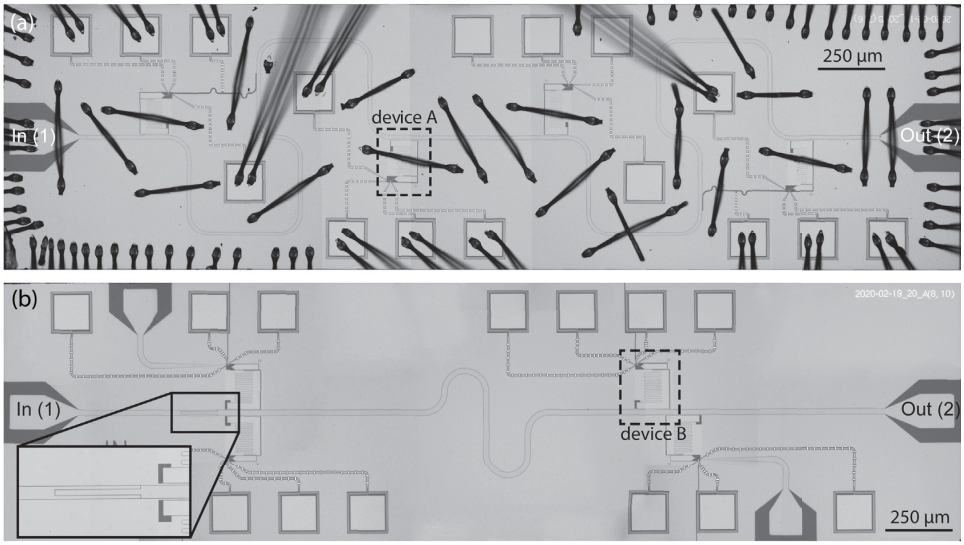

Figure 6.13: **Chip design.** (a) The chip of device A, containing four nearly identical devices coupled to the same transmission line. The image is taken after wire-bonding onto a PCB. (b) The chip of device B, incorporating an input capacitor in the transmission line (enlarged in inset). The image is taken before wire-bonding onto a PCB.

Optical microscope images of the chips containing devices A and B are shown in Figs. 6.13(a) and (b), respectively. Each chip, 7 mm long and 2 mm wide, consists of four devices coupled to the same transmission line. For the chip containing device A, only one device was functional. Out of the other three, one did not have a nanowire, another contained three nanowires stuck together, and for the third device a gate electrode showed no response. The chip of device B includes an on-chip capacitor on the input port of the transmission line to increase the signal-to-noise ratio. For this chip only two of the devices were bonded: device B, which was functional, and another device that did

not show any response to the electrostatic gates. The two unbonded devices were dismissed based on prior optical inspection, containing two and no nanowires respectively.

FLUX CONTROL WITH IN-PLANE MAGNETIC FIELD

In all measurements we control the external flux ϕ_{ext} with the in-plane component of the magnetic field perpendicular to the nanowire, B_y, as illustrated in Fig. 6.14 (Wesdorp et al., 2023), for which one flux quantum corresponds to 2.2 mT. This is done since flux tuning with the out-of-plane magnetic field B_x led to strong hysteric behaviour in the resonator as well as flux jumps in the SQUID loop. We attribute these effects to Abrikosov vortex generation and the presence of superconducting loops on the chip, causing screening currents.

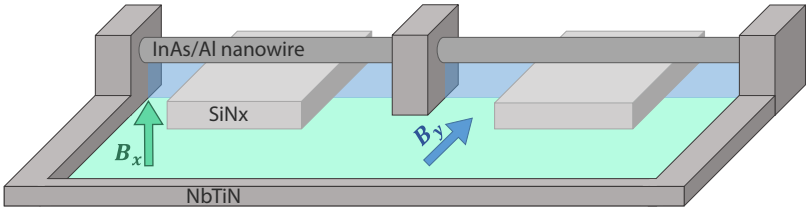

Figure 6.14: **Flux control with B_y.** The nanowire is elevated with respect to the NbTiN plane due to the gate dielectric. This defines a loop area perpendicular to B_y. B_y can therefore be used to control the flux through the SQUID loop while keeping the out-of-plane field component (B_x) fixed, reducing the occurance of external flux jumps.

CRYOGENIC AND ROOM TEMPERATURE MEASUREMENT SETUP

Both devices are measured in the same Triton dilution refrigerator with a base temperature of 20 mK. As shown in Fig. 6.15, it contains an input RF line, an output RF line and multiple DC gate lines. The DC gate lines are filtered at base temperature with multiple low-pass filters connected in series. The input RF line contains attenuators and low-pass filters at different temperature stages, as indicated. The output RF line contains a travelling wave parametric amplifier (TWPA) at the 20 mK temperature stage, a high-electron-mobility transistor (HEMT) amplifier at the 4 K stage, and an additional amplifier at room temperature. A three-axis vector magnet (x-axis not shown) is thermally anchored to the 4 K temperature stage, with the device under study mounted at its center. The B_z component of the magnetic field is controlled with a MercuryiPS current source while the B_x and B_y axes are controlled with Yokogawa GS200 and GS610 current sources respectively. At room temperature a vector network analyzer (VNA) is connected to the input and output RF lines for spectroscopy at frequency f_{r}. On the input line, this signal is then combined with the qubit drive tone at frequency f_{t} for two-tone spectroscopy. A separate tone at f_{r} only used for time-domain measurements is also combined onto this line. For time-domain measurements the output signal is additionally split off into a separate branch and down-converted to 25 MHz to be measured with a Zurich Instruments ultra-high frequency lock-in amplifier.

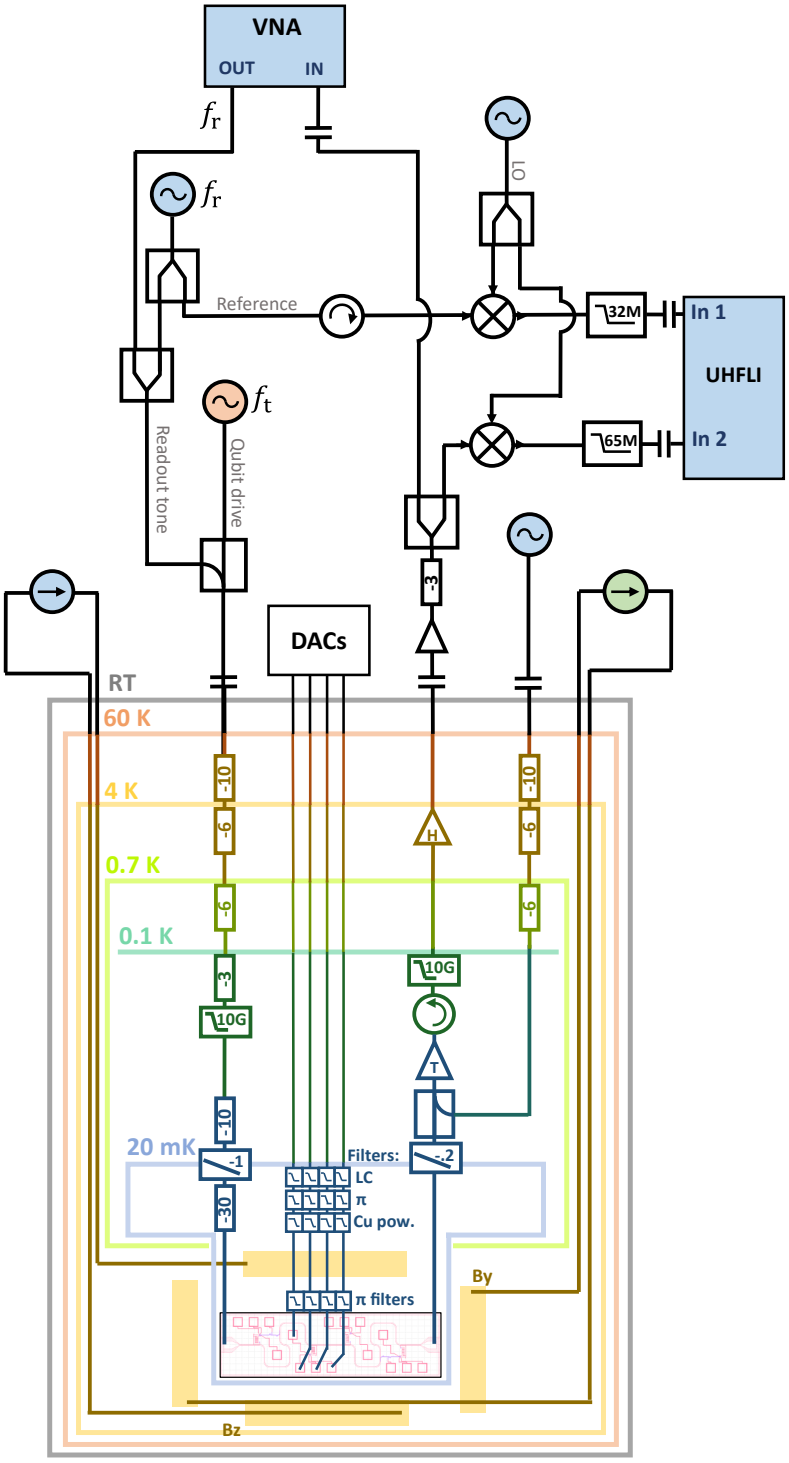

Figure 6.15: **Measurement setup at cryogenic and room temperatures.**

FLUX JUMPS IN DEVICE A WHEN $|B| < 9$ mT

For all measurements of device A, the value of the applied magnetic field is kept above 10 mT to prevent flux jumps observed when $|B| < 9$ mT. In particular, for Figs. 6.3 to 6.5 in the main text, $B_z = 10$ mT. The reason for this is purely technical. Device A contains various on-chip aluminium wire-bonds connecting separate sections of the ground plane together. Below the critical magnetic field of aluminium (~10 mT (Luthi et al., 2018)) these wire bonds create superconducting loops close to the device region, and have a significant cross-section perpendicular to the chip plane. In this regime, the application of an in-plane magnetic field B_y generates unwanted currents across these superconducting loops, which in turn result in multiple jumps observed in the flux through the SQUID loop (Fig. 6.16), making it impossible to reliably control ϕ_{ext}. Applying a field $|B| > 9$ mT turns the aluminium wire bonds normal and prevents the unwanted flux jumps, as shown in Fig. 6.16(a). As this magnetic field is small compared to other energy scales involved, it should not affect the physics under study. We further note that the absence of superconducting loops containing wire-bonds in device B made it possible to measure this device at $B_z = 0$ mT without suffering from similar flux jumps.

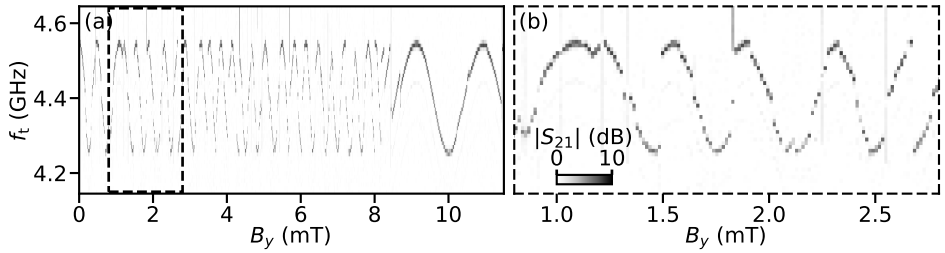

Figure 6.16: **Flux jumps under |B| = 9 mT for device A.** Multiple flux jumps and a distorted periodicity observed at low magnetic fields disappear when $|B| > 9$ mT. Here, $B_z = B_x = 0$

6.8.3. BASIC CHARACTERIZATION AND TUNE UP OF DEVICE A

REFERENCE JUNCTION CHARACTERIZATION

In this section we investigate the basic behaviour of the reference junction versus junction gate voltage V_J and magnetic field B_z when the quantum dot junction is completely closed. This information is used to choose a V_J set-point, $V_J = 640$ mV, which maintains a good SQUID asymmetry in all regimes of interest. Figs. 6.17(a) and (b) show the V_J dependencies of the resonator and transmon frequencies, respectively. As V_J is varied, different junction channels open sequentially (Hart et al., 2019; Spanton et al., 2017), with transparencies that increase non-monotonically due to mesoscopic fluctuations at the junction. This in turn affects the transmon's E_J and results in the observed fluctuations of its frequency.

The B_z dependencies of f_{01} and $f_{02}/2$ at $V_J = 640$ mV are shown in Fig. 6.17(e). From this we estimate both the transmon island charging energy E_c (not to be confused with U, the charging energy of the quantum dot junction) and the parameters of reference junction potential used in this section to match the measurements to the numerical calculations. Illustrated in this figure is a fit of the data with a Josephson potential gov-

erned by a single Andreev level at the junction $V(B,\delta) = -\Delta(B)\sqrt{1 - T\sin^2\frac{\delta}{2}}$. Here $\Delta(B) = \Delta\sqrt{1-(B/B_c)^2}$ is the field dependent superconducting gap (Luthi et al., 2018), Δ is the superconducting gap at zero field, B_c is the critical magnetic field and T is the transparency of the junction. As the fit is not constrained well enough to provide a unique solution, we fix $\Delta/h = 60$ GHz based on recent experiments on the same nanowires (Splitthoff et al., 2022). We obtain $E_c/h = 306$ MHz, $T = 0.58$, and $B_c = 413$ mT, resulting in an effective $E_J \sim \Delta T/4 = 8.7$ GHz. A similar procedure is then performed for $V_j = E_J(1-\cos\delta)$, resulting in $E_c/h = 210$ MHz and $E_J/h = 12.8$ GHz.

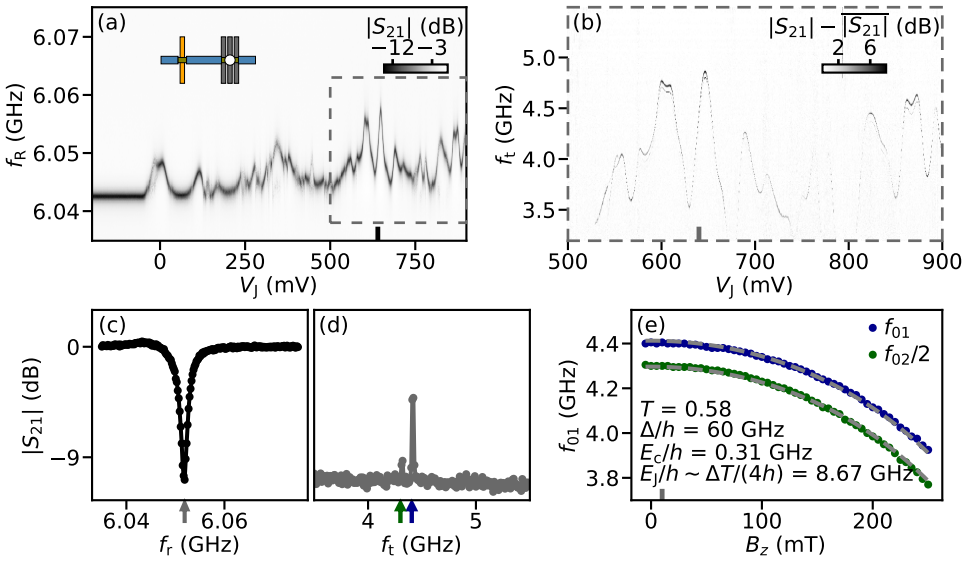

Figure 6.17: **Reference junction characterization for device A.** (a) V_J dependence of single-tone spectroscopy when the quantum dot junction is pinched-off ($V_C = 52.4$ mV, $V_L = 470$ mV, $V_R = 373$ mV). At low V_J values the reference junction is pinched-off and $E_J \sim 0$, thus the resonator is at its bare resonance frequency. As V_J increases, the resonator frequency increases non-monotonically due to mesoscopic fluctuations of the overall increasing transmission of different junction channels. (b) V_J-dependence of two-tone spectroscopy for the V_J range indicated in (a) with a dashed line rectangle. The black lines in (a) and (b) indicate the $V_J = 640$ mV set-point which sets the transmon frequency to its set-point used for the main text figures, $f_{01} = f_{01}^0 = 4.4$ GHz. (c) Line-cut of (a) at the V_J set-point, showing a resonance. (d) Line-cut of (b) at the V_J set-point, showing two peaks. The highest peak, at higher frequency, appears when the second tone frequency matches the transmon frequency ($f_t = f_{01}^0$). The lower peak corresponds to $f_{02}/2$ and shows the anharmonicity of the transmon. For (d), the first tone frequency f_r is fixed at the bottom of the resonance, indicated with a grey arrow in (c). (e) B_z evolution of f_{01}^0 and $f_{02}/2$ at $V_J = 640$ mV.

We can use these parameters to estimate the experimentally-realized SQUID asymmetry $\alpha_S = E_J/E_{J,QD}$ where $E_{J,QD}$ denotes the effective quantum dot junction Josephson energy. To do so we estimate $E_{J,QD}$ from the calculated qubit frequencies of the singlet and doublet obtained through the relation $\hbar\omega_{01} \approx \sqrt{8E_{J,QD}E_c} - E_c$ (Koch et al., 2007). We find that $\alpha_S > 10$ for almost all of the parameter range, exceeding 30 for low values of V_t. The asymmetry is at its smallest for the upper values of V_t in the vicinity of $\xi = 0$, where we find a minimum asymmetry $\alpha_S = 4$. We note that the effects of these variations in

asymmetry are fully captured by the numerical model; its effects are predominantly on the modulation of the qubit transition frequency with flux and not on the position of the singlet-doublet transition boundaries.

QUANTUM DOT JUNCTION CHARACTERIZATION

In this section we show the basic behaviour of the quantum dot gates when the reference junction is closed. Fig. 6.18 shows effective pinch-off curves for all three quantum dot gates ramped together (a) and for each of them separately, when the other two are kept at 1250 mV (b-d). This shows that each of the three quantum dot gates can independently pinch off the quantum dot junction even if the other gates are in the open regime, signifying strong lever arms and good gate alignment. We note that these are not pinch-off curves as encountered in conventional tunnel spectroscopy. They reflect the voltages at which there is no longer a measurable transmon transition frequency mediated by the quantum dot junction, which could either be due to low tunneling rates or a full depletion of the quantum dot.

We further note that the gate setpoint chosen for the measurements shown in the main text should not be directly compared to the individual pinch-off curves shown here. In panels (b-d) the non-varying quantum dot gates are kept fully open at 1250 mV which, due to cross coupling between gates, results in lower pinch-off values than those at the gate setpoint used for the measurements in the main text.

DEVICE TUNE UP

This section describes the process of tuning up the quantum dot gates to the setpoint used for the main text figures. We start by closing the reference junction ($V_J = -200$ mV) and going to a point in quantum dot gate voltages near pinchoff ($V_C = 100$ mV, $V_L = 250$ mV and $V_R = 400$ mV, see Fig. 6.18). Monitoring the frequency of the resonator while varying one of the gates reveals small shifts away from its bare frequency which resemble the shape expected for quantum dot resonances (Fig. 6.19(a)). Fixing the readout frequency f_r at the bare frequency of the resonator, one can map out the regions where these shifts happen on a two-dimensional map versus the left and right gates (Fig. 6.19(b)). In such maps, a pixel with a dark color indicates the resonator is not shifted from its bare frequency while a bright pixel indicates a shift of the resonator frequency, which we can use to identify potential regions of interest.

After identifying such a region in V_L-V_R space, we open the reference junction to its set-point $V_J = 640$ mV, which lifts the reference transmon frequency to $f_{01}^0 = 4.4$ GHz, closer to the bare resonator frequency. This magnifies the dispersive shift of the resonator and, furthermore, brings the external flux into the picture. As shown in Fig. 6.19(e), the asymmetric SQUID behaves as expected for different quantum dot gate setpoints. The reference junction sets the reference value for the transmon frequency, f_{01}^0, and the quantum dot contributes with small variations above or below this setpoint due to constructive or destructive interference, respectively.

Fixing $\phi_{ext} = 0$ and repeating the initial measurement versus V_R with the reference junction open reveals much stronger deviations of the resonant frequency than before (Fig. 6.19(c)). Importantly, the observed resonant frequency is now discontinuous, which, as detailed in the main text, is a signature of a singlet-doublet transition of the quantum dot junction. We tentatively identify the regions for which the resonator frequency is

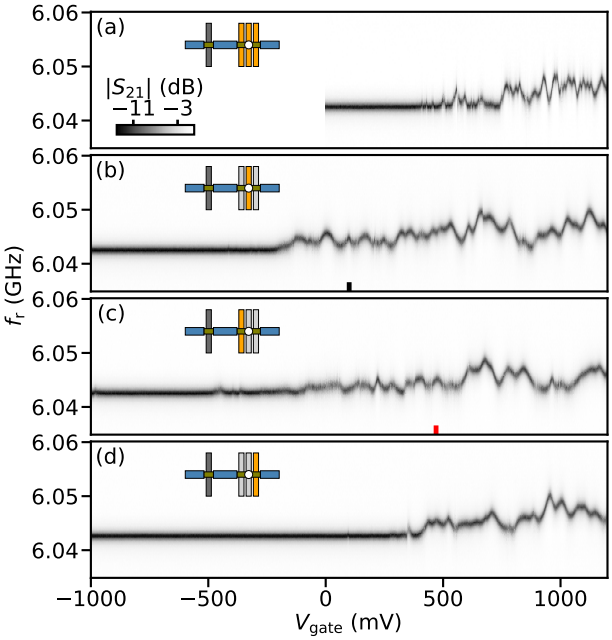

Figure 6.18: **Quantum dot gates characterization for device A.** (a) Gate voltage dependence ($V_L = V_C = V_R = V_{gate}$) of single-tone spectroscopy, showing how the quantum dot junction is pinched off at V_{gate} values lower than 300 mV. (b-d) V_C, V_L and V_R dependence, respectively of single-tone spectroscopy. In each panel, the two unused gates are kept at 1250 mV. This shows how each of the three quantum dot gates can independently pinch off the quantum dot junction. For all panels, the reference junction is closed ($V_J = -200$ mV). The black line in (b) indicates the value of $V_C = 100$ mV at which Fig. 6.19 is taken. The red line in (c) indicates the fixed value of $V_L = 470$ mV at which all main text figures are taken.

shifted to lower values as doublet regions and perform single frequency readout versus V_R and V_L, now with f_r fixed at the resonator frequency corresponding to doublet regions (Fig. 6.19(d)). The resulting two-dimensional map reveals regions for which the transmission amplitude signal is low (dark regions in Fig. 6.19(d)) which we identify as potential regions with a doublet ground state.

The next step for tuning up is identifying an isolated region where the quantum dot is in a doublet ground state and exploring the behaviour versus the central quantum dot gate. This is shown in Fig. 6.20. As V_C is varied at $\phi_{ext} = 0$ (Fig. 6.20(c)), the resonator first shows a displacement towards higher frequencies to then abruptly drop to a lower frequency, to then finally go back to the higher frequencies once-more. As detailed in the main text, we identify this behaviour with a singlet-doublet transition as the relative level of the quantum dot ξ is being varied. Figs. 6.20(a) and (b) show how this central doublet ground state region varies with each of the two lateral quantum dot gates. In both cases we observe a dome shape, resembling the behaviour we would expect when varying the tunnel coupling between quantum dot and leads. However, these dome shapes are rotated in V_C-V_R and V_C-V_L space. This is understood as the result of cross coupling between the different quantum dot gates.

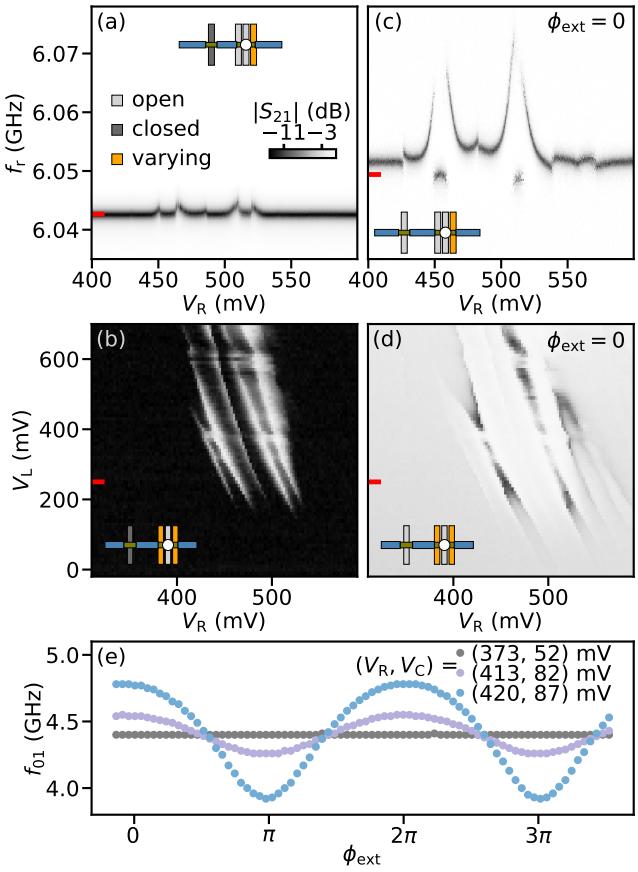

Figure 6.19: **Quantum dot tune up for device A.** (a) Single-tone spectroscopy measured at V_L = 250 mV, exhibiting two small resonances. Here the reference junction is fully closed (V_J = -200 mV). The red line indicates the readout frequency used in panel (b). (b) Single frequency readout of the resonator. Bright colors indicate a shift in the resonance frequency, marking the onset of supercurrent through the dot. The red line indicates the V_L value of panel (a). (c) Same as panel (a) but with the reference junction opened to the V_J = 640 mV setpoint used throughout the manuscript. The two junctions in parallel form a SQUID, increasing the qubit frequency and in turn the resonance frequency. Measured at ϕ_{ext} = 0. (d) Same as panel (b) but with the reference junction set to V_J = 640 mV and ϕ_{ext} = 0, measured at the frequency indicated with a red line in (c). For (a-d), V_C = 100 mV (close to pinchoff), indicated with a black line in Fig. 6.18. (e) f_{01} versus ϕ_{ext} at fixed V_J = 640 mV, for three quantum dot gates setpoints corresponding to a quantum dot junction which is fully closed (grey), slightly open (violet) or very open (blue) showing the DC SQUID behaviour of the two parallel Josephson junctions.

After identifying the cross coupling effect between different quantum dot gates, we define a new set of virtual gates in an attempt to tune the model parameters independently. We fix V_L =470 mV (set-point kept for all results shown in the main text) and focus on V_R-V_C space. Fig. 6.21(b) shows the dome shape previously identified in V_R-V_C space. We identify a line along the dome (indicated with a dashed line) for which the quantum dot level appears to be fixed and define new plunger virtual gate (V_P, perpendicular to

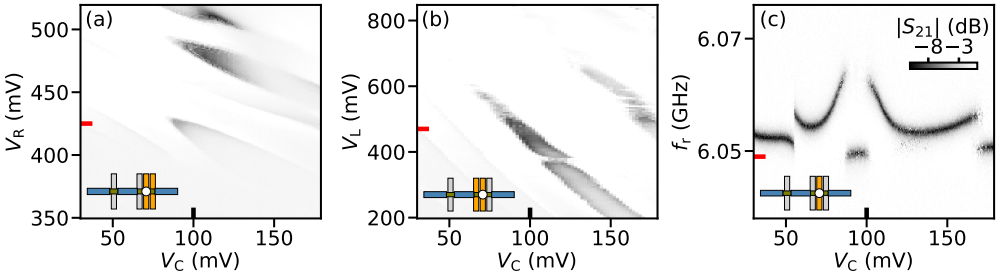

Figure 6.20: **Quantum dot gate dependence for device A.** (a) Single frequency readout of the resonator at the frequency indicated in Fig. 6.19(c) with a red line, performed versus V_C and V_R for fixed V_L = 470 mV. (b) Same as (a) but versus V_C and V_L and for fixed V_R = 425 mV. (c) Single-tone spectroscopy versus V_C, measured at V_L = 470 mV and V_R = 425 mV, revealing a quantum dot resonance. For all panels $\phi_{ext} = 0$.

this line) and right tunnel virtual gate (V_T, along this line) (see Fig. 6.21(d)). This rotated gate frame is the one used for the main text. Note that this routine does not guarantee that V_P does not affect the tunneling rates. It rather ensures that V_T does not (strongly) affect the quantum dot level ξ.

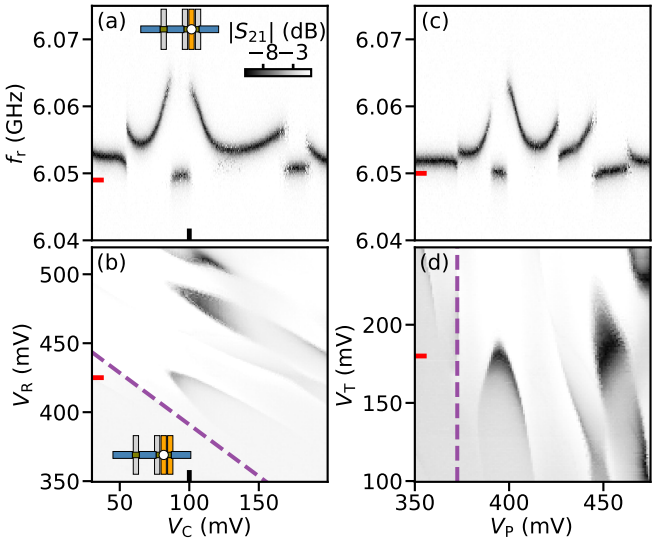

Figure 6.21: **Gate compensation for device A.** (a) Single-tone spectroscopy versus V_C at V_R = 427 mV. (b) Single frequency readout of the resonator measured versus the central (V_C) and right (V_R) quantum dot gate voltages, performed at a at fixed V_L 470 mV. The red line indicates the V_R value of panel (a). (c) Resonator spectroscopy versus V_P at V_T = 180 mV. (d) Same as (b) but in the transformed coordinate frame, measured vs. the virtual plunger (V_P) and right tunnel (V_T) gate voltages. In (a) and (c), the red lines indicate the readout frequencies used in panels (b) and (d), respectively. For all panels $\phi_{ext} = 0$.

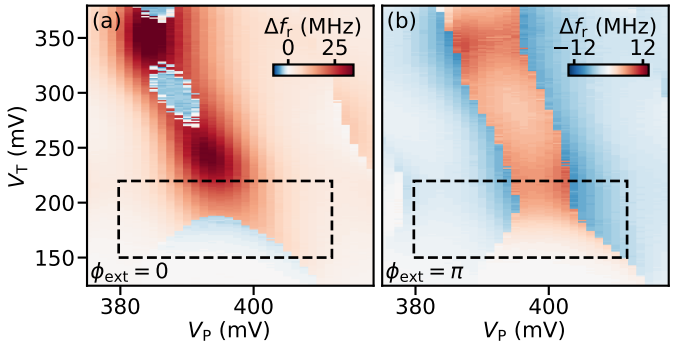

Figure 6.22: **Extended V_T dependence.** (a) Δf_r versus V_P and V_T at $\phi_{ext} = 0$, revealing singlet (red) and doublet (blue) ground state regions separated by sharp transitions. (b) Same as (a) but for $\phi_{ext} = \pi$. We note that the plunger gate axis is shifted by about 5 mV with respect to (a) and the data shown in the main text, which we speculate is due to an irreproducible gate jump. Dashed rectangles indicate the gate ranges in which the measurements of Fig. 6.5 of the main text are taken.

LARGER TUNNEL VOLTAGE RANGE

In Fig. 6.22 we show the behaviour of the singlet and doublet regions beyond the V_T range investigated in Fig. 6.5 of the main text. At $\phi_{ext} = \pi$ we do not observe the doublet phase boundary fully closing for any V_T. According to theory, this should only occur if $\xi \approx 0$ and $\Gamma_L \approx \Gamma_R$ are maintained at each gate setting in the experiment. That this condition would remain satisfied for any V_T is implausible given the cross-coupling present in the system. We instead speculate that at higher gate voltages the tunnel rates cease to be a monotonically increasing function, which is substantiated by the tunnel gate dependence at $\phi_{ext} = 0$. Here we observe a temporary recovery of the doublet region at higher V_T, which should not occur for increasing values of Γ. We further speculate that in this regime of increasingly large Γ/U the dot can eventually be tuned to a different charge configuration, involving energy levels not captured by the single-level model.

We note that for these measurements only single tone spectroscopy was performed. We therefore plot $\Delta f_r = f_{res} - f^0_{res}$, where f^0_{res} denotes the resonator frequency with the quantum dot junction pinched off. Its qualitative interpretation is the same as that of Δf_{01} used in the main text.

STATE SELECTIVE SPECTROSCOPY

For the measurements performed close to singlet-doublet transitions, single-tone spectroscopy simultaneously shows two resonances whose relative depth varies with the distance from the transition. This is once more illustrated in Fig. 6.23, which shows single-tone spectroscopy at several different V_P regions while ϕ_{ext} is varied. It corresponds to the measurements of Fig. 6.4 of the main text. In panels (a) and (d) we observe only a single resonance; at these plunger gate values the quantum dot junction is sufficiently deep in the singlet and doublet parity sector respectively that only one state is occupied. However, at the plunger gate values between these two regimes (panels (c-d)) the behaviour is more complex. We simultaneously observe two resonances and their depth becomes a function of flux.

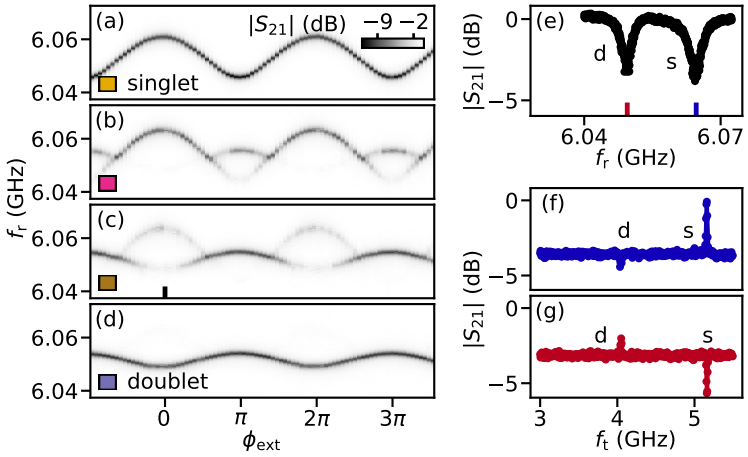

Figure 6.23: **State selective spectroscopy.** (a-d) ϕ_{ext} dependence of single-tone spectroscopy at four representative V_P values, indicated in Fig. 6.3 in the main text. Traces at intermediate V_P values show two resonances simultaneously due to switches on timescales faster than the integration time. (e) Linecut of (c) at $\phi_{ext} = 0$, indicated by a black line in (c). (f) Two-tone spectroscopy at the same settings as in (e), with the first tone at the frequency of the singlet resonance. The measurement shows a peak at the transmon frequency of the singlet state. (g) Same as (f) but with the readout frequency corresponding to the doublet resonance, which shows a peak at the transmon frequency of the doublet state.

For the two-tone spectroscopy measurements in the main text we make use of the averaged occupation of the states captured in the single-tone spectroscopy measurement to identify most occupied state. This can be inferred from the relative depth of the resonances: for example in Fig. 6.23(e) the most occupied state is the singlet, albeit by a small margin. This in turn allows us to do state selective two-tone spectroscopy, revealing the transmon transition that corresponds to the most occupied state of the system. To do so we fix the frequency of the first tone f_r at the bottom of the deepest resonance, corresponding to the most populated sector of the system. We illustrate this in Figs. 6.23(f) and (g), where by fixing f_r at the bottom of the resonance corresponding to the singlet (doublet) state we observe a peak only when f_t is equal to the transmon frequency corresponding to the singlet (doublet) state. It is this peak position that we report as f_{01}.

6.8.4. MAGNETIC FIELD DEPENDENCE OF DEVICE A

In this section we elaborate on the analysis of the data shown in Fig. 6.6(c) in the main text. When varying both ϕ_{ext} and B_z in a measurement, one has to consider the possibility of an unwanted misalignment of the magnetic field with respect to the nanowire axis. This, in combination with the multiple orders of magnitude difference between the applied B_z (hundreds of mT) and the B_x (less than 1 μT) or B_y (several mT) needed to thread a flux quantum through the SQUID loop, can result in big changes of the $\phi_{ext} = 0$ point for different values of B_z. Therefore, one has to re-calibrate the value of B_y that corresponds to $\phi_{ext} = 0$ for each B_z value. To do so, we use the flux dependence of f_{01} at a gate point for which the quantum dot junction ground state remains a singlet for the whole B_z range as a reference for identifying $\phi_{ext} = 0$. This gate point is indicated with a

grey cross in Fig. 6.24(a).

The measurement shown in Fig. 6(c) is therefore performed as follows:

for each B_z value **do**
  apply B_z
  for each B_y value **do**
    apply B_y
    measure f_{01} at the grey gate point
    measure f_{01} at the green gate point
  end for
end for

For each B_z value we then reconstruct the B_y dependence of ϕ_{ext} through the dependence of the reference gate point (grey). Furthermore, we use this method to identify points in B_y where flux jumps happen and correct for them. While they almost never occur for small magnetic fields, and none of the other data required such a correction, we found that at increasing B_z jumps would occur more often. We believe this is due to a small misalignment between B_z and the plane of the chip. The resulting corrected ϕ_{ext} reference is shown in Fig. 6.24(b), while Fig. 6.24(d) shows several linecuts.

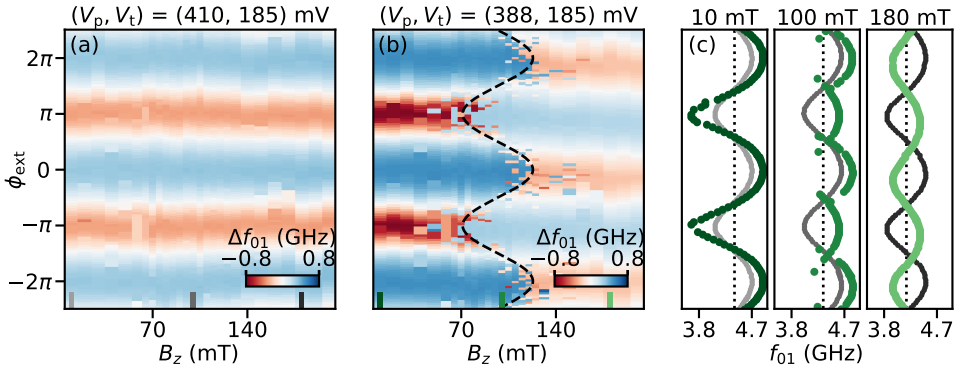

Figure 6.24: **Data analysis for magnetic field dependence of device A.** (a) and (b) show Δf_{01} versus B_z and ϕ_{ext}, measured the two gate points indicated in Fig. 6.6 with grey and green markers, respectively. In (a), the singlet is the ground state for all B_z. This gate point is used to identify a flux reference for each B_z. For (b), there is a singlet-doublet ground state transition with B_z, where the sinusoidal dashed line serves as a guide for the eye. (c) f_{01} versus ϕ_{ext} for the three B_z values indicated in (a) and (b). The dotted line indicates f_{01}^0, which decreases with B_z as shown in Fig. 6.17(e).

6.8.5. PARITY LIFETIME EXTRACTION PROCEDURE

In this section we elaborate on the analysis method for extracting the characteristic lifetimes of the singlet and doublet states, T_s and T_d. We start with a continuous measurement at a fixed readout frequency where we monitor the demodulated output signal integrated in time bins of $t_{\text{int}} = 2.3\,\mu\text{s}$. This reveals a complex random telegraph signal jumping between two states in the (I,Q)-plane. The histogram of the acquired (I,Q) points shows two states (Fig. 6.25(a)) whose centers define an axis X. A segment of the measured telegraph signal, projected onto this X axis, is shown in Fig. 6.25(c). Taking the

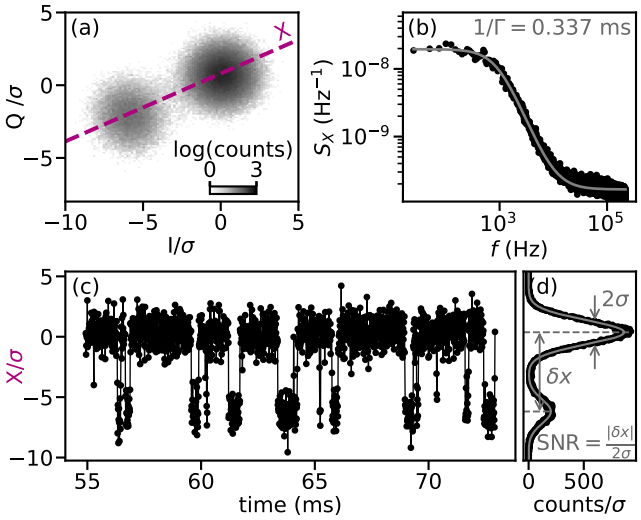

Figure 6.25: **Parity lifetime analysis.** (a) Logarithmic-scale histogram of the resonator response in the (I,Q)-plane after integrating a 2 s time trace with time bins of $t_{\text{int}} = 11.4\,\mu\text{s}$. It exhibits two separate Gaussian distributions whose centers define an axis, X, indicated with a dashed line. (b) Power spectral density (black) of an unintegrated 2 s time trace projected onto the X axis. In grey, best fit of a Lorentzian lineshape with a white noise background (Eq. (6.14)). (c) 18 ms cut of the integrated response projected onto the X axis, revealing jumps between two distinct states. (d) 1D histogram of the response in (a) projected onto the X axis (black) and the best fit of a double Gaussian line-shape (grey, Eq. (6.13)). For all panels $V_{\text{L}} = 325\,\text{mV}$, $V_{\text{T}} = -60\,\text{mV}$, $V_{\text{P}} = 551.4\,\text{mV}$, $B_z = 0$ and $\phi_{\text{ext}} = 0$.

histogram along this axis results in a double Gaussian distribution (Fig. 6.25(d)) that is well-described by

$$g(x) = \frac{A_1}{\sqrt{2\pi\sigma^2}} e^{\frac{-(x-x_1)^2}{2\sigma^2}} + \frac{A_2}{\sqrt{2\pi\sigma^2}} e^{\frac{-(x-x_2)^2}{2\sigma^2}} \tag{6.13}$$

Here, $A_{1,2}$ are the relative populations of singlet and doublet occupation, $x_{1,2}$ are the centers of each Gaussian and σ is their standard deviation. For the data shown in Fig. 6.25, the fit results in $A_1 = 2169\sigma$, $A_2 = 506\sigma$, $x_1 = 0.37\sigma$ and $x_2 = -6.19\sigma$, from which we determine the $\text{SNR} = |x_1 - x_2|/2\sigma = 3.28$.

From the time domain information of the signal we construct its power spectral density (PSD), which is its squared discrete Fourier transform (Fig. 6.25(b))

$$S_X(f) = \frac{\Delta t}{N\pi} \left| \sum_{n=1}^{N} X(n\Delta t) e^{-i2\pi f n \Delta t} \right|^2 \tag{6.14}$$

where $X(t)$ is the measured signal (as projected onto the previously defined X-axis), $\Delta t = 2.3\,\mu\text{s}$ is the discrete time bin in which the data is measured, $N = \frac{T}{\Delta t}$ is the number of points and T is the total signal length. In practice we use Welch's method with a Hanning window (Welch, 1967) to calculate the power spectral density, dividing the trace into 50 sections of length 40 ms that overlap by 20 ms and averaging the power spectral density of all segments. This results in a spectrum that is well fit by a single Lorentzian of the

form

$$S(f) = A\frac{4\Gamma}{(2\Gamma)^2 + (2\pi f)^2} + B, \tag{6.15}$$

from which we obtain $1/\Gamma = 0.337$ ms, $A = 5.75 \cdot 10^{-5}$ and $B = 1.65 \cdot 10^{-10}$ Hz^{-1}.

Combining the amplitude ratio $R = A_1/A_2$ obtained from the Gaussian fit of the two quadratures and the Γ value obtained from the Lorentzian fit of the PSD, we calculate

$$T_s = 1/\Gamma_s = \frac{1+R}{2\Gamma R}, \qquad T_d = 1/\Gamma_d = \frac{1+R}{2\Gamma} \tag{6.16}$$

to obtain $T_s = 0.89$ ms, $T_d = 0.21$ ms.

6.8.6. EXTENDED PARITY LIFETIME DATA

PARITY LIFETIMES LINECUT VERSUS FLUX

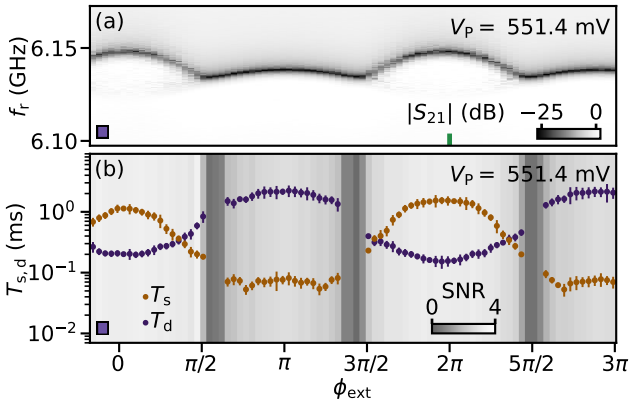

Figure 6.26: **Flux dependence of parity lifetimes** (a) ϕ_{ext} dependence of single-tone spectroscopy at V_P = 551.4 mV. (b) ϕ_{ext} dependence of the parity lifetimes extracted following the analysis in Fig. 6.25 at V_P = 551.4 mV. Markers indicate the mean and error bars indicate the maximum and minimum values of 10 consecutive 2 s time traces. SNR = $\frac{|\delta x|}{2\sigma}$ is shown in greyscale in the background. For points where SNR < 1, the extracted parity lifetimes are not shown as we do not consider them reliable. Measured at the same V_T, V_L and B_z as for Fig. 6.25.

Fig. 6.26 shows the flux dependence of the lifetimes of the singlet and doublet states at V_P = 554.4 mV, which accompanies main text Fig. 6.7. We find that both singlet and doublet lifetimes show an approximate sinusoidal dependence on the applied flux. As discussed in the main text, this flux dependence most likely originates from the oscillation of the singlet-doublet energy gap with flux. However it could also be indicative of a coherent suppression of the tunneling rates (Pop et al., 2014). We further note that the sudden drops in SNR are due to crossings of the transmon frequencies of the singlet and doublet states. At these points both resonator frequencies become indistinguishable and their lifetimes can not be measured.

POWER AND TEMPERATURE DEPENDENCE OF PARITY LIFETIMES

Here we present additional data on the readout power and temperature dependence of the parity lifetimes shown in Fig. 6.7 of the main text. The power dependence at four

selected points across a phase boundary is shown in Figs. 6.27(c-f). Away from the transition (purple) and right on top of the transition (green) the readout power does not have a strong effect on the extracted lifetimes in the investigated range. For plunger gate values V_P closer to the transition, however, the asymmetry of the lifetimes decreases with power (blue). Although the origin of this dependence is not clear, we conjecture it is related to parity pumping effects (Wesdorp et al., 2023).

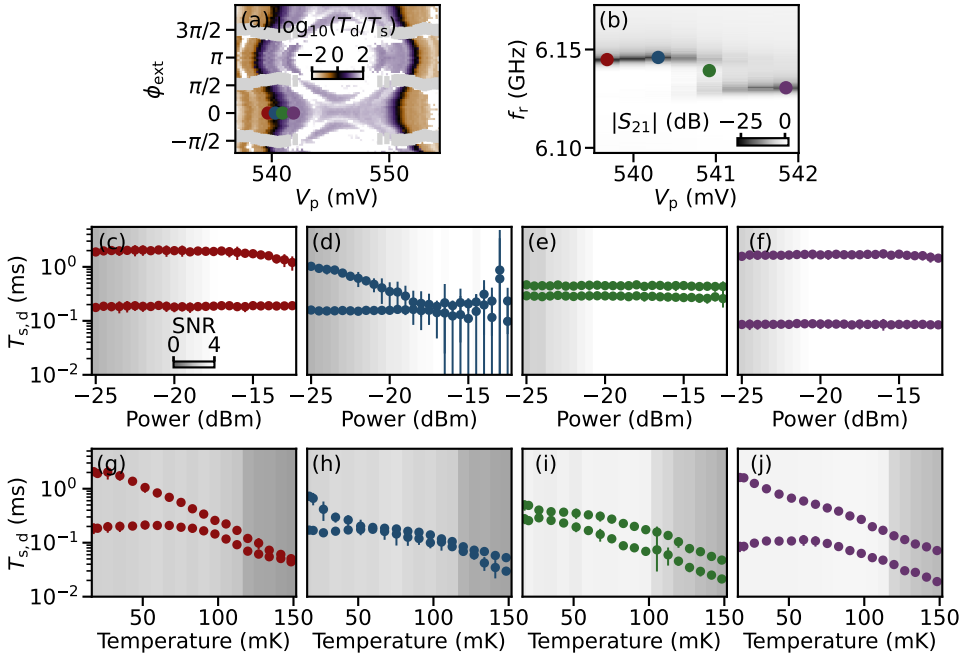

Figure 6.27: **Power and temperature dependence of parity lifetimes across the singlet-doublet transition** (a) 2D map of $\log_{10}(T_d/T_s)$ versus V_P and ϕ_{ext}, extracted from a 2 s time trace for each pixel. This is the same panel as Fig. 6.7(e) in the main text. (b) V_P dependence of single-tone spectroscopy at $\phi_{ext} = 0$, across a singlet/doublet transition. For (a) and (b), the mixing chamber temperature is 18 mK and the readout power is −22 dBm. (c-f) Readout power dependence at 18 mK of the extracted parity lifetimes at the plunger points indicated in (a) and (b). Markers indicate the mean and error bars indicate the maximum and minimum values of 10 consecutive 2 s time traces. The SNR is shown in greyscale in the background. For points where SNR < 1, the extracted parity lifetimes are discarded. (g-j) Same as (c-d) but versus temperature and at a power of −22 dBm. All powers are given at the fridge input.

Temperature dependencies at the same gate points, measured at a readout power of -22 dBm at the fridge input, are shown in Figs. 6.27(g-j). Here the mixing chamber temperature of the dilution refrigerator is measured with a ruthenium oxide resistance thermometer and increased in a controlled step-wise fashion with a variable-output heater mounted on the mixing chamber plate. We observe different effects of temperature for each of the gate points. In general, there is a temperature independent regime at low temperatures, followed by a temperature dependent drop above a certain characteristic temperature, which varies over tens of mK for different gate points. For some of the

gate points, however, the temperature independent contribution is absent and the effect of increased mixing chamber temperature starts immediately at base temperature (Fig. 6.27(i)). These results are indicative of non-equilibrium effects playing a role in the physics of the devices under study, their exact behaviour dependent on the energy level configuration of the quantum dot junction.

PARITY LIFETIMES VERSUS TUNNEL GATE

To complement the data shown in Fig. 6.7 of the main text, taken at $V_T = -60$ mV, we also show the V_T dependence of the parity lifetimes at $\phi_{ext} = 0$ in Fig. 6.28. As for device A, the doublet ground state region exhibits a dome shape in V_P and V_T space, and at the transition between singlet and doublet ground states the lifetimes for both states become equal. Away from the transition, the lifetime asymmetry increases and the lifetimes differ by more than one order of magnitude. We note that the gate compensation of device B was not ideal, resulting in a small tilt of the dome.

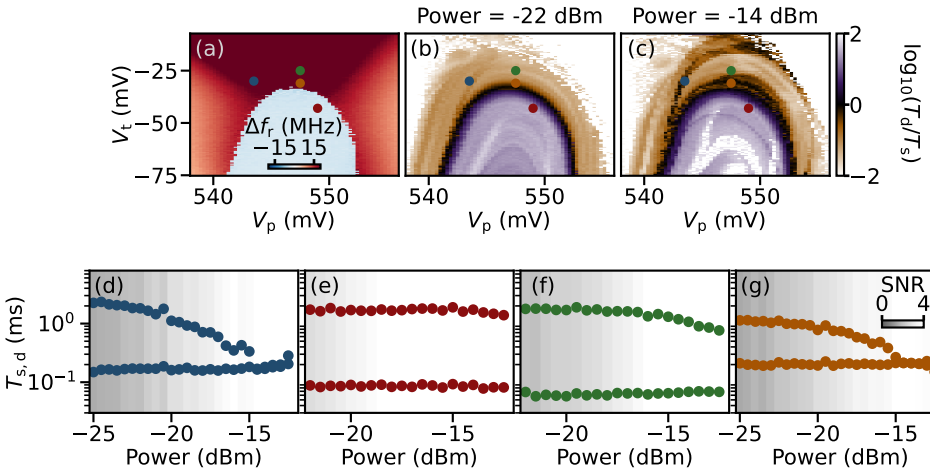

Figure 6.28: **Tunnel, plunger and power dependence of parity lifetimes** (a) $\Delta f_r = f_{res} - f_{res}^0$ versus V_P and V_T measured at $\phi_{ext} = 0$. It shows a regions of constructive and destructive interference, separated by sharp dome-like boundary. (b) Two-dimensional map of $\log_{10}(T_d/T_s)$ versus V_P and V_T, measured at a power of −22 dBm. (c) Same as (b) but for a power of −14 dBm. (d-e) Power dependence of the extracted parity lifetimes at the gate points indicated in (a-c). All powers are given at the fridge input.

Similarly to the behaviour shown in the main text for ϕ_{ext} and V_P, in this case we also observe contours of equal ratio where the lifetime asymmetry abruptly increases or decreases. For higher readout power these contours become accentuated, as shown in Fig. 6.28(c). Furthermore, for higher power the region with similar lifetimes around the ground state transition becomes wider. This is due to the parity lifetimes having a different dependence on power for different regions in gate space. For most regions in gate space there is again almost no dependence on readout power in the range explored (Fig. 6.28(e,f)). However, on special gate regions, such as close to ground state transitions (Fig. 6.28(g)) and on top of the observed contours (Fig. 6.28(d)), the lifetime asymmetry decreases rapidly with power, similar to the effect shown in Fig. 6.27.

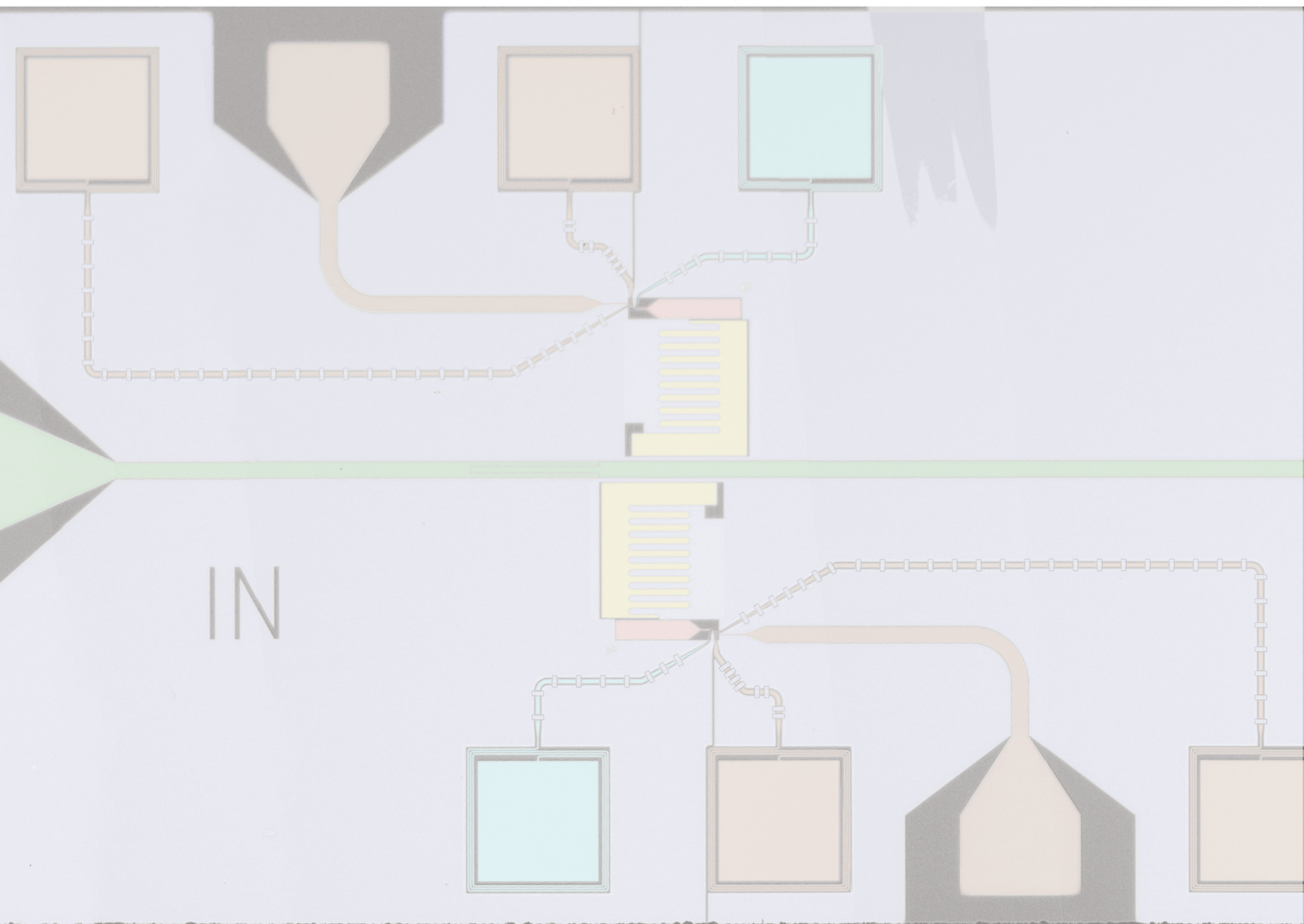
IN

7

SPECTROSCOPY OF SPIN-SPLIT ANDREEV LEVELS IN A QUANTUM DOT WITH SUPERCONDUCTING LEADS

We use a hybrid superconductor-semiconductor transmon device to perform spectroscopy of a quantum dot Josephson junction tuned to be in a spin-1/2 ground state with an unpaired quasiparticle. Due to spin-orbit coupling, we resolve two flux-sensitive branches in the transmon spectrum, depending on the spin of the quasi-particle. A finite magnetic field shifts the two branches in energy, favoring one spin state and resulting in the anomalous Josephson effect. We demonstrate the excitation of the direct spin-flip transition using all-electrical control. Manipulation and control of the spin-flip transition enable the future implementation of charging energy protected Andreev spin qubits.

The work in this chapter has been published as: A. Bargerbos*, **M. Pita-Vidal***, R. Žitko, L.J. Splitthoff, L. Grünhaupt, J.J. Wesdorp, Y. Liu, L.P. Kouwenhoven, R. Aguado, C.K. Andersen, A. Kou, and B. van Heck, Spectroscopy of spin-split Andreev levels in a quantum dot with superconducting leads, Physical Review Letters, **131**, 097001 (2023). * Equal contributions.

7.1. INTRODUCTION

In the confined geometry of a Josephson junction, the Andreev reflection of an electron into a hole at a normal-superconducting interface results in discrete Andreev bound states (ABS) (Bagwell, 1992; Beenakker, 1991; Bretheau et al., 2013; Furusaki and Tsukada, 1990; Kulik, 1969; Sauls, 2018). ABS are of fundamental importance from the perspective of mesoscopic superconductivity and are also at the basis of several qubit proposals (Chtchelkatchev and Nazarov, 2003; Despósito and Yeyati, 2001; Padurariu and Nazarov, 2010; Zazunov et al., 2003). In particular, when an ABS is populated by a single quasiparticle, the trapped quasi-particle can serve as the superconducting version of a spin qubit. In the presence of spin-orbit coupling, the Josephson phase difference ϕ may break the spin degeneracy, coupling the spin degree of freedom to the supercurrent across the junction (Béri et al., 2008; Chtchelkatchev and Nazarov, 2003) and allowing for direct integration of spin qubits into superconducting circuits for remote communication, transduction, or hybrid qubit platforms (Aguado, 2020; Lauk et al., 2020; Spethmann et al., 2022).

Experimental work on InAs/Al nanowire Josephson junctions has shown the presence of the predicted spin-split ABS (Hays et al., 2020; Metzger et al., 2021; Tosi et al., 2018), culminating in the first demonstration of coherent Andreev spin qubit manipulation (Hays et al., 2021). These remarkable experiments were operated in a regime in which the spin-1/2 junction states were an excited manifold and were thus susceptible to qubit leakage via quasiparticle escape or recombination, bringing the junction back into its spin-zero ground state. Furthermore, the direct manipulation of the spin states proved unfeasible, likely due to the smallness of relevant matrix elements (Park and Yeyati, 2017), requiring complex excitation schemes involving auxiliary levels (Cerrillo et al., 2021; Hays et al., 2021).

In Chapter 6 we showed that embedding a gate-controlled quantum dot in the InAs/Al Josephson junction makes it possible to tune its ground state to be an odd-parity spin-1/2 state. In this doublet phase, the lifetime of the trapped quasi-particle can exceed 1 ms, likely benefiting from the large charging energy of the quantum dot suppressing quasiparticle poisoning events.

In this Letter, employing the same transmon techniques as in Chapter 6, we report the detection of the spin-orbit-induced spin-splitting of the doublet states of a quantum dot Josephson junction. The energy difference between spin states is smaller than the electron temperature, which would make it difficult to detect in transport measurements. We also demonstrate that the spin-split states populations, as well as the spin-selective transmon frequencies, can be controlled via external magnetic fields smaller than 40 mT. In the presence of magnetic field, we furthermore observe the anomalous Josephson effect: a shift of the minimum of the energy-phase relation to a value ϕ_0 which is neither 0 nor π or, equivalently, the presence of a non-zero equilibrium supercurrent at $\phi = 0$ (Brunetti et al., 2013; Szombati et al., 2016; Yokoyama et al., 2014; Zazunov et al., 2009). Finally, we show that the spin states can be directly manipulated by applying microwaves to a bottom gate, via the electric dipole spin resonance (EDSR) (Flindt et al., 2006; Golovach et al., 2006; Nadj-Perge et al., 2010; Nowack et al., 2007; Rashba and Efros, 2003; van den Berg et al., 2013). Our experiment is directly comparable to, and inspired by, the theoretical proposal of Padurariu and Nazarov (2010), which we use to model the

data, combined with further understanding based on a modified single-impurity Anderson model (SIAM).

7.2. DEVICE & CONCEPTUAL OVERVIEW

At the core of our experiment lies the quantum dot Josephson junction, which is hosted in a nominally 10 µm-long InAs/Al superconductor-semiconductor nanowire with a 110 nm-wide hexagonal core and a 6 nm-thick shell covering two facets (Krogstrup et al., 2015). The quantum dot is electrostatically defined in a 200 nm-long wet-etched InAs section using three bottom gate electrodes with voltages V_L, V_C and V_R, and its superconducting leads are formed by the flanking InAs/Al sections [Fig. 7.1(a)]. The bottom gates can be used to control the occupation of the quantum dot and its coupling to the superconducting electrodes. This results in two possible ground states of the quantum dot junction: either a spin-zero or a spin-1/2 state. We are particularly interested in the latter case [Fig. 7.1(b)], where the ground state manifold is spanned by the two components, $|\downarrow\rangle$ and $|\uparrow\rangle$, of a Kramers doublet, and a minimal model for the potential energy of the quantum dot junction is given by (Padurariu and Nazarov, 2010)

$$U(\phi) = E_0 \cos(\phi) - E_{SO}\, \vec{\sigma}\cdot\vec{n} \sin(\phi) + \frac{1}{2}\vec{E}_Z \cdot \vec{\sigma}\,. \tag{7.1}$$

Here, $\vec{\sigma}$ is the spin operator, $\vec{n}$ is a unit vector along the spin-polarization direction set by the spin-orbit interaction, and E_{SO} and E_0 are the spin-dependent and spin-independent Cooper pair tunneling rates across the quantum dot junction. Note that the term proportional to E_0 has a minimum at $\phi = \pi$. This π-shift originates from the odd occupancy of the junction (Glazman and Matveev, 1989; Spivak and Kivelson, 1991) and distinguishes the Josephson energy from that of a conventional tunnel junction. Finally, $\vec{E}_Z$ is a Zeeman field arising in the presence of an external magnetic field.

The energy scales E_0 and E_{SO} can be understood as follows (Padurariu and Nazarov, 2010): Cooper pair tunneling occurs via a sequence of single-electron co-tunneling processes through the quantum dot energy levels. The spin-independent component E_0 arises from those sequences in which both electrons co-tunnel through the same energy level. The amplitude for these sequences is the same whether the initial state of the quantum dot junction is $|\downarrow\rangle$ or $|\uparrow\rangle$. On the other hand, E_{SO} arises from tunneling processes in which one electron co-tunnels through the singly-occupied level, involving a spin rotation, while the second one co-tunnels through a different level. Since in the presence of spin-orbit coupling the single-electron tunneling amplitudes can be spin-dependent, for these processes the *pair* tunneling amplitude may depend on the spin of the initial state.

The two potential energy branches of the doublet states at $\vec{E}_Z = \vec{0}$, $E_{\downarrow,\uparrow} = E_0 \cos\phi \pm E_{SO}\sin\phi$, are sinusoidals with an amplitude of $\sqrt{E_0^2 + E_{SO}^2}$ and minima at a phase ϕ_0 of $\pi \pm \arctan(E_{SO}/E_0)$, see Fig. 7.1(c). If $E_{SO} = 0$, the potential energy reduces to the well-known π-junction behavior without spin-splitting. At non-zero E_{SO}, the shift of the minima away from $\phi = 0, \pi$ is a precursor (Padurariu and Nazarov, 2010) to the anomalous Josephson effect (Brunetti et al., 2013; Zazunov et al., 2009); while at $\phi = 0$ there will be instantaneous supercurrents on timescales short compared to the spin lifetime,

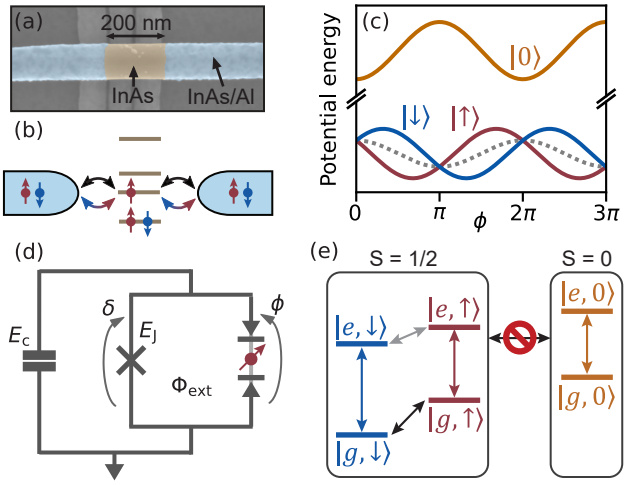

Figure 7.1: (a) False-colored scanning electron micrograph of the quantum dot junction. (b) Conceptual diagram of the quantum dot junction with multiple energy levels. Black and blue-to-red arrows denote the spin-conserving and spin-flipping tunnel couplings, respectively. (c) Josephson potential U versus the superconducting phase difference between the leads ϕ, shown for different quantum dot junction states: the singlet state in orange, and the two doublet states in red and blue. The dotted gray line indicates the potential of the doublet states in the absence of the E_{SO} term. (d) Circuit model for a transmon with charging energy E_c and a grounded SQUID formed by the parallel combination of a quantum dot junction and a reference Josephson junction with Josephson energy E_J. δ denotes the phase difference across the reference junction, and Φ_{ext} is the external magnetic flux through the SQUID loop. (e) Level diagram of the joint transmon-quantum dot junction system. The transmon transition frequencies $|g\rangle \leftrightarrow |e\rangle$ (vertical arrows) depend on the quantum dot junction state. Coherent microwave transitions between singlet and doublet are forbidden. However, intra-doublet spin-flip transitions are possible (diagonal arrows).

7

the time-averaged current will be zero due to thermal fluctuations. For completeness, in Fig. 7.1(c) we also show the potential energy E_s of the lowest-energy singlet state $|0\rangle$, with a minimum at $\phi = 0$, as expected for a conventional Josephson junction.

We can derive the occurrence of both E_0 and E_{SO} within a minimally-extended SIAM with superconducting leads. The SIAM is a simple model widely used to understand quantum dot junctions, containing a single energy level coupled to the leads via spin-conserving tunneling events (Choi et al., 2004; Glazman and Matveev, 1989; Kadlecová et al., 2019; Karrasch et al., 2008; Luitz et al., 2012; Martín-Rodero and Levy Yeyati, 2011; Meden, 2019; Oguri et al., 2004; Tanaka et al., 2007; Yoshioka and Ohashi, 2000). Only two extensions to the SIAM are required to generate the spin-splitting term E_{SO}: (i) spin-flipping single-electron tunneling between the leads and the energy level (Barakov and Nazarov, 2022; Danon and Nazarov, 2009; Padurariu and Nazarov, 2010; Spethmann et al., 2022) and (ii) inter-lead tunneling, resulting from integrating out the additional quantum dot energy levels. These results are derived in Sec. 7.7.1 of the Supplementary Material, together with a validation based on numerical renormalization group calculations (See Sec. 7.7). In view of the strong spin-orbit coupling in InAs (Fasth et al., 2007; Liang and Gao, 2012) and the confinement on the order of 100 nm (Chang et al., 2013; van Dam et al., 2006; van Veen et al., 2019), we expect both spin-flipping and spin-conserving

tunneling, as well as additional quantum dot levels, to be present in our device. Note that within this model, the energy E_0 in Eq. (7.1) may have either sign depending on the relative strength of the two terms. While both situations may occur at different gate settings in the same device, the tuning procedure to find a doublet ground state relies on the detection of a π-shift (see Chapter 6). Thus, our experiment naturally selects the case $E_0 > 0$, justifying the sign choice in Eq. (7.1).

To resolve the predicted spin-splitting we follow the method introduced in Chapter 6 and incorporate the quantum dot junction into the superconducting quantum interference device (SQUID) of a transmon circuit [Fig. 7.1(d)] (Koch et al., 2007). The different potential energies corresponding to the states $|0\rangle$, $|\downarrow\rangle$, or $|\uparrow\rangle$ give rise to distinct transition frequencies of the transmon circuit [Fig. 7.1(e)], which can be detected and distinguished via standard circuit quantum electrodynamics techniques (Blais et al., 2004, 2021). We refer to the Supplementary Materials for further details on the device implementation (Sec. 7.7.2).

7.3. TRANSMON BASED SPIN SPECTROSCOPY

To study the system in the regime of interest, we tune the quantum dot junction to a spin-1/2 ground state, as detailed in Sec. 7.7, where we refer to this setpoint as gate setpoint A[1]. This is followed by a two-tone spectroscopy measurement for which we apply both tones through the feedline and detect the transmon transition frequency as a function of the applied flux Φ_{ext}. The flux is tuned with a small in-plane external magnetic field applied perpendicular to the wire (Wesdorp et al., 2022), requiring a 1.8 mT field for adding one flux quantum through the SQUID. We note that, since the reference junction is tuned to have a Josephson energy $E_J/h = 12.5$ GHz, much higher than that of the quantum dot junction, the phase difference across the latter is well approximated by $\phi_{\text{ext}} = 2e\Phi_{\text{ext}}/\hbar$.

In Fig. 7.2(a), we show the typical flux dispersion observed in two-tone spectroscopy when the gate voltages are such that the ground state is a singlet, with the maximum frequency occurring at $\phi_{\text{ext}} = 0$. In fact, this measurement serves as a calibration of the applied flux, which is assumed to be an integer multiple of the flux quantum when the transmon frequency is maximal. In contrast, when the ground state is electrostatically set to be a doublet, the transition spectrum displays two shifted frequency branches, with maxima at $\phi_{\text{ext}} = \phi_0 \neq 0, \pi$ [Fig. 7.2(b)]. The measured spectrum is in good agreement with that predicted by a transmon circuit model with the potential energy of Eq. (7.1), with $E_0/h = 190$ MHz and $E_{\text{SO}}/h = 300$ MHz. The latter corresponds to a temperature scale of 14 mK, indicating that transmon-based spectroscopy can experimentally resolve the spin-orbit splitting of the doublet state well below the thermal broadening that typically limits tunneling spectroscopy experiments. Furthermore, the simultaneous observation of both transmon branches is indicative of a large thermal occupation of the excited spin state, which prevents the splitting from being observable in switching current measurements as the two contributions to the current cancel out.

We note that tuning the junction to a spin-1/2 ground state is not a sufficient condi-

[1] Precise gate voltage values for different gate configurations are reported in the Supplementary Materials of Sec. 7.7.

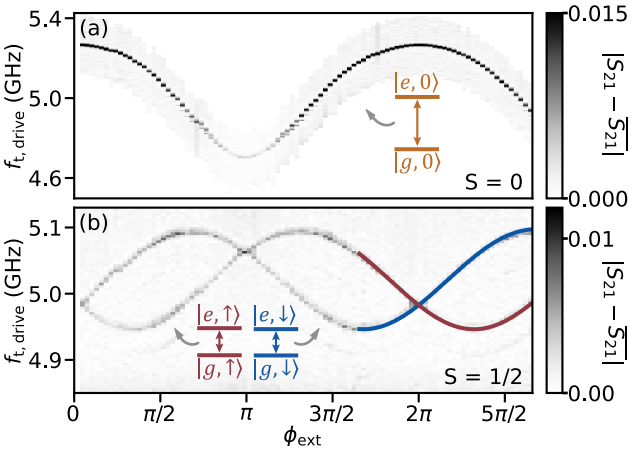

Figure 7.2: Comparison of singlet and spin-split doublet ground states in transmon two-tone spectroscopy. (a) Transmitted microwave signal versus external flux, ϕ_{ext}, and transmon drive frequency $f_{t,drive}$ for the quantum dot junction in the singlet state. (b) Same as (a) for the doublet state, at gate setpoint A, revealing the spin-splitting of the doublet state. The two ground states occur for two different gate voltage settings, as detailed in Chapter 6 and Sec. 7.7. Solid lines show fits to a transmon circuit model containing Eq. (7.1).

tion to observe the spin-splitting in the transition spectrum. By tuning the quantum dot to different resonances, corresponding to a quasi-particle trapped to different levels of the quantum dot, we frequently find instances of doublets without the predicted splitting, such as the one studied in detail in Chapter 6. There are also doublet states that show a small, MHz-size spin-splitting comparable to the transmon linewidth, as well as doublet states with larger splittings than shown in Fig. 7.2(b). This range of behaviours is shown in the Supplementary Materials . We attribute this variability to mesoscopic fluctuations (Padurariu and Nazarov, 2010), due to factors outside of our experimental control, such as disorder and confinement effects on the quantum dot wave functions.

7.4. MAGNETIC FIELD DEPENDENCE

The transition spectrum is affected by magnetic field through the Zeeman interaction and depends sensitively on the field direction with respect to the spin-orbit direction $\vec{n}$. This is shown in Fig. 7.3, which shows the behaviour for two limiting cases: $B_\parallel$, the direction along $\vec{n}$, and $B_\perp$, the direction perpendicular to $\vec{n}$ and in the chip plane. The evolution for intermediate directions and the procedure used to infer $\vec{n}$ are discussed in Supplementary Materials. The flux dispersion of the transition frequencies is only weakly affected by increasing $B_\parallel$[2]. Moreover, one of the two spin branches gradually disappears [Fig. 7.3(a)] until at $B_\parallel \gtrsim 23$ mT only a single spectroscopic line remains visible [Fig. 7.3(b)]. In this regime, the minimum transmon transition frequency of the single-valued dispersion is shifted by ϕ_0 away from $\phi_{ext} = 0$. This is a consequence of a ϕ_0-shift of the maximum of the energy-phase relation away from $\phi = 0$, as the trans-

[2]We attribute the field-dependent change in flux dispersion to the renormalization of the impurity g-factor by coupling to the leads, known as the impurity Knight shift (Pavešić et al., 2023b).

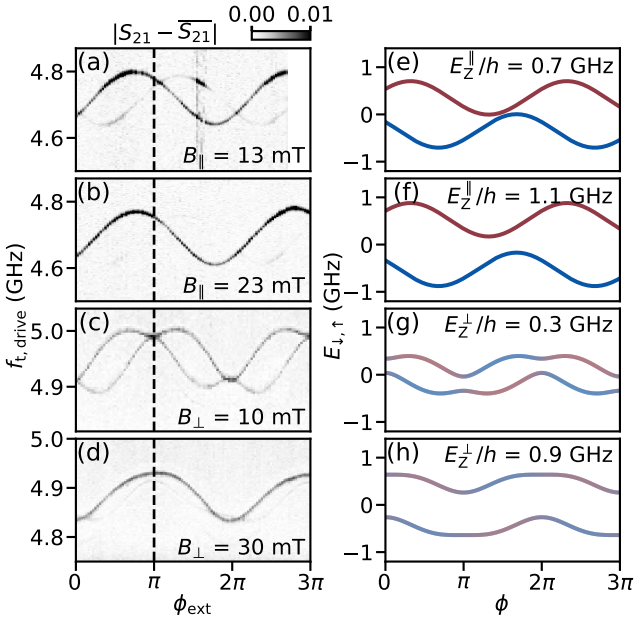

Figure 7.3: Magnetic field dependence of the doublet states for gate setpoint A. (a-d) Transmon spectroscopy versus ϕ_{ext} for a magnetic field applied either parallel (a,b) or perpendicular (c,d) to the inferred spin-orbit direction $\vec{n}$. The vertical dashed lines indicate $\phi_{ext} = \pi$. (e-f) Numerically calculated ϕ-dependence of the Josephson potential for the two doublet states, obtained by diagonalizing the model in Eq. (7.1), in the presence of parallel (e-f) and perpendicular (g-h) Zeeman field. Blue and red colors denote $|\downarrow\rangle$ and $|\uparrow\rangle$ spin polarization, respectively, with a blend of the two indicating mixing of the states. Panels (e-h) are not fits to the data of (a-d). Instead, together with the contribution from the reference junction, constitute the potentials that determine the transmon energy levels and serve to build a qualitative understanding (see text).

mon transition frequency is given by the Josephson inductance, the second derivative of the energy-phase relationship. This observation therefore demonstrates the presence of the anomalous Josephson effect (Brunetti et al., 2013; Sharov and Zaikin, 2005; Szombati et al., 2016; Yokoyama et al., 2014; Zazunov et al., 2009). In contrast, increasing the magnetic field along the $B_\perp$ direction appears to couple the two spectroscopic lines, leading to branches with two minima per flux period [Fig. 7.3(c)]. At even higher fields this behaviour is lifted, and once-more only one of the two transmon branches persists [Fig. 7.3(d)]. In this case, however, the ϕ_0-offset has strongly decreased.

The observed behaviour can be qualitatively understood from Eq. (7.1) by considering the cases in which the Zeeman field is respectively parallel or perpendicular to the spin-orbit direction. A parallel field $E_Z^\parallel$ separates the doublet potentials in energy without distorting their phase dependence [Fig. 7.3(e-f)]. As the energy separation increases, the thermal population of the higher-energy state decreases and, with it, so does the visibility of the corresponding transmon frequency branch. As the transmon frequency is insensitive to overall shifts in the energy-phase relation, it remains largely unaffected by the ϕ-independent field-induced energy shift. A Zeeman term $E_Z^\perp$ perpendicular to the spin-orbit direction instead couples the two states and opens up an

avoided crossing in the Josephson potential [Fig. 7.3(g)]. This results in the peculiar flux dependence seen in spectroscopy for moderate fields [Fig. 7.3(c)]. Finally, when $E_Z^{\perp}$ becomes much larger than E_{SO}, the doublet states instead polarize along the applied field direction [Fig. 7.3(h)], suppressing the ϕ_0-offset (Szombati et al., 2016; Zazunov et al., 2009).

We note that, at this gate setpoint, the $\vec{n}$ direction does not appear to be directly related to the orientation of the nanowire, as it points 13 degrees away from the nanowire axis. Moreover, this direction is found to be unique to each region in gate space, as discussed in the Supplementary Materials. This behavior differs from that of long single-gated semiconducting Josephson junctions, where the $\vec{n}$ direction is perpendicular to the nanowire axis (Strambini et al., 2020; Tosi et al., 2018). We attribute this variability to mesoscopic fluctuations of the junction wavefunctions and of the direction of the electrostatic field when the gate setpoint is changed (Han et al., 2023).

7.5. DIRECT DRIVING OF SPIN FLIP TRANSITIONS

In order to use the doublet states as a superconducting spin qubit (Chtchelkatchev and Nazarov, 2003; Padurariu and Nazarov, 2010), the ability to drive transitions between the doublet states is crucial. Encouragingly, a recent work by our group indicates that spin-flip transitions of ABS are possible in the presence of an external magnetic field (Wesdorp et al., 2022). Further motivated by all-electrical microwave excitation of spins in quantum dots via EDSR (Nadj-Perge et al., 2010; Nowack et al., 2007), we apply a microwave tone directly to the central gate to excite the doublet states. For this, we tune the transmon frequency close to the resonator frequency, enhancing its dispersive shift. In addition, we tune away from the gate setpoint investigated so far (gate setpoint A) to a parameter regime with a larger spin-splitting $E_{SO}/h = 560\,\text{MHz}$ (gate setpoint B) to maximize the visibility of the doublet splitting (See Supplementary Materials).

Applying a microwave drive to the central gate electrode, we find that a low-frequency transition of up to 1 GHz can be detected for a vanishing applied magnetic field[3], as also shown by Metzger et al. (2021) [Fig. 7.4(a)]. Its poor visibility is potentially due to the lack of magnetic field, which reduces the efficacy of EDSR (Flindt et al., 2006; Golovach et al., 2006), as well as to the large thermal population of the excited state, which reduces the achievable change in dispersive shift. This large thermal population can be expected from the fact that the spin-flip transition energy corresponds to an effective temperature range of 0 to 50 mK, below the typical electron temperatures found in transport and transmon (Jin et al., 2015) experiments, 35 mK to 100 mK. At elevated $B_{\parallel}$ the transition frequency rises and becomes well-resolved [Fig. 7.4(b)]. For an applied perpendicular field the transition frequency increases more slowly, and its flux periodicity is half that of the transition in the parallel field direction [Fig. 7.4(c)]. Note that the $\vec{n}$ direction found for gate setpoint B (72 degrees away from the nanowire axis) differs from that of gate setpoint A, and that therefore $B_{\parallel}$ and $B_{\perp}$ in Fig. 7.4 point in different directions than in Fig. 7.3.

The observed behaviour is consistent with the expected transitions between the dou-

[3] The tuning of the external flux requires a small magnetic field, which for the data in Fig. 7.4(a) ranges from −1.5 mT to 0.7 mT.

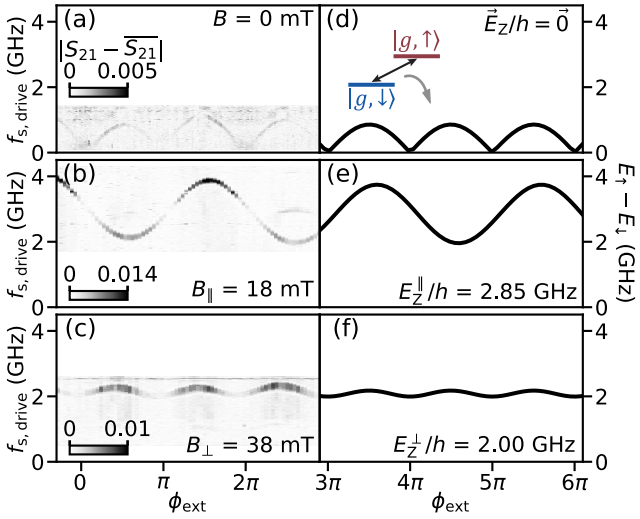

Figure 7.4: Direct spin-flip spectroscopy for gate setpoint B. (a-c) Measured flux dependence of the direct $|g,\downarrow\rangle \leftrightarrow |g,\uparrow\rangle$ transition frequency for no (a), parallel (b), and perpendicular (c) magnetic field relative to $\vec{n}$. (d-f) Numerically calculated flux dependence of the $|g,\downarrow\rangle \leftrightarrow |g,\uparrow\rangle$ transition frequency for no (d), parallel (e), and perpendicular (f) Zeeman fields relative to $\vec{n}$.

blet states [Fig. 7.4(d-f)], with the period-halving in perpendicular field being a result of the avoided crossings between the spin branches [c.f. Fig. 7.3(g)]. The comparison to the model furthermore allows us to estimate the effective Landé g-factors in the parallel and perpendicular directions, $g_\parallel = 11$ and $g_\perp = 3.8$ respectively. We note that the value and the anisotropy of the g-factor depend strongly on the gate voltages (see Supplementar Materials), likely tied to an interplay of spin-orbit coupling and confinement, beyond the scope of the model considered here (Csonka et al., 2008; Kiselev et al., 1998; Schroer et al., 2011; Winkler et al., 2017).

7.6. CONCLUSIONS

To conclude, our microwave measurements have revealed the rich spin structure of energy levels in a quantum dot Josephson junction and the occurrence of the anomalous Josephson effect. These findings are promising for applications in superconducting spintronics (Linder and Robinson, 2015; Shukrinov, 2022). The ability to directly drive spin-flip transitions between the doublet states has strong implications for the nascent field of Andreev spin qubits (Chtchelkatchev and Nazarov, 2003; Padurariu and Nazarov, 2010), since so far their coherent manipulation relied on fine-tuned Raman transitions through auxiliary levels (Cerrillo et al., 2021; Hays et al., 2021). Having direct, all-electrical access to these transitions promises simpler and faster qubit manipulation (Nadj-Perge et al., 2010; van den Berg et al., 2013). Furthermore, the polarization of the doublet states at elevated magnetic fields eliminates the unwanted excited state population observed in previous investigations (Hays et al., 2020, 2021). Finally, the demonstrated tunability of the transition frequency, enabled by both flux and magnetic field, is

a necessary ingredient for scalable networks of such qubits (Spethmann et al., 2022).

7.7. SUPPLEMENTARY INFORMATION

7.7.1. THEORY

To solidify our understanding of the results and of the mechanisms that govern the size of the spin splitting, we set up a minimal model that is able to reproduce the qualitative features observed experimentally. Our starting point is an extension of the single-impurity Anderson model (SIAM) for a quantum dot (QD) attached to two superconducting leads (Meden, 2019), see Fig. 7.5. Compared to the standard SIAM, our model also contains spin-flip tunneling between the impurity and the leads due to the presence of spin-orbit coupling, as well as an additional direct tunneling term between the leads. The non-interacting part of the Hamiltonian is

$$\begin{aligned} H_0 = &\sum_{\sigma} \epsilon d_\sigma^\dagger d_\sigma + E_x S_x + E_y S_y + E_z S_z \\ &+ \sum_{i,k\sigma} \epsilon_k c_{i,k\sigma}^\dagger c_{i,k\sigma} + \sum_{i,k} \Delta_i \left(e^{i\phi_i} c_{i,k\uparrow}^\dagger c_{i,k\downarrow}^\dagger + \text{H.c.} \right) \\ &+ \sum_{i,k\sigma} \left(V_{i,k} c_{i,k\sigma}^\dagger d_\sigma + \text{H.c.} \right) + \sum_{i,k\sigma} \left(i W_{i,k} c_{i,k\sigma}^\dagger d_{\bar{\sigma}} + \text{H.c.} \right) \\ &+ \sum_{k,k',\sigma} \left(t c_{\text{L},k\sigma}^\dagger c_{\text{R},k'\sigma} + \text{H.c.} \right). \end{aligned} \tag{7.2}$$

The first line describes the QD level ϵ closest to the Fermi level (the "resonant" level), subject to an external magnetic field $\vec{E}_Z$ with the components E_x, E_y and E_z expressed in units of energy (i.e., as Zeeman energy contributions). The operator $d_\sigma^\dagger$ is the creation operator for an electron in the resonant level, and S_x, S_y, S_z are impurity spin operators. The second line describes two superconductors with the dispersion relation ϵ_k and order parameters $\Delta_i \exp(i\phi_i)$. The operator $c_{i,k\sigma}^\dagger$ is the creation operator for an electron in the left (i = L) or right (i = R) superconductor, in level k and with spin σ. The third line describes the QD-superconductor hybridisation; we include both spin-preserving and spin-flipping processes with amplitudes $V_{i,k}$ and $W_{i,k}$, respectively. The notation $\bar{\sigma}$ denotes spin inversion, $\bar{\uparrow} = \downarrow$, $\bar{\downarrow} = \uparrow$. Alternatively, we may characterize the tunnel barriers via tunneling rates $\Gamma_\text{L} = \pi\rho|V_{\text{L},k_F}|^2$ or $\Gamma_\text{R} = \pi\rho|V_{\text{R},k_F}|^2$ for spin-preserving processes, and $\gamma_\text{L} = \pi\rho|W_{\text{L},k_F}|^2$ or $\gamma_\text{R} = \pi\rho|W_{\text{R},k_F}|^2$ for spin-flip tunneling. Here ρ is the normal-state density of states and we took the matrix elements at the Fermi level, hence at $k = k_F$. Finally, the last line accounts for the presence of all other ("non-resonant") levels in the QD: the electron can also cotunnel through the QD via those high-lying levels, which provides another conduction pathway through the dot. Formally, we may consider this term to arise from integrating out all other levels in the QD, so that

$$t = \sum_{l,k,k'} \frac{V_{\text{L},k;l}^* V_{\text{R},k';l}}{\Delta\epsilon_l}, \tag{7.3}$$

where we sum over all "non-resonant" levels, $V_{\text{L/R},k;l}$ are the corresponding tunneling amplitude, while $\Delta\epsilon_l$ are the energy levels. (For simplicity, we are disregarding interactions and spin-flip processes.) The inter-lead hopping term makes the model resemble

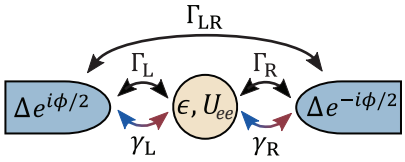

Figure 7.5: Model diagram of the quantum dot junction. Two *s*-wave superconductors are connected via tunnelling rates to a single level quantum dot. $\Gamma_{L,R}$ and $\gamma_{L,R}$ denote, respectively, the spin-conserving and spin-flipping tunneling rates between the superconducting leads and quantum dot. Γ_{LR} denotes a spin-conserving effective tunneling rate between the superconducting leads via all remaining energy levels, with $\Gamma_{LR} = \pi\rho|t|^2$.

those for a QD embedded in a nanoscopic Aharonov-Bohm ring (Karrasch and Meden, 2009). The model breaks down if the level spacing is too small (less than the scale of $\Gamma_{L/R}$): in that case one should use a multi-orbital Anderson impurity model instead.

In addition to this last term, we could also include the spin-flip tunneling through high-lying levels, however this brings about no new qualitative effect. As we will show, for what follows, the important element is that the ratio of spin-flip to spin-preserving tunneling rate is different for the resonant level and for the aggregate tunneling rate through all remaining non-resonant levels. This generic situation is expected to hold in most circumstances due to mesoscopic variability of tunneling matrix elements for different QD levels. The hopping elements, $V_{i,k}$, $W_{i,k}$ and t, are in general complex-valued ("directional"): if we reverse the electron flow direction, the amplitude needs to be complex conjugated.

The interacting part of the Hamiltonian is standard:

$$H_{\text{int}} = U_{ee} n_\uparrow n_\downarrow, \tag{7.4}$$

where U_{ee} is the electron-electron repulsion on the QD and $n_\sigma = d_\sigma^\dagger d_\sigma$ is the occupancy operator.

The model is analytically tractable in the regime $\Delta_L, \Delta_R \gg U_{ee}$ (the "superconducting atomic limit"(Affleck et al., 2000; Karrasch et al., 2008; Meng et al., 2009; Oguri et al., 2004; Rozhkov and Arovas, 2000; Tanaka et al., 2007; Vecino et al., 2003)) and in the regime $\Gamma_L, \Gamma_R \ll U_{ee}$ (the perturbative limit). We find that it is particularly instructive to integrate out the superconducting electrons and compute the hybridization matrix for this Hamiltonian. This leads to relatively simple closed-form expressions that can be used to construct a highly simplified model. Such a model nevertheless seems to be sufficient to account for the full range of the observed behaviors. The analytic calculations may be verified with explicit calculations using the numerical renormalization group (NRG) techniques, probing their validity over a wide range of parameters.

ANALYTICS

We work in the 4 × 4 Nambu representation with

$$d_a^\dagger = \begin{pmatrix} d_\uparrow^\dagger & d_\downarrow & d_\downarrow^\dagger & d_\uparrow \end{pmatrix}. \tag{7.5}$$

Similar notation is used for the c_k operators in the superconducting leads. We will use indexes from the beginning of the alphabet, $a, b, \ldots$, to denote the Nambu-space index

1,2,3,4. We define the Green's function (GF) matrices $G_{ab}(z) = \langle\langle d_a; d_b^\dagger\rangle\rangle_z$ and $F_{ab,ik}(z) = \langle\langle d_a; c_{ik,b}^\dagger\rangle\rangle_z$; here $\langle\langle A;B\rangle\rangle_z$ denotes the Laplace transform of the Green's function, $\langle\langle A;B\rangle\rangle_z = \int_0^\infty e^{izt}\langle\langle A;B\rangle\rangle_t \mathrm{d}t$, where $\langle\langle A;B\rangle\rangle_t = -i\Theta(t)\langle\{A(t),B(0)\}\rangle$ is the retarded GF. In this notation, the equations of motion (EOMs) take the form $z\langle\langle A;B\rangle\rangle_z = \langle\{A,B\}\rangle + \langle\langle A;[H,B]\rangle\rangle_z$. The EOM for the QD take the form

$$z\mathbf{G}(z) = \mathscr{I} + \mathbf{G}(z)\mathbf{H}_0 + \sum_{i,k}\mathbf{F}_{ik}(z)\mathbf{V}_{ik} + \mathbf{U}(z). \tag{7.6}$$

Here the argument $z = \omega + i\delta$ is complex frequency, $\mathscr{I}$ is the identity matrix, $\mathbf{H}_0$ corresponds to the Nambu matrix representation of the non-interacting part of the impurity Hamiltonian:

$$\mathbf{H}_0 = \begin{pmatrix} \epsilon + E_z/2 & 0 & (E_x - iE_y)/2 & 0 \\ 0 & -\epsilon + E_z/2 & 0 & -(E_x - iE_y)/2 \\ (E_x + iE_y)/2 & 0 & \epsilon - E_z/2 & 0 \\ 0 & -(E_x + iE_y)/2 & 0 & -\epsilon - E_z/2 \end{pmatrix}, \tag{7.7}$$

$\mathbf{V}_{ik}$ contains the hopping matrix elements:

$$\mathbf{V}_{ik} = \begin{pmatrix} V_{i,k} & 0 & iW_{i,k} & 0 \\ 0 & -V_{i,k}^* & 0 & iW_{i,k}^* \\ iW_{i,k} & 0 & V_{i,k} & 0 \\ 0 & iW_{i,k}^* & 0 & -V_{i,k}^* \end{pmatrix}, \tag{7.8}$$

and $\mathbf{U}(z)$ contains the contributions of the interacting part of the Hamiltonian, H_{int}. The EOMs for mixed GFs F_{ik} (dropping the frequency argument z in GFs for clarity) may be written as

$$\begin{aligned} \mathbf{F}_{\mathrm{L}k}[z\mathscr{I} - \mathbf{H}_{\mathrm{L}k}] &= \mathbf{G}\mathbf{V}_{\mathrm{L}k}^\dagger + \mathscr{F}_{\mathrm{R}}\mathbf{T}^*, \\ \mathbf{F}_{\mathrm{R}k}[z\mathscr{I} - \mathbf{H}_{\mathrm{R}k}] &= \mathbf{G}\mathbf{V}_{\mathrm{L}k}^\dagger + \mathscr{F}_{\mathrm{L}}\mathbf{T}, \end{aligned} \tag{7.9}$$

with

$$\mathbf{H}_{ik} = \begin{pmatrix} \epsilon_k & e^{+i\phi_i}\Delta_i & 0 & 0 \\ e^{-i\phi_i}\Delta_i & -\epsilon_k & 0 & 0 \\ 0 & 0 & \epsilon_k & -e^{i\phi_1}\Delta_1 \\ 0 & 0 & -e^{-i\phi_1}\Delta_1 & -\epsilon_k \end{pmatrix}, \tag{7.10}$$

$$\mathbf{T} = \begin{pmatrix} t & 0 & 0 & 0 \\ 0 & -t^* & 0 & 0 \\ 0 & 0 & t & 0 \\ 0 & 0 & 0 & -t^* \end{pmatrix}, \tag{7.11}$$

and

$$\mathscr{F}_i = \sum_k \mathbf{F}_{ik}. \tag{7.12}$$

Using the lead propagator $\mathbf{G}_{ik} = [z\mathscr{I} - \mathbf{H}_{ik}]^{-1}$, this may be rewritten as

$$\begin{aligned} \mathbf{F}_{\mathrm{L}k} &= \mathbf{G}\mathbf{V}_{\mathrm{L}k}^\dagger\mathbf{G}_{\mathrm{L}k} + \mathscr{F}_{\mathrm{R}}\mathbf{T}^*\mathbf{G}_{\mathrm{L}k}, \\ \mathbf{F}_{\mathrm{R}k} &= \mathbf{G}\mathbf{V}_{\mathrm{R}k}^\dagger\mathbf{G}_{\mathrm{R}k} + \mathscr{F}_{\mathrm{L}}\mathbf{T}\mathbf{G}_{\mathrm{R}k}. \end{aligned} \tag{7.13}$$

We now assume that V_{ik} and W_{ik} do not depend on k, i.e., $V_{ik} \equiv V_i$ and $W_{ik} \equiv W_i$; this is a reasonable approximation for the relevant bath levels in the vicinity of the Fermi level. We define $\mathbf{G}_i = \sum_k \mathbf{G}_{ik}$ and we sum the EOMs over k:

$$\begin{aligned} \mathscr{F}_{\mathrm{L}} &= \mathbf{G}\mathbf{V}_{\mathrm{L}}^{\dagger}\mathbf{G}_{\mathrm{L}} + \mathscr{F}_{\mathrm{R}}\mathbf{T}^{*}\mathbf{G}_{\mathrm{L}}, \\ \mathscr{F}_{\mathrm{R}} &= \mathbf{G}\mathbf{V}_{\mathrm{R}}^{\dagger}\mathbf{G}_{\mathrm{R}} + \mathscr{F}_{\mathrm{L}}\mathbf{T}\mathbf{G}_{\mathrm{R}}. \end{aligned} \tag{7.14}$$

or

$$\begin{pmatrix} \mathscr{F}_{\mathrm{L}} & \mathscr{F}_{\mathrm{R}} \end{pmatrix} \begin{pmatrix} \mathscr{I} & -\mathbf{T}\mathbf{G}_{\mathrm{R}} \\ -\mathbf{T}^{*}\mathbf{G}_{\mathrm{L}} & \mathscr{I} \end{pmatrix} = \mathbf{G} \begin{pmatrix} \mathbf{V}_{\mathrm{L}}^{\dagger}\mathbf{G}_{\mathrm{L}} & \mathbf{V}_{\mathrm{R}}^{\dagger}\mathbf{G}_{\mathrm{R}} \end{pmatrix}. \tag{7.15}$$

The important observation here is that $\mathscr{F}_i$ are proportional to $\mathbf{G}$. This means that the third term in the EOM Eq. (7.6) can be written as

$$\sum_{ik} \mathbf{F}_{ik}(z)\mathbf{V}_{ik} = \mathbf{G}(z)\mathbf{\Delta}(z), \tag{7.16}$$

where $\mathbf{\Delta}(z)$ is the hybridization matrix which describes the renormalization of the QD level due to electron excursions in the superconducting leads. Eq. (7.15) can be solved for each $\mathscr{F}_i$ individually, but the expressions are very lengthy and not very informative. Instead, we proceed with calculating the hybridization matrix $\mathbf{\Delta}(z) = [\mathbf{G}(z)]^{-1}\sum_i \mathscr{F}_i\mathbf{V}_i$. We furthermore assume that t is real and introduce the dimensionless quantity $\tilde{t} = \pi\rho t$. We also set $\phi_{\mathrm{L}} = \phi/2$ and $\phi_{\mathrm{R}} = -\phi/2$. Finally, we take the large-Δ limit of the lead propagator

$$\mathbf{G}_{ik} = \frac{1}{z^2 - (\Delta_i^2 + \epsilon_k^2)} \begin{pmatrix} z+\epsilon_k & e^{i\phi_1}\Delta_i & 0 & 0 \\ e^{-i\phi_i}\Delta_i & z-\epsilon_k & 0 & 0 \\ 0 & 0 & z+\epsilon_k & -e^{i\phi_i}\Delta_i \\ 0 & 0 & -e^{-i\phi_i}\Delta_i & z-\epsilon_k \end{pmatrix} \tag{7.17}$$

to obtain

$$\mathbf{G}_i = \sum_k \mathbf{G}_{ik} = -\pi\rho \begin{pmatrix} 0 & e^{i\phi_i} & 0 & 0 \\ e^{-i\phi_i} & 0 & 0 & 0 \\ 0 & 0 & 0 & -e^{i\phi_i} \\ 0 & 0 & -e^{-i\phi_i} & 0 \end{pmatrix}. \tag{7.18}$$

With these assumptions and simplifications in place, the hybridisation matrix can be written as

$$\mathbf{\Delta}(z) = \frac{\pi\rho}{1 + 2\tilde{t}^2\cos\phi + \tilde{t}^4} \begin{pmatrix} -2a & b & -2c & 0 \\ b^* & 2a & 0 & 2c \\ -2c & 0 & -2a & -b \\ 0 & 2c & -b^* & 2a \end{pmatrix}, \tag{7.19}$$

where we introduced the following notation

$$\begin{aligned} a &= (V_{\mathrm{L}}V_{\mathrm{R}} + W_{\mathrm{L}}W_{\mathrm{R}})\tilde{t}(\tilde{t}^2 + \cos\phi), \\ b_i &= V_i^2 + W_i^2, \\ b &= e^{-i\phi/2}(b_{\mathrm{R}} + \tilde{t}^2 b_{\mathrm{L}}) + e^{+i\phi/2}(b_{\mathrm{L}} + b_{\mathrm{R}}\tilde{t}^2), \\ c &= (V_{\mathrm{R}}W_{\mathrm{L}} - V_{\mathrm{L}}W_{\mathrm{R}})\tilde{t}\sin\phi. \end{aligned} \tag{7.20}$$

The key feature of this expression is that this matrix includes terms in the out-of-diagonal 2×2 blocks. These correspond to the presence of an effective magnetic field in the x direction that induces the spin polarization along this same direction. The particular direction (x) results from the assumed form of the spin-orbit-coupling terms in Eq. (7.2) and from assuming real $V_{\mathrm{L,R}}$, $W_{\mathrm{L,R}}$ and t. In terms of second quantization operators, the hybridisation matrix corresponds to the following form:

$$\Delta_{\mathrm{hyb}} = \frac{\pi\rho}{1+2\tilde{t}^2\cos\phi+\tilde{t}^4}\left(-2a\sum_\sigma d_\sigma^\dagger d_\sigma - 4cS_x + b d_\uparrow^\dagger d_\downarrow^\dagger + b^* d_\downarrow d_\uparrow + \mathrm{const.}\right). \tag{7.21}$$

Not all terms contribute in both spin sectors. The pairing terms proportional to b are only relevant in the spin-singlet sector, while the effective spin-splitting terms proportional to c are only relevant in the spin-doublet sector. The potential term proportional to a contributes in both subspaces. Since we are interested only in the $S=1/2$ subspace, in the following we concentrate on this particular 2×2 subspace. We find that the effective Hamiltonian of the doublet sector in the $\uparrow,\downarrow$-basis is given by

$$H_{\mathrm{eff}} = \begin{pmatrix} \epsilon+E_z/2 & \left(E_x-iE_y\right)/2 \\ \left(E_x+iE_y\right)/2 & \epsilon-E_z/2 \end{pmatrix} - \frac{2\pi\rho}{1+2\tilde{t}^2\cos\phi+\tilde{t}^4}\begin{pmatrix} a & c \\ c & a \end{pmatrix}. \tag{7.22}$$

This model is exact in the double limit $U_{ee}\to 0$, $\Delta_{\mathrm{L,R}}\to\infty$. In general, one expects correction factors to parameters that depend on both $\Delta_{\mathrm{L,R}}$ and U_{ee}, which control the energy cost of charge fluctuations from the doublet state. These corrections can be accurately computed using the NRG method. Nevertheless, the general form remains the same, as confirmed by numerical calculations, see below. Most importantly, the conditions for the matrix element c to be non-zero, as revealed in this calculation, hold fully generally, and are the following: a) the presence of additional QD levels (i.e., nonzero parameter t in the generalized SIAM), b) the presence of both spin-preserving and spin-flip tunneling (so that the combination $V_{\mathrm{R}}W_{\mathrm{L}}-V_{\mathrm{L}}W_{\mathrm{R}}$ is non-zero, which is expected to be generally true except in cases of accidental cancellation), c) finite phase bias ϕ.

We need to note that in the superconducting atomic limit the doublet state in the standard superconducting-SIAM model does not depend on the phase bias ϕ, as can be checked by taking the limit $W_{\mathrm{L,R}}\to 0$ and $t\to 0$ in Eq. (7.22). However, away from the superconducting atomic limit an additional diagonal term $E_D\cos(\phi)$ arises, with $E_D>0$. This term is generated by fourth-order processing in hopping (second order in hybridisation) and has a minimum at $\phi=\pi$ (Spivak and Kivelson, 1991), as typical for Josephson junctions with an odd-parity ground state.

Assuming $V_{\mathrm{L}}=V_{\mathrm{R}}\equiv V$, $W_{\mathrm{L}}=-W_{\mathrm{R}}\equiv W$ (note that this sign for W_i choice merely reflects the sign convention in the Hamiltonian and actually corresponds to the symmetric situation with the same amplitude for the left SC to QD and for the QD to right SC spin-flip tunneling), and defining

$$\Gamma_V=\pi\rho V^2,\quad \Gamma_W=\pi\rho W^2,$$

the second term of Eq. (7.22) can be written as

$$\frac{2\tilde{t}}{1+2\tilde{t}^2\cos\phi+\tilde{t}^4}\begin{pmatrix} (\Gamma_V-\Gamma_W)\left(\tilde{t}^2+\cos\phi\right) & 2\sqrt{\Gamma_V\Gamma_W}\sin\phi \\ 2\sqrt{\Gamma_V\Gamma_W}\sin\phi & (\Gamma_V-\Gamma_W)\left(\tilde{t}^2+\cos\phi\right)\end{pmatrix}. \tag{7.23}$$

Assuming that $\tilde{t} \ll 1$, we can simplify the model further by performing a series expansion to obtain

$$2\tilde{t}\begin{pmatrix}(\Gamma_V-\Gamma_W)\cos\phi & 2\sqrt{\Gamma_V\Gamma_W}\sin\phi\\ 2\sqrt{\Gamma_V\Gamma_W}\sin\phi & (\Gamma_V-\Gamma_W)\cos\phi\end{pmatrix}. \tag{7.24}$$

Defining

$$E_t = 2\tilde{t}\,(\Gamma_V-\Gamma_W), \quad E_{\mathrm{SO}} = 4\tilde{t}\sqrt{\Gamma_V\Gamma_W}, \tag{7.25}$$

we find the approximate small $\tilde{t}$ Hamiltonian given by (up to a constant):

$$H_{\mathrm{eff}} = \begin{pmatrix}E_z/2 & \left(E_x-iE_y\right)/2\\ \left(E_x+iE_y\right)/2 & -E_z/2\end{pmatrix} - \begin{pmatrix}E_t\cos\phi & E_{\mathrm{SO}}\sin\phi\\ E_{\mathrm{SO}}\sin\phi & E_t\cos\phi\end{pmatrix}. \tag{7.26}$$

This expression takes the form of the phenomenological potential for the transmon circuit given by main text Eq. (7.1). Given that there is a potential cancellation of the E_t term, it is prudent to include in the model an addition term of the form $E_D\cos(\phi)$ from processes that are higher-order in hybridisation. This term will combine with $-E_t\cos(\phi)$ to produce the $+E_0\cos(\phi)$ potential with $E_0 = E_D - E_t$ in Eq. (7.1). Note that E_0 can take either a positive or negative sign.

Within the limit considered here, we find that E_{SO} depends on each of the three types of coupling in the model: spin-conserving, spin-flipping, and direct lead-lead tunneling. All three have to be present for the spin-splitting to occur. Furthermore, it may happen that the cosine term drops out if the prefactors of all contributions add up to zero, resulting in a Josephson potential shifted by $\pi/2$ compared to the singlet state. This fine-tuned situation is indeed encountered in the experiment as discussed later in the Supplementary Materials.

It is instructive to evaluate the eigenvalues of the isolated quantum dot junction. In the simplified model of Eq. (7.1) these are given by

$$E_{\uparrow,\downarrow} = E_0\cos\phi \pm \frac{1}{2}\sqrt{E_y^2+E_z^2+\left(E_x-2E_{\mathrm{SO}}\sin\phi\right)^2}. \tag{7.27}$$

For $E_y = E_z = 0$, this simplifies to

$$E_{\uparrow,\downarrow} = E_0\cos\phi \pm \left(E_x/2 - E_{\mathrm{SO}}\sin\phi\right) \tag{7.28}$$

The Zeeman field parallel to E_{SO} enters as a constant offset, which does not change the curvature of the potential and does not affect the transmon frequency. Furthermore, this results in the spin-flip transition frequency given by

$$E_\uparrow - E_\downarrow = E_x - 2E_{\mathrm{SO}}\sin\phi \tag{7.29}$$

which is linear in the applied Zeeman field. Setting $E_x = E_y = 0$ instead, we find

$$E_{\uparrow,\downarrow} = E_0\cos\phi \pm \frac{1}{2}\sqrt{E_z^2+4E_{\mathrm{SO}}^2\sin^2\phi} \tag{7.30}$$

Here the E_z term does enter the curvature of the potential, thus affecting the transmon frequency. Furthermore, the resulting in the spin-flip qubit transition frequency is given by

$$E_\uparrow - E_\downarrow = \sqrt{E_z^2+4E_{\mathrm{SO}}^2\sin^2\phi} \tag{7.31}$$

The presence of the $\sin^2\phi$ term results in the doubling in periodicity we observe in the perpendicular field dependence of main text Fig. 7.4(c) compared to the parallel field dependence of Fig. 7.4(b).

NRG CALCULATIONS

The proposed model has very little symmetry: the spin-orbit coupling fully breaks the rotational SU(2) spin symmetry, and the BCS mean-field approximation breaks the U(1) charge conservation. The only remaining symmetry is Z_2 fermionic number parity (even or odd total number of electrons in the system). Furthermore, the Hamiltonian has complex-valued matrix elements. Nevertheless, the quantum impurity problem can still be solved using the conventional impurity solver, the numerical renormalization group (NRG), albeit at quite significant computational cost. The NRG method consists of discretizing the continua (two superconducting baths), their transformation into Wilson tight-binding chains, and an iterative diagonalization of the resulting chain/ladder Hamiltonian. We performed a very coarse discretization with the discretization parameter $\Lambda = 8$; nonetheless, for the purposes of computing energy splitting, this remains a surprisingly good approximation. We retain up to 3000 states in each NRG step. On 8 cores of an AMD EPYC 7452 processor, such NRG calculations take approximately 15 minutes for each parameter set. The band is assumed to have a constant density of states in the interval $[-D : D]$. In the following, all model parameters will be given in units of half-bandwidth D.

We first verify the findings from the analytics, specifically the spin splitting induced by the combination of the spin-flip scattering, the presence of multiple levels in the QD (represented by the interdot tunneling term t), and finite superconducting phase difference between the two SC contacts, as described by the $E_{\mathrm{SO}}\sin\phi$ terms in the effective Hamilotinian with $E_{\mathrm{SO}} = 4\tilde{t}\sqrt{\Gamma_V\Gamma_W} = 4\tilde{t}\Gamma_V\sqrt{\Gamma_W/\Gamma_V}$, see Eqs. (7.25) and (7.25). In Fig. 7.6 we plot the dependence of the splitting $E_\uparrow - E_\downarrow$ as a function of key parameters. We indeed observe that the splitting is linear in the hybridisation Γ for fixed Γ_W/Γ_V ratio, in the ratio $W/V = \sqrt{\Gamma_W/\Gamma_V}$ and in the hopping t. Finally, we also ascertain the $\sin(\phi)$ dependence of the splitting. We have thus confirmed that the splitting is linear in t, Γ, W/V, and ϕ for small parameter values.

The dependence on other model parameters, in particular U_{ee} and Δ, is not simple. The parameters U_{ee} and Δ control the energy cost of charge fluctuations, and the behavior depends not only on their ratio, but also on their values compared to the hybridisation Γ as well as the bandwidth D. The simplest case is the linear regime of small parameter Γ, where the splitting is simply inversely proportional to $1/(U_{ee}/2 + \Delta)$ to a good approximation, see Fig. 7.7(a). For larger Γ, we observe deviations from this simple form, see Fig. 7.7(b). It is also instructive to consider the dependence on Δ at fixed U_{ee}. The limit of small U_{ee} is merely of academic interest, because the doublet state is then a (highly) excited state: we find a roughly linear dependence on Δ, see Fig. 7.7(c). For large U_{ee}, however, we find a complex dependence that furthermore depends on the value of Γ, showing a cross-over from quadratic dependence for $\Delta \ll \Gamma$ to a roughly linear dependence for $\Delta \gtrsim \Gamma$, see Fig. 7.7(d). From these plots we conclude that the dependence on U_{ee}, Δ and Γ (when Γ is not small) is highly non-trivial and should in general be computed numerically (e.g. using the NRG method).

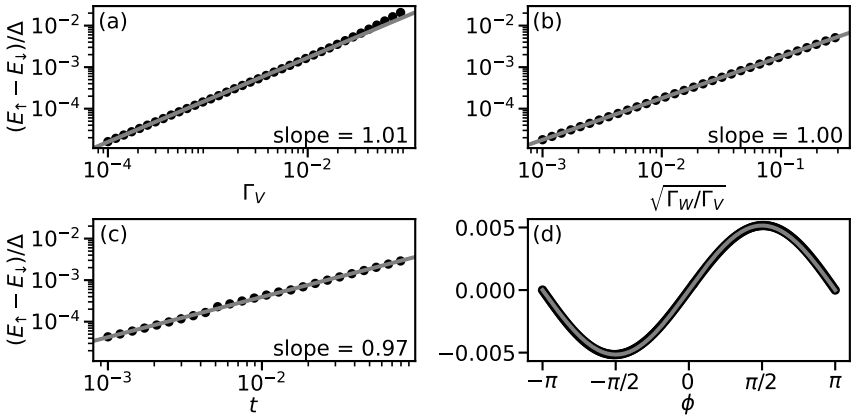

Figure 7.6: Scaling of the induced spin splitting in the doublet state with parameters Γ_V, Γ_W, and t, as well as the ϕ-dependence. Unless stated otherwise, the parameter set is $U_{ee} = 1$, $\epsilon = -U_{ee}/2$, $\Gamma_V = 0.02$, $\Gamma_W = \Gamma_V/5$, $t = 0.1$, $\Delta = 0.01$, $\phi = \pi/4$. (a) Γ_V-dependence, demonstrating the linearity of splitting as a function of the hybridisation strength, with small non-linear corrections for large Γ_V. (b) Γ_W/Γ_V-dependence, demonstrating the linearity of splitting as a function of the ratio of spin-flip over spin-preserving tunneling processes to the impurity orbital in resonance. (c) t-dependence, demonstrating the linearity of splitting as a function of cotunneling through non-resonant impurity levels. (d) ϕ-dependence, showing a very clean $\sin(\phi)$ behavior of the spin-splitting, as predicted by the reduced analytical model.

In Fig. 7.8 we explore the three contributions to the doublet potential: the conventional doublet $E_D\cos(\phi)$ potential with the minima at $\phi = \pm\pi$, the $E_{\mathrm{SO}}\sin(\phi)$ potential due to spin-flip scattering with minima at $\phi = \pm\pi/2$, as well as the $-E_t\cos(\phi)$ potential due to cotunneling though the multiple levels of the QD with minimum at $\phi = 0$, see Fig. 7.8. We plot the results for a range of t starting from zero; this case serves as a reference from which we extract the standard E_D part. With increasing t, both E_{SO} as well as E_t increase. This displaces the minima in the effective potential from $\phi = \pm\pi$ towards $\phi = \pm\pi/2$. When E_t becomes equal to E_D, the $\cos(\phi)$ part of the potential cancels out. For $E_t > E_D$, the minima move past $\phi = \pm\pi/2$ and tend toward $\phi = 0$.

A major time-saving procedure is to incorporate the effects of the external magnetic field as a perturbation to the results of an NRG calculation for a Hamiltonian without any field terms. This ploy rests on the observation that the impurity spin operators are exactly marginal (in the renormalization-group sense): their matrix elements remain of the same order of magnitude throughout the NRG iteration, i.e., they neither blow up nor decay to zero. The method may hence be dubbed the "marginal-operator trick". The idea is to perform the NRG iteration of spin operators S_x, S_y, S_z through unitary transformations to find the effective spin operators in the NRG eigenbasis in the low-energy sector. These are then added to the effective Hamiltonian with bare Zeeman energies E_x, E_y, E_z:

$$H_{\mathrm{eff}} = \sum_w E(w)\,|w\rangle\langle w| + E_x\tilde{S}_x + E_y\tilde{S}_y + E_z\tilde{S}_z. \tag{7.32}$$

Here w indexes the eigenstates $|w\rangle$ with eigenenergies $E(w)$, while $\tilde{S}_i$ are the trans-

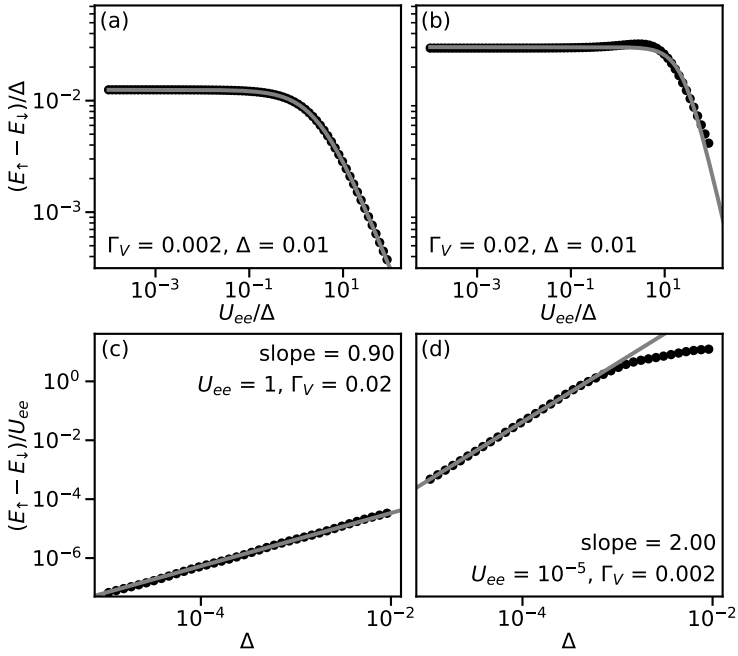

Figure 7.7: Scaling of the induced spin splitting in the doublet state with parameters U_{ee} and Δ. Other parameters as in Fig. 7.6. (a) U_{ee}-dependence at $\Gamma_V = 0.002$ showing the cross-over from the $U_{ee} \ll \Delta$ regime to the $U_{ee} \gg \Delta$ regime. (b) Same as a, but for stronger hybridisation $\Gamma_V = 0.02$, showing the more complex behavior away from the low-Γ_V limit. (c) Δ-dependence at $\Gamma_V = 0.02$, showing that the splitting is roughly proportional to Δ in the $U_{ee} \gg \Gamma, \Delta$ regime. (d) Same as (c), but for $\Gamma_V = 0.002$ and much smaller $U_{ee} = 10^{-5}$ (non-interacting limit), showing quadratic scaling for $\Delta \ll \Gamma$ that crosses over into linear scaling for $\Delta \gg \Gamma$.

7

formed spin matrices in this same basis. The basis can be truncated to a small number of levels; in many cases it is sufficient to retain solely the subgap states. This effective Hamiltonian may then be diagonalized at negligible numerical cost for arbitrary values of E_x, E_y and E_z. In case where only two (subgap) states are retained one can even write down closed-form expressions for eigenenergies and eigenstates. The marginal-operator trick is a good approximation up to Zeeman energies comparable to the BCS energy gap Δ, as it has been ascertained by comparisons with the NRG calculations with the Zeeman terms included from the outset, see Fig. 7.9. This method is clearly very generally applicable to any problem involving marginal operators in the Hamiltonian, obviating the need for costly parameter sweeps in multidimensional spaces.

TRANSMON DIAGONALIZATION

Having established how to calculate an effective potential in the doublet sector, we now turn to its inclusion in the Hamiltonian of the encompassing transmon circuit (Koch et al., 2007):

$$H = -4E_c\partial_\phi^2 + E_J(1-\cos\delta) + U(\phi), \tag{7.33}$$

where E_c and E_J denote the charging energy of the transmon island and the Josephson energy of the reference junction, respectively, and $U(\phi)$ denotes the effective doublet

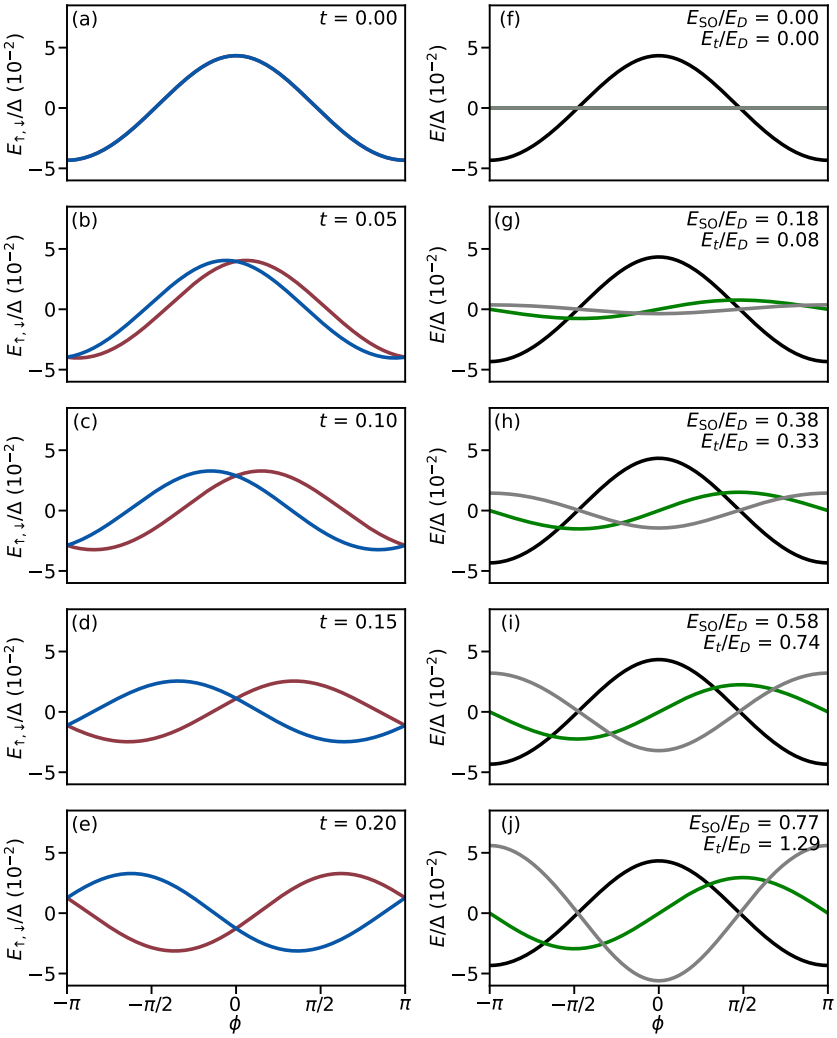

Figure 7.8: Decomposition of the doublet potential energy into its components. We show the results for various values of t, as indicated for each panel. All plots have the same axis ranges in order to permit direct comparison of magnitudes. (a-e) Total potential for the two spin states. (f-g) $E_D\cos(\phi)$ potential, common to all cases (black), $-E_t\cos(\phi)$ (green) and $E_{SO}\sin(\phi)$ (grey) contributions. We find $E_D = 4.33\,10^{-3}$ (same for all t) and the E_t/E_D and E_{SO}/E_D ratios indicated for each panel. Other model parameters are $U_{ee} = 1$, $\epsilon = -U_{ee}/2$, $\Delta = 0.1$, $\Gamma_V = 0.2$, $\Gamma_W/\Gamma_V = 1/5$.

potential of main text Eq. (7.1). The two phase drops across the quantum dot junction (ϕ) and across the reference junction (δ) are connected according to $\phi - \delta = \phi_{ext}$, where $\phi_{ext} = (2e/\hbar)\Phi_{ext}$ is the phase difference resulting from the externally applied magnetic flux through the SQUID loop, Φ_{ext} [Fig. 7.1(d)].

Following Refs. (Bargerbos et al., 2020; Kringhøj et al., 2020), we numerically diago-

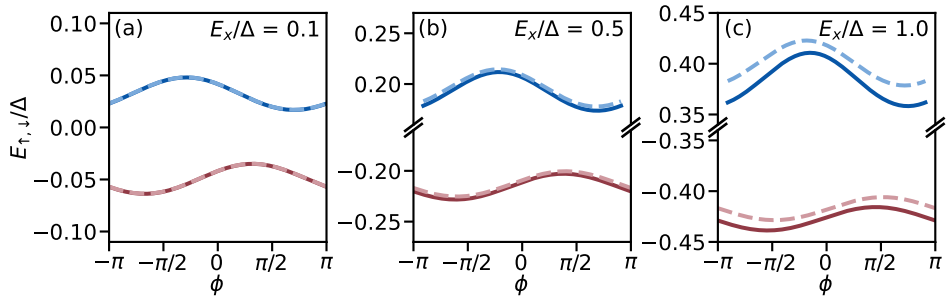

Figure 7.9: Comparison of the energies of the doublet subgap states as a function of the phase bias computed using the standard NRG procedure (solid lines) and using the "marginal-operator trick" approximation (discontinuous lines). Vertical scale is the same for all panels. Model parameters are $U_{ee} = 1.5$, $\Gamma_L = \Gamma_R \equiv \Gamma = 0.2$, $\gamma_L = \gamma_R = 0.2\Gamma$, $t = 0.1$, $\epsilon = 0.1 - U_{ee}/2$, $\Delta = 0.1$.

nalize Eq. 7.33 in the phase basis. This results in the energy levels E_n as well as the associated transition frequencies $f_{nm} = (E_m - E_n)/h$, capturing both the transmon and the spin-flip transitions. Having calculated the transition frequencies, fits can be made to the data. This is done to obtain the estimates for the effective model parameters found in the main text and in the next sections, using $E_c/h = 284\,\text{MHz}$ and $E_J/h = 12.4\,\text{GHz}$ to $12.7\,\text{GHz}$ as reference junction parameters. Note that the reference junction gate voltage is generally held fixed in the experiment, and that the range in E_J is the result of cross-coupling between the quantum dot and reference junction gate lines.

Here we note that the sinusoidal reference junction potential used in Eq. (7.33) is that of a conventional superconductor-insulator-superconductor (SIS) tunnel junction, governed by many weakly transparent channels. Previous work has found that nanowire-based Josephson junctions are more accurately described by several or even a single transport channel, leading to a more skewed potential shape (Kringhøj et al., 2018). This can result in a reduction of the the qubit anharmonicity, and thus an underestimation of E_c when using the SIS potential. However, the inclusion of a more involved potential introduces additional fitting parameters, and obtaining unique solutions is not guaranteed. This holds in particular because the reference junction is operated far from its pinchoff voltage, such that several channels are expected to contribute to the potential. We therefore choose to use the SIS potential throughout the Letter. In practice, this choice affects the value of E_c that is extracted from the fit, which in turn rescales the extracted values of E_0 and E_{SO}.

7.7.2. DEVICE AND EXPERIMENTAL SETUP

DEVICE OVERVIEW

The physical implementation of the device studied is shown in Fig. 6.2. It is analogous to that of Chapter 6, repeated here for convenience. The chip, 7 mm long and 2 mm wide, consists of four devices coupled to a single transmission line with an input capacitor to increase the directionality of the outgoing signal [Fig. 6.2(b)]. For the experiments performed in this Letter only two of the devices were wire-bonded: the device measured in the main text, and a second device, which was not functional.

For each device, a lumped element readout resonator is capacitively coupled to the feedline [Fig. 7.10(c)]. The resonator is additionally capacitively coupled to the transmon island, which is connected to ground via a SQUID loop formed by the reference and quantum dot junctions [Fig. 7.10(d)]. Both junctions are implemented on a single 10 um-long epitaxial superconductor-semiconductor nanowire with a 110 nm-wide hexagonal InAs core and a 6 nm-thick Al shell covering two of its facets, in turn covered by a thin layer of aluminium oxide. The growth conditions were almost identical to those detailed by Krogstrup et al. (2015), with the only two differences being that this time the As/In ratio is 12, smaller than in Krogstrup et al. (2015), and that the oxidation of the Al shell is now performed in-situ, for better control, reproducibility and homogeneity of the oxide layer covering the shell. Inspection of the nanowire batch, performed under a scanning electron microscope directly after growth, indicated an average wire length of $9.93\pm 0.92\,\mu$m and an average wire diameter of 111 ± 5 nm. For the device investigated here, the two facets of the aluminum shell are situated on the top part of the nanowire. The two junctions are defined in two uncovered nanowire sections (110 nm-long for the reference junction and 200 nm-long for the quantum dot junction). A zoom-in of the the quantum dot junction is shown in Fig. 7.10(e). The reference junction is controlled by a single 110 nm-wide electrostatic gate, set at a DC voltage V_J. The quantum dot junction is defined by three 40 nm-wide gates separated from each other by 40 nm. We note that in Fig. 7.1(e) the gates appear wider (and the gaps between gates appear smaller) than stated due to distortion by the gate dielectric layer. The outer two gates are set at DC voltages V_L and V_R. The central gate is connected to a bias-tee formed by a 100 kΩ resistor and a 100 pF capacitor. This permits the simultaneous application of a DC signal V_C to control the level of the quantum dot junction and a microwave tone $f_\mathrm{s,drive}$ to drive the spin-flip transition.

NANOFABRICATION DETAILS

The device fabrication occurs in several steps using standard nanofabrication techniques. It is identical to that described in Chapter 6, and repeated here for the sake of completeness. The substrate consists of 525 µm-thick high-resistivity silicon, covered in 100 nm of low pressure chemical vapor deposited Si_3N_4. On top of this, a 20 nm thick NbTiN film is sputtered, into which the gate electrodes and circuit elements are patterned using an electron-beam lithography mask and SF_6/O_2 reactive ion etching. Subsequently, 30 nm of Si_3N_4 dielectric is deposited on top of the gate electrodes using plasma enhanced chemical vapor deposition and then etched with a buffered oxide etchant. The nanowire is then deterministically placed on top of the dielectric using a nanomanipulator and an optical microscope. After placement, two sections of the aluminium shell

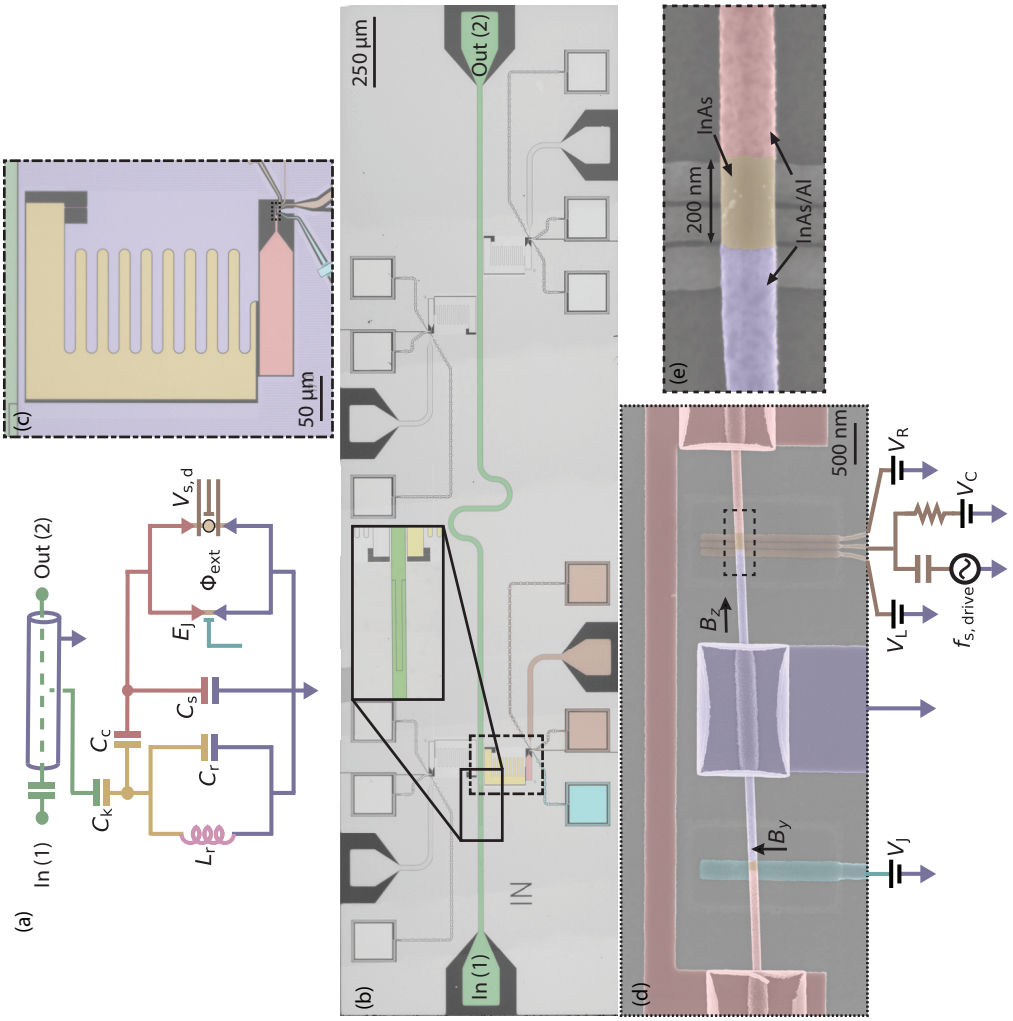

Figure 7.10: **Device overview.** (a) Diagram of the microwave circuit. A coplanar waveguide transmission line with an input capacitor (green center conductor) is capacitively coupled to a grounded LC resonator. The resonator consists of an island (yellow) capacitively and inductively (pink) shunted to ground (blue). The resonator is in turn capacitively coupled to a transmon island (red), which is shunted to ground capacitively as well as via two parallel Josephson junctions. (b) Chip containing four nearly identical devices coupled to the same transmission line, which has an input capacitor, enlarged in inset. (c) False-colored optical microscope image of the device showing the qubit island, the resonator island, the resonator inductor, the transmission line, the electrostatic gates and ground. (d) False-colored scanning electron micrograph (SEM) of the measured device, showing the InAs/Al nanowire into which the junctions are defined. The B_y component of the magnetic field is used to tune Φ_{ext} (Wesdorp et al., 2023). B_z is the magnetic field component parallel to the nanowire. (e) False-colored SEM of the measured device, showing the quantum dot junction in which the quantum dot is gate defined. The three bottom gates have a width and spacing of 40 nm, although this is obfuscated by the dielectric layer placed on top.

are selectively removed by wet etching with MF-321 developer. These sections form the quantum dot junction and the reference junction, with lengths 200 nm and 110 nm respectively. After the junction etch, the nanowire is contacted to the transmon island and to ground by an argon milling step followed by the deposition of 150 nm-thick sputtered NbTiN. Finally, the chip is diced into 2 by 7 millimeters, glued onto a solid copper block with silver epoxy, and connected to a custom-made printed circuit board using aluminium wirebonds.

CRYOGENIC AND ROOM TEMPERATURE MEASUREMENT SETUP

The device was measured in a Triton dilution refrigerator with a base temperature of 20 mK. As shown in Fig. 7.11, the setup contains an input RF line, an output RF line, an additional RF line for driving the spin-flip transition, and multiple DC gate lines. The DC gate lines are filtered at base temperature with multiple low-pass filters connected in series. The input and drive RF lines contain attenuators and low-pass filters at different temperature stages, as indicated. The output RF line contains a traveling wave parametric amplifier (TWPA) at the 20 mK temperature stage, a high-electron-mobility transistor (HEMT) amplifier at the 4 K stage, and an additional amplifier at room temperature. A three-axis vector magnet (x-axis not shown) is thermally anchored to the 4 K temperature stage, with the device under study mounted at its center. The three magnet coils are controlled with Yokogawa GS610 current sources. At room temperature, a vector network analyzer (VNA) is connected to the input and output RF lines for spectroscopy at frequency f_r. On the input line, this signal is then combined with the transmon drive tone at frequency $f_{t,drive}$, for two-tone spectroscopy. The spin-flip drive tone at frequency $f_{s,drive}$ is sent through the additional RF line.

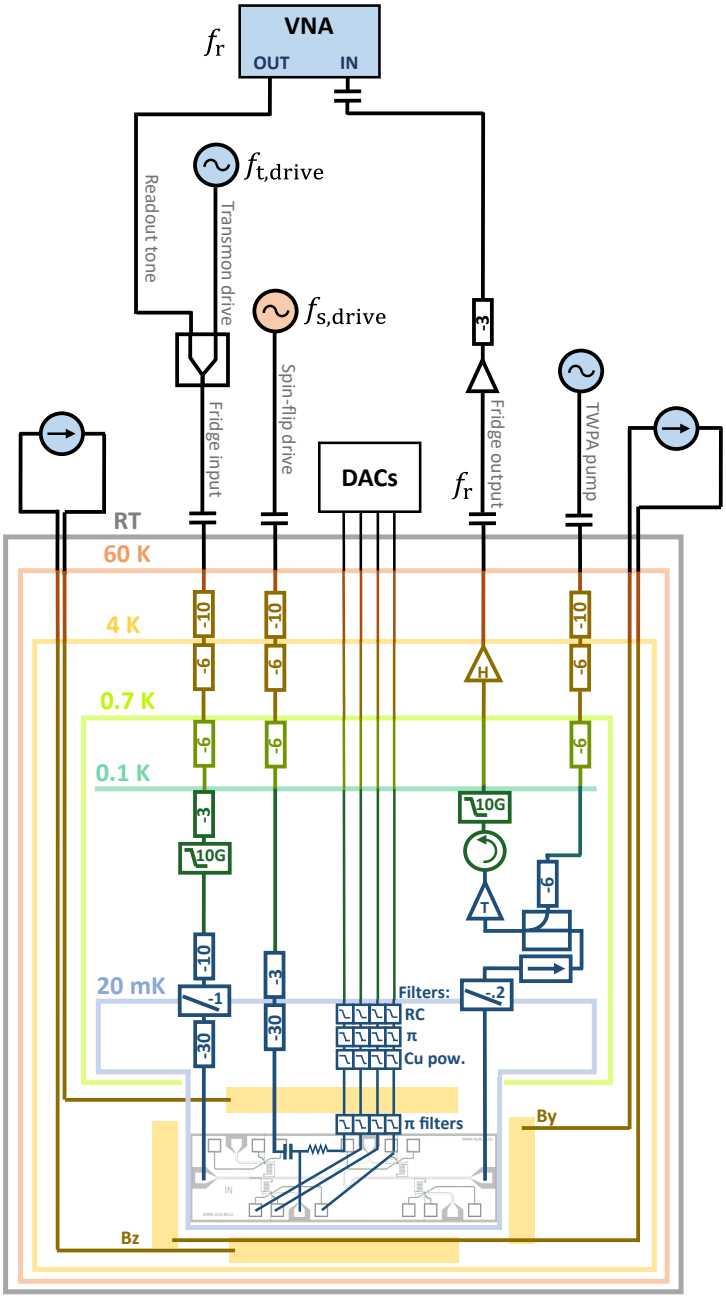

Figure 7.11: **Measurement setup at cryogenic and room temperatures.**

7.7.3. BASIC CHARACTERIZATION AND TUNE UP

This section describes how the device is tuned to its gate setpoints.

We start by characterizing the effect of the electrostatic gates, which control each of the two Josephson junctions. Fig. 7.12(a) shows the basic behaviour of the reference junction versus junction gate voltage V_J when the quantum dot junction is completely closed. As V_J is varied, different junction channels open sequentially (Hart et al., 2019; Spanton et al., 2017), with transparencies that increase non-monotonically due to mesoscopic fluctuations. This in turn affects the E_J of the transmon, allowing for in-situ tunability of its frequency, and the transmon then affects the resonator through its dispersive shift (Blais et al., 2004), resulting in the observed change in resonator frequency. We use this to choose a V_J set-point which maintains a good SQUID asymmetry in all regimes of interest. The black line in Fig. 7.12(a) indicates $V_J = 3860$ mV, the setpoint used in Figs. 7.3(a-b) in the main text. After a small non-reproducible gate jump in the reference junction the setpoint was retuned to $V_J = 4064.5$ mV, which was used for all other data shown in the main text. For all resonances explored, we maintained $E_J/E_c > 40$.

We start by characterizing the effect of the electrostatic gates, which control each of the two Josephson junctions. Fig. 7.12(a) shows the basic behaviour of the reference junction versus junction gate voltage V_J when the quantum dot junction is completely closed. As V_J is varied, different junction channels open sequentially (Hart et al., 2019; Spanton et al., 2017), with transparencies that increase non-monotonically due to mesoscopic fluctuations. This in turn affects the E_J of the transmon, allowing for in-situ tunability of its frequency, and the transmon then affects the resonator through its dispersive shift (Blais et al., 2004), resulting in the observed change in resonator frequency. We use this to choose a V_J set-point which maintains a good SQUID asymmetry in all regimes of interest. The black line in Fig. 7.12(a) indicates $V_J = 3860$ mV, the setpoint used in Figs. 7.3(a-b) in the main text, which fixes the transmon frequency at $f_t = 4.7$ GHz. After changing the quantum dot junction from gate setpoint A to gate setpoint B and due to cross-coupling between the quantum dot and reference gates, the reference junction started exhibiting poisoning behavior. Therefore, its setpoint was then set to $V_J = 4064.5$ mV, fixing the transmon frequency at $f_t = 4.95$ GHz, which was used for all other data shown in the main text. Fig. 7.12(b) shows a measurement taken at the moment when the V_J value was changed from its $V_J = 3860$ mV to its $V_J = 4064.5$ mV setpoint, both indicated with black lines. For all resonances explored, we maintained $E_J/E_c > 40$.

In Figs. 7.12(c-f) we show analogous measurements where we vary the quantum dot gate voltages when the reference junction is closed. We first measure an effective pinch-off curve for all three quantum dot gates ramped together [Fig. 7.12(c)], before sweeping each gate separately, with the other two quantum dot gates kept at 2000 mV [Figs. 7.12(d-f)]. This shows that each of the three quantum dot gates can independently pinch off the quantum dot junction, even if the other gates are in the open regime, signifying strong lever arms and good gate alignment. Note that these are not pinch-off curves as encountered in conventional tunnel spectroscopy; they reflect the voltages at which there is no longer a measurable transmon transition frequency mediated by the quantum dot junction, which could either be due to low tunneling rates or a full depletion of the quantum dot.

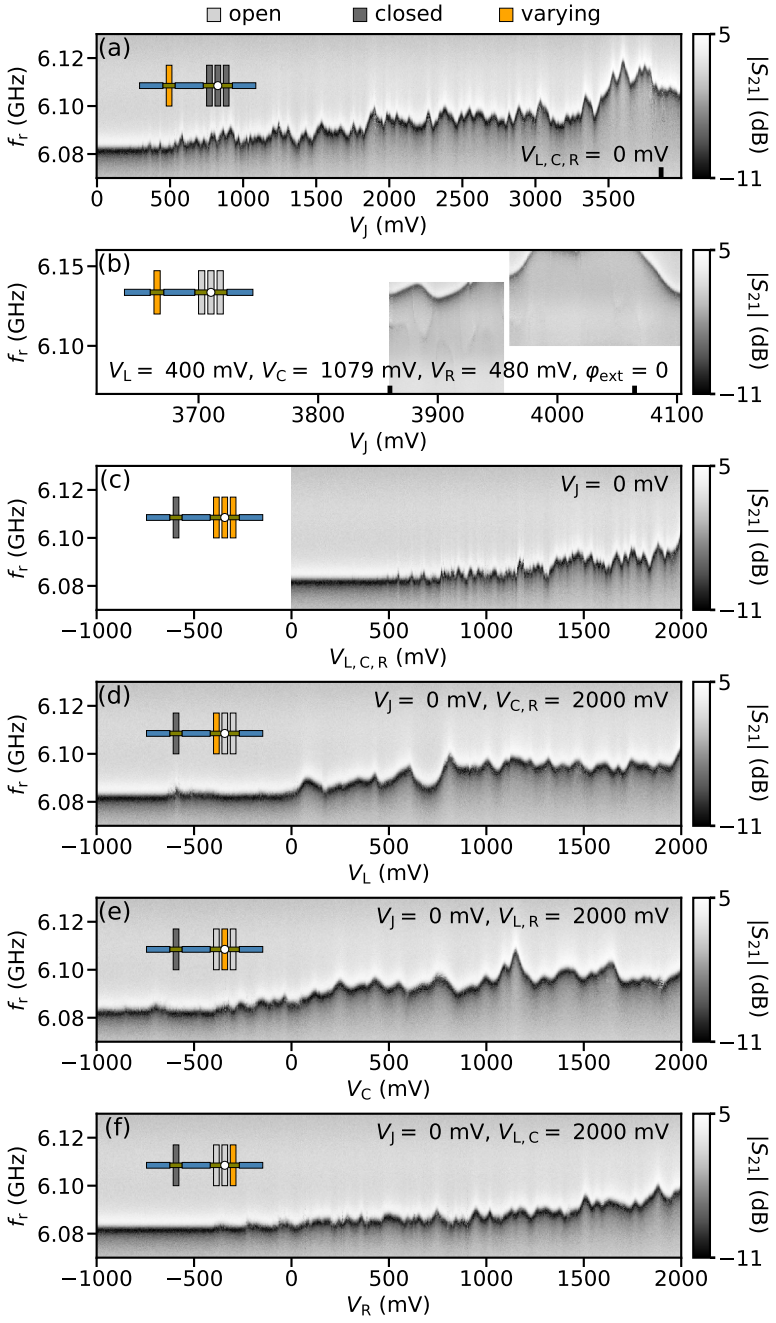

Figure 7.12: **Electrostatic gates characterization.** Transmission amplitude as a function of frequency of a single tone f_r and gate voltage. For each panel, the inset indicates which gate is being varied (orange) and which ones are set to a value above (light grey) or below (dark grey) their pinch-off value.

The subsequent tuning procedure for finding an isolated quantum dot resonance is discussed in detail in Chapter 6, summarized here for the specific resonances used in the main text. First we close the reference junction and go to a point in quantum dot gate voltages near pinchoff. Fixing the readout frequency f_r at the bare frequency of the resonator, one can then map out the regions where dispersive shifts occur on a two-dimensional map versus the left and right quantum dot gates, with the central gate held fixed. This signifies regions in which there is a supercurrent flowing through the quantum dot junction. After identifying such a region in V_L-V_R space, we subsequently open the reference junction, which lifts the reference transmon frequency closer to the bare resonator frequency. This magnifies the dispersive shift of the resonator and, furthermore, brings the external flux into the picture. Fixing $\phi_{ext} = 0$ and repeating the initial measurement then reveals much stronger deviations of the resonant frequency due to the enhanced dispersive shift.

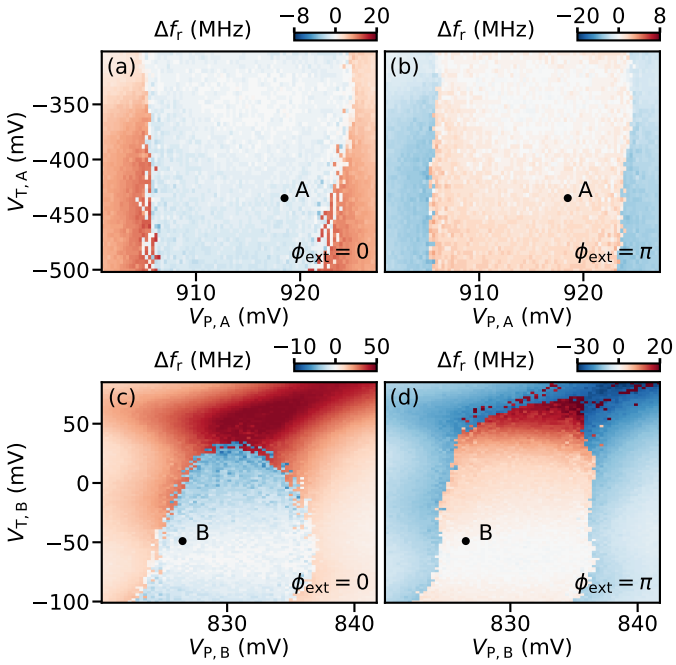

Figure 7.13: (a,c) Shift of the resonator resonance frequency with respect to its value when the quantum dot junction is fully closed, Δf_r, versus V_P and V_T at $\phi_{ext} = 0$, revealing singlet (red) and doublet (blue) ground state regions separated by sharp transitions for resonance A (a) and resonance B (c). (b,d) Same as (a,c) but for $\phi_{ext} = \pi$.

Using this approach we identify isolated quantum dot resonances, and subsequently explore their evolution versus the central quantum dot gate. This is shown in Fig. 7.13, where we furthermore account for cross coupling between the different quantum dot gates by defining a new set of virtual gates. For simplicity we fix V_L and focus on the rotated V_R-V_C space, denoted as the V_P-V_T-space. Note that this compensation scheme

is unique for each isolated region we explore. Fixing $\phi_{\text{ext}} = 0$ and varying the central dot gate, the resonator first shows a displacement towards higher frequencies to then abruptly drop to a lower frequency, to then finally go back to the higher frequencies once-more [Fig. 7.13(a,c)]. This behaviour is reversed for $\phi_{\text{ext}} = \pi$ [Fig. 7.13(b,d)], and can be identified as a singlet-doublet transition resulting from the relative level of the quantum dot is being varied by V_{P}. We note that in the V_{T} direction we do not always find the expected dome shape characteristic of singlet-doublet transitions; while such a shape does develop for resonance B [Fig. 7.13(c-d)], the doublet phase of resonance A [Fig. 7.13(a-b)] remains open even at elevated tunnel gate voltages. This is potentially a result of a non-monotonic dependence of tunnel rates on the gate voltage.

7.7.4. EXTENDED DATA

SPIN-ORBIT SPLITTING AT DIFFERENT RESONANCES

As discussed in the main text, we find a wide variety of phase-dependent splittings depending on the quantum dot resonance studied. This is shown in Fig. 7.14, portraying a range of resonances all the way from an even phase dependence with no splitting (panel d) to resonances that have a fully odd phase dependence (panel b). By Fitting the potentials with the transmon Hamiltonian, we extract a set of effective parameters for each resonance, tabulated in Table 7.1.

	V_{L} (mV)	V_{C} (mV)	V_{R} (mV)	E_0/h (GHz)	E_{SO}/h (GHz)
A	79.0	1020.0	363.0	0.18	0.28
B	430.0	531.0	635.2	0.00	0.56
C	430.0	520.0	652.0	0.11	0.56
D	430.0	614.8	335.0	0.50	0.00
E	430.0	655.2	305.2	0.23	0.05

Table 7.1: Quantum dot junction gate voltage set points and extracted model parameters for the five panels in Fig. 7.14.

SPIN-ORBIT SPLITTING WITHIN THE SAME RESONANCE

Within the extended SIAM model, E_{SO} and E_0 are expected to depend on Γ_V, Γ_W, and $\tilde{t}$ (see Sec. 7.7.1). One would therefore expect that these quantities can also vary within a single resonance, as the gate voltages tune the relative energy levels as well as the tunnel barriers of the quantum dot. This is indeed observed in the experiment: as shown in Fig. 7.15(a,b) for resonance A, we find that both effective doublet parameters vary with the rotated plunger and tunnel gates. In particular, both E_0 and E_{SO} show an increase towards the boundary of the singlet doublet transition, i.e. towards the edges of the Coulomb diamond. This is in line with the predictions of Padurariu and Nazarov (2010), as in the middle of the Coulomb diamond the energy cost of adding an electron to the quantum dot is maximal and the high energy of the intermediate states reduces the probability of Cooper pair tunneling. Additionally, contrary to initial expectation, the magnitude of the effective parameters appears to decrease for larger tunnel gate values. While the tunnel gate is expected to increase the tunnel rates, and thus the effective parameters, we note that in practice the situation is highly complex; there are up to

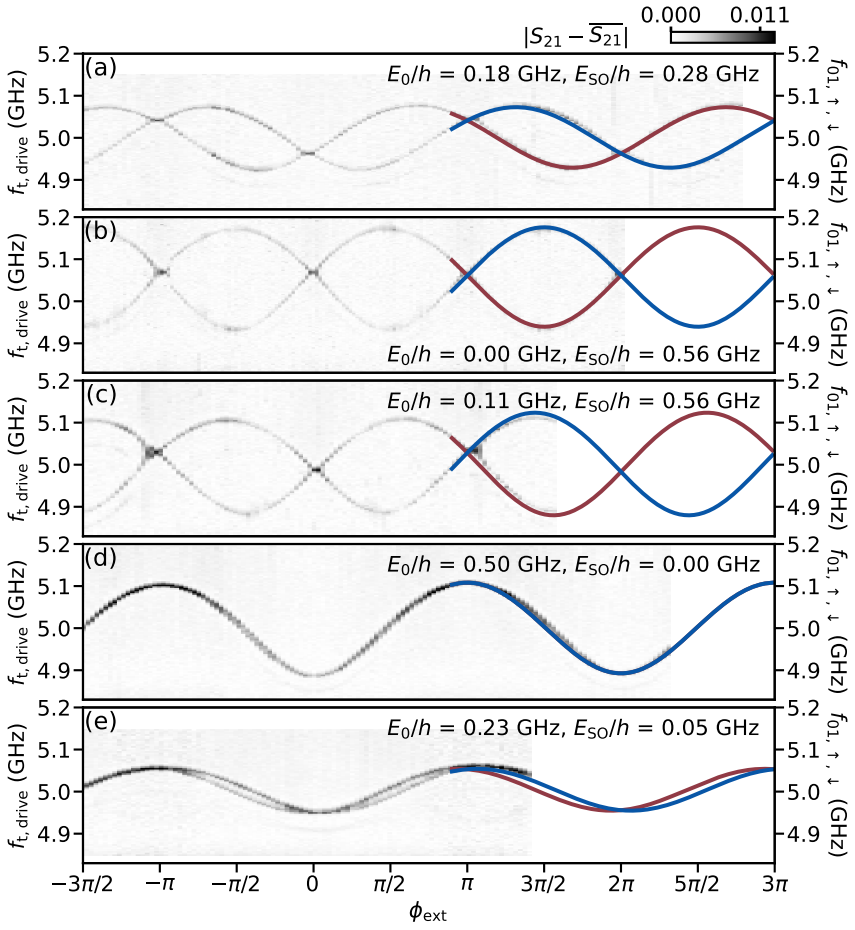

Figure 7.14: **Spin-splitting energies at different resonances.** Flux dependence of transmon spectroscopy taken at different points in quantum dot gate space, indicated in Table 7.1. In all cases, the quantum dot junction is in a doublet state. Different panels show different spin-splitting energies. (a) and (b) are gate setpoints A and B of the main text, respectively.

three gate voltages that control five model parameters ($\Gamma^{L,R}_{V,W}$, $\tilde{t}$), with potentially non-monotonic dependencies as well as cross-coupling. A full understanding of such a system will require a more detailed study of such dependencies, which we leave for future work. At this stage we instead emphasize the gate-tunability of these quantities, allowing for in-situ fine-tuning of the model parameters

Furthermore, we also find that the effective Landé g-factor g^* depends on gate voltage [Fig. 7.15(c)], in line with previous results on quantum dots in InAs nanowires, demonstrating its electric gate tunability (Csonka et al., 2008). This could be of relevance for qubit applications, as the tunability can be used to rapidly drive spin states in and out of resonance with a static magnetic field induced electron spin resonance condition.

Finally, we note that the observed gate dependence of g^* is distinct from that of E_{SO} and E_0, supporting the assertion that its origin is tied to a complex interplay of spin-orbit coupling and confinement, beyond the model considered here (Kiselev et al., 1998; Schroer et al., 2011; Winkler et al., 2017).

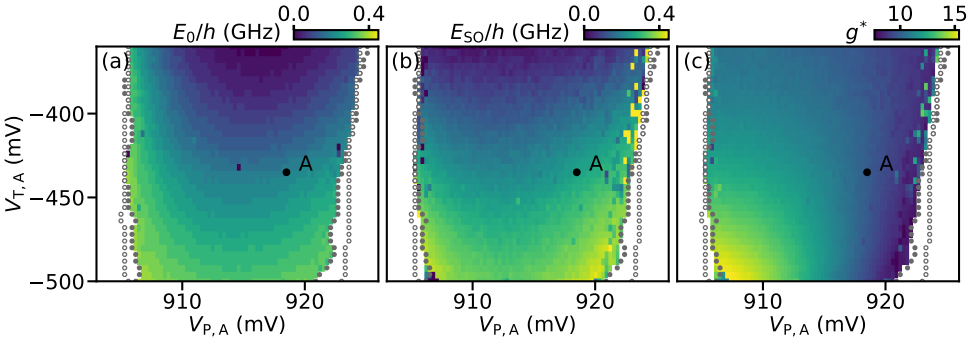

Figure 7.15: **Gate dependence within resonance A.** (a) Magnitude of E_0 extracted from transmon qubit spectroscopy at $\phi_{ext} = 0, \pi$ versus rotated plunger and tunnel gate voltages, at a magnetic field of 18 mT applied parallel to the nanowire. (b) Same as (a) for E_{SO}, extracted from spin-flip spectroscopy at $\phi_{ext} = \pi/2, 3\pi/2$. (c) Same as (b) for g^*, extracted from the same measurement as (b).

MAGNETIC FIELD ANGLE DEPENDENCE AND DETERMINATION OF THE SPIN-SPLITTING DIRECTION

In this Section we detail the method used to determine the direction of the spin-orbit interaction at a fixed gate point. This is done by comparing the angle dependence of transmon and spin-flip spectroscopy to the predictions of the model discussed in Sec. 7.7.1. For this it is useful to define a coordinate space determined by the nanowire direction, Z, the on-chip direction perpendicular to the nanowire, Y, and the direction perpendicular to the chip, X. We then define $\theta \in [0, 180)$ as the polar angle with respect to the Z direction and $\phi \in [0, 360)$ as the azimuthal angle [see Fig. 7.16], such that $B_x = B_r \cos(\phi)\sin(\theta)$, $B_y = B_r \sin(\phi)\sin(\theta)$ and $B_z = B_r \cos(\theta)$. Note that the cartesian field directions B_x, B_y and B_x set a frame of reference and should not be confused with the directions $B_\parallel$ and $B_\perp$ presented in the main text, which are specific for each gate setpoint. With this convention, $\phi = 90$ is the plane of the chip, while $\phi = 0$ is the plane perpendicular to the chip containing the nanowire. In each of these two planes, we first fix the magnitude of the applied magnetic field, B_r, and measure the evolution of transmon and spin-flip spectroscopy while varying θ in steps of two degrees. For each plane we determine the angle for which the applied field is perpendicular to the spin-splitting direction, $\theta_{\perp,0}$ and $\theta_{\perp,90}$, by comparison to the theory model. The cross product of these two directions determines the direction parallel to the spin-splitting term.

Representative data of such a measurement for resonance A is shown in Fig. 7.16(a-b), where we fix $\phi = 90$ and find $\theta_{\perp,90} = 78$. Performing an analogous measurement in the $\phi = 0$ plane, we determine $\theta_{\perp,0} = 86$. From these two, we obtain $(\theta_s, \phi_s) = (167, 72)$ as the spin-splitting direction of resonance A. This is 13 degrees away from the nanowire axis. Furthermore, we generally find that the measured spin-split direction varies depending

on which quantum dot resonance is studied; for resonance B of the main text we obtain a spin-splitting direction of $(\theta_s, \phi_s) = (72, 45)$, which is 84 degrees away from the spin-splitting direction of resonance A.

We can furthermore estimate the effective Landé g-factor from the evolution of the spin-flip transition frequency versus the angle of the magnetic field. Shown in Fig. 7.16(c) for resonance A, the effective g-factor varies from 3 to 11 depending on the angle, minimal for magnetic fields perpendicular to the spin-orbit direction. The measured behaviour is well-described by a simple cosine, in line with previous results on quantum dots in InAs nanowires (Schroer et al., 2011).

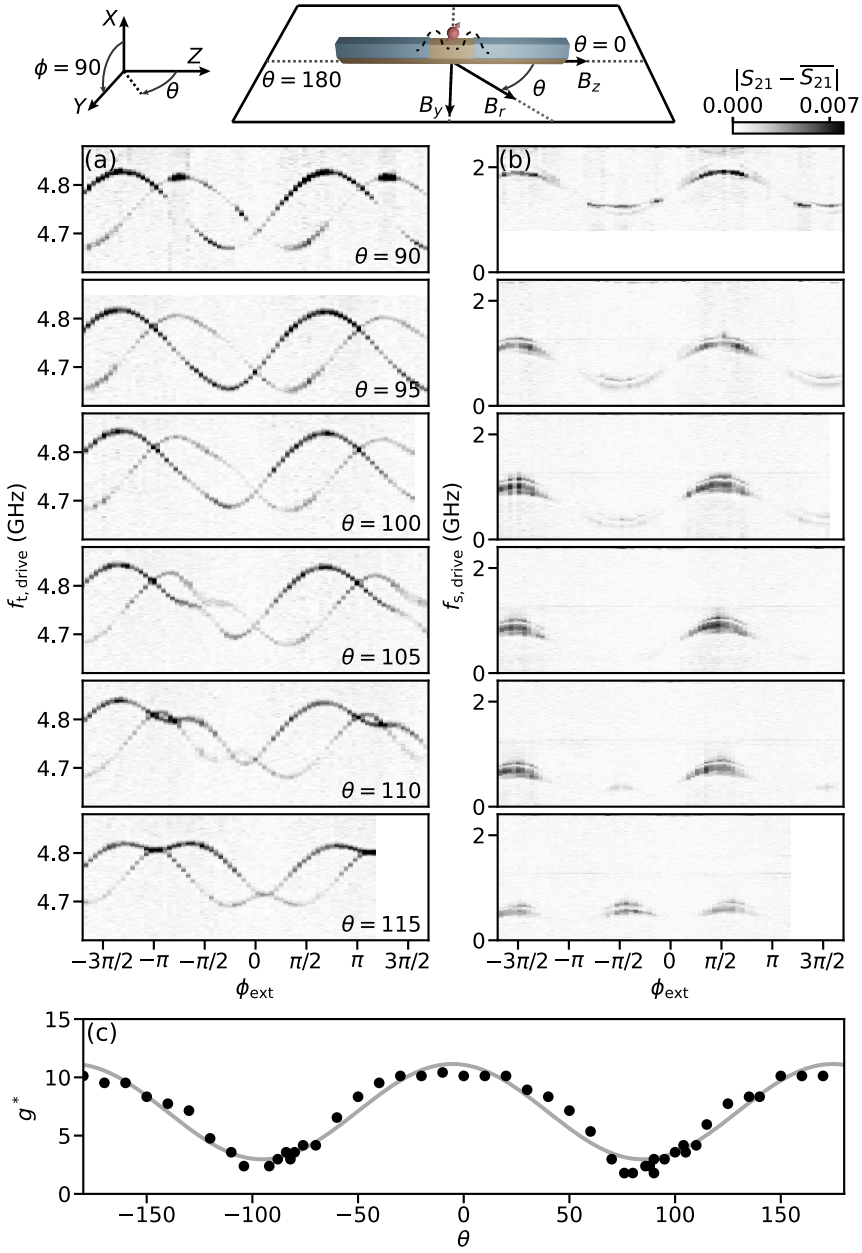

Figure 7.16: **Magnetic field angle dependence of resonance A.** (a-b) Flux dependence of transmon (left column) and spin-flip (right column) transitions for different magnetic field directions, for a fixed total magnetic field $B_r = 12\,\text{mT}$. Each row corresponds to a different magnetic field orientation on the chip plane, $\phi = 90$, determined by the angle θ with respect to the nanowire direction (see diagram at the top). All panels share the same color bar. (c) Effective Landé g-factor g^* versus θ. Markers show data extracted from spin-flip spectroscopy at 12 mT, and the solid line shows a fit with a cosine.

SPIN-FLIP SPECTROSCOPY ENABLED BY SPIN-ORBIT SPLITTING

As discussed in the main text, we do not rely on driving transitions of the transmon circuit to perform spectroscopy of the junction's excitation spectrum. While in principle possible by using three microwave tones, this could result in limitations due to the finite transmon lifetime as well as undesired mixing processes between the different tones. Instead, we use the dispersive shift from the transmon's ground state to induce a doublet-state-dependent shift on the resonator, similar to how the island parity of offset-charge sensitive transmon qubits can be distinguished (Serniak et al., 2019; Uilhoorn et al., 2021). As the difference between the transmon frequencies of both doublet states is small, inducing a sizeable dispersive shift larger than the resonator's linewidth requires us to tune the spin-dependent transmon qubit frequency close to that of the resonator [Fig. 7.10(a-b)]. Having done so, we can observe the spin-flip transition directly with conventional two-tone spectroscopy, where the first tone is applied at the frequency of the readout resonator, and the second tone at the spin-flip frequency [Fig. 7.10(c)]. The transmon, off-resonant from both tones, remains in its ground state during the measurement.

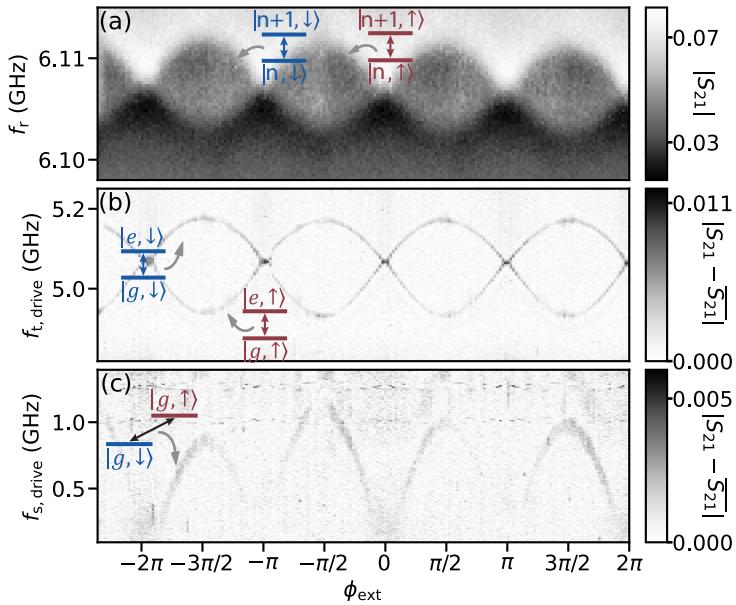

Figure 7.17: **Spin-flip two-tone spectroscopy.** (a) Flux dependence of single-tone spectroscopy showing the resonator frequency. Each of the two visible branches corresponds to a different spin state of the quantum dot junction. (b) Flux dependence of two-tone spectroscopy showing the transmon frequency. The continuous lines denote the two transmon branches corresponding to the two possible spin states of the quantum dot junction. They are the result from the same fit as in Fig. 7.14. (c) Flux dependence of two-tone spectroscopy showing the spin-flip frequency. The continuous line denotes the spin-flip transition frequency obtained from the same fit as in Fig. 7.14.

8

DIRECT MANIPULATION OF A SUPERCONDUCTING SPIN QUBIT STRONGLY COUPLED TO A TRANSMON QUBIT

Il mio Pinocchio fragile, parente artigianale di ordigni costruiti su scala industriale.

Fabrizio De André

Spin qubits in semiconductors are currently one of the most promising architectures for quantum computing. However, they face challenges in realizing multi-qubit interactions over extended distances. Superconducting spin qubits provide a promising alternative by encoding a qubit in the spin degree of freedom of an Andreev level. Such an Andreev spin qubit could leverage the advantages of circuit quantum electrodynamics, enabled by an intrinsic spin-supercurrent coupling. The first realization of an Andreev spin qubit encoded the qubit in the excited states of a semiconducting weak-link, leading to frequent decay out of the computational subspace. Additionally, rapid qubit manipulation was hindered by the need for indirect Raman transitions. Here, we exploit an electrostatically-defined quantum dot Josephson junction with large charging energy, which leads to a spin-split doublet ground state. Additionally, we use a magnetic field to tune the qubit frequency over a frequency range of 10 GHz and to investigate the qubit performance using direct spin manipulation. Using an all-electric microwave drive we achieve Rabi frequencies exceeding 200 MHz. We furthermore embed the Andreev spin qubit in a superconducting transmon qubit, demonstrating strong coherent qubit-qubit coupling. These results are a crucial step towards a hybrid architecture that combines the beneficial aspects of both superconducting and semiconductor qubits.

The work in this chapter has been published as: **M. Pita-Vidal***, A. Bargerbos*, R. Žitko, L.J. Splitthoff, L. Grünhaupt, J.J. Wesdorp, Y. Liu, L.P. Kouwenhoven, R. Aguado, B. van Heck, A. Kou, and C.K. Andersen, Direct manipulation of a superconducting spin qubit strongly coupled to a transmon qubit, Nature Physics, DOI: 10.1038/s41567-023-02071-x, (2023). * Equal contributions.

8.1. INTRODUCTION

Spin qubits in semiconductors (Hanson et al., 2007; Loss and DiVincenzo, 1998) and transmon qubits in superconducting circuits (Koch et al., 2007) are currently two of the most promising platforms for quantum computing. Spin qubits are promising from a scalability standpoint due to their small footprint and compatibility with industrial semiconductor processing (Zwerver et al., 2022). However, despite encouraging progress in recent years (Borjans et al., 2020; Harvey-Collard et al., 2022; Landig et al., 2018; Mi et al., 2018; Samkharadze et al., 2018; Yu et al., 2023), spin qubit architectures face challenges in realizing multi-qubit interactions over extended distances. Transmon-based circuits currently boast some of the largest numbers of qubits on a single device (Arute et al., 2019; IBM Quantum, 2022a), and are readily controlled, read out, and coupled over long distances due to the use of circuit quantum electrodynamics (QED) techniques (Blais et al., 2004, 2021; Wallraff et al., 2004). However, transmon qubits have a small anharmonicity, limiting the speed of qubit operations, and they are relatively large (typically 0.01 to 1 mm^2 per qubit), which leads to large chip sizes and makes transmons susceptible to cross-coupling with distant control elements.

A potential route to leverage the benefits of both superconducting qubits and spin qubits is to encode a qubit in the spin degree of freedom of a quasi-particle occupying an Andreev bound state in a Josephson junction (Chtchelkatchev and Nazarov, 2003; Padurariu and Nazarov, 2010). These states are confined by Andreev reflections at the superconducting interfaces and, thus, are localized in a small and well-defined region, similarly to conventional spin qubits. Furthermore, in the presence of spin-orbit interaction (SOI), the supercurrent across the Josephson junction becomes spin-dependent (Béri et al., 2008; Chtchelkatchev and Nazarov, 2003), which allows for interfacing with superconducting circuit elements. Such a superconducting spin qubit has recently been realized in the weak link of a superconductor-semiconductor hybrid nanowire (Hays et al., 2021), where it was named the Andreev spin qubit (ASQ). This first implementation showed that an ASQ can be efficiently read out using standard circuit QED techniques. However, qubit control was hindered by frequent leakage out of the computational subspace of the qubit, formed by higher energy Andreev levels of the junction. Additionally, due to the selection rules of the system in the absence of a magnetic field (Park and Yeyati, 2017), direct driving of the ASQ is partly suppressed (Metzger et al., 2021) and qubit manipulation may require virtual driving of auxiliary states to induce qubit transitions (Hays et al., 2021).

In this work, we utilize previous insights from semiconducting spin-orbit qubits (SOQ) (Nadj-Perge et al., 2010; Nowack et al., 2007) to construct an ASQ using a quantum dot within a Josephson junction, building on the work of Chapters 6 and 7. To enhance the confinement of the quantum dot, we implement it in a Josephson junction shorter than that from Ref. (Hays et al., 2021) and we use three electrostatic bottom gates. These two features lead to an enhanced charging energy of the dot compared to that in previous implementations of Andreev spin qubits, such that it can be exploited to deterministically prepare the quantum dot into a doublet phase with well-defined spin-split states; see Chapter 7. As a consequence, the computational subspace of the qubit is now formed by the lowest energy states of the junction in the doublet phase. Moreover, this charging energy enhances the parity lifetime of the doublet subspace to the millisecond

regime, therefore providing protection against leakage resulting from parity switches of the junction (Padurariu and Nazarov, 2010). Furthermore, this design allows for fast and direct qubit control through spin-orbit mediated electric dipole spin resonance (EDSR) (Golovach et al., 2006; Nadj-Perge et al., 2010; Nowack et al., 2007; van den Berg et al., 2013). We additionally demonstrate the magnetic field tunability of the qubit transition frequency over a frequency range of more than 10 GHz, pushing the device into a parameter regime inaccessible to previous experiments, which allows us to investigate the origin of dephasing. At elevated qubit frequencies, this moreover results in a suppression of the population of the excited state, facilitating qubit manipulation and readout without any additional steps needed for initialization of the qubit beyond the qubit relaxation. Finally, the intrinsic coupling between the spin degree of freedom and the supercurrent facilitates strong coherent coupling between the ASQ and a transmon qubit.

8.2. ANDREEV SPIN QUBIT

We implement the ASQ in a quantum dot Josephson junction formed in a hybrid InAs/Al semiconducting-superconducting nanowire, see Fig. 8.1(a). The quantum dot is electrostatically defined by three gate electrodes under an uncovered InAs section of the nanowire and tunnel-coupled to the superconducting segments (see Chapter 6). In the limit of weak coupling between the superconducting part of the nanowire and the quantum dot, and in the presence of a magnetic field, the ASQ can be described by the effective Hamiltonian

$$H_s = E_0 \cos(\phi) - E_{SO}\,\vec{\sigma}\cdot\vec{n}\sin(\phi) + \frac{1}{2}\vec{E}_Z\cdot\vec{\sigma}, \tag{8.1}$$

where ϕ is the phase difference across the junction, $\vec{\sigma}$ is the spin operator, $\vec{n}$ is a unit vector along the zero-field spin-polarization direction, set by the SOI, and $\vec{E}_Z$ is a Zeeman field arising in the presence of an external magnetic field. E_0 denotes the effective Josephson energy of the quantum dot junction, common for both spin states. We note that the the term proportional to E_0 has a minimum at $\phi = \pi$, originating from the odd occupancy of the junction. In turn, E_{SO} denotes the spin-dependent contribution to the energy of the junction. It originates from the occurrence of electron co-tunneling accompanied by a spin flip, and it is finite only if SOI is present and multiple levels of the quantum dot are involved in the co-tunneling sequence (Padurariu and Nazarov, 2010). The difference between the energies of the $|\downarrow\rangle$ and $|\uparrow\rangle$ eigenstates of Eq. (8.1) determines the ASQ qubit frequency $f_s = E_\uparrow - E_\downarrow$, as depicted in Fig. 8.1(b). For readout and control, we embed the ASQ into a superconducting transmon circuit, as illustrated in Fig. 8.1(c). The transmon circuit consists of a capacitor, with charging energy E_c, shunting a superconducting quantum interference device (SQUID) formed by the parallel combination of a gate-tunable Josephson junction with Josephson energy E_J, and the quantum dot Josephson junction hosting the ASQ. We operate in the regime $E_J/\sqrt{E_0^2 + E_{SO}^2} > 20$ so that the phase difference ϕ across the quantum dot Josephson junction can be controlled through the magnetic flux through the SQUID loop $\Phi_{ext} = \phi_{ext}\Phi_0/(2\pi)$, where $\Phi_0 = h/2e$ is the magnetic flux quantum. Due to the presence of the E_{SO} term, the transmon frequency f_t becomes spin-dependent. We exploit this fact to readout the ASQ state by capacitively coupling the transmon circuit to a readout resonator. Due to the transmon-resonator dispersive coupling, the resonator frequency in turn becomes spin-dependent

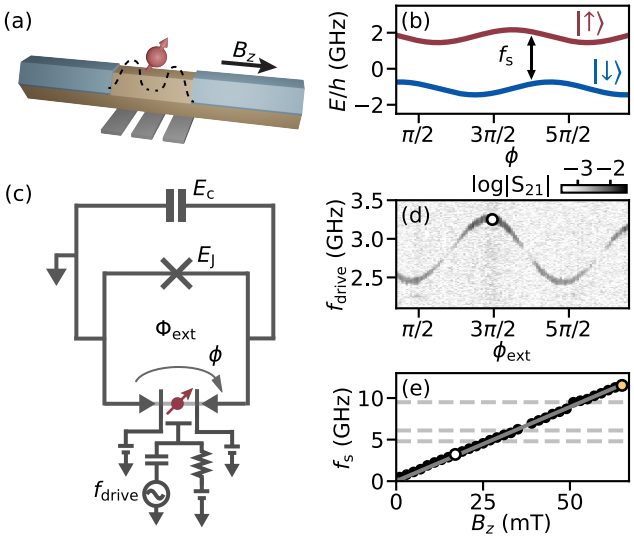

Figure 8.1: (a) Schematic depiction of an Andreev spin qubit in a hybrid superconductor-semiconductor nanowire. The qubit is formed in a gate-defined quantum dot with an odd number of electrons and is coupled to superconducting leads. The dashed line is a sketch of the potential landscape created by the gates. (b) Eigenenergies of the Andreev spin qubit levels as a function of the phase difference ϕ, as described by the effective model of Eq. 8.1. The frequency of the qubit spin-flip transition $|\downarrow\rangle \leftrightarrow |\uparrow\rangle$ is denoted by f_s. In this panel the component of the Zeeman energy parallel to the zero-field spin-polarization direction is $E_Z^{\parallel} = 2.9\,\text{GHz}$. (c) Circuit model of the Andreev spin qubit embedded in a transmon circuit. The spin state is manipulated by a microwave drive, at frequency f_{drive}, applied to the central gate electrode. The transmon island, with charging energy E_c, is connected to ground by a SQUID formed by the parallel combination of the ASQ and a reference Josephson junction. Here, ϕ denotes the superconducting phase difference across the quantum dot junction, while Φ_{ext} is the externally applied magnetic flux through the SQUID loop. (d) Transmission through the readout circuit as a function of the external flux and the applied drive frequency, measured at a magnetic field $B_z = 17\,\text{mT}$ parallel to the nanowire (see Fig. 8.5). (e) Extracted qubit frequency f_s versus B_z (markers), measured at $\phi_{\text{ext}} = 3\pi/2$. The data is fitted with a linear dependence (solid line), resulting in an effective Landé g-factor of $g^* = 12.7 \pm 0.2$. Horizontal dashed lines denote the first and second transmon frequencies, as well as the readout resonator frequency.

and probing the readout resonator therefore leads to a spin-dependent response. Spectroscopy of the spinful Andreev levels can, thus, be performed using standard two-tone circuit QED techniques (see Fig. 7.17). Finally, the spin-flipping qubit transition can be directly driven, while maintaining the transmon in its ground state, by applying a microwave tone on the central quantum dot gate (Metzger et al., 2021; Wesdorp et al., 2022). Such microwave drive allows for all-electrical manipulation through EDSR (Nadj-Perge et al., 2010; Nowack et al., 2007). For further details about the device implementation and setup, see the Supplementary Information in Sec. 8.6.

Following the gate-tuning strategy described in Chapter 6, we prepare the quantum dot junction in a regime where it is occupied by an odd number of electrons, with $E_0/h = 211\,\text{MHz}$ and $E_{\text{SO}}/h = 305\,\text{MHz}$ and with a parity lifetime of 2.8 ms. In this regime, the qubit states $|\uparrow\rangle$ and $|\downarrow\rangle$ are the lowest energy levels of the system, and the qubit subspace is separated from higher lying states by a frequency gap of at least 20 GHz (see Sup-

plementary Materials). After fixing the gate voltages of the quantum dot, we investigate the tunability of the spin-flip transition f_s by applying a microwave tone at frequency f_{drive} and performing dispersive readout of the transmon qubit. As shown in Fig. 7.1(d), we can finely control f_s by applying a magnetic flux through the SQUID loop [1], although the visibility of the measurement signal is reduced around $\phi_{ext} = 0, \pi$, where the spin-dependent transmon frequencies are degenerate. By applying an external magnetic field along the nanowire B_z of up to 65 mT, the qubit frequency can be varied from 250 MHz to 12 GHz, see Fig. 7.1(e). The magnetic field direction is chosen to maximize the magnetic field compatibility of the Al shell of the nanowire and is generally not aligned with the spin-orbit direction $\vec{n}$ (Han et al., 2023).

8.3. QUBIT COHERENCE

To perform coherent manipulation of the spin states we fix $B_z = 65$ mT and $\phi_{ext} = 3\pi/2$, setting $f_s = 11.5$ GHz, where the residual population of the excited state is suppressed to less than 5 %, facilitating qubit manipulation and readout (see Fig. 8.10). We observe Rabi oscillations between the qubit states $|\uparrow\rangle$ and $|\downarrow\rangle$ by applying a Gaussian microwave pulse with a carrier frequency at the spin-flip transition frequency $f_{drive} = f_s$, see Fig. 8.2. Here, the Gaussian pulses are truncated so that the total pulse length is 2.5 times the Gaussian full width at half maximum (FWHM). As shown in Fig. 8.2(a), we resolve up to 10 oscillations by varying the amplitude and duration of the pulse envelope. The population transfer between the spin states, as measured by the dispersive readout scheme, follows the expected time-dependence of a standard Rabi oscillation, as shown in Fig. 8.2(b), from which we extract the Rabi frequency for each pulse amplitude. For a fixed Rabi frequency, we calibrate the FWHM needed for π and $\pi/2$ pulses for single qubit manipulation.

In contrast to previous approaches to implementing Andreev spin qubits, we drive the qubit transition directly and do not rely on auxiliary energy levels in the junction (Cerrillo et al., 2021; Hays et al., 2021). This is motivated by recent work by our group, indicating that spin-flip transitions of Andreev bound states can be activated by a magnetic field; see Ref. (Wesdorp et al., 2022) and Chapter 7.

As expected for a two-level system, the Rabi frequency is linear over a wide range of pulse amplitudes. It only starts to deviate from this linear dependence for strong drive amplitudes, see Fig. 8.2(c). This deviation is due to saturation of the maximum power provided by the room-temperature electronics. We measure Rabi frequencies larger than 200 MHz, exceeding the largest Rabi frequencies achieved in SOQ (van den Berg et al., 2013) and more than an order of magnitude faster than previous results for the ASQ (Hays et al., 2021). We observe that the Rabi frequency is approaching the anharmonicity of typical transmon qubits, with no indications of higher order levels being driven. The two-level nature of the ASQ thus intrinsically supports faster single qubit gates than standard transmon qubits (Werninghaus et al., 2021).

Next, we characterize the lifetime of the ASQ by applying a π pulse and reading out the qubit state after a delay time τ. We obtain an exponential decay with a characteristic

[1] We attribute the shift of the minima and maxima of the spin-flip frequency away from $\pi/2$ and $3\pi/2$ to the phase-dependent renormalization of the impurity g-factor by coupling to the leads, known as the impurity Knight shift (Pavešić et al., 2023b).

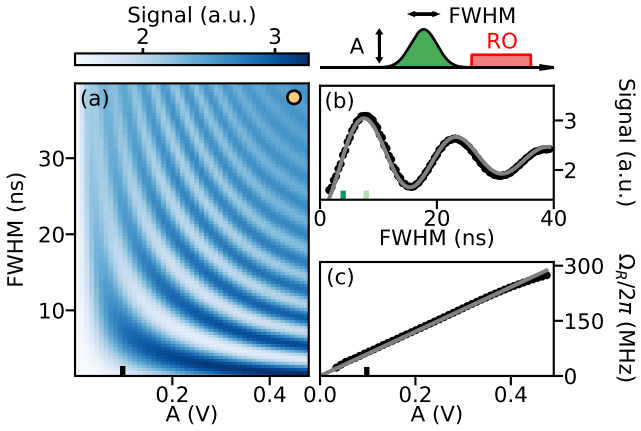

Figure 8.2: Coherent manipulation of the Andreev spin qubit for $f_s = 11.5\,\text{GHz}$ at $B_z = 65\,\text{mT}$. (a) Rabi oscillations for a range of Gaussian pulses characterized by their amplitude A at the waveform generator output and their full width at half maximum (FWHM), see pulse sequence. As also indicated in the pulse sequence, the Rabi pulse is immediately followed by a readout (RO) pulse (red, not to scale). (b) Rabi oscillation corresponding to $A = 0.1\,\text{V}$, fit with $a\cos(t\Omega_R)\exp(t/t_d)$ (solid line). The fit yields a decay time $t_d = 27\,\text{ns}$. (c) Extracted Rabi frequencies versus pulse amplitude, fit with a linear equation (solid line).

time $T_1 = 24.4 \pm 0.5\,\mu\text{s}$ at $B_z = 65\,\text{mT}$, see Fig. 8.3(a). As a function of magnetic field, T_1 varies between 10 and 40 µs for qubit frequencies above the transmon frequency. We conjecture that the observed lifetime is limited by Purcell-like decay from coupling to the transmon, given the short transmon lifetime of around 250 ns. For B_z closer to zero, T_1 drops down to around 1 µs (see Fig. 8.13). This is in contrast to the near-zero-field lifetimes found in previous ASQ experiments (Hays et al., 2020, 2021), which were in the range of 10 µs to 50 µs. The cause of this discrepancy is unknown, but a potential reason is an enhanced resonant exchange with the nuclear spins in InAs due to stronger strain in the nanowire, which may vary for different nanowires depending on the exact growth conditions (Stockill et al., 2016).

To characterize the coherence time of the qubit, we apply two $\pi/2$ pulses separated by a delay time, after which we read out the qubit state. From this experiment we extract a Ramsey coherence time of $T_{2R} = 11 \pm 1\,\text{ns}$, see Fig. 8.3(b), much smaller than T_1, and thus indicative of strong dephasing. Dephasing that originates from slow noise compared to the spin dynamics can be partially cancelled using a Hahn-echo sequence (Hahn, 1950), which introduces a π pulse halfway between the two $\pi/2$ pulses. This echo sequence increases the measured coherence time by more than three times, to $T_{2E} = 37 \pm 4\,\text{ns}$, see Fig. 8.3(c).

The coherence time of the qubit can be further enhanced by using dynamical decoupling pulse sequences, which serve to filter out faster environmental fluctuations. We apply Carr–Purcell (CP) sequences (Barthel et al., 2010; Bylander et al., 2011; Carr and Purcell, 1954), interleaving a varying number of equidistant π pulses, n_π, in between two $\pi/2$ pulses. As n_π increases, higher frequency noise is cancelled out, extending the decoherence times. We reach T_2 times up to more than 90 ns for $n_\pi = 7$, at which stage we are most likely limited by decoherence during the π pulses, see Fig. 8.3(d). We subsequently

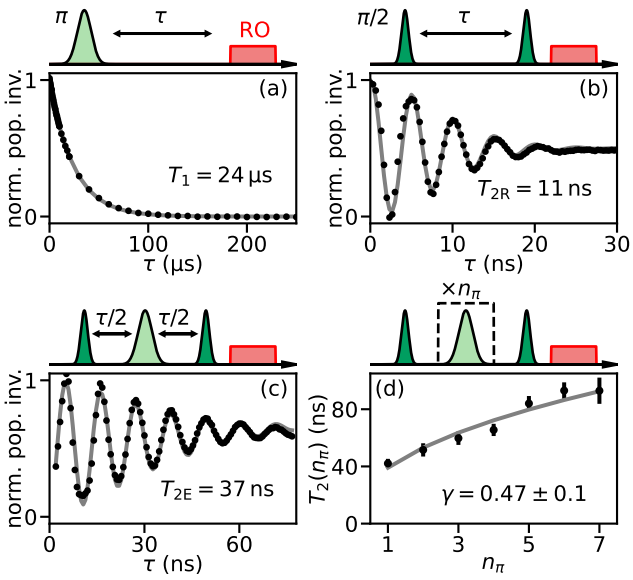

Figure 8.3: Coherence of the Andreev spin qubit at the same setpoint as Fig. 8.2. (a) Qubit lifetime, (b) Ramsey, (c) Hahn-echo and (d) CPMG experiments. Solid lines indicate fits to the data. For (b-d) oscillations are introduced into the decay by adding a phase proportional to the delay time for the final $\pi/2$-pulse. The data of (a-c) is obtained using a π-pulse ($\pi/2$-pulse) of FWHM = 8 ns (4 ns), while for (d) this is 4 ns (2 ns). For (a-c) we plot the normalized population inversion, where each sub-panel is individually normalized to the resulting fit.

fit the n_π dependence of T_2 with a power law $T_2(n_\pi) \propto n_\pi^\gamma$. Assuming a noise power spectral density of the form $f^{1/\beta}$, we expect the relation $\beta = \gamma/(1-\gamma)$ (Bylander et al., 2011; Cywiński et al., 2008; Medford et al., 2012). The observed scaling with $\gamma = 0.47 \pm 0.1$ therefore suggests that the decoherence is governed by noise with a $1/f$ spectral density in the frequency range 25 to 100 MHz.

There are several potential sources of dephasing that are compatible with a $1/f$ noise spectral density, such as flux noise through the SQUID loop and charge noise (Braumüller et al., 2020; Schreier et al., 2008). We exclude the former, as we do not observe an increase of coherence times at the flux sweet spots (see Fig. 8.15). Similarly, no consistent trend is observed when varying the gate voltages, nor when increasing the magnetic field strength. The latter indicates that charge noise is likely not the dominant contributor to dephasing, given that EDSR becomes more effective at coupling charge noise to the qubit at elevated fields (Golovach et al., 2006; Nadj-Perge et al., 2010; Nowack et al., 2007; van den Berg et al., 2013). Additionally, based on the evolution of the Rabi decay time with increasing pulse amplitudes (Malinowski et al., 2017), the size of the charge fluctuations required to cause the observed amount of dephasing is estimated to be 0.25 mV, significantly larger than what is expected to originate from the gate lines (see Fig. 8.17). However, the contribution of charge fluctuations originating elsewhere, such as in the dielectric material on the device, could still be contributing to the dephasing. Given that the sensitivity to fluctuations in environmental offset charge on the transmon island is suppressed by the large $E_J/E_c > 30$ ratio, it is furthermore unlikely that the

ASQ dephasing originates from offset-charge-dependent fluctuations of the transmon frequency qubit (Koch et al., 2007).

Another potential source of dephasing originates from the dynamics of the spinful nuclei in the nanowire, which may couple to the ASQ as a result of the hyperfine interaction. It has previously been shown that these dynamics can lead to longitudinal Overhauser field fluctuations with a $1/f$ spectral density (Malinowski et al., 2017b). Moreover, this effect is expected to be particularly strong in InAs due to the large nuclear spin of indium ($I = 9/2$) and should not be strongly affected by magnetic field in the B_z range investigated here, which is not enough to polarize the nuclear spins. Corroborated by the fact that the extracted T_{2R} and T_{2E} times are strikingly similar to those found for the weak-link InAs ASQ (Hays et al., 2021), the InAs SOQ (Nadj-Perge et al., 2010) and the InSb SOQ (van den Berg et al., 2013), we conjecture that the nuclear environment provides a significant contribution to the decoherence of the ASQ.

8.4. ASQ-TRANSMON COUPLING

One of the main characteristics of the ASQ is the intrinsic coupling between the spin degree of freedom and the supercurrent across the quantum dot Josephson junction. We have so far only exploited this coupling for read-out of the qubit state using circuit QED techniques. Now, we demonstrate the observation of coherent coupling of the ASQ with the transmon qubit.

A first signature of a coherent coupling is the presence of transitions that involve both qubits, in addition to the single-qubit transitions, see Fig. 8.4(a). At zero applied magnetic field, we spectroscopically detect two of such transitions at $f_t + f_s$ and $f_t - f_s$, where f_t is the transmon frequency, see Fig. 8.4(b). We classify them based on a fit with the joint Hamiltonian of the total ASQ-transmon circuit of Fig. 8.1(c), given by

$$H_{tot} = -4E_c\partial_\phi^2 - E_J\cos(\phi - \phi_{ext}) + H_s(\phi). \tag{8.2}$$

We identify the additional observed resonances as the double excitation $|g\downarrow\rangle \leftrightarrow |e\uparrow\rangle$ and the $|g\uparrow\rangle \leftrightarrow |e\downarrow\rangle$ SWAP transitions, where $|g\rangle$ and $|e\rangle$ denote the ground and first excited transmon states, respectively. These transitions could be used to construct entanglement and two qubit gates between the two different qubit platforms, provided the transitions can be driven at a faster rate than the decoherence rates of either qubit.

Additionally, one of the hallmarks of strong coherent coupling is the appearance of an avoided level crossing when both qubit frequencies are made equal, $f_t \approx f_s$. In this case the $|e,\downarrow\rangle$ and $|g,\uparrow\rangle$ states are expected to hybridize into superposition states with a frequency splitting of $2J$, see Fig. 8.4(c). At $B_z = 28$ mT this splitting can be readily observed in the experiment. By varying the external flux ϕ_{ext} such that the ASQ frequency f_s crosses the transmon frequency f_t, we find avoided crossings with a minimum frequency splitting $2J/(2\pi) = 2 \times 52$ MHz, as shown in Fig. 8.4(d). As J is four times larger than the decoherence rate of the ASQ, $1/T_{2R} \approx 14 \times 2\pi$ MHz and one order of magnitude larger than the decoherence rate of the transmon, $\approx 1.2 \times 2\pi$ MHz, the coupling between the two qubits falls into the strong coupling regime. This result establishes the first realization of a direct strong coupling between a spin qubit and a superconducting qubit, in contrast to the results of Ref. (Landig et al., 2019), where a high-impedance bus res-

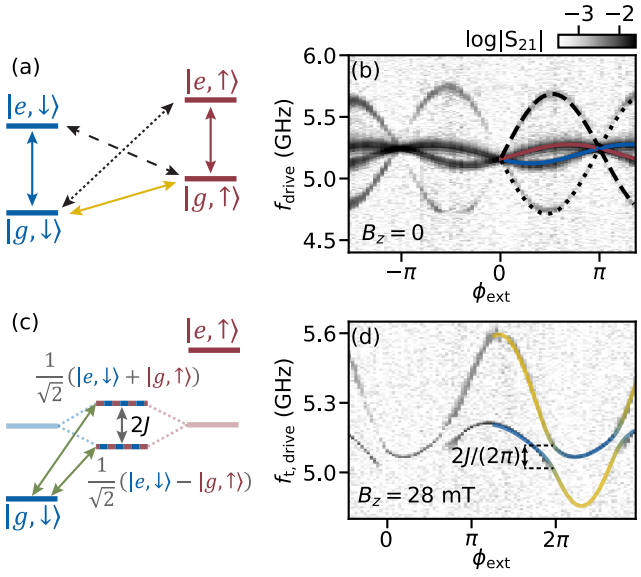

Figure 8.4: Coherent ASQ-transmon coupling. (a) Frequency diagram of the joint ASQ-transmon circuit of Fig. 8.1(c) at large detuning between ASQ and transmon qubit energy levels. In addition to the two spin-conserving transmon transitions (solid red and blue) and the transmon-conserving spin qubit transition (solid yellow), two additional transitions involving both qubits can take place in the presence of coherent coupling between them (dashed and dotted black). (b) Two-tone spectroscopy of the joint two-qubit system at $B_z = 0$. In addition to the two spin-dependent branches of the transmon qubit frequency, two additional transitions appear. Overlaid are transition frequencies obtained from the model of Eq 8.2. (c) Frequency diagram of the joint ASQ-transmon circuit for $|e,\downarrow\rangle = |g,\uparrow\rangle$. In the presence of coherent coupling, the two qubits hybridize into states with a frequency splitting of $2J$. Green arrows denote the transitions from ground to the two hybridized states. (d) Two-tone spectroscopy versus external flux at $B_z = 28\,\mathrm{mT}$, where $f_{\mathrm{s}} \approx f_{\mathrm{t}}$. This results in avoided crossings between the two qubit frequencies. Overlaid are the transition frequencies obtained from the model of Eq. 8.2. Their colors denote the expectation value of the spin degree of freedom of the excited state and go from $|\downarrow\rangle$ (blue) for the transmon transition to $|\uparrow\rangle$ (yellow) for the spin-flip transition. $f_{\mathrm{t,drive}}$ denotes the frequency of the second tone, sent through the readout resonator.

onator was required to mediate the coupling between spin and transmon qubit through virtual photons.

Analytical estimates predict that the coupling $J \propto E_{\mathrm{SO}}\phi_{\mathrm{zpf}}\sin(\theta)$, where ϕ_{zpf} is the magnitude of zero-point fluctuation of the transmon phase, and θ is the angle between the Zeeman field and the spin-orbit direction; see Sec. 8.6. This suggests that by choosing a resonance with a larger E_{SO} and by aligning the magnetic field perpendicular to the spin-orbit direction, coupling rates of hundreds of MHz can be achieved, which would enable rapid two-qubit gates between the transmon and the ASQ and potentially allow for the study of light-matter interactions in the ultrastrong coupling regime (Forn-Díaz et al., 2019; Scarlino et al., 2022).

8.5. TOWARDS NEW PLATFORMS AND MULTIPLE ASQ

We have implemented an Andreev spin qubit, where the spin degree of freedom of a quasi-particle in a quantum dot with superconducting leads encodes the qubit state. The qubit subspace is stabilized by the charging energy of the quantum dot and direct microwave driving of the transitions is possible without the requirement of auxiliary levels. The qubit coherence was found to be comparable to previous results for qubits implemented in InAs or InSb nanowires (Hays et al., 2021; Nadj-Perge et al., 2010; van den Berg et al., 2013). Our results suggest that the nuclear environment contributes strongly to the ASQ decoherence, although the contribution of charge noise can not be fully neglected. This limitation motivates future investigation of alternative material platforms for ASQs, such as superconductor-proximitized nuclear-spin-free semiconductors (de Leon et al., 2021), e.g. isotopically purified germanium (Hendrickx et al., 2018; Scappucci et al., 2021; Tosato et al., 2023).

We furthermore observed direct strong coherent coupling between the ASQ and a transmon qubit. Such strong coupling showcases the advantage of the intrinsic spin-supercurrent coupling, allowing the ASQ to be readily integrated into a circuit QED architecture. Our results open avenues towards multi-qubit devices: we propose to leverage the fact that transmon qubits can be readily coupled together using capacitive coupling, useful for mediating interactions between multiple ASQ. Furthermore, our results are a crucial step towards the coupling of distant Andreev spin qubits through bus resonators or a shared inductance (Padurariu and Nazarov, 2010), as well as short-distance coupling through wavefunction overlap (Spethmann et al., 2022).

AUTHOR CONTRIBUTIONS

A.B., M.P.V., and A.K. conceived the experiment. Y.L. developed and provided the nanowire materials. A.B., M.P.V., L.S., L.G. and J.J.W prepared the experimental setup and data acquisition tools. L.S. deposited the nanowires. A.B. and M.P.V. designed and fabricated the device, performed the measurements and analysed the data, with continuous feedback from L.S., L.G., J.J.W, B.v.H, A.K. and C.K.A. R.A., B.v.H. and R.Z. provided theory support during and after the measurements. A.B., M.P.V. and B.v.H. wrote the code to compute the circuit energy levels and extract experimental parameters. L.P.K., R.A., B.v.H., A.K. and C.K.A. supervised the work. A.B., M.P.V., and C.K.A. wrote the manuscript with feedback from all authors.

DATA AVALABILITY

The data and analysis code that support the findings of this study are openly available in 4TU.ResearchData at `https://doi.org/10.4121/c.6073271`.

8.6. SUPPLEMENTARY INFORMATION

8.6.1. MODELING OF JOINT ASQ-TRANSMON SYSTEM

NUMERICAL DIAGONALIZATION

In order to obtain the transition frequencies of the joint ASQ-transmon system, we combine the Hamiltonian of the ASQ [Eq. (8.1) in the main text] with the Hamiltonian of the transmon, as indicated in Eq. (8.2) of the main text. This combined Hamiltonian is numerically diagonalized in the phase basis following the procedure in Refs. (Bargerbos et al., 2020; Kringhøj et al., 2020). This results in the transmon and ASQ energy levels E_n, as well as the associated transition frequencies $f_{nm} = (E_m - E_n)/h$. These frequencies are used in Figs. 8.1 and 8.4 to fit the spectroscopy measurements.

ESTIMATE OF QUBIT-QUBIT COUPLING STRENGTH

As demonstrated in Fig. 8.4, we observe avoided crossings between the transmon and the ASQ transitions, which is indicative of strong coherent coupling. In this section we derive how the coupling strength depends on the model parameters.

We start by combining Eq. (8.1) and (8.2) of the main text into the effective Hamiltonian

$$H_{\text{tot}} = H_{\text{tmon}} + H_{\text{Z}} + H_{\text{coupling}}, \tag{8.3}$$

with the individual terms given as

$$H_{\text{tmon}} = -4E_{\text{c}}\partial_{\phi}^2 - E_{\text{J}}\cos(\phi) - E_0\cos\left(\phi - \phi_{\text{ext}}\right), \tag{8.4}$$

$$H_{\text{Z}} = \frac{1}{2}\begin{pmatrix} E_{\text{Z}}^{\perp} & E_{\text{Z}}^{\parallel} \\ E_{\text{Z}}^{\parallel} & -E_{\text{Z}}^{\perp} \end{pmatrix} = \frac{|\vec{E}_{\text{Z}}|}{2}\begin{pmatrix} \sin(\theta) & \cos(\theta) \\ \cos(\theta) & -\sin(\theta) \end{pmatrix} \tag{8.5}$$

$$H_{\text{coupling}} = -E_{\text{SO}}\sin(\phi - \phi_{\text{ext}})\sigma_x. \tag{8.6}$$

Here, σ_x is the x Pauli matrix and θ is the angle between the Zeeman field $\vec{E}_{\text{Z}}$ and the spin-orbit direction, such that $E_{\text{Z}}^{\parallel} = |\vec{E}_{\text{Z}}|\cos\theta$ and $E_{\text{Z}}^{\perp} = |\vec{E}_{\text{Z}}|\sin\theta$. Next, we write the coupling term H_{coupling} in the eigenbasis of H_{Z}, which is given by the states

$$|v_1\rangle = [\cos(\theta/2), \sin(\theta/2)]\,,\ |v_2\rangle = [-\sin(\theta/2), \cos(\theta/2)]\,. \tag{8.7}$$

We identify that

$$\langle v_1|\sigma_x|v_2\rangle = \langle v_2|\sigma_x|v_1\rangle = \cos\theta \tag{8.8}$$

and

$$\langle v_1|\sigma_x|v_1\rangle = -\langle v_2|\sigma_x|v_2\rangle = \sin\theta, \tag{8.9}$$

such that σ_x becomes $\cos(\theta)\sigma_{\overline{x}} + \sin(\theta)\sigma_{\overline{z}}$ in the $\{|v_1\rangle, |v_2\rangle\}$ spin basis.

We rewrite H_{coupling} and expand to first order in ϕ, valid in the transmon limit $E_{\text{J}} \gg E_{\text{c}}$, where $\langle\phi\rangle \ll 1$, which results in

$$H_{\text{coupling}} = E_{\text{SO}}\left[\cos(\phi)\sin\left(\phi_{\text{ext}}\right) - \cos\left(\phi_{\text{ext}}\right)\sin(\phi)\right]\sigma_x \tag{8.10}$$

$$\approx E_{\text{SO}}\left[\sin(\phi_{\text{ext}}) - \phi\cos(\phi_{\text{ext}})\right]\sigma_x. \tag{8.11}$$

Therefore, in the spin eigenbasis, we obtain

$$H_{\text{coupling}} \approx E_{\text{SO}} \left[\sin(\phi_{\text{ext}}) - \phi\cos(\phi_{\text{ext}})\right] \left[\cos(\theta)\sigma_{\overline{x}} + \sin(\theta)\sigma_{\overline{z}}\right]. \tag{8.12}$$

This term of the Hamiltonian couples the ASQ to the transmon via the phase operator ϕ of the transmon and is, thus, reminiscent of a dipole coupling. In the transmon regime, we can express the operator ϕ in terms of the zero point fluctuations of the phase, ϕ_{zpf}, and the bosonic creation and annihilation transmon operators, $c^\dagger$ and c respectively: $\phi = \phi_{\text{zpf}}\left(c^\dagger + c\right)$. Inserting this operator into Eq. (8.12), we obtain

$$H_{\text{coupling}} \approx \left[E_{\text{SO}}\sin(\phi_{\text{ext}}) - E_{\text{SO}}\phi_{\text{zpf}}\left(c^\dagger + c\right)\cos(\phi_{\text{ext}})\right] \left[\cos(\theta)\sigma_{\overline{x}} + \sin(\theta)\sigma_{\overline{z}}\right] \tag{8.13}$$

$$= E_{\text{SO}}\sin(\phi_{\text{ext}}) \left[\cos(\theta)\sigma_{\overline{x}} + \sin(\theta)\sigma_{\overline{z}}\right] + \hbar J_{\overline{x}}\left(c^\dagger + c\right)\sigma_{\overline{x}} + \hbar J_{\overline{z}}\left(c^\dagger + c\right)\sigma_{\overline{z}}. \tag{8.14}$$

In this expression, we have the transversal and longitudinal coupling strengths

$$\hbar J_{\overline{x}} = E_{\text{SO}}\cos(\phi_{\text{ext}})\phi_{\text{zpf}}\cos(\theta),\ \hbar J_{\overline{z}} = E_{\text{SO}}\cos(\phi_{\text{ext}})\phi_{\text{zpf}}\sin(\theta). \tag{8.15}$$

From fitting the spectroscopy data we find a charging energy of $E_{\text{c}}/h = 284$ MHz and a Josephson energy of $E_{\text{J}}/h = 13.1$ GHz, which results in $\phi_{\text{zpf}} = [2E_{\text{c}}/E_{\text{J,eff}}(\phi_{\text{ext}})]^{1/4} \leq 0.46$ where

$$E_{\text{J,eff}}(\phi_{\text{ext}}) = (E_{\text{J}} + E_0)\sqrt{\cos^2(\phi_{\text{ext}}) + \left(\frac{E_{\text{J}} - E_0}{E_{\text{J}} + E_0}\right)^2 \sin^2(\phi_{\text{ext}})}. \tag{8.16}$$

For $E_{\text{SO}}/h = 309$ MHz, this results on a transverse coupling of up to $J_{\overline{x}}/(2\pi) = 145$ MHz when $\phi_{\text{ext}} = 0$ and the magnetic field is applied perpendicular to the spin-orbit direction. In the fit of Fig. 8.4 we instead find an avoided crossing of $2J_{\overline{x}}/(2\pi) = 2 \times 52$ MHz, corresponding to a Zeeman field at an angle of $\theta = 35.6°$ with respect to the spin-orbit direction.

8.6.2. DEVICE AND EXPERIMENTAL SETUP

DEVICE OVERVIEW

Fig. 8.5 shows an overview of the device including the different elements forming the superconducting circuit used for readout and control of the qubits. The device under investigation in this work is the same as the one used in Chapter 7, where further details about its physical implementation and fabrication can be found.

CRYOGENIC AND ROOM TEMPERATURE MEASUREMENT SETUP

The device was measured in a Triton dilution refrigerator with a base temperature of ≈ 20 mK. Details of the wiring at room and cryogenic temperatures are shown in Fig. 8.6. The setup contains an input radio-frequency (RF) line, an output RF line, an extra RF line for the spin-flip drive tone and multiple direct current (DC) lines, used to tune the electrostatic gate voltages. The DC gate lines are filtered at base temperature with multiple low-pass filters connected in series. The input and drive RF lines contain attenuators and low-pass filters at different temperature stages, as indicated. In turn, the output RF line contains amplifiers at different temperature stages: a travelling wave parametric amplifier (TWPA) at the mixing chamber plate (≈ 20 mK), a high-electron-mobility transistor (HEMT) amplifier at the 4 K stage, and an additional amplifier at room temperature.

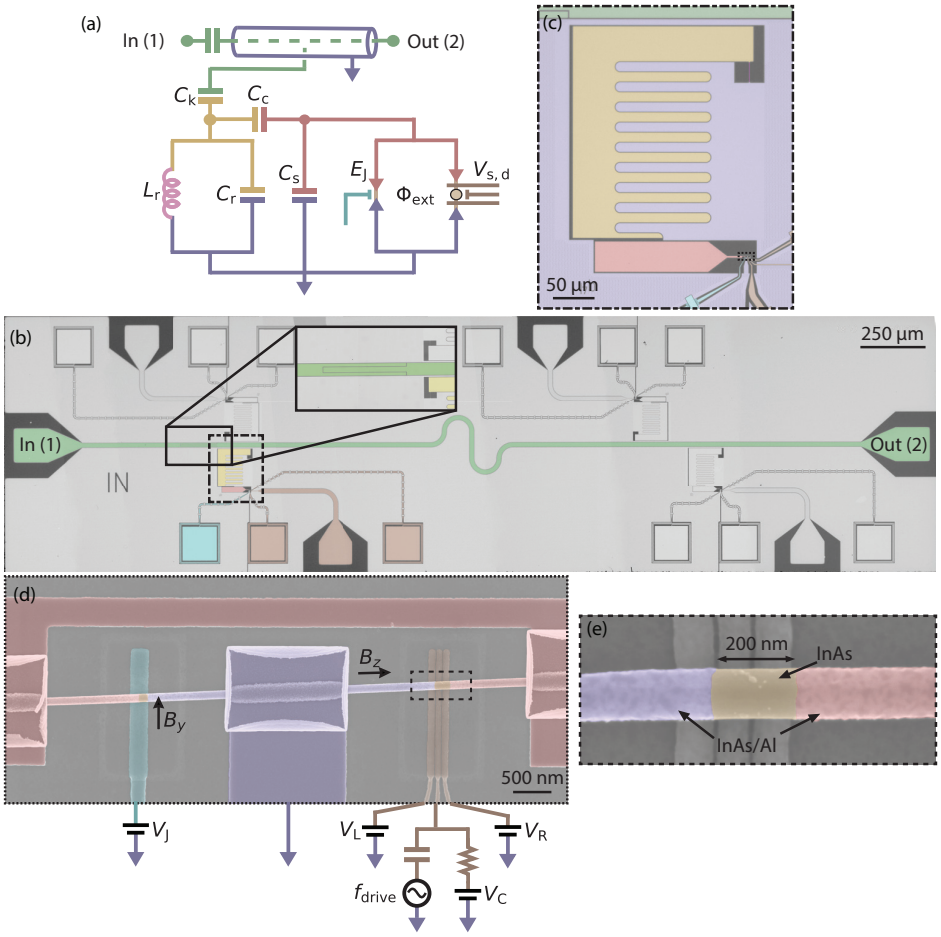

Figure 8.5: **Device overview.** (a) Diagram of the microwave circuit. A coplanar waveguide transmission line with an input capacitor (green center conductor) is capacitively coupled to a grounded LC resonator. The resonator consists of an island (yellow) capacitively and inductively (pink) shunted to ground (blue). The resonator is in turn capacitively coupled to a transmon island (red), which is shunted to ground capacitively as well as via two parallel Josephson junctions. (b) Chip containing four nearly identical devices coupled to the same transmission line, which has a capacitor at its input port, enlarged in the inset. (c) False-colored optical microscope image of the device showing the qubit island, the resonator island, the resonator inductor, the transmission line, the electrostatic gates and ground. (d) False-colored scanning electron micrograph (SEM) of the measured device, showing the InAs/Al nanowire into which the junctions are defined. The B_y component of the magnetic field is used to tune Φ_{ext} (Wesdorp et al., 2022). B_z is the magnetic field component parallel to the nanowire. (e) False-colored SEM of the measured device, showing the junction in which the quantum dot is gate defined. The three bottom gates have a width and spacing of 40 nm, although this is obfuscated by the dielectric layer placed on top.

A three-axis vector magnet (x-axis not shown) is thermally anchored to the 4 K temperature stage, with the device under study mounted at its center. The three magnet coils are controlled with Yokogawa GS610 current sources. At room temperature, a vec-

tor network analyzer (VNA) is connected to the input and output RF lines for spectroscopy at frequency f_r. On the input line, this signal is then combined with the IQ-modulated transmon drive tone at frequency $f_{t,drive}$. A separate IQ-modulated tone at f_r, only used for time-domain measurements, is also combined onto this line. The IQ-modulated spin-flip drive tone at frequency f_{drive} is sent through the drive line. For time-domain measurements the output signal is additionally split off into a separate branch and down-converted to be measured with a Quantum Machines OPX.

BASIC CHARACTERIZATION AND TUNE UP

The basic characterization and tune-up of the device proceeds such as detailed in Chapter 6, while the specific tune-up of the quantum dot resonance investigated in this device is detailed in the supplement of Chapter 7, where it is labeled as resonance A. A brief summary is as follows: We first characterize the gate dependence of the reference junction with the dot fully closed, and fix V_J such that $E_J \gg \sqrt{E_0^2 + E_{SO}^2}$, to ensure the phase drop set by ϕ_{ext} happens mostly at the quantum dot junction. Furthermore, we choose E_J such that the transmon frequency f_t is close to the readout resonator frequency ≈ 6.11 GHz to obtain a large dispersive shift for two-tone spectroscopy and qubit readout. For the results shown in this work, we used $V_J = 3860$ mV. We then investigate the gate dependence of the quantum dot junction with the reference junction fully closed, determining the pinchoff voltages of the three quantum dot gates. Next, we open the reference junction to its gate set-point and explore the quantum dot junction gate space at both $\phi_{ext} = 0$ and $\phi_{ext} = \pi$ to identify regions that show a π-shift in phase. For a given π-shifted region, we measure explicit ϕ_{ext} dependence of the transmon to identify a resonance with a spin splitting comparable to the spin-independent Josephson energy. Finally, we choose a gate set-point in the selected resonance. For the results shown here, the setpoint chosen for the three quantum dot gates was $V_L = 363$ mV, $V_C = 1000$ mV and $V_C = 81$ mV, which corresponds to $V_{T,A} = -423.6$ mV, $V_{P,A} = 909.5$ mV in the rotated gate frame shown in Fig. 7.13 of Chapter 7.

SUMMARY OF DEVICE PARAMETERS

Resonator frequency, f_r	6.084 GHz	Transmon charging energy, E_c/h	284 MHz
Resonator-transmon coupling, g/h	163 MHz	Reference junction Josephson energy, E_J/h	13.1 GHz
Transmon frequency, f_t	5.1 GHz	Transmon Echo time, T_{2E}^t	330 ns
Transmon decay time, T_1^t	251 ns	ASQ E_0/h	211 MHz
Transmon Ramsey time, T_{2R}^t	141 ns	ASQ E_{SO}/h	305 MHz

Table 8.1: Values of relevant device parameters.

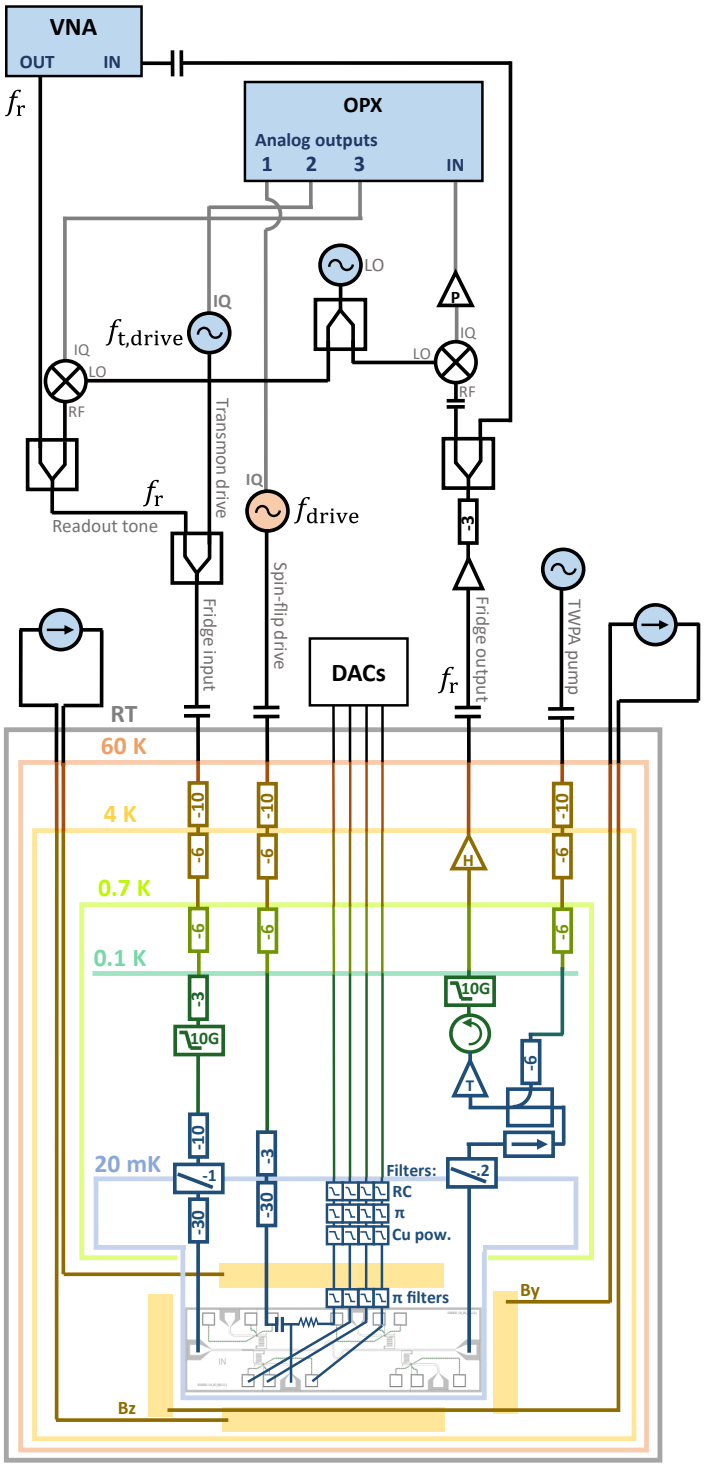

Figure 8.6: Measurement setup at cryogenic and room temperatures.

8.6.3. EXTENDED DATASET

EXTENDED TWO-TONE SPECTROSCOPY DATA

Fig. 8.7 shows extended two-tone spectroscopy measurements at the setpoint of main text Fig. 8.4(b), performed over a range of 20 GHz. It reveals several additional transition frequencies: panels (a) and (b) contain the higher-lying transmon transitions f_{03} and f_{02}, respectively, while panel (c) shows five different transitions. These are the four transitions also shown in Fig. 8.4(b) and, above that, the resonator transition frequency. Panel (d) exhibits two low-frequency transitions: the bright top transition is the direct spin-flip transition with the transmon in its ground state, while the dark lower transition results from the direct spin-flip transition with the transmon in its excited state. The latter transition is visible as a result of a residual excited state population of the transmon. No other auxiliary transitions are found between 0 and 20 GHz, nor does any transition develop for magnetic fields up to 65 mT. We further note that the measurement of panel (d) requires a large drive power (31 dBm more than for the measurement shown in Fig. 8.1 of the main text), and that visibility is reduced compared to panel (c), which is expected since the matrix elements for the EDSR driving is suppressed in the absence of an external magnetic field.

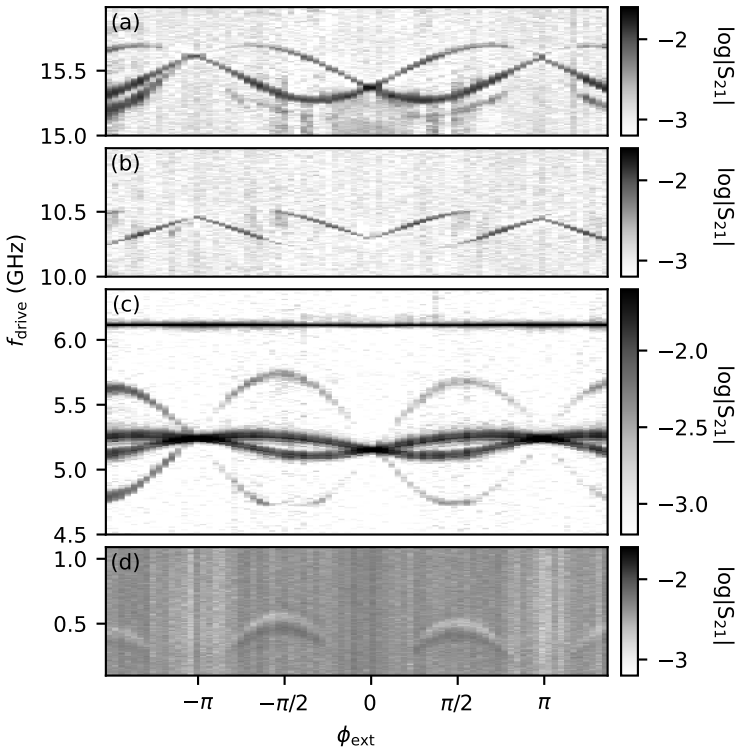

Figure 8.7: Normalized two-tone spectroscopy measurement of the transition spectrum versus external flux. Input power at the top of the spin-flip drive line is −36 dBm for (a-b), −46 dBm for (c) and −6 dBm for (d).

SINGLE SHOT ASSIGNMENT FIDELITY

The time domain measurements in the main text are obtained by averaging over many shots. We now estimate the assignment fidelity of ASQ readout at the setpoint used for the coherence measurements in the main text ($B_z = 65$ mT and $\phi_{\text{ext}} = 3\pi/2$). To do so, we measure the IQ quadrature response of the readout resonator for the qubit prepared in the ground state [Fig. 8.8(a)] and for the qubit prepared in the excited state [Fig. 8.8(b)], after applying an 8-ns π-pulse. In both cases we read out for 500 ns, more than 40 times shorter than T_1, and wait for $5T_1$ between different measurements to let the qubit decay back to its ground state. We find an assignment fidelity of $F = 1 - (P(\downarrow \mid \uparrow) - P(\uparrow \mid \downarrow))/2 = 80\%$ [Fig. 8.8(d)], where $P(a|b)$ denotes the probability of measuring the qubit to be in state a after preparing it in state b. The fidelity is predominantly set by assignment errors for the excited state limited by decoherence during the excitation as the π-pulse duration is comparable to T_2. Longer readout times therefore do not significantly improve the assignment fidelity. However, shorter π pulses would likely lead to improved performance although this experiment was not performed on the current device.

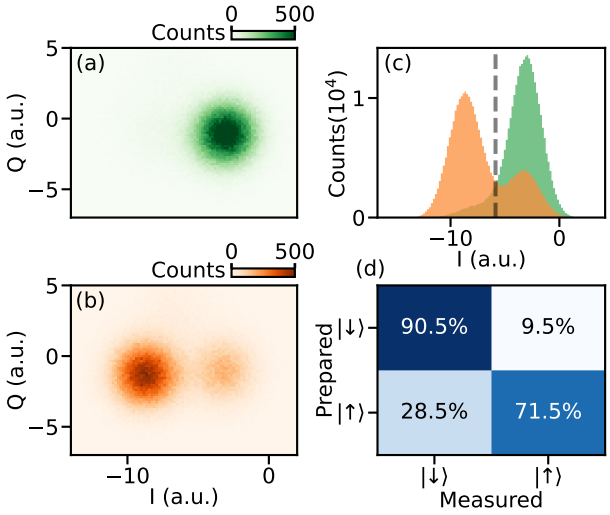

Figure 8.8: Single shot assignment fidelity. (a) Histogram in the complex plane of 3×10^5 sequential shots separated by 200 µs and integrated for 500 ns in the absence of an excitation pulse. (b) Same as (a) in the presence of a π-pulse with a FWHM of 8 ns preceding each shot. (c) Histograms of the I-quadrature response of the preceding panels. Green and orange colors correspond to panels (a) and (b), respectively. (d) Extracted single-shot fidelity's based on the threshold indicated in (c) with a gray dashed line.

PARITY LIFETIME

One of the advantages of using a quantum dot junction over a semiconducting weak link is that the charging energy of the quantum dot allows us to select an operational setpoint for which the doublet states are the lowest energy states of the system (Padurariu and Nazarov, 2010). Therefore, the charging energy is expected to protect against qubit leakage via quasiparticle escape or recombination, which would take the junction outside of the computational space of the qubit. To confirm this protection, we measure the

quasiparticle poisoning times of the junction around the gate setpoint used in the main text.

Shown in Fig. 8.9(a), two resonances are visible as the central quantum dot gate V_C is varied around its setpoint $V_C = 1000\,\text{mV}$, at $\phi_{ext} = 0$. Following the methods of Chapter 6, we identify the outer two V_C regions as having a singlet ground state (spin-zero) and the central region as having a doublet ground state (spin-1/2). For each gate point, we subsequently monitor the transmon circuit in real time and determine the switching time of the quantum dot junction parity. T_s and T_d denote the characteristic times for which the quantum dot maintains a singlet or doublet occupation, respectively. The extracted times are shown in Fig. 8.9(b). Note that this measurement is performed at $\phi_{ext} = 0$, where the $|\uparrow\rangle$ and $|\downarrow\rangle$ states result in equal transmon frequencies, thus becoming indistinguishable using our readout scheme. The spin-flip times T_{spin} are therefore not resolved here, as opposed to the experiments of Ref. (Hays et al., 2020).

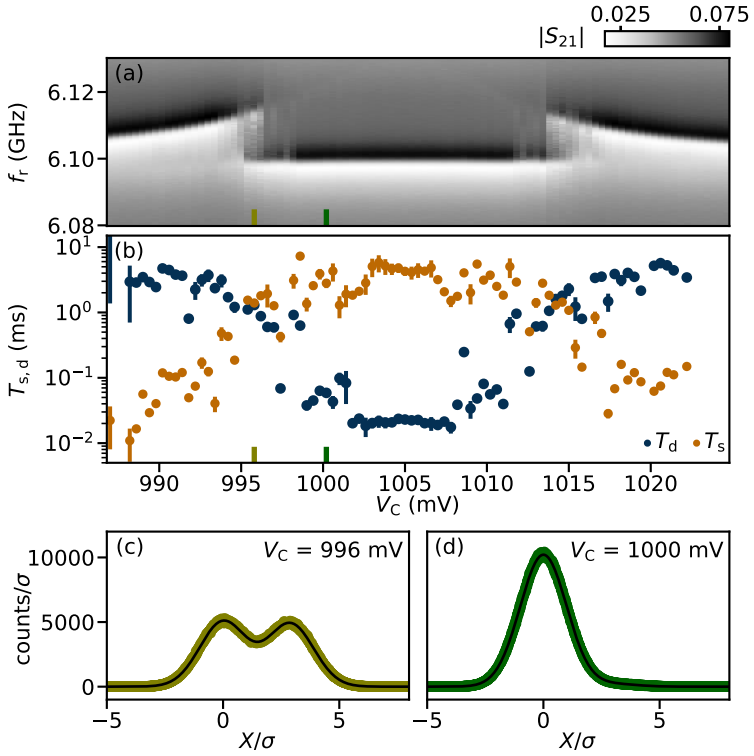

Figure 8.9: Gate dependence of parity lifetimes. (a) V_C dependence of $|S_{21}|$ at $\phi_{ext} = 0$. (b) V_C dependence of the extracted lifetimes. Markers indicate the mean while error bars indicate the maximum and minimum values of 10 consecutive time traces. (c) In yellow, 1D histogram of a continuously measured 17 s-long time trace integrated in time bins of $t_{int} = 4.3\,\mu\text{s}$, at $V_C = 996\,\text{mV}$. In black, best fit to a double Gaussian shape. (d) Same as (c) but at $V_C = 1000\,\text{mV}$.

We observe that, for the outer two regions, where the ground state is the spin-0 state, the doublet switching time T_d ranges from a few µs to hundreds of µs, but is always

much shorter than the singlet switching time T_s. Close to the singlet-doublet ground state transition, both times become similar and of the order of 1 ms, which can be seen in Fig. 8.9(c) for $V_C = 996$ mV, where the histogram of a continuous time trace, integrated in time bins of $t_{int} = 4.3$ µs, shows two Gaussians with equal amplitudes. In the central region, where the doublet states are the lowest energy states, the situation is reversed and, away from the singlet-doublet transition, T_d is consistently above 1 ms. The imbalance between average singlet and doublet occupation is shown in Fig. 8.9(d) for the setpoint used in the main text, $V_C = 1000$ mV. In this case we measure $T_s = 59$ µs and $T_d = 2.8$ ms. The latter is much larger than that of weak-link junctions, typically found to be in the range 10-500 µs (Hays et al., 2018, 2020, 2021; Janvier et al., 2015; Wesdorp et al., 2023), and thus demonstrates the advantage of using a quantum dot junction. In particular, for the weak-link ASQ (Hays et al., 2021) the authors measured a parity lifetime $T_{parity} = 22$ µs and a spin-flip time $T_{spin} = 17$ µs, such that the parity lifetime was a relevant limitation to the qubit T_1. In contrast, we find that $T_d \gg T_1$ such that the lifetime of the ASQ studied in this work is not limited by parity switches.

EXCITED STATE POPULATION

Similar to what is found in previous works investigating the doublet states of SNS junctions (Hays et al., 2020, 2021; Wesdorp et al., 2022), we observe that both $|\uparrow\rangle$ and $|\downarrow\rangle$ of the quantum dot junction are occupied at $B_z = 0$ mT, even in the absence of a drive. As such, we observe simultaneously both of the transmon branches corresponding to each spin state [see Fig. 8.4(b)]. We hypothesize that this residual excited state population is the result of excitations of either thermal or non-equilibrium origin, as the maximum zero-field ASQ transition frequency $f_s \approx 600$ MHz, when expressed in units of temperature ($T_{eff} = h f_s / k_B$, where k_B is Boltzmann's constant), corresponds to an effective temperature scale of $T_{eff} \approx 30$ mK, below the typical electron temperatures found in transport and transmon (Jin et al., 2015) experiments, 35 mK to 100 mK.

To investigate the residual population further, we monitor the transmon circuit in real-time, now at $\phi_{ext} = 3\pi/2$ so that we are maximally sensitive to changes in the spin state. At $B_z = 0$ mT, the IQ histogram of 2.5×10^5 sequential measurements confirms the presence of two populated states, as shown in Fig. 8.10(a). From a double Gaussian fit, we extract a ratio of state occupations of $P(\uparrow)/P(\downarrow) = 0.7$. Upon increasing the qubit frequency f_s with the magnetic field B_z, we find that the excited state population is strongly reduced, in line with expectation [Fig. 8.10(d)]. However, the ASQ frequency first crosses the transmon and then the resonator frequencies between 20 and 30 mT, preventing the measurement of the spin states occupancy over a range of frequencies. Measuring again at $B_z = 65$ mT, where $f_s = 11.53$ GHz, we find at most 4% remaining excited state population, see Fig. 8.10(b). Here, the remaining excited state population is expected to be predominantly due to assignment errors, similar to those found in Fig. 8.8(a).

To extract the effective temperature of the ASQ, we subsequently fit the frequency dependence of the ratio of populations to a Boltzmann distribution,

$$P(\uparrow)/P(\downarrow) = \exp\left(-h f_s/(k_B T_{eff})\right), \tag{8.17}$$

where h and k_B are the Planck and Boltzmann constants, respectively. This leads to reasonable agreement with the data, resulting in an effective temperature of $T_{eff} = 100 \pm 8$ mK [see Fig. 8.10(d)].

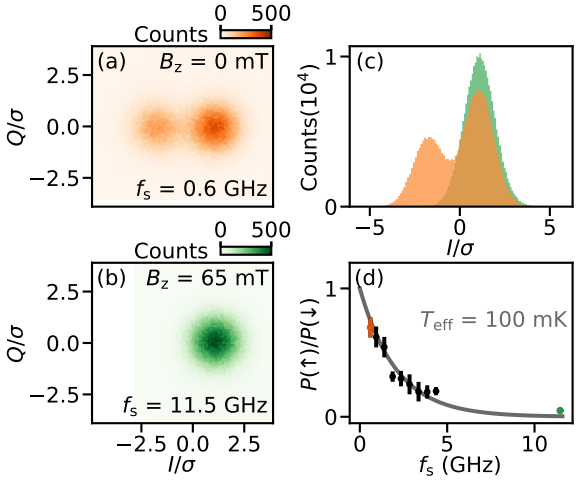

Figure 8.10: Excited state population of the spin states. (a) Histogram in the complex plane of 2.5×10^5 sequential shots, integrated for 500 ns in the absence of an excitation pulse. Measured at $B_z = 0$ mT and $f_s = 0.6$ GHz. (b) Same as (a) at $B_z = 65$ mT and $f_s = 11.5$ GHz. (c) Histograms of the I-quadrature response of the preceding panels (a in orange, b in green). (d) Extracted excited state population versus spin qubit frequency f_s, as tuned with the magnetic field B_z. Data (markers) are fit with a Boltzmann equation (see text) resulting in an effective temperature of 100 mK.

CP DATA

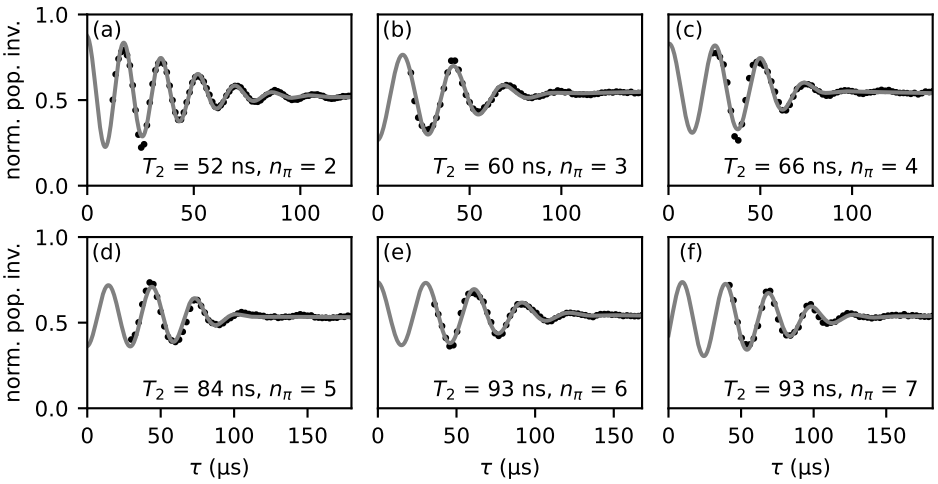

Figure 8.11: Extended CP experiment data. Solid lines indicate fits to the data (see text). All data is normalized to the visibility of a preceding Rabi oscillation measurement, and the data is obtained using a π-pulse ($\pi/2$-pulse) with a FWHM of 4 ns (2 ns). The oscillations are introduced into the decay by adding a phase proportional to the delay time for the final $\pi/2$-pulse.

In this section we provide further data for the CP measurements shown in Fig. 8.3(d)

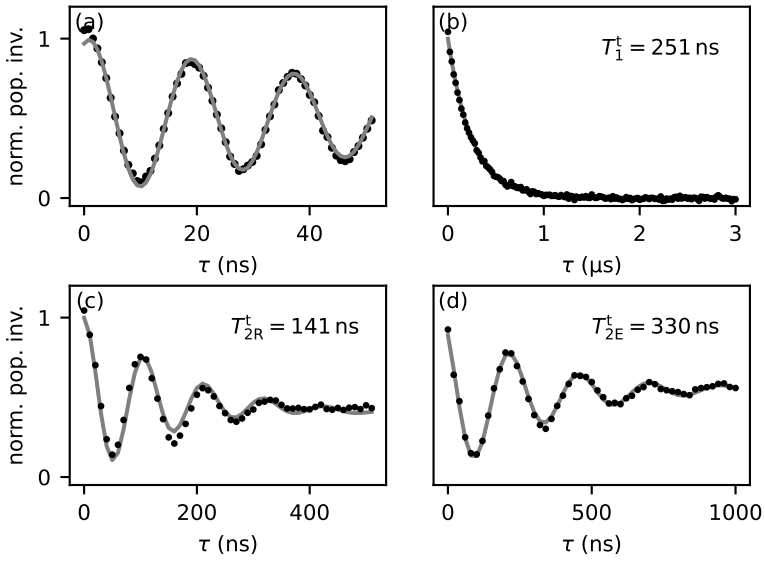

Figure 8.12: Coherence of the transmon qubit at $B_z = 65$ mT. (a) Rabi oscillations, (b) qubit lifetime, (c) Ramsey and (d) Hahn-echo experiments. Solid lines indicate fits to the data. For (c-d) oscillations are introduced into the decay by adding a phase proportional to the delay time for the final $\pi/2$-pulse. We plot the normalized population inversion, where each sub-panel is individually normalized to the resulting fit. $\phi_{\text{ext}} = 3\pi/2$ for all panels.

in the main text. As discussed, the CP sequence is constructed as follows: for each n_π, we apply a $\pi/2$-pulse, followed by n_π equidistant π-pulses and a final $\pi/2$-pulse. All pulses are composed of a Gaussian envelope and have a FWHM of 2 ns and 4 ns for the $\pi/2$- and π-pulses, respectively. The separation between the centers of consecutive π-pulses is τ/n_π and the separation between a $\pi/2$ pulse and its nearest π pulse is $\tau/(2n_\pi)$, resulting in a total delay time τ between the center of the two $\pi/2$ pulses. Fig. 8.11 shows CP measurements for n_π values ranging from 2 to 7, accompanied by a fit to the expression

$$a\cos\left(\tau\Omega - \phi\right)\exp\left(-\left(\tau/T_2\right)^{d+1}\right) + c + e\tau, \tag{8.18}$$

from which we extract the $T_2(n_\pi)$ values reported in Fig. 8.3(d). Note that the maximum waveform generator output power puts a limit on the minimum delay time τ for which the sequence can be generated, as the Gaussian pulses overlap for short delay times compared to the pulse width. This results in the absence of data for short τ in Fig. 8.11.

TRANSMON QUBIT COHERENCE

We characterize the transmon performance at the flux and gate bias point used in the main text using standard time-domain techniques, see Fig. 8.12.

ASQ COHERENCE VERSUS CONTROL PARAMETERS

In this section we provide additional data showing the dependence of the ASQ lifetime and coherence times on different control parameters. They are extracted by fitting their respective time evolutions using the same expressions employed in Fig. 8.3 of the main text:

$$T_1: \quad a\exp\left(t/T_1\right)+c \tag{8.19}$$

$$T_{2R}: \quad a\cos\left(t\Omega-\phi\right)\exp\left(-\left(t/T_{2R}\right)^{d+1}\right)+c \tag{8.20}$$

$$T_{2E}: \quad a\cos\left(t\Omega-\phi\right)\exp\left(-\left(t/T_{2E}\right)^{d+1}\right)+c+et \tag{8.21}$$

Here, a, c, d, e, ϕ, Γ, T_1, T_{2R} and T_{2E} are fit parameters. For T_{2R} and T_{2E}, Ω accounts for the combination of detuning and the oscillations introduced by adding a phase proportional to the delay time for the final $\pi/2$-pulse.

ASQ LIFETIME VERSUS MAGNETIC FIELD

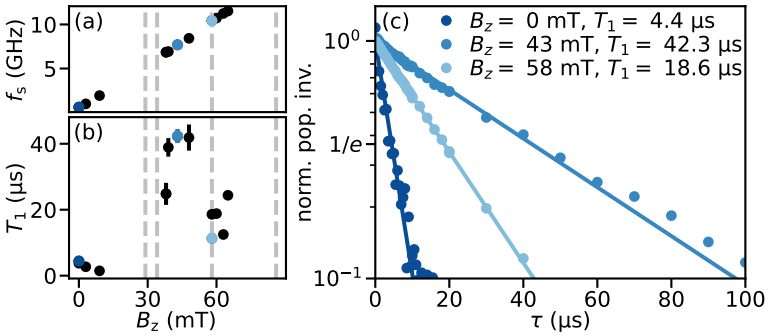

Figure 8.13: (a) Spin qubit frequency, f_s, as a function of magnetic field, B_z. (b) Spin qubit lifetime, T_1 as a function of magnetic field. Dashed lines in (a-b) indicate the magnetic fields at which f_s crosses the first three transmon frequencies f_{0j} and the resonator frequency [c.f. Fig. 8.7]. (c) Representative qubit lifetime measurements, fit with an exponential decay.

We start by investigating the evolution of the ASQ lifetime T_1 versus magnetic fields between 0 and 65 mT. As shown in Fig. 8.13(b), the qubit lifetime varies strongly, from around 1 μs close to zero magnetic field and up to 40 μs at intermediate fields, before once-more decreasing to approximately 20 μs. For intermediate magnetic fields between 15 mT and 35 mT, the measurement of the qubit lifetime is hindered by the vicinity to the transmon and resonator transition frequencies. In this region it is not possible to drive the ASQ independently as, due to the capacitance between the gate drive line and the transmon island, the transmon qubit is also excited. This simultaneous driving of both qubits impedes the distinction of the response coming from each of them.

The strong reduction of T_1 at low fields is potentially due to resonant exchange with the nuclear spins in InAs (Stockill et al., 2016); given the large g-factor of the ASQ, this process only takes places at low magnetic fields. This is supported by the finding that at elevated magnetic fields, in the range 45 mT to 50 mT, we find the ASQ lifetime to exceed

40 µs. Further investigation would be needed to determine the origin of the magnetic field dependence of T_1 near zero field. At even higher fields we observe a drop of the lifetime to around 20 µs. As discussed in the main text, we conjecture the ASQ lifetime found in these regimes is limited by Purcell-like decay from coupling to the transmon, given the short transmon lifetime of around 250 ns [Fig. 8.12(b)].

To support the assertion that the reduction in the ASQ lifetime for qubit frequencies in the proximity of the transmon transitions is due to Purcell-like decay, we investigate whether the transmon lifetime is enhanced by proximity to the ASQ. Fig. 8.14 shows the transmon lifetime T_1^{t} for three different detunings between transmon and ASQ. When the qubits are detuned from each other, we measure $T_1^{\mathrm{t}} \approx 250$ ns. However, when the transmon is resonant with the ASQ, its lifetime is enhanced by almost factor of two, reaching 470 ± 5 ns. This is consistent with hybridization of the two qubits, given that $T_1^{\mathrm{s}} \gg T_1^{\mathrm{t}}$, and supports that the lifetime of the ASQ can be decreased by vicinity to the transmon modes. These findings furthermore compliment the the observations discussed surrounding main text Fig. 8.4, serving as an additional signature of coherent coupling.

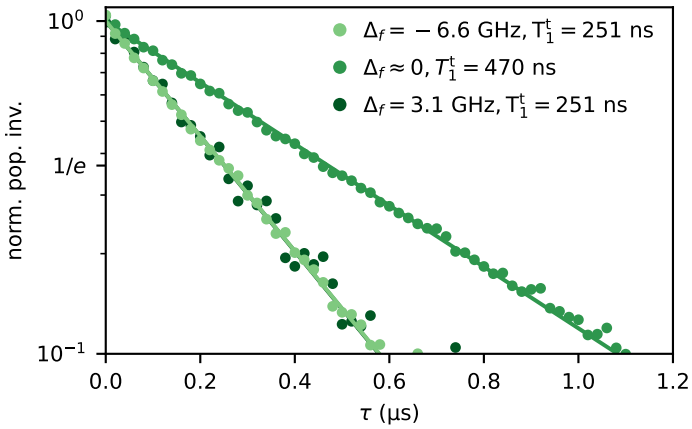

Figure 8.14: Transmon qubit lifetime T_1^{t} at $\phi_{\mathrm{ext}} = 3\pi/2$ and as a function of detuning $\Delta_f = f_{\mathrm{t}} - f_{\mathrm{s}}$ from the spin qubit frequency as tuned with the magnetic field. Detunings $\Delta_f = 3.1$, 0 and -6.6 GHz correspond to $B_z = 9$, 28 and 65 mT, respectively.

INDEPENDENCE OF ASQ COHERENCE ON GATE VOLTAGES, MAGNETIC FIELD AND FLUX

We investigate the effect of different sources of noise by measuring the dependence of the $T_{2\mathrm{R}}$ and $T_{2\mathrm{E}}$ coherence times on gate voltage, magnetic field, and flux.

The B_z dependence of coherence times is shown in Fig. 8.15(a), for which we do not observe a measurable dependence over the B_z range investigated. Therefore charge noise is likely not the dominant contribution to qubit dephasing since, if it was the case, an increase in B_z would increase the effectiveness of EDSR at coupling charge noise to the qubit, which would result on a reduction of the decoherence times. In contrast, this B_z-independence of coherence times is compatible with nuclear magnetic noise being a strong contribution to qubit dephasing; due to the small magnetic moment of the nuclei

spin, a magnetic fields of 65 mT do not yet lead to a significant nuclear splitting. As a result of this we do not reach the regime of strong nuclear spin polarization, such that the precession of the nuclear bath in the external fields still leads to a significant Overhauser field for the range of fields explored. Additionally, the Overhauser field could have a field-independent component originating from the quadrupolar coupling of the nuclei to electric field gradients, induced by strain in the nanowire (Krogstrup et al., 2015; Stockill et al., 2016). A more complete understanding of the system will require further investigation.

Next, we consider the dependence of coherence times on the external flux ϕ_{ext}. As shown in Fig. 8.15(b), we again do not find a pronounced dependence of the coherence times. In particular, we do not observe an increase of the T_2 times near the sweet spots at $\phi_{\text{ext}} = \pm\pi/2$. From this we conclude that flux noise does not strongly contribute to dephasing.

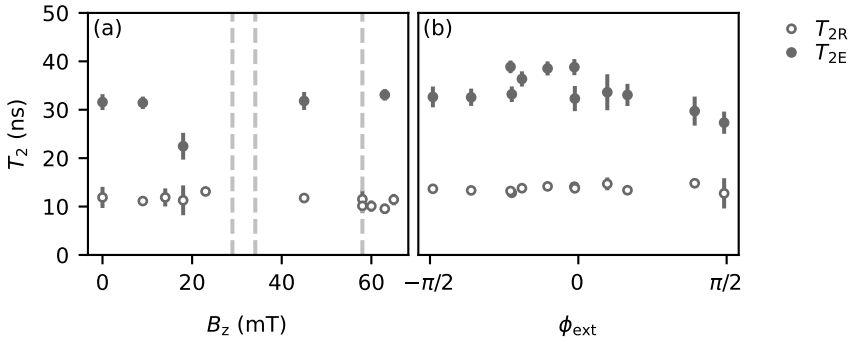

Figure 8.15: Dependence of the spin qubit coherence on the external magnetic field (a) and the external flux (b). The dashed lines in (a) indicate the magnetic fields at which f_s crosses the transmon transition frequencies f_{01} and f_{02} as well as the resonator frequency.

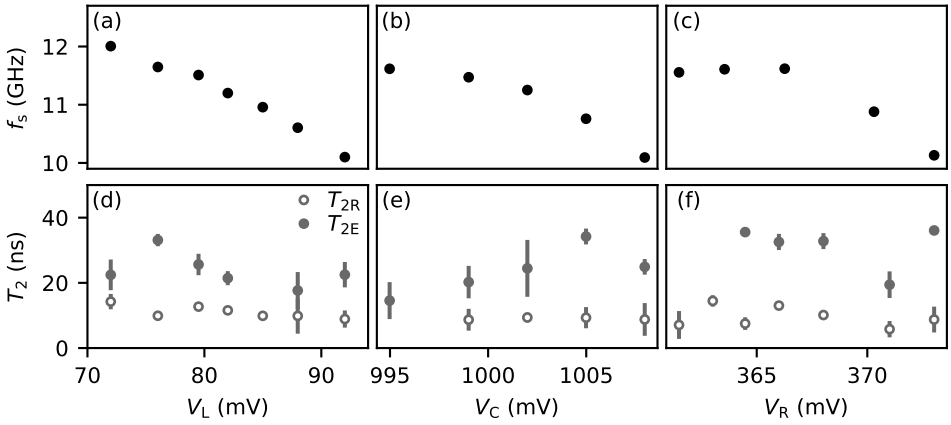

Figure 8.16: Dependence of the spin qubit coherence on the three quantum dot gates. (a-c) Spin qubit frequency versus gate voltage. (d-f) Ramsey and Hahn echo T_2 times versus gate voltage.

Finally we investigate the dependence of coherence times on the voltages applied to the three gate electrodes situated underneath the quantum dot junction [see Fig. 8.5(e)]. As shown in Fig. 8.16, we do not find a clear correlation between $T_{2\mathrm{R}}$ or $T_{2\mathrm{E}}$ and the slope of the qubit frequency versus any of the three gate voltages. This indicates that voltage noise also does not provide a large contribution to the dephasing rate. However, although we measure T_2 in the vicinity of the available sweet spots of the individual gate electrodes, we did not find a simultaneous sweet spot for all three quantum dot gates, and the effect of voltage noise cannot be entirely ruled out. Further investigation of the qubit's susceptibility to voltage and magnetic noise based on the Rabi decay times are discussed in the next section.

ESTIMATING THE AMPLITUDE OF CHARGE AND MAGNETIC NOISE FLUCTUATIONS

A method for estimating upper bounds on the amplitude of fluctuations originating from different noise sources is provided in Ref. (Malinowski et al., 2017), where the authors study the relation between the Rabi frequency, $f_{\mathrm{R}} = \Omega_{\mathrm{R}}/2\pi$, and the Rabi decay time, T_{R}. These quantities, respectively shown in Figs. 8.17(a) and (b), can be extracted from a fit to the Rabi signal with the expression $a\cos(t\Omega_R)\exp(\mathrm{t}/\mathrm{T_R}) + c$, where t denotes the full-width half maximum of the applied Gaussian pulse, see Fig. 8.2. We fit the extracted decay times to the model of Ref. (Malinowski et al., 2017)

$$\left(\frac{1}{T_{\mathrm{R}}}\right)^2 = \frac{\sigma_f^4}{4f_{\mathrm{R}}^2} + C^2 f_{\mathrm{R}}^2, \tag{8.22}$$

where σ_f is the standard deviation of the fluctuations of the qubit frequency f_{s} due to noise in the control and model parameters and C is a measure of noise of the drive field. The data is fitted up to the region where the Rabi frequency stops being linear as a function of the pulse amplitude A, indicated with grey markers in Fig. 8.17, and extract $\sigma_f = 39.7\,\mathrm{MHz}$ and $C = 0.25$.

If we assume that the dominating contribution to σ_f originates from noise in just one control parameter, we can obtain upper bounds on the noise amplitude for various types of noise. Since the coherence time is mostly independent on the external flux [Fig. 8.15], we focus only on two possible origins of decoherence: voltage noise and nuclear magnetic noise. We first determine the susceptibility of the qubit frequency with respect to the external parameters (V_{L}, V_{C}, V_{R}, $B_\parallel$ and $B_\perp$) at the ASQ operational setpoint, calculated as the partial derivatives of the qubit frequency with respect to each parameter. From two-tone spectroscopy measurements, we find the susceptibilities with respect to the left, central and right quantum dot gates of $S_{\mathrm{L}} \approx 0.16\,\mathrm{GHz/mV}$, $S_{\mathrm{C}} \approx 0.07\,\mathrm{GHz/mV}$ and $S_{\mathrm{R}} \approx 0.08\,\mathrm{GHz/mV}$, respectively, and the susceptibilities to the parallel and perpendicular magnetic fields of $S_\parallel \approx 0.18\,\mathrm{GHz/mT}$ and $S_\perp \approx 0.05\,\mathrm{GHz/mT}$, respectively.

We start by evaluating the contribution of voltage noise on the DC lines. Considering noise from the gate with highest susceptibility we obtain an upper bound of $\sigma_{\mathrm{L}} < \sigma_f/S_{\mathrm{L}} = 0.25\,\mathrm{mV}$ for the standard deviation of the gate voltage fluctuations. While this agrees with the gate noise observed in Ref. (Hays et al., 2021), where the estimated standard deviation of the voltage gate fluctuations was $\sigma_V = 0.24\,\mathrm{mV}$, we do not expect fluctuations of this magnitude to be present in our system. Previous experiments measured in the same experimental setup [Fig. 8.6] observed gate stability below 60 μeV for similar

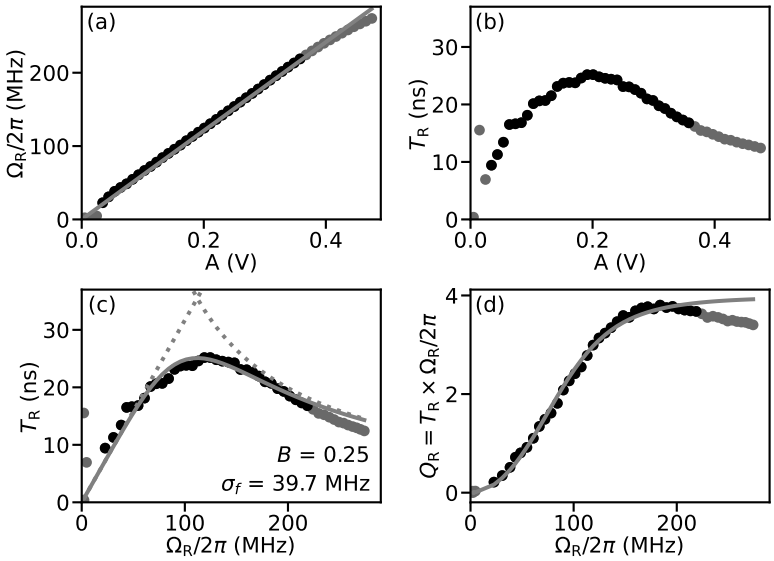

Figure 8.17: (a) Rabi frequency versus pulse amplitude (markers) and fit to a linear dependence (line). Same data as in Fig. 8.2. (b) Rabi decay time versus pulse amplitude (markers). Grey markers denote the points for which the data deviates from the linear dependence in (a). (c) Rabi decay time versus Rabi frequency (markers) an result of a fit of the black markers to Eq. 8.22 (continuous line). The dotted lines show the individual contributions of the two summands in Eq. 8.22. (d) Rabi quality factor $Q = T_R f_R$ versus Rabi frequency (markers) and result of the same fit as in (c) (line).

device geometries (Bargerbos et al., 2020). Furthermore, the DC lines used to control the gate electrodes are strongly filtered with a sequence of 9 kHz RC filters, 80 MHz to 5 GHz π filters and, finally, custom made copper powder filters, all mounted at the mixing chamber stage. and an additional set of 80 MHz π filter on the printed circuit board. The left and right gates additionally have first order LC filters on-chip, with an expected cutoff frequency of 200 MHz. We therefore suspect that the dominant contribution to σ_f does not arise from gate voltage fluctuations on the DC lines. However, charge fluctuations on the device, unrelated to the gate control, could still limit the coherence time.

Alternatively, the gate voltage noise could originate from the RF drive line connected to the central gate electrode. This would result in an upper bound to gate voltage noise of $\sigma_C < \sigma_f / S_C = 0.57$ mV, which corresponds to an effective power of -53 dBm at the sample. Given the -55 dB attenuation of the drive line [Fig. 8.6], this would correspond to a noise power of 2 dBm at the fridge input, which we consider implausible. Furthermore, the RF line is connected via both a DC block and a bias tee, providing strong high-pass filtering.

Next, we consider the contribution of nuclear magnetic noise. We estimate upper bounds to the longitudinal and transverse magnetic fluctuations of $\sigma_\parallel < \sigma_f / S_\parallel = 0.22$ mT and $\sigma_\perp < \sigma_f / S_\perp = 0.80$ mT, respectively. These estimates are comparable to the values obtained for InAs and InSb spin-orbit qubits in previous works: $\sigma_B = 0.66$ mT (Nadj-Perge et al., 2010) and $\sigma_B = 0.16$ mT (van den Berg et al., 2013), respectively. Nuclear

magnetic noise is therefore a plausible dominating contribution to the dephasing observed in the ASQ. However, we emphasize that these calculations are only an estimate and that further investigation is needed to discern between the different possible causes of dephasing.

VIRTUAL-PHOTON-MEDIATED ASQ–RESONATOR COUPLING

In this section we provide additional data showing coherent coupling between the readout resonator and the Andreev spin qubit. As shown in Fig. 8.18, we observe avoided crossings between the ASQ and resonator transitions when they are on resonance, at B_z = 36.5 mT. This coherent coupling is of note, as the ASQ and readout resonator are not directly coupled. However, both are directly and strongly coupled to the transmon qubit, detuned by 900 MHz in this case, which mediates a strong virtual coupling. This effect is analogous to the work of Ref. (Landig et al., 2019) where, instead, a resonator mediated virtual coupling between a transmon and a spin qubit.

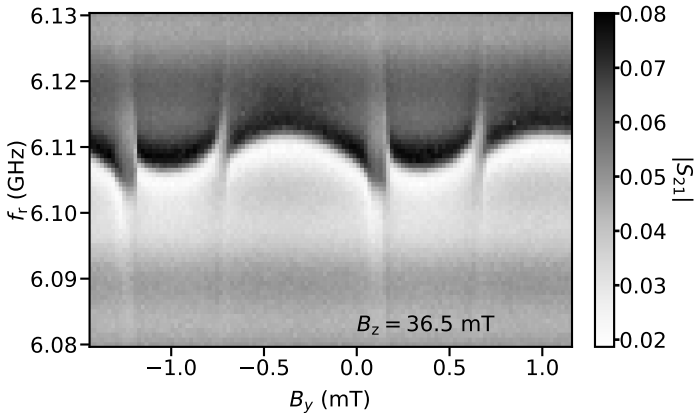

Figure 8.18: Single-tone spectroscopy of the readout resonator versus the magnetic field in the chip plane and perpendicular to the nanowire, B_y, for B_z = 36.5 mT.

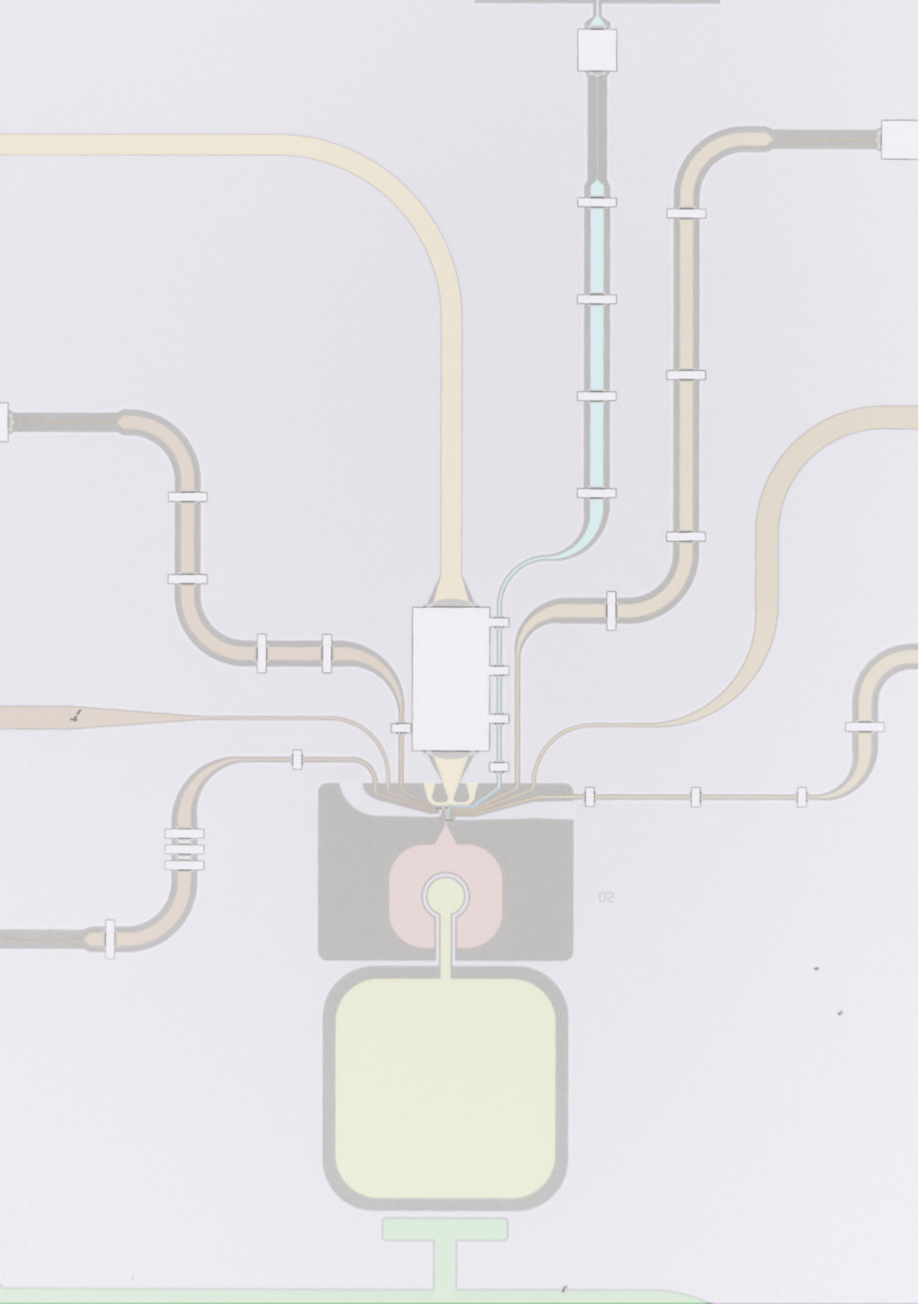
D2

9

STRONG TUNABLE COUPLING BETWEEN TWO DISTANT SUPERCONDUCTING SPIN QUBITS

Superconducting (or Andreev) spin qubits have recently emerged as an alternative qubit platform with realizations in semiconductor-superconductor hybrid nanowires (Hays et al., 2021) (see Chapter 8). In these qubits, the spin degree of freedom is intrinsically coupled to the supercurrent across a Josephson junction via the spin-orbit interaction, which facilitates fast, high-fidelity spin readout using circuit quantum electrodynamics techniques (Hays et al., 2020). Moreover, this spin-supercurrent coupling has been predicted to facilitate inductive multi-qubit coupling (Chtchelkatchev and Nazarov, 2003; Padurariu and Nazarov, 2010). In this work, we demonstrate a strong supercurrent-mediated coupling between two distant Andreev spin qubits. This qubit-qubit interaction is of the longitudinal type and we show that it is both gate- and flux-tunable up to a coupling strength of 178 MHz. Finally, we find that the coupling can be switched off in-situ using a magnetic flux. Our results demonstrate that integrating microscopic spin states into a superconducting qubit architecture can combine the advantages of both semiconductors and superconducting circuits and pave the way to fast two-qubit gates between remote spins.

The work in this chapter is currently under peer review and is available at: **M. Pita-Vidal**[*], J. J. Wesdorp[*], L. J. Splitthoff, A. Bargerbos, Y. Liu, L. P. Kouwenhoven, and C. K. Andersen, Strong tunable coupling between two distant superconducting spin qubits, arXiv:2307.15654. [*] Equal contributions.

Semiconducting spin qubits (Hanson et al., 2007; Loss and DiVincenzo, 1998) have proven to be a promising platform for quantum information processing. In such qubits, quantum information is encoded in the spin degree of freedom of electrons or holes localized in quantum dots, which leads to long lifetimes and a naturally large energy separation between computational and non-computational states. Moreover, their small size makes them attractive candidates for large-scale quantum devices (Burkard et al., 2023; Vandersypen et al., 2017). However, it remains challenging to engineer a direct spin-spin coupling between remote spin-qubits as their interaction strength decays rapidly with distance. Ongoing efforts to overcome this challenge focus on engineering a coupling between distant spin-qubits mediated by microwave photons in superconducting resonators (Borjans et al., 2020; Harvey-Collard et al., 2022; Landig et al., 2018; Mi et al., 2018; Samkharadze et al., 2018; Yu et al., 2023). For such photon-mediated spin-spin coupling, the interaction strength is currently limited to the order of 10 MHz, which makes the implementation of fast, long-range two-qubit gates an outstanding challenge (Burkard et al., 2023; Harvey-Collard et al., 2022). Moreover, the transverse character of the coupling puts a constraint on the available qubit frequencies.

An alternative approach to engineer remote spin-spin coupling is to embed the spin-qubit into a Josephson junction creating a so-called Andreev spin qubit (ASQ) (Hays et al., 2021), where the qubit states carry a spin-dependent supercurrent (Hays et al., 2020, 2021; Tosi et al., 2018; Wesdorp et al., 2022; Wesdorp et al., 2023), as discussed in Chapters 7 and 8. Recent experiments have demonstrated that a single ASQ can be operated coherently with strong coupling of the spin states to superconducting circuits (Hays et al., 2021) (see Chapter 8). Similarly, it has been predicted that large spin-dependent supercurrents can lead to strong, longitudinal, long-range and tunable spin-spin coupling (Chtchelkatchev and Nazarov, 2003; Padurariu and Nazarov, 2010), thus, overcoming the challenges imposed by the coupling being only a second-order interaction in previous photon-mediated implementations of spin-spin coupling as well as circumventing any strong constraints on the qubit frequencies.

Here, we investigate the supercurrent-mediated coupling between two ASQs by analyzing the influence of a shared Josephson inductance on the coupling strength using the setup in Fig. 9.1. Specifically, we design a device formed by two Andreev spin qubits, ASQ1 and ASQ2, connected in parallel to a third Josephson junction with gate-tunable Josephson inductance, thus defining two superconducting loops (Fig. 9.1a). Microscopically, the longitudinal coupling between the qubits directly results from the main characteristic of Andreev spin qubits: their spin to supercurrent coupling. The phase-dependent frequency of one qubit results in a spin-state-dependent circulating supercurrent through the loop arm containing the other qubit. We show that the qubit-qubit coupling in this configuration can be in-situ controlled by the flux through the superconducting loops as well as by changing the Josephson inductance of the shared junction using an electrostatic gate. In particular, we reach the strong longitudinal coupling regime where the coupling strength is larger than the qubit linewidths. Moreover, we show that the coupling can be switched fully off for particular values of the flux, which makes this platform appealing as an alternative for implementing fast flux-controlled two-qubit gates between spin qubits.

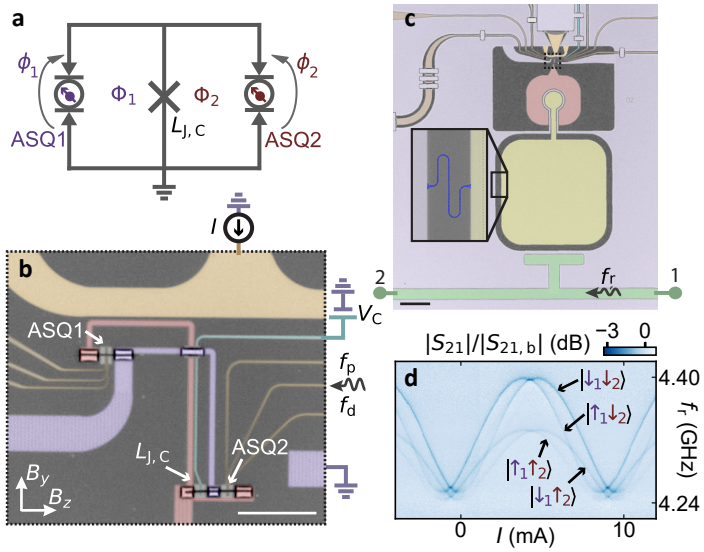

Figure 9.1: **Device and readout. a** Circuit diagram of two coupled Andreev spin qubits (ASQ1 and ASQ2) connected to a coupling junction with a tunable Josephson inductance $L_{J,C}$. Φ_1 and Φ_2 are the magnetic fluxes through the two loops. **b** False-colored optical microscope image of the device. The ASQs are placed between a transmon island (red) and ground (purple). The three Josephson junctions are implemented in two separate Al/InAs nanowires, with one containing ASQ1 and the other containing ASQ2 and the coupling junction. The in-plane magnetic field directions are denoted as B_z and B_y, approximately parallel and perpendicular to the nanowires axis, respectively. Additional flux control is achieved through the applied current I in the flux line (amber). Each ASQ is electrostatically controlled by three gates below the nanowire (brown), while the coupling junction is controlled by one gate line (cyan). The drive tones f_d and f_p are applied through the central gate of ASQ2. See Sec. 9.6 for further details about the geometry of the loops area. **c** Zoomed out false-colored optical microscope image showing the transmon island (red) capacitively coupled to a lumped-element readout resonator, consisting of a capacitor (yellow) and an inductor (blue, inset). The resonator is further capacitively coupled to a coplanar waveguide (green center conductor) with input and output ports labeled as 1 and 2, respectively. A readout tone f_r is applied through the waveguide. Scale bars in **b** and **c** correspond to 10 µm and 100 µm, respectively. **d** Amplitude of the transmission through the readout circuit, $|S_{21}|$, divided by the background, $|S_{21,b}|$, as a function of the current through the flux line, I. The measurement is performed at a magnetic field of $B_z = 0$ with a fixed $\Phi_2 \sim -\Phi_0/4$, set by $B_y = -1.04$ mT.

9.1. DEVICE

In our device, each ASQ is hosted in a quantum dot Josephson junction which is implemented in a separate Al/InAs nanowire and controlled by three electrostatic gates placed beneath the nanowires (Fig. 9.1b). Throughout this work, the gate voltages are fixed as specified in Sec. 9.6. Moreover, we define an additional regular Josephson junction with gate-tunable Josephson inductance $L_{J,C}$ in one of the nanowires. The nanowires are galvanically connected to a NbTiN circuit which defines the superconducting loops forming a double-loop superconducting quantum interference device (SQUID). We denote by Φ_1 and Φ_2 the external magnetic fluxes through each of the loops. The qubit frequency for ASQi, f_i, where $i = 1,2$, is set by the energy difference between the spin-states, $|\uparrow_i\rangle$ and $|\downarrow_i\rangle$, which is controlled by the magnetic field due to the Zeeman effect. We denote the in-plane magnetic field directions as B_z, approximately along the nanowires, and B_y,

approximately perpendicular to the nanowires. See also Sec. 9.6 for additional details on the field alignment. The B_y component of the magnetic field is moreover used to tune Φ_1 and Φ_2. Note that, while B_y is applied in the chip plane, it still threads flux through the loops due to the elevation of the nanowires with respect to the NbTiN circuitry. This reduces flux jumps compared to using out-of-plane field B_x for flux tuning, as discussed in Ref. (Wesdorp et al., 2022). Φ_1 and Φ_2 set the phase drops over the junctions, $\phi_1 \sim \frac{2\pi}{\Phi_0}\Phi_1$ and $\phi_2 \sim \frac{2\pi}{\Phi_0}\Phi_2$ in the limit of small $L_{J,C}$, where Φ_0 denotes the magnetic flux quantum. The current through the flux line, I, tunes Φ_1 and leaves Φ_2 nearly unaffected, as the loop corresponding to Φ_2 is placed near the symmetry axis of the flux line (see Sec. 9.6). The drive pulses, with frequencies f_d and f_p, are sent through the central gate of ASQ2 and are used to drive both qubits. We find that it is possible to drive ASQ1 using the gate line of ASQ2 possibly due to cross-coupling between the gate lines corresponding to both qubits or to cross-coupling between the gate line and the transmon island. The coupling junction is controlled by a single electrostatic gate whose voltage, V_C, is varied to tune $L_{J,C}$ (Doh, 2005).

To enable readout of the ASQ states, the double-loop SQUID in which the ASQs are hosted is placed between a superconducting island (red) and ground (purple), forming a transmon circuit (de Lange et al., 2015; Koch et al., 2007; Larsen et al., 2015) (Fig. 9.1b, c). These circuit elements are implemented in 20 nm-thick NbTiN for magnetic field compatibility (Kringhøj et al., 2021; Kroll et al., 2018, 2019; Samkharadze et al., 2016; Uilhoorn et al., 2021; Wesdorp et al., 2022) (see Chapter 5). The transmon frequency depends on the energy-phase relation of the double-loop SQUID, which in turn depends on the states of both ASQs, as discussed in Chapter 7. The transmon is subsequently dispersively coupled to a lumped element readout resonator, which is coupled to a feedline implemented with a coplanar waveguide and monitored in transmission using a probe tone at frequency f_r. The readout mechanism is illustrated in Fig. 9.1d, which shows the four possible frequencies of the readout resonator, caused by the different dispersive shifts of the four spin states of the combined ASQ1-ASQ2 system (Blais et al., 2004): $\{|\uparrow_1\uparrow_2\rangle, |\uparrow_1\downarrow_2\rangle, |\downarrow_1,\uparrow_2\rangle, |\downarrow_1\downarrow_2\rangle\}$. Note that spin is not a well defined quantum number for these states[1]. The measurement is taken at zero magnetic field where all spin states are thermally occupied on average, since the energy splitting between them is between 0.5 and 1 GHz (see Sec. 9.6), which is smaller than typical effective temperatures on the order of 100 mK observed in these devices (see Chapter 8). Therefore, the lines corresponding to all four states are visible. This result already illustrates the presence of two separate ASQs in the system. We will now move on to the characterization of these qubits before we turn our attention to the two-qubit coupling.

9.2. INDIVIDUAL ANDREEV SPIN QUBIT CHARACTERIZATION

We first characterize each ASQ separately, while the junction containing the other qubit is pinched-off electrostatically using the voltages on its gates (Fig. 9.2), following the methods of Chapter 8. To set the qubit frequencies, we apply a magnetic field $B_r = 35$ mT

[1] In an ASQ, the spin is hybridized with spatial degrees of freedom, and thus the eigenstates are rather pseudo-spin states. Similar to previous works (Hays et al., 2021) and Chapter 8, we will refer to the eigenstates as spins for simplicity.

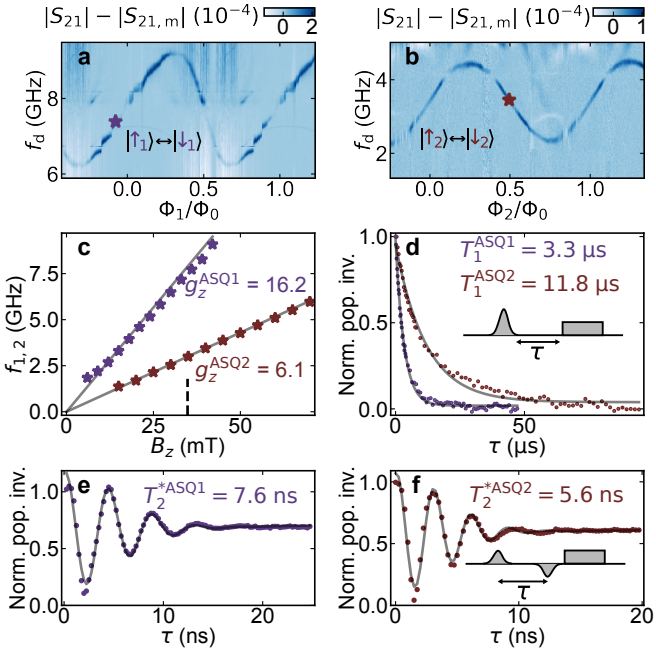

Figure 9.2: **Individual Andreev spin qubit properties**. **a, b** Readout signal amplitude with the median background subtracted, $|S_{21}| - |S_{21,\mathrm{m}}|$, showing qubit spectroscopy of ASQ1 (versus Φ_1) and ASQ2 (versus Φ_2), respectively. During spectroscopy of one qubit, the other qubit is turned off by setting its gates to -1 V. We set $B_r = 35$ mT for both panels (indicated in **c** with a dashed line). **c** Qubit frequency versus B_z for both ASQs. f_i is calculated as the average between its maximum and minimum values versus flux. The grey lines indicate a linear fit to the data from which we extract the g-factors indicated in the labels. **d** Energy decay time (T_1) measurements of both ASQs at the frequency setpoints indicated in **a**, **b** ($f_1 = 7.4$ GHz and $f_2 = 3.4$ GHz, respectively). The experiment was performed by sending a π-pulse followed, after a delay τ, by a readout pulse (see inset). **e**, **f** Measurements of the coherence times (T_2^*) of ASQ1 and ASQ2 at the same setpoints, measured using a Ramsey experiment. Oscillations with a period of 4 ns (for **e**) and 3 ns (for **f**) are realized by adding a phase to the final $\pi/2$ pulse proportional to the delay time τ. The pulse sequence is shown in the inset for a phase of π. T_2^* is extracted by fitting a sine with a Gaussian decay envelope. The experiments were performed using Gaussian pulses with a FWHM of 4 ns. All datasets are averaged over $3 \cdot 10^5$ shots, readout time ranges from 1 to 2 µs and the total measurment time for $T_2^{*,\mathrm{ASQ}i}$ ranges from around 10 min for ASQ1 to around 30 min for ASQ2. The normalized population inversion on the y-axis of panels **d**-**f** is defined as the the measured signal normalized by the signal difference between having sent no pulse and a π-pulse before the readout pulse.

in the y-z plane, 0.1 radians away from the B_z direction (see Sec. 9.6). This field sets $f_1 \in [6, 9]$ GHz and $f_2 \in [2, 4.5]$ GHz for ASQ1 and ASQ2, respectively. We note that the qubit frequencies are significantly different due to mesoscopic fluctuations in the gate-dependence of the spin-orbit direction and g-factor of each ASQ, see also Fig. 9.2 and Sec. 9.6. Qubit spectroscopy is then performed by monitoring the transmission through the feedline near the readout-resonator frequency, while applying a drive tone with frequency f_d to the central gate line of ASQ2, see Fig. 9.2a, b. On resonance with the qubit transition, we observe a strong change in transmission because spin-orbit coupling and a magnetic field enable electrical driving of the spin (Metzger et al., 2021; Wesdorp et al.,

2022), as discussed in Chapter 7. The qubit frequencies, f_1 and f_2, can be tuned by flux, as shown in Fig. 9.2a and b. Note that the phase dispersion is expected to be sinusoidal, see Ref. (Padurariu and Nazarov, 2010; Pavešić et al., 2023b), as is the case for ASQ2. However, for ASQ1 we rather observe a skewed sine. From the ratio of the inductance of ASQ1 and $L_{J,C}$ we rule out a non-linear flux-phase relation, so the skewness is currently of unknown origin and could be related to higher orbitals in the quantum dot. While flux tuning provides fine-tuning of the qubit frequency within a frequency band of a few GHz set by the spin-orbit coupling strength, we can also tune the qubit frequencies over a larger range by varying the magnetic field, due to the Zeeman effect. From the magnetic field dependence of the frequencies we extract the g-factor of each ASQ, see Fig. 9.2c. We find that the different g-factors are consistent with earlier work (Vaitiekėnas et al., 2018; Wesdorp et al., 2022) and with Chapter 7, see also Sec. 9.6.

Next, we characterize the coherence properties of each ASQ at the frequencies indicated with markers in Fig. 9.2a and b. At these setpoints, we extract energy decay times of $T_1^{\mathrm{ASQ1}} = 3.3 \pm 0.1\,\mu\mathrm{s}$ and $T_1^{\mathrm{ASQ2}} = 11.8 \pm 0.4\,\mu\mathrm{s}$ for ASQ1 and ASQ2, respectively, where the reported uncertainties are the 1σ confidence intervals from the fit. These decay-times are to a large extent limited by Purcell decay to the transmon qubit (see Sec. 9.6). Furthermore, from a Ramsey experiment, we extract dephasing times of $T_2^{*\mathrm{ASQ1}} = 7.6 \pm 0.2\,\mathrm{ns}$ and $T_2^{*\mathrm{ASQ2}} = 5.6 \pm 0.2\,\mathrm{ns}$ for ASQ1 and ASQ2, respectively, which are comparable to times found in earlier works (Hays et al., 2021) (see Chapter 8). For these measurements, we use Gaussian pulses with a full width at half-maximum (FWHM) of 4 ns, which is comparable to T_2^*. Therefore, the $\pi/2$ pulses cannot be considered instantaneous, which is the conventional assumption in a Ramsey experiment. Rather, a non-zero overlap of the pulses of order T_2^* can result in an overestimation of the extracted T_2^*, as further discussed in Sec. 9.6. Therefore, these numbers should be interpreted as an upper bound to the pure dephasing times. Furthermore, we extract echo times of $T_{2\mathrm{E}}^{\mathrm{ASQ1}} = 17.3 \pm 0.4\,\mathrm{ns}$ and $T_{2\mathrm{E}}^{\mathrm{ASQ2}} = 17.4 \pm 0.4\,\mathrm{ns}$, see Sec. 9.6, three times larger than T_2^*, which points at low-frequency noise being a strong contributor to dephasing, consistent with previous observations in InAs-based spin qubits (Hays et al., 2021; Nadj-Perge et al., 2010) and Chapter 8.

9.3. LONGITUDINAL COUPLING

Having two Andreev spin qubits, we describe the joint system by the following Hamiltonian with the two qubits coupled longitudinally with coupling strength J (Padurariu and Nazarov, 2010):

$$H = -\frac{\hbar\omega_1}{2}\sigma_1^z - \frac{\hbar\omega_2}{2}\sigma_2^z - \frac{hJ}{2}\sigma_1^z\sigma_2^z, \tag{9.1}$$

where $\omega_i = 2\pi f_i$ and $\sigma_i^z = |{\downarrow}_i\rangle\langle{\downarrow}_i| - |{\uparrow}_i\rangle\langle{\uparrow}_i|$ denote the phase-dependent spin-flip frequency and the z Pauli matrix of ASQi, respectively, h is the Planck constant and $\hbar = h/(2\pi)$. In this description, the longitudinal term $\frac{-hJ}{2}\sigma_1^z\sigma_2^z$ originates from the fact that the spin-dependent supercurrent of ASQ1 induces a spin-dependent phase difference over ASQ2, thus changing its transition frequency by $\pm J$, and vice versa. Importantly, the longitudinal coupling does not arise from direct wavefunction overlap (Spethmann et al., 2022) or magnetic interactions as the spins are separated by a distance of approx-

imately 25µm. From this physical understanding of the interaction, we can express the coupling strength J as a function of the circuit parameters by (Padurariu and Nazarov, 2010)

$$J(L_{\mathrm{J,C}},\Phi_1,\Phi_2) = \frac{1}{2h}\frac{L_{\mathrm{J,C}}L_{\mathrm{ASQ}}(\Phi_1,\Phi_2)}{L_{\mathrm{J,C}}+L_{\mathrm{ASQ}}(\Phi_1,\Phi_2)} I_1(\Phi_1)I_2(\Phi_2). \tag{9.2}$$

Here, we define $L_{\mathrm{ASQ}}(\Phi_1,\Phi_2)$ as the total spin-independent inductance of the two ASQs in parallel and the spin-dependence is captured by $I_i(\Phi_i)$, which denotes the difference in supercurrent across ASQi for its two possible spin states. In this expression, one of the main features of the device becomes apparent: the coupling is tunable with flux and can be switched to zero when either I_1 or I_2 are set to zero.

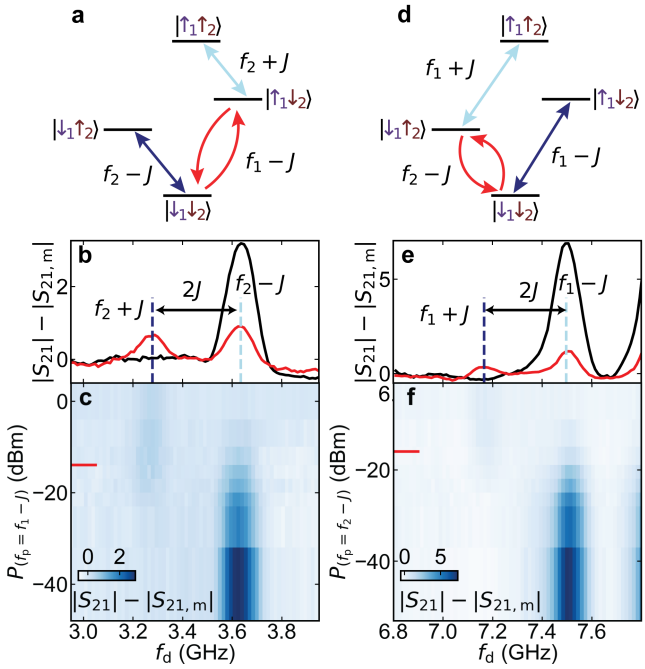

Figure 9.3: **Strong longitudinal coupling between the two Andreev spin qubits.** **a** Energy level diagram of the combined ASQ1-ASQ2 system with the levels (horizontal black lines) labeled by the states of both qubits (ASQ1 in purple, ASQ2 in maroon). The diagonal arrows denote the two different transition frequencies ($f_2 \pm J$) of ASQ2 depending on the state of ASQ1. Note that J is negative in this illustration and for the data presented in this figure. **b** Spectroscopy of ASQ2 as a function of the drive frequency f_d. The black and red lines indicate the readout signal amplitude with the background subtracted, $|S_{21}|-|S_{21,\mathrm{m}}|$, with and without a pump tone resonant with ASQ1 at frequency $f_\mathrm{p} = f_1 - J$, respectively. The pump tone is indicated with red arrows in **a**. **c** Power dependence of the pump tone. The red line indicates the power used for the red line in **c**. We indicate the power at the source output. **d**-**f** Similar to panels **a**-**c**, but with the roles of ASQ1 and ASQ2 exchanged. In this case, the pump tone drives ASQ2 at a frequency $f_\mathrm{p} = f_2 - J$, while performing spectroscopy of ASQ1.

We now proceed to investigate the spin-spin coupling at the same gate voltages and magnetic field used for Fig. 9.2. To this end, we open both loops simultaneously and set Φ_1 and Φ_2 at points where the slopes of the qubit frequencies $\partial f_i/\partial\Phi_i \propto I_i$ are large,

close to $\Phi_1 \sim 0$ and $\Phi_2 \sim \Phi_0/2$. When the two qubits are longitudinally coupled, the transition frequency of each of them depends on the state of the other, as schematically depicted in Fig. 9.3a and d. In each panel, the blue arrows indicate the two possible frequencies of one qubit, separated by twice the coupling strength, J, for the two possible states of the other qubit. To determine the magnitude of the coupling strength, we perform the following measurements: First, we determine $f_2 - J$ by performing qubit spectroscopy of ASQ2 starting from the ground state, $|\downarrow_1\downarrow_2\rangle$, where ASQ1 is in the spin-down state (black trace in Fig. 9.3b). Then, we repeat the spectroscopy while applying another continuous pump tone at a frequency f_p resonant with the spin-flip transition of ASQ1, driving $|\downarrow_1\downarrow_2\rangle \leftrightarrow |\uparrow_1\downarrow_2\rangle$. The presence of this additional tone results in ASQ1 being in a mixture of $|\downarrow_1\rangle$ and $|\uparrow_1\rangle$. When performing spectroscopy of ASQ2 under these conditions (red trace in Fig. 9.3b), we observe the emergence of a second peak corresponding to the shifted frequency of ASQ2 due to ASQ1 having population in its excited state, $|\uparrow_1\rangle$. This frequency splitting arises from the longitudinal coupling term and, thus, we determine the value of $J = -178 \pm 3$ MHz from a double Gaussian fit as half of the difference between the two frequencies (see Sec. 9.6 for details on the fit procedure). Since the coupling term is symmetric with respect to the two qubits, we should observe the same frequency splitting when we exchange the roles of ASQ1 and ASQ2, see Fig. 9.3e (note that the increase in amplitude around 7.8 GHz is unrelated to the ASQs but due to a resonance of the traveling wave parametric amplifier). From this measurement, we extract a value of $J = -165 \pm 4$ MHz similar to the value we extracted before. We speculate that the modest difference between the values of J extracted from the measurements of both qubits may be due to temporal instabilities, which we found to be present in the system. We additionally measure the qubit spectroscopy as a function of the pump tone power, shown in Fig. 9.3c and f, and we observe a power dependence on the peak amplitude. At low powers, not enough excited population is generated in the ASQ while the second peak gradually appears at higher powers. At too high powers, the readout resonator shifts too much due to the non-linearity of the resonator mode and it becomes more lossy, which results in a reduced signal (at even higher power both peaks fully disappears). Additional data and a numerical analysis of the expected pump power dependence and relative peak heights, in agreement with the experimental observations, can be found in Sec. 9.6.

Next, we compare the extracted value of J to the linewidth of the ASQ transitions and find $J = 165\,\mathrm{MHz} > 28\,\mathrm{MHz} = 1/(2\pi T_2^{*\mathrm{ASQ2}})$, indicating that the system is in the strong longitudinal coupling regime. This value of J puts a speed limit for a controlled-Z two-qubit gate at a time of $t = 1/(4J) = 1.4\,\mathrm{ns}$ and a coherence limit on the average gate fidelity of around 85%, which will be explored in future experiments. Such a two-qubit gate, combined with single qubit rotations, enables a universal set of gates. On the other hand, such a fast gate would require distortion-free flux pulses Rol et al. (2020), with a rise time much smaller than the gate time of 1.5 ns. This two-qubit gate time is much faster than typical fast two-qubit gates with superconducting qubits ($10 - 45\,\mathrm{ns}$ (Arute et al., 2019; Rol et al., 2019)) and comparable to the fastest short distance exchange gates in spin qubits coupled via directly overlapping wavefunctions (He et al., 2019; Hendrickx et al., 2021; Loss and DiVincenzo, 1998).

9.4. TUNABILITY OF THE COUPLING STRENGTH

We have so far investigated the coupling strength at fixed gate voltages and flux. We now investigate the dependence of J on different control parameters and demonstrate that it is tunable as predicted by Eq. (9.2) (Padurariu and Nazarov, 2010). We vary Φ_1 using the flux line, see Fig. 9.4a, and find that the coupling strength is directly proportional to I_1, as expected. The current difference across ASQ1, I_1, is extracted from a measurement of the qubit frequency as a function of flux as shown in Fig. 9.4d. Note that, by varying the flux, we not only vary the magnitude of J, but also switch its sign, crossing zero coupling. Thus, the two ASQs can be fully uncoupled by setting $J = 0$ at the flux points which maximize or minimize $f_i(\Phi_i)$, and where thus $I_i = 0$, for either one of the qubits. The coinciding of zero coupling with these frequency-extrema is useful as these are the first-order flux-insensitive points of the qubit transition frequency. Two representative situations in which the ASQs are coupled and uncoupled at nearby flux points are shown in Fig. 9.4b and c, respectively. The data was measured and analyzed using the same procedure as described for Fig. 9.3.

We overlay the Φ_1-dependence of the coupling strength with the expected dependence from Eq. (9.2). The values of $L_{J,C} = 8.4\,\text{nH}$ and $I_2 \sim h\partial f_2/\partial\Phi_2|_{\Phi_2=0.51\Phi_0} = -2.52\,\text{nA}$ are fixed and independently extracted from measurements of the transmon frequency and of $f_2(\Phi_2)$, respectively. $L_{ASQ}(\Phi_1)$ is calculated as the parallel combination of the spin-independent Josephson inductances of both qubits, which are determined from separate transmon spectroscopy measurements (see Sec. 9.6) and $I_1(\Phi_1) \sim h\partial f_1/\partial\Phi_1$ is estimated from Fig. 9.4d. As shown in Fig. 9.4a, the measured $J(\Phi_1)$ is in good agreement with Eq. (9.2).

Finally, we investigate the $L_{J,C}$ tunability of J by fixing $\Phi_1 = -0.07\Phi_0$, which sets $I_1 = 2.16\,\text{nA}$, and varying the value of V_C(see Sec. 9.6 for the corresponding qubit parameters). We observe an increase of the magnitude of J as the value of $L_{J,C}$ is increased, as shown in Fig. 9.4e. The measured data follows to a large extent the dependence expected from Eq. (9.2), indicated with a continuous line in Fig. 9.4e. The $|J|$ increase is limited to a maximum when the coupling junction $L_{J,C}$ becomes comparable to the finite spin-independent inductance L_{ASQ} of the ASQs. For the solid line in Fig. 9.4e we use the independently measured value $L_{ASQ}(\Phi_1 = -0.07\Phi_0, \Phi_2 = 0.51\Phi_0) = 102.0\,\text{nH}$. For comparison, the dashed line depicts the limit of $L_{ASQ} \gg L_{J,C}$.

9.5. CONCLUSIONS

In conclusion, we have extended earlier results demonstrating single Andreev spin qubits (Hays et al., 2021) (see Chapter 8) and integrated two InAs/Al-based ASQs within a single transmon circuit. The two ASQs are separated by around 25 µm, two orders of magnitude larger than the size of the individual qubit wavefunctions. Both ASQs showed comparable coherence properties to those reported in prior work (Hays et al., 2021) (see Chapter 8). We have shown strong supercurrent-mediated coupling between the two Andreev spin qubits and found that the coupling strength, J, can be tuned with either a magnetic flux or an electrical voltage. In particular, we have shown that J can be fully suppressed using a magnetic flux. This switchability of the coupling is essential for the use of longitudinally coupled Andreev spin qubits to perform quantum computation.

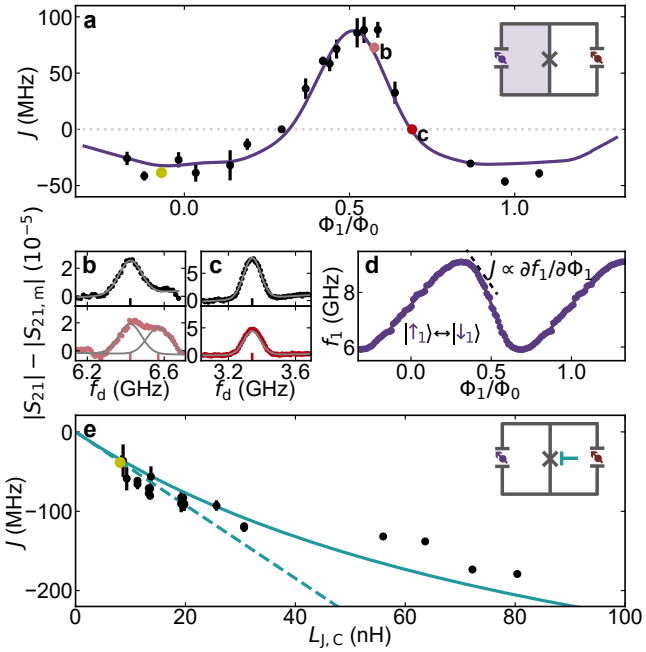

Figure 9.4: **Tunability of the coupling strength.** **a** Qubit-qubit coupling strength, J, as a function of flux in the loop containing ASQ1, Φ_1, see also inset, at fixed $\Phi_2 \sim 0.51\Phi_0$. The markers and error bars represent the best-fit values of J (see panels **b, c**) and their estimated standard errors (one-sigma confidence intervals), respectively. The purple line shows the expected dependence from Eq. (9.2). **b, c** Representative fits at two Φ_1 points highlighted with colored (and letter marked) markers in **a**. The signal measured in the absence of a pump tone (black markers) is fit with a single Gaussian (black line), to determine $f_i - J$ (vertical black line in the x axis). The signal measured in the presence of a pump tone at the other ASQ (colored markers) is additionally fitted (colored line) to determine $f_i + J$. The grey lines in **b** show the two individual Gaussians. **d** Frequency of ASQ1, f_1, versus Φ_1 (markers) and interpolation (line) used to estimate $I_1(\Phi_1) \sim h\partial f_1/\partial\Phi_1$. **e** Qubit-qubit coupling strength J at fixed $\Phi_1 = -0.07\Phi_0$ and as a function of $L_{J,C}$, which is varied using the gate-voltage at the coupling junction (see inset). The continuous line shows the dependence from Eq. (9.2), while the dashed line shows a linear dependence $Jh = L_{J,C} I_1 I_2/2$. The yellow marker in **a** and in **e** is a shared point between the two panels.

Furthermore, the high sign and magnitude tunability of J could have applications for the use of Andreev spin qubits to perform analog quantum simulations. More generally, Andreev spin qubits could in the future provide an independent platform for quantum computing and simulation or, alternatively, they may be incorporated into existing spin qubit platforms and serve as readout modules or long-distance couplers. Independently of the precise use-case for Andreev spin qubits, we emphasize that strong spin-spin coupling as demonstrated here will be an essential requirement although smaller dephasing rates would be desired.

Previous works suggest that one possible mechanism limiting dephasing is coupling to the large nuclear spins of InAs (Hays et al., 2021; Nadj-Perge et al., 2010) (see Chapter 8). While the origin of dephasing must be further investigated, this suggests that a possible route to increase the dephasing times is implementing Andreev spin qubits

in an alternative nuclear-spin-free material such as germanium (Hendrickx et al., 2018; Scappucci et al., 2021; Tosato et al., 2023; Valentini et al., 2023). We expect that future efforts using alternative materials could both provide a path towards integration in more established semiconductor-based quantum architecture as well as strongly increased coherence times. If longer coherence times can be achieved, in combination with the strong qubit-qubit coupling demonstrated here, Andreev spin qubits will emerge as an encouraging platform for the realization of high-fidelity two-qubit gates between remote spins.

DATA AVAILABILITY

Data as well as processing and plotting scripts are available online at `https://doi.org/10.4121/e10185d0-026e-480f-bbaa-3448c6e1b9a2`.

AUTHOR CONTRIBUTIONS

J.J.W., M.P.V., and C.K.A. conceived the experiment. Y.L. developed and provided the nanowire materials. J.J.W, M.P.V., L.S. and A.B. prepared the experimental setup and data acquisition tools. L.S. deposited the nanowires. J.J.W, M.P.V. and A.B designed the device. J.J.W and M.P.V. fabricated the device, performed the measurements and analysed the data, with continuous feedback from L.S., A.B. and C.K.A. L.P.K. and C.K.A. supervised the work. J.J.W., M.P.V., and C.K.A. wrote the manuscript with feedback from all authors.

9.6. SUPPLEMENTARY INFORMATION

9.6.1. THEORETICAL DESCRIPTION OF LONGITUDINAL ASQ-ASQ COUPLING

Note that the notation used in this section to refer to the spin-dependent and spin-independent Josephson energies is changed with respect to the notation used in Chapters 7 and 8. While we used E_{SO} and E_0 before, respectively, we now use $E^{\sigma}_{\mathrm{J,i}}$ and $E^{I}_{\mathrm{J,i}}$, respectively, where $i \in \{1,2\}$ denotes the qubit.

GENERAL DESCRIPTION OF THE ESTIMATION OF J USED IN THE MAIN TEXT

We derive a general expression for the coupling strength J in terms of Andreev current operators. The derived expression facilitates the data analysis presented in the main text, where we use the experimentally obtained current-phase relationship, which differs from that expected from the ideal quantum dot junction theory (Padurariu and Nazarov, 2010) (see Sec. 7.7 in Chapter 7). The current operator for each individual ASQ can be expressed as $\hat{I}_i = -\frac{2\pi}{\Phi_0}\frac{\partial H_i}{\partial \phi_i}$, where $i = 1,2$. Here, $\Phi_0 = h/2e$ denotes the magnetic flux quantum, $H_i = -\frac{\hbar\omega_i(\phi_i)}{2}\sigma_i^z$ in the subspace of the two spinful doublet states, ϕ_i is the phase drop across ASQi, σ_i^z is the z Pauli matrix for ASQi and the z axis is chosen along the spin-polarization direction for each qubit. As a result, the current operator can be related to the qubit frequency by

$$\hat{I}_i = \frac{\pi h}{\Phi_0}\frac{\partial f_i(\phi_i)}{\partial \phi_i}\sigma_i^z = \frac{I_i}{2}\sigma_i^z, \tag{9.3}$$

where we have defined the amplitude of the spin-dependent current $I_i = \frac{2\pi h}{\Phi_0}\frac{\partial f_i(\phi_i)}{\partial \phi_i} \approx h\frac{\partial f_i(\Phi_i)}{\partial \Phi_i}$ as in the main text, where the last approximation holds in the limit of $L_{\mathrm{J,C}} \ll L^I_{\mathrm{J},i}, L^\sigma_{\mathrm{J},i} \forall i$, such that the phase drop can be directly related to the external flux applied through the loop: $\phi_i = \frac{2\pi}{\Phi_0}\Phi_i$. In the subspace of the doublet states for each ASQ we can expand the two-qubit Hamiltonian to first order around the phase bias ϕ_1, given by the perturbation of the current through ASQ2, $\delta\phi_1 = \frac{2\pi}{\Phi_0} M\hat{I}_2$. Here, M denotes an effective mutual inductance that determines how much phase drops over ASQ1 due to a current in ASQ2. We obtain

$$\begin{aligned} H &= H_1(\phi_1 + \delta\phi_1) + H_2(\phi_2) \\ &= H_1(\phi_1 + \frac{2\pi}{\Phi_0} M\hat{I}_2) + H_2(\phi_2) \\ &\approx H_1(\phi_1) + \frac{2\pi}{\Phi_0}\frac{\partial H_1(\phi_1)}{\partial \phi_1} M\hat{I}_2 + H_2(\phi_2) \\ &= H_1(\phi_1) + H_2(\phi_2) - M\hat{I}_1\hat{I}_2 \\ &= -\frac{\hbar\omega_1}{2}\sigma_1^z - \frac{\hbar\omega_2}{2}\sigma_2^z - \frac{1}{4}MI_1I_2\sigma_1^z\sigma_2^z. \end{aligned} \tag{9.4}$$

In the limit of $L_{\mathrm{J,C}} \ll L^\sigma_{\mathrm{J},i}\forall i$, where $L^\sigma_{\mathrm{J},i}$ is the spin-dependent Josephson inductance of ASQi, M is given by the parallel combination of the spin-independent inductances of the three SQUID branches, $M = \frac{L_{\mathrm{J,C}}L_{\mathrm{ASQ}}}{L_{\mathrm{J,C}}+L_{\mathrm{ASQ}}}$. Here, $L_{\mathrm{ASQ}}(\phi_1,\phi_2)$ is the parallel combination of the spin-independent Josephson inductances of the ASQs:

$$\frac{1}{L_{\mathrm{ASQ}}(\phi_1,\phi_2)} = \frac{\cos(\phi_1)}{L^I_{\mathrm{J},1}} + \frac{\cos(\phi_2)}{L^I_{\mathrm{J},2}}.$$

By comparison to Eq. 9.1, we thus find

$$J = \frac{M}{2h} I_1 I_2 = \frac{1}{2h}\frac{L_{\mathrm{J,C}}L_{\mathrm{ASQ}}}{L_{\mathrm{J,C}}+L_{\mathrm{ASQ}}} I_1 I_2. \tag{9.5}$$

ANALYTICAL AND NUMERICAL CALCULATION OF J ASSUMING A SINUSOIDAL CURRENT-PHASE RELATION

As discussed in Sec. 7.7 of Chapter 7, a simple model of the Hamiltonian for each ASQ is given by (Padurariu and Nazarov, 2010)

$$H_i(\phi_i) = -E^I_{\mathrm{J},i}\cos\phi_i + E^\sigma_{\mathrm{J},i}\sigma_i^z \sin\phi_i, \tag{9.6}$$

where $E^I_{\mathrm{J},i} = \Phi_0^2/(4\pi^2 L^I_{\mathrm{J},i})$ and $E^\sigma_{\mathrm{J},i} = \Phi_0^2/(4\pi^2 L^\sigma_{\mathrm{J},i})$ denote the spin-independent and spin-dependent Josephson energies, respectively. The total Hamiltonian of the coupled system of Fig.9.1(a) is thus

$$H(\phi) = H_1(\varphi_1 - \phi) + H_2(\varphi_2 - \phi) + E_{\mathrm{J,C}}\cos(\phi) \tag{9.7}$$

$$= -E^I_{\mathrm{J},1}\cos(\varphi_1 - \phi) + E^\sigma_{\mathrm{J},1}\sigma_1^z \sin(\phi - \varphi_1) - E^I_{\mathrm{J},2}\cos(\varphi_2 - \phi) + E^\sigma_{\mathrm{J},2}\sigma_2^z \sin(\varphi_2 - \phi) - E_{\mathrm{J,C}}\cos\phi, \tag{9.8}$$

where $E_{\mathrm{J,C}} = \Phi_0^2/(4\pi^2 L_{\mathrm{J,C}})$ and the reduced flux, $\varphi_i = 2\pi\Phi_i/\Phi_0$, is the magnetic flux through the loop containing ASQi expressed in units of phase.

Analytical solution Following Ref. (Padurariu and Nazarov, 2010), assuming the energy-phase relation in Eq. (9.6), the lowest order in $E^{\sigma}_{\mathrm{J},1}/E_{\mathrm{J,C}}$ and $E^{\sigma}_{\mathrm{J},2}/E_{\mathrm{J,C}}$ yields the coupling energy in the form

$$J = -2\frac{E^{\sigma}_{\mathrm{J},1}E^{\sigma}_{\mathrm{J},2}}{|\tilde{E}|}\cos(\varphi_{\tilde{E}}-\varphi_1)\cos(\varphi_{\tilde{E}}-\varphi_2), \tag{9.9}$$

where

$$\tilde{E} = E^{I}_{\mathrm{J},1}e^{i\varphi_1} + E^{I}_{\mathrm{J},2}e^{i\varphi_2} + E_{\mathrm{J,C}}. \tag{9.10}$$

Numerical diagonalization To go beyond the limit of Eq. (9.9), i.e. for strong coupling, where the phase-drop on each ASQ is no longer linearly related to the applied flux, we solve the eigenenergies of the system numerically. For a given set of parameters, the energies of the four possible states of the qubit-qubit system ($E_{\uparrow\uparrow}$, $E_{\downarrow\uparrow}$, $E_{\uparrow\downarrow}$ and $E_{\downarrow\downarrow}$) are obtained as the minima in ϕ of the four eigenvalues of $H(\phi)$. From these four energies, we calculate the coupling strength J given the longitudinal (or Ising) type coupling Hamiltonian presented in Eq. 9.1. In this situation, the four eigenenergies of the coupled system are

$$E_{\uparrow\uparrow} = \frac{\hbar\omega_1}{2} + \frac{\hbar\omega_2}{2} + \frac{hJ}{2}, \tag{9.11}$$

$$E_{\downarrow\uparrow} = -\frac{\hbar\omega_1}{2} + \frac{\hbar\omega_2}{2} - \frac{hJ}{2}, \tag{9.12}$$

$$E_{\uparrow\downarrow} = \frac{\hbar\omega_1}{2} - \frac{\hbar\omega_2}{2} - \frac{hJ}{2}, \tag{9.13}$$

$$E_{\downarrow\downarrow} = -\frac{\hbar\omega_1}{2} - \frac{\hbar\omega_2}{2} + \frac{hJ}{2}. \tag{9.14}$$

Thus, from the numerically solved eigenenergies, we can find J as

$$J = \frac{1}{2h}(E_{\uparrow\uparrow} - E_{\uparrow\downarrow} - E_{\downarrow\uparrow} + E_{\downarrow\downarrow}). \tag{9.15}$$

Numerics including the transmon degree of freedom To fit the transmon spectroscopy data presented in Sec. 9.6.3 and 9.6.6, we add a charging energy term to Eq. (9.8) corresponding to the transmon island and numerically diagonalize the resulting Hamiltonian in the phase basis (Bargerbos et al., 2020; Kringhøj et al., 2020b)

$$H_{\mathrm{Transmon}} = -4E_{\mathrm{c}}\partial^2_{\phi} + H(\phi) \tag{9.16}$$

where E_{c} denotes the charging energy of the transmon island and $H(\phi)$ is defined in Eq. (9.8).

METHOD COMPARISON

Given the different approaches to calculate J, we now compare the different methods assuming the sinusoidal energy-phase of Eq. (9.6), see Figs. 9.5 and 9.6. The analytical expression of Eq. (9.9) is indicated with dashed lines. The continuous lines are obtained numerically from exact diagonalization of the total Hamiltonian in Eq. (9.8) using Eq. (9.15). The numerical diagonalization and the analytical expression of Eq. (9.9)

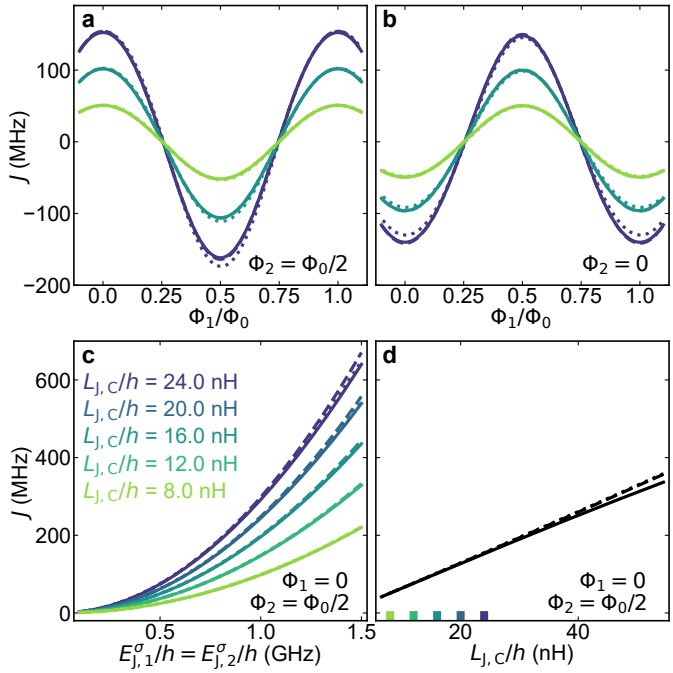

Figure 9.5: **Qubit-qubit coupling strength J as a function of model parameters.** **a**, **b** Φ_1 dependence of the coupling strength J at fixed $\Phi_2 = \Phi_0/2$ and $\Phi_2 = 0$, respectively. **c** $E^{\sigma}_{\mathrm{J},i}$ dependence of J at fixed $\Phi_1 = 0$ and $\Phi_1 = \Phi_0/2$, for various $L_{\mathrm{J,C}}$ values. **d** $L_{\mathrm{J,C}}$ dependence of J at fixed $\Phi_1 = 0$ and $\Phi_1 = \Phi_0/2$. For all panels $E^{\sigma}_{\mathrm{J},1}/h = 0.82\,\mathrm{GHz}$, $E^{\sigma}_{\mathrm{J},2}/h = 0.63\,\mathrm{GHz}$, $E^{I}_{\mathrm{J},1}/h = 0.2\,\mathrm{GHz}$ and $E^{I}_{\mathrm{J},2}/h = 0.3\,\mathrm{GHz}$, excepting for panel c where the values of $E^{\sigma}_{\mathrm{J},1}$ and $E^{\sigma}_{\mathrm{J},2}$ are varied. The continuous lines indicate the results obtained from direct diagonalization of Hamiltonian (9.8) using Eq. (9.15), the dashed lines, which mostly fall on top of the solid lines, indicate the analytic limit of Eq. (9.9) (Padurariu and Nazarov, 2010) and the dotted lines indicate the limit of Eq. (9.5) used in the main text. Note that, for panel **d**, the values of $I_i \sim h\frac{\partial f_i(\Phi_i)}{\partial \Phi_i}$ are calculated for each value of $L_{\mathrm{J,C}}$. This differs from what is done in Fig. 9.4e, where the values of I_i are estimated at a fixed $L_{\mathrm{J,C}}$ point and used for the complete $L_{\mathrm{J,C}}$ range.

9

show near perfect agreement. Only when $E^{\sigma}_{J,i} \sim E_{J,C}$ (Fig. 9.5(c)) a slight deviation is visible since Eq. (9.9) is only valid in the limit $E^{\sigma}_{J,i} \ll E_{J,C}$. We then test the estimate of J on the sinusoidal energy-phase relation of Eq. (9.6) using Eq. (9.5), which is also used in the main text for the experimentally obtained energy-phase relation. This is shown with dotted lines, for different sets of parameters. In Fig. 9.5 we use parameters corresponding to the limit $L_{\mathrm{J,C}} \ll L^{\sigma}_{\mathrm{J},i}, L^{I}_{\mathrm{J},i} \forall i$ and, given the agreement between the different methods, we note that the approximations made in Sec. 9.6.1 are valid. Thus, the general estimate from Eq. (9.5) (dotted line) agrees well with the exact value of J found by numerical diagonalization of the full Hamiltonian, as expected. To illustrate the estimates obtained from the different methods outside of this limit, we use values of $E^{I}_{\mathrm{J},i}$ in Fig. 9.6 that instead deviate from the limit $L_{\mathrm{J,C}} \ll L^{I}_{\mathrm{J},i} \forall i$. In this case, we see that the estimate from Eq. (9.5) deviates strongly from the exact numerical calculation due to the non-linear flux-phase relation.

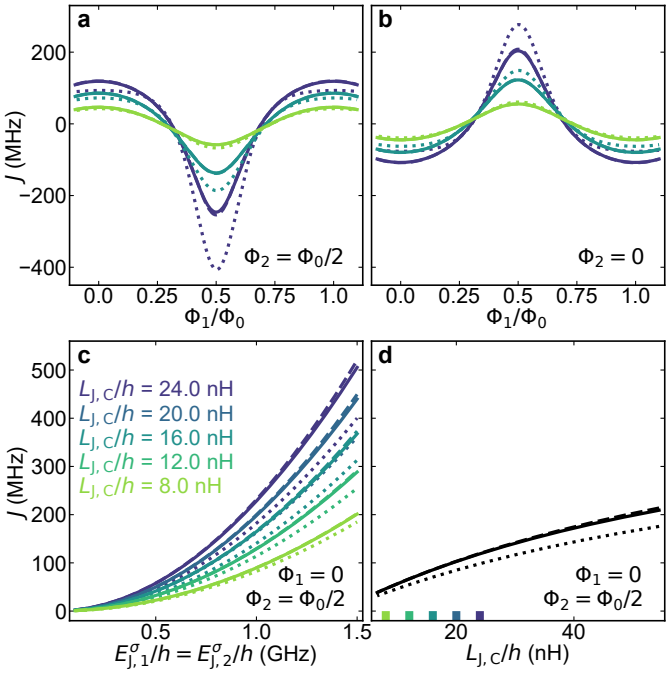

Figure 9.6: Same as Fig. 9.5 but for $E^I_{\mathrm{J},1}/h = 2.30$ GHz and $E^I_{\mathrm{J},2}/h = 0.45$ GHz.

MASTER EQUATION APPROACH TO LONGITUDINAL COUPLING EXPERIMENT

We now present a simple master equation simulation to investigate the effect of the drives on the coupled two-qubit system in presence of decay. We solve the Lindblad master equation for the time evolution of the system density matrix, ρ, of the following form

$$\dot{\rho} = \left[\rho, H'\right] - \sum_n \frac{1}{2}\left[2C_n\rho C_n^\dagger - \rho C_n^\dagger C_n - C_n^\dagger C_n \rho\right], \tag{9.17}$$

where H' describes the two-qubit system in the rotating frame of the two drives, which have certain detuning Δ_i from qubit i. This results in the following Hamiltonian

$$H'/\hbar = \frac{\Delta_1}{2}\sigma_2^z + \frac{\Delta_2}{2}\sigma_2^z + \frac{\Omega_{p1}}{2}\sigma_1^x + \frac{\Omega_{p2}}{2}\sigma_2^x + 2\pi\frac{J}{2}\sigma_1^z\sigma_2^z, \tag{9.18}$$

where Ω_{pi} denotes the drive amplitude of the tone near qubit i and $\Delta_i = \omega_i - \omega_{pi}$ is the detuning of that drive frequency with the qubit frequency. Additionally, we apply the collapse operators C_n on the individual qubits to simulate the effect of finite T_1 and T_2: $C_n \in \{\sqrt{\gamma_{1,1}}\sigma_1^-, \sqrt{\gamma_{\phi_1}/2}\sigma_1^z\sqrt{\gamma_{1,2}}\sigma_2^-, \sqrt{\gamma_{\phi_2}/2}\sigma_2^z\}$, where $\gamma_{1,i} = 1/T_1^{\mathrm{ASQ}i}$, $\gamma_{\phi_i} = 1/T_2^{\mathrm{ASQ}i}$, $\sigma_i^+ = |\uparrow_i\rangle\langle\downarrow_i|$ and $\sigma_i^- = |\downarrow_i\rangle\langle\uparrow_i|$. We then solve Eq. (9.17) for the steady state solution using Qutip (Johansson et al., 2013). From the above evolution of the master equation under a certain drive amplitude, we obtain the populations of the states $\{|\uparrow_1\uparrow_2\rangle, |\uparrow_1\downarrow_2\rangle, |\downarrow_1,\uparrow_2\rangle, |\downarrow_1\downarrow_2\rangle\}$. Then, assuming a dispersive shift for each state and a linewidth of the resonator mode,

we calculate the signal as the sum of populations times the displaced Lorentzians corresponding to each state and subtract the median for each linecut as is done with the experimental data. We compare the data measured in Fig. 9.3 to the master equation simulation with realistic parameters, as shown in Fig. 9.7. The simulations reproduce the main features seen in the data.

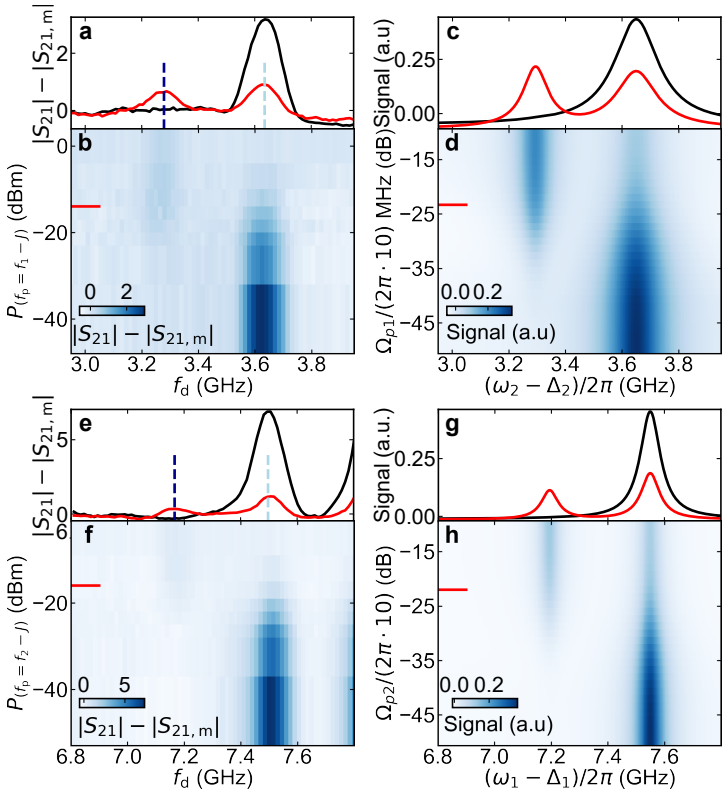

Figure 9.7: **Comparison between experiment and master-equation simulation. a-b, e-f** Experimental data of longitudinal coupling measurement repeated from Fig. 9.3. **c-d, g-h** Results of master equation simulations of the corresponding experimental data. **c-d** ASQ1 is driven with a pump tone at $f_p = f_1 - J$, while doing spectroscopy on ASQ2. **g**-h ASQ2 is driven with a pump tone at $f_p = f_2 - J$, while doing spectroscopy on ASQ1. We use the following parameters: the spectroscopy drive amplitude for ASQi is set to $\Omega_{pi}/2\pi = 2$ MHz which power broadens the observed linewidths similar to the experiment. The drive frequency of the third tone is set such that $\Delta_i = -J$, and the power is shown on the y-axis of the 2D maps in dB, similar to the experiment. T_1 and T_2^* are set to their values shown in Fig. 9.2 using the collapse operators and $\omega_i/(2\pi)$ of ASQi are set to $f_i - J$. The dispersive shifts are assumed larger than the linewidth of the resonator here such that the signal is only sensitive to the change in $|{\downarrow_1}{\downarrow_2}\rangle$ population. In all simulations, we fix $J = 178$ MHz.

The peak height difference between the drive being on and off (black and red linecuts in Fig. 9.7) depends on the difference between the initial and final populations $P_{\downarrow\downarrow}$ of $|{\downarrow_1}{\downarrow_2}\rangle$ in the limit of large dispersive shift, which we consider here for simplicity. Consider the case where we apply a spectroscopy tone at $f_2 - J$ on ASQ2, in the absence of a pump tone. In steady state, we get $P_{\downarrow\downarrow} = P_{\downarrow\uparrow} = 0.5$ and $P_{\uparrow\uparrow} = P_{\uparrow\downarrow} = 0$ due to the spec-

troscopy saturating ASQ2. Now, if we set a separate pump tone driving ASQ1 at $f_p = f_1 - J$ to a sufficiently high amplitude Ω_{p1}, we obtain $P_{\downarrow\downarrow} = P_{\downarrow\uparrow} = P_{\uparrow\downarrow} = 0.33$. Thus the height of the driven peak at $f_2 + J$ (red right peak) should be the height of the undriven (black) peak divided by a factor of $0.5/(0.5 - 0.33) \sim 2.94$ (as opposed to a factor of 2 which one might naively expect). The residual lowering of the peak observed in the experiment, we attribute to additional losses in the resonator mode under a strong drive. The height of the peak at $f_2 - J$, on the other hand, is expected to have a similar height if no T_1 decay is present. In presence of finite and similar T_1 for ASQ1 and ASQ2, however, the final populations end up becoming $P_{\downarrow\downarrow} = P_{\downarrow\uparrow} = P_{\uparrow\downarrow} = P_{\uparrow\uparrow} = 0.25$, thus increasing the signal at $f_2 - J$ and leading to a higher peak reaching half the height of the undriven peak at $f_2 + J$ (as also seen in in Fig. 9.7(d)). However, beyond these limiting cases, depending on the exact ratio of the T_1 lifetimes of ASQ1 and ASQ2 the steady-state populations will vary.

9.6.2. METHODS

DEVICE OVERVIEW

The physical implementation of the device investigated is shown in Fig. 9.8. The chip, 6 mm long and 6 mm wide, consists of two devices coupled to a single transmission line with an input capacitor to increase the directionality of the outgoing signal (Fig. 9.8h). For the experiments performed here, only the device discussed in the main text, highlighted in Fig. 9.8g, was measured. The resonator of the second device (uncolored device in Fig. 9.8g) was not functional and thus was not investigated.

For each device, a lumped element readout resonator is capacitively coupled to the feedline (Fig. 9.8e). The resonator is additionally capacitively coupled to the transmon island, which is connected to ground via three Josephson junctions in parallel (the coupling junction, ASQ1 and ASQ2) defining two loops (Fig. 9.8b). The three junctions are implemented on two separate Al/InAs nanowires. The junctions are defined by etching the aluminum shell of the nanowire in a 95 nm-long subsection for the coupling junction and 215 nm-long subsections for each of the ASQ junctions. The coupling junction is controlled by a single 200 nm-wide electrostatic gate centered at the middle of the junction, controlled with a DC voltage V_C. Each of the quantum dot junctions is defined by three gates consisting of two 50 nm wide tunnel gates (L, R) surrounding a 60 nm wide plunger gate (P), separated from each other by 45 nm (Fig. 9.8c, d). We define the DC voltages used for the left and right tunnel gates as V_{LP1} and V_{R1} for ASQ1 or V_{L2} and V_{R2} for ASQ2. The plunger gate of ASQ1 is also set to V_{LP1} because it was shorted to the left tunnel gate due to a fabrication imperfection. All gate lines except for the plunger lines incorporate a fourth-order Chebyshev LC-LC filter with a cut-off frequency at 2 GHz. The first and second inductive elements, of 5.2 nH and 6.1 nH respectively, are implemented using thin strips of NbTiN with widths of 3.5 µm and 300 nm, respectively. The first and second capacitive elements, of 2.45 pF and 2.08 pF respectively, are implemented with parallel plate capacitors. The plunger gate of ASQ2 is connected to a bias-tee on the printed circuit board formed by a 100 kΩ resistor and a 100 pF capacitor. This permits the simultaneous application of a DC signal, V_{P2}, to control the level of the quantum dot junction, and microwave tones, f_d and f_p, to drive either of the spin-flip transitions or the transmon. We also drive ASQ1 using the same gate line, because the bias-tee at the plunger gate of ASQ1 was not functional. The flux through the loop containing ASQ1

is controlled using a flux line (shown in amber). Its design in the area of the loops was inspired by Ref. (Rot, 2022). We furthermore incorporate a 25 pF parallel plate capacitor near the end of the flux line which, together with the 1 nH inductance of the rest of the flux line, implements an LC low-pass filter with a cut-off at 1 GHz.

SUMMARY OF DEVICE PARAMETERS

Bare resonator frequency, $f_{r,0}$	4.229 GHz	Resonator Q_c	1.3k
Resonator Q_i	~ 35k	Transmon decay time, T_1^t	53.6 ns
Resonator-transmon coupling, g/h	~ 287 MHz	Transmon Ramsey time, T_{2R}^t	80.0 ns
Transmon charging energy, E_c/h	200 MHz		

Table 9.1: **Values of relevant device parameters.** The resonator bare frequency and quality factors are measured when all electrostatic gates are at −1000 mV and thus all three junctions are pinched off (see Fig. 9.12). The transmon charging energy is extracted from the transmon anharmonicity in two-tone spectroscopy. The resonator-transmon coupling is extracted from a single-tone spectroscopy measurement at their anti-crossing (see Fig. 9.14). The transmon coherence values were measured with both ASQs in pinch off and at V_C = 1500 mV, which sets the transmon frequency to f_t = 5.45 GHz.

NANOFABRICATION DETAILS

The device fabrication occurs in several steps identical to that described in Chapter 6, and repeated here for the sake of completeness. The substrate consists of 525 µm-thick high-resistivity silicon, covered in 100 nm of low-pressure chemical vapor deposited Si_3N_4. In the first step, a 4-inch wafer of such substrate is cleaned by submerging it for 5 min in HNO_3 while ultasonicating, followed by two short H_2O immersions to rinse the HNO_3 residues. Afterwards, a 20 nm-thick NbTiN film is sputtered on top of the substrate using an *AJA International ATC 1800* sputtering system. Subsequently, Ti/Pd e-beam alignment markers are patterned on the wafer, which is thereafter diced into smaller individual dies of approximately 12 mm×12 mm. In the next step, the gate electrodes and the rest of the NbTiN circuit elements are patterned on one die covered by 110 nm-thick *AR-P 6200* (positive) e-beam resist using electron-beam lithography. The structures are then etched using SF_6/O_2 reactive ion etching for 47 s. Subsequently, 28 nm of Si_3N_4 dielectric are deposited on top of the gate electrodes using plasma-enhanced chemical vapor deposition and etched in patterns with a buffered oxide etchant (for 3 min). This dielectric is used as a gate dielectric, as well as as the dielectric for the crossovers at the DC gate lines and flux line and for the crossover that generates the twist in the loop containing ASQ1.

The nanowires are deterministically placed on top of the dielectric using a nanomanipulator and an optical microscope. These nanowires are ~10 µm-long epitaxial superconductor - semiconductor nanowires with a 110 nm-wide hexagonal InAs core and a 6 nm-thick Al shell covering two of their facets, in turn covered by a thin layer of aluminium oxide. The growth conditions were almost identical to those detailed in Ref. (Krogstrup et al., 2015), with the only two differences being that this time the As/In ratio was 12, smaller than in Ref. (Krogstrup et al., 2015), and that the oxidation of the Al

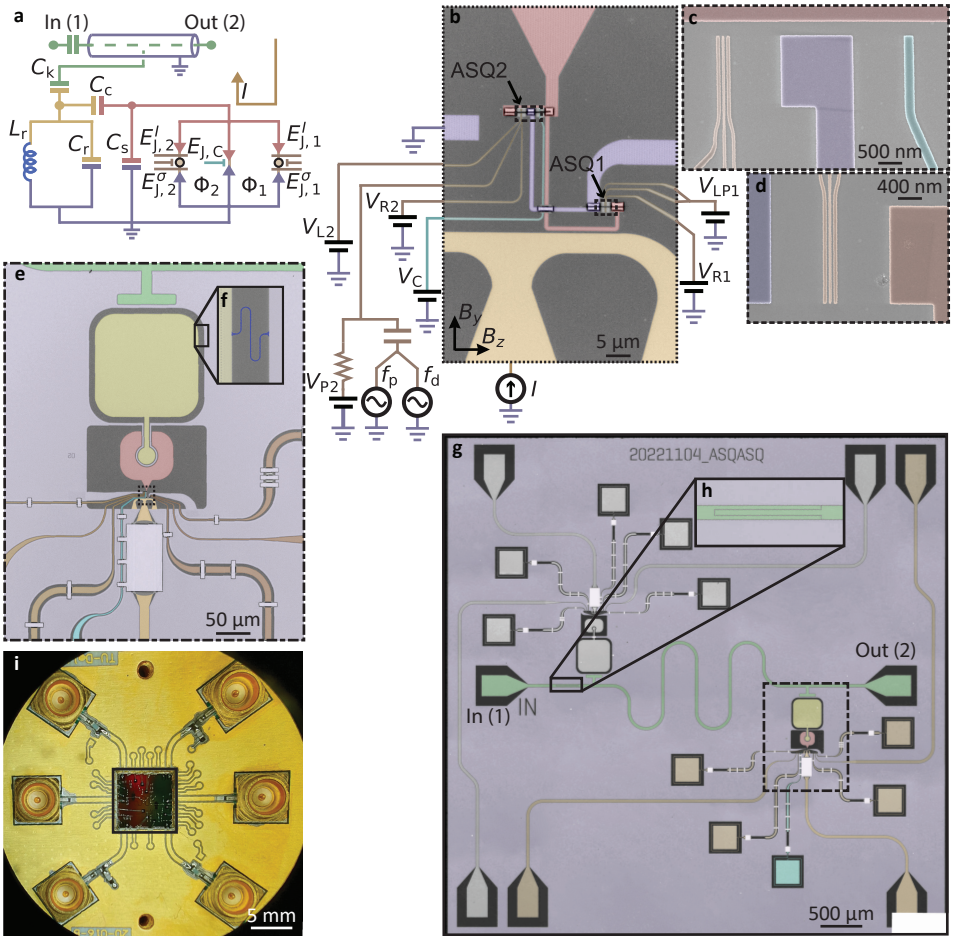

Figure 9.8: **Device overview.** **a** Diagram of the full microwave circuit. A coplanar waveguide (green center conductor) transmission line with an input capacitor is capacitively coupled to a grounded LC resonator. The resonator consists of an island (yellow) capacitively and inductively (blue) shunted to ground (purple). The resonator is in turn capacitively coupled to a transmon island (red), which is shunted to ground capacitively as well as via three parallel Josephson junctions. The coupling junction is controlled by a single electrostatic gate (cyan) and each of the two Andreev spin qubits is controlled by three electrostatic gates (brown). The RF drive tones f_d and f_p are sent through the plunger gate of ASQ2. The current through the flux line (amber), I, controls the flux thread through the loop containing ASQ1, Φ_1, and leaves Φ_2 nearly unaffected. **b** False-colored optical microscope image of the loops area. The three Josepshon junctions are implemented in two separate Al/InAs nanowires, one of them containing the coupling junction and ASQ2 and the other containing ASQ1. The B_y component of the magnetic field is used to tune Φ_1 and Φ_2, see Fig. 9.9 for a detailed sketch of the loops geometry. B_z is the magnetic field component approximately parallel to the nanowires axis. **c**, **d** False colored scanning electron microscope (SEM) images of the gates areas taken before the deposition of the gate dielectric and nanowire. **e** False-colored optical microscope image of the device showing the qubit island (red), the resonator island (yellow), the 200 nm-wide resonator inductor (blue, enlarged in **f**), the transmission line (green), the electrostatic gates (brown and cyan) the flux line (amber) and ground (purple). **g** False-colored optical microscope image of the whole 6×6 mm chip containing two nearly identical devices coupled to the same transmission line, which has an input capacitor, enlarged in **h**. The measured device is false-colored, while the second device was not investigated. **i** Chip mounted on a printed circuit board (PCB).

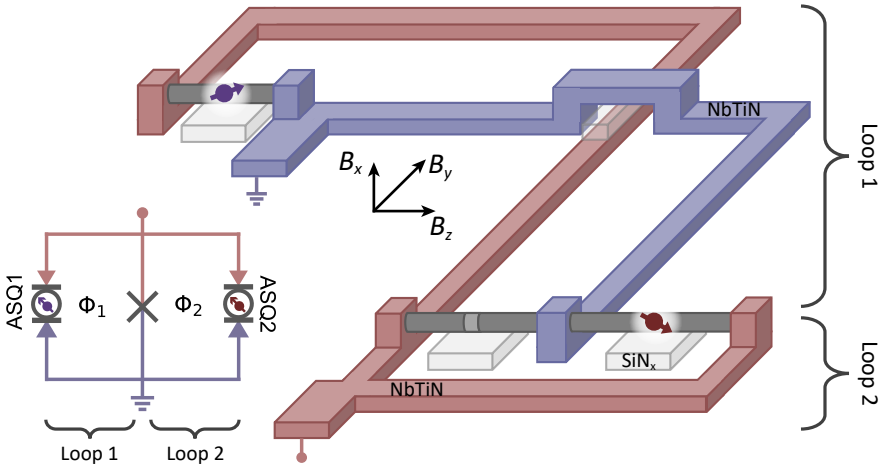

Figure 9.9: **Loops geometry.** Diagram of the loops area shown in Fig. 9.8b. Red and purple NbTiN segments denote segments connected to the transmon island and ground, respectively. The loop containing the coupling junction and ASQ2 (loop 2) is a planar loop with the same geometry as those in Chapters 6, 7 and 8. The loop containing the coupling junction and ASQ1 (loop 1) is a twisted gradiometric loop formed by two subloops. Equal of out-of-plane magnetic fields B_x through each of the two subloops result in nearly opposite contributions to the flux Φ_1, rendering loop 1 nearly insensitive to out-of-plane magnetic field noise. The nanowires are elevated with respect to the NbTiN plane due to the gate dielectric (light grey). This defines, for each loop, a loop area perpendicular to B_y. B_y can thus be used to control the flux through the loops while keeping the out-of-plane field component (B_x) fixed, reducing the occurrence of external flux jumps (Wesdorp et al., 2022).

shell was now performed in-situ, for better control, reproducibility and homogeneity of the oxide layer covering the shell. Inspection of the nanowire batch, performed under a scanning electron microscope directly after growth, indicated an average wire length of $9.93 \pm 0.92\,\mu$m and an average wire diameter of 111 ± 5 nm.

After nanowire placement, three subsections of the aluminium shells are selectively removed by wet etching for 55 s with *MF-321* developer. These subsections form the two quantum dot junctions and the coupling junction, with lengths 215 nm and 95 nm, respectively. After the junctions etch, the nanowires are contacted to the transmon island and to ground by a 110 s argon milling step followed by the deposition of 150 nm-thick sputtered NbTiN. Finally, the chip is diced into 6 by 6 millimeters, glued onto a solid gold-plated copper block with silver epoxy, and connected to a custom-made printed circuit board using aluminium wire-bonds (Fig. 9.8g).

CRYOGENIC AND ROOM TEMPERATURE MEASUREMENT SETUP

The device was measured in an *Oxford instruments Triton* dilution refrigerator with a base temperature of approximately 20 mK. Details of the wiring at room and cryogenic temperatures are shown in Fig. 9.10. The setup contains an input radio-frequency (RF) line, an output RF line, an extra RF line for the drive tones, a flux-bias line and multiple direct current (DC) lines used to tune the electrostatic gate voltages. The DC gate lines are filtered at base temperature with multiple low-pass filters connected in series.

The input, flux and drive RF lines contain attenuators and low-pass filters at different temperature stages, as indicated. In turn, the output RF line contains amplifiers at different temperature stages: a traveling wave parametric amplifier (TWPA) at the mixing chamber plate ($\approx 20\,\mathrm{mK}$), a high-electron-mobility transistor (HEMT) amplifier at the 4 K stage, and an additional amplifier at room temperature.

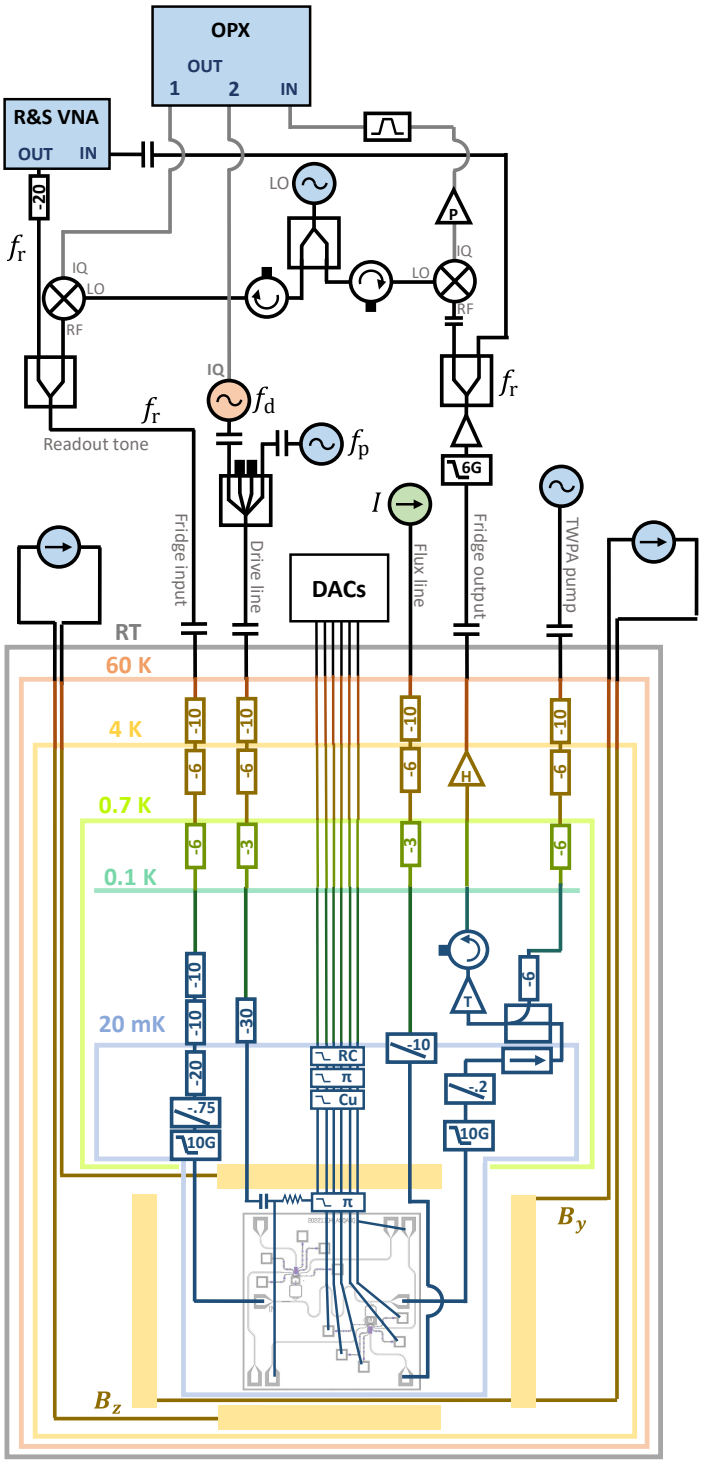

Figure 9.10: **Measurement setup.**

A three-axis vector magnet, for which the y and z coils are illustrated by yellow rectangles in Fig. 9.10 (x-axis not shown), is thermally anchored to the 4 K temperature stage, with the device under study mounted at its center. The three magnet coils are controlled with *Yokogawa GS610* current sources. The current through the flux line, I, is controlled with a *Yokogawa GS200* current source. At room temperature, a vector network analyzer (VNA) is connected to the input and output RF lines for spectroscopy at frequency f_r. On the input line, this signal is combined with a separate IQ-modulated tone also at f_r, only used for time-domain measurements. The IQ-modulated drive tone at frequency f_d and the pump tone at frequency f_p are both sent through the drive line. For time-domain measurements, the output signal is additionally split off into a separate branch and down-converted to be measured with a *Quantum Machines OPX*.

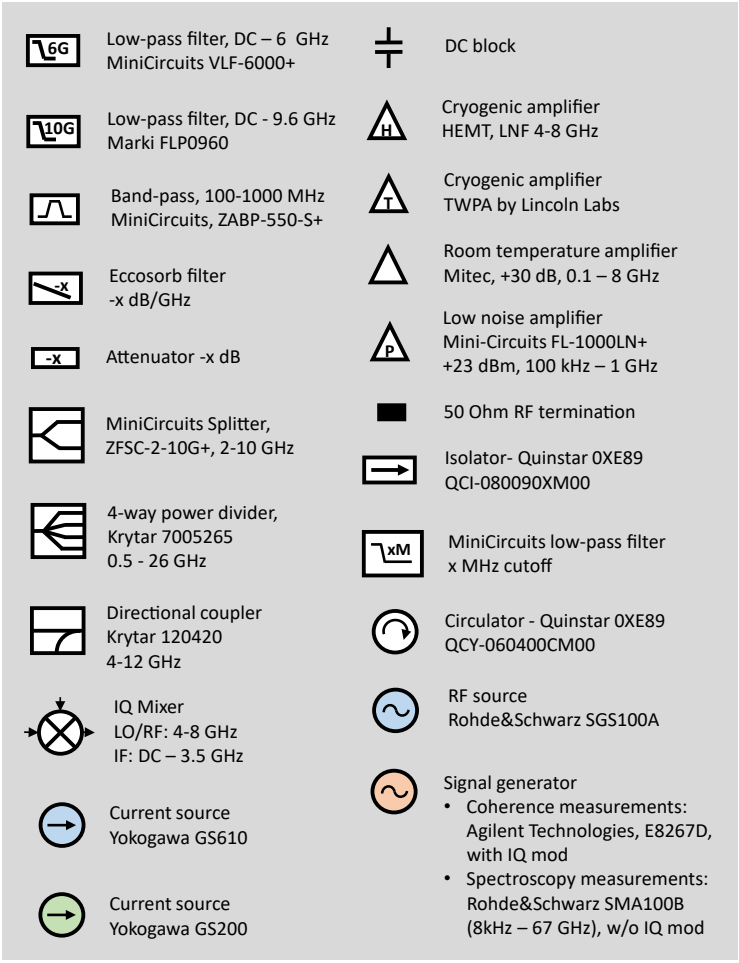

Figure 9.11: **Legend of Fig. 9.10.**

DATA PROCESSING

Background subtraction for single-tone and two-tone spectroscopy measurements For all single-tone spectroscopy measurements shown in the main text and Supplementary Information, we plot the amplitude of the transmitted signal, $|S_{21}|$, with the frequency-dependent background, $|S_{21,\mathrm{b}}(f_\mathrm{r})|$, divided out, in dB: $10\log_{10}(|S_{21}|/|S_{21,\mathrm{b}}|)$. The background is extracted from an independent measurement of the transmission through the feedline as a function of V_C. To determine the background for each f_r we do not consider transmission data for which the resonator frequency is more than 20 MHz close to f_r, so that the presence of the resonator does not impact the extracted background.

For two-tone spectroscopy measurements, we instead plot the transmitted signal, $|S_{21}|$, with the frequency-independent background, $|S_{21,\mathrm{m}}|$, subtracted: $|S_{21}| - |S_{21,\mathrm{m}}|$. In this case, the background is defined as the median of $|S_{21}|$ of each frequency trace.

Gaussian fits to extract J from spectroscopy measurements To extract the value of the coupling strength from the peak splitting observed in spectroscopy measurements, we follow the following procedure:

1. We first fit the two-tone spectroscopy signal in the absence of a pump tone with a single Gaussian function of the form

$$\frac{A}{\sqrt{2\pi\sigma^2}}\exp\left(\frac{-(f_\mathrm{d}-f_a)^2}{2\sigma^2}\right)+Bf_\mathrm{d}+C, \tag{9.19}$$

   from which we extract the position of the first peak, f_a, and its width, σ.

2. Next, we fit the two-tone spectroscopy signal in the presence of a pump tone with a double Gaussian function of the form

$$\frac{A_a}{\sqrt{2\pi\sigma^2}}\exp\left(\frac{-(f_\mathrm{d}-f_a)^2}{2\sigma^2}\right)+\frac{A_b}{\sqrt{2\pi\sigma^2}}\exp\left(\frac{-(f_\mathrm{d}-f_b)^2}{2\sigma^2}\right)+Bf_\mathrm{d}+C, \tag{9.20}$$

   for which the peak widths σ, as well as the position of the first peak, f_a, are fixed to their values extracted from the previous fit. From this fit, we extract the position of the second peak, f_b, as well as the chi-square of the fit, χ^2_double.

3. Next, we repeat a fit to the two-tone spectroscopy signal in the presence of a pump tone with a single Gaussian function (Eq. (9.19)) and extract the chi-square of the fit, χ^2_single.

4. To determine whether a double Gaussian fits better than a single Gaussian, we compare the goodness of fit of a double and single Gaussian fit.
   If $(\chi^2_\mathrm{single}-\chi^2_\mathrm{double})/\chi^2_\mathrm{double} \geq 0.1$, we conclude that the data shows two peaks and extract J as $J=(f_a-f_b)/2$ and the error of J as the error of f_b extracted from the double Gaussian fit (its one-sigma confidence interval).

5. If, else, $(\chi^2_\mathrm{single}-\chi^2_\mathrm{double})/\chi^2_\mathrm{double} < 0.1$, we conclude that the data shows a single peak and thus $J=0$.

Determination of the flux axis To determine the flux axis for data that we display in the main text as a function of Φ_i, we map the corresponding flux control parameter (I for the loop containing ASQ1 and B_y for the loop containing ASQ2) to the fluxes Φ_1 and Φ_2. To do so, we need to determine the value of the control parameter corresponding to $\Phi_i = 0$ (denoted as $I_{\Phi_1=0}$ and $B_{y,\Phi_2=0}$, respectively) as well as the one flux quanta (denoted as I_{Φ_0} and B_{y,Φ_0}, respectively). The former is independently determined for each separate measurement, from fits of the data to the expected transitions.

The values of the flux quanta ($I_{\Phi_0} = 9.62\,\mathrm{mA}$ for Φ_1 and $B_{y,\Phi_0} = 3.16\,\mathrm{mT}$ for Φ_2) are fixed throughout all main text and supplementary figures and is extracted from fits to the data in Fig. 9.2a and b. The data in Fig. 9.2b is fitted with a sinusoidal dependence of the form

$$2E^{\sigma}_{\mathrm{J},2} \sin\left(2\pi \frac{B_y - B_{y,\Phi_2=0}}{B_{y,\Phi_0}}\right) + C, \tag{9.21}$$

as expected for a quantum dot Josephson junction (Padurariu and Nazarov, 2010) (see Sec. 7.7 in Chapter 7). The data in Fig. 9.2a is instead fitted with a phenomenological skewed sinusoidal dependence of the form

$$2E^{\sigma}_{\mathrm{J},1} \sin\left(2\pi \frac{I - I_{\Phi_1=0}}{I_{\Phi_0}} + S \sin\left(2\pi \frac{I - I_{\Phi_1=0}}{I_{\Phi_0}}\right)\right) + C, \tag{9.22}$$

where $-1 < S < 1$ is the skewness parameter. For the data in Fig. 9.1a, we extract $S = -0.39$. The observed skewness of the spin-flip is, to our knowledge, not predicted by existing models (Padurariu and Nazarov, 2010), so further investigation is needed to explain its origin.

9.6.3. BASIC CHARACTERIZATION AND TUNEUP

READOUT RESONATOR CHARACTERIZATION

In this subsection, we perform a fit to a bare resonator spectroscopy trace and extract the resonator parameters shown in Tab. 9.1. The result of a single-tone resonator trace, performed with all Josephson junctions pinched off, is shown with black markers in Fig. 9.12. The grey lines show the best fit of the complex transmission to the expected dependence (Flanigan, 2023; Khalil et al., 2012)

$$S_{21}(f_\mathrm{r}) = 1 - \frac{1 + i\alpha}{1 + \frac{Q_\mathrm{c}}{Q_\mathrm{i}} + 2Q_\mathrm{c} i \frac{f_\mathrm{r} - f_{\mathrm{r},0}}{f_{\mathrm{r},0}}}, \tag{9.23}$$

where $f_{\mathrm{r},0}$ is the bare resonator resonance frequency, Q_c and Q_i are the coupling and internal quality factors, respectively, and α is a real number to account for the resonator asymmetry.

GATE AND FLUX CHARACTERIZATION

Throughout this manuscript, we use B_y, which affects both Φ_1 and Φ_2, to tune Φ_2 and the current through the flux line, I, to tune Φ_1. Fig. 9.13a shows the B_y tunability of Φ_2, for which the period corresponds to 3.25 mT. Note that this value is slightly larger than the actual flux quantum due to the small flux jumps present in the signal. Fig. 9.13c and

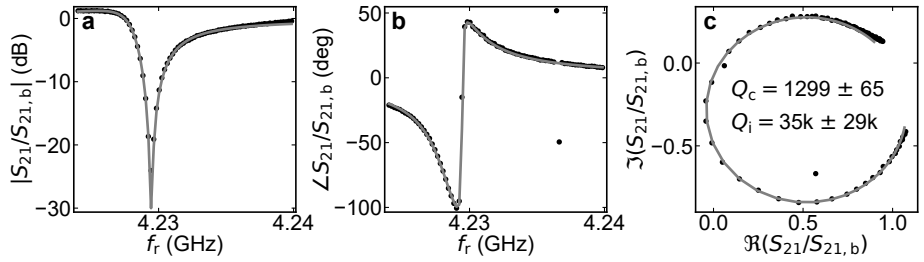

Figure 9.12: **Single-tone spectroscopy of the resonator and quality factor extraction.** All panels show the measured data (black markers) and a fit to Eq. (9.23) (grey line). **a** and **b** show, respectively, the amplitude and phase of the S_{21} signal as a function of frequency. **c** shows the imaginary and real parts of the complex S_{21} signal. From the fit, we extract a resonator bare frequency of $f_{r,0} = 4.22850\,\text{GHz} \pm 91\,\text{kHz}$ and the quality factors indicated in **c**.

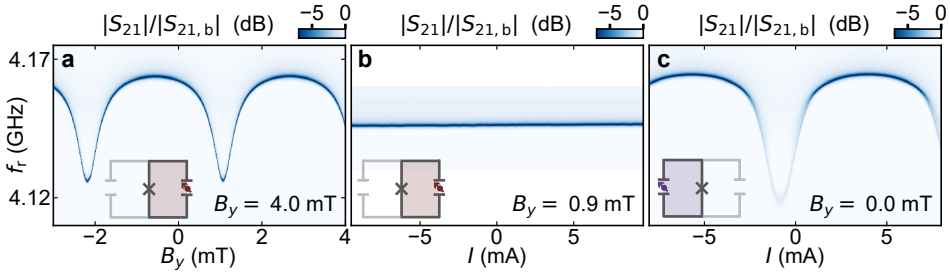

Figure 9.13: **Flux control.** Amplitude of the transmission through the readout circuit, $|S_{21}|$, with background, $|S_{21,b}|$, divided out. **a**, **b** With ASQ1 closed ($V_{LP1} = V_{R1} = -1000\,\text{mV}$) and ASQ2 open to a singlet state with large Josephson energy. **a** shows the dependence on B_y, which tunes Φ_2, while **b** shows the dependence on the current through the flux line, I, which leaves Φ_2 unaffected. **c** With ASQ1 open to a singlet state with large Josephson energy and ASQ2 closed ($V_{L2} = V_{P2} = V_{R2} = -1000\,\text{mV}$), plotted versus I, which controls Φ_1. For all panels, $B_x = B_z = 0$ and $V_C = 1995\,\text{mV}$.

b show how the current through the flux line, I, controls Φ_1, for which a flux quantum corresponds to 9.61 mA, while leaving Φ_2 unaffected.

We now investigate the performance of all electrostatic gates. Fig. 9.14 shows the resonator frequency, measured by single-tone spectroscopy, while various combinations of gates are varied. In all cases, only at most one of the three junctions is open, thus not defining any loops. All junctions can be fully pinched off using any of the gates that control them while leaving the rest of the gates open, which confirms the proper functionality of all gates.

Panels a-c show the effect of varying the gates of ASQ1 either simultaneously (a) or separately (b, c). Note that the left and plunger gates of ASQ1 are connected to each other on-chip and thus are always set at the same voltage, V_{LP1}, while the right gate of ASQ1 is set at voltage V_{R1}. The effect of the left, plunger and right gates of ASQ2, respectively set at voltages V_{L2}, V_{P2} and V_{R2}, is shown in panels e-h. Although the pinch-off voltages for ASQ2 are slightly lower, this junction displays a behavior similar to that of ASQ1. Panel d shows the effect of V_C, the voltage of the coupling Josephson junction gate, which tunes $E_{J,C}$. By varying V_C, the transmon frequency can be tuned to values above the bare

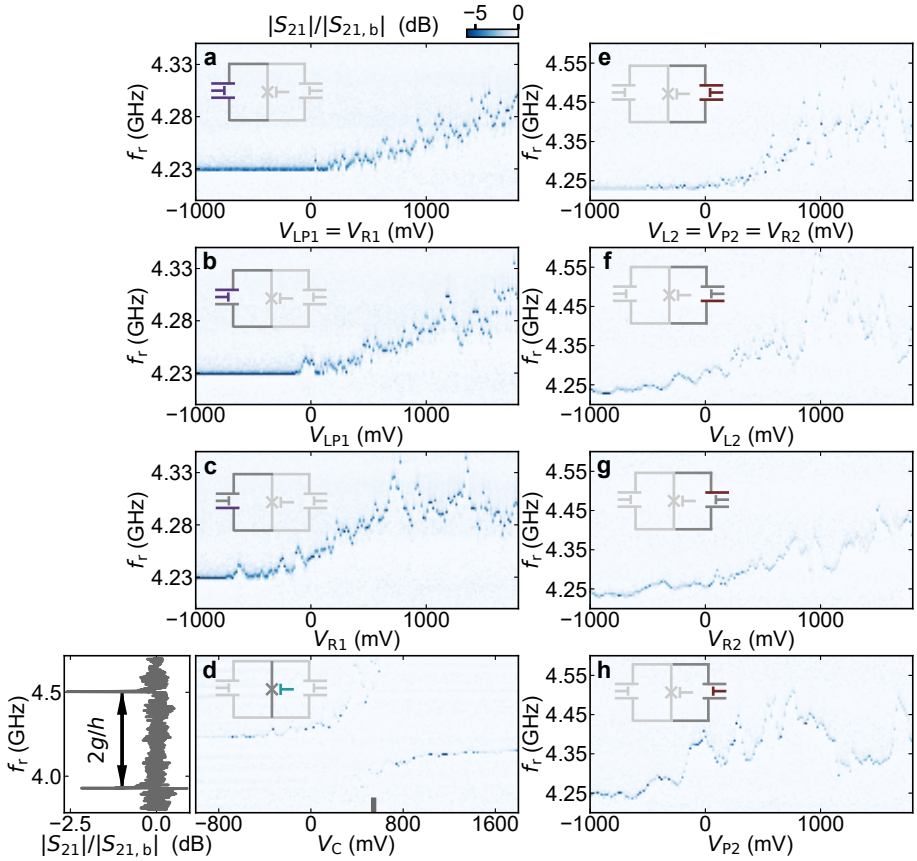

Figure 9.14: **Individual characterization of electrostatic gates.** All panels show single-tone spectroscopy of the resonator versus different gate voltages. The gate voltages that are being varied in each case are highlighted with colors in the insets. Dark grey shaded gates indicate open gates set to 1800 mV. Light grey shaded gates indicate closed gates set to −1000 mV. The panel to the left of **d** shows a line cut of the data in **d** taken at the V_C value indicated with a grey line in the x-axis. From this line cut we extract the transmon-resonator coupling energy g.

resonator frequency, thus resulting in an avoided crossing between the resonator and transmon frequencies at around $V_C = 500$ mV. We find a transmon-resonator coupling strength $g/h \sim 287$ MHz as half of the distance between the two resonances observed at the avoided crossing.

Next, we measure the V_C-dependence of the transmon frequency f_t with both ASQs pinched off, from which we calibrate the V_C to $E_{J,C}$ map which is used for the data processing behind Fig. 9.4.

The black markers in Fig. 9.15a show the transmon frequency as a function of V_C, measured directly after the data shown in Fig. 9.4 and at the same magnetic field conditions ($B_r = 35$ mT applied in the chip plane and six degrees away from the z direction). For comparison, we also show the transmon frequencies measured while taking the data

in Fig. fig:fig4e (teal markers), with both ASQs open. In this case, the measured frequencies deviate from the black markers, since they instead result from a parallel combination of $E_{J,C}$ and the Josephson energies of both qubits. The black markers in Fig. 9.15a are used to determine the V_C-dependence of $E_{J,C}$ shown in Fig. 9.15b, given the value of E_c independently determined from a measurement of the transmon anharmonicity (see Tab. 9.1). These data are used to determine the x-axis of Fig. 9.4e.

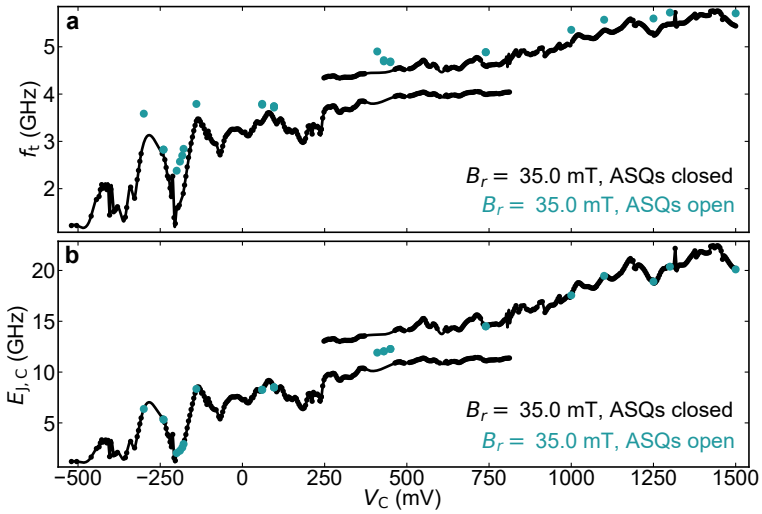

Figure 9.15: **Coupling junction characterization a** Transmon frequency, f_t, versus the coupling junction gate voltage, V_C, extracted by peak-finding in two-tone spectroscopy data. The black markers are taken at the magnetic field conditions at which we measured Fig. 9.4 but with both ASQ junctions fully closed (all quantum dot gates set to −1000 mV). The continuous line is a cubic interpolation to the measured data. The teal markers indicate the V_C, f_t points at which we measured longitudinal coupling in Fig. fig:fig4e. Note that, the teal markers deviate from the black markers, because there f_t is determined by the combination of $E_{J,C}$, $E^I_{J,1}$, $E^I_{J,1}$, $E^\sigma_{J,1}$, $E^\sigma_{J,1}$, Φ_1 and Φ_2, and not solely by $E_{J,C}$ as for the black markers. **b** Coupling junction Josephson energy $E_{J,C}$ versus V_C obtained directly from the corresponding data in **a**, given the measured E_c value specified in Tab. 9.1. The mapping between V_C and $E_{J,C}$ indicated with a continuous black line is used to obtain the x-axis of Fig. 9.4e.

9

ASQ GATE SETPOINTS

In this subsection, we discuss the tune-up of each individual ASQs, which results in the chosen gate setpoints specified in Tab. 9.2.

The tune-up of ASQ1 is presented in Fig. 9.16. We first set the junction containing ASQ2 to pinch-off by setting its three gates to −1000 mV and set the ASQ1 gates to a region where we detect a sizable spin-splitting energy in a low-resolution measurement. From the transmon frequency at $\Phi_1 = 0, \Phi_0/2$ we estimate the spin-independent Josephson energy $E^I_{J,1}$ and map it out over a region in gate space using the two gate voltages of ASQ1 (Fig. 9.16a). Then, we proceed to investigating the value of the spin-dependent Josephson energy, $E^\sigma_{J,1}$. One way of doing so would be directly mapping out the spin-flip frequency f_1 in gate space. However, the visibility of the transition is significantly

reduced at $B = 0$ due to the thermal population of the ASQ as well as to the smaller matrix element from driving the spin transition. We instead perform Φ_1-dependent transmon spectroscopy at a few selected gate points indicated with markers in Fig. 9.16a (Fig. 9.16b-g). For each gate setpoint we estimate the values of $E^{\sigma}_{\mathrm{J},1}/h$ by matching the distance between transmon frequencies at $\Phi_1 = \Phi_0/4$ to its theoretically expected value extracted from numerical diagonalization of Eq. (9.16) in the phase basis. Similarly, $E^{I}_{\mathrm{J},1}$ is estimated by fitting the measured transmon frequencies at $\Phi_1 = 0, \Phi_0/2$ to their theoretically expected values. The resulting quantities are indicated as labels on each panel. We choose the gate setpoint used for ASQ1 in the main text by maximizing $E^{\sigma}_{\mathrm{J},1}$ while keeping the value of $E^{I}_{\mathrm{J},1}$ low, since a high value negatively impacts the maximal coupling strength J. The chosen ASQ1 gate setpoint (see Tab. 9.2) is indicated in Fig. 9.16a with a purple marker.

Next, we pinch off the junction containing ASQ1 to tune-up the gate configuration of ASQ2. We perform an investigation analogous to the one detailed above, as shown in Fig. 9.17. Fig. 9.17a is measured in the same way as Fig. 9.16a and displays the evolution of $E^{I}_{\mathrm{J},2}$ with the tunnel gates, $V_{\mathrm{L}2}$ and $V_{\mathrm{R}2}$, while $V_{\mathrm{P}2}$ is kept at 0 mV. Fig. 9.17b shows the tunnel gate dependence of $E^{\sigma}_{\mathrm{J},2}$, determined from direct spin-flip spectroscopy of ASQ2 at $B = 0$: $E^{\sigma}_{\mathrm{J},2}/h = f_2(B = 0, \Phi_2 = \Phi_0/4)/2$. Similarly to the strategy for ASQ1, we choose a gate setpoint for ASQ2 by maximizing $E^{\sigma}_{\mathrm{J},2}$ while keeping $E^{I}_{\mathrm{J},2}$ as low as possible. However, for some gate points in this region of gate space, a singlet state is also slightly visible in transmon spectroscopy (as can be seen in Fig. 9.17c, around $\Phi_2 = 0$). The presence of the singlet state indicates that the singlet phase of the system is only separated by an energy gap comparable to the thermal energy of the system. Consequently, while choosing the ASQ2 setpoint we also minimize the visibility of the singlet state. The chosen setpoint (see Tab. 9.2 is indicated in Fig. 9.17a and b with a maroon marker).

Finally, we perform in-field spin-flip spectroscopy of both ASQs, as well as transmon spectroscopy at zero field, to more accurately determine their Josephson energies detailed in Tab. 9.2.

	$V_{\mathrm{L}i}$ (mV)	$V_{\mathrm{P}i}$ (mV)	$V_{\mathrm{R}i}$ (mV)	$E^{I}_{\mathrm{J},i}/h$ (GHz)	$E^{\sigma}_{\mathrm{J},i}/h$ (GHz)
ASQ1	62.0	62.0	350.0	2.29	0.82
ASQ2	206.50	0.0	-624.0	0.45	0.63

Table 9.2: ASQ1 and ASQ2 gate voltage set points and extracted model parameters from the measurements in Fig. 9.18.

The spin-flip spectroscopy shown in Fig. 9.18a and b is performed under the same magnetic field conditions as the ones where we measured coupling in the main text. We extract $E^{\sigma}_{\mathrm{J},1}/h = 0.82\,\mathrm{GHz}$ and $E^{\sigma}_{\mathrm{J},2}/h = 0.63\,\mathrm{GHz}$ from fits of a skewed and non-skewed sine, respectively, to the measured data (see Sec. 9.6.2). The $E^{\sigma}_{\mathrm{J},i}/h =$ values are determined as one fourth of the flux dispersion of the fit result. $E^{I}_{\mathrm{J},1}/h = 2.29\,\mathrm{GHz}$ and $E^{I}_{\mathrm{J},2}/h = 0.45\,\mathrm{GHz}$ are determined similarly to how it was done for Figs. 9.16 and 9.17, by fitting the Φ_i-dependent data to the expected transmon frequencies obtained by numerical diagonalization of the Hamiltonian in Eq. (9.16) at Φ_i being integer multiples of

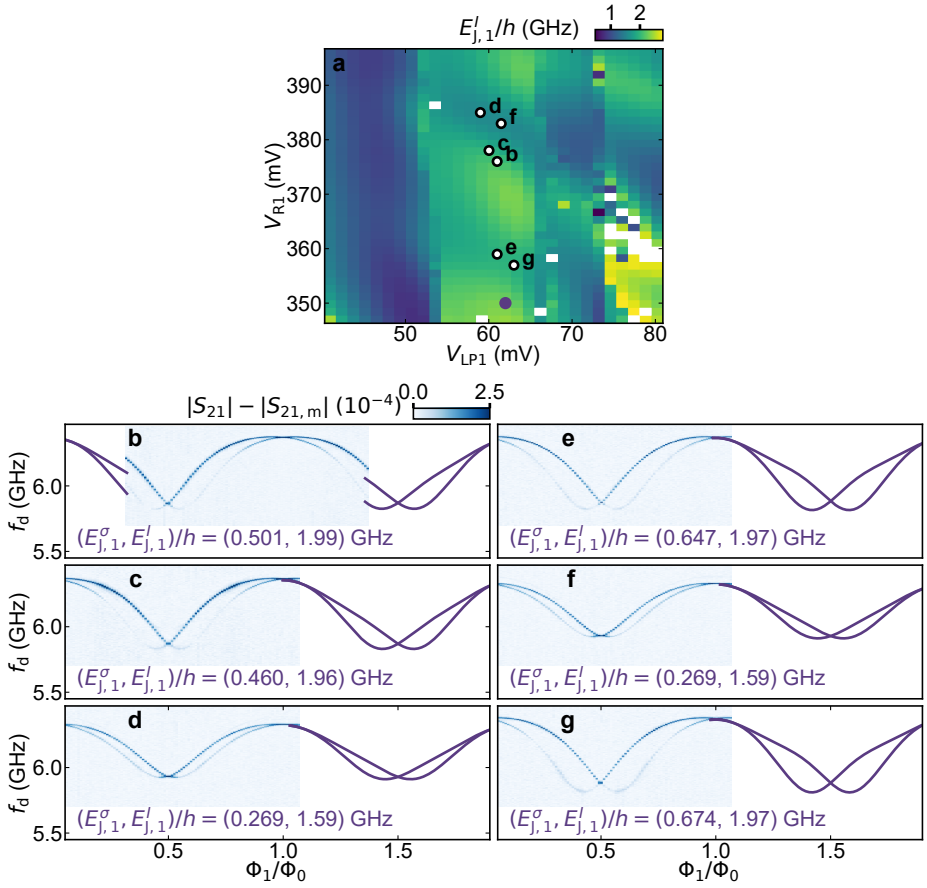

Figure 9.16: **ASQ1 gate dependence around its gate setpoint. a** Estimate of spin-independent Josephson energy of ASQ1, $E^I_{J,1}$, versus the two gate voltages of ASQ1, obtained from two-tone spectroscopy measurements of the transmon transitions at $B_r = 0$ and at two different flux values: $\Phi_1 = 0$ and $\Phi_1 = \Phi_0/2$. The purple marker indicates the gate setpoint of ASQ1 in the main text. **b** - **g** Transmon spectroscopy at various gate configurations, indicated with markers in **a**. The values of $E^I_{J,1}/h$ indicated in the labels are extracted by fitting the measured transmon frequencies at $\Phi_1 = 0$ and $\Phi_1 = \Phi_0/2$ to their theoretical values. The value of $E^\sigma_{J,1}/h$ is extracted from the distance between transmon frequencies at $\Phi_1 = \Phi_0/4$. The continuous lines are the corresponding transmon frequencies obtained by numerical diagonalization of an adapted Eq. (9.16) in which the spin-dependent potential of ASQ1 is replaced by a skewed sinusoidal shape $E^\sigma_{J,1}\sigma^z_1 \sin(\varphi_1 + S\sin\varphi_1)$, where $\varphi_1 = \frac{2\pi}{\Phi_0}\Phi_1$. Panels **b** - **g** share the color map.

$\Phi_0/2$. In both cases, we fix the spin-dependent part of the transmon potential to that extracted from the fits in Fig. 9.18a and b.

ANDREEV SPIN QUBIT READOUT

In the main text (Fig. 9.1d) we discussed how, when both loops are open, we observe four possible resonator frequencies, depending on the four possible spin states of the ASQ1-ASQ2 system, $\{|\uparrow_1\uparrow_2\rangle, |\uparrow_1\downarrow_2\rangle, |\downarrow_1,\uparrow_2\rangle, |\downarrow_1\downarrow_2\rangle\}$. This allows us to perform two-tone

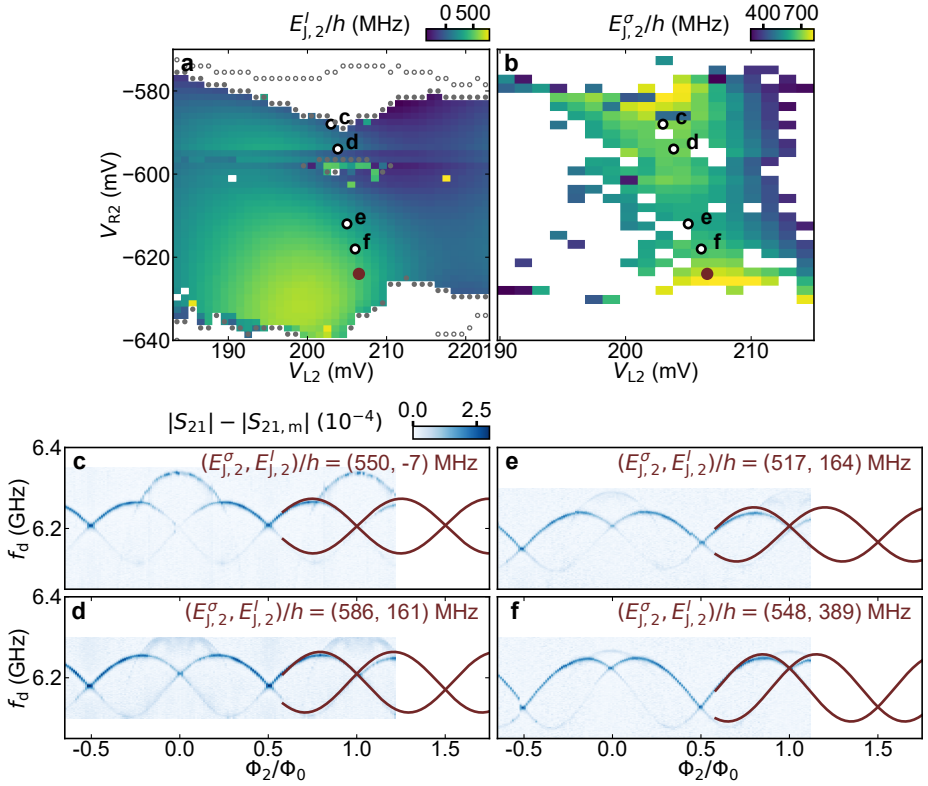

Figure 9.17: **ASQ2 gate dependence around its gate setpoint.** **a** Estimate of spin-independent Josephson energy of ASQ2, $E^I_{J,2}/h$, versus the two tunnel gates of ASQ2, for fixed $V_{P2} = 0$, obtained from two-tone spectroscopy measurements of the transmon transitions at $B_r = 0$ and at two different flux values: $\Phi_2 = 0$ and $\Phi_2 = \Phi_0/2$. The open and filled grey markers indicate the boundaries of the singlet-doublet transition at $\Phi_2 = 0$ and $\Phi_2 = \Phi_0/2$, respectively. **b** Estimate of spin-dependent Josephson energy of ASQ2, $E^\sigma_{J,2}/h$, versus the two tunnel gates of ASQ2, for fixed $V_{P2} = 0$, obtained from two-tone spectroscopy measurements of the spin-flip transition, f_2, at $B_r = 0$ and $\Phi_2 = \Phi_0/4$. The maroon marker in **a** and **b** indicates the gate setpoint of ASQ2 in the main text. **c** - **f** Transmon spectroscopy at various gate configurations indicated with markers in **a** and **b**. The values of $E^I_{J,2}/h$ indicated in the labels are extracted by fitting the measured transmon frequencies at $\Phi_2 = 0$ and $\Phi_2 = \Phi_0/2$ to their theoretical values. The value of $E^\sigma_{J,2}/h$ is extracted from the distance between transmon frequencies at $\Phi_2 = \Phi_0/4$. The continuous lines are the corresponding transmon frequencies obtained by numerical diagonalization of Eq. (9.16). Panels **c** - **f** share the color map.

spectroscopy of either one of the two qubit transitions, f_1 and f_2, which are present when both ASQ junctions are open. Here, we show the analogous situation when only *one* out of the two ASQs is open, while the junction containing the other one is fully pinched off (Fig. 9.19).

Fig. 9.19a shows the Φ_1-dependence of resonator spectroscopy, at zero magnetic field and when only ASQ1 is open. In this case, we observe two branches of the resonator frequency, corresponding to the two possible states of ASQ1: $|\uparrow_1\rangle$ or $|\downarrow_1\rangle$). The different visibility of each of the branches is a consequence of the different thermal populations

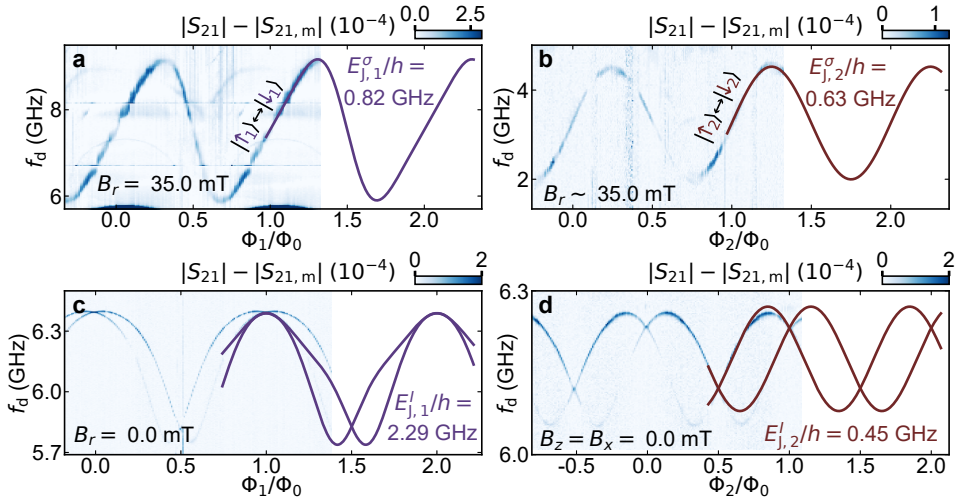

Figure 9.18: **Parameter estimation for both ASQs. a** Spin-flip spectroscopy of ASQ1 versus Φ_1, at $B_r = 35$ mT. The line shows a fit to a skewed sinusoidal dependence (Eq. (9.22)) from which we extract the value of $E^{\sigma}_{J,1}/h = 0.82$ GHz. **b** Spin-flip spectroscopy of ASQ2 versus Φ_2, at $B_r \sim 35$ mT. The line shows a fit to a sinusoidal dependence (Eq. (9.21)) from which we extract the value of $E^{\sigma}_{J,2}/h = 0.63$ GHz. **c** Transmon spectroscopy versus Φ_1, at $B_r = 0$ mT with ASQ1 open to its setpoint (see Tab. 9.2) and ASQ2 closed. The two transmon frequencies correspond to the two possible states of ASQ1. **d** Transmon spectroscopy versus Φ_2, at $B_r = 0$ mT with ASQ2 open to its setpoint (see Tab. 9.2) and ASQ1 closed. The two transmon frequencies correspond to the two possible states of ASQ2. For **a** and **b**, $V_C = 1500$ mV, while for **c** and **d**, $V_C = 1995$ mV. The continuous lines in **c** and **d** show the transmon transition spectrum given the spin-dependent part of the ASQ potentials found in **a**, **b** and the measured value of E_c (see Tab. 9.1). In both cases, the frequencies are obtained by numerical diagonalization of the Hamiltonian in Eq. (9.16) and are best fits of the measured data at Φ_i being integer multiples of $\Phi_0/2$. From these transmon spectra, we extract the values of the spin-independent Josephson energies $E^{I}_{J,1}/h = 2.29$ GHz and $E^{I}_{J,2}/h = 0.45$ GHz.

of the two states at $B_r = 0$. This is expected, since the spin-splitting of ASQ1 varies with flux reaching up to $2E^{\sigma}_{J,1}/h = 1.64$ GHz, comparable, when transformed into an effective temperature, to typical electron temperatures found in other experiments (Jin et al., 2015; Uilhoorn et al., 2021) (see Chapter 8). Fig. 9.19b shows the analogous situation but now for ASQ2. In this case, the resonator also displays two separate frequencies. After fixing B_y so that $\Phi_2 \sim -\Phi_0/4$ and so that the separation between the resonator frequencies corresponding to $|\uparrow_2\rangle$ and $|\downarrow_2\rangle$ is sizable, we open ASQ1 to its setpoint. In such situation, when performing resonator spectroscopy versus Φ_1, we observe four different transitions, labeled with their corresponding states in Fig. 9.19c. Note that, in this case, the difference in visibility becomes more perceptible due to the larger energy separation between the different states $\{|\uparrow_1\uparrow_2\rangle, |\uparrow_1\downarrow_2\rangle, |\downarrow_1,\uparrow_2\rangle, |\downarrow_1\downarrow_2\rangle\}$.

MAGNETIC FIELD ANGLE DEPENDENCE AND DETERMINATION OF THE SPIN-SPLITTING DIRECTION

In this subsection, we specify the measurements performed to determine the zero-field spin-polarization direction for each Andreev spin qubit. For each qubit, we perform spin-flip spectroscopy measurements, like those shown in Fig. 9.18a and b, for differ-

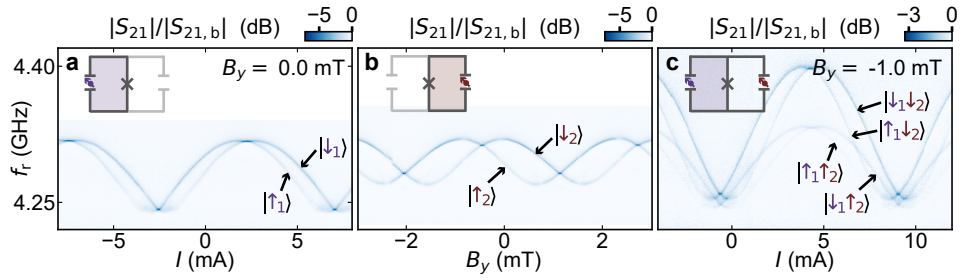

Figure 9.19: **Readout.** Amplitude of the transmission through the readout circuit, $|S_{21}|$, with background, $|S_{21,b}|$, divided out. **a** With ASQ1 open at its setpoint (see Tab. 9.2) and ASQ2 closed ($V_{L2} = V_{P2} = V_{R2} = -1000\,\text{mV}$). **b** With ASQ1 closed ($V_{LP1} = V_{R1} = -1000\,\text{mV}$) and ASQ2 open at its setpoint (see Tab. 9.2). **c** With both ASQ1 and ASQ2 open, as also displayed in Fig. 9.1d. **a, c** are plotted vs. the current through the flux line I, which controls Φ_1. **b** is plotted vs. B_y, which controls Φ_2. For all panels, $B_x = B_z = 0$ and $V_C = 180\,\text{mV}$.

ent magnetic field directions. As reported also in Chapter 7, we observe that both the flux dispersion of the spin-flip transition, df, as well as the g-factor, depend strongly on the direction of the applied magnetic field. To determine these quantities, the maxima, $f_i^{\max}$, and minima, $f_i^{\min}$, of the spin-flip frequencies are first extracted by hand from two-tone spectroscopy measurements of the spin-flip transition, analogous to those in Fig. 9.18a, b. The g-factors are calculated from the average of these maximum and minimum frequencies, as $g = (f_i^{\max} + f_i^{\min})/(2\mu_B B_r)$, where μ_B is the Bohr magnetron and B_r is the magnitude of the applied magnetic field. The frequency dispersion is determined as $df = (f_i^{\max} - f_i^{\min})/2$. The dependence of g and df on the magnetic field direction is shown in Fig. 9.20 with purple and maroon markers for ASQ1 and ASQ2, respectively.

First, we investigate the dependence on the angle within the chip plane and away from the nanowires axis, $\theta_{\phi=90}$. $\theta_{\phi=90} = 0$ indicates that the field is applied approximately along the nanowires axis, while $\theta_{\phi=90} = 90$ degrees indicates that the field is applied in-plane but approximately perpendicular to the nanowire axis. We find that the g-factor of ASQ1 depends strongly on $\theta_{\phi=90}$, while that of ASQ2 stays almost constant, fluctuating only between 5.5 and 6.5 (Fig. 9.20a). Within this plane, the g-factor of ASQ1 is found to be maximal when the magnetic field B_r is applied approximately along the nanowires axis, while for ASQ2 it is maximized for $\theta_{\phi=90} \sim 31$ degrees away from the nanowire axis. Performing the same experiment while varying the field direction in the x-z plane, the plane perpendicular to the chip and containing the nanowires axis, we observe a similar dependence (Fig. 9.20c). This time, the ASQ1 g-factor is again maximized along the nanowires axis, while that of ASQ2 becomes maximal when B_r is applied $\theta_{\phi=0} \sim 60$ degrees away from the nanowires axis. This variability of the g-factor dependence for different configurations is consistent with previous observations of quantum dots implemented in InAs nanowires and is thought to be due to mesoscopic fluctuations of the electrostatic environment at the quantum dot (Han et al., 2023) (as detailed in Chapter 7).

To learn about the zero-field spin-polarization direction of each qubit, we now focus on the field-direction dependence of the flux dispersion of the spin-flip transition.

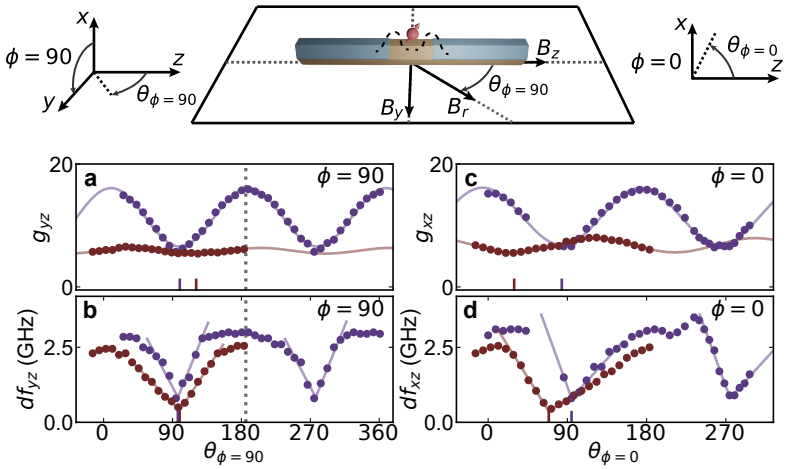

Figure 9.20: **Magnetic field angle dependence.** **a** g-factor for both ASQs for varying magnetic field direction in the chip plane, $y-z$, plotted as a function of the angle between the applied field and the nanowire axis, $\theta_{\phi=90}$. The g-factor is calculated as the average between its maximum and minimum values versus flux. Data points corresponding to ASQ1 and ASQ2 are colored purple and maroon, respectively. The continuous lines are cosinusoidal fits to the data. **b** Flux-dispersion of the spin-flip, df_{yz}, for both ASQs versus $\theta_{\phi=90}$. df_{yz} is calculated as the difference between the maximum and minimum of the spin-flip frequency f_i versus flux. The continuous lines are fits to the data around their minima and the colored vertical lines on the x-axis indicate the positions of the minima extracted from the fits, which are interpreted as the directions perpendicular to the zero-field spin-polarization direction for each qubit. Note that these lines do not coincide with the minima of the g-factors found in **a**. The vertical dotted lines in **a**, **b** indicate the field angle along which all measurements in the main text, except for Fig. 9.2c,d, were taken. **c**, **d** Same as **a**, **b** but in the $x-z$ plane, the plane perpendicular to the chip which contains the nanowires axis.

We denote by df the difference in frequency between the maximum and minimum of the spin-flip frequency versus flux. When the field is applied along the zero-field spin-polarization direction, we expect that $df = 4E^{\sigma}_{\mathrm{J},i}$ (see Sec. 9.6.1). However, when a component of the applied magnetic field is perpendicular to the zero-field spin-polarization direction, df is reduced due to the hybridization of the two spin states (see Chapter 7). Fig. 9.20b shows the $\theta_{\phi=90}$ dependence of df for both ASQs. We find that, in both cases, df becomes minimal at a direction approximately perpendicular to the nanowire axis. We also perform a similar experiment in the x-z plane (see Fig. 9.20d). The extracted angles constitute two of the directions perpendicular to the spin-polarization axis. Their cross-product thus returns the zero-field spin polarization directions for each qubit, which are indicated in Tab. 9.3 in spherical coordinates, where $\theta_{||}$ denotes the polar angle away from the nanowire axis and $\phi_{||}$ denotes the azimuthal angle measured away from the x-axis (see Fig. 9.20). The angle between this direction and the direction of the applied magnetic field in Figs. 9.3 and 9.4 ($\theta = 185, \phi = 90$) is indicated in the last column of Tab. 9.3.

The angle used for all measurements in the main text, except for Fig. 9.2c,d, is indicated with vertical dotted lines in Fig. 9.20a and b. We chose this angle following various considerations. First, we wanted to minimize the field component perpendicular to the

spin directions of each of the ASQs. The reason for this is that we expect transverse qubit-qubit coupling terms to emerge under the presence of a large perpendicular Zeeman energy compared to $E^{\sigma}_{\mathrm{J,i}}$, at the cost of the longitudinal component. Second, we wanted to maximize the difference in g-factors to avoid crossings between the qubit frequencies versus flux. This enables the possibility of spectroscopically measuring the coupling strength at every flux point. Finally, we chose the total field magnitude $B_r = 35\,\mathrm{mT}$ to set the ASQ frequencies at setpoints that did not cross neither the resonator nor any transmon transition frequency for any value of flux.

	$\theta_{\|\|}$	$\phi_{\|\|}$	α
ASQ1	8.54	54.76	5.1
ASQ2	22.73	157.15	21.5

Table 9.3: **Zero-field spin-polarization directions for ASQ1 and ASQ2 in degrees.** The zero-field spin-polarization direction $(\theta_{||}, \phi_{||})$ is calculated as the vector product of the two perpendicular directions indicated with colored lines in the x-axis of Fig. 9.20b,d. α denotes the angle between the field applied in the main text measurements and the spin-polarization direction for each qubit.

9.6.4. SUPPLEMENTARY COHERENCE DATA

We now describe the functions used for extracting the coherence times quoted in the main text. To determine T_1 we fit an exponential decay

$$y(t) = a \cdot \exp[t/T_1] + c \tag{9.24}$$

where a, T_1 and c are free fit parameters. For Ramsey and Hahn echo (see Fig. 9.21) experiments we fit a sinusoide with a exponential decay envelope and sloped background

$$y(t) = a \cdot \cos\left(\frac{2\pi}{p}t - \phi\right) \cdot \exp\left[(-t/T_2)^{d+1}\right] + c + et \tag{9.25}$$

where a, T_2, ϕ, c, e and p are free fit parameters and d was fixed to 1, resulting in a Gaussian decay envelope. We found that $d = 1$ gave the least χ-squared in the fit compared to $d = 0, 2$. The tilted background was included to compensate for a slightly non-linear Rabi response.

HAHN ECHO DECAY TIME MEASUREMENTS OF ASQ1 AND ASQ2

To verify the slow nature of the noise causing dephasing, we performed Hahn-echo experiments with artificial detuning, shown in Fig. 9.21. The resulting data was fit using Eq. (9.25). Note that for these measurement we found that the data was not always within the range of the identity and π-pulse calibration points. We suspect this is due to the additional echo pulse inducing leakage to other states outside the spin-subspace. We therefore normalized the data setting 0 and 1 to the minimum and maximum of the fit envelope at $\tau = 0$ instead of using the calibration points as was done in the main text.

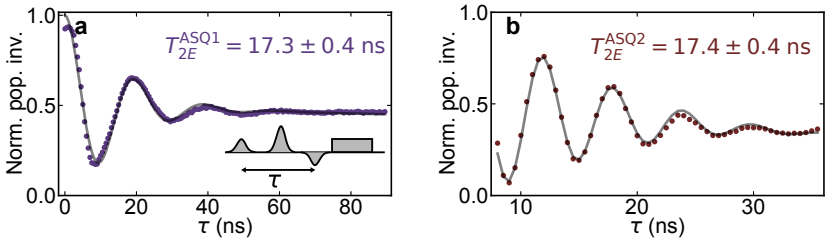

Figure 9.21: **Hahn echo experiment on ASQ1 and ASQ2. a, b** Measurement of T_2-echo for ASQ1 and ASQ2, respectively, with artificial detuning at the setpoints indicated in Fig. 9.2. The pulse sequence is shown in the inset of **a**. This is the same sequence as used in the Ramsey experiment, but with a π-pulse added between the two $\pi/2$ pulses. In **a**, an artificial detuning corresponding to a period of 20 ns was set and in **b** it was set to 6 ns. This data was taken using Gaussian pulses with FWHM of 4 ns and averaged over $3 \cdot 10^5$ shots for each data point. The y-axis is normalized using the fit (for details, see the accompanying text in Section 9.6.4).

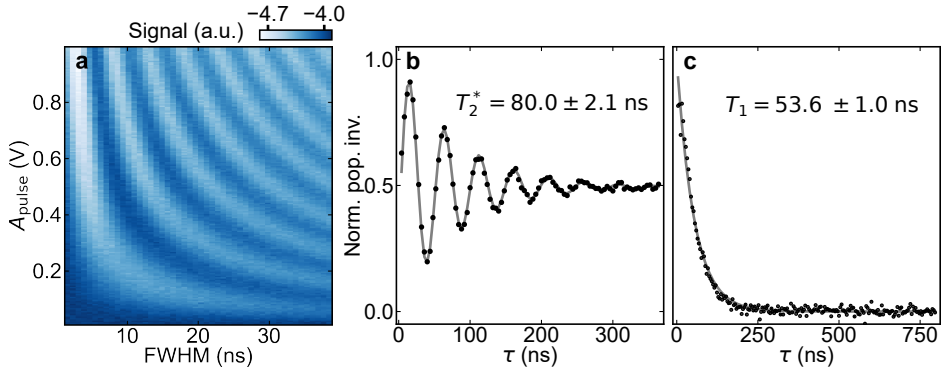

Figure 9.22: **Transmon coherence properties.** **a** Rabi oscillations versus the full-width at half maximum (FWHM) and amplitude of the Gaussian pulse. **b** Standard T_2^* measurement using a Ramsey sequence with Gaussian pulses of FWHM = 5.5 ns. The fit to Eq. (9.25) (grey line) was performed here with $d = 0$. **c** T_1 measurement. For panels **b** and **c** the data was normalized using the fitted scaling constants of Eqs. (9.24) and (9.25).

9

COHERENCE PROPERTIES OF THE TRANSMON

Although the transmon was used in this work to facilitate spin readout, we now demonstrate its coherence properties. Fig. 9.22 shows measurements of the transmon's Rabi oscillations, Ramsey coherence time and energy decay time.

The transmon T_1 was found to be lower than that of previous implementations of a transmon using gate-tunable nanowires (Bargerbos et al., 2023; Casparis et al., 2016; Kringhøj et al., 2021; Larsen et al., 2015; Luthi et al., 2018) (see Chapter 8), which we suspect may be due to it being too strongly coupled to the flux-bias line or drive lines. This in turn limits the ASQs T_1 due to Purcell decay via the transmon. Given a transmon T_1 of 53.6 ns, we can estimate the limit set by Purcell decay for each ASQ. At their setpoints in Fig. 9.2, the detunings from the transmon were 1.7 GHz and 2.2 GHz for ASQ1 and ASQ2, respectively. From measurements of the avoided crossing between the ASQ spin-flip and transmon transitions under similar conditions, we extract that the cou-

pling strengths between transmon and ASQ are in the range 50 MHz to 100 MHz for both qubits. These quantities allow us to estimate the Purcell limit of T_1 for both qubits to be 14-56 µs for ASQ2 and 23-92 µs for ASQ1. The higher harmonics of the transmon can reduce these lifetimes even more, especially for ASQ1 which resides close to the first higher harmonic. However, we did not measure the lifetime of that transition.

SCALING OF EXTRACTED T2* WITH PULSE LENGTH

Due to the short dephasing time of ASQs with respect to the pulse length, the pulse length influences the observed life time of the ASQs when the pulses are (partly) overlapping (see Fig. 9.23). This is the case because, during the part of the decay time τ, the ASQ is being driven. Therefore, care should be taken when pulses of length comparable to T_2^* are used. In the main text we report values obtained using short 4 ns FWHM pulses.

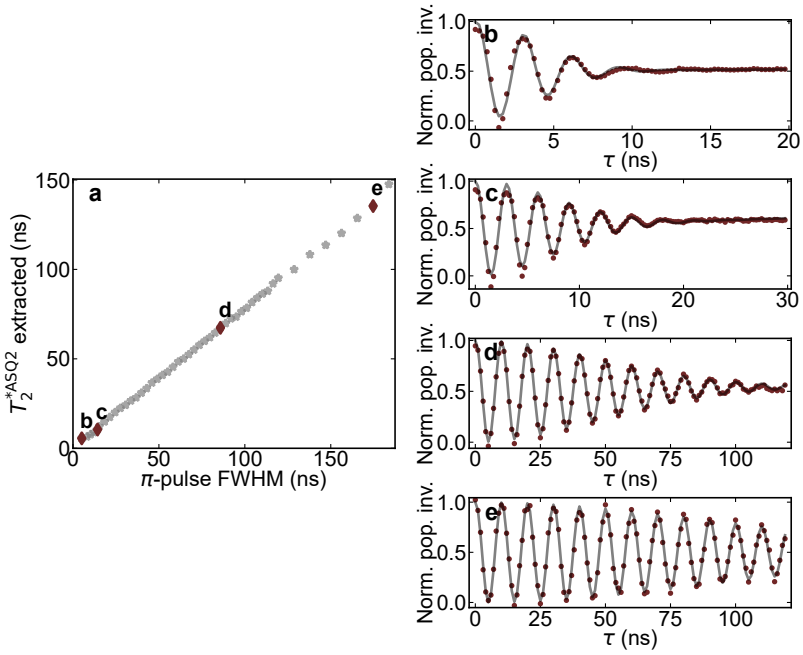

Figure 9.23: **Effect of overlapping pulses on the extracted T_2^{*ASQ2} for ASQ2.** **a** Extracted T_2^{*ASQ2} by performing Ramsey experiments on ASQ2 as a function of the $\pi/2$-pulse FWHM. For each data point we reduced the amplitude of the $\pi/2$-pulse by the same factor as we increased the pulse length to keep an approximate $\pi/2$-pulse, using the calibration for the shortest pulse length. **b**-**d** Examples of the data with T_2^{*ASQ2} fits indicated with maroon markers in **a**. The artificial detuning period was varied with pulse length to make sure there were enough points in each period and enough oscillations in the length of the traces.

SINGLE-SHOT READOUT CONTRAST OF INDIVIDUAL ASQS

In Fig. 9.24 we show examples of single-shot readout outcomes. These are measured at the setpoints used in the main text and at magnetic field settings of the main text for ASQ1 and for ASQ2 we go to a higher magnetic field in order to reduce thermal popula-

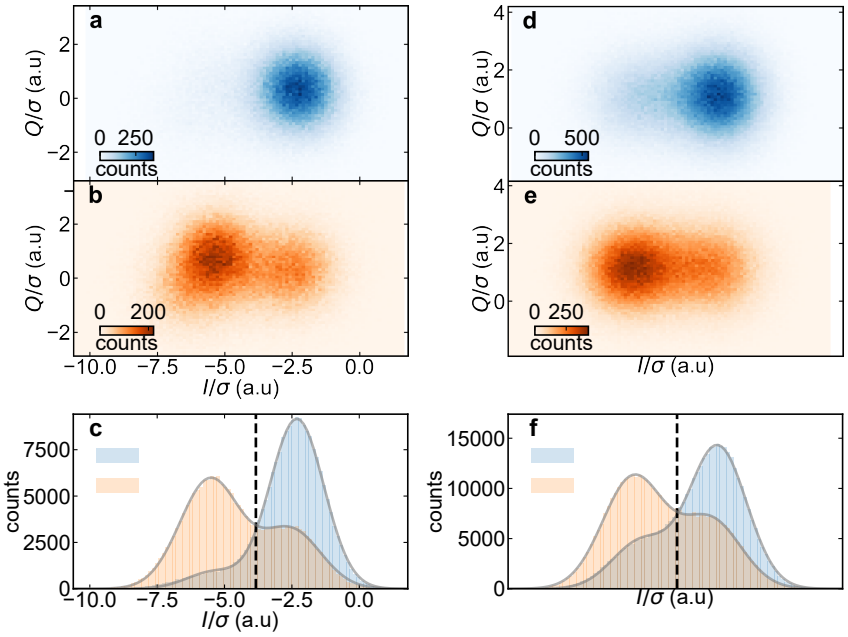

Figure 9.24: **Individual qubit readout shots**. **a**-**c** Histograms of single shot readout of ASQ1 near the maximum of the transition ($I = -2$ mA) at $B_z = 35$ mT (same setpoint as for the coherence measurements in the main text). **a**, **b** Histogram of single shot measurements in the $I-Q$ plane after initializing in $|\downarrow_1\rangle$ and $|\uparrow_1\rangle$, respectively. **c** Projection of the data in **a** and **b** along the I-axis fitted with a double Gaussian function (grey line) for each initialization. A 1000 ns readout pulse and a ~2 ns FWHM π-pulse were used. The black dashed line in **c** indicates the optimal threshold to distinguish spin-up from spin-down states and is used to calculate the fidelity F. **d**-**f** Histograms of single-shot readout of ASQ2 at $B_z = 80$ mT for a 1500 ns-long readout pulse and a ~ 4.7 ns FWHM π-pulse, at $B_y = 5.96$ mT.

tion of the excited spin state. We obtain an average signal-to-noise ratio for distinguishing spin-up and spin-down, based on double Gaussian fits to the up and down initializations SNR $= |\mu_\uparrow - \mu_\downarrow|/(2\sigma)$ where μ_i, σ are the mean and width of the fitted Gaussian corresponding to state i, of 1.5 and 1.3 in a integration time of 1 µs, 1.5 µs for ASQ1 and ASQ2 respectively. Note that we use the fit parameters of the initialization without a π-pulse here as the pulse can cause excitations of other states, which we suspect to be the transmon excited states, visible as an extra tail in the Gaussian corresponding to the excited spin state in Fig. 9.24b, c. Additionally, these values are strongly flux and magnetic field dependent and thus could be optimized further in future works, as we did not perform an exhaustive study here.

The SNR is a measurement of the pure readout contrast, rather than the more standard readout fidelity $F = 1 - P(\uparrow|\downarrow)/2 - P(\downarrow|\uparrow)/2$, where $P(a|b)$ denotes the probability of obtaining state a when preparing state b. This is because F includes the effects of thermal population and imperfect π-pulse, due to dephasing during the π-pulse and imperfect calibrations. At the main text gate setpoint, and the magnetic field settings mentioned above using the indicated threshold (black dashed line in Fig. 9.24) we ob-

tain $F = 0.75$ and $F = 0.67$ for ASQ1 and ASQ2 respectively.

9.6.5. SUPPORTING DATA FOR THE LONGITUDINAL COUPLING MEASUREMENTS

Fig. 9.25 shows data taken in the same way as in Fig. 9.3 and under the same field, gate and flux conditions, but for varying frequency of the pump tone f_p. We find that, when f_p matches the transition frequency of one of the qubits, and thus continuously drives it to its excited state, the frequency of the other qubit splits in two, as discussed in the main text (red lines in Fig. 9.25c and d). When the pump tone frequency instead does not match the transition frequency of the first qubit, the frequency of the second qubit does not split, as expected (black lines in Fig. 9.25c and d). This confirms that the frequency splitting observed in the main text is indeed the result of both states of the other ASQ being populated.

In Fig. 9.26 we perform a similar experiment for two fixed pump frequencies away from the spin-flip transitions and as a function of the pump tone power. For Fig. 9.26a and b, the pump tone drives the transmon transition and for Fig. 9.26c and d its frequency is set to a value $f_p = 5.8\,\text{GHz}$ where no transition is driven. In neither of the two cases do we observe a splitting of any of the two ASQ transitions at any power, as expected. Note that the instability that can be observed in the measured transition frequencies was also observed versus time and is thus unrelated to the presence of the pump tone.

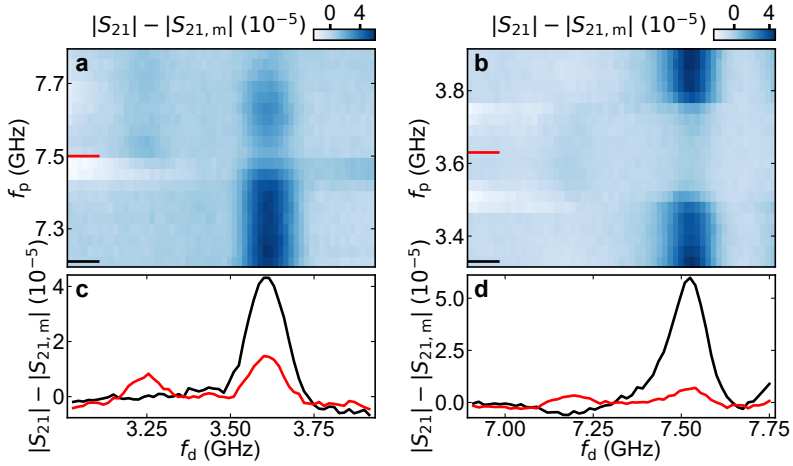

Figure 9.25: **Third tone frequency dependence of the longitudinal coupling signal. a** Spectroscopy of ASQ2 as a function of the drive frequency f_d while continuously applying a pump tone at varying frequency f_p. The red line indicates the pump tone frequency used in Fig. 9.3b and d, $f_p = f_1 - J$. **b** Same as in **a** but with the roles of ASQ1 and ASQ2 exchanged. In this case, the pump tone has a frequency close to that of ASQ2, while performing spectroscopy of ASQ1. **c** and **d** show line-cuts of **a** and **b**, respectively, at two fixed pump frequencies indicated in **a** and **b** with color matching lines.

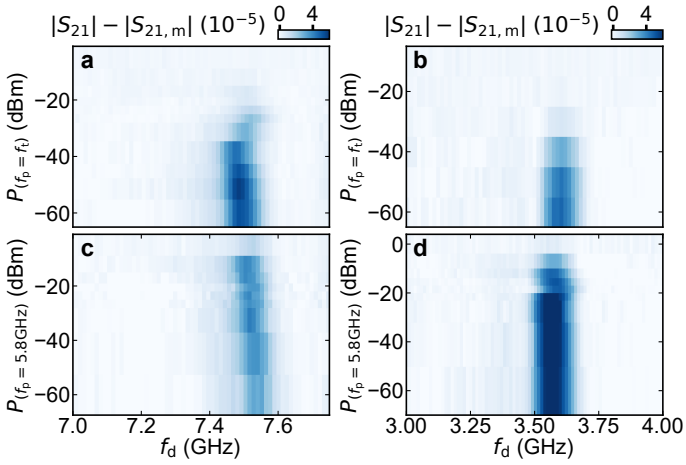

Figure 9.26: **Qubit spectroscopy while driving at different frequencies with the third pump tone. a** Two-tone spectroscopy of ASQ1 while driving with the third pump tone at the transmon frequency $f_p = f_t$ with varying power. **c** Same as **a** but for $f_p = 5.8$ GHz, not in resonance with any visible transition. **b** and **d** Same as **a** and **c** but for ASQ2.

9.6.6. LONGITUDINAL COUPLING AT DIFFERENT GATE SEPOINT

In this subsection, we present longitudinal coupling measurements similar to those in the main text, but now taken at a different gate configuration for both Andreev spin qubits. The new gate setpoints, at which the two qubits are set for all results discussed in this subsection, are indicated in Tab. 9.4.

	V_{Li} (mV)	V_{Pi} (mV)	V_{Ri} (mV)	$E^I_{J,i}/h$ (GHz)	$E^\sigma_{J,i}/h$ (GHz)
ASQ1	61.0	61.0	376.0	1.79	0.66
ASQ2	53.0	0.0	-700.0	0.53	1.3

Table 9.4: ASQ1 and ASQ2 gate voltage set points and extracted model parameters from the measurements in Fig. 9.27 .

We start by performing basic characterization measurements. The values of the spin-independent, $E^I_{J,i}$, and spin-dependent, $E^\sigma_{J,i}$, Josephson energies for both qubits are extracted from spin-flip and transmon spectroscopy measurements (see Fig. 9.27). Fig. 9.27a and b show in-field spectroscopy of the ASQ1 and ASQ2 spin-flip transitions, respectively. The values of $E^\sigma_{J,1}$ and $E^\sigma_{J,2}$ are extracted from fits to a skewed (Eq. 9.22) and a non-skewed (Eq. 9.21) sinusoidal relation, respectively. Fig. 9.27c and d show transmon spectroscopy measurements performed at zero magnetic field, each with only one of the two ASQs open (ASQ1 in panel c and ASQ2 in panel d). The values of $E^I_{J,i}$ are estimated by fitting the measured transmon transitions with Eq. 9.16 at Φ_i being integer multiples of $\Phi_0/2$.

Before investigating the longitudinal coupling strength at the new gate setpoints, we characterize their magnetic field dependence. The characterization is done analogously

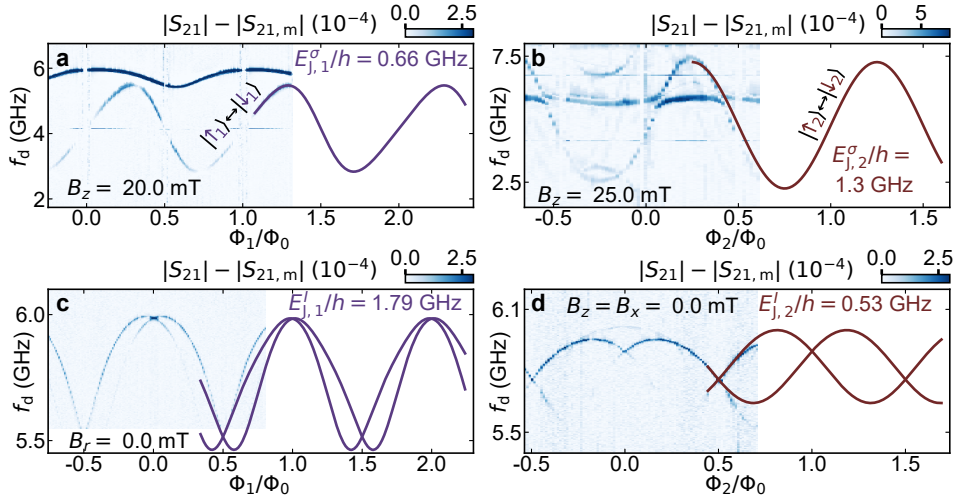

Figure 9.27: **Parameter estimation for both ASQs at the gate setpoints specified in Tab. 9.4.** **a** Spin-flip spectroscopy of ASQ1 versus Φ_1, at B_z = 20 mT. The line shows a fit to a skewed sinusoidal dependence (Eq. 9.22) from which we extract the value of $E^{\sigma}_{J,1}/h$ = 0.66 GHz. **b** Spin-flip spectroscopy of ASQ2 versus Φ_2, at $B_z \sim$ 25 mT. The line shows a fit to a sinusoidal dependence (Eq. 9.21) from which we extract the value of $E^{\sigma}_{J,2}/h$ = 1.3 GHz. **c** Transmon spectroscopy versus Φ_1, at B_r = 0 mT with ASQ1 open to its setpoint (see Tab. 9.4) and ASQ2 closed. The two transmon frequencies correspond to the two possible states of ASQ1. **d** Transmon spectroscopy versus Φ_2, at B_r = 0 mT with ASQ2 open to its setpoint (see Tab. 9.4) and ASQ1 closed. The two transmon frequencies correspond to the two possible states of ASQ2. For all panels, V_C = 1500 mV. The lines in **c** and **d** show the transmon transition spectrum given the spin-dependent part of the ASQ potentials found in **a**, **b** and the measured value of E_c (see Tab. 9.1). The lines in **c** and **d** are best fits to the measured data at Φ_i being integer multiples of $\Phi_0/2$. From these transmon spectra, we estimate the values of the spin-independent Josephson energies $E^{I}_{J,1}/h$ = 1.79 GHz and $E^{I}_{J,2}/h$ = 0.53 GHz.

to that for the previous gate setpoint (discussed around Fig. 9.20) and can be found in the data repository. The relevant extracted parameters are summarized in Tab. 9.5. By performing spin-flip spectroscopy of each of the two qubits at different field directions, we extract their g-factors on the chip plane, which range between 6 and 15 for ASQ1 and between 9 and 15 for ASQ2. The values along the B_z and B_y directions are reported in Tab. 9.5. As before, we determine the spin-flip polarization direction for ASQ1 by finding two perpendicular directions in the $y-z$ and $x-z$ planes. The resulting spin-polarization direction is reported in Tab. 9.5 and is this time found to be approximately 1.85 degrees away from the nanowire axis. For ASQ2 we did not determine the full spin-orbit direction as we only data measured in the $y-z$ plane.

Next, we measure the longitudinal coupling energy at the selected gate setpoints in the same way as for Fig. 9.3. Fig. 9.28a-d show a longitudinal coupling measurement for fixed control parameters B_z = 25 mT, $\Phi_1 = 0.1\Phi_0$, $\Phi_2 = 0.48\Phi_0$ and V_C = 180 mV. These parameters set f_1 = 4.7 GHz, f_2 = 5.3 GHz and $L_{J,C}$ = 22.3 nH. Similarly to Fig. 9.3, we find that the frequency of each of the qubits splits by $2J$ when the other qubit is driven with a pump tone f_p. From spectroscopy of ASQ2 while ASQ1 is driven (Fig. 9.28a, b), we find $J = -110.0 \pm 3.2$ MHz, while from spectroscopy of ASQ1 while ASQ2 is driven

	$g_z^{\mathrm{ASQ}i}$	$g_y^{\mathrm{ASQ}i}$	$\theta_{\|\|}$	$\phi_{\|\|}$	α
ASQ1	14.9	6.7	1.85	64.4	1.36
ASQ2	14.1	-	-	-	-

Table 9.5: **Summary of g-factors and relevant angles for ASQ1 and ASQ2 at their alternative setpoint.** The zero-field spin-polarization direction ($\theta_{||}$,$\phi_{||}$ in spherical coordinates) is calculated as the vector product of the two perpendicular directions $\theta_{yz,\perp}$ and $\theta_{xz,\perp}$. α denotes the angle between the field applied for the longitudinal coupling measurements of Fig. 9.28 and the spin-polarization direction for each qubit.

(Fig. 9.28c, d), we find -107.0 ± 3.1 MHz. These two values are equal within their one-sigma confidence intervals, consistent with the theory prediction.

Finally, we investigate the flux and $L_{\mathrm{J,C}}$ dependence of the coupling strength, similarly to how it is done in Fig. 9.4. Fig. 9.28e, f show the tunability of J at the setpoint of Tab. 9.4. These measurements are taken at the same B_z and Φ_2 conditions as in Fig. 9.28a-d, which result on a fixed supercurrent difference through ASQ2, $I_2 = -5.6$ nA. Panel e shows the Φ_1 dependence of J at $V_{\mathrm{C}} = 180$ mV, which fixes $L_{\mathrm{J,C}} = 22.3$ nH. Similarly to what was found in the main text, we observe that J can take both positive and negative values and that it follows a similar shape as that predicted by Eq. 9.5. We however note that, especially around $\Phi_1 = \Phi_0$, the data deviates from the behavior predicted by Eq. 9.5. This is due to the fact that this data is not taken for parameters consistent with the limit $L_{\mathrm{J,C}} \ll L^{\sigma}_{\mathrm{J},i}, L^{I}_{\mathrm{J},i} \forall i$. As shown in Fig. 9.6, when this limit is not met Eq. 9.5 overestimates the value of J in the region of $\Phi_1 \sim \Phi_0$.

Finally, Fig. 9.28f shows the evolution of J with $L_{\mathrm{J,C}}$ at a fixed $\Phi_1 = 1.1\Phi_0$ setpoint, indicated with a yellow marker in Fig. 9.28e, which sets $I_1 = 1.7$ nA. As expected, we find an increase of the magnitude of J with $L_{\mathrm{J,C}}$, which is proportional, with a scaling factor $A = 0.79 \pm 0.02$, to Eq. 9.2 given $L_{\mathrm{ASQ}} = \frac{\Phi_0^2}{4\pi^2} / (E^I_{\mathrm{J},1} \cos(\frac{2\pi}{\Phi_0}\Phi_1) + E^I_{\mathrm{J},2} \cos(\frac{2\pi}{\Phi_0}\Phi_2)) = 176.9$ nH.

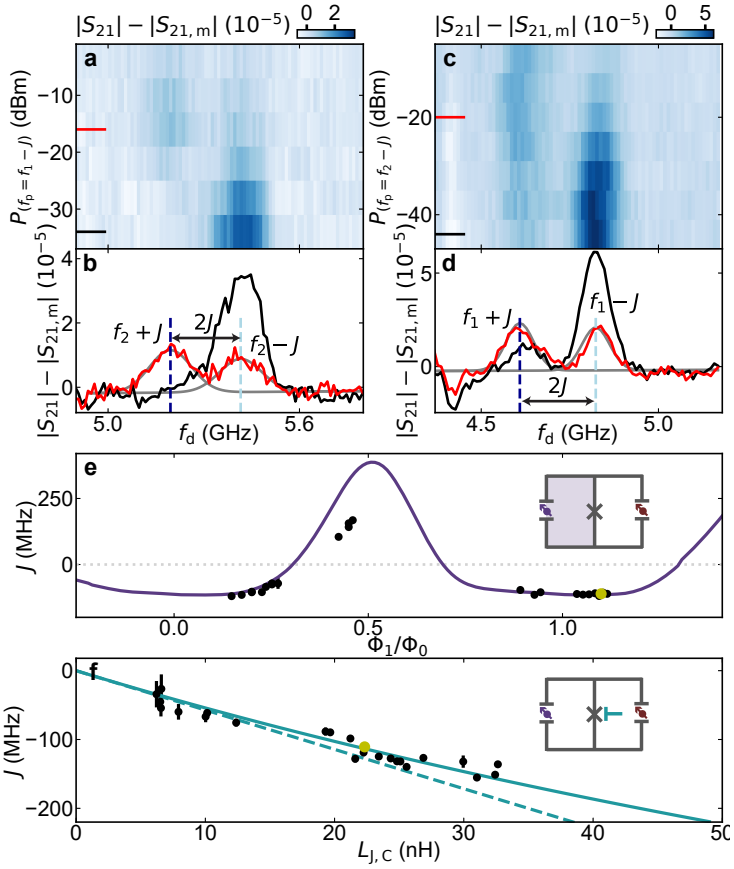

Figure 9.28: **Longitudinal coupling between the two Andreev spin qubits at different gate setpoint.** Data measured and processed in the same way as for Figs. 9.3 and 9.4 in the main text, but now for alternative ASQ1 and ASQ2 gate setpoints, reported in Tab. 9.4. **a** Spectroscopy of ASQ2 as a function of the drive frequency, f_d and the power of a pump tone resonant with ASQ1 at frequency $f_\mathrm{p} = f_1 - J$. **b** Linecuts of **a** at the powers indicated with color-matching lines. The grey line shows the result of a double-Gaussian fit to the signal in red (see Sec. 9.6.2) and the vertical lines indicate the best-fit values of the two Gaussian centers. **c**, **d** Similar to the situation of **a**, **b**, but with the roles of ASQ1 and ASQ2 exchanged. In this case, the pump tone drives ASQ2 at a frequency $f_\mathrm{p} = f_2 - J$, while performing spectroscopy of ASQ1. The longitudinal coupling strength, J, extracted from the fits is -110.0 ± 3.2 MHz and -107.0 ± 3.1 MHz, respectively for **b** and **d**. For **a** - **d**, $\Phi_1 = 0.1\Phi_0$. **e** Qubit-qubit coupling strength, J, as a function of flux in the loop for ASQ1, Φ_1, see also inset. The values of J are determined from a double Gaussian fit to a spectroscopy trace of one ASQ taken while driving the other ASQ. The markers and error bars represent the best-fit values and their estimated standard errors (one-sigma confidence intervals), respectively. The purple line shows the expected dependence $hJ(\Phi_1) = A\frac{L_{\mathrm{J,C}}L_{\mathrm{ASQ}}}{L_{\mathrm{J,C}}+L_{\mathrm{ASQ}}} I_1(\Phi_1) I_2/2$ for the value of A extracted from panel **f**. **f** Qubit-qubit coupling strength J at fixed $\Phi_1 = 1.1\Phi_0$ and as a function of $L_{\mathrm{J,C}}$, which is varied using the gate-voltage at the coupling junction (see inset). The continuous line shows a fit to the dependence $hJ(L_{\mathrm{J,C}}) = A\frac{L_{\mathrm{J,C}}L_{\mathrm{ASQ}}}{L_{\mathrm{J,C}}+L_{\mathrm{ASQ}}} I_1 I_2/2$. We extract a value $A = 0.79 \pm 0.02$ from this fit. The dashed line shows the linear dependence $hJ(L_{\mathrm{J,C}}) = AL_{\mathrm{J,C}} I_1 I_2/2$. The yellow marker in **e** and in **f** is a shared point between the two panels. For all panels, $B_z = 25$ mT, $B_y = 0.25$ mT, $B_x = 0.0$ mT and $\Phi_2 = 0.48\Phi_0$.

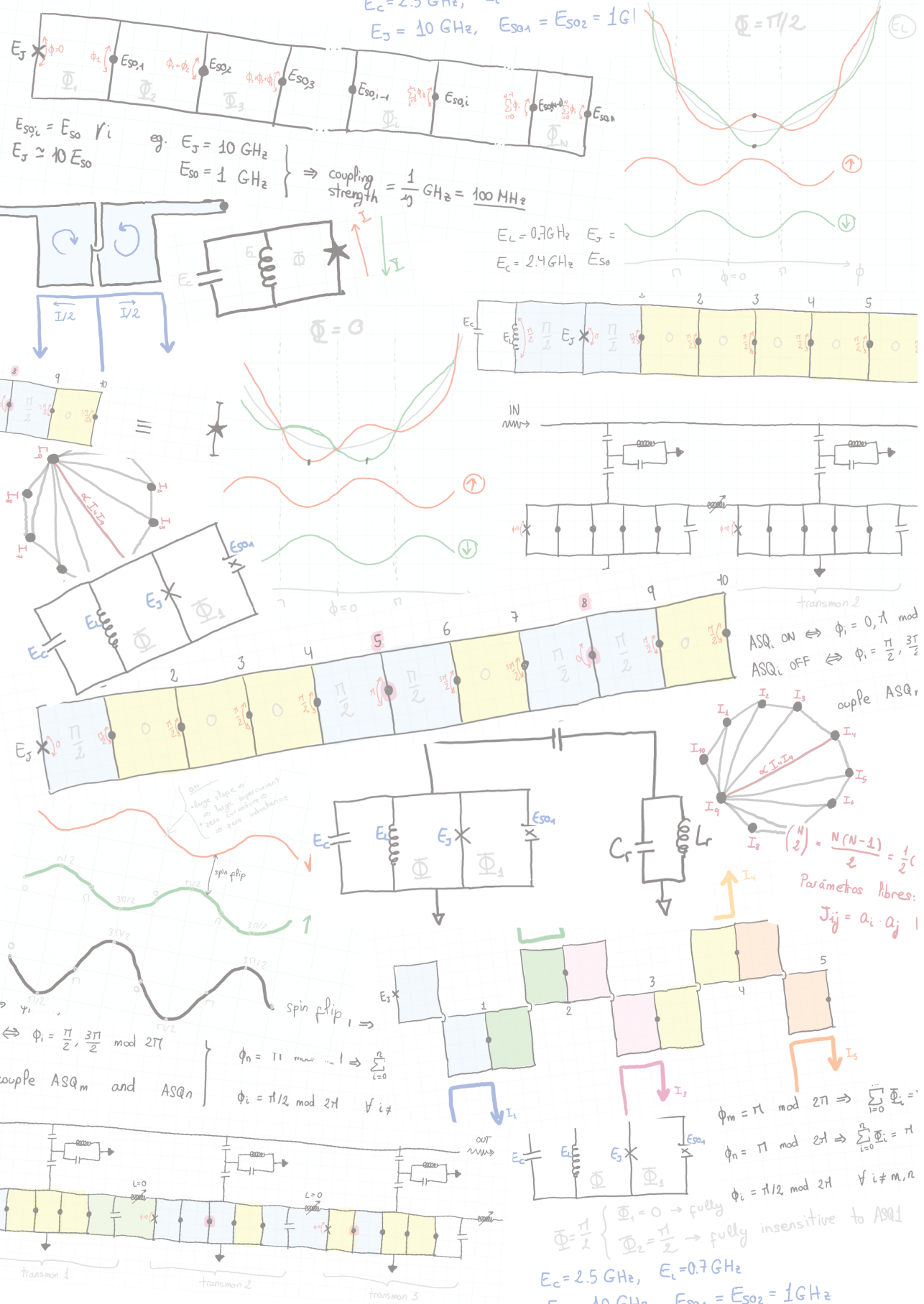
$E_J = 10\ GHz$, $E_{so1} = E_{so2} = 1G$
$E_{so,i} = E_{so}\ \forall i$
$E_J \simeq 10\, E_{so}$
eg. $E_J = 10\ GHz$, $E_{so} = 1\ GHz$ ⇒ coupling strength $= \frac{1}{10}\ GHz = 100\ MHz$
$E_C = 0.7 GHz$ $E_J =$
$E_C = 2.4 GHz$ E_{so}
$\Phi = \pi/2$
$\Phi = 0$
$\phi = 0$
π
ϕ
$I/2$
$I/2$
I
IN
transmon 2
$\propto I_i I_j$
E_{so1}
E_J
E_C
E_L
Φ_1
Φ_2
Φ
ASQ$_i$ ON ⇔ $\phi_i = 0, \pi$ mod
ASQ$_i$ OFF ⇔ $\phi_i = \frac{\pi}{2}, \frac{3\pi}{2}$
couple ASQ
$\binom{N}{2} = \frac{N(N-1)}{2} = \frac{1}{2}$
Parámetros libres:
$J_{ij} = a_i \cdot a_j$
spin flip
$\Leftrightarrow \phi_i = \frac{\pi}{2}, \frac{3\pi}{2}$ mod 2π
couple ASQ$_m$ and ASQ$_n$
$\phi_n = \pi$ mod 2π ⇒ $\sum_{i=0}^{n} \phi_i =$
$\phi_i = \pi/2$ mod 2π $\forall i \neq$
$\Phi = \frac{\pi}{2}$ { $\Phi_1 = 0$ → fully
$\Phi_2 = \frac{\pi}{2}$ → fully insensitive to ASQ1
$E_C = 2.5\ GHz$, $E_L = 0.7\ GHz$
$E_J = 10\ GHz$, $E_{so1} = E_{so2} = 1GHz$
transmon 1
transmon 2
transmon 3
L=0
out

10

BLUEPRINT FOR ALL-TO-ALL CONNECTED SUPERCONDUCTING SPIN QUBITS

Andreev (or superconducting) spin qubits (ASQs) have recently emerged as a promising qubit platform with realizations in semiconductor-superconductor hybrid nanowire Josephson junctions. While experiments have successfully coupled two distant ASQs, a scalable architecture for extending this coupling to multiple distant qubits has not been proposed. In this work, we introduce an architecture that achieves all-to-all connectivity between multiple remote ASQs. Our approach enables selective connectivity between any qubit pair while maintaining all other qubit pairs uncoupled. Furthermore, we demonstrate the feasibility of efficient readout using circuit quantum electrodynamics techniques and compare different readout configurations. This architecture shows promise both for gate-based quantum computing and for analog quantum simulation applications by offering higher qubit connectivity than alternative solid-state platforms.

To date, the two most scalable solid-state qubit platforms are semiconducting spin qubits and superconducting qubits. Recent experiments in these architectures have realized systems with tens and hundreds of coupled qubits, respectively (Borsoi et al., 2023; IBM Quantum, 2022b; Philips et al., 2022), as well as two-qubit gates with fidelities above 99 % (Barends et al., 2014; Hong et al., 2020; Mądzik et al., 2022; Mills et al., 2022; Noiri et al., 2022; Sheldon et al., 2016; Xue et al., 2022). However, both platforms are currently limited to low qubit connectivity, often restricted to nearest neighbors in planar grids, and typically featuring at most four to five connections per qubit (Boter et al., 2022; Li et al., 2018; Tadokoro et al., 2021; Vandersypen et al., 2017; Versluis et al., 2017). This sparse connectivity results in a considerable overhead in qubit count, both when it comes to gate-based quantum computation applications (Bravyi and Kitaev, 1998; Dennis et al., 2002; Google Quantum AI, 2023; Krinner et al., 2022; Zhao et al., 2022) and to analog quantum simulation applications (Cai et al., 2014).

Andreev (or superconducting) spin qubits (ASQs) have recently emerged as a promising hybrid qubit platform. Their state is encoded in the spin of a quasiparticle localized within a semiconducting quantum dot tunnel-coupled to two superconducting leads (Chtchelkatchev and Nazarov, 2003; Padurariu and Nazarov, 2010). Recent experimental realizations have explored systems with a single ASQ (Hays et al., 2021) (Chapter 8) as well as the supercurrent-mediated coupling between two distant ASQs (Chapter 9). Yet, no experiments involving more than two ASQs have been reported. An architecture for coupling multiple qubits to each other via wavefunction overlap has been proposed (Spethmann et al., 2022). However, this architecture enables the short-distance coupling of nearest-neighbour qubits in a planar layout, sharing the same connectivity constraints as semiconducting spin qubits and superconducting qubits.

Here, we introduce an architecture that offers a solution to the connectivity challenge. Our design allows for the coupling of multiple distant ASQs at a distance in a fully connected and scalable way. We demonstrate that this architecture permits selective connectivity between any qubit pair within the system while maintaining all other qubit pairs uncoupled. Furthermore, we illustrate how this system can efficiently perform quantum simulations of highly connected Ising models with a reduced qubit count and a smaller footprint compared to alternative solid-state platforms. The proposed architecture also facilitates sequential, individual, or joint qubit readout. Finally, we outline an experimental protocol for systematically tuning up the system to its operational setpoint.

10.1. CONCEPT

The circuit model of the device is shown in Fig. 10.1(a). It consists of a coupling junction, with Josephson energy E_J and phase drop ϕ across it, connected in parallel to a number, N, of Andreev spin qubits. The subspace of each ASQ is spanned by two spin states, denoted as $|\downarrow_i\rangle$ and $\langle\downarrow_i|$ for ASQi, where $1 \leq i \leq N$ is the qubit index. This configuration defines N loops through which magnetic fluxes, Φ_i, are threaded, as indicated.

The individual ASQs are implemented using semiconducting quantum dot Josephson junctions with substantial quantum dot charging energy (see Chapters 6, 7, 8 and 9). Each ASQ is characterized by a spin-dependent and a spin-independent Josephson energy, denoted as $E_{\mathrm{SO},i}$ and $E_{\mathrm{J},i}$, respectively (see Chapter 7). As discussed in Sec. 7.7.1

and Fig. 7.14, the values of $E_{\mathrm{SO},i}$ and $E_{\mathrm{J},i}$ can be tuned independently via electrostatic gates arriving at each qubit location (not shown in Fig. 10.1). The Hamiltonian of ASQi can be expressed in terms of these Josephson energies as

$$H_i(\phi_i) = E_{\mathrm{J},i}\sigma_i^0 \cos\left(\phi_i\right) - E_{\mathrm{SO},i}\sigma_i^z \sin\left(\phi_i\right) + \frac{1}{2}\vec{E}_{\mathrm{Z},i}\cdot\vec{\sigma}_i\,, \tag{10.1}$$

where $\sigma_i^z = |\uparrow_i\rangle\langle\uparrow_i| - |\downarrow_i\rangle\langle\downarrow_i|$ and σ_i^0 denote the z Pauli operator and the identity operator of ASQi, respectively, $\vec{\sigma}_i$ is the vector of x, y and z Pauli operators of ASQi and $\vec{E}_{\mathrm{Z},i}$ is the externally applied Zeeman field expressed in the coordinate system of ASQi.

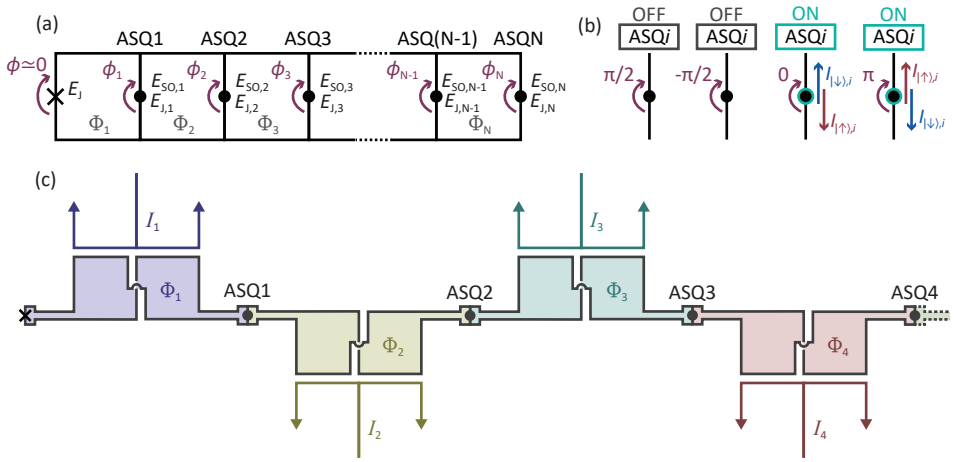

Figure 10.1: **Scalability of superconducting spin qubits.** (a) Circuit diagram of N superconducting Andreev spin qubits connected in parallel to a coupling Josephson junction with Josephson energy E_{J}, thus defining N loops. ASQi has spin-independent and spin-dependent Josephson energies $E_{\mathrm{J},i}$ and $E_{\mathrm{SO},i}$, respectively. The magnetic flux through loop i is denoted as Φ_i. The phase drop across ASQi is denoted as ϕ_i and that across the coupling junction as ϕ. The system is operated in the regime $E_{\mathrm{J}} \gg E_{\mathrm{J},i}, E_{\mathrm{SO},i}\ \forall i$, which results in $\phi \simeq 0$. (b) Diagrams of four possible phase setpoints for an ASQ. When $\phi_i = \pi/2, -\pi/2$ the spin-dependent component of the supercurrent vanishes and the qubit is labeled as OFF. When instead $\phi_i = 0, \pi$ the spin-dependent component of the supercurrent is maximal and the qubit is labeled as ON. (c) Example of a design that minimizes the flux cross-coupling between loops. Each loop is implemented with a twisted gradiometric geometry that renders it insensitive to global magnetic field noise. The two subloops of each loop, shaded with the same color, have identical areas. The magnetic flux through each loop is controlled with a flux bias line, indicated with a color-matching line.

To lowest order in $E_{\mathrm{SO},i}/E_{\mathrm{J}}$ and $E_{\mathrm{J},i}/E_{\mathrm{J}}\ \forall i$, the phase drop through the coupling junction becomes $\phi = 0$ and each ϕ_i is determined by the cumulative flux values from 1 to i,

$$\phi_i = \sum_{j=1}^{i} \varphi_j, \tag{10.2}$$

where $\varphi_i = 2\pi\Phi_i/\Phi_0$, $\Phi_0 = h/(2e)$ is the magnetic flux quantum, h is the Planck constant and e is the absolute value of the electron charge. Therefore, by controlling the external fluxes, one can independently fix the values of all phase drops ϕ_i.

Fig. 10.1(b) illustrates the four extreme phase configurations for ASQi, determined by the value of the spin-dependent component of the supercurrent through it, $I_{s,i}$. Taking the phase derivative of the ASQ Hamiltonian (Eq. 10.1) and assuming a magnetic field aligned with the spin-polarization direction, $\vec{E}_{Z,i} = E_Z \sigma_i^z$, we obtain its current operator,

$$\mathscr{I}_i = \frac{\pi}{\Phi_0} \frac{\partial H_i(\phi_i)}{\partial \phi_i} = \frac{I_{s,i}}{2} \sigma_i^z + I_{0,i} \sigma_i^0, \tag{10.3}$$

where $I_{0,i}$ represents a spin-independent component and the spin-dependent supercurrent is

$$I_{s,i} = \frac{2\pi}{\Phi_0} E_{SO,i} \cos(\phi_i). \tag{10.4}$$

Notably, when ϕ_i is either $\pi/2$ or $-\pi/2$, $I_{s,i}$ vanishes, rendering the supercurrent identical for both qubit states. On the contrary, when ϕ_i is either 0 or π, the spin-dependent component of the supercurrent is maximal. Throughout this chapter, we refer to these two setpoints as OFF and ON, as depicted in Fig. 10.1(b).

In practice, the fluxes through adjacent loops can be tuned independently and with maximal addressability using the geometry illustrated in Fig. 10.1(c). Each loop is implemented with a twisted gradiometric loop geometry similar to that of loop 1 in Chapter 9 (see Fig. 9.9). Each loop is inductively coupled to a flux bias line with current I_i and a symmetrical design at its end, where currents flow in opposite directions. This combination of the loop and flux bias line designs maximizes their coupling while minimizing unwanted cross-coupling to other loops, for various reasons. Firstly, the two opposite currents on the flux line induce contributions to the flux through the loop that add up due to its twisted geometry. Secondly, the generated magnetic field decreases with distance faster than for monopole flux line configurations, resulting in reduced magnetic fields at the locations of other loops. Thirdly, the gradiometric loop design reduces the sensitivity to homogeneous fields, again reducing the unwanted cross-coupling, as well as the sensitivity to global magnetic noise. We envision two possible driving mechanisms: either using the same flux bias lines for driving the Andreev spin qubits via supercurrent or connecting drive lines to the electrostatic gates to address each qubit via the electric dipole spin resonance (EDSR) mechanism (Golovach et al., 2006; Nowack et al., 2007).

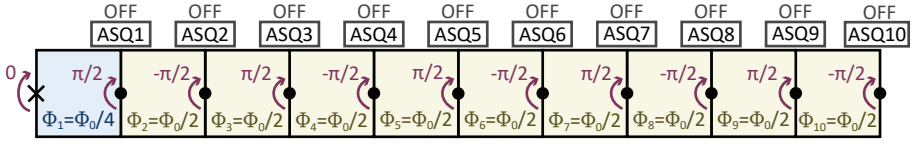

Figure 10.2: **Idling flux configuration.** Chain with $N = 10$ showing the flux setpoint for an idling configuration in which all qubits are uncoupled. $\Phi_1 = \Phi_0/4$ and $\Phi_i = \Phi_0/2\ \forall i > 1$ set alternating phase drops of $\pi/2$ and $-\pi/2$ for all qubits.

The system's global configuration can be adjusted by varying the flux setpoints of all qubits. An idling configuration where all qubits are OFF is shown in Fig. 10.1(c). By setting $\Phi_1 = \Phi_0/4$, ASQ1 is set to its OFF state, with $\phi_1 = \pi/2$. In turn, $\Phi_i = \Phi_0/2\ \forall i > 1$

result in alternating phase drops of $\pi/2$ and $-\pi/2$ for all other qubits, rendering them OFF as well. Consequently, in this configuration all qubits are uncoupled.

10.2. ALL-TO-ALL SELECTIVE COUPLING

When the external magnetic field is applied along the spin-polarization direction for all qubits, $\vec{E}_{Z,i} = E_Z \sigma_i^z$, the qubits become pairwise longitudinally coupled to each other[1], as detailed in Ref. (Padurariu and Nazarov, 2010) for the case of $N = 2$ (see Chapter 9). In this situation, the Hamiltonian describing the longitudinally coupled system can be expressed in the ASQ basis as

$$H_{\mathrm{ASQ}} = \sum_{i=1}^{N} \left(\frac{1}{2} E_i \sigma_i^z + \sum_{j<i}^{N} \frac{1}{2} J_{ij} \sigma_i^z \sigma_j^z \right) + C, \tag{10.5}$$

where E_i is the energy of qubit i, J_{ij} represents the longitudinal coupling energy between qubits i and j and C denotes an inconsequential spin-independent term. Following Ref. (Padurariu and Nazarov, 2010), to first order in $E_{\mathrm{SO},i}/E_{\mathrm{J}}$ we have that

$$J_{ij} = -2 \frac{E_{\mathrm{SO},i} E_{\mathrm{SO},j}}{|\tilde{E}|} \cos\left(\sum_{k=1}^{i} \varphi_k - \varphi_{\tilde{E}}\right) \cos\left(\sum_{k=1}^{j} \varphi_k - \varphi_{\tilde{E}}\right), \tag{10.6}$$

where

$$\tilde{E} = E_{\mathrm{J}} + \sum_{l=1}^{N} E_{\mathrm{J},l} e^{i \sum_{k=1}^{l} \varphi_k} \tag{10.7}$$

is the total spin-independent Josephson energy of the system and $\varphi_{\tilde{E}}$ is the argument of $\tilde{E}$. Therefore, to maximize the qubit-qubit coupling strength one needs to maximize $E_{\mathrm{SO},i}$ and keep $E_{\mathrm{J}} \gg E_{\mathrm{J},i}\ \forall i$.

In the limit of $E_{\mathrm{J},i}/E_{\mathrm{J}} \to 0\ \forall i$, the $\varphi_{\tilde{E}}$ term in the cosine vanishes. In such situation, it directly follows from Eq. 10.6 that, when two qubits are ON (with $\sum_{i=k}^{i} \varphi_k = 0, \pi$), the coupling between them is maximal. Conversely, when either one of the two qubits is OFF (with $\sum_{k=1}^{i} \varphi_k = \pm\pi/2$), the coupling between them becomes zero. Fig. 10.3(a) and (b) illustrate two possible flux configurations to selectively couple two pairs of qubits in this scenario.

Away from this limit, the ON and OFF flux setpoints deviate from their exact $0, \pi$ and $\pm\pi/2$ values by an amount, $\varphi_{\tilde{E}}$, that depends on the exact global flux configuration. However, it is still possible to recover the ideal scenario of maximal ON-ON coupling and vanishing OFF-OFF and ON-OFF couplings by adjusting the ON and OFF flux values according to the $\varphi_{\tilde{E}}$ offset. This offset can be independently measured in a separate calibration experiment. Consequently, at the corrected flux setpoints, non-zero values $E_{\mathrm{J},i}$ do not affect the unwanted couplings and only start reducing the magnitude of the wanted coupling substantially when their values become comparable to E_{J}.

Fig. 10.3(c) and (d) show the resulting coupling strengths for two realistic parameter sets, for $N = 10$ and $N = 30$, respectively. The couplings are displayed for a situation in

[1] Note that sizable perpendicular Zeeman components might introduce undesired transverse coupling terms between ASQs. See Sec. 10.7.2.

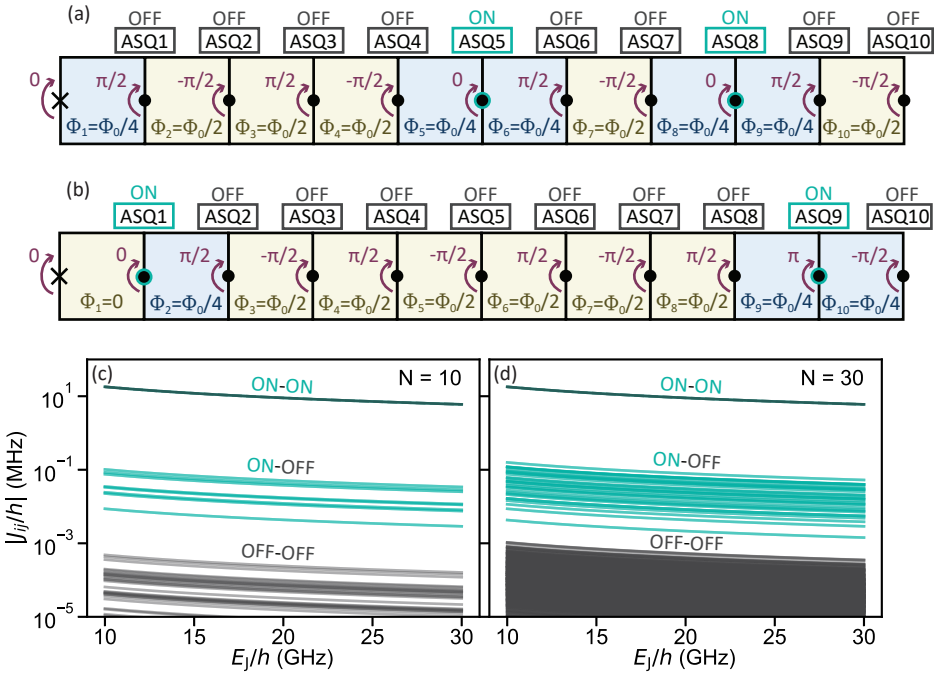

Figure 10.3: **All-to-all selective coupling.** (a) and (b) Two chains with $N = 10$ showing two example flux setpoints needed for selective two-qubit coupling that deviate from the idling configuration in Fig. 10.1(c), as indicated. This modifies the phase drops across two qubits, labeled as ON, to be either 0 or π, thus maximizing their spin-dependent supercurrent. In these configurations, the two selected qubits are longitudinally coupled to each other while the rest of the qubits remain uncoupled. (c) - (d) Absolute value of the qubit-qubit coupling strength, $|J_{ij}|$ obtained from Eq. 10.6, for two parameter configurations. For each panel, the dark green line indicates the coupling strength between the two qubits that are ON, n and m, the light green lines indicate the (undesired) coupling strength between either n or m and another qubit and the grey lines indicate the (undesired) coupling strength between any other pair of qubits. (c) For $N = 10$, $n = 3$, $m = 8$, $E_{\mathrm{SO},i}/h = 300$ MHz and $E_{\mathrm{J},i}/h = 0\ \forall i$. The fluxes deviate from their target value by an amount $\Delta\Phi_i$. The $\Delta\Phi_i$ take random values from a uniform distribution between plus and minus $0.001\Phi_0$. (d) Same as (c) but for $N = 30$, $n = 6$ and $m = 18$. In both cases, the ON-ON coupling strengths are around two orders of magnitude larger than the ON-OFF coupling strengths.

which two qubits, ASQn and ASQm, are coupled to each other while the rest of the qubits are kept near their corrected OFF flux setpoints but deviate from them, each by a random value drawn from a uniform distribution between plus and minus $0.001\Phi_0$. These deviations correspond to errors in the flux bias lines currents of less 10 µA (see Chapter 9), well above the resolution of typical current sources (Yokogawa, 2021), and thus well within experimental reach. We find ON-ON coupling strengths of around 10 MHz that slowly decrease with increasing E_J. Additionally, the unwanted ON-OFF and OFF-OFF couplings remain significantly lower than the ON-ON coupling strength, by around 2 and 4 orders of magnitude, respectively.

By flux pulsing, this selective coupling scheme enables the implementation of CPHASE gates between any qubit pair within the system (Ma et al., 2023). In particular, cou-

pling strengths of more than 10 MHz would allow to realize CPHASE gates in less than $t = h/(4J) = 25$ ns. Starting from an idling configuration, only the fluxes of the loops adjacent to the two selected qubits must be swept to reach the coupling configuration shown in Fig. 10.3(a) and (b). Importantly, during pulsing, the two fluxes adjacent to qubit m must be adjusted simultaneously to prevent undesired coupling between qubits m and $m+1$. Note that, during operation of a CPHASE gate, the qubits leave their flux sweet spot (OFF) and become sensitive to flux noise (ON). Continuous dynamical decoupling, requiring only microwave control, can be applied during gate operation to narrow down the frequency range of noise affecting the qubits (Ma et al., 2023).

10.3. QUANTUM SIMULATION OF HIGHLY CONNECTED ISING SYSTEMS

Beyond its use for digital gate-based quantum computation schemes, the system introduced in Fig. 10.1 holds potential for applications in analog quantum simulation. The Hamiltonian presented in Eq. 10.5, which corresponds to a Zeeman field aligned with all qubits, directly maps the Hamiltonian of an all-to-all longitudinally connected Ising model. More generally, when the Zeeman field has components perpendicular to the spin directions, $\vec{E}_{Z,i} = E_Z^z \sigma_i^z + E_Z^x \sigma_i^z$, the coupling Hamiltonian also includes transverse $\sigma_i^x \sigma_j^x$ terms (see Sec. 10.7):

$$H_{\mathrm{ASQ}} = \sum_{i=1}^{N} \left(\frac{1}{2} E_i \sigma_i^z + \sum_{j<i}^{N} \frac{1}{2} J_{ij}^{zz} \sigma_i^z \sigma_j^z + \sum_{j<i}^{N} \frac{1}{2} J_{ij}^{xx} \sigma_i^x \sigma_j^x \right) + C. \tag{10.8}$$

Here, J_{ij}^{zz} and J_{ij}^{xx} denote the longitudinal and transverse coupling energies, respectively.

Classically, efficient simulation is possible only for sparsely connected longitudinal systems with planar couplings. However, when either transverse terms are present in a planar system or when the system exhibits higher connectivity, only nondeterministic polynomial time (NP)-hard classical exact solutions exist (Barahona, 1982). Sparsely connected flux qubit systems have been used to approach the solution of some problems more efficiently using quantum annealing (Albash and Lidar, 2018; Kadowaki and Nishimori, 1998; Somma et al., 2012). Nonetheless, these systems have sparse connectivity, which requires an initial embedding of the desired problem into the qubit system at the cost of sacrificial qubits, thereby substantially increasing the qubit count requirements (Cai et al., 2014). Due to their high connectivity, Andreev spin qubits constitute a promising solid-state platform well-suited for simulating a broader range of problems without requiring sacrificial qubits. Specifically, this system can be used to explore the spin dynamics without the need for Trotterization (Kim et al., 2023). The system presented here extends the range of Ising problems that can be simulated quantumly to encompass all partitioning problems, defined by $J_{ij}^{zz} = a_i^z a_j^z$ and $J_{ij}^{xx} = a_i^x a_j^x$. Moreover, the tuning of the system from its fully uncoupled idling state (Fig. 10.1(c)) to a fully coupled state (Fig. 10.4(a) or (b)), only requires the adjustment of the adjustment of the flux through loop 1 by a quarter of a flux quantum. This provides straightforward control over the evolution time of an analog quantum simulation by only pulsing a single flux line. Note, however, that a generic Ising system has a total of $(N^2 - N)/2$ independent

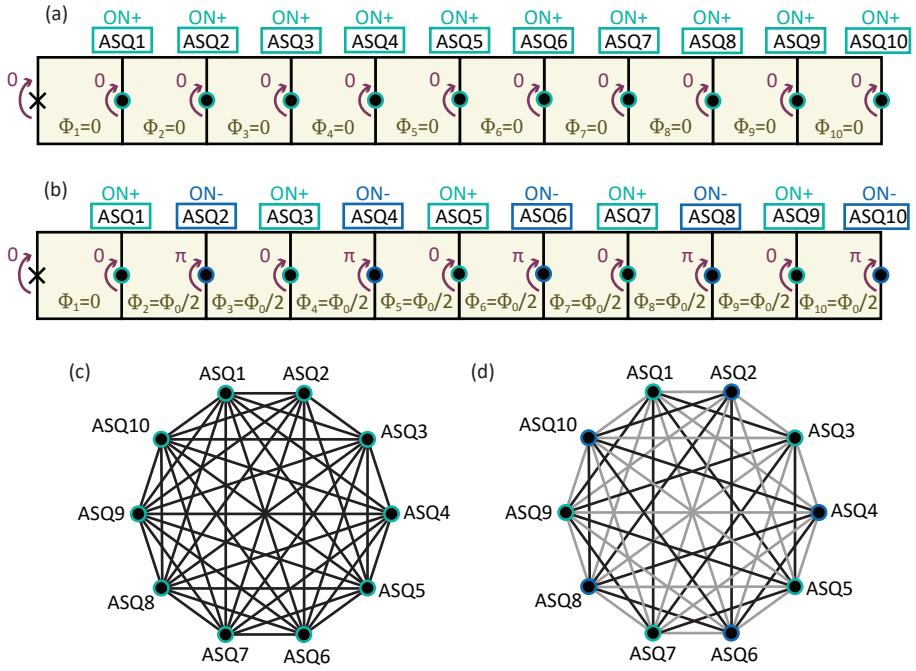

Figure 10.4: **Quantum simulation with ASQs.** (a) and (b) Circuit diagrams for $N = 10$ exemplifying two flux configurations in which all qubits are coupled to each other, thus mapping a highly connected Ising system. (c) and (d) Graph diagrams indicating the couplings (edges) between each pair of qubits (nodes). Panels (c) and (d) correspond to the flux configurations depicted in (a) and (b), respectively. For (c), all coupling strengths have equal sign $J_{ij} = -|J_{ij}|\ \forall i, j$ (black edges). For (d), the coupling strengths have either a negative sign, $J_{ij} = -|J_{ij}|$ if $|i-j| = 2n$ (black edges), or a positive sign, $J_{ij} = +|J_{ij}|$ if $|i-j| = 2n+1$ (grey edges), with n being an integer number.

couplings, meaning that the ASQ system studied here, with N free parameters, cannot simulate all possible configurations of the Ising model.

10.4. READOUT

The spin-supercurrent coupling of superconducting spin qubits provides a means for reading out their state through the use of circuit Quantum Electrodynamics techniques, as discussed in Chapters 8, 9, and Refs. (Hays et al., 2020, 2021). In this section, we detail different readout alternatives that depend on the readout circuitry and on the specific qubits that need to be measured[2]. In Fig. 10.5 we present a protocol for sequentially reading out the state of all qubits, one by one, in the computational basis. This can be achieved using either a transmon or a fluxonium circuit. Subsequently, in 10.6, we discuss how to selectively read out the state of a single qubit while keeping all qubits un-

[2]Note that, if the $E_{SO,i}/E_J$ ratio needs to be reduced further by increasing E_J to the THz range, an alternative readout method involves replacing the coupling junction with a linear inductor and using a readout resonator with a geometry analogous to that in Ref. (Fatemi et al., 2022; Hays et al., 2020, 2021; Wesdorp et al., 2022; Wesdorp et al., 2023).

coupled. Lastly, in Sec. 10.4.3, we instead present the simultaneous readout of multiple qubits to determine the total number of qubits that are in their excited state. Note that, in all cases, the readout circuit must be detuned from all ASQ frequencies to prevent transverse coupling between the qubits and the readout.

10.4.1. SEQUENTIAL READOUT OF ALL QUBITS

Fig. 10.5 outlines the protocol for the sequential readout of all qubits. The readout protocol starts with all qubits in their ON state. In this situation, their relative phases change, but the state in the computational Z^N basis remains conserved as the coupling is longitudinal, thus preserving the measurement result. For reading out each of the qubits, they are sequentially switched to their OFF state one by one (an example for qubit 5 is shown in Fig. 10.5(a)). We discuss two alternative circuits for selectively reading out the state of a qubit when it is OFF while being insensitive to the states of the qubits that are ON.

TRANSMON READOUT

The first alternative employs a transmon circuit, as depicted in Fig. 10.5(b), for simplicity for the case $N = 1$. The transmon consists of a capacitor, with charging energy E_c, connected in parallel to the coupling and ASQ junctions. Its Hamiltonian can be expressed as

$$H_t(\phi) = -4E_c(\hat{n} - n_g)^2 + E_J\left(1 - \cos\left(\phi\right)\right) + H_{ASQ}(\phi), \tag{10.9}$$

where $H_{ASQ}(\phi)$ denotes the Hamiltonian of all ASQs in parallel, which depends on all fluxes, $\hat{n}$ is the conjugate charge of ϕ, and n_g is the offset charge in the transmon island, expressed in units of the Cooper pair charge $2e$.

As shown in Fig. 10.5(c), when a qubit is in its ON setpoint ($\varphi_1 = 0$), the transmon's eigenstates have the same energy independently of the qubit state ($|\uparrow\rangle$ or $|\downarrow\rangle$). Consequently, the transmon transition frequencies are identical for both qubit states (see Fig. 10.5(h)). If the ASQ is instead in its OFF state, the transmon eigenenergies change depending on the qubit state (red and blue in Fig. 10.5(d)). This results in distinguishable transmon transition frequencies for $|\uparrow\rangle$ and $|\downarrow\rangle$. Fig. 10.5(j) shows the resulting frequencies of a readout resonator capacitively coupled to the transmon with a coupling energy g. The resonator frequencies are different when the qubit is in its OFF setpoint and identical when it is ON, thus allowing to selectively readout the state of individual OFF qubits.

FLUXONIUM READOUT

An alternative readout circuit to realize the same protocol is a magnetic field resilient fluxonium circuit, shown in Fig. 10.5(c). Its Hamiltonian can be expressed as

$$H_f(\phi) = -4E_c\hat{n}^2 + \frac{1}{2}E_L(\phi - \varphi)^2 + E_J\left(1 - \cos\left(\phi\right)\right) + H_{ASQ}(\phi), \tag{10.10}$$

where E_L is the inductive energy of the fluxonium shunting inductor and $\varphi = 2\pi\Phi/\Phi_0$ denotes the reduced flux through the loop formed by the inductor and the coupling junction. If the fluxonium flux is set to $\varphi = \pi/2$, a fluxonium circuit can be used to selectively read out qubits in their OFF state, analogously to the transmon case (see Fig. 10.5(f, g, i, k)).

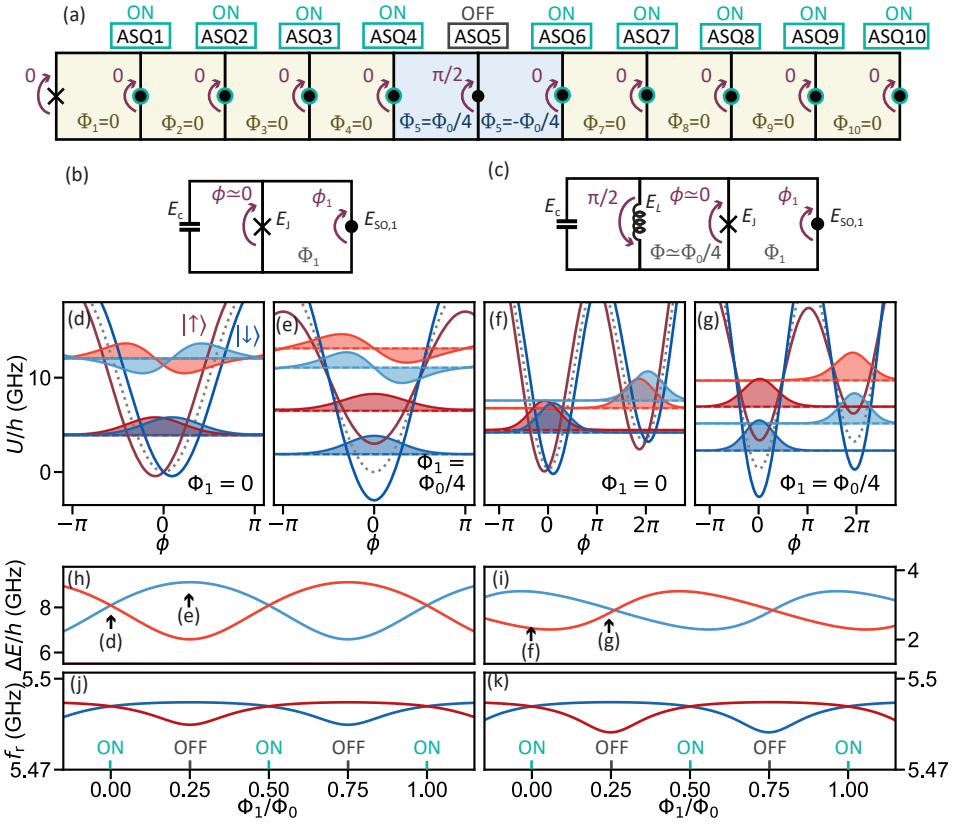

Figure 10.5: **Sequential readout of qubits in their OFF state.** (a) Circuit diagram for $N = 10$ exemplifying the flux configuration for reading out the state of qubit 5. All qubits except for ASQ5 are ON, and thus longitudinally coupled. This makes their phases evolve but does not change their state in the computational Z^N basis. The phase drop $\phi_5 \sim \pi/2$ sets ASQ5 OFF. (b) and (c) Two alternative readout circuits, shown for the case $N = 1$ for simplicity. (b) Transmon readout circuit diagram. A capacitor with charging energy E_c is connected in parallel to the Andreev spin qubits, as in Chapters 6, 7, 8 and 9. (c) Fluxonium readout circuit diagram. A capacitor with charging energy E_c and an inductor with inductive energy E_L are connected in parallel to the Andreev spin qubits, as in Chapter 5. The inductor and the coupling junction define a loop. The magnetic flux through this loop is denoted as Φ. (d) and (e) Transmon potential versus the phase drop across the coupling junction, ϕ, for $\Phi_1 = 0$ (ON) and $\Phi_1 = \Phi_0/4$ (OFF), respectively. In both cases, $E_{J,1} = 0$, $E_c/h = 1.0\,\text{GHz}$ and $E_J/h = 10.0\,\text{GHz}$. The dotted lines indicate the case $E_{SO,1} = 0$. Colored lines indicate the two possible potentials depending on the state of the ASQ, for $E_{SO,1}/h = 3\,\text{GHz}$. The color-filled regions represent the wavefunctions of the two lowest energy scales in each case, in arbitrary units. (f) and (g) Same as (d) and (e) but for the fluxonium circuit with $E_L/h = 0.3\,\text{GHz}$ and at $\Phi = \Phi_0/4$. (h) First transmon transition frequency versus flux for the two possible spin states, $|\uparrow\rangle$ and $|\downarrow\rangle$, indicated with red and blue, respectively. (j) Frequency of a readout resonator with bare frequency $f_{r,0} = 5.5\,\text{GHz}$ capacitively coupled to the transmon with a resonator-transmon coupling strength $g/h = 200\,\text{MHz}$. Different spin states result in different resonator frequencies when the qubit is OFF and in identical resonator frequencies when the qubit is ON. (i) First fluxonium transition versus flux for the two possible spin states. As opposed to the transmon behavior, the fluxonium frequencies are different when the qubit is ON. (k) Same as (j) but for a readout resonator capacitively coupled to the fluxonium with resonator-fluxonium coupling strength $g/h = 200\,\text{MHz}$. As the resonator is sensitive to the fluxonium ground state and not to its first transition, the resonator does not follow the fluxonium frequency and instead has a dependence analogous to that of the transmon case, allowing to read out the state of the qubit when it is OFF.

10.4.2. SELECTIVE READOUT OF ONE QUBIT

In certain applications, such as ancilla-based parity readout, there's a need to selectively read out the state of an individual qubit without affecting the states of other qubits. To facilitate this selective readout, we introduce the protocol illustrated in Fig. 10.6. This method consists of configuring all qubits to their OFF setpoints, ensuring they remain uncoupled. Simultaneously, the specific qubit that needs to be measured is set to its ON setpoint (see Fig. 10.6(a)). As only one qubit is ON, it does not interact with any of the other qubits.

To read the state of the qubit in the ON setpoint, we use a fluxonium circuit as the one shown in Fig. 10.6(b). This circuit is tuned to a precise flux φ setpoint positioned near an avoided crossing between a fluxonium transition and the readout resonator. Fig. 10.6(c) and (d) show a crossing between the second fluxonium transition and the readout resonator as φ is varied, for the ON and OFF qubit setpoints, respectively. By setting φ close to this crossing, the frequency of the readout resonator depends on the ASQ state when the ASQ is ON and remains unaffected when it is OFF. This approach enables the selective readout of the state of an individual qubit in the ON state while being insensitive to all other qubits that are in the OFF state. Note however that there is a balance between the proximity to the avoided crossing and the number of readout photons, as the closer the flux point is to the avoided crossing the higher the hybridization between the readout resonator and the fluxonium states.

10.4.3. JOINT READOUT OF ALL QUBITS

In situations where the $E_{\mathrm{SO},i}$ values of all qubits are similar, there is a third readout option available, which allows to differentiate between various joint states based on the total number of qubits that are in their $|\uparrow_i\rangle$ state. This joint readout protocol entails configuring all qubits to their OFF flux setpoints, which leaves them uncoupled and thereby does not affect their state. As a result, all joint states with the same number of qubits in their $|\uparrow_i\rangle$ state lead to the same dispersive shift on the resonator. In total, there are N different resonator frequencies, each corresponding to a different total number of $|\uparrow_i\rangle$ spins. This configuration has several potential applications:

- **Direct counting of excited qubits**. If the dispersive shifts and resonator linewidths are designed so that the N resulting IQ blobs can be distinguished, this configuration allows for the direct count of the total number of $|\uparrow_i\rangle$ spins. This measurement could be applied as an error syndrome for quantum error correction, although further research is needed to detail how this can be done.
- **State initialization**. By selecting a specific readout frequency to distinguish the $|\downarrow_0\downarrow_1 ... \downarrow_N\rangle$ state from all other states, this approach can be employed for state preparation, to initialize the system in this state (Johnson et al., 2012).
- **Fidelity benchmarking**. The ability to differentiate the $|\downarrow_0\downarrow_1 ... \downarrow_N\rangle$ state from all other states can be used to benchmark gate sequences that should have the global ground state as their final state.
- **Quantum simulation**. Finally, in quantum simulation, distinguishing states with a fixed number of $|\uparrow_i\rangle$ spins from all other states can be useful to verify if the final

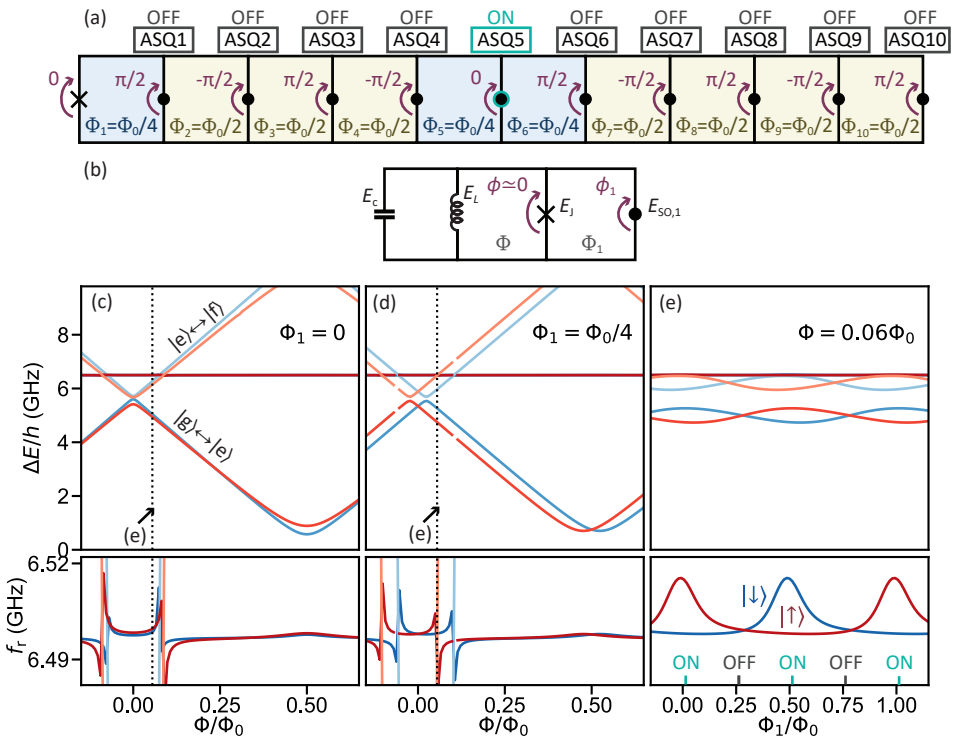

Figure 10.6: **Selective readout of a qubit in its ON state.** (a) Circuit diagram for $N = 10$ exemplifying the flux configuration for reading out the state of qubit 5. The phase drop $\phi_5 \sim 0$ sets ASQ5 ON, while all other qubits are OFF and thus uncoupled. (b) Same as Fig. 10.5(c). In this case, the value of Φ is not fixed. $E_c/h = 4.0\,\text{GHz}$, $E_{SO,1}/h = 1.5\,\text{GHz}$, $f_{r,0} = 6.6\,\text{GHz}$, $g/h = 300\,\text{MHz}$ and the other parameters are the same as in Fig. 10.5. (c), (d) and (e) Show the fluxonium (top) and resonator (bottom) frequencies for different flux configurations. For (c) and (d) the ASQ is ON and OFF, respectively. As Φ is varied, there are different anticrossings between the resonator and the fluxonium. (e) Shows the Φ_1 dependence when Φ is fixed near one of such anticrossings, resulting in equal resonator frequencies when the ASQ is OFF and in different resonator frequencies when it is ON. This allows selectively reading out the qubit in its ON setpoint.

state falls within the correct subspace, confirming the accuracy of the simulation.

These diverse applications underline the versatility of the ASQ system. However, further research is essential to address specific implementation details.

10

10.5. TUNE-UP PROTOCOL

Implementing each Andreev spin qubit in a semiconducting Josephson junction permits pinching it off (i.e. setting both of its Josephson energies to zero) by electrostatic gating. In this section, we explain how, by selectively pinching off different combinations of qubits, the system can be sequentially tuned up to its operational configuration, as depicted in Fig. 10.7.

The tune-up process follows the procedure outlined in Chapters 8 and 9 for the $N = 1$ and $N = 2$ cases, respectively. In the initial step, illustrated in Fig. 10.7(a), all ASQs

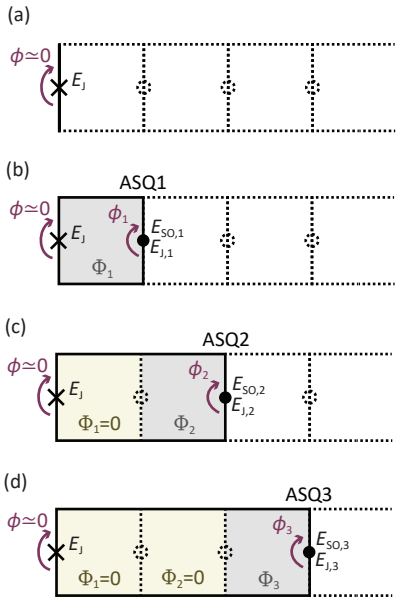

Figure 10.7: **Sequential qubit tune-up.** Each panel shows the circuit diagram of the loops array in different configurations, at subsequent steps in the tune-up process. (a) All qubits are pinched off with their electrostatic gates so that $E_{\mathrm{SO},i} = E_{\mathrm{J},i} = 0\ \forall i$. In this configuration, there are no loops and the value of E_J can be directly determined. (b) While keeping the rest of ASQs pinched off, ASQ1 is tuned up with its electrostatic gates following the procedure described in Chapter 7 (Sec. 7.7.3). This allows to fix the desired values of $E_{\mathrm{SO},1}$ and $E_{\mathrm{J},1}$, as well as to determine the I_1 setpoints that set $\Phi_1 = 0, \Phi_0$. (c) Subsequently, the flux setpoint of ASQ1 is fixed at $\Phi_1 = 0$ and the electrostatic gates of ASQ1 are pinched off. Following a procedure analogous to that in (b) one can set the values of $E_{\mathrm{SO},2}$ and $E_{\mathrm{J},2}$ and determine the the I_2 setpoints that set $\Phi_2 = 0, \Phi_0$. (d) Same as (b) and (c) but for ASQ3.

are pinched off and the coupling junction is characterized. As the E_c and E_L values are known by design, the value of E_J can be determined from the measured frequency of the transmon or fluxonium readout circuitry. If the coupling junction is implemented with a semiconducting Josephson junction, E_J can be electrostatically set at this step to a target value much larger than the target value for all $E_{\mathrm{SO},i}$ and $E_{\mathrm{J},i}$.

Subsequent steps involve selectively pinching off all ASQs except one, allowing it to be tuned up independently. This configuration is shown in Fig. 10.7(b), (c) and (d) for qubits 1, 2 and 3, respectively. This sequential approach permits the investigation of each qubit's gate and magnetic field dependence, enabling the selection of an optimal setpoint as follows:

Initially, the gate space is mapped out at zero magnetic field to identify regions with sizable $E_{\mathrm{SO},i}$ and low $E_{\mathrm{J},i}$. This optimization aims to maximize the coupling strength (see to Eq. 10.6). An efficient way to perform this mapping is by detecting a frequency splitting of the readout resonator at fixed flux points (see Sec. 10.4).

Subsequently, the magnetic field is set to a non-zero value, allowing for the investigation of the magnetic field dependence. This step provides access to the spin-polarization direction and the g-factor at each gate setpoint.

During operation, the global magnetic field will be fixed at a predetermined value and direction, chosen to align with the chip plane to maximize the magnetic field resilience of the readout circuitry (see Chapter 4) (Feldstein i Bofill, 2022; Graaf et al., 2012; Kroll et al., 2019; Samkharadze et al., 2016; Zollitsch et al., 2019). Therefore, for each ASQ, a gate setpoint is selected so that the spin-polarization direction aligns with the preferred direction relative to the chosen magnetic field operation direction. This relative alignment depends on the application. For gate-based quantum computing, the operation is simplified if only longitudinal coupling terms are present (as in Eq. 10.5), and thus the spin direction must be chosen to be aligned the the Zeeman field direction. For quantum simulation of Ising systems, however, the spin direction can be adjusted to determine the ratio between longitudinal and transverse coupling terms. Note that the precise values of the g-factors at the chosen setpoint are not of relevance for qubit operation, as the qubits couple longitudinally. The only consideration regarding the g-factors is that the qubit frequencies should not match the frequencies of the readout resonator or the readout superconducting qubit and that they lay within an experimentally accessible frequency band. Once the setpoint for one qubit is determined in this manner, its junction can be pinched off, and the next qubit can be characterized and tuned up similarly.

The change in the global magnetic field during the preceding steps alters the $\Phi_i(I_i)$ mappings. Therefore, these mappings can be determined in a subsequent round of tune-up steps, carried out after fixing the global magnetic field at its operational setpoint. In this phase, each qubit is sequentially opened (i.e. set to its gate setpoint) and an I_i dependence is performed to determine the I_i values that set $\Phi_i = 0$ and $\Phi_i = \Phi_0$, as indicated in Fig. 10.7.

10.6. DISCUSSION

In the preceding sections, we discussed the potential of highly connected Andreev spin qubits for quantum computing and quantum simulation tasks. Our analysis focused on an estimation of the coupling strength to first order in $E_{\mathrm{SO},i}/E_\mathrm{J}$, as detailed in Sec. 10.2. However, it is crucial to consider the contribution of the spin-dependent inductance of each ASQ, which becomes significant away from the limit $E_{\mathrm{SO},i}/E_\mathrm{J} \to 0$ (see Sec. 10.7). These contributions introduce higher-order coupling terms of the form $\epsilon_k J_{ij}\sigma_i^z\sigma_j^z\sigma_k^z$, where $\epsilon_k \approx E_{\mathrm{SO},k}/E_\mathrm{J}$. For instance, the experimentally realistic values of $E_{\mathrm{SO},i}/h$ =300 MHz$\forall\, i$ and E_J/h =30 GHz discussed in Fig. 10.3 result in an ON-ON coupling of $J_{ij}/h = 6$ MHz and unwanted higher-order coupling terms of $J_{ijk}/h = 60$ kHz

Alternatively, to reduce the $E_{\mathrm{SO},i}/E_\mathrm{J}$ ratio and, consequently, mitigate the magnitude of higher-order terms, one can reduce the inductance of the coupling junction. Achieving a reduction to $E_{\mathrm{SO},i}/E_\mathrm{J} = 1/1000$ within experimentally attainable parameters can be realized by setting $E_{\mathrm{SO},i}/h = 1$ GHz $\forall\, i$ and $E_\mathrm{J}/h = 1000$ GHz. This, in turn, sets the ON-ON coupling to $J_{ij}/h = 2$ MHz. Under these conditions, the higher-order coupling terms have an amplitude of $J_{ijk}/h = 2$ kHz. This magnitude of E_J can be achieved by replacing the coupling junction with a linear inductor and using a resonator, instead of a transmon or fluxonium, for readout (Fatemi et al., 2022; Hays et al., 2020, 2021; Wesdorp et al., 2022; Wesdorp et al., 2023).

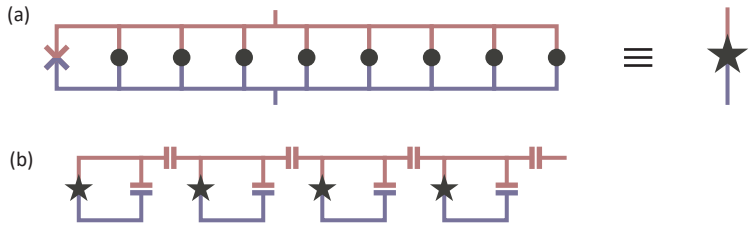

Figure 10.8: **Quantum computing with superconducting spin qubits.** (a) One cluster of N coupled ASQs is represented with a star symbol and implements a logical qubit. (b) Each cluster is read out with a transmon circuit. Different clusters are capacitively coupled to each other to mediate inter-cluster coupling.

The presence of higher-order terms can limit the two-qubit gate fidelity, imposing a constraint, $N_{\max}$, on the maximum number of qubits in the system. To scale up beyond this limit, we envision defining independent unit cells, each containing $N_{\max}$ qubits, as illustrated in Fig. 10.8(a). A potential architecture for coupling different clusters to each other involves capacitively coupling the readout circuit of two separate clusters (Fig. 10.8(b)). This hierarchical approach provides a scalable path for creating larger quantum processors while mitigating the impact of higher-order coupling terms.

To conclude, we have presented an approach for scaling up Andreev spin qubits in a highly connected way. Our work demonstrates the ability to control the magnitude of the coupling strength between any pair of qubits, independently of their physical distance, by varying the applied flux. This feature enables the realization of fast two-qubit gates across the entire system. Moreover, as all couplings are of the longitudinal type, the coupling strength remains independent of the relative qubit frequencies. This characteristic offers great flexibility for increasing the qubit count without encountering issues associated with frequency crowding.

When it comes to gate-based digital quantum computation, this enhanced qubit connectivity opens up opportunities for exploring alternative quantum error correction codes, potentially requiring fewer physical qubits per logical qubit compared to existing surface codes (Bravyi et al., 2023). Regarding analog quantum simulation of Ising systems, the all-to-all connectivity extends the range of NP-hard problems that can be readily simulated without the need for sacrificial qubits, presenting an advantageous alternative to other superconducting qubit approaches.

10.7. SUPPLEMENTARY INFORMATION

10.7.1. HIGHER ORDER LONGITUDINAL COUPLING TERMS

Away from the limit $E_{\mathrm{SO},i}/E_{\mathrm{J}} \to 0$ it becomes essential to account for modifications to the coupling described in Eq. 10.6 due to the presence of a state-dependent parallel inductance. This inductance introduces a modification to $\tilde{E}$, resulting in

$$\tilde{E} = E_{\mathrm{J}} + \sum_{l=1}^{N} E_{\mathrm{J},l} e^{i\sum_{k=1}^{l}\varphi_k} + \sum_{l=1}^{N} \sigma_l^z E_{\mathrm{SO},l} e^{i(\frac{\pi}{2}+\sum_{k=1}^{l}\varphi_k)}. \tag{10.11}$$

The $E_{\mathrm{SO},i}/E_{\mathrm{J}}$ term gives rise to higher order coupling terms of the form $\sigma_i^z\sigma_j^z\sigma_k^z$ that

can be found by Taylor expanding Eq. 10.6 around $E_{\mathrm{SO},i}/E_{\mathrm{J}} = 0$. The second-order contribution from the denominator yields

$$J_{ij}^{(2)} = J_{ij}^{(1)} \left(1 - \sum_{l=1}^{N} \sigma_l^z E_{\mathrm{SO},l} e^{i\left(\frac{\pi}{2} + \sum_{k=1}^{l} \varphi_k\right)}\right), \tag{10.12}$$

where $J_{ij}^{(1)}$ is the first-order approximation from Eq. 10.6. This results in a contribution to the three-qubit coupling terms, $J_{ijk}\sigma_i^z\sigma_j^z\sigma_k^z$, that is a factor of $E_{\mathrm{J}}/E_{\mathrm{SO},k}$ times smaller than the two-qubit coupling terms J_{ij} (i.e. $J_{ijk} = E_{\mathrm{SO},k}/E_{\mathrm{J}} J_{ij}$).

Additionally, Eq. 10.11 results in a σ_k^z-dependent contribution to $\varphi_{\tilde{E}}$. This contribution can be as high as

$$\varphi_{\tilde{E}} = \tan^{-1}\left(\frac{\sum_{k=1}^{N} E_{\mathrm{SO},k}\sigma_k^z}{E_{\mathrm{J}}}\right) \approx \frac{\sum_{k=1}^{N} E_{\mathrm{SO},k}\sigma_k^z}{E_{\mathrm{J}}} \tag{10.13}$$

when all qubits are OFF. Here, the approximation is again made to first order in $E_{\mathrm{SO},k}/E_{\mathrm{J}}$. Similarly, this introduces a second contribution to the three-qubit coupling terms, given by

$$J_{ijk} = J_{ij}^{(0)} \frac{E_{\mathrm{SO},k}}{E_{\mathrm{J}}} \sigma_k^z. \tag{10.14}$$

Once again, this term is scaled by a factor of $E_{\mathrm{SO},k}/E_{\mathrm{J}}$ compared to the two-qubit coupling terms.

10.7.2. TRANSVERSE COUPLING UNDER THE PRESENCE OF A PERPENDICULAR ZEEMAN FIELD

For the sake of simplicity and without loss of generality, we consider the case $N = 2$. The Hamiltonian of the coupled system, expressed in the eigenbasis of the system at zero magnetic field, is given by

$$H_{\mathrm{ASQ}} = \frac{1}{2}E_1\sigma_1^z + \frac{1}{2}E_2\sigma_2^z + \frac{1}{2}J_{12}\sigma_1^z\sigma_2^z. \tag{10.15}$$

If a perpendicular magnetic field is applied, the eigenstates of each of the two qubits are no longer the same. In particular, the Hamiltonian of ASQi becomes

$$H_i(\phi_i) = E_{\mathrm{J},i}\sigma_i^0 \cos(\phi_i) - E_{\mathrm{SO},i}\sigma_i^z \sin(\phi_i) + \frac{1}{2}E_{\mathrm{Z}} \cos(\theta_i)\sigma_i^z + \frac{1}{2}E_{\mathrm{Z}} \sin(\theta_i)\sigma_i^x, \tag{10.16}$$

where E_{Z} represents the magnitude of the magnetic field and θ_i is the angle between the direction of the external magnetic field and the zero-field spin direction of ASQi. In the limit of $E_{\mathrm{Z}} \gg E_{\mathrm{SO},i}\ \forall i$, the eigenstates of ASQ$i$, expressed in its original basis, become

$$|\downarrow_i\rangle = \left(\cos\left(\frac{\theta_i}{2}\right), \sin\left(\frac{\theta_i}{2}\right)\right), \qquad |\uparrow_i\rangle = \left(-\sin\left(\frac{\theta_i}{2}\right), \cos\left(\frac{\theta_i}{2}\right)\right). \tag{10.17}$$

Consequently, σ_i^z and σ_i^x, expressed in the new $\{|\downarrow_i\rangle, |\uparrow_i\rangle\}$ basis, become

$$\sigma_i^z = \cos(\theta_i)\sigma_i^{\overline{z}} + \sin(\theta_i)\sigma_i^{\overline{x}}, \qquad \sigma_i^x = \cos(\theta_i)\sigma_i^{\overline{x}} + \sin(\theta_i)\sigma_i^{\overline{z}}. \tag{10.18}$$

This leads to the coupling Hamiltonian, expressed in the new spin eigenbasis

$$\begin{aligned} H_{\mathrm{ASQ}} = & \frac{1}{2}E_1\sigma_1^{\overline{z}} + \frac{1}{2}E_2\sigma_2^{\overline{z}} \\ & + \frac{1}{2}J_{12}\cos(\theta_1)\cos(\theta_2)\sigma_1^{\overline{z}}\sigma_2^{\overline{z}} \\ & + \frac{1}{2}J_{12}\sin(\theta_1)\cos(\theta_2)\sigma_1^{\overline{x}}\sigma_2^{\overline{z}} \\ & + \frac{1}{2}J_{12}\cos(\theta_1)\sin(\theta_2)\sigma_1^{\overline{z}}\sigma_2^{\overline{x}} \\ & + \frac{1}{2}J_{12}\sin(\theta_1)\sin(\theta_2)\sigma_1^{\overline{x}}\sigma_2^{\overline{x}}. \end{aligned} \tag{10.19}$$

This expression comprises both transversal (XX) and longitudinal (ZZ) coupling terms, along with ZX and XZ terms, with amplitudes

$$\begin{aligned} & J_{12}^{zz}J_{12}\cos(\theta_1)\cos(\theta_2), \\ & J_{12}^{xz}J_{12}\sin(\theta_1)\cos(\theta_2), \\ & J_{12}^{zx}J_{12}\cos(\theta_1)\sin(\theta_2) \text{ and} \\ & J_{12}^{xx}J_{12}\sin(\theta_1)\sin(\theta_2). \end{aligned} \tag{10.20}$$

If the Zeeman field is perpendicular to both qubits, $\theta_1 = \theta_2 = \pi/2$, the longitudinal, XZ and ZX terms vanish, leaving only the transverse coupling term with an amplitude of $J_{12}^{xx} = J_{12}$.

11

OUTLOOK

I'd rather describe [a follow-up project] as a second mountain that is usually covered by thick fog but is now visible because you have climbed to the top of a neighboring mountain.

Bernard van Heck

- Work related to Sec. 11.1.3 has been published as:L. Pavešić, **M. Pita-Vidal**, A. Bargerbosa and R. Žitko, Impurity Knight shift in quantum dot Josephson junctions. SciPost Phys.(2023).
- Work related to Sec. 11.1.2 is currently under peer review and is available at: T. Vakhtel, P. Kurilovich, **M. Pita-Vidal**, A. Bargerbos, V. Fatemi and B. van Heck, Tunneling of fluxons via a Josephson resonant level. arXiv:2310.03102.

In the preceding chapters, we have presented various experimental results and discussed their novelty. We now shift our perspective by 180 degrees and instead focus on what has *not* been explored within this thesis. As anyone who's ever witnessed the unfolding of doctoral research could have easily anticipated, it didn't go according to plan. It never does.

While it might not have been apparent thus far, the original goal of this thesis was the pursuit of Majorana bound states. It turns out we didn't find them. The reason for this, to our current understanding, is that the level of disorder in the nanowires that we employed was too high (Das Sarma and Pan, 2021). Sec. 11.1.1 provides a concise presentation of potential experiments that could reveal signatures of a topological transition in the nanowire using a fluxonium circuit. We underline that such a "Majorana sensor" could be adaptable to other junction materials. Furthermore, we describe alternative experiments that could be performed with this and other of the devices investigated in the preceding chapters, requiring little to no modifications. Some of these experiments were part of the "protected qubits" plan suggested in the first-year proposal for this thesis that, unsurprisingly, also remains unrealized. In Sec. 11.1.2 we discuss the application of a nanowire fluxonium to find signatures of the amplitude of 4π quantum phase slips (QPS) at the junction surpassing that of 2π-QPS, a consequence of a mechanism analogous to Landau-Zenner tunneling in the presence of a highly transparent junction channel. Expanding on this concept in Sec. 11.2, we explore the potential use of this 4π-QPS enhancement to implement a type of Hamiltonian-protected qubit.

Finally, we turn to describing follow-up experiments that could be performed to further research the physics of SQDS devices. In Sec. 11.1.3, we highlight certain aspects of the physics observed in Chapters 6 and 7 that call for further research and delve into how to investigate them with our devices. Finally, in Sec. 11.3 we address the main challenges of superconducting spin qubits and elaborate on how they could be addressed in future experiments.

11.1. cQED AS A TOOL TO INVESTIGATE CONDENSED MATTER SYSTEMS

The circuit quantum electrodynamics (cQED) techniques developed over the past years by the superconducting qubit community not only are useful to address and readout superconducting qubit processors. As we tried to exploit throughout this thesis, they also constitute a versatile toolkit for probing condensed matter phenomena. Microwave techniques provide access to device properties that go beyond those that can be probed with traditional direct current (DC) transport experiments. Furthermore, they are generally less invasive than transport techniques and provide higher energy and time resolution (Aguado, 2020; Clerk et al., 2020). In general, low-frequency methodologies are limited to probing the conductance or resistance of the device, while high-frequency techniques can also unveil its reactive properties. Moreover, the energy resolution of traditional DC transport techniques, such as tunnel spectroscopy, is typically limited to the order of $h\cdot$1 GHz due to thermal broadening (see Appendix A for a conversion guide on energy units). In contrast, cQED two-tone spectroscopy measurements offer a much higher energy resolution, limited by the coherence times of the circuits used and typi-

cally below $h\cdot 10\,\mathrm{MHz}$. Throughout this thesis, we have harnessed both of these features, employing microwaves to access the inductance of nanowire junctions[1] with high energy resolution.

11.1.1. FLUXONIUM AS A PROBE OF THE FRACTIONAL JOSEPHSON EFFECT

As has also been proposed for a nanowire transmon (Ávila et al., 2020; Avila et al., 2020b; Ginossar and Grosfeld, 2014; Hassler et al., 2011; Hyart et al., 2013), a nanowire fluxonium —similar to the one discussed in Chapter 5— can function as a sensor of topological phases of matter[2]. In particular, it serves as a non-invasive probe of the 4π (or fractional) Josephson effect (Pekker et al., 2013).

Imagine a scenario wherein the two proximitized sections of the nanowire transition into a topological state, thereby generating four Majorana bound states (MBSs) at their ends. These MBSs, denoted by γ_i, with $i \in \{0,1,2,3\}$, in Fig. 11.1(a), would drastically modify the fluxonium spectrum as a result of the fractional Josephson effect. Consequently, this device, if combined with other signatures, can contribute to identifying the presence of MBSs. Moreover, such cQED integration would facilitate the extraction of information about the MBSs that is not readily accessible via low-frequency transport techniques. Firstly, using a nanowire fluxonium one can spectroscopically quantify the coupling of the two adjacent MBSs across a Josephson junction, γ_1 and γ_2, surpassing the resolution achievable with conventional transport methods. Secondly, a nanowire fluxonium permits the exploration of the time dynamics of the Majorana parity, influenced by quasiparticle-poisoning events, similarly to how we did in Chapter 6. Lastly, the four MBSs would encode the state of a qubit with a topologically protected state on which unprotected operations can be performed with microwave pulses, complementing the non-universal set of protected braiding operations on Majorana-based qubits. The state of the topological qubit could moreover be read out in fast timescales exploiting the cQED architecture it is embedded in.

In what follows, we start by describing the Majorana signatures in a fluxonium spectrum, then turn to exploring how one could operate on the topological qubit using microwaves and, lastly, we discuss potential alterations of the junction material or configuration.

MAJORANA DETECTION

Fig. 11.1(a) presents the circuit model of a nanowire fluxonium for which the superconducting nanowire sections are in the topological regime. The coupling between γ_1 and γ_2, which depends on the overlap of their wavefunctions, results in a 4π-periodic Josephson term with energy scale E_M. The corresponding fluxonium Hamiltonian, H_f, can be

[1] Note that, while not explored here, microwave techniques also offer a wide range of possibilities when it comes to probing the conductive and capacitive properties of the device under test. See for instance Refs. (de Jong et al., 2019; van Veen et al., 2019; Vigneau et al., 2023).

[2] An alternative approach for finding signatures of topological phases of matter has also been suggested (Bøttcher, 2022; Bøttcher et al., 2023; Phan et al., 2022). Integrating a superconducting material into a superconducting resonator (Splitthoff et al., 2022) permits probing the temperature dependence of its superfluid density, which can give insights into the order parameter symmetry. This approach, while not within our scope, can be used to reveal signatures of unconventional superconductivity and has been proposed for investigating two-dimensional superconductors such as tungsten ditelluride WTe_2 (Bøttcher, 2022; Fatemi et al., 2018; Sajadi et al., 2018) or the superconducting phase of twisted bilayer graphene (Cao et al., 2018).

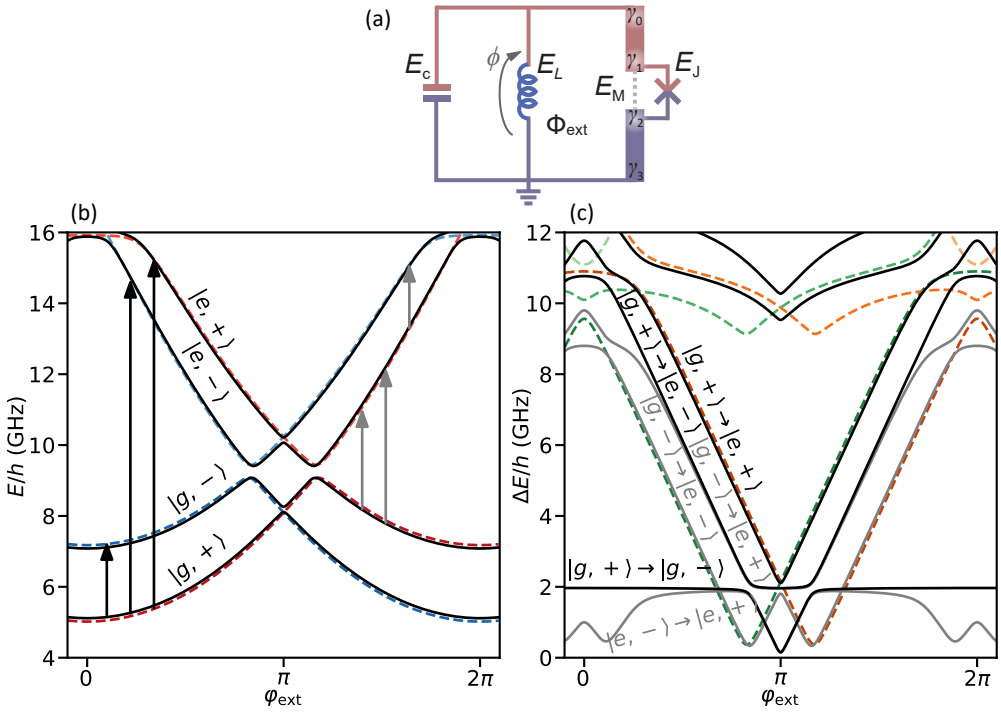

Figure 11.1: **Fluxonium circuit as a detector of the fractional Josephson effect.** (a) Circuit model of a nanowire fluxonium with coupling E_M between the inner Majoranas, γ_1 and γ_2. The couplings between inner and outer Majoranas, E_M^{10} and E_M^{23}, resulting from the finite size of the nanowire, are not indicated. The 2π periodic component of the junction potential, the capacitor and the inductor are characterized by the energies E_J, E_L, and E_c, respectively. The loop formed by the inductor and the nanowire junction is threaded by an external magnetic flux, Φ_{ext}. (b) Energy levels obtained by diagonalizing Hamiltonian 11.2 with $E_L/h = 0.4$ GHz, $E_J/h = 7.0$ GHz, $E_c/h = 2.3$ GHz and $E_M/h = 1.0$ GHz, as a function of the reduced flux $\varphi_{ext} = 2\pi\Phi_{ext}/\Phi_0$. The dashed colored lines correspond to the ideal case $E_M^{01}/h = E_M^{23}/h = 0.0$ GHz, with red and blue colors denoting different $i\gamma_1\gamma_2$ parities. The continuous black lines correspond to the case $E_M^{01}/h = E_M^{23}/h = 0.2$ GHz, where the $i\gamma_1\gamma_2$ parity is not well defined. Labels to the quantum states are assigned by comparison to the spectrum without couplings. (c) Frequencies of transitions between the energy levels shown in (b). The colored dashed lines correspond to parity-conserving transitions inside the subspaces with fixed $i\gamma_1\gamma_2$ parity, for the $E_M^{01}/h = E_M^{23}/h = 0.0$ GHz case. Orange and green lines correspond to different $i\gamma_1\gamma_2$ parities and start, in each case, from the ground state. When couplings are considered, extra transitions appear between initial and end states with opposite parity. Black and grey lines denote transitions starting from the lowest energy level and from excited levels, respectively, indicated by color-matching arrows in (b).

expressed in terms of the phase drop across the inductor, ϕ, and its conjugated charge, n, as (Manucharyan et al., 2009; Pekker et al., 2013)

$$H_f = 4E_c n^2 + \frac{1}{2}E_L\phi^2 + U_J(\phi - \varphi_{ext}) - E_M i\gamma_1\gamma_2 \cos\left(\frac{\phi - \varphi_{ext}}{2}\right), \tag{11.1}$$

where $U_J(\delta)$ denotes, as in Chapter 2, the conventional 2π-periodic component of the energy-phase relation of the Josephson junciton. Fig. 11.1(b) and (c) show how the presence of the E_M term drastically alters the fluxonium spectrum in comparison to the triv-

ial scenario investigated in Chapter 5. Each transition frequency splits in two, corresponding to the two possible fermionic parities, $i\gamma_1\gamma_2 \in \{|+\rangle, |-\rangle\}$, of the inner Majoranas (dashed lines in Fig. 11.1(c)). If the coupling energy, E_M, is larger than the spectroscopic linewidth, one can thus detect the emergence of Majoranas by detecting these split transitions. Note, moreover, that a fluxonium offers advantages compared the use of a transmon to detect the fractional effect. As E_M and E_J are tuned by the same electrostatic gate knob, maximizing E_M in a transmon can lead to complications with the transmon frequency moving beyond its measurable range. The fluxonium introduces extra tunability with flux, which allows to maximize E_M without worrying about the value of E_J.

We should note, however, that qualitatively different spectra can arise from Hamiltonian 11.1, depending on the value of E_M. The split-lines spectrum shown in Fig. 11.1(c) is obtained for $E_M < \pi^2/E_L$, while a different type of spectrum, with minima at $\varphi_{ext} = 2\pi\Phi_{ext}/\Phi_0 = 0, 2\pi$, is obtained when $E_M > \pi^2/E_L$. Both spectra are 4π-periodic for fixed $i\gamma_1\gamma_2$ parity and show parity-protected crossings of lines corresponding to different $i\gamma_1\gamma_2$. Both are qualitatively different from the trivial version, with minima at $\varphi_{ext} = \pi, 3\pi$ and without protected crossings. Therefore, in this idealized scenario, these spectroscopic features could be used to robustly find signatures of MBSs at both sides of the junction.

However, the finite size of real devices would introduce coupling between the two parity branches, modifying the spectrum. Such finite-size effects can be accounted for by introducing coupling terms between the inner and outer Majoranas with energies E_M^{01} and E_M^{12}, respectively in each of the two topological sections (Pekker et al., 2013). We obtain

$$H = H_f + E_M^{01} i\gamma_0\gamma_1 + E_M^{23} i\gamma_2\gamma_3. \tag{11.2}$$

As shown in Fig. 11.1(c), the E_M^{01} and E_M^{23} terms break the crossings between levels of different parity. If these couplings are weak compared to E_M, which can be achieved using long topological wires, the states are superpositions of opposite $i\gamma_1\gamma_2$ parities at the anticrossings, yet still retain a well-defined parity away from them. In such scenario, one would observe the parity conserving transitions (orange and green lines) away from $\varphi_{ext} = \pi$ and the transitions starting from the lowest energy state (black lines) in the vicinity of $\varphi_{ext} = \pi$.

An additional experiment to confirm the 4π-periodicity of the spectrum for fixed $i\gamma_1\gamma_2$ would be to do external flux sweeps. These sweeps should be performed fast enough to avoid adiabatically changing parity at the avoided crossings at π and 3π and also fast compared to the quasiparticle poisoning rates. Since the $i\gamma_1\gamma_2$ parity should not change over the duration of such measurement, we should see that a flux sweep of 2π ends up in a state different than the initial state, while a flux sweep of 4π is necessary to recover the initial state.

Moreover, the observation of a spectrum with signatures of MBSs would enable the investigation of the quasiparticle poisoning rates on the Majorana qubit state. By operating at a point away from $\varphi_{ext} = \pi$ and monitoring the time dynamics of changes between parity branches, individual QPP events can be detected.

Importantly, it's worth noting that a highly transmissive trivial Andreev bound state could mimic the effect of MBSs at the junction, with the crossing being protected by the parity of fluxons in the loop rather than by the $i\gamma_1\gamma_2$ parity, leading to the same qualitative results for all experiments proposed here. Similarly, the presence of quasi-Majoranas

at both sides of the junction would result in the same signatures as for spatially-separated Majorana bound states, as the fractional Josephson effect is the result of a local interaction which thus does not provide information about the bulk phase being trivial or topological (Vuik et al., 2019). Consequently, the described spectroscopic signatures would never constitute, in isolation, conclusive proof of a topological transition on the nanowire.

Finally, we note that, when trying to obtain signatures of the fractional Josephson effect with a nanowire fluxonium, different design aspects should be considered. First, using long nanowires can help suppress finite-size effects, thus minimizing E_{M}^{01} and E_{M}^{23}. Similarly, even if MBSs emerge at the ends of the junction, if they don't couple to each other with a strength larger than the spectroscopic linewidth one can not resolve them spectroscopically. Consequently, minimizing the junction length, thus increasing E_{M}, would be advisable for obtaining robust signatures of E_{M}.

TOPOLOGICAL QUBIT OPERATION AND READOUT WITH A NANOWIRE FLUXONIUM

This section assumes the scenario in which Majoranas are isolated at both ends of the junction while preserving negligible inner-outer Majorana couplings. Under these circumstances, one can exploit the techniques offered by the circuit Quantum Electrodynamics integration to read out and manipulate the Majorana state. Assuming a fixed total parity $-\gamma_0\gamma_1\gamma_2\gamma_3 = \pm 1$, the $|+\rangle$ and $|-\rangle$ $i\gamma_1\gamma_2$ parity states effectively encode the state of a qubit. As discussed earlier, different fluxonium transitions are available depending on the Majorana qubit state (orange or green in Fig. 11.1(c)). Consequently, the corresponding dispersive shifts on the readout resonator depend on the Majorana qubit state, enabling fast qubit state readout via standard cQED techniques.

Moreover, one can perform quantum operations on the Majorana qubit using microwave pulses. As the $|g,-\rangle \leftrightarrow |g,+\rangle$ and the $|e,-\rangle \leftrightarrow |e,+\rangle$ transitions are degenerate for a certain φ_{ext} range, the Majorana qubit transition, $|-\rangle \leftrightarrow |+\rangle$, can be addressed independently of the fluxonium state. By driving it, one can therefore perform single qubit rotations on the Majorana qubit. Alternatively, if the matrix element for this transition is too low, due to the opposite parity of the Majorana states involved, one could flux-pulse to $\varphi_{\mathrm{ext}} = \pi$, where both Majorna states mix and coherent oscillations between them occur, to perform X rotations of the topological qubit.

MODIFICATIONS OF A NANOWIRE FLUXONIUM FOR MBS DETECTION AND ALTERNATIVE MATERIALS

The experiments discussed above rely upon the presence of MBSs at the junction ends. However, over the past years, it has become clear to the physics community that the currently available materials lack the pristine quality necessary for consistent Majorana bound state isolation. The search for Majorana signatures using a nanowire fluxonium should thus be accompanied by the replacement of the junction by up-to-date choices as more promising platforms for MBS isolation become available.

One promising platform for the controlled emergence of Majorana bound states is an artificially defined Kitaev chain (Kitaev, 2001). Encouraging preliminary outcomes have demonstrated the feasibility of constructing a Kitaev chain by interleaving quantum dots and proximitized nanowire segments (Bordin et al., 2023; Dvir et al., 2023; Wang et al., 2022, 2023). These artificial Kitaev chains effectively model the Hamiltonian of a

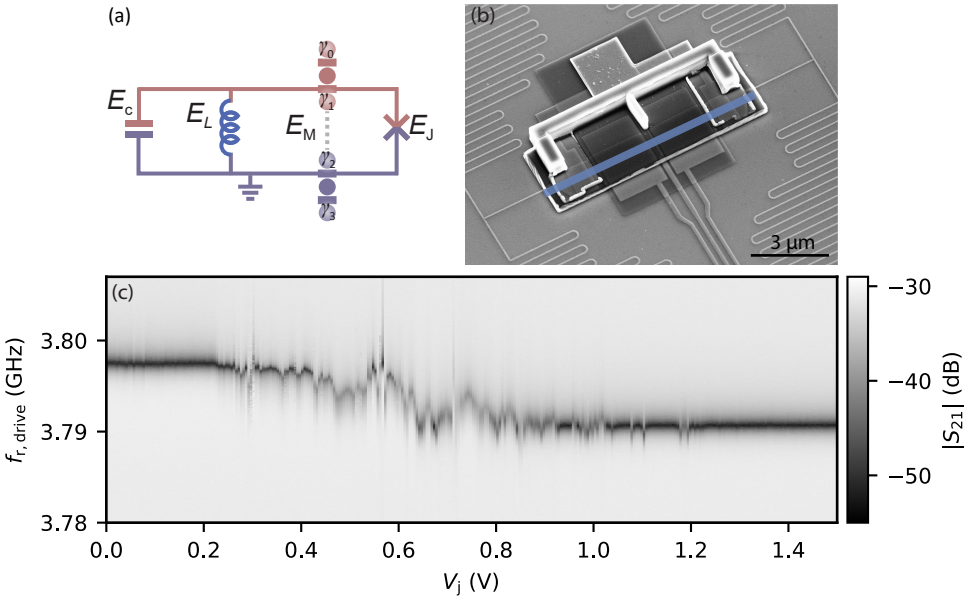

Figure 11.2: **Shadow-wall fluxonium.** (a) Circuit model of a fluxonium for which the Josephson junction is replaced by the parallel combination of a Josephson junction and a second arm formed by two artificial Kitaev chains placed in series. (b) Scanning electron microscope (SEM) image of a nanowire fluxonium for which the junction is fabricated using the shadow-wall technique. The aluminium is deposited from the side of the shadow-wall opposite to the nanowire and the thin nozzle close to the center shadows the junction area. The blue line indicates the position of the nanowire. (c) Electrostatic gate dependence of the resonator resonance frequency.

nanowire which, by tuning electrostatic and magnetic control parameters, can be transitioned from a trivial to a topological regime (Dvir et al., 2023). These controlled devices can in principle withstand higher degrees of material disorder than previous approaches. Fig. 11.2(a) presents a conceptual schematic of a fluxonium for which the two superconducting nanowire sections have been replaced by two artificially defined Kitaev chains that host Majorana bound states at their ends (see Ref. (Pino et al., 2023) for an analogous idea with a transmon circuit). As opposed to a continuous nanowire configuration (Fig. 11.1(a)), the 2π-peridic component of the junction's potential in such Kitaev chain configuration is not expected to be larger than approximately $E_J/h \sim 100$ MHz (Bouman et al., 2020). To address this, in Fig. 11.2(a) we incorporate an additional trivial junction in parallel to independently set the value of E_J to the regime of interest.

In the long-term perspective, the platform that offers the highest flexibility for implementing Kitaev chains are two-dimensional electron gases (2DEGs) (Wang et al., 2023). However, the cQED integration of 2DEG-based devices is not straightforward[3]. A successful alternative that is directly compatible with cQED integration (Wesdorp and *et al.*,

[3] Note, however, that promising results have been obtained either by etching away the 2DEG and buffer layers across the chip (Casparis et al., 2018) or by using flip-chip approaches (Hinderling et al., 2023; Hinderling et al., 2023b).

2023b) involves defining the Kitaev chain on an InSb nanowire using the shadow-wall lithography technique (Borsoi et al., 2021; Heedt et al., 2021). This technique consists in fabricating approximately 1 µm-tall structures next to the nanowire, followed by the deposition of an aluminium film at an angle. In this way, the walls selectively shadow parts of the nanowire and enable the deposition of superconducting films while retaining the non-proximitized sections pristine.

A device that incorporates the use of the shadow-wall technique into a fluxonium circuit is shown in Fig. 11.2(b). While not including any resemblance to the Kitaev chains, this highly simplified device serves as a proof-of-concept for the compatibility of shadow-wall lithography with the fluxonium spectroscopy technique discussed in Chapter 5. As shown in Fig. 11.2(c), we find that the resonator resonance frequency depends non-monotonically on the junction gate, a preliminary result that demonstrates this compatibility. For a more exhaustive exploration of the simultaneous use of shadow-wall lithography and microwave techniques, see Ref. (Wesdorp and *et al.*, 2023b).

To conclude this section, we note that the technique discussed here is adaptable to the investigation of materials beyond InAs or InSb hybrids. By replicating a similar fluxonium geometry and substituting the Josephson junction material with a two-dimensional material (Kroll et al., 2018; Wang et al., 2019) it becomes possible to probe, for instance, superconductor-proximitized edge states in a quantum spin Hall insulators (Dolcini et al., 2015; Fu and Kane, 2008; Wu et al., 2018). Alternatively, a hybrid fluxonium could be used to detect topological transitions in proximitized germanium (Ge) Josephson junctions (Laubscher et al., 2023; Luethi et al., 2023; Luethi et al., 2023b), a platform that offers lower disorder levels than InSb or InAs (Mizokuchi et al., 2018; Stehouwer et al., 2023). Two-dimensional hole gases in Ge have a large spin-orbit interaction and can be proximitized with superconductors (Aggarwal et al., 2021; Hendrickx et al., 2019; Tosato et al., 2023; Valentini et al., 2023; Vigneau et al., 2019), making it a competitive candidate for hosting Majoranas, thus diversifying the landscape of available platforms.

11.1.2. FLUXONIUM AS A DETECTOR OF DIRECT 4π QUANTUM PHASE SLIPS

Beyond its role in probing topological effects, a nanowire fluxonium can provide insights into trivial phenomena in semiconducting nanowires, such as the presence of highly transparent channels. Recently, colleagues in our research group have observed effects of a nanowire transmon when the junction transparency, T, approaches unity that can not be explained by considering only the lowest energy branch of the ABS potential (see Sec. 2.1.1) (Averin, 1999; Bargerbos et al., 2020; Kringhøj et al., 2020; Vakhtel and van Heck, 2023).

These deviations from the standard behavior can be understood as the suppression of 2π quantum phase slips (QPS) across the junction, a consequence of imaginary-time Landau-Zenner tunneling (ILZT) between the lower and upper branches of the Andreev potential (Averin, 1999). Fig. 11.3 shows the implications of considering both even branches of the Andreev potential when $T \to 1$. 2π-QPS, characterized by energy $E_s^{2\pi}$, couple states localized in neighboring potential wells (such as the wells at $\phi = 0$ and $\phi = 2\pi$). This coupling is due to tunneling through the barrier that separates the wells (Astafiev et al., 2012; Matveev et al., 2002; Mooij and Harmans, 2005; Mooij and Nazarov, 2006; Pop et al., 2010). Similarly, 4π-QPS, characterized by energy $E_s^{4\pi}$, couple states lo-

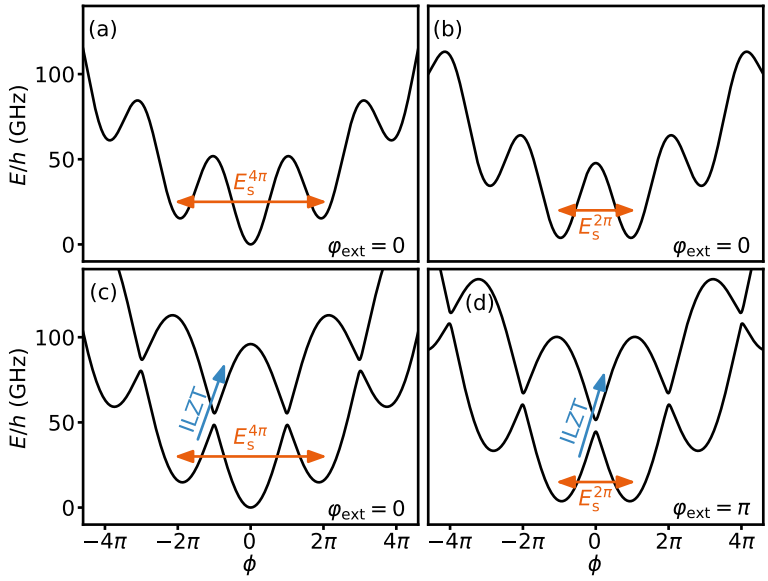

Figure 11.3: 2π **and** 4π **quantum phase slips in a fluxonium with different junction potential models.** All panels show a fluxonium potential (in black) consisting of a parabolic background from the E_L term plus a 2π-periodic Josephson term at different flux values, as indicated in the labels. In (a) and (b), the Josephson potential term is a cosine $E_J \cos(\phi - \varphi_{ext})$. In (c) and (d), the Josephson potential term is that of a single highly transparent channel $\pm\Delta\sqrt{1 - T\sin^2\left((\phi - \varphi_{ext})/2\right)}$. Orange arrows indicate tunneling processes between nearest-neighbor wells (2π quantum phase slips) or between next-nearest-neighbor wells (4π quantum phase slips). Blue arrows indicate Landau-Zenner tunneling between the ground and the excited branches of the Andreev bound state potential.

calized in next-nearest neighbor wells, separated by 4π. When E_J is large compared to the energies of the fluxon states, the amplitude of quantum phase slips is reduced. In this regime of rare QPS and if one only considers the lower branch of the Andreev potential, 4π-QPS are a second order processes in $E_s^{2\pi}$: $E_s^{4\pi} \propto {E_s^{2\pi}}^2$ (Manucharyan, 2012; Vakhtel and *et al.*, 2023b).

However, as explored in our recent work (Vakhtel and *et al.*, 2023b), this relationship is modified when the second ABS branch is accounted for (see Fig. 11.3(c) and (d)). When T approaches unity, the reduction of the energy gap between the lower and upper branches at $\phi = \pi$ amplifies the impact of ILZT, resulting in the suppression of 2π-QPS in favor of 4π-QPS. At $T = 1$, $E_s^{2\pi}$ exactly vanishes, rendering the subspaces of states localized at even and odd multiples of $\phi = 2\pi$ entirely uncoupled.

Nanowire transmons only offer indirect access to this high T effect, via the implications of the suppressed 2π-QPS in a reduced charge dispersion (Averin, 1999; Bargerbos et al., 2020; Kringhøj et al., 2020; Vakhtel and van Heck, 2023). In contrast, a nanowire fluxonium permits the direct and independent resolution of the 4π- and 2π-QPS characteristic energies, $E_s^{2\pi}$ and $E_s^{4\pi}$, respectively (Manucharyan, 2012; Manucharyan et al., 2009, 2012). If the Josephson junction is part of a superconducting loop, as in the case of a fluxonium circuit, quantum phase slips couple states with different fluxon num-

bers[4], differing by one for 2π-QPS or two for 4π-QPS (Manucharyan et al., 2009). The $E_s^{2\pi}$ and $E_s^{4\pi}$ amplitudes become experimentally accessible in the fluxonium transition spectrum, as shown in Fig. 11.4(a). Fluxon states localized at integer values of $\phi/2\pi$ have a well-defined number of fluxons in the loop. The ground state at $\varphi_{ext} = 0$, for example, is localized at $\phi = 0$ (Fig. 11.3(a)) (zero fluxons) while the one at $\varphi_{ext} = 2\pi$ is localized at $\phi = 2\pi$ (one fluxon). In the absence of 2π-QPS, the energies of these two states would perfectly cross at $\varphi_{ext} = \pi$. However, 2π-QPS hybridize states with adjacent fluxon numbers and lift all degeneracies between nearest neighbor parabolas at half-integer values of $\varphi_{ext}/(2\pi)$. Analogously, 4π-QPS mix states that differ by two fluxons and lead to avoided crossings between next nearest neighbor parabolas at integer values of $\varphi_{ext}/2\pi$. The magnitudes of $E_s^{2\pi}$ and $E_s^{4\pi}$ are thus accessible by spectroscopy measurements, as shown in Fig. 11.4(a).

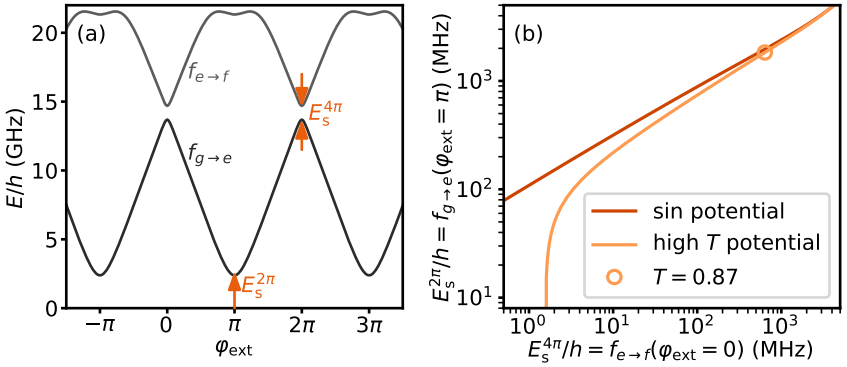

Figure 11.4: **Spectroscopy of suppressed $E_s^{2\pi}$ with respect to $E_s^{4\pi}$.** (a) Flux dependence of the transition energies, starting from the ground state, for a fluxonium with a sinusoidal junction potential and $E_c/h = 5.5$ GHz, $E_L/h = 0.3$ GHz and $E_J/h = 11$ GHz. The $E_s^{2\pi}$ and $E_s^{4\pi}$ quantum phase slip amplitudes, indicated with orange arrows, can be directly resolved in the spectrum at $\varphi_{ext} = \pi$ and $\varphi_{ext} = 2\pi$, respectively. (b) $E_s^{2\pi}$ versus $E_s^{4\pi}$ for different potential models. The behavior for the model considering two ABSs deviates from that of the sinusoidal model above a threshold T_c and results in a suppressed $E_s^{2\pi}$ with respect to $E_s^{4\pi}$ due to Landau-Zenner tunneling.

Fig. 11.4(b) shows the different evolution of the quantum phase slip amplitudes depending on the junction potential model. Specifically, we plot the dependence of $E_s^{4\pi}$ on $E_s^{2\pi}$ for the sinusoidal and double-branch junction potential models, as E_J or T are varied, respectively[5]. As expected, as E_J or T increase, both $E_s^{2\pi}$ and $E_s^{4\pi}$ decrease and, in the high E_J regime, the $E_s^{4\pi} \propto {E_s^{2\pi}}^2$, relationship emerges. For details on how the proportionality factor depends on the system's parameters, see Ref. (Vakhtel and *et al.*,

[4]The fluxon number is the number of 2π twists that the superconducting phase accumulates around the loop.

[5]To simulate the two-level Andreev potential case we use the two-level Hamiltonian proposed by Zazunov et al. (2003)

$$H_{2ABS} = 4E_c n^2 + \frac{1}{2}E_L(\phi - \varphi_{ext})^2 - \Delta\begin{pmatrix} 0 & -ze^{-ir\phi/2} \\ -z^* e^{ir\phi/2} & 0 \end{pmatrix} \tag{11.3}$$

with $z = \cos(\phi/2) + ir\sin(\phi/2)$ and $r = \sqrt{1-T}$, which agrees better with the predictions from the single-level potentials at low T than other options in the literature (Ivanov and Feigel'man, 1998; Ivanov and Feigel'man, 1999; Zazunov et al., 2005).

2023b). However, above a certain threshold transparency, T_c, which depends on the parameter regime, the effect of ILZT reduces $E_s^{2\pi}$ and results in strong deviations from the quadratic $E_s^{2\pi}$ vs. $E_s^{4\pi}$ relation (see Ref. (Vakhtel and *et al.*, 2023b) for quantitative analytical expressions). Interestingly, as discussed in Ref. (Vakhtel and *et al.*, 2023b), for some intermediate parameter regimes, these two possible paths resulting in 4π-QPS destructively interfere, bringing the amplitude of 4π-QPS to zero before it revives again (not shown in Fig. 11.4). We propose to use a nanowire fluxonium to detect this signature of direct 4π quantum phase slips activated by the higher energy ABS branch. Moreover, in Sec. 11.2 we suggest to exploit this high T effect to implement a protected qubit.

11.1.3. FURTHER EXPERIMENTS WITH AN SQDS TRANSMON

The experiments conducted in Chapters 6, 7, 8, and 9 demonstrate the transmon's efficacy as a spectroscopic tool to access the inductance of a quantum dot junction's ground state, as well as the transition energies between its states. Notably, its sensitivity is on the order of megahertz, which corresponds to a picoampere supercurrent sensitivity (see Appendix A), thereby enabling the measurement of supercurrents beyond the reach of conventional transport techniques. As elaborated on by Bargerbos (2023b), this device also holds promise for investigating the ground state properties of Josephson junctions incorporating other configurations of quantum dots. One could, for instance, envision using a transmon to map out the phase diagram of a double quantum dot junction (Bouman et al., 2020; Ortega-Taberner et al., 2023; Saldaña et al., 2018; Steffensen et al., 2022) or to investigate more complex combinations of quantum dots and junctions that are not numerically tractable, possibly in the presence of a Zeeman magnetic field.

In this section, we instead focus on describing two aspects that could be further researched with the *same* junction geometry as in Chapters 6, 7, 8 and 9. While investigating a single quantum dot tunnel-coupled to two superconducting leads, we identified two intriguing phenomena that deserve further attention: the physics of the doublet "chimney" (Pavešič et al., 2023) and the Knight shift on the doublet states under a magnetic field (Pavešić et al., 2023b). Both phenomena are not explained to low order perturbation theory and can thus be easily missed when doing an analytic study of the SIAM. Yet, their detection becomes feasible using either the experimental spectroscopic techniques or the numerical renormalization group methods presented in this thesis.

PHYSICS OF THE CHIMNEY

In Chapter 6 we measured a phase diagram at $\varphi_{\text{ext}} = \pi$ with showed a characteristic "chimney" shape for the doublet region (see Fig. 6.5(b)). We found that, in the proximity of $\xi = 0$, the ground state was always a doublet, independently of the magnitude of the coupling to the leads, Γ. While this regime had been theoretically predicted (Rozhkov et al., 2001; Tanaka et al., 2007), it had not yet been observed experimentally. Moreover, the nature of its doublet ground state lacked an intuitive understanding. Specifically, the persistence of the doublet ground state under strong tunnel coupling to the leads is, at first sight, counterintuitive. In general, a screened singlet ground state is expected at large coupling strengths, involving one spin localized in the quantum dot that is screened by an uncoupled quasiparticle on the leads.

Following our experimental observation of the chimney, the nature of this doublet

state was further investigated theoretically by our collaborators (Pavešič et al., 2023). Within low-order perturbation theory, the singlet and doublet ground states are found to be degenerate at the chimney. Pavešić *et al.* revealed that, in this situation, the natures of the singlet and doublet states close to $\xi = 0$ are very similar. Both states have a YSR-like character, hosting an individual electron on the dot which is fully screened by antiferromagnetic coupling a quasiparticle from the leads. The doublet state includes an additional quasiparticle on the leads. The even phase dependence of this extra quasiparticle enables interactions with the quasiparticle in the quantum dot, lowering the energy of the doublet state with respect to the singlet.

This follow-up work deepened our comprehension of the doublet state's nature. Related questions that could still be explored experimentally are, for instance, the investigation of the parity dynamics in the chimney. In particular, as the coupling to the leads increases, the singlet and doublet states approach degeneracy exponentially. This would possibly result in equal characteristic lifetimes independently of the tunnel gates which could be mapped out versus the different control parameters. Additionally, it could be interesting to compare the dominating dephasing mechanisms in this parameter regime to those deep in the dome, where the doublet states are of very different nature.

KNIGHT SHIFT

During our exploration of spin-flip spectroscopy under magnetic fields, reported in Chapters 7 and 8, we encountered an unexpected feature. We found that the maximum of the spin-flip transition, $f_s(\varphi_{ext})$, shifted away from $\varphi_{ext} = \pi/2, 3\pi/2$ under the presence of a magnetic field (see Fig. 11.5(a)-(f), as well as Fig. 8.1 and 7.3). Additionally, the flux-dispersion of the frequency increased as a function of the magnetic field. This effect, while inconsistent with the minimal model of Eq. (7.1), can be phenomenologically accounted for by introducing an additional term proportional to $\cos(\varphi_{ext})$, alongside the expected $\sin(\varphi_{ext})$ dependence due to the E_{SO} term:

$$f_s(\varphi_{ext}) = A\sin(\varphi_{ext}) + B\cos(\varphi_{ext}) + C, \tag{11.4}$$

where $A = 2E_{SO}$, $C = E_Z$ is the Zeeman energy and the term proportinal to B remained unexplained. Furthermore, NRG calculations corroborated the existence of this shift, while it is not predicted analytically to first order in the coupling to the leads (see Sec. 7.7.1).

The origin of this phase shift was subsequently investigated in collaborative research (Pavešić et al., 2023b). The experimental data exhibits that the amplitude of the cosine term, B, depends linearly on the magnetic field (as shown in Fig. 11.5(i)). Such effect can be accounted for by considering a renormalization of the g-factor determined by the factor κ

$$g_{eff} = g(1-\kappa). \tag{11.5}$$

A similar renormalization, known as the impurity Knight shift, is known to occur for impurities coupled to a metallic or a single superconducting bath. Here, we consider a variant of this effect caused by the exchange interaction between the local quasiparticle in the quantum dot and the continuum of Bogoliubov quasiparticles in the leads.

Different contributions to the renormalization parameter, κ, can be obtained from a perturbative calculation in the limit of small coupling to the leads, Γ. In particular, as all odd-order contributions in electron hopping vanish, we focus on the second and

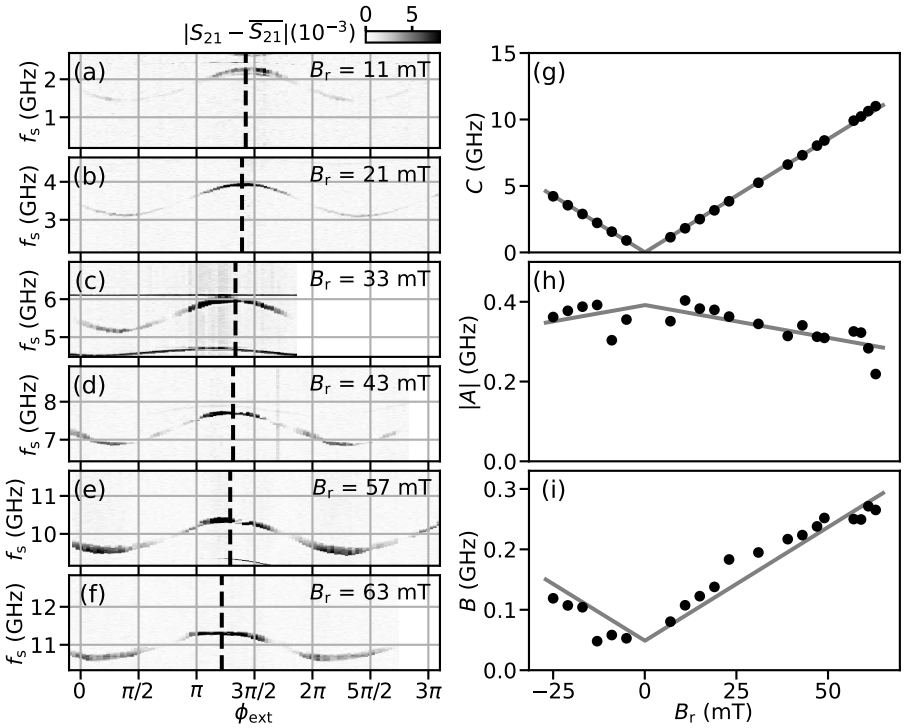

Figure 11.5: **Experimental observation of the Knight shift.** (a)-(f) Spin-flip spectroscopy of the device from Chapters 7 and 8. Measured flux dependence of the $|\downarrow\rangle \leftrightarrow |\uparrow\rangle$ transition for a range of magnetic fields applied parallel to the spin direction. The vertical dashed lines mark the positions of maximal frequency and are extracted from fits to the dependence $f_s = A\sin(\varphi_{ext}) + B\sin(\varphi_{ext}) + C$ (see Eq. 11.4). (g), (h) and (i) Decomposition of the data into constant, sine and cosine terms, respectively, as a function of the applied magnetic field.

fourth-order terms. The leading term, $\bar{\kappa}$, is linear in Γ (quadratic in electron hopping) and does not depend on phase. In contrast, the subleading term is quadratic in Γ (quartic in electron hopping) and, importantly, has a cosinusoidal dependence on ϕ. This cosine dependence originates from the phase dependence of the hybridization between the quantum dot and the leads. We obtain

$$\kappa(\phi) = \bar{\kappa} - \frac{\Delta_\kappa}{2}\cos\phi. \tag{11.6}$$

Consequently, the potential energy can be expressed as

$$U(\phi) = E_0\cos\phi - E_{SO}\vec{\sigma}\cdot\vec{n}\sin\phi + \frac{1}{2}g[1-\kappa(\phi)]\mu_B\vec{\sigma}\cdot\vec{B}, \tag{11.7}$$

where $\vec{n}$ denotes a unit vector along the spin polarization direction at zero field, $\vec{\sigma}$ is the vector of x, y and z Pauli operators and $\vec{B}$ is an externally applied magnetic field. For a magnetic field, $\vec{B} = B_r\vec{n}$, applied along $\vec{n}$, the transition energy is then given by the difference

$$E_s = |E_\uparrow - E_\downarrow| = E_Z(1-\bar{\kappa}) - 2E_{SO}\sin\phi + \frac{E_Z\Delta_\kappa}{2}\cos\phi, \tag{11.8}$$

where $E_Z = g\mu_B B_r$ is the Zeeman energy. This takes the same shape as Eq. 11.4 found experimentally.

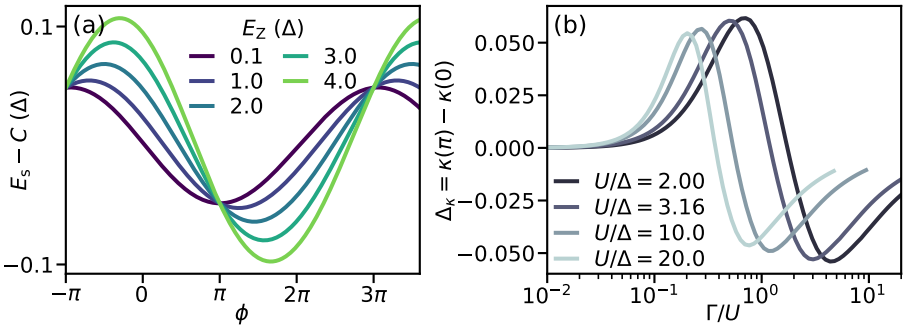

Figure 11.6: **NRG investigation of the Knight shift.** (a) Spin-flip transition energy, $E_s = |E_\uparrow - E_\downarrow|$ versus the phase drop across the junction, ϕ. Different lines correspond to different parallel magnetic fields, as indicated on the label. In each case, we subtract the average energy, denoted by C. The data are extracted from NRG calculations of the extended SIAM presented in Chapter 7. (b) Difference between κ values for $\phi = 0$ and $\phi = \pi$, $\Delta_\kappa = \kappa(\pi) - \kappa(0)$ versus Γ/U and for several U/Δ values. This quantity corresponds to the amplitude of the cosine term of Eq. 11.6. $D = 100\Delta$.

Performing NRG calculations allows investigating the effect away from the low Γ limit. Fig. 11.6(a) shows the transition energy E_s obtained from NRG calculations as the magnetic field increases, reproducing our experimental results. Interestingly, as Γ/U increases, higher harmonic terms $\kappa \propto \cos(n\phi)$ emmerge. These terms arise from higher-order processes in electron hopping and have not yet been explored experimentally.

This shift constitutes a magnetic-field-tunable coupling between the quantum dot spin and the Josephson current which, notably, does not require the presence of a spin-orbit interaction term. To confirm this experimentally, it would be insightful to identify signatures of this Knight shift in either a doublet resonance with $E_{SO} = 0$ or even in a material without spin-orbit interaction. Exploiting this effect holds promise for applications to implement Andreev spin qubits in materials without spin-orbit interaction, as further discussed in Sec. 11.3.2.

Importantly, the NRG study from Pavešić et al. (2023b) allows us to determine the dependence of the cosine amplitude, Δ_κ, on the different control parameters. As shown in Fig. 11.6(b), we find that Δ_κ is absent in the low Γ/U limit and starts increasing at around $\Gamma/U \sim 0.1$, a regime readily accessible experimentally (see Fig. 6.5). Over a wide range of experimentally attainable parameters, the value of Δ_κ reaches 0.05. For a typical qubit frequency of 10 GHz, this would translate into a frequency dispersion of 500 MHz, comparable to typical amplitudes of the sine term originating from the spin-orbit interaction at the material.

11.2. HAMILTONIAN-PROTECTED HYBRID QUBITS

As discussed in Sec. 2.1.1 and 11.1.2, the energy-phase relationship of nanowire Josephson junctions can drastically deviate from a standard 2π-periodic cosinusoidal relation in various ways. In Sec. 2.1.1 we saw that, when highly transparent channels are present,

higher $\cos(m\phi)$ harmonics with $m > 1$ become relevant. Similarly, in Sec. 11.1.2 we discussed how, in the limit of maximal transparency, 2π quantum phase slips vanish in favor of 4π quantum phase slips. This effectively transforms the junction potential into a 4π-periodic function. Here, we delve into how to harness these unconventional junction potentials to construct Hamiltonian-protected superconducting qubits (Aguado, 2020; Clerk et al., 2020). In particular, we focus on how to exploit the even $\cos(2m\phi)$, $m \in \mathbb{N}$, junction harmonics to implement a Cooper pair parity protected qubit (Gladchenko et al., 2009; Larsen et al., 2020; Schrade et al., 2022; Smith et al., 2020) and on how to exploit a $\cos(\phi/2)$ junction potential to implement a fluxon parity protected qubit (Kalashnikov et al., 2020; Vakhtel and *et al.*, 2023b).

11.2.1. NANOWIRE $\cos(2\phi)$ QUBIT (PROTECTED BY COOPER PAIR PARITY)

A $\cos(2\phi)$ qubit consists of a superconducting island with charging energy E_c connected to ground via a Josephson junction with a π-periodic energy-phase relation, as illustrated in Fig. 11.7(a) (Gladchenko et al., 2009; Smith et al., 2020). Its Hamiltonian can be written as

$$H_{2\phi}(\phi) = 4E_c(\hat{n} - n_g)^2 + E_{J,2}\cos(2\phi), \tag{11.9}$$

where ϕ represents the phase across the junction, $\hat{n}$ is its conjugate charge, and n_g denotes an offset charge on the island. Higher potential $\cos(2m\phi)$ terms could also be present without affecting the qubit's behavior in a qualitative manner.

The protection of this qubit arises from the Josephson element's π-periodic potential, which suppresses coherent charge transport in units of $2e$ (single Cooper pairs) but allows coherent charge transport in units of $4e$ (pairs of Cooper pairs). Consequently, the two lowest energy states, $|g\rangle$ and $|e\rangle$, become nearly degenerate and localize in subspaces with different Cooper pair parities on the island. Fig. 11.7 illustrates the wavefunctions of $|g\rangle$ and $|e\rangle$ for different $E_{J,2}/E_c$ ratios. When $E_{J,2}/E_c \gtrsim 1$, these states exhibit different Cooper pair parities (green and orange in Fig. 11.7(c)), while for $E_{J,2}/E_c \gg 1$, they are localized in different potential wells (Fig. 11.7(d)). In both cases, the vanishing transition matrix elements between $|g\rangle$ and $|e\rangle$ result in suppressed qubit decay. Moreover, in the regime of large $E_{J,2}/E_c$, the wavefunctions of the computational states delocalize in charge space, effectively mitigating dephasing due to charge noise. This inherent Hamiltonian protection, simultaneously against decay and dephasing, positions the $\cos(2\phi)$ qubit as a promising candidate compared to other qubit types.

To implement a $\cos(2\phi)$ element using nanowire Josephson junctions, one can leverage the higher harmonics in their energy-phase relationship when highly transparent channels are present (Eq. 2.7) (Bozkurt and Fatemi, 2023; de Lange et al., 2015; Larsen, 2018; Larsen et al., 2020; Schrade et al., 2022). The potential $U_{SNS}(\phi)$, being an even function, can be expressed through its Fourier decomposition

$$U_{SNS}(\phi) = \sum_{m\geq 1} E_{J,m}(\{T_i\})\cos(m\phi) \tag{11.10}$$

where the $E_{J,m}$ components increase with increasing junction transparencies (Lüthi, 2019). To cancel out the odd harmonics, two such nanowire junctions can be connected in parallel within a SQUID configuration. If the SQUID is threaded by half a flux quantum, the odd harmonics cancel out (since $\cos\big((2m+1)(\phi+\pi)\big) = -\cos\big((2m+1)(\phi)\big)$) while the

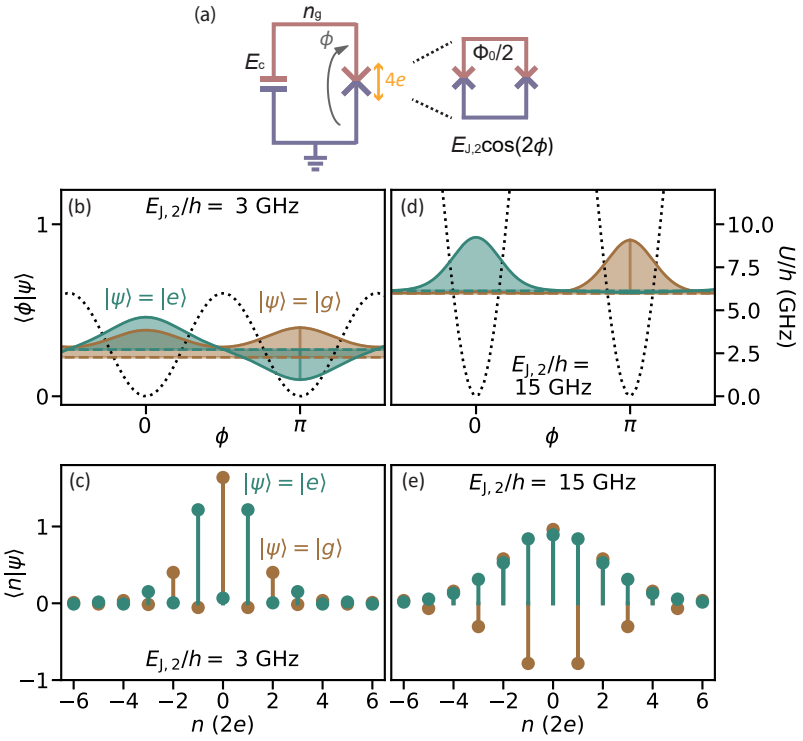

Figure 11.7: **Nanowire cos(2ϕ) qubit.** (a) Circuit model of a cos(2ϕ) qubit. It consists of an island (red) connected to ground (purple) by a cos(2ϕ) element and a capacitor. Only pairs of Cooper pairs can tunnel through the cos(2ϕ) junction (orange). External voltage noise couples capacitively to the island and results in charge, n_g, noise. Inset: the cos(2ϕ) element can be implemented by the parallel combination of two highly transparent nanowire Josephson junctions. (b) Potential of the nanowire junction SQUID (dotted black line) and wavefunctions of the ground, $|g\rangle$, and first excited, $|e\rangle$, states in the phase basis, in arbitrary units and offset by their eigenenergy. The two eigenstates are the symmetric and antisymmetric combinations of wave functions localized in the 0 and π potential wells. (c) Wavefunctions of $|g\rangle$ and $|e\rangle$ in the charge basis, in arbitrary units. The two eigenstates are localized in subspaces with different Cooper pair parity. For (b) and (c), $E_{J,2}/h = 3$ GHz. (d, e) Same as (b, c) but for $E_{J,2}/h = 15$ GHz. In the phase basis, the eigenstates are localized in different potential wells (d), while in the charge basis, they are the symmetric and antisymmetric superpositions of wave functions localized in subspaces with different Cooper pair parity (e). For all panels $E_c/h = 0.35$ GHz, $n_g = 0$.

even harmonics combine (since $\cos\left(2m(\phi+\pi)\right) = \cos\left(2m\phi\right)$). If the junctions are identical, the result is a π-periodic potential. Having to tune the flux to half a flux quantum, however, requires a relatively large loop and results in sensitivity to flux noise. An alternative is to define a quantum dot in one of the two junctions and tune it so that it is in a doublet ground state and thus has a π-offset energy-phase relation (Szombati et al., 2016; van Dam et al., 2006). This alternative approach reduces the loop size, mitigating the sensitivity to flux noise.

The circuit presented in Fig. 11.7(a) offers a simpler design compared to alternative implementations of cos(2ϕ) qubits (Groszkowski et al., 2018; Smith et al., 2020). Moreover, the *in situ* tunability of the junction transparency permits investigating both pro-

tected and unprotected regimes within the same device.

While the literature on $\cos(2\phi)$ qubits is more sparse than that on other types of qubits, such as the transmon, recent results prove that $\cos(2\phi)$ qubits can quickly learn from the expertise developed in other sub-fields. Refs. (Leroux and Blais, 2023; Schrade et al., 2022), for instance, set a first stone in the path towards scalability of $\cos(2\phi)$ qubits by proposing two-qubit gates inspired on cat and transmon qubits, respectively. A similar approach can be used in the future to further explore some of the challenges that persist in the area of nanowire-based $\cos(2\phi)$, listed below. Firstly, while the sensitivity to n_g noise is significantly reduced in the high $E_{J,2}/E_c$ regime, the introduction of a nanowire junction SQUID renders the system sensitive to junction charge noise and flux noise. The magnitude and implications of this sensitivity should be analyzed in detail in further studies. Additionally, due to the unique mesoscopic characteristics of each semiconducting junction, the likelihood of all odd $E_{J,2m+1}$ terms being identical in both junctions is exceedingly low. This would introduce a non-zero 2π-periodic component in the potential, which, while compatible with the Hamiltonian protection against decay, should be minimized (Larsen et al., 2020; Schrade et al., 2022). Finally, reaching the high $E_{J,2}/E_c$ regime might pose challenges due to the relatively small magnitudes of higher-order harmonics in nanowire junctions. Strategies to address this issue include implementing large capacitors to reduce E_c and harnessing highly transparent junction channels in the presence of a resonant level (Bargerbos et al., 2020; Kringhøj et al., 2020).

11.2.2. NANOWIRE $\cos(\phi/2)$ QUBIT (PROTECTED BY FLUXON PARITY)

We now delve into the physics of a nanowire-based $\cos(\phi/2)$ qubit that leverages the suppression of 2π quantum phase slips within a highly transparent Josephson junction (Kalashnikov et al., 2020; Vakhtel and *et al.*, 2023b). As discussed in Sec. 11.1.2, when the energy gap between the lower and upper branches of the Andreev potential approaches zero, states with different fluxon parities do not couple to each other. In this high-transparency regime, a nanowire Josephson junction effectively has a $\pm\cos(\phi/2)$ potential, exhibiting different potentials for states with different fluxon parity. If such a junction is connected in parallel to a capacitor with charging energy E_c and an inductor with inductive energy E_L (Fig. 11.8), the total Hamiltonian becomes

$$H_{\phi/2}(\phi) = -4E_c\hat{n}^2 + \frac{1}{2}E_L(\phi-\varphi_{ext})^2 \pm E_J\cos(\phi/2) + E_J, \tag{11.11}$$

where φ_{ext} is the reduced flux through the loop.

The two lowest eigenstates of the system are shown in Fig. 11.8 for two different E_L values. In both scenarios, $|g\rangle$ and $|e\rangle$ are characterized by a different parity of fluxons in the loop (Fig. 11.8(b) and (d)). Consequently, these two states are uncoupled from each other, resulting in protection against decay. For the limit of low E_L (Fig. 11.8(c) and (d)), the states moreover delocalize in phase space, suppressing dephasing due to flux noise, a concept recently demonstrated in the blochnium qubit (Pechenezhskiy et al., 2020). Therefore, in this limit, the Hamiltonian offers simultaneous protection against decay and dephasing, analogously to the $\cos(2\phi)$ case.

Previous attempts to implement a $\cos(\phi/2)$ element, like the bifluxon (Kalashnikov et al., 2020), combined conventional SIS Josephson junctions with more complex circuit geometries. While offering higher circuit simplicity and *in situ* tunability in and

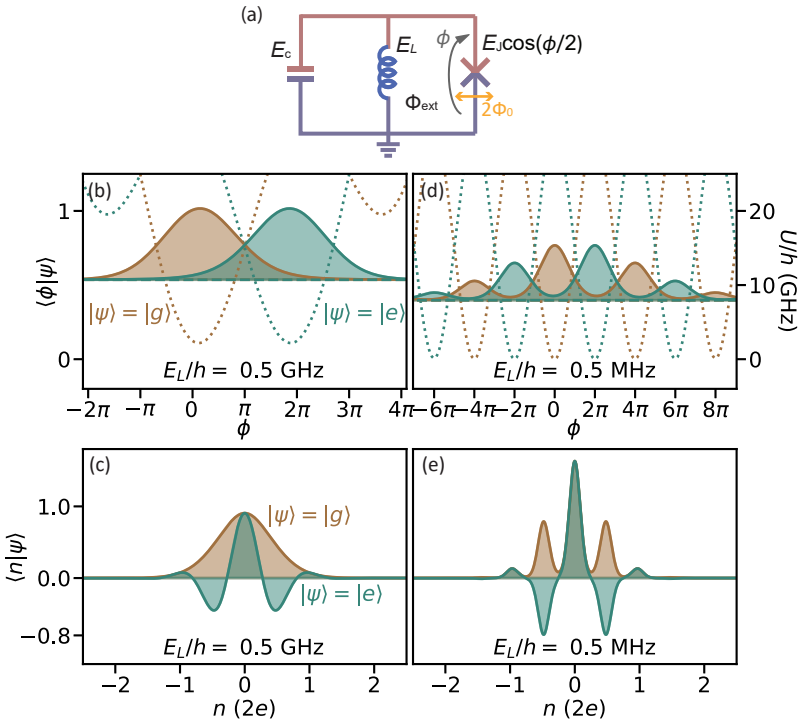

Figure 11.8: **Nanowire cos(ϕ/2) qubit.** (a) Circuit model of a cos (ϕ/2) qubit. It consists of a cos(ϕ/2) junction, a capacitor and an inductor connected in parallel. Only pairs of fluxons can tunnel through the cos(ϕ/2) junction (orange). External magnetic noise couples inductively to the loop formed by the junction and the inductor and results in flux, Φ_{ext}, noise. (b) The potential of the nanowire junction and the inductor in parallel is shown with dotted lines. Different colors correspond to different fluxon parity. Filled regions indicate the wavefunctions of the ground, $|g\rangle$, and first excited, $|e\rangle$, states in the phase basis, in arbitrary units and offset by their eigenenergy. (c) Wavefunctions of $|g\rangle$ and $|e\rangle$ in the charge basis, in arbitrary units. For (b) and (c), $E_L/h = 0.5$ GHz. (d, e) Same as (b, c) but for $E_L/h = 0.5$ MHz, unrealistically low. The two eigenstates are localized in subspaces with different fluxon parity (d). For all panels $E_c/h = 10.0$ GHz, $\Phi_{ext} = \Phi_0/2$ and $E_j/h = 15$ GHz.

out of the protected regime, the suggested nanowire implementation of cos(ϕ/2) also poses various challenges that should be further investigated. First, and similarly to the cos (2ϕ) case, the electrostatic junction tunability introduces sensitivity to junction gate noise. Moreover, the values of E_L required to delocalize the wavefunction in phase are currently lower than experimentally achievable[6]. This calls for further research in alternative materials with large kinetic inductance, such as titanium nitride (Shearrow et al., 2018) or granular aluminium (Kamenov et al., 2020; Maleeva et al., 2018), as well as in substrate-free inductors (Pechenezhskiy et al., 2020).

11

[6]To the best of our knowledge, the current record in the literature stands at $E_L/h = 66.5$ MHz (Pechenezhskiy et al., 2020).

11.3. SUPERCONDUCTING SPIN QUBITS. WHAT'S NEXT?

Throughout this thesis, we investigated superconducting spin qubits and highlighted their primary characteristics. Firstly, ASQs emerge as a unique bridge between semiconducting and superconducting qubits, a result of their native coupling between spin and supercurrent degrees of freedom. Furthermore, various intrinsic advantages set them apart from other solid-state qubit platforms. In comparison to semiconducting spin qubits, ASQs offer fast circuit Quantum Electrodynamics (cQED) readout capabilities and strong coupling across longer distances. When compared to transmon qubits, ASQs have a large transition frequency separation, fast manipulation without leakage limitations and a compact footprint. Moreover, their native longitudinal interactions address the issue of frequency crowding when scaling up. Finally, their possibility for high qubit connectivity, as discussed in Chapter 10, holds promise for enhanced scalability by reducing the qubit number overhead for quantum error correction.

However, the development of Andreev spin qubits is still in its infancy and thus faces numerous challenges yet to be addressed:

- **Noise sensitivity**. ASQs exhibit exceptionally short dephasing times when compared to other qubit platforms, primarily due to their sensitivity to various noise sources. These sources include charge noise, nuclear spin fluctuations, quasiparticle poisoning and flux noise. Distinguishing between these origins and pinpointing the primary contributors to dephasing calls for further research. Fortunately, the extensive knowledge gained in the semiconducting and superconducting qubit communities over the years provides several potential avenues to enhance qubit coherence, as discussed in Sec. 11.3.1

- **Flux sensitivity of the coupling strength around the OFF setpoint**. Superconducting spin qubits are uncoupled at their flux sweet spots, at zero and half flux. However, deviations from these sweet spots lead to linearly increasing longitudinal qubit-qubit coupling energy, giving rise to unwanted coupling terms. While this is an intrinsic challenge for ASQs, realistic experimental flux errors should maintain the ON-OFF coupling ratio below 1/100. Consequently, this issue will only become relevant when the two-qubit gate fidelity exceeds 99.99 %.

- **Selective readout challenges in the $\mathbf{E_J/E_{SO}}$ limit**. In Chapter 10 we introduced a fluxonium-based readout method for selectively reading out a qubit in its ON state while keeping other qubits uncoupled. Furthermore, we found that the gate fidelity can be increased by increasing the E_J/E_{SO} ratio. However, for large E_J values in the THz range, the fluxonium readout has to be replaced by resonator readout, which is incompatible with the selective readout method introduced. While the sequential and joint readout protocols discussed in Chapter 10 are still possible, further research is needed to explore alternative selective readout methods in the large E_J/E_{SO} limit.

- **Leakage due to quasiparticle poisoning**. The measured decay times in this work (around 1 to 50 µs) are substantially lower than the doublet lifetimes (around 1 to 5 ms), primarily due to Purcell decay induced by the relatively poor coherence of the readout circuitry. However, as the ASQ T_1 times improve in future experiments,

the leakage to the singlet state may become a limiting factor. Sec. 11.3.2 offers insights into potential strategies for addressing this challenge by enhancing doublet lifetimes.

- **Higher-order coupling terms in multiqubit systems**. In the context of multiqubit systems, the qubit-state-dependent inductance of all qubits introduces higher-order coupling terms that reduce the multiqubit gate fidelity as the number of qubits in the system increases. This sets a qubit number limit, $N_{\max}$, which calls for further research in novel approaches to intercouple different unit cells, as introduced in Chapter 10.

In the subsequent sections, we discuss potential follow-up experiments that can offer deeper insights into the physics of superconducting spin qubits. Additionally, we provide suggestions to tackle the challenges presented above.

11.3.1. ORIGIN OF DEPHASING

NUCLEAR SPIN NOISE

The coherence of the Andreev spin qubits presented in this thesis is influenced by several mechanisms. One of these factors is the hyperfine interaction between the qubit spin and the nuclear spins of the In and As atoms within the electron wavefunction (Chekhovich et al., 2013; Cywiński et al., 2009; Khaetskii et al., 2002). This interaction is usually described semi-clasically in terms of an effective background Overhauser magnetic field generated by the nuclei. On the one hand, random flip-flops of the nuclear spins result in non-Markovian low-frequency fluctuations of the Overhauser field generated along the externally applied magnetic field direction. Moreover, the precession of the nuclear spins around the external field direction leads to higher-frequency fluctuations of the Overhauser field, typically in the megahertz range, at narrow frequency bands determined by the relative Larmor precession frequencies of the different nuclei. The longitudinal projection of these fluctuations also couples to the qubit electron spin via the Zeeman effect, ultimately contributing to decoherence.

This mechanism can be distinguished from others based on the dependence of the measured coherence times on various external parameters. A recent numerical simulation in Ref. (Hoffman et al., 2023) explicitly examined the interaction between an Andreev spin qubit and a surrounding bath of nuclear spins. This simulation accounted for the effects of many Overhauser fluctuators and the hyperfine dipole-dipole interactions. The results offer qualitative predictions of the dependence of dephasing on the magnetic field and the external flux. Comparing these predictions to the Ramsey and Hann echo measurements performed in Chapter 8 suggests that interaction with nuclear spins stands as the dominant dephasing mechanism in our case. Furthermore, the flux (in)dependence (see Fig. 8.15) indicates that not only local dipole-dipole interactions, but also long-range dipole-dipole interactions, influence the qubit coherence.

While these initial models provide valuable insights, further experimental research is necessary to distinguish between different sources of dephasing. Potential experimental approaches include the use of refocusing techniques such as CPMG dynamical decoupling to explore the high-frequency noise spectrum (Malinowski et al., 2017b,c). Alternatively, investigations could be directed towards the relationship between deco-

herence and different magnetic field and spin-polarization directions. This may allow to determine whether decoherence is more pronounced along specific spin polarization directions. Finally, it's worth noting that the polarization of nuclear spins with high magnetic fields is anticipated to mitigate the influence of nuclear spins and enhance qubit coherence (Huthmacher et al., 2018; Stockill et al., 2016). While it would likely not constitute the optimal operational field for other reasons, exploring coherence times at higher magnetic fields than those considered in this thesis could yield further insights into the origins of dephasing.

CHARGE NOISE

The presence of spin-orbit interaction (SOI) in the material offers significant advantages for the operation of Andreev spin qubits, introducing several unique features. First, it results in spin-supercurrent coupling without the need for high magnetic fields. This coupling is a fundamental characteristic of ASQs and is harnessed for qubit-qubit interactions and cQED-based readout. Furthermore, when combined with a perpendicular magnetic field component, it provides a means to drive the spin-flip transition via the supercurrent matrix element. Moreover, SOI directly enables the possibility of driving the spin-flip transition through EDSR (Golovach et al., 2006; Nowack et al., 2007).

However, the intrinsic charge-spin coupling resulting from SOI can also be detrimental, as it renders the qubit susceptible to charge noise (Hendrickx et al., 2023; Lawrie, 2022). Charge noise can originate from two-level systems (TLSs) located in the dielectrics and material interfaces surrounding the qubit or can alternatively be introduced through the electrostatic gate lines. In either case, it results in a $1/B$ magnetic field dependence of the charge noise contribution to the dephasing time (Lawrie, 2022). The absence of this $1/B$ dependence in the measurements conducted in Chapter 8 (see Fig. 8.15) corroborates the hypothesis that, at present, charge noise is not the primary factor limiting coherence. However, this could change in future devices once the contribution of the hyperfine mechanism is reduced (see Sec. 11.3.2). Consequently, it is important to further investigate and mitigate the sensitivity to charge noise. In forthcoming experiments, one promising approach to gain deeper insights into this mechanism is to systematically measure qubit coherence at higher magnetic fields and explore its dependence on field direction and strength.

FLUX NOISE

Another noise source that can induce dephasing of the ASQ is magnetic noise coupling to the qubit through flux. Conveniently, the OFF setpoints at zero and half flux constitute sweet spots where the qubit frequency is, to first order, insensitive to flux. However, the flux sensitivity is maximized at the ON setpoint, where the flux is swept to couple two qubits.

At the moment, the absence of a discernible dependence of coherence times over the entire flux range (see Fig. 8.15) suggests that flux noise is not the primary dephasing mechanism. However, it can become a relevant factor in future generations of devices with improved coherence, leading to enhanced decoherence at the operational point during the execution of two-qubit gates. In this scenario, one strategy to mitigate the impact of flux noise is continuous dynamical decoupling during flux pulsing (Viola and Lloyd, 1998). This technique requires only microwave control and has been shown to

improve the decoherence times of fluxonium qubits away from their flux sweet spot (Ma et al., 2023).

It is worth noting that, in the context of gate operation, the noise sensitivity of ASQs to flux noise is conceptually analogous to the sensitivity of traditional semiconducting spin qubits to detuning at the exchange ON operational point. This flux-sensitivity during two-qubit gates is also observed in other flux-sensitive qubits like fluxoniums and flux qubits. For instance, in the case of fluxonium qubits, this sensitivity can lead to reductions in T_2 by approximately an order of magnitude away from the sweet spot (Nguyen et al., 2019). However, ASQs distinguish themselves by having a more favorable sweet spot and reduced sensitivity to flux noise due to the shallower slope of their frequency-versus-flux relationship (Nguyen et al., 2019; Orgiazzi et al., 2016).

QUASIPARTICLE POISONING

An additional effect that can perturb the qubit state is quasiparticle poisoning (QPP). A change in the quasiparticle number within the quantum dot leads to unwanted leakage out of the computational space. As discussed in Chapters 6 and 8, we measured doublet lifetimes on the order of a few milliseconds at gate setpoints near the singlet-doublet transition (i.e. close to the top of the dome).

As the energy decay and the dephasing times are currently limited to microsecond and nanosecond timescales, respectively, quasiparticle poisoning does not currently constitute a limiting factor. However, we anticipate that the values of ASQ T_1 will improve if read out with superconducting circuits with higher coherence than in this thesis. For the experiments presented here, the energy lifetimes were partially Purcell-limited, but the lifetimes of semiconducting spin qubits are typically orders of magnitude longer (see for instance Ref. (Lawrie et al., 2020) for 32 ms T_1 in germanium hole spin qubits).

Hence, it is reasonable to consider that in future generations of superconducting spin qubits, QPP times on the order of milliseconds may emerge as a limiting factor for T_1. Further experiments to investigate this mechanism include probing the QPP rates across a wider range in gate space than previously examined in Chapter 6. Specifically, we anticipate longer doublet lifetimes in regions with lower Γ and, consequently, reduced coupling to the leads. Therefore, we recommend investigating the QPP rates in regions positioned lower within the dome in future experiments.

11.3.2. IMPROVED SUPERCONDUCTING SPIN QUBITS

NUCLEAR SPIN FREE MATERIALS

The Ramsey coherence times of ASQs found in this thesis are of the order of 10 ns. While very short, these times are strikingly similar to those found in early implementations of spin qubits in materials such as InAs (Nadj-Perge et al., 2010), InSb (van den Berg et al., 2013) and GaAs (Koppens et al., 2005, 2008; Petta et al., 2005). A common feature shared by these III-V materials is that they are composed of atoms with a high abundance of magnetic nuclei, as shown in Tab. 11.1. As discussed in Sec. 11.3.1, nuclear spins can lead to decoherence of spin qubits.

These reduced ASQ dephasing times can potentially be extended using strategies that have proven successful for III-V semiconducting spin qubits, even in the presence of a high concentration of nuclear spins. One approach is to use CPMG-based dynamical

Element	Isotopes	I	Natural abundance
In	^{115}In	9/2	95.71 %
	^{113}In	9/2	4.29 %
As	^{75}As	3/2	100.00 %
Ga	^{69}Ga	3/2	60.11 %
	^{71}Ga	3/2	39.89 %
Ge	^{70}Ge	0	20.38 %
	^{72}Ge	0	27.31 %
	^{74}Ge	0	36.72 %
	^{76}Ge	0	7.83 %
	^{73}Ge	9/2	7.76 %
Si	^{28}Si	0	92.2 %
	^{30}Si	0	3.1 %
	^{29}Si	1/2	4.7 %
C	^{12}C	0	99 %
	^{13}C	1/2	1 %

Table 11.1: Natural abundance of isotopes with different nuclear spin number, I, of various elements.

decoupling to selectively filter out the nuclear spin noise. As discussed in Refs. (Malinowski et al., 2017c) and (Bluhm et al., 2011), this method can extend T_2 by orders of magnitude, reaching nearly 1 ms and 0.2 ms, respectively. Given the similarity between In and Ga in terms of the number of spinful isotopes and high nuclear spins (see Tab. 11.1), it would be interesting to explore analogous spectral decoupling techniques in the context of Andreev spin qubits. Another method is to use dynamic nuclear polarization. This technique prevents nuclear–nuclear flip-flops and reduces the randomness in the nuclear field (Bluhm et al., 2010; Foletti et al., 2009). However, as it has been mainly developed for singlet-triplet qubits, an adaptation of the technique would be needed before using it for Andreev spin qubits.

An alternative approach adopted in the semiconducting spin qubit community is to enhance spin qubit coherence not by reducing sensitivity to nuclear spin noise but by eliminating nuclear spins altogether. This can be accomplished by hosting the qubits in materials with a notably reduced presence of nuclear spins, such as silicon (Kawakami et al., 2014; Tyryshkin et al., 2012) and germanium (Hendrickx et al., 2018; Scappucci et al., 2021; Tosato et al., 2023). Note that these materials not only possess a significantly lower total natural abundance of isotopes with a non-zero nuclear spin number, but they also feature a single isotopic species with a non-zero I. Consequently, the Larmor precession of their nuclei does not introduce high-frequency transverse noise that affects the spin qubit coherence.

The success achieved in switching to nuclear-spin-free materials within the area of semiconducting spin qubits motivates future investigation of alternative material platforms for ASQs. Apart from being a nuclear-spin-free semiconductor, the chosen mate-

rial should also be compatible with superconductor proximitization and, ideally[7], should have a sizable spin-orbit interaction. Germanium emerges as a promising candidate that fulfills these characteristics (Hendrickx et al., 2018; Tosato et al., 2023; Valentini et al., 2023). Furthermore, high-quality growth methods for germanium, as demonstrated in recent research (Stehouwer et al., 2023), result in high mobility, reinforcing its suitability for the next generation of Andreev spin qubits. Moreover, recent experiments showing the compatibility of Ge quantum dots with a circuit quantum electrodynamics architecture are encouraging for the implementation of Ge superconducting spin qubits (De Palma et al., 2023; Valentini et al., 2023).

Nevertheless, even in these materials with reduced presence of magnetic nuclei, a small number of nuclei with high spin are typically present. As discussed in Ref. (Lawrie, 2022), these nuclei could become the limiting dephasing mechanism in advanced spin qubits with reduced charge noise in the near future. An approach to further mitigate the impact of nuclear spins is to use isotopically enriched materials with a reduced abundance of the isotopes with non-zero nuclear spins (Itoh and Watanabe, 2014). This approach has demonstrated remarkable success in enhancing the dephasing times of semiconducting spin qubits in silicon by several orders of magnitude (Veldhorst et al., 2014, 2015; Yoneda et al., 2018). Hence, we propose to implement next-generation Andreev spin qubits using isotopically purified germanium, offering a path toward improved qubit performance and reduced sensitivity to nuclear noise.

SUPERCONDUCTING SPIN QUBITS WITHOUT SPIN-ORBIT INTERACTION

An alternative route for implementing Andreev spin qubits involves exploiting the Knight shift effect discussed in Sec. 11.1.3 to mediate the spin-supercurrent coupling (Pavešić et al., 2023b). This approach opens up the possibility of implementing ASQs in alternative materials without spin-orbit interaction, thereby reducing their susceptibility to charge noise. A promising platform are quantum dots defined in isotopically purified graphene (Banszerus et al., 2022; Eich et al., 2018; Güttinger et al., 2010; Itoh and Watanabe, 2014; Kroll et al., 2018; Wang et al., 2019) (see Tab. 11.1). Note that, even in the absence of spin-orbit interaction, some degree of charge noise sensitivity may persist due to the dependence of the qubit frequency on the configuration of electrostatic gates (see Sec. 7.7). In the absence of spin-orbit interaction, the EDSR driving strength vanishes. An alternative in this scenario would be to drive the qubit transition through the supercurrent matrix element.

OPTIMIZING SETPOINTS IN GATE SPACE AND MAGNETIC FIELD

Throughout the experiments performed in this thesis, we have operated the Andreev spin qubits at gate setpoints not far from the singlet-doublet transition, near the top of the dome. To enhance the quasiparticle lifetimes in next-generation ASQs, it would be advantageous to operate them at lower Γ/U and larger U/Δ. In the limit of low Γ/U, however, the supercurrent across the dot is reduced. Similarly, as shown in Fig. 11.6(b), an intermediate Γ/U parameter regime is preferred for maximizing the Knight shift amplitude in ASQ implementations in materials without SOI. Therefore, a balance should

[7] See next subsection for ASQs without spin-orbit interaction.

be found so that the spin-supercurrent coupling is remains sufficiently large for qubit-qubit coupling and readout.

As for the optimal magnetic field setpoint, it depends on whether the chosen material has spin-orbit interaction. For Knight-shift-based implementations (in materials without SOI) high magnetic field is needed to maximize the Knight shift amplitude. In this context, the absence of spin-orbit coupling eliminates challenges derived from enhanced charge noise at elevated magnetic fields.

Conversely, for ASQ implementations in materials featuring SOI, the dephasing rates increase linearly with magnetic field. In such cases, it is beneficial to operate the qubits at low magnetic fields. This technique has been shown to lead to higher coherence times in semiconducting spin qubits (Hendrickx et al., 2023; Lawrie, 2022).

11.3.3. FURTHER MULTIQUBIT EXPERIMENTS

FURTHER EXPERIMENTS WITH THE DEVICE OF CHAPTER 8

Multiqubit experiments that could be performed with the single ASQ device from Chapter 8 include:

- **ASQ-transmon iSWAP gate.** The transverse coupling between the ASQ and the transmon illustrated in Fig. 8.4 opens up the possibility of implementing a two-qubit gate. This can be achieved by pulsing the flux to the anticrossing and allowing the system to evolve for the appropriate duration. The outcome of such an experiment would constitute the first realization of an entangling gate between a superconducting qubit and a semiconducting qubit, complementing previous spectroscopic results (Landig et al., 2019; Scarlino et al., 2019).

- **Ultrastrong coupling regime.** The transversely coupled ASQ-transmon system could be investigated at lower magnetic fields than in Chapter 8. In this parameter regime, the qubit frequencies can become comparable to the coupling strength, leading to the onset of the ultrastrong coupling regime (Forn-Díaz et al., 2010; Forn-Díaz et al., 2017; Forn-Díaz et al., 2019; Frisk Kockum et al., 2019; Niemczyk et al., 2010; Scarlino et al., 2022). Such a regime offers the opportunity to investigate light-matter interaction beyond the rotating wave approximation, when the counter-rotating terms become substantial.

FURTHER EXPERIMENTS WITH THE DEVICE OF CHAPTER 9

Multiqubit experiments that could be performed with the double ASQ device from Chapter 9 include:

- **Explore transverse ASQ-ASQ coupling.** As elaborated on in Sec. 10.7.2, we expect transverse ASQ-ASQ coupling terms to emerge under the application of a perpendicular magnetic field. A potential future experiment is to spectroscopically investigate the strength of this transverse coupling, which would appear as an avoided crossing between the two qubits.

- **ASQ-ASQ CPHASE gate.** As briefly mentioned in Chapter 9, the possibility of switching on and off the longitudinal coupling between two Andreev spin qubits can be

harnessed to implement an entangling two-qubit gate by pulsing the flux. The total Hamiltonian of the coupled system, in the basis $\{|\downarrow_1\downarrow_2\rangle, |\uparrow_1\downarrow_2\rangle, |\downarrow_1\uparrow_2\rangle, |\uparrow_1\uparrow_2\rangle\}$, can be written with respect to the energy of the ground state, as (see Sec. 2.4.2)

$$H = (-\frac{E_1}{2} - \frac{E_2}{2} + \frac{J}{2})\sigma_1^0\sigma_2^0 + \begin{pmatrix} 0 & 0 & 0 & 0 \\ 0 & E_1 - J & 0 & 0 \\ 0 & 0 & E_2 - J & 0 \\ 0 & 0 & 0 & E_1 + E_2 \end{pmatrix}, \tag{11.12}$$

where σ_i^0 represents the identity operator in the subspace of qubit i. If the system is pulsed to the coupled flux setpoint for an amount of time t, it evolves following the unitary operator $U_{ZZ}(t) = e^{iHt}$

$$U_{ZZ}(t) = e^{i\xi_0}\begin{pmatrix} 1 & 0 & 0 & 0 \\ 0 & e^{i\xi_1} & 0 & 0 \\ 0 & 0 & e^{i\xi_2} & 0 \\ 0 & 0 & 0 & e^{i(\xi_1+\xi_2+\phi)} \end{pmatrix} = e^{i\xi_0} Z_1(\xi_1) Z_2(\xi_2) ZZ(\phi), \tag{11.13}$$

where $\xi_i = (E_i - J)t$ and $\phi = Jt$. Up to an inconsequential global phase $\xi_0 = (-\frac{E_1}{2} - \frac{E_2}{2} + \frac{J}{2})t$, this corresponds to two individual qubit rotations around the Z axis, $Z_i(\xi_i)$, and a CPHASE two-qubit gate with phase ϕ, denoted as $ZZ(\phi)$. When $\phi = Jt = \pi$, it corresponds to a controlled-Z gate. The single qubit rotations can be corrected without any time cost using virtual-Z gates (McKay et al., 2017).

- **ASQ-ASQ CNOT gate.** Alternatively, a controlled-NOT (CNOT) gate can be implemented by selectively driving single-qubit transitions of the longitudinally coupled system, as discussed in Refs. (Chuang et al., 1998; Gershenfeld and Chuang, 1997; Linden et al., 1998; Orlando et al., 1999; Plantenberg et al., 2007). As the frequency of one ASQ depends on the state of the other ASQ, conditional rotations can be implemented by selectively driving one of the two split frequencies, with any one of the two qubits serving as control. For instance, a microwave pulse at the frequency of the $|\uparrow_1\downarrow_2\rangle \leftrightarrow |\uparrow_1\uparrow_2\rangle$ transition drives an X rotation of ASQ2 conditional on ASQ1 being in its $|\uparrow_1\rangle$ state. The corresponding unitary operator is

$$U_{|\uparrow_1\downarrow_2\rangle\leftrightarrow|\uparrow_1\uparrow_2\rangle}(t) = \begin{pmatrix} 1 & 0 & 0 & 0 \\ 0 & 1 & 0 & 0 \\ 0 & 0 & \cos(\omega t/2) & i\sin(\omega t/2) \\ 0 & 0 & i\sin(\omega t/2) & \cos(\omega t/2) \end{pmatrix}, \tag{11.14}$$

where t represents the pulse duration and ω the Rabi frequency. This unitary implements a CNOT gate if $\omega t = \pi$, up to a single qubit Z rotation in the control qubit, which can be canceled out with a virtual-Z gate (McKay et al., 2017). The execution time for this controlled-NOT operation is determined by the minimum between the coupling strength and the single-qubit Rabi frequency.

Note, however, that this protocol is performed under the constant presence of an always-on longitudinal coupling, resulting in the simultaneous application of the

controlled-Z unitary described above. Consequently, this protocol is not practical for more complex quantum algorithms. However, this experiment is still interesting as a simple proof of principle of an entangling two-qubit gate between Andreev spin qubits. In particular, this conditional gate can be used to generate a maximally entangled Bell state that requires just two microwave pulses applied to the ground state. First, a single-qubit rotation transforms $|\downarrow_1\downarrow_2\rangle$ into the superposition state $|\psi\rangle = \frac{1}{\sqrt{2}}(|\downarrow_1\rangle + |\uparrow_1\rangle)|\downarrow_2\rangle$. Then, the conditional rotation pulse results into $U_{\text{CNOT}}|\psi\rangle = \frac{1}{\sqrt{2}}(|\downarrow_1\downarrow_2\rangle + |\uparrow_1\uparrow_2\rangle)$, which is a Bell state of two distant spins.

- **Transmon-mediated ASQ-ASQ gate.** Alternative remote spin-spin coupling experiments mediated by virtual resonator photons (Harvey-Collard et al., 2022) can inspire yet a third type of gate between Andreev spin qubits. In the double-ASQ device from Chapter 9, both ASQs are transversely coupled to the transmon qubit if a perpendicular magnetic field component is present. This system could be exploited to implement two-qubit gates between distant ASQs without the need for flux pulsing, by mediating the coupling via virtual transmon excitations.

- **Supercurrent-mediated coupling between distant spin and charge qubits.** By configuring any of the two SQDS junctions in the device from Chapter 9 to be in a singlet ground state, an Andreev level qubit (ALQ) can be formed (Janvier et al., 2015; Zazunov et al., 2003, 2005). In an ALQ, the qubit is encoded within the subspace of the two singlet states. We propose using the same supercurrent-mediated architecture to couple not only distant spin degrees of freedom but also distant charge degrees of freedom. Two configurations leading to ASQ-ALQ and ALQ-ALQ couplings, respectively, are illustrated in Fig. 11.9(a) and (b). Note that, in these cases, non-diagonal terms of the ALQ current operator in the qubit basis introduce both longitudinal and transverse qubit-qubit coupling terms, even in the absence of perpendicular field components (Zazunov et al., 2003, 2005).

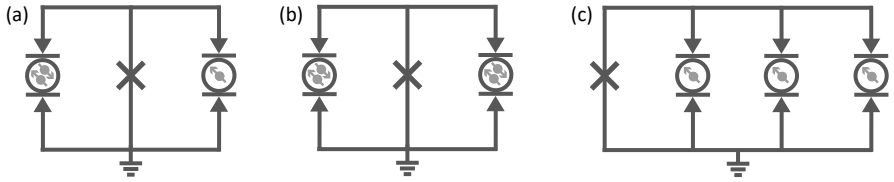

Figure 11.9: **Other supercurrent-mediated coupling experiments between Andreev level or spin qubits.** (a) Coupling between an Andreev level qubit (ALQ) and an Andreev spin qubit (ASQ). (b) Coupling between two ALQs. (c) Minimal test device for the selective coupling architecture presented in Chapter 10, for $N = 3$.

- **Multiqubit experiments with N > 2.** While requiring modifications to the device configuration from Chapter 9, we finally suggest experimentally implementing the system presented in Fig. 11.9(c), with $N = 3$ ASQs. This experiment would serve as a test of the scalability approach presented in Chapter 10.

A

ENERGY UNITS CONVERSION CHEAT SHEET

Throughout this thesis, we predominantly express frequencies, f, in units of GHz. Similarly, energies are most often given in terms of their corresponding frequency using the conversion $E = hf$, where h is the Planck constant. However, in DC transport experiments, energy scales are typically depicted in units of meV. Likewise, Josephson junctions are frequently characterized by their critical current I_c, rather than by their Josephson energy E_J. To facilitate easier data interpretation for researchers more userd to different units, this appendix provides quick conversion values for the temperature, inductance, supercurrent, and capacitance corresponding to 1 GHz (refer to Fig. A.1).

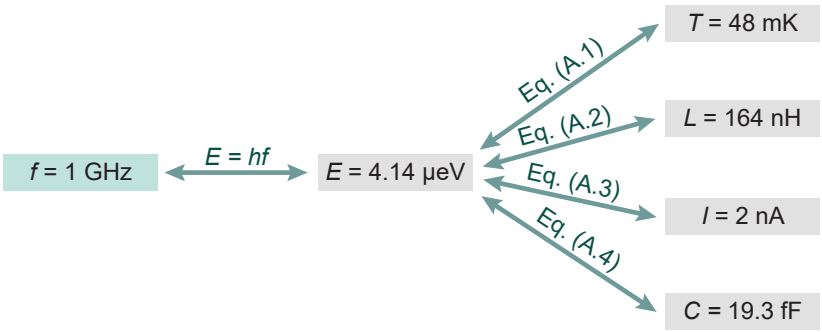

Figure A.1: **Energy units conversion.**

To perform the unit conversions, we employ the relations shown below. These depict the correspondence between thermal (E_T), inductive (E_L), Josephson (E_J), and charging (E_c) energies with respect to temperature (T), inductance (L), critical current (I_c), and capacitance (C), respectively.

$$E_T = K_\mathrm{B}\,T, \quad \text{(A.1)} \qquad E_L = \frac{\Phi_0^2}{4\pi^2 L}, \quad \text{(A.2)} \qquad E_\mathrm{J} = \frac{\Phi_0}{2\pi} I_\mathrm{c}, \quad \text{(A.3)} \qquad E_\mathrm{c} = \frac{e^2}{2C}. \quad \text{(A.4)}$$

In the equations above, K_B is Boltzmann's constant, Φ_0 denotes the superconducting magnetic flux quantum, and e represents the absolute value of the electron charge.

B

TIME EVOLUTION OF NBTIN DEPOSITION PARAMETERS

In this appendix we report on the monitoring of different standard recipes performed on the AJA International ATC 1800 sputtering system, nicknamed SuperAJA, of the Kavli Nnolab Delft. We focus on the properties and deposition conditions of a NbTiN film obtained by sputtering on a 70/30 NbTi target with a purity of 99.99 % under a nitrogen atmosphere. The film is obtained using the following standard sputtering recipe:

- Main chamber pressure before loading: 1×10^{-9} Torr to 1×10^{-8} Torr.
- Load lock pressure before loading: below 1×10^{-6} Torr.
- Argon flow: 50 sccm.
- Nitrogen gas flow: 3.5 sccm.
- Power applied to the NbTi target: 250 W.
- Pressure in the chamber during deposition: 2.3 mTorr.
- Wafer holder rotating during sputtering.
- Target thickness: 100 nm

This recipe was developed to optimize the film properties. As discussed in Iossad (2002), high process pressures result in films with high resistivity, reduced critical temperature and no stress, resulting from the low mobility of the adatoms during deposition. Too low process pressures instead lead to the formation of crystalline grains separated by argon-filled grain boundaries. This in turn results in elevated compressive stress and, again, in reduced critical temperature. The intermediate process pressure

The monitoring data reported in this appendix was collected by: Chung-Kai Yang, Chung Ting Ke, Marta Pita-Vidal and Ivan Kulesh.

of, in our case, 2.3 mTorr, results in the formation of columnar grains with little defects in between, which leads to optimum critical temperature and to a moderate degree of compressive stress, thus facilitating liftoff. Similarly, we use an intermediate nitrogen flow that maximizes the critical temperature of the resulting film for nearly depleted targets Iossad (2002). Note, however, that, while the nitrogen flow is fixed throughout this thesis, its optimum value varies over time as the target becomes depleted, with the optimum nitrogen flow for a new target being approximately twice that of an almost depleted target (Iossad, 2002).

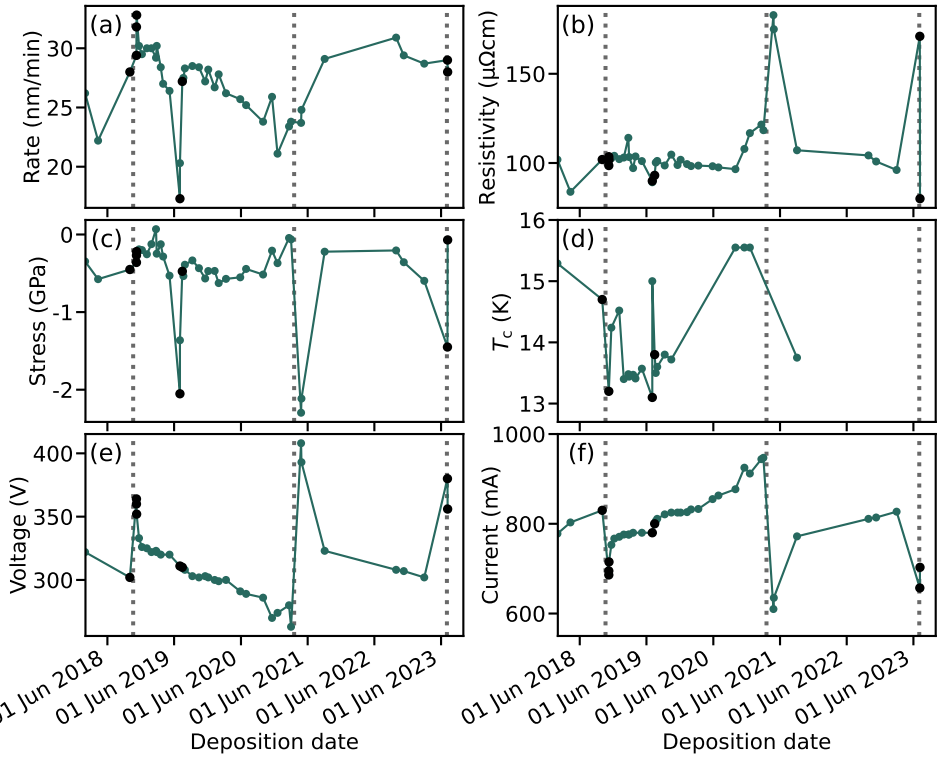

Figure B.1: **Monitoring of NbTiN sputtering parameters.** (a) Deposition rate, (b) room temperature resistivity of the film, (c) film stress, (d) critical temperature, (e) voltage and (f) current readings on the DC source during sputtering. Dark teal markers indicate depositions for which the final thickness was between 80 nm and 120 nm, while black markers indicate depositions for which the final thickness was outside of this range. The continuous lines are guides for the eye connecting adjacent markers. The dotted lines indicate NbTi target changes.

The monitoring results, obtained in the period 2018 - 2023 for three different NbTi targets, are shown in Fig. B.1, where the target change times are indicated with vertical lines. Between target changes, most deposition parameters drift over time as the target is consumed, as expected. Right after a target change, we find abrupt changes for most monitored parameters that go back to their standard ranges after the target has been conditioned by a total deposition time of the order of a few hours. Such stabilization after

intensive sputtering is associated with the formation of a so-called "race-track" erosion profile on the NbTi target.

For each deposition, we determine the **deposition rate** by measuring the film thickness with a Bruker Dektak XT profilometer at five nearby points around the center of the wafer. We find that the deposition rate ranges from 20 to 30 nm/min and shows a descending trend between target changes (Fig. B.1(a)). For all depositions, we target a film thickness of 100 nm by updating the total sputtering time based on the previously determined rate. The deposition rounds for which the final thickness deviated highly from this target are indicated with black markers in Fig. B.1.

The film **resistivity**, ρ, at room temperature is determined using a Lucas Labs / Signatone Pro4, as shown in Fig. C.1(c) in appendix C. As shown in Fig. B.1(b), we find that the resistivity stays constant at around 100 µΩcm, showing only desviations from this value before and after a target change. A raise in film resistivity can thus be used as a signature of the NbTi target being nearly consumed.

We determine the film **stress** using a Flexus Toho FLX-2320 stress meter. In general, a compressive (negative) stress of less than approximately -100 MPa is desired to facilitate liftoff. We find values between -200 and -800 MPa that don't show a strong correlation with the deposition date, as shown in Fig. B.1(c). Right after a target change we however observe an abrupt increase in the film stress magnitude before it is stabilized again after the target has been conditioned.

The film **critical temperature** was determined only for some of the films by dicing a rectangular piece of wafer and measuring its four-probe resistance versus temperature, both while ramping the temperature downwards and upwards. The reported T_c value is the average between the two measurements.

Finally, we also monitor the **voltage**, V, and **current**, I, readings on the DC source to attain a power $P = IV = 250\,\mathrm{W}$ during sputtering, as they are a useful measure for detecting when a new NbTi target change is needed. As shown in Fig. B.1(e) and (f), the source voltage and current smoothly decrease and increase, respectively, as the NbTi target is consumed, signaling the need for a target change when the deposition current reaches a threshold.

Although with less frequency, we also monitored the argon etch rate at the same instrument, as we use it for all of our devices to mill the aluminium oxide on the nanowire shell before contact deposition. We monitor the etching rate of silicon oxide with the following recipe:

- Power: 100 W.
- Argon flow: 50 sccm.
- Pressure: 3 mTorr.
- Total etch time: 600 s.

The etch rate over time is shown in Fig. B.2.

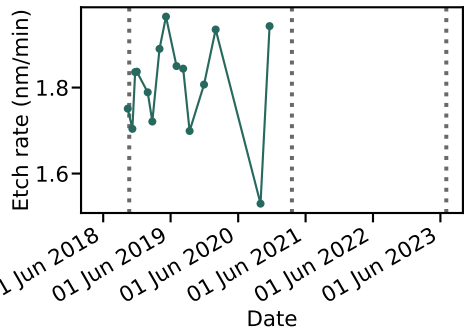

Figure B.2: **Monitoring of Ar milling etch rate.**

C

KINETIC INDUCTANCE MEASUREMENTS ON NBTIN FILMS

Throughout the years 2018 - 2023, we characterized multiple NbTiN thin films of varying thicknesses, all deposited using the sputtering recipe detailed in Appendix B. Here, we present a summary of various film parameters extracted from our measurements: the measured critical temperature T_c, the measured room temperature sheet resistance R_s, the kinetic inductance estimated from the previous two quantities L_k^{est} (Annunziata et al., 2010) and the kinetic inductance extracted from measurements of resonator devices at cryogenic temperatures L_k^{meas}. These values are shown in Tab. C.1 for different film thicknesses, t.

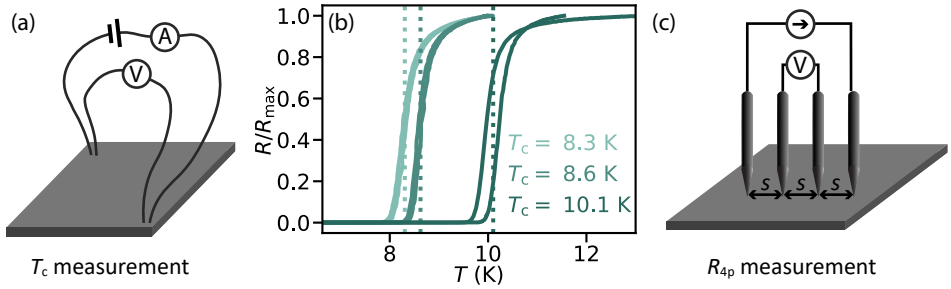

Figure C.1: **Thin film characterization.** (a) Four-probe measurement of the resistance of a NbTiN film, used to determine the critical temperature, T_c. The voltmeter and amperemeter independently determine the voltage drop, V, and current, I, through the film. Each of them is connected to two corners of a small chip. (b) Resistance of various NbTiN films as a function of temperature, T. Different colors correspond, from lighter to darker, to thicknesses t = 11 nm, 11 nm and 20 nm. For each thickness, two measurements are shown. The first, taken while ramping T from higher to lower values, underestimates the extracted T_c. The second, taken while varying T from lower to higher values, overestimates T_c. The value of T_c indicated as a vertical dotted line, as well as in the label, is the average of the two measurements. (c) Four-point probe sheet resistance measurement, performed with four aligned and equidistant probes, separated by s = 1.016 mm. The probes are placed on the center of a small chip or on different positions of a 4-inch wafer.

To determine the critical temperature of a film, we measure its resistance as a function of temperature. For most samples, we employed a four-probe configuration to determine the sample resistance, as shown for three different films in Fig. C.1(a). This configuration ensures that the current and voltage electrodes are connected separately, thus eliminating the lead and contact resistances from the measurement. Measurements of contact resistance while ramping the temperature downwards or upwards, respectively underestimate and overestimate T_c (Fig. C.1(b)). Therefore, the values reported in Tab.C.1 represent the average of the results of these two measurements. The measurements shown in Fig. C.1(b) were performed using a cryogenic insert system (nicknamed the Gecko) for the t =11 nm-thick films and an *Oxford Instruments Heliox* insert for the t =20 nm-thick film.

To determine the sheet resistance R_s, we use a *Lucas Labs* / *Signatone Pro4* manual sheet resistivity measurement system. This system utilizes the four-point probe technique (or Kelvin technique) (Kikken, 2018; Topsøe, 1966), as illustrated in Fig. C.1(c). The technique involves using four aligned and equidistant probes with spacing $s = 1.016$ mm between them. The outer two probes are used to source a DC current, I, while the inner two probes measure the DC voltage drop, V, to determine the four-probe resistance R_{4p}. For $t \ll s$ and chip size much greater than s, the sheet resistance calculation simplifies to

$$R_s = \frac{\pi}{\ln(2)} R_{4p}. \tag{C.1}$$

Note that in Tab. C.1 we report the sheet resistance determined from Eq. C.1, without including geometric correction factors to account for the exact geometry of the chips. As some of the measured samples had square shapes with sizes of order 1 to 2 cm, this could result in inaccuracies of up to 5 % on the reported R_s values (Topsøe, 1966).

The film kinetic inductance originates from the inertial mass of the charge carriers. As discussed in Ref. (Annunziata et al., 2010), at low-temperature it can be estimated from the critical temperature, T_c, and the sheet resistance at room temperature, R_s. For $T \ll T_c$ we can estimate L_k as

$$L_k^{\text{est}}(T \ll T_c) = \frac{R_s h}{2\pi^2 1.76 K_B T_c}, \tag{C.2}$$

where h and K_B denote Planck's and Boltzmann's constants, respectively.

Thinner films exhibit lower T_c and higher R_s, resulting in larger kinetic inductances. For low thicknesses, t, the kinetic inductance strongly depends on t and, therefore, also on the deposition time. As this time is manually controlled, and the deposition rate is approximately 0.5 nm/s (see Appendix B), differences of around 1 s can have an impact on L_k of tens of pH/□, explaining the non-monotonic behavior of the reported values at low t.

Deposition date	t (nm)	T_c (K)	R_s (Ω/□)	L_k^{est}(pH/□)	L_k^{meas}(pH/□)	Used in
AUG-2018	7	7.2	348	67		
OCT-2018	9	7.6	199	36	41	Chapter 5
JAN-2020	9	n.m.	200 - 270	35 - 55	n.m.	
MAR-2020	10	n.m.	158 - 208	28 - 35	42-45	
AUG-2018	11	8.3-8.5	153	25		
FEB-2020	20	n.m.	n.m.	n.m.	15	Chapter 6
APR-2021	20	n.m.	n.m.	n.m.	11.8	Chapters 7 and 8, Chapter 4 Sec. 4.2 and 4.1 and Ref. (Feldstein i Bofill, 2022)
MAY-2021	20	n.m.	57-69	7 - 10	14.8	Ref. (Bargerbos et al., 2023) and Chapter 4 Sec. 4.1
FEB-2022	20	n.m.	59 - 75	9 - 11.5	n.m.	
AUG-2021	20	n.m.	n.m.	n.m.	7.6	Ref. (Rot, 2022; Wesdorp and *et al.*, 2023b)
2020	22	10.6	87	11.3	14.5	Ref. (Wesdorp et al., 2022; Wesdorp et al., 2023)
MAR-2018	22	10.1	66	9.7		
AUG-2021	40	n.m.	27 - 37	3.8 - 5.0	5.31	Ref. (Splitthoff et al., 2022)
2020-2023	100	13.5 - 13.7	9.5 - 10.5	~1	n.m.	

Table C.1: Measured and estimated properties of NbTiN films with different thicknesses at the center of the wafer, t, determined from the deposition rate and the deposition time. T_c denotes the measured critical temperature, R_s denotes the measured sheet resistance at room temperature, L_k^{est} denotes the kinetic inductance estimated using Eq. C.2 and L_k^{meas} is the kinetic inductance value extracted from measurements of resonators. n.m. means not measured. When we give a range for R_s it is due to the value varying across a 4-inch wafer. The lowest sheet resistance value corresponds to the center of the wafer and the highest to ~1 cm away from the wafer edge.

D

NANOFABRICATION RECIPES

Some of you may use this book solely for the recipes, and there is nothing wrong with that. I'll still like you. I've done my best to write them as clearly and concisely as possible, and I guarantee each and every one of them will work as advertised (provided you follow the instructions). If they don't work for you, I want to hear about it!

J. Kenji López-Alt

In this appendix, we present a comprehensive nanofabrication recipe employed for the fabrication of the devices discussed in this thesis. Unless otherwise specified, all fabrication steps were carried out at the Kavli Nanolab of Delft University of Technology. It is important to note that certain details may vary depending on the specific sample, as indicated.

We begin in Sec. D.1 by providing a description of the substrate preparation process. Subsequently, in Sec. D.2, we outline the steps conducted prior to nanowire deposition, including the patterning of the superconducting circuitry in the base layer and the definition of the gate dielectric. The nanofabrication steps related to the nanowire are elaborated in Sec. D.3, encompassing the processes of growth, deposition, junction etching, and contacting. Finally, in Sec. D.4, we describe the final preparation steps required for the devices to be measured. This includes dicing the devices into smaller pieces suitable for mounting on the printed circuit board (PCB), as well as the process of wirebonding them to the PCB.

D.1. WAFER PREPARATION

D.1.1. GLOBAL SUBSTRATE DIELECTRIC DEPOSITION

1. We use high resistivity silicon wafers with a diameter of 4 inches provided by Topsil, with the following specifications:

    - Material: High-purity silicon with N-type dopants.

- Orientation: (1-0-0) ±0.5.
- Resistivity: Greater than 1×10^4 Ωcm.
- Thickness: (525 ± 10) µm.
- Front side finishing: Polished.

2. A batch of 25 wafers is simultaneously processed at the Else Kooi lab of the TU Delft, as follows:

   (a) Hydrofluoric acid (HF) 0.55 % cleaning step to remove native oxide on silicon.

   (b) Deposition of (100 ± 1) nm-thick low-pressure (about 250 MPa) chemical vapor deposited (LPCVD) silicon nitride.

3. All wafers are subsequently sealed in a wafer box and stored in a cleanroom environment until further use.

D.1.2. WAFER CLEANING

Individual 4-inch wafers undergo the following cleaning process:

1. The wafer is submerged in fuming nitric acid (HNO_3) and sonicated at maximum power for 5 min.

2. The wafer is rinsed by submerging it in deionized water (DI H_2O) for 5 s to remove HNO_3 residues.

3. The previous step is repeated a second time.

4. The wafer is finally dried using a wafer spinner.

D.1.3. NBTIN DEPOSITION

1. Immediately after cleaning, NbTiN is sputtered on the entire 4-inch wafer using an AJA International ATC 1800 sputtering system. The deposition is carried out under the conditions and with the recipe specified in Appendix B, but with varying final thickness.

2. The pre-sputtering time (with the shutter closed) is always set to 2 min.

3. The deposition time is determined based on the desired target thickness and the latest measured deposition rate (see Appendix B).

4. The room temperature resistivity of the wafer is determined by multiple four-probe measurements at different distances from the wafer center. The measurements are performed with a Lucas Labs / Signatone Pro4 Resistivity System. The measured values are used to estimate the kinetic inductance at different parts of the wafer (see Appendix C). The kinetic inductance is always found to be larger closer to the wafer edges than at the center.

D.1.4. EBEAM ALIGNMENT MARKERS DEPOSITION

The exact recipe varies for the different chapters depending on the material used, as indicated.

1. We first apply positive e-beam resist, as follows:
   (a) Spin resist MMA8.5 = EL 8% (from MicroChem) at 4000 rpm. Expected thickness 220 nm.
   (b) Bake the resist for 2 minutes at 185 °C.
   (c) Allow the chip to cool down for 2 minutes.
   (d) Spin resist PMMA 950 A4 (from MicroChem) at 4000 rpm. Expected thickness 210 nm.
   (e) Bake the resist for 5 minutes at 185 °C.
2. Markers of size $20 \times 20 \mu m^2$ are patterned using a Raith EBPG-5200 e-beam with the following specifications:
   - Acceleration voltage: 100 kV
   - Dose: $1400\,\mu C cm^{-2}$.
   - Beam current: around 100 nA.
   - Beam spot size: around 50 nm.
3. The resist is developed as follows:
   (a) Submerge the wafer in a solution of MIBK:IPA 1:1 at room temperature for 1 min 50 s.
   (b) Submerge the wafer in IPA at room temperature for 30 s.
   (c) Dry the wafer with nitrogen.
4. This is followed by a descum step under oxygen plasma at a PVA Tepla 300 system.
   - Power: 100 W.
   - Oxigen gas flow: 200 ml/min.
   - Time: 1 min.
   - A Faraday grid is used.
5. For Chapter 5, Ti/Au markers are evaporated using a Temescal evaporator, as follows:
   (a) Deposit 7 nm of Ti at a rate of 0.5 Å/s while rotating the holder at 10 rpm.
   (b) Deposit 83 nm of Au at a rate of 2 Å/s while rotating the holder at 10 rpm.
6. For device A in Chapter 6, Ti/Pt markers are evaporated using a Temescal evaporator(see discussion around Fig. 3.9), as follows:
   (a) Deposit 5 nm of Ti at a rate of 0.5 Å/s while rotating the holder at 10 rpm.

(b) Deposit 15 nm of Pt at a rate of 1 Å/s while rotating the holder at 10 rpm.

(c) Wait 20 min for substrate cooldown.

(d) Deposit 15 nm of Pt at a rate of 1 Å/s while rotating the holder at 10 rpm.

(e) Wait 20 min for substrate cooldown.

(f) Deposit 25 nm of Pt at a rate of 1 Å/s while rotating the holder at 10 rpm.

7. For device B in Chapter 6 and for Chapters 7, 8 and 9, Ti/Pd markers are evaporated using an AJA International evaporator, as follows:

(a) Deposit 10 nm of Ti at a rate of 0.5 Å/s while rotating the holder at 10 rpm.

(b) Deposit 80 nm of Pd at a rate of 1 Å/s while rotating the holder at 10 rpm.

8. Finally, the markers are lifted off using the following steps:

(a) Submerge the wafer in acetone at 50 °C for 3 h.

(b) Sonicate the wafer at medium power for 5 min.

(c) Submerge the wafer in IPA at room temperature for 30 s.

(d) Dry the wafer with nitrogen.

D.1.5. DICING

1. We apply a protective dicing resist as follows:

(a) Spin resist AZ9260 at 1500 rpm for 1 min. Expected thickness 14 µm.

(b) Bake the resist for 2 minutes at 110 °C.

2. The wafer is then diced into small individual chips with approximate dimensions of 1.05×0.85 cm^2 (for Chapter 5) or 1.5×1.5 cm^2 (for all other experimental chapters) using a DAD3220 dicer from Disco Hi-Tec Europe GMbH. The dicing details are as follows:

- Blade type: NBC ZB 1050.
- Blade height: 50 µm for a foil height of 70 µm, resulting in a 20 µm cut into the foil.
- Spindle revollutions: 30 000 rpm.
- Feed speed: 1.0 for Chapter 5 and for device A in Chapter 6, 2.0 for all other experimetal chapters.
- ESD reducing cooling liquid: DI H_2O with CO_2 bubbler.
- Without waiting until any particular water resistivity is reached.

3. The dicer resist is left on the chip until it is used for device fabrication.

D.2. SUBSTRATE PREPARATION PRE-NANOWIRE

D.2.1. SUPERCONDUCTING CIRCUITRY ETCHING

The initial nanofabrication step for each chip involves patterning the superconducting circuit elements on the base layer. This process is carried out as follows:

1. Before processing a chip, the first step is to strip the dicing resist, as follows:
   (a) Submerge the chip in acetone at 50 °C for 2 h with a magnetic stirrer.
   (b) Submerge the chip in PRS-3000 at 80 °C while sonicating at maximum power for around 10 min.
   (c) Submerge the chip in DI H_2O at room temperature for 10 s.
   (d) Submerge the chip in DI H_2O at room temperature for 30 s.
   (e) Submerge the chip in IPA at room temperature for 10 s.
   (f) Dry the chip with nitrogen.
2. Then, positive e-beam resist is applied as follows:
   (a) For Chapter 5 and for device A in Chapter 6: Spin resist CSAR (AR-P) 6200.09 at 4000 rpm for 1 min. Expected thickness 200 nm.
   (b) For device B in Chapter 6 and for all subsequent experimental chapters: Spin resist CSAR (AR-P) 6200.04 at 2000 rpm for 1 min. Expected thickness 110 nm.
   (c) Bake the resist at 185 °C for 5 to 10 minutes depending on the device.
3. All superconducting structures are patterned at the e-beam (Raith EBPG-5200) with the following specifications:
   - Acceleration voltage: 100 kV
   - Doses: from 180 to 270 μCcm^{-2} for the finer beam layers and from 450 to 500 μCcm^{-2} for the coarse and medium holes layers.
   - Beam current: around 1000 pA for the fine layers and around 200 nA for the coarser layers.
   - Beam spot size: ranging from around 20 nm for the finer layers to 200 nm for the coarser layers.
4. The resist is developed as follows:
   (a) Submerge the chip in pentylacetate at room temperature for 1 min.
   (b) Submerge the chip in a solution of MIBK:IPA 1:3 at room temperature for 1 min 50 s.
   (c) Submerge the chip in IPA for 30 s.
   (d) Dry the chip with nitrogen (except for Chapter 6).
5. Only for Chapter 6, we finish the development with a critical point drying (CPD) step to more carefully develop fine features like the narrow electrostatic gates. This is done using a Leica CPD.

6. Reactive ion etching of the NbTiN layer:
    - For Chapter 5, we use a Laybold Heraeus etcher (nicknamed "old F1"). Etching details:
        - Pressure: 8 µbar.
        - SF_6 flow: 13.75 sccm.
        - O_2 flow: 4 sccm.
        - RF power: 64 W.
        - Pre-conditioning time: 5 min.
        - Total etch time: 30 s.
        - NbTiN etch rate: 0.45 nm/s.
    - For device A in Chapter 6, we use a different Laybold Heraeus etcher (nicknamed "F3"). Etching details:
        - Pressure: 6 µbar.
        - SF_6 flow: 13.75 sccm.
        - O_2 flow: 4 sccm.
        - RF power: 50 W.
        - Pre-conditioning time: 5 min.
        - Total etch time: 50 s.
        - NbTiN etch rate: 0.65 nm/s.
        - CSAR resist etch rate: 1.85 nm/s.
        - SiN etch rate: 4.0 nm/s.
    - For device B in Chapter 6 and for Chapters 7, 8 and 9, we use a Sentech Etchlab 200 etcher (nicknamed "new F1"). Etching details:
        - Pressure: 8 µbar.
        - SF_6 flow: 13.5 sccm.
        - O_2 flow: 3.5 sccm.
        - RF power: 50 W.
        - Pre-conditioning time: 5 min.
        - Total etch time: 47 s.
        - NbTiN etch rate: ~ 0.70 nm/s.
        - CSAR resist etch rate: ~ 1.5 nm/s.
7. The resist is stripped as follows:
    (a) Submerge the chip in PRS-3000 at 80 °C for 2 h to 4 h, depending on the device, with a magnetic stirrer.
    (b) Submerge the chip in DI H_2O at room temperature for 10 s.
    (c) Submerge the chip in DI H_2O at room temperature for 10 s.
    (d) Submerge the chip in IPA at room temperature for 30 s.

(e) Dry the chip with nitrogen.

8. Finally, we perform scanning electron microscope (SEM) inspection of selected features (using a FEI NovaNano, a Hitachi S4800 or a Hitachi Regulus 8230 depending on the device).

   (a) For Chapter 5, we occasionally perform SEM imaging of the fluxonium superinductor to ensure its connectivity and measure its width.

   (b) For Chapters 6, 7, 8 and 9, we perform SEM imaging of all gate lines to measure their widths and spacings and detect any potential shorts or disconnections.

   (c) Acceleration voltages used for imaging range from 1.5 to 5 kV.

   (d) Emission current ~ 10μA.

D.2.2. GATE DIELECTRIC

In this step, we deposit the dielectric that sits in between the bottom electrostatic gates and the nanowire for all devices. In the next step, we also fabricate other pieces of dielectric, like the capacitor dielectric for the fluxonium parallel-plate capacitor in Chapter 5, the gate jumps over the superinductive loop in the same chapter, the dielectric for the capacitive parts of the gate-line filters in Chapters 6, 7, 8 and 9 or for the jump forming the twisted loop in Chapter 9.

1. Plasma enhanced chemical vapor deposition (PECVD) of Si_3N_4 is performed using a Plasmalab 80 Plus instrument from Oxford Instruments Plasma Technology, under the following conditions:

   - Table heater: 300 °C.
   - Pressure: 650 mbar.
   - LF power: forward 20 W, pulsed time 8 W.
   - RF power: forward 20 W, pulsed time 12 W.
   - SiH_4 flow: 20 sccm.
   - NH_3 flow: 20 sccm.
   - N_2 flow: 980 sccm
   - We add, next to the sample, a silicon witness chip of around 2×2 cm^2.
   - Expected deposition rate: it is calculated from the result of previous deposition, but it is typically around 0.20 nm/s.
   - Target thickness: 28 nm.

2. The resulting dielectric thickness is sometimes monitored under a Woollam M-2000 (XI-210) ellipsometer.

3. Then, negative e-beam resist is applied as follows:

   (a) Spin primer AR200-80 at 4000 rpm for 1 min.

(b) Bake resist at 190 °C for 2 minutes.

(c) Let the chip cool down for a couple of minutes.

(d) Spin resist AR N 7500-18 at 4000 rpm for 1 min.

(e) Bake resist at 95 °C for 3 minutes.

4. The dielectric structures are then patterned at the e-beam (Raith EBPG-5200) with the following specifications:

   - Acceleration voltage: 100 kV
   - Doses: from 900 μCcm^{-2} to 1000 μCcm^{-2}.
   - Beam current: around 400 pA for the bottom gate dielectric and other fine regions and around 200 nA for the gate-line overjump dielectric and other coarse layers.
   - Beam spot size: around 20 nm for the bottom gate dielectric and other fine regions and around 100 nm for the gate-line overjump dielectric and other coarse layers.

5. The resist is developed as follows:

   (a) Submerge in AS300-47 at room temperature for 2 min.

   (b) Submerge in DI H_2O for 1 min.

   (c) Dry with nitrogen.

6. The resist is post-baked under the following conditions:

   - For Chapter 5 and for device A in Chapter 6: at 140 °C for 2 min.
   - For device B in Chapter 6 and for Chapters 7 and 8: at 110 °C for 1 min.
   - For Chapter 9: at 100 °C for 1 min.

7. The PECVD silicon nitride is then wet etched as follows:

   (a) Submerge in J. T. Bakker 20:1 buffered oxide etchant (BOE) with surfactant for 3 min. Wear protective gear as it contains HF.

   (b) Submerge in DI H_2O for 5 s.

   (c) Submerge in DI H_2O for 10 s.

   (d) Dry with nitrogen.

8. Finally, the remaining resist is stripped as follows:

   (a) Submerge in AR600-71 at room temperature, with a magnetic stirrer, for 1 h.

   (b) Submerge in DI H_2O at room temperature for 1 min.

   (c) Submerge in IPA at room temperature for 30 s.

   (d) Dry with nitrogen.

D.2.3. THICK NBTIN DEPOSITION

This step is only followed for the devices presented in Chapter 5 but not for any of the devices presented in other Chapters.

1. We first apply positive e-beam resist, as follows:
   (a) Spin resist PMMA 495 A6 (from MicroChem) at 4000 rpm. Expected thickness 300 nm.
   (b) Bake resist for 5 minutes at 185 °C.
   (c) Let the chip cool down for about 2 min.
   (d) Spin resist PMMA 950 A3 (from MicroChem) at 4000 rpm. Expected thickness 100 nm.
   (e) Bake resist for 10 minutes at 185 °C.
2. The thick NbTiN structures (the feedline, the flux lines (not used), part of the gate lines, the top capacitor pads and the bonding pads) are patterned using a Raith EBPG-5200 e-beam with the following specifications:
   - Acceleration voltage: 100 kV
   - Doses: 1800 μCcm^{-2}.
   - Beam current: around 1000 pA for the fine structures (capacitor pad and gates overjump) and around 300 nA for the coarser structures.
   - Beam spot size: around 20 nm for the fine structures and around 120 nm for the coarse structures.
3. The resist is developed as follows:
   (a) Submerge in a solution of MIBK:IPA 3:1 at room temperature for 1 min.
   (b) Submerge in IPA at room temperature for 30 s.
   (c) Dry with nitrogen.
4. NbTiN is sputtered using an AJA International ATC 1800 sputtering system, under the conditions and with the recipe specified in Appendix B, but now targetting a thickness of 55 nm.
5. Then, lift-off is performed as follows:
   (a) Submerge in acetone at 50 °C for 1 h.
   (b) Sonicate at high power for 5 min.
   (c) Blow nitrogen through a plastic pipette to facilitate the lift-off process.
   (d) Submerge in IPA at room temperature for 30 s.
   (e) Dry with nitrogen.
6. The final step before the nanowire deposition is the general inspection of the chip to make sure its quality is good enough to proceed to the next steps. This involves the following steps:

(a) Optical inspection of the feedline, flux lines, gate lines including filters and all other structures to detect potential shorts to the ground plane.

(b) Probe all lines at a probe station and make sure they are not shorted, neither to ground nor to each other.

(c) For the devices without an input capacitor, probe the feedline resistance to get a second estimate of the film's kinetic inductance.

7. For some of the devices (Chapters 5 and 6) we perform a descum step of the chip prior to nanowire deposition. This is done under oxygen plasma at a PVA Tepla 300.

   - Power: 200 W.
   - Oxigen gas flow: 200 mL/min.
   - Time: 10 min.
   - With Faraday grid.

D.3. INCORPORATION OF THE NANOWIRE

D.3.1. NANOWIRE GROWTH

The Al-proximitized InAs nanowires used in this thesis were grown by our collaborator Yu Liu at the University of Copenhagen. The nanowires are grown by the vapor-liqud-solid (VLS) method in a molecular beam epitaxy (MBE) machine and have hexagonal cross-section. The aluminium shell (6 nm-thick) is deposited on two of the nanowire facets right after growth without breaking the vacuum. For further details of the nanowire growth, we refer you to Ref. (Krogstrup et al., 2015) as well as to Sec. 7.7.

In this thesis we use two different batches of nanowires with similar characteristics:

- For Chapter 5, we use a nanowire batch grown in May 2018 (QDEV758) for which the average wire diamter is 80 ± 5 nm and the average wire length is $7 \pm 2\mu$m.
- For Chapters 6, 7, 8 and 9, we instead use a nanowire batch grown in July 2020 (QDEV1042) for which the average wire diameter is 111 ± 5 nm and the average wire length is $9.9 \pm 1\mu$m.

D.3.2. NANOWIRE DEPOSITION

The deposition is performed manually using a micromanipulator. For Chapter 5 the deposition was performed by Kongyi Li and for all other chapters by Lukas J. Splitthoff. Roughly speaking, this process consists of the following steps:

1. The growth chip is inspected under an optical microscope. By changing the focal point one can select a nanowire that stands vertically straight and that does not look damaged.

2. The wire is picked up manually using a tungsten needle attached to a micromanipulator. The wire is pushed with the needle a few microns above its base, which makes the wire break and stay attached to the needle.

3. The wire is then deposited horizontally onto the substrate. The micromanipulator allows for x and y control of the target position and allows determining the final nanowire location with micrometer accuracy.

4. Finally, the nanowire can be slightly pushed to improve its alignment with the pre-patterned structures (gates and contacts).

D.3.3. JUNCTION ETCH FOR CHAPTER 5

In this step, we selectively wet etch the epitaxial aluminum covering the nanowire in the junction area.

1. We first spin resist PMMA 950 A4 at 4000 rpm.

2. We bake the resist for 5 min at 185 °C.

3. Subsequently, the junction area is patterned using a Raith EBPG-5200 e-beam with the following specifications:

   - Acceleration voltage: 100 kV
   - Dose: 200 $\mu C cm^{-2}$.
   - Beam current: around 1200 pA.
   - Beam spot size: around 20 nm.

4. The resist is then developed as follows:

   (a) Submerge the chip in a solution of MIBK:IPA 1:3 at room temperature for 1 min.

   (b) Submerge the chip in IPA at room temperature for 30 s.

   (c) Dry with nitrogen directly without rinsing

5. Then, we wet etch the junction as follows:

   (a) Submerge the chip in Transene D, at 48.2 °C, for 12 s.

   (b) Submerge the chip in DI H_2O, at room temperature, for 3 s.

   (c) Submerge the chip again in DI H_2O, at room temperature, for 15 s.

   (d) Submerge the chip again in DI H_2O, at room temperature, for 15 s.

   (e) Dry with nitrogen.

6. The resist is not stripped and is left covering the chip.

D.3.4. JUNCTION ETCH FOR ALL OTHER EXPERIMENTAL CHAPTERS

In this step, we selectively wet etch the epitaxial aluminum covering the nanowire in the junctions areas.

1. We start by depositing an adhesion promoter (HMDS) on the surface of the chip.

   (a) First, the chip is pre-baked for 10 min at 150 °C.

   (b) Then the HMDS primer is deposited using a Delta RC80 apparatus.

2. Then, we spin resist PMMA 950 A4 at 4000 rpm.
3. We bake the resist for 5 min at 185 °C.
4. Subsequently, the junction area is patterned using a Raith EBPG-5200 e-beam with the following specifications:
   - Acceleration voltage: 100 kV
   - Dose: 1700 μCcm^{-2}.
   - Beam current: around 90 pA.
   - Beam spot size: around 60 nm.
5. The resist is then developed as follows:
   (a) Submerge the chip in a solution of H_2O:IPA 1:3 at 6 °C for 1 min.
   (b) Dry with nitrogen directly without rinsing
6. Then, we wet etch the junction as follows:
   (a) Submerge the chip in MF321, at room temperature, using a teflon holder and for 55 s.
   (b) Submerge the chip in DI H_2O, at room temperature, for 5 s.
   (c) Submerge the chip again in DI H_2O, at room temperature, for 5 s.
   (d) Submerge the chip again in DI H_2O, at room temperature, for 30 s.
   (e) Submerge the chip in IPA, at room temperature, for 30 s.
   (f) Dry with nitrogen.
7. The resist is not stripped and is left covering the chip.

D.3.5. CONTACTING

The nanowire is contacted to the pre-patterned superconducting circuitry using sputtered NbTiN patches. For some of the devices, we use this same step to deposit NbTiN in other parts of the chip as well, like for the capacitive parts of the gate-line filters in Chapters 6, 7, 8 and 9 and for the jump forming the twisted loop in Chapter 9.

1. We first apply positive e-beam resist, as follows:
   (a) Spin resist PMMA 495 A4 (from MicroChem) at 4000 rpm. Expected thickness 200 nm.
   (b) Bake resist for 5 minutes at 185 °C.
2. The NbTiN structures are patterned using a Raith EBPG-5200 e-beam with the following specifications:
   - Acceleration voltage: 100 kV

- Doses: from 1400 to 1800 μCcm^{-2}.
- Beam current: around 1000 pA for the contacts and and around 240 nA for coarser structures.
- Beam spot size: around 20 nm for Chapter 5 and and around 150 nm for coarser structures.

3. The resist is developed as follows:
   (a) Submerge in a solution of MIBK:IPA 3:1 at room temperature for 1 min.
   (b) Submerge in IPA at room temperature for 30 s.
   (c) Dry with nitrogen.

4. Then we perform an Ar milling step using an AJA International ATC 1800 sputtering system, under the following conditions:
   - Power: 50 W.
   - Argon flow: 50 sccm.
   - Pressure: 3 mTorr.
   - Total etch time: 180 s for Chapter 5 and 110 s for all other chapters.

5. NbTiN is sputtered using an AJA International ATC 1800 sputtering system, with the same recipe as in Sec. D.1 but now targetting a thickness of 120 nm.

6. Then, lift-off is performed as follows:
   (a) Submerge in acetone at 50 °C for 1 h.
   (b) Blow nitrogen through a plastic pipette to facilitate the lift-off process.
   (c) Submerge in IPA at room temperature for 30 s.
   (d) Dry with nitrogen.

D.4. FINAL STEPS

D.4.1. DICING

Finally, we dice the chip into individual dies of the correct size to fit in the PCB. For all chapters except for Chapter 9, we use 7×2 mm^2 chips, while for Chapter 9 we use 6×6 mm^2 chips. We follow the same dicing procedure as in Sec. D.1 except that now we monitor the water resistivity of the dicing water and only dice the chips when it is below 1 Ω. This is done to minimize the risk of electrostatic discharge (ESD) damaging the nanowires.

D.4.2. WIREBONDING

After dicing, the devices are mounted on a printed circuit board (PCB) using either vacuum grease (for Chapter 5) or silver paint (for all other chapters). Afterwards, they are electrically connected to the PCB using a wirebonder. The devices investigated in Chapter 5, as well as some of the resonator test devices presented in Chapter 4, were wirebonded on a Westbond system. All other devices were bonded using a Bondtec 5630. In both cases, we first bond on the PCB and then on the chip. We use the following bond parameters:

For the Westbond:

- First bond (on PCB): power around 190, time 85 ms and force 25 g.
- Second bond (on chip): power around 210, time 85 ms and force 25 g.

For the Bondtec:

- First bond (on PCB): power around 120, time 35 ms and force 22 to 35 g.
- Second bond (on chip): power around 135, time 40 ms and force 22 to 35 g.

BIBLIOGRAPHY

I. Affleck, J.-S. Caux, and A. M. Zagoskin. Andreev scattering and Josephson current in a one-dimensional electron liquid. *Phys Rev B*, 62, 2000. ISSN 0163-1829. doi: 10.1103/physrevb.62.1433. [Cited on page(s) 147].

F. Afshar, S. Nazarpour, and A. Cirera. Survey of the theory and experimental measurements of residual stress in Pd thin film. *Journal of Applied Physics*, 108(9):093513, 11 2010. ISSN 0021-8979. doi: 10.1063/1.3505725. URL https://doi.org/10.1063/1.3505725. [Cited on page(s) 39].

K. Aggarwal, A. Hofmann, D. Jirovec, I. Prieto, A. Sammak, M. Botifoll, S. Martí-Sánchez, M. Veldhorst, J. Arbiol, G. Scappucci, J. Danon, and G. Katsaros. Enhancement of proximity-induced superconductivity in a planar Ge hole gas. *Phys. Rev. Res.*, 3: L022005, Apr 2021. doi: 10.1103/PhysRevResearch.3.L022005. URL https://link.aps.org/doi/10.1103/PhysRevResearch.3.L022005. [Cited on page(s) 268].

R. Aguado. A perspective on semiconductor-based superconducting qubits. *Appl Phys Lett*, 117(24), Dec. 2020. doi: 10.1063/5.0024124. [Cited on page(s) 138, 262, 275].

S. Ahn, H. Pan, B. Woods, T. D. Stanescu, and S. Das Sarma. Estimating disorder and its adverse effects in semiconductor Majorana nanowires. *Phys. Rev. Materials*, 5, Dec. 2021. doi: 10.1103/PhysRevMaterials.5.124602. [Cited on page(s) 109].

A. Akhmerov and G. Steele. Open Data Policy of the Quantum Nanoscience Department, TU Delft. *Zenodo*, Feb. 2019. doi: 10.5281/ZENODO.2556949. [Cited on page(s) 53].

T. Albash and D. A. Lidar. Demonstration of a scaling advantage for a quantum annealer over simulated annealing. *Phys. Rev. X*, 8:031016, Jul 2018. doi: 10.1103/PhysRevX.8.031016. URL https://link.aps.org/doi/10.1103/PhysRevX.8.031016. [Cited on page(s) 249].

A. F. Andreev. The thermal conductivity of the intermediate state in superconductors. *ZhETF*, 46:1823, November 1964. URL http://www.jetp.ac.ru/cgi-bin/dn/e_019_05_1228.pd. [Cited on page(s) 10].

A. J. Annunziata, D. F. Santavicca, L. Frunzio, G. Catelani, M. J. Rooks, A. Frydman, and D. E. Prober. Tunable superconducting nanoinductors. *Nanotechnology*, 21(44): 445202, 2010. doi: doi.org/10.1088/0957-4484/21/44/445202. [Cited on page(s) 65, 73, 295, 296].

A. E. Antipov, A. Bargerbos, G. W. Winkler, B. Bauer, E. Rossi, and R. M. Lutchyn. Effects of gate-induced electric fields on semiconductor Majorana nanowires. *Phys. Rev. X*, 8: 031041, Aug 2018. doi: 10.1103/PhysRevX.8.031041. [Cited on page(s) 117].

F. Arute, K. Arya, R. Babbush, D. Bacon, J. C. Bardin, et al. Quantum supremacy using a programmable superconducting processor. *Nature*, 574(7779), Oct. 2019. doi: 10.1038/s41586-019-1666-5. [Cited on page(s) 17, 172, 206].

O. V. Astafiev, L. B. Ioffe, S. Kafanov, Y. A. Pashkin, K. Y. Arutyunov, D. Shahar, O. Cohen, and J. S. Tsai. Coherent quantum phase slip. *Nature*, 484(7394):355–358, 2012. ISSN 1476-4687. doi: 10.1038/nature10930. [Cited on page(s) 75, 268].

D. V. Averin. Coulomb blockade in superconducting quantum point contacts. *Phys. Rev. Lett.*, 82:3685–3688, May 1999. doi: 10.1103/PhysRevLett.82.3685. [Cited on page(s) 268, 269].

J. Ávila, E. Prada, P. San-Jose, and R. Aguado. Superconducting islands with topological Josephson junctions based on semiconductor nanowires. *Phys. Rev. B*, 102:094518, Sep 2020. doi: 10.1103/PhysRevB.102.094518. URL https://link.aps.org/doi/10.1103/PhysRevB.102.094518. [Cited on page(s) 99, 109, 263].

J. Avila, E. Prada, P. San-Jose, and R. Aguado. Majorana oscillations and parity crossings in semiconductor-nanowire-based transmon qubits. *Phys. Rev. Research*, 2(3), Mar. 2020b. ISSN 2643-1564. doi: 10.1103/physrevresearch.2.033493. [Cited on page(s) 99, 109, 263].

P. F. Bagwell. Suppression of the Josephson current through a narrow, mesoscopic, semiconductor channel by a single impurity. *Phys Rev Lett*, 46(19), Nov. 1992. ISSN 0163-1829. doi: 10.1103/PhysRevB.46.12573. [Cited on page(s) 138].

L. Banszerus, K. Hecker, S. Möller, E. Icking, K. Watanabe, T. Taniguchi, C. Volk, and C. Stampfer. Spin relaxation in a single-electron graphene quantum dot. *Nature Communications*, 13(1):3637, Jun 2022. ISSN 2041-1723. doi: 10.1038/s41467-022-31231-5. URL https://doi.org/10.1038/s41467-022-31231-5. [Cited on page(s) 284].

F. Barahona. On the computational complexity of Ising spin glass models. *Journal of Physics A: Mathematical and General*, 15(10):3241, oct 1982. doi: 10.1088/0305-4470/15/10/028. URL https://dx.doi.org/10.1088/0305-4470/15/10/028. [Cited on page(s) 249].

H. Barakov and Y. V. Nazarov. Supercurrent in the presence of direct transmission and a resonant localized state. *arXiv e-prints*, Jan. 2022. [Cited on page(s) 140].

R. Barends, J. Kelly, A. Megrant, A. Veitia, D. Sank, E. Jeffrey, T. C. White, J. Mutus, A. G. Fowler, B. Campbell, Y. Chen, Z. Chen, B. Chiaro, A. Dunsworth, C. Neill, P. O'Malley, P. Roushan, A. Vainsencher, J. Wenner, A. N. Korotkov, A. N. Cleland, and J. M. Martinis. Superconducting quantum circuits at the surface code threshold for fault tolerance. *Nature*, 508(7497):500–503, Apr 2014. ISSN 1476-4687. doi: 10.1038/nature13171. URL https://doi.org/10.1038/nature13171. [Cited on page(s) 244].

A. Bargerbos. Nanowire Josephson junctions in superconducting circuits. *PhD thesis*, 2023b. [Cited on page(s) 45, 271].

A. Bargerbos, W. Uilhoorn, C.-K. Yang, P. Krogstrup, L. P. Kouwenhoven, G. de Lange, B. van Heck, and A. Kou. Observation of vanishing charge dispersion of a nearly open superconducting island. *Phys. Rev. Lett.*, 124:246802, Jun 2020. doi: 10.1103/PhysRevLett.124.246802. [Cited on page(s) 67, 84, 100, 155, 181, 196, 211, 268, 269, 277].

A. Bargerbos, L. J. Splitthoff, M. Pita-Vidal, J. J. Wesdorp, Y. Liu, P. Krogstrup, L. P. Kouwenhoven, C. K. Andersen, and L. Grünhaupt. Mitigation of quasiparticle loss in superconducting qubits by phonon scattering. *Phys. Rev. Appl.*, 19:024014, Feb 2023. doi: 10.1103/PhysRevApplied.19.024014. URL https://link.aps.org/doi/10.1103/PhysRevApplied.19.024014. [Cited on page(s) 234, 297].

C. Barthel, J. Medford, C. M. Marcus, M. P. Hanson, and A. C. Gossard. Interlaced dynamical decoupling and coherent operation of a singlet-triplet qubit. *Phys Rev Lett*, 105, Dec. 2010. doi: 10.1103/PhysRevLett.105.266808. [Cited on page(s) 176].

G. Batey, S. Chappell, M. Cuthbert, M. Erfani, A. Matthews, and G. Teleberg. A rapid sample-exchange mechanism for cryogen-free dilution refrigerators compatible with multiple high-frequency signal connections. *Cryogenics*, 60:24–32, 2014. ISSN 0011-2275. doi: https://doi.org/10.1016/j.cryogenics.2014.01.007. URL https://www.sciencedirect.com/science/article/pii/S0011227514000150. [Cited on page(s) 44].

C. W. J. Beenakker. Universal limit of critical-current fluctuations in mesoscopic Josephson junctions. *Phys. Rev. Lett.*, 67:3836–3839, Dec 1991. doi: 10.1103/PhysRevLett.67.3836. [Cited on page(s) 10, 84, 138].

B. Béri, J. H. Bardarson, and C. W. J. Beenakker. Splitting of Andreev levels in a Josephson junction by spin-orbit coupling. *Phys Rev B*, 77(4), Jan. 2008. doi: 10.1103/physrevb.77.045311. [Cited on page(s) 138, 172].

A. Blais, R.-S. Huang, A. Wallraff, S. M. Girvin, and R. J. Schoelkopf. Cavity quantum electrodynamics for superconducting electrical circuits: An architecture for quantum computation. *Phys. Rev. A*, 69:062320, Jun 2004. doi: 10.1103/PhysRevA.69.062320. [Cited on page(s) 16, 17, 24, 25, 72, 95, 99, 141, 161, 172, 202].

A. Blais, J. Gambetta, A. Wallraff, D. I. Schuster, S. M. Girvin, M. H. Devoret, and R. J. Schoelkopf. Quantum-information processing with circuit quantum electrodynamics. *Phys. Rev. A*, 75:032329, Mar 2007. doi: 10.1103/PhysRevA.75.032329. [Cited on page(s) 17].

A. Blais, A. L. Grimsmo, S. M. Girvin, and A. Wallraff. Circuit quantum electrodynamics. *Rev Mod Phys*, 93, May 2021. ISSN 1539-0756. doi: 10.1103/REVMODPHYS.93.025005/FIGURES/34/MEDIUM. [Cited on page(s) 15, 97, 141, 172].

H. Bluhm, S. Foletti, D. Mahalu, V. Umansky, and A. Yacoby. Enhancing the coherence of a spin qubit by operating it as a feedback loop that controls its nuclear spin bath. *Phys. Rev. Lett.*, 105:216803, Nov 2010. doi: 10.1103/PhysRevLett.105.216803. URL https://link.aps.org/doi/10.1103/PhysRevLett.105.216803. [Cited on page(s) 283].

H. Bluhm, S. Foletti, I. Neder, M. Rudner, D. Mahalu, V. Umansky, and A. Yacoby. Dephasing time of GaAs electron-spin qubits coupled to a nuclear bath exceeding 200 μs. *Nature Physics*, 7(2):109–113, Feb 2011. ISSN 1745-2481. doi: 10.1038/nphys1856. URL https://doi.org/10.1038/nphys1856. [Cited on page(s) 283].

A. Bordin, X. Li, D. van Driel, J. C. Wolff, Q. Wang, S. L. D. ten Haaf, G. Wang, N. van Loo, L. P. Kouwenhoven, and T. Dvir. Crossed Andreev reflection and elastic co-tunneling in a three-site Kitaev chain nanowire device. *arXiv e-prints*, art. arXiv:2306.07696, jun 2023. doi: 10.48550/arXiv.2306.07696. [Cited on page(s) 266].

F. Borjans, X. G. Croot, X. Mi, M. J. Gullans, and J. R. Petta. Resonant microwave-mediated interactions between distant electron spins. *Nature*, 577(7789), Jan. 2020. ISSN 1476-4687. doi: 10.1038/s41586-019-1867-y. [Cited on page(s) 172, 200].

F. Borsoi, G. P. Mazur, N. van Loo, M. P. Nowak, L. Bourdet, K. Li, S. Korneychuk, A. Fursina, J. Wang, V. Levajac, E. Memisevic, G. Badawy, S. Gazibegovic, K. van Hoogdalem, E. P. A. M. Bakkers, L. P. Kouwenhoven, S. Heedt, and M. Quintero-Pérez. Single-shot fabrication of semiconducting–superconducting nanowire devices. *Adv Funct Mater*, 31(34), June 2021. ISSN 1616-301X. doi: 10.1002/adfm.202102388. [Cited on page(s) 268].

F. Borsoi, N. W. Hendrickx, V. John, M. Meyer, S. Motz, F. van Riggelen, A. Sammak, S. L. de Snoo, G. Scappucci, and M. Veldhorst. Shared control of a 16 semiconductor quantum dot crossbar array. *Nature Nanotechnology*, Aug 2023. ISSN 1748-3395. doi: 10.1038/s41565-023-01491-3. URL https://doi.org/10.1038/s41565-023-01491-3. [Cited on page(s) 244].

J. M. Boter, J. P. Dehollain, J. P. van Dijk, Y. Xu, T. Hensgens, R. Versluis, H. W. Naus, J. S. Clarke, M. Veldhorst, F. Sebastiano, and L. M. Vandersypen. Spiderweb array: A sparse spin-qubit array. *Phys. Rev. Appl.*, 18:024053, Aug 2022. doi: 10.1103/PhysRevApplied.18.024053. URL https://link.aps.org/doi/10.1103/PhysRevApplied.18.024053. [Cited on page(s) 244].

C. G. L. Bøttcher. New avenues in circuit QED: from quantum information to quantum sensing. *PhD Thesis*, 2022. URL https://nrs.harvard.edu/URN-3:HUL.INSTREPOS:37372164. [Cited on page(s) 263].

C. G. L. Bøttcher, S. P. Harvey, S. Fallahi, G. C. Gardner, M. J. Manfra, U. Vool, S. D. Bartlett, and A. Yacoby. Parametric longitudinal coupling between a high-impedance superconducting resonator and a semiconductor quantum dot singlet-triplet spin qubit. *Nature Communications*, 13(1):4773, Aug 2022. ISSN 2041-1723. doi: 10.1038/s41467-022-32236-w. URL https://doi.org/10.1038/s41467-022-32236-w. [Cited on page(s) 26].

C. G. L. Bøttcher, N. R. Poniatowski, A. Grankin, M. E. Wesson, Z. Yan, U. Vool, V. M. Galitski, and A. Yacoby. Circuit QED detection of induced two-fold anisotropic pairing in a hybrid superconductor-ferromagnet bilayer. *arXiv e-prints*, art. arXiv:2306.08043, June 2023. doi: 10.48550/arXiv.2306.08043. [Cited on page(s) 263].

V. Bouchiat, D. Vion, P. Joyez, D. Esteve, and M. H. Devoret. Quantum coherence with a single Cooper pair. *Phys Scripta*, T76(1), Jan. 1998. ISSN 0031-8949. doi: 10.1238/Physica.Topical.076a00165. [Cited on page(s) 18].

D. Bouman, R. J. J. van Gulik, G. Steffensen, D. Pataki, P. Boross, P. Krogstrup, J. Nygård, J. Paaske, A. Pályi, and A. Geresdi. Triplet-blockaded Josephson supercurrent in double quantum dots. *Phys. Rev. B*, 102:220505, Dec 2020. doi: 10.1103/PhysRevB.102.220505. URL https://link.aps.org/doi/10.1103/PhysRevB.102.220505. [Cited on page(s) 267, 271].

A. M. Bozkurt and V. Fatemi. Josephson tunnel junction arrays and Andreev weak links: what's the difference? In J.-E. Wegrowe, J. S. Friedman, and M. Razeghi, editors, *Spintronics XVI*, volume 12656, page 1265607. International Society for Optics and Photonics, SPIE, 2023. doi: 10.1117/12.2678477. URL https://doi.org/10.1117/12.2678477. [Cited on page(s) 275].

J. Braumüller, L. Ding, A. P. Vepsäläinen, Y. Sung, M. Kjaergaard, T. Menke, R. Winik, D. Kim, B. M. Niedzielski, A. Melville, J. L. Yoder, C. F. Hirjibehedin, T. P. Orlando, S. Gustavsson, and W. D. Oliver. Characterizing and optimizing qubit coherence based on SQUID geometry. *Phys. Rev. Applied*, 13(5), May 2020. doi: 10.1103/physrevapplied.13.054079. [Cited on page(s) 177].

S. Bravyi, A. W. Cross, J. M. Gambetta, D. Maslov, P. Rall, and T. J. Yoder. High-threshold and low-overhead fault-tolerant quantum memory. *arXiv e-prints*, art. arXiv:2308.07915, Aug. 2023. doi: 10.48550/arXiv.2308.07915. [Cited on page(s) 257].

S. B. Bravyi and A. Y. Kitaev. Quantum codes on a lattice with boundary. *arXiv e-prints*, art. quant-ph/9811052, Nov. 1998. doi: 10.48550/arXiv.quant-ph/9811052. [Cited on page(s) 244].

L. Bretheau. Localized excitations in superconducting atomic contacts: Probing the Andreev doublet. *PhD Thesis*, 2013. URL https://pastel.hal.science/pastel-00862029. Paris-Saclay University. [Cited on page(s) 10].

L. Bretheau, Ç. Ö. Girit, H. Pothier, D. Esteve, and C. Urbina. Exciting Andreev pairs in a superconducting atomic contact. *Nature*, 499:312 EP –, Jul 2013. doi: 10.1038/nature12315. [Cited on page(s) 10, 138].

A. Brunetti, A. Zazunov, A. Kundu, and R. Egger. Anomalous Josephson current, incipient time-reversal symmetry breaking, and Majorana bound states in interacting multilevel dots. *Phys Rev B*, 88(14), Oct. 2013. doi: 10.1103/physrevb.88.144515. [Cited on page(s) 138, 139, 143].

R. Bulla, T. A. Costi, and T. Pruschke. The numerical renormalization group method for quantum impurity systems. *Rev Mod Phys*, 80(2), Apr. 2008. ISSN 0034-6861. doi: 10.1103/revmodphys.80.395. [Cited on page(s) 12, 96, 112].

G. Burkard, T. D. Ladd, A. Pan, J. M. Nichol, and J. R. Petta. Semiconductor spin qubits. *Rev. Mod. Phys.*, 95:025003, Jun 2023. doi: 10.1103/RevModPhys.95.025003. URL https://link.aps.org/doi/10.1103/RevModPhys.95.025003. [Cited on page(s) 15, 200].

J. Bylander, S. Gustavsson, F. Yan, F. Yoshihara, K. Harrabi, G. Fitch, D. G. Cory, Y. Nakamura, J.-S. Tsai, and W. D. Oliver. Noise spectroscopy through dynamical decoupling with a superconducting flux qubit. *Nat Phys*, 7(7), July 2011. ISSN 1745-2481. doi: 10.1038/nphys1994. [Cited on page(s) 176, 177].

J. Cai, W. G. Macready, and A. Roy. A practical heuristic for finding graph minors. *arXiv e-prints*, art. arXiv:1406.2741, June 2014. doi: 10.48550/arXiv.1406.2741. [Cited on page(s) 244, 249].

Y. Cao, V. Fatemi, S. Fang, K. Watanabe, T. Taniguchi, E. Kaxiras, and P. Jarillo-Herrero. Unconventional superconductivity in magic-angle graphene superlattices. *Nature*, 556(7699):43–50, Apr 2018. ISSN 1476-4687. doi: 10.1038/nature26160. URL https://doi.org/10.1038/nature26160. [Cited on page(s) 263].

Y. Cao, D. Rodan-Legrain, O. Rubies-Bigorda, J. M. Park, K. Watanabe, T. Taniguchi, and P. Jarillo-Herrero. Tunable correlated states and spin-polarized phases in twisted bilayer–bilayer graphene. *Nature*, 583(7815):215–220, Jul 2020. ISSN 1476-4687. doi: 10.1038/s41586-020-2260-6. [Cited on page(s) 83].

H. Y. Carr and E. M. Purcell. Effects of diffusion on free precession in nuclear magnetic resonance experiments. *Phys Rev*, 94, May 1954. doi: 10.1103/PhysRev.94.630. [Cited on page(s) 176].

L. Casparis, T. W. Larsen, M. S. Olsen, F. Kuemmeth, P. Krogstrup, J. Nygård, K. D. Petersson, and C. M. Marcus. Gatemon benchmarking and two-qubit operations. *Phys. Rev. Lett.*, 116:150505, Apr 2016. doi: 10.1103/PhysRevLett.116.150505. [Cited on page(s) 234].

L. Casparis, M. R. Connolly, M. Kjaergaard, N. J. Pearson, A. Kringhøj, T. W. Larsen, F. Kuemmeth, T. Wang, C. Thomas, S. Gronin, G. C. Gardner, M. J. Manfra, C. M. Marcus, and K. D. Petersson. Superconducting gatemon qubit based on a proximitized two-dimensional electron gas. *Nature Nanotechnology*, 13(10):915–919, 2018. doi: 10.1038/s41565-018-0207-y. [Cited on page(s) 72, 267].

J. Cerrillo, M. Hays, V. Fatemi, and A. L. Yeyati. Spin coherent manipulation in Josephson weak links. *Phys. Rev. Research*, 3(2), May 2021. doi: 10.1103/physrevresearch.3.l022012. [Cited on page(s) 138, 145, 175].

W. Chang, V. E. Manucharyan, T. S. Jespersen, J. Nygård, and C. M. Marcus. Tunneling spectroscopy of quasiparticle bound states in a spinful Josephson junction. *Phys Rev Lett*, 110(21), May 2013. ISSN 0031-9007. doi: 10.1103/PhysRevLett.110.217005. [Cited on page(s) 13, 94, 140].

E. A. Chekhovich, M. N. Makhonin, A. I. Tartakovskii, A. Yacoby, H. Bluhm, K. C. Nowack, and L. M. K. Vandersypen. Nuclear spin effects in semiconductor quantum dots. *Nature Materials*, 12(6):494–504, Jun 2013. ISSN 1476-4660. doi: 10.1038/nmat3652. URL https://doi.org/10.1038/nmat3652. [Cited on page(s) 280].

I. Chiorescu, Y. Nakamura, C. J. P. M. Harmans, and J. E. Mooij. Coherent quantum dynamics of a superconducting flux qubit. *Science*, 299(5614):1869–1871, 2003. ISSN 0036-8075. doi: 10.1126/science.1081045. [Cited on page(s) 17].

I. Chiorescu, P. Bertet, K. Semba, Y. Nakamura, C. J. P. M. Harmans, and J. E. Mooij. Coherent dynamics of a flux qubit coupled to a harmonic oscillator. *Nature*, 431(7005): 159–162, 2004. ISSN 1476-4687. doi: 10.1038/nature02831. [Cited on page(s) 17, 72].

M.-S. Choi, M. Lee, K. Kang, and W. Belzig. Kondo effect and Josephson current through a quantum dot between two superconductors. *Phys Rev B*, 70, July 2004. doi: 10.1103/PhysRevB.70.020502. [Cited on page(s) 94, 140].

N. M. Chtchelkatchev and Y. V. Nazarov. Andreev quantum dots for spin manipulation. *Phys Rev Lett*, 90(22), June 2003. ISSN 1079-7114. doi: 10.1103/PhysRevLett.90.226806. [Cited on page(s) 15, 16, 25, 26, 94, 109, 138, 144, 145, 172, 199, 200, 244].

I. L. Chuang, L. M. K. Vandersypen, X. Zhou, D. W. Leung, and S. Lloyd. Experimental realization of a quantum algorithm. *Nature*, 393(6681):143–146, May 1998. ISSN 1476-4687. doi: 10.1038/30181. URL https://doi.org/10.1038/30181. [Cited on page(s) 26, 286].

A. A. Clerk, K. W. Lehnert, P. Bertet, J. R. Petta, and Y. Nakamura. Hybrid quantum systems with circuit quantum electrodynamics. *Nature Physics*, 16(3):257–267, Mar 2020. ISSN 1745-2481. doi: 10.1038/s41567-020-0797-9. URL https://doi.org/10.1038/s41567-020-0797-9. [Cited on page(s) 262, 275].

J. P. Cleuziou, W. Wernsdorfer, V. Bouchiat, T. Ondarcuhu, and M. Monthioux. Carbon nanotube superconducting quantum interference device. *Nat Nanotechnol*, 1(1), Oct. 2006. ISSN 1748-3395. doi: 10.1038/nnano.2006.54. URL http://www.nature.com/naturenanotechnology. [Cited on page(s) 94, 103].

M. C. Collodo, J. Herrmann, N. Lacroix, C. K. Andersen, A. Remm, S. Lazar, J.-C. Besse, T. Walter, A. Wallraff, and C. Eichler. Implementation of conditional phase gates based on tunable zz interactions. *Phys. Rev. Lett.*, 125:240502, Dec 2020. doi: 10.1103/PhysRevLett.125.240502. URL https://link.aps.org/doi/10.1103/PhysRevLett.125.240502. [Cited on page(s) 25, 26].

S. Csonka, L. Hofstetter, F. Freitag, S. Oberholzer, C. Schönenberger, T. S. Jespersen, M. Aagesen, and J. Nygård. Giant fluctuations and gate control of the g-factor in InAs nanowire quantum dots. *Nano Lett.*, 8(11), Oct. 2008. doi: 10.1021/nl802418w. [Cited on page(s) 145, 165].

L. Cywiński, R. M. Lutchyn, C. P. Nave, and S. Das Sarma. How to enhance dephasing time in superconducting qubits. *Phys Rev B*, 77, May 2008. doi: 10.1103/PhysRevB.77.174509. [Cited on page(s) 177].

L. Cywiński, W. M. Witzel, and S. Das Sarma. Pure quantum dephasing of a solid-state electron spin qubit in a large nuclear spin bath coupled by long-range hyperfine-mediated interactions. *Phys. Rev. B*, 79:245314, Jun 2009. doi: 10.1103/PhysRevB.79.245314. URL https://link.aps.org/doi/10.1103/PhysRevB.79.245314. [Cited on page(s) 280].

A. J. Daley, I. Bloch, C. Kokail, S. Flannigan, N. Pearson, M. Troyer, and P. Zoller. Practical quantum advantage in quantum simulation. *Nature*, 607(7920):667–676, Jul 2022. ISSN 1476-4687. doi: 10.1038/s41586-022-04940-6. URL https://doi.org/10.1038/s41586-022-04940-6. [Cited on page(s) 17].

J. Danon and Y. V. Nazarov. Pauli spin blockade in the presence of strong spin-orbit coupling. *Phys Rev B*, 80(4), July 2009. doi: 10.1103/physrevb.80.041301. [Cited on page(s) 140].

S. Das Sarma and H. Pan. Disorder-induced zero-bias peaks in Majorana nanowires. *Phys. Rev. B*, 103:195158, May 2021. doi: 10.1103/PhysRevB.103.195158. URL https://link.aps.org/doi/10.1103/PhysRevB.103.195158. [Cited on page(s) 262].

I. M. Dayton, T. Sage, E. C. Gingrich, M. G. Loving, T. F. Ambrose, N. P. Siwak, S. Keebaugh, C. Kirby, D. L. Miller, A. Y. Herr, Q. P. Herr, and O. Naaman. Experimental demonstration of a Josephson magnetic memory cell with a programmable π-junction. *IEEE Magnetics Letters*, 9, 2018. doi: 10.1109/LMAG.2018.2801820. [Cited on page(s) 109].

D. de Jong, J. van Veen, L. Binci, A. Singh, P. Krogstrup, L. P. Kouwenhoven, W. Pfaff, and J. D. Watson. Rapid detection of coherent tunneling in an InAs nanowire quantum dot through dispersive gate sensing. *Phys. Rev. Appl.*, 11:044061, Apr 2019. doi: 10.1103/PhysRevApplied.11.044061. URL https://link.aps.org/doi/10.1103/PhysRevApplied.11.044061. [Cited on page(s) 263].

D. de Jong, C. G. Prosko, D. M. A. Waardenburg, L. Han, F. K. Malinowski, P. Krogstrup, L. P. Kouwenhoven, J. V. Koski, and W. Pfaff. Rapid microwave-only characterization and readout of quantum dots using multiplexed gigahertz-frequency resonators. *Phys. Rev. Applied*, 16(1), July 2021. doi: 10.1103/physrevapplied.16.014007. [Cited on page(s) 117].

G. de Lange, B. van Heck, A. Bruno, D. J. van Woerkom, A. Geresdi, S. R. Plissard, E. P. A. M. Bakkers, A. R. Akhmerov, and L. DiCarlo. Realization of microwave quantum circuits using hybrid superconducting-semiconducting nanowire Josephson elements. *Phys. Rev. Lett.*, 115:127002, Sep 2015. doi: 10.1103/PhysRevLett.115.127002. [Cited on page(s) 10, 72, 77, 94, 202, 275].

N. P. de Leon, K. M. Itoh, D. Kim, K. K. Mehta, T. E. Northup, H. Paik, B. S. Palmer, N. Samarth, S. Sangtawesin, and D. W. Steuerman. Materials challenges and opportunities for quantum computing hardware. *Science*, 372, Apr. 2021. doi: 10.1126/science.abb2823. [Cited on page(s) 180].

F. De Palma, F. Oppliger, W. Jang, S. Bosco, M. Janík, S. Calcaterra, G. Katsaros, G. Isella, D. Loss, and P. Scarlino. Strong hole-photon coupling in planar Ge: probing the charge degree and Wigner molecule states. *arXiv e-prints*, art. arXiv:2310.20661, Oct. 2023. doi: 10.48550/arXiv.2310.20661. [Cited on page(s) 284].

P. J. de Visser, J. J. A. Baselmans, S. J. C. Yates, P. Diener, A. Endo, and T. M. Klapwijk. Microwave-induced excess quasiparticles in superconducting resonators measured through correlated conductivity fluctuations. *Applied Physics Letters*, 100(16):162601, 04 2012. ISSN 0003-6951. doi: 10.1063/1.4704151. URL https://doi.org/10.1063/1.4704151. [Cited on page(s) 63].

P. J. de Visser, D. J. Goldie, P. Diener, S. Withington, J. J. A. Baselmans, and T. M. Klapwijk. Evidence of a nonequilibrium distribution of quasiparticles in the microwave response of a superconducting aluminum resonator. *Phys. Rev. Lett.*, 112:047004, Jan

2014. doi: 10.1103/PhysRevLett.112.047004. URL https://link.aps.org/doi/10.1103/PhysRevLett.112.047004. [Cited on page(s) 62, 63].

R. S. Deacon, Y. Tanaka, A. Oiwa, R. Sakano, K. Yoshida, K. Shibata, K. Hirakawa, and S. Tarucha. Tunneling spectroscopy of Andreev energy levels in a quantum dot coupled to a superconductor. *Phys Rev Lett*, 104(7), Feb. 2010. ISSN 1079-7114. doi: 10.1103/PhysRevLett.104.076805. [Cited on page(s) 13, 94].

R. Delagrange, D. J. Luitz, R. Weil, A. Kasumov, V. Meden, H. Bouchiat, and R. Deblock. Manipulating the magnetic state of a carbon nanotube Josephson junction using the superconducting phase. *Phys Rev B*, 91(24), June 2015. ISSN 1550-235X. doi: 10.1103/PhysRevB.91.241401. [Cited on page(s) 13, 94, 102, 103].

R. Delagrange, R. Weil, A. Kasumov, M. Ferrier, H. Bouchiat, and R. Deblock. $0-\pi$ quantum transition in a carbon nanotube Josephson junction: Universal phase dependence and orbital degeneracy. *Phys Rev B*, 93(19), May 2016. ISSN 2469-9969. doi: 10.1103/PhysRevB.93.195437. [Cited on page(s) 13].

R. Delagrange, R. Weil, A. Kasumov, M. Ferrier, H. Bouchiat, and R. Deblock. $0-\pi$ Quantum transition in a carbon nanotube Josephson junction: Universal phase dependence and orbital degeneracy. *Phys. B Condens. Matter*, 536, May 2018. ISSN 0921-4526. doi: 10.1016/j.physb.2017.09.034. URL https://www.sciencedirect.com/science/article/pii/S0921452617306208. [Cited on page(s) 13, 94, 103].

M. L. Della Rocca, M. Chauvin, B. Huard, H. Pothier, D. Esteve, and C. Urbina. Measurement of the current-phase relation of superconducting atomic contacts. *Phys Rev Lett*, 99, Sept. 2007. doi: 10.1103/PhysRevLett.99.127005. [Cited on page(s) 96].

E. Dennis, A. Kitaev, A. Landahl, and J. Preskill. Topological quantum memory. *Journal of Mathematical Physics*, 43(9):4452–4505, 08 2002. ISSN 0022-2488. doi: 10.1063/1.1499754. URL https://doi.org/10.1063/1.1499754. [Cited on page(s) 244].

M. A. Despósito and A. L. Yeyati. Controlled dephasing of Andreev states in superconducting quantum point contacts. *Phys Rev B*, 64(14), Sept. 2001. doi: 10.1103/physrevb.64.140511. [Cited on page(s) 138].

M. H. Devoret. Does Brian Josephson's gauge-invariant phase difference live on a line or a circle? *Journal of Superconductivity and Novel Magnetism*, 34(6):1633–1642, may 2021. doi: 10.1007/s10948-020-05784-9. [Cited on page(s) 18].

L. DiCarlo, J. M. Chow, J. M. Gambetta, L. S. Bishop, B. R. Johnson, D. I. Schuster, J. Majer, A. Blais, L. Frunzio, S. M. Girvin, and R. J. Schoelkopf. Demonstration of two-qubit algorithms with a superconducting quantum processor. *Nature*, 460:240 EP –, Jun 2009. doi: 10.1038/nature08121. [Cited on page(s) 17].

N. Didier, J. Bourassa, and A. Blais. Fast quantum nondemolition readout by parametric modulation of longitudinal qubit-oscillator interaction. *Phys. Rev. Lett.*, 115:203601, Nov 2015. doi: 10.1103/PhysRevLett.115.203601. URL https://link.aps.org/doi/10.1103/PhysRevLett.115.203601. [Cited on page(s) 26].

L. Ding, M. Hays, Y. Sung, B. Kannan, J. An, A. Di Paolo, A. H. Karamlou, T. M. Hazard, K. Azar, D. K. Kim, B. M. Niedzielski, A. Melville, M. E. Schwartz, J. L. Yoder, T. P. Orlando, S. Gustavsson, J. A. Grover, K. Serniak, and W. D. Oliver. High-fidelity, frequency-flexible two-qubit fluxonium gates with a transmon coupler. *Phys. Rev. X*, 13:031035, Sep 2023. doi: 10.1103/PhysRevX.13.031035. URL https://link.aps.org/doi/10.1103/PhysRevX.13.031035. [Cited on page(s) 17].

Y.-J. Doh. Tunable Supercurrent Through Semiconductor Nanowires. *Science*, 309(5732): 272–275, July 2005. ISSN 0036-8075, 1095-9203. doi: 10.1126/science.1113523. [Cited on page(s) 202].

F. Dolcini, M. Houzet, and J. S. Meyer. Topological Josephson ϕ_0 junctions. *Phys. Rev. B*, 92:035428, Jul 2015. doi: 10.1103/PhysRevB.92.035428. [Cited on page(s) 83, 268].

T. Dvir, G. Wang, N. van Loo, C.-X. Liu, G. P. Mazur, A. Bordin, S. L. D. ten Haaf, J.-Y. Wang, D. van Driel, F. Zatelli, X. Li, F. K. Malinowski, S. Gazibegovic, G. Badawy, E. P. A. M. Bakkers, M. Wimmer, and L. P. Kouwenhoven. Realization of a minimal Kitaev chain in coupled quantum dots. *Nature*, 614(7948):445–450, Feb 2023. ISSN 1476-4687. doi: 10.1038/s41586-022-05585-1. URL https://doi.org/10.1038/s41586-022-05585-1. [Cited on page(s) 266, 267].

M. Eich, F. c. v. Herman, R. Pisoni, H. Overweg, A. Kurzmann, Y. Lee, P. Rickhaus, K. Watanabe, T. Taniguchi, M. Sigrist, T. Ihn, and K. Ensslin. Spin and valley states in gate-defined bilayer graphene quantum dots. *Phys. Rev. X*, 8:031023, Jul 2018. doi: 10.1103/PhysRevX.8.031023. URL https://link.aps.org/doi/10.1103/PhysRevX.8.031023. [Cited on page(s) 284].

A. Eichler, R. Deblock, M. Weiss, C. Karrasch, V. Meden, C. Schönenberger, and H. Bouchiat. Tuning the Josephson current in carbon nanotubes with the Kondo effect. *Phys Rev B*, 79, Apr. 2009. doi: 10.1103/PhysRevB.79.161407. [Cited on page(s) 94].

S. D. Escribano, A. Levy Yeyati, R. Aguado, E. Prada, and P. San-Jose. Fluxoid-induced pairing suppression and near-zero modes in quantum dots coupled to full-shell nanowires. *Phys Rev B*, 105, Jan. 2022. doi: 10.1103/PhysRevB.105.045418. [Cited on page(s) 103].

C. Fasth, A. Fuhrer, L. Samuelson, V. N. Golovach, and D. Loss. Direct measurement of the spin-orbit interaction in a two-electron InAs nanowire quantum dot. *Phys Rev Lett*, 98(26), June 2007. doi: 10.1103/physrevlett.98.266801. [Cited on page(s) 140].

V. Fatemi, S. Wu, Y. Cao, L. Bretheau, Q. D. Gibson, K. Watanabe, T. Taniguchi, R. J. Cava, and P. Jarillo-Herrero. Electrically tunable low-density superconductivity in a monolayer topological insulator. *Science*, 362(6417):926–929, 2018. doi: 10.1126/science.aar4642. URL https://www.science.org/doi/abs/10.1126/science.aar4642. [Cited on page(s) 263].

V. Fatemi, P. D. Kurilovich, M. Hays, D. Bouman, T. Connolly, S. Diamond, N. E. Frattini, V. D. Kurilovich, P. Krogstrup, J. Nygård, A. Geresdi, L. I. Glazman, and M. H. Devoret. Microwave susceptibility observation of interacting many-body Andreev states. *Phys. Rev. Lett.*, 129:227701, Nov 2022. doi: 10.1103/PhysRevLett.129.227701. URL https:

//link.aps.org/doi/10.1103/PhysRevLett.129.227701. [Cited on page(s) 94, 109, 250, 256].

D. Feldstein i Bofill. Magnetic field resilient lumped element superconducting resonators. *Master Thesis*, 2022. URL http://resolver.tudelft.nl/uuid:777aaeac-d4a8-4a5a-ad78-e4d99f6d06c8. [Cited on page(s) 55, 58, 59, 60, 61, 63, 256, 297].

D. Flanigan, 2023. To perform the fits we used the code available in the following GitHub repository: https://github.com/danielflanigan/resonator. [Cited on page(s) 223].

C. Flindt, A. S. Sørensen, and K. Flensberg. Spin-orbit mediated control of spin qubits. *Phys Rev Lett*, 97(24), Dec. 2006. ISSN 0031-9007. doi: 10.1103/physrevlett.97.240501. [Cited on page(s) 138, 144].

S. Foletti, H. Bluhm, D. Mahalu, V. Umansky, and A. Yacoby. Universal quantum control of two-electron spin quantum bits using dynamic nuclear polarization. *Nature Physics*, 5(12):903–908, Dec 2009. ISSN 1745-2481. doi: 10.1038/nphys1424. URL https://doi.org/10.1038/nphys1424. [Cited on page(s) 283].

P. Forn-Díaz, J. Lisenfeld, D. Marcos, J. J. García-Ripoll, E. Solano, C. J. P. M. Harmans, and J. E. Mooij. Observation of the Bloch-Siegert shift in a qubit-oscillator system in the ultrastrong coupling regime. *Phys. Rev. Lett.*, 105:237001, Nov 2010. doi: 10.1103/PhysRevLett.105.237001. URL https://link.aps.org/doi/10.1103/PhysRevLett.105.237001. [Cited on page(s) 285].

P. Forn-Díaz, J. García-Ripoll, B. Peropadre, J. Orgiazzi, M. Yurtalan, R. Belyansky, C. Wilson, and A. Lupascu. Ultrastrong coupling of a single artificial atom to an electromagnetic continuum in the nonperturbative regime. *Nature Physics*, 13(1):39–43, Jan 2017. ISSN 1745-2481. doi: 10.1038/nphys3905. URL https://doi.org/10.1038/nphys3905. [Cited on page(s) 285].

P. Forn-Díaz, L. Lamata, E. Rico, J. Kono, and E. Solano. Ultrastrong coupling regimes of light-matter interaction. *Rev Mod Phys*, 91(2):025005, jun 2019. doi: 10.1103/revmodphys.91.025005. [Cited on page(s) 179, 285].

S. Friedel. How to Calculate a Capacitance Matrix in COMSOL Multiphysics, 2017. [Cited on page(s) 35].

A. Frisk Kockum, A. Miranowicz, S. De Liberato, S. Savasta, and F. Nori. Ultrastrong coupling between light and matter. *Nature Reviews Physics*, 1(1):19–40, Jan 2019. ISSN 2522-5820. doi: 10.1038/s42254-018-0006-2. URL https://doi.org/10.1038/s42254-018-0006-2. [Cited on page(s) 285].

L. Fu and C. L. Kane. Superconducting proximity effect and Majorana fermions at the surface of a topological insulator. *Phys. Rev. Lett.*, 100:096407, Mar 2008. doi: 10.1103/PhysRevLett.100.096407. URL https://link.aps.org/doi/10.1103/PhysRevLett.100.096407. [Cited on page(s) 268].

I. C. Fulga, A. Haim, A. R. Akhmerov, and Y. Oreg. Adaptive tuning of Majorana fermions in a quantum dot chain. *New J Phys*, 15, Apr. 2013. ISSN 1367-2630. doi: 10.1088/1367-2630/15/4/045020. [Cited on page(s) 109].

A. Furusaki and M. Tsukada. A unified theory of clean Josephson junctions. *Phys. B Condens. Matter*, 165-166, Aug. 1990. doi: 10.1016/s0921-4526(09)80069-0. [Cited on page(s) 138].

A. García Corral, D. M. T. van Zanten, K. J. Franke, H. Courtois, S. Florens, and C. B. Winkelmann. Magnetic-field-induced transition in a quantum dot coupled to a superconductor. *Phys. Rev. Research*, 2, Mar. 2020. doi: 10.1103/PhysRevResearch.2.012065. [Cited on page(s) 94].

N. A. Gershenfeld and I. L. Chuang. Bulk spin-resonance quantum computation. *Science*, 275(5298):350–356, 1997. doi: 10.1126/science.275.5298.350. URL https://www.science.org/doi/abs/10.1126/science.275.5298.350. [Cited on page(s) 25, 26, 286].

E. Ginossar and E. Grosfeld. Microwave transitions as a signature of coherent parity mixing effects in the Majorana-transmon qubit. *Nature Communications*, 5(1):4772, 2014. ISSN 2041-1723. doi: 10.1038/ncomms5772. [Cited on page(s) 72, 109, 263].

S. M. Girvin. Circuit QED: superconducting qubits coupled to microwave photons. In *Quantum Machines: Measurement and Control of Engineered Quantum Systems: Lecture Notes of the Les Houches Summer School: Volume 96, July 2011*. Oxford University Press, 06 2014. ISBN 9780199681181. doi: 10.1093/acprof:oso/9780199681181.003.0003. URL https://doi.org/10.1093/acprof:oso/9780199681181.003.0003. [Cited on page(s) 32].

S. M. Girvin. Circuit QED: Superconducting qubits coupled to microwave photons. *Lecture Notes of the 12th Capri Spring School on Transport in Nanostructures*, 2016. URL http://www.capri-school.eu/capri16/lectureres/master_cqed_les_houches.pdf. [Cited on page(s) 15, 16, 17].

S. Gladchenko, D. Olaya, E. Dupont-Ferrier, B. Douçot, L. B. Ioffe, and M. E. Gershenson. Superconducting nanocircuits for topologically protected qubits. *Nature Physics*, 5(1):48–53, Jan 2009. ISSN 1745-2481. doi: 10.1038/nphys1151. URL https://doi.org/10.1038/nphys1151. [Cited on page(s) 275].

L. Glazman and K. Matveev. Resonant Josephson current through Kondo impurities in a tunnel barrier. *JETP Lett*, 49(10), May 1989. ISSN 0021-3640. URL http://adsabs.harvard.edu/abs/1989JETPL..49..659G. [Cited on page(s) 94, 139, 140].

L. I. Glazman and G. Catelani. Bogoliubov quasiparticles in superconducting qubits. *SciPost Phys. Lect. Notes*, 2021. doi: 10.21468/SciPostPhysLectNotes.31. [Cited on page(s) 108, 119].

M. F. Goffman, C. Urbina, H. Pothier, J. Nygård, C. M. Marcus, and P. Krogstrup. Conduction channels of an InAs-Al nanowire Josephson weak link. *New Journal of Physics*, 19 (9):092002, sep 2017. doi: 10.1088/1367-2630/aa7641. [Cited on page(s) 10].

D. J. Goldie and S. Withington. Non-equilibrium superconductivity in quantum-sensing superconducting resonators. *Superconductor Science and Technology*, 26(1):015004, nov 2012. doi: 10.1088/0953-2048/26/1/015004. URL https://dx.doi.org/10.1088/0953-2048/26/1/015004. [Cited on page(s) 63].

V. N. Golovach, M. Borhani, and D. Loss. Electric-dipole-induced spin resonance in quantum dots. *Phys Rev B*, 74(16), Oct. 2006. doi: 10.1103/physrevb.74.165319. [Cited on page(s) 138, 144, 173, 177, 246, 281].

A. A. Golubov, M. Y. Kupriyanov, and E. Il'ichev. The current-phase relation in Josephson junctions. *Rev Mod Phys*, 76(2), Apr. 2004. ISSN 0034-6861. doi: 10.1103/RevModPhys.76.411. [Cited on page(s) 8].

Google Quantum AI. Suppressing quantum errors by scaling a surface code logical qubit. *Nature*, 614(7949):676–681, Feb 2023. ISSN 1476-4687. doi: 10.1038/s41586-022-05434-1. URL https://doi.org/10.1038/s41586-022-05434-1. [Cited on page(s) 17, 244].

Google Quantum AI. Phase transition in random circuit sampling. *arXiv e-prints*, art. arXiv:2304.11119, Apr. 2023b. doi: 10.48550/arXiv.2304.11119. [Cited on page(s) 17].

S. E. d. Graaf, A. V. Danilov, A. Adamyan, T. Bauch, and S. E. Kubatkin. Magnetic field resilient superconducting fractal resonators for coupling to free spins. *Journal of Applied Physics*, 112(12):123905, 12 2012. ISSN 0021-8979. doi: 10.1063/1.4769208. URL https://doi.org/10.1063/1.4769208. [Cited on page(s) 63, 64, 256].

P. Groszkowski, A. D. Paolo, A. L. Grimsmo, A. Blais, D. I. Schuster, A. A. Houck, and J. Koch. Coherence properties of the $0-\pi$ qubit. *New J Phys*, 20(4), Apr. 2018. doi: 10.1088/1367-2630/aab7cd. [Cited on page(s) 276].

L. Grünhaupt, N. Maleeva, S. T. Skacel, M. Calvo, F. Levy-Bertrand, A. V. Ustinov, H. Rotzinger, A. Monfardini, G. Catelani, and I. M. Pop. Loss mechanisms and quasiparticle dynamics in superconducting microwave resonators made of thin-film granular aluminum. *Phys. Rev. Lett.*, 121:117001, Sep 2018. doi: 10.1103/PhysRevLett.121.117001. [Cited on page(s) 73].

L. Grünhaupt, M. Spiecker, D. Gusenkova, N. Maleeva, S. T. Skacel, I. Takmakov, F. Valenti, P. Winkel, H. Rotzinger, W. Wernsdorfer, A. V. Ustinov, and I. M. Pop. Granular aluminium as a superconducting material for high-impedance quantum circuits. *Nature Materials*, 18(8):816–819, 2019. ISSN 1476-4660. doi: 10.1038/s41563-019-0350-3. [Cited on page(s) 73].

J. Güttinger, T. Frey, C. Stampfer, T. Ihn, and K. Ensslin. Spin states in graphene quantum dots. *Phys. Rev. Lett.*, 105:116801, Sep 2010. doi: 10.1103/PhysRevLett.105.116801. URL https://link.aps.org/doi/10.1103/PhysRevLett.105.116801. [Cited on page(s) 284].

E. L. Hahn. Spin echoes. *Phys Rev*, 80, Nov. 1950. doi: 10.1103/PhysRev.80.580. [Cited on page(s) 176].

L. Han, M. Chan, D. de Jong, C. Prosko, G. Badawy, S. Gazibegovic, E. P. Bakkers, L. P. Kouwenhoven, F. K. Malinowski, and W. Pfaff. Variable and orbital-dependent spin-orbit field orientations in an InSb double quantum dot characterized via dispersive gate sensing. *Phys. Rev. Appl.*, 19:014063, Jan 2023. doi: 10.1103/PhysRevApplied.19.014063. URL https://link.aps.org/doi/10.1103/PhysRevApplied.19.014063. [Cited on page(s) 144, 175, 231].

R. Hanson, L. P. Kouwenhoven, J. R. Petta, S. Tarucha, and L. M. K. Vandersypen. Spins in few-electron quantum dots. *Rev Mod Phys*, 79, Oct. 2007. doi: 10.1103/RevModPhys.79.1217. [Cited on page(s) 15, 172, 200].

S. Hart, Z. Cui, G. Ménard, M. Deng, A. E. Antipov, R. M. Lutchyn, P. Krogstrup, C. M. Marcus, and K. A. Moler. Current-phase relations of InAs nanowire Josephson junctions: From interacting to multimode regimes. *Phys. Rev. B*, 100:064523, Aug 2019. doi: 10.1103/PhysRevB.100.064523. [Cited on page(s) 10, 72, 123, 161].

P. Harvey-Collard, G. Zheng, J. Dijkema, N. Samkharadze, A. Sammak, G. Scappucci, and L. M. K. Vandersypen. On-Chip Microwave Filters for High-Impedance Resonators with Gate-Defined Quantum Dots. *Physical Review Applied*, 14(3):034025, Sept. 2020. ISSN 2331-7019. doi: 10.1103/PhysRevApplied.14.034025. [Cited on page(s) 33].

P. Harvey-Collard, J. Dijkema, G. Zheng, A. Sammak, G. Scappucci, and L. M. Vandersypen. Coherent spin-spin coupling mediated by virtual microwave photons. *Phys. Rev. X*, 12(2), May 2022. doi: 10.1103/physrevx.12.021026. [Cited on page(s) 172, 200, 287].

F. Hassler, A. R. Akhmerov, and C. W. J. Beenakker. The top-transmon: a hybrid superconducting qubit for parity-protected quantum computation. *New Journal of Physics*, 13(9):095004, sep 2011. doi: 10.1088/1367-2630/13/9/095004. [Cited on page(s) 72, 263].

M. Hays. Realizing an Andreev spin qubit. *PhD Thesis*, 2021. doi: https://doi.org/10.1007/978-3-030-83879-9. Yale University. [Cited on page(s) 16].

M. Hays, G. de Lange, K. Serniak, D. J. van Woerkom, D. Bouman, P. Krogstrup, J. Nygård, A. Geresdi, and M. H. Devoret. Direct microwave measurement of Andreev-bound-state dynamics in a semiconductor-nanowire Josephson junction. *Phys. Rev. Lett.*, 121:047001, Jul 2018. doi: 10.1103/PhysRevLett.121.047001. [Cited on page(s) 16, 72, 94, 106, 107, 189].

M. Hays, V. Fatemi, K. Serniak, D. Bouman, S. Diamond, G. de Lange, P. Krogstrup, J. Nygård, A. Geresdi, and M. H. Devoret. Continuous monitoring of a trapped superconducting spin. *Nature Physics*, Jul 2020. ISSN 1745-2481. doi: 10.1038/s41567-020-0952-3. [Cited on page(s) 16, 72, 94, 106, 107, 138, 145, 176, 188, 189, 199, 200, 250, 256].

M. Hays, V. Fatemi, D. Bouman, J. Cerrillo, S. Diamond, K. Serniak, T. Connolly, P. Krogstrup, J. Nygård, A. L. Yeyati, A. Geresdi, and M. H. Devoret. Coherent manipulation of an Andreev spin qubit. *Science*, 373(6553), July 2021. doi: 10.1126/science.abf0345. [Cited on page(s) 15, 16, 94, 107, 138, 145, 172, 175, 176, 178, 180, 189, 195, 199, 200, 202, 204, 207, 208, 244, 250, 256].

T. M. Hazard, A. Gyenis, A. Di Paolo, A. T. Asfaw, S. A. Lyon, A. Blais, and A. A. Houck. Nanowire superinductance fluxonium qubit. *Phys. Rev. Lett.*, 122:010504, Jan 2019. doi: 10.1103/PhysRevLett.122.010504. URL https://link.aps.org/doi/10.1103/PhysRevLett.122.010504. [Cited on page(s) 73, 84].

Y. He, S. K. Gorman, D. Keith, L. Kranz, J. G. Keizer, and M. Y. Simmons. A two-qubit gate between phosphorus donor electrons in silicon. *Nature*, 571(7765):371–375, July 2019. ISSN 0028-0836, 1476-4687. doi: 10.1038/s41586-019-1381-2. [Cited on page(s) 206].

S. Heedt, M. Quintero-Pérez, F. Borsoi, A. Fursina, N. van Loo, G. P. Mazur, M. P. Nowak, M. Ammerlaan, K. Li, S. Korneychuk, J. Shen, M. A. Y. van de Poll, G. Badawy, S. Gazibegovic, N. de Jong, P. Aseev, K. van Hoogdalem, E. P. A. M. Bakkers, and L. P. Kouwenhoven. Shadow-wall lithography of ballistic superconductor–semiconductor quantum devices. *Nat Commun*, 12(1), Aug. 2021. ISSN 2041-1723. doi: 10.1038/s41467-021-25100-w. [Cited on page(s) 268].

J. Heinsoo, C. K. Andersen, A. Remm, S. Krinner, T. Walter, Y. Salathé, S. Gasparinetti, J.-C. Besse, A. Potočnik, A. Wallraff, and C. Eichler. Rapid high-fidelity multiplexed readout of superconducting qubits. *Phys. Rev. Applied*, 10, Sept. 2018. doi: 10.1103/PhysRevApplied.10.034040. [Cited on page(s) 106].

N. W. Hendrickx, D. P. Franke, A. Sammak, M. Kouwenhoven, D. Sabbagh, L. Yeoh, R. Li, M. L. V. Tagliaferri, M. Virgilio, G. Capellini, G. Scappucci, and M. Veldhorst. Gate-controlled quantum dots and superconductivity in planar germanium. *Nat Commun*, 9(1), July 2018. ISSN 2041-1723. doi: 10.1038/s41467-018-05299-x. [Cited on page(s) 180, 209, 283, 284].

N. W. Hendrickx, M. L. V. Tagliaferri, M. Kouwenhoven, R. Li, D. P. Franke, A. Sammak, A. Brinkman, G. Scappucci, and M. Veldhorst. Ballistic supercurrent discretization and micrometer-long Josephson coupling in germanium. *Phys. Rev. B*, 99:075435, Feb 2019. doi: 10.1103/PhysRevB.99.075435. URL https://link.aps.org/doi/10.1103/PhysRevB.99.075435. [Cited on page(s) 268].

N. W. Hendrickx, W. I. L. Lawrie, M. Russ, F. Van Riggelen, S. L. De Snoo, R. N. Schouten, A. Sammak, G. Scappucci, and M. Veldhorst. A four-qubit germanium quantum processor. *Nature*, 591(7851):580–585, Mar. 2021. ISSN 0028-0836, 1476-4687. doi: 10.1038/s41586-021-03332-6. [Cited on page(s) 206].

N. W. Hendrickx, L. Massai, M. Mergenthaler, F. Schupp, S. Paredes, S. W. Bedell, G. Salis, and A. Fuhrer. Sweet-spot operation of a germanium hole spin qubit with highly anisotropic noise sensitivity. *arXiv e-prints*, art. arXiv:2305.13150, May 2023. doi: 10.48550/arXiv.2305.13150. [Cited on page(s) 281, 285].

C. Hermansen, A. Levy Yeyati, and J. Paaske. Inductive microwave response of Yu-Shiba-Rusinov states. *Phys Rev B*, 105, Feb. 2022. doi: 10.1103/PhysRevB.105.054503. [Cited on page(s) 94].

T. Hime, P. A. Reichardt, B. L. T. Plourde, T. L. Robertson, C.-E. Wu, A. V. Ustinov, and J. Clarke. Solid-state qubits with current-controlled coupling. *Science*, 314(5804):1427–1429, 2006. doi: 10.1126/science.1134388. URL https://www.science.org/doi/abs/10.1126/science.1134388. [Cited on page(s) 26].

M. Hinderling, D. Sabonis, S. Paredes, D. Haxell, M. Coraiola, S. ten Kate, E. Cheah, F. Krizek, R. Schott, W. Wegscheider, and F. Nichele. Flip-chip-based microwave spectroscopy of Andreev bound states in a planar Josephson junction. *Phys. Rev. Appl.*, 19:054026, May 2023. doi: 10.1103/PhysRevApplied.19.054026. URL https://link.aps.org/doi/10.1103/PhysRevApplied.19.054026. [Cited on page(s) 267].

M. Hinderling, S. C. ten Kate, D. Z. Haxell, M. Coraiola, S. Paredes, E. Cheah, F. Krizek, R. Schott, W. Wegscheider, D. Sabonis, and F. Nichele. Flip-chip-based fast inductive parity readout of a planar superconducting island. *arXiv e-prints*, art. arXiv:2307.06718, July 2023b. doi: 10.48550/arXiv.2307.06718. [Cited on page(s) 267].

S. Hoffman, M. Hays, T. Hazar, K. Serniak, and C. Tahan. Decoherence mechanisms in Andreev spin qubits. *March Meeting of the APS, S67.3*, 2023. URL https://meetings.aps.org/Meeting/MAR23/Session/S67.3. [Cited on page(s) 280].

S. S. Hong, A. T. Papageorge, P. Sivarajah, G. Crossman, N. Didier, A. M. Polloreno, E. A. Sete, S. W. Turkowski, M. P. da Silva, and B. R. Johnson. Demonstration of a parametrically activated entangling gate protected from flux noise. *Phys. Rev. A*, 101:012302, Jan 2020. doi: 10.1103/PhysRevA.101.012302. URL https://link.aps.org/doi/10.1103/PhysRevA.101.012302. [Cited on page(s) 244].

A. A. Houck, J. A. Schreier, B. R. Johnson, J. M. Chow, J. Koch, J. M. Gambetta, D. I. Schuster, L. Frunzio, M. H. Devoret, S. M. Girvin, and R. J. Schoelkopf. Controlling the spontaneous emission of a superconducting transmon qubit. *Phys. Rev. Lett.*, 101:080502, Aug 2008. doi: 10.1103/PhysRevLett.101.080502. URL https://link.aps.org/doi/10.1103/PhysRevLett.101.080502. [Cited on page(s) 25].

Y. Huang, H. Pan, C.-X. Liu, J. D. Sau, T. D. Stanescu, and S. Das Sarma. Metamorphosis of Andreev bound states into Majorana bound states in pristine nanowires. *Phys. Rev. B*, 98:144511, Oct 2018. [Cited on page(s) 83].

L. Huthmacher, R. Stockill, E. Clarke, M. Hugues, C. Le Gall, and M. Atatüre. Coherence of a dynamically decoupled quantum-dot hole spin. *Phys. Rev. B*, 97:241413, Jun 2018. doi: 10.1103/PhysRevB.97.241413. URL https://link.aps.org/doi/10.1103/PhysRevB.97.241413. [Cited on page(s) 281].

T. Hyart, B. van Heck, I. C. Fulga, M. Burrello, A. R. Akhmerov, and C. W. J. Beenakker. Flux-controlled quantum computation with Majorana fermions. *Phys. Rev. B*, 88: 035121, Jul 2013. doi: 10.1103/PhysRevB.88.035121. [Cited on page(s) 72, 263].

IBM Quantum. Compute resources. https://quantum-computing.ibm.com/services?services=systems, 2022a. Accessed: 2022-06-13. [Cited on page(s) 172].

IBM Quantum. Compute resources. https://quantum-computing.ibm.com/services?services=systems, 2022b. Accessed: Oct-2023. [Cited on page(s) 244].

N. Iossad. Metal nitrides for superconducting tunnel detectors. *PhD Thesis*, 2002. URL http://resolver.tudelft.nl/uuid:d4ec36d6-50b8-4617-bd01-17eb3d2aae12. [Cited on page(s) 291, 292].

K. M. Itoh and H. Watanabe. Isotope engineering of silicon and diamond for quantum computing and sensing applications. *MRS Communications*, 4(4):143–157, Dec 2014. ISSN 2159-6867. doi: 10.1557/mrc.2014.32. URL https://doi.org/10.1557/mrc.2014.32. [Cited on page(s) 284].

D. A. Ivanov and M. V. Feigel'man. Coulomb effects in a ballistic one-channel s-s-s device. *Physics-Uspekhi*, 41(2):197–201, feb 1998. doi: 10.1070/pu1998v041n02abeh000363. [Cited on page(s) 270].

D. A. Ivanov and M. V. Feigel'man. Two-level Hamiltonian of a superconducting quantum point contact. *Phys. Rev. B*, 59:8444–8446, Apr 1999. doi: 10.1103/PhysRevB.59.8444. [Cited on page(s) 270].

C. Janvier, L. Tosi, L. Bretheau, Ç. O. Girit, M. Stern, P. Bertet, P. Joyez, D. Vion, D. Esteve, M. F. Goffman, H. Pothier, and C. Urbina. Coherent manipulation of Andreev states in superconducting atomic contacts. *Science*, 349(6253), Sept. 2015. doi: 10.1126/science.aab2179. [Cited on page(s) 72, 94, 107, 189, 287].

X. Jin, A. Kamal, A. Sears, T. Gudmundsen, D. Hover, J. Miloshi, R. Slattery, F. Yan, J. Yoder, T. Orlando, S. Gustavsson, and W. Oliver. Thermal and residual excited-state population in a 3D transmon qubit. *Phys Rev Lett*, 114(24), June 2015. doi: 10.1103/physrevlett.114.240501. [Cited on page(s) 144, 189, 230].

J. Johansson, P. Nation, and F. Nori. Qutip 2: A python framework for the dynamics of open quantum systems. *Computer Physics Communications*, 184(4):1234–1240, 2013. ISSN 0010-4655. doi: https://doi.org/10.1016/j.cpc.2012.11.019. URL https://www.sciencedirect.com/science/article/pii/S0010465512003955. [Cited on page(s) 213].

J. E. Johnson, C. Macklin, D. H. Slichter, R. Vijay, E. B. Weingarten, J. Clarke, and I. Siddiqi. Heralded state preparation in a superconducting qubit. *Phys. Rev. Lett.*, 109:050506, Aug 2012. doi: 10.1103/PhysRevLett.109.050506. URL https://link.aps.org/doi/10.1103/PhysRevLett.109.050506. [Cited on page(s) 253].

J. Jones. Course 10 - Nuclear magnetic resonance quantum computation. In D. Estève, J.-M. Raimond, and J. Dalibard, editors, *Quantum Entanglement and Information Processing*, volume 79 of *Les Houches*, pages 357–400. Elsevier, 2004. doi: https://doi.org/10.1016/S0924-8099(03)80034-3. URL https://www.sciencedirect.com/science/article/pii/S0924809903800343. [Cited on page(s) 25].

J. Jones and E. Knill. Efficient refocusing of one-spin and two-spin interactions for NMR quantum computation. *Journal of Magnetic Resonance*, 141(2):322–325, 1999. ISSN 1090-7807. doi: https://doi.org/10.1006/jmre.1999.1890. URL https://www.sciencedirect.com/science/article/pii/S1090780799918906. [Cited on page(s) 26].

H. I. Jørgensen, K. Grove-Rasmussen, K. Flensberg, and P. E. Lindelof. Critical and excess current through an open quantum dot: Temperature and magnetic-field dependence. *Phys Rev B*, 79, Apr. 2009. doi: 10.1103/PhysRevB.79.155441. [Cited on page(s) 94].

B. Josephson. Possible new effects in superconductive tunnelling. *Physics Letters*, 1 (7):251–253, 1962. ISSN 0031-9163. doi: https://doi.org/10.1016/0031-9163(62)91369-0. URL https://www.sciencedirect.com/science/article/pii/0031916362913690. [Cited on page(s) 8].

H. I. Jørgensen, T. Novotný, K. Grove-Rasmussen, K. Flensberg, and P. E. Lindelof. Critical current 0-π transition in designed Josephson quantum dot junctions. *Nano Letters*, 7(8):2441–2445, 2007. doi: 10.1021/nl071152w. URL https://doi.org/10.1021/nl071152w. PMID: 17637018. [Cited on page(s) 13, 94, 103].

A. Kadlecová, M. Žonda, and T. Novotný. Quantum dot attached to superconducting leads: Relation between symmetric and asymmetric coupling. *Phys Rev B*, 95(19), May 2017. doi: 10.1103/physrevb.95.195114. [Cited on page(s) 103, 112].

A. Kadlecová, M. Žonda, V. Pokorný, and T. Novotný. Practical guide to quantum phase transitions in quantum-dot-based tunable Josephson junctions. *Phys. Rev. Applied*, 11, Apr. 2019. doi: 10.1103/PhysRevApplied.11.044094. [Cited on page(s) 94, 103, 140].

T. Kadowaki and H. Nishimori. Quantum annealing in the transverse Ising model. *Phys. Rev. E*, 58:5355–5363, Nov 1998. doi: 10.1103/PhysRevE.58.5355. URL https://link.aps.org/doi/10.1103/PhysRevE.58.5355. [Cited on page(s) 249].

K. Kalashnikov, W. T. Hsieh, W. Zhang, W.-S. Lu, P. Kamenov, A. Di Paolo, A. Blais, M. E. Gershenson, and M. Bell. Bifluxon: Fluxon-parity-protected superconducting qubit. *PRX Quantum*, 1:010307, Sep 2020. doi: 10.1103/PRXQuantum.1.010307. [Cited on page(s) 73, 275, 277].

P. Kamenov, W.-S. Lu, K. Kalashnikov, T. DiNapoli, M. T. Bell, and M. E. Gershenson. Granular aluminum meandered superinductors for quantum circuits. *Phys. Rev. Appl.*, 13: 054051, May 2020. doi: 10.1103/PhysRevApplied.13.054051. URL https://link.aps.org/doi/10.1103/PhysRevApplied.13.054051. [Cited on page(s) 278].

H. Kamerlingh Onnes. The liquefaction of helium. *Commun. Phys. Lab. Univ. Leiden*, page 108, 1908. [Cited on page(s) 2].

H. Kamerlingh Onnes. Further experiments with liquid helium. B. On the change in the resistance of pure metals at very low temperatures, etc. III. The resistance of platinum at helium temperatures. *Koninklijke Nederlandse Akademie van Wetenschappen Proceedings Series B Physical Sciences*, 1911. [Cited on page(s) 2].

C. Karrasch and V. Meden. Supercurrent and multiple singlet-doublet phase transitions of a quantum dot Josephson junction inside an Aharonov-Bohm ring. *Phys Rev B*, 79 (4), Jan. 2009. doi: 10.1103/physrevb.79.045110. [Cited on page(s) 147].

C. Karrasch, A. Oguri, and V. Meden. Josephson current through a single Anderson impurity coupled to BCS leads. *Phys Rev B*, 77, 2008. ISSN 1098-0121. doi: 10.1103/physrevb.77.024517. [Cited on page(s) 94, 140, 147].

T. Karzig, C. Knapp, R. M. Lutchyn, P. Bonderson, M. B. Hastings, C. Nayak, J. Alicea, K. Flensberg, S. Plugge, Y. Oreg, C. M. Marcus, and M. H. Freedman. Scalable designs

for quasiparticle-poisoning-protected topological quantum computation with Majorana zero modes. *Phys. Rev. B*, 95:235305, Jun 2017. doi: 10.1103/PhysRevB.95.235305. [Cited on page(s) 94, 109].

E. Kawakami, P. Scarlino, D. R. Ward, F. R. Braakman, D. E. Savage, M. G. Lagally, M. Friesen, S. N. Coppersmith, M. A. Eriksson, and L. M. K. Vandersypen. Electrical control of a long-lived spin qubit in a Si/SiGe quantum dot. *Nature Nanotechnology*, 9(9):666–670, Sep 2014. ISSN 1748-3395. doi: 10.1038/nnano.2014.153. URL https://doi.org/10.1038/nnano.2014.153. [Cited on page(s) 283].

A. Keselman, C. Murthy, B. van Heck, and B. Bauer. Spectral response of Josephson junctions with low-energy quasiparticles. *SciPost Physics*, 7(4), May 2019. doi: 10.21468/SciPostPhys.7.4.050. [Cited on page(s) 99, 109].

A. V. Khaetskii, D. Loss, and L. Glazman. Electron spin decoherence in quantum dots due to interaction with nuclei. *Phys. Rev. Lett.*, 88:186802, Apr 2002. doi: 10.1103/PhysRevLett.88.186802. URL https://link.aps.org/doi/10.1103/PhysRevLett.88.186802. [Cited on page(s) 280].

M. S. Khalil, M. J. A. Stoutimore, F. C. Wellstood, and K. D. Osborn. An analysis method for asymmetric resonator transmission applied to superconducting devices. *Journal of Applied Physics*, 111(5):054510, 2012. URL https://aip.scitation.org/doi/10.1063/1.3692073. [Cited on page(s) 60, 62, 223].

S. P. Kikken. Measuring film resistivity: understanding and refining the four-point probe set-up. *Bachelor Thesis*, 2018. [Cited on page(s) 296].

Y. Kim, A. Eddins, S. Anand, K. X. Wei, E. van den Berg, S. Rosenblatt, H. Nayfeh, Y. Wu, M. Zaletel, K. Temme, and A. Kandala. Evidence for the utility of quantum computing before fault tolerance. *Nature*, 618(7965):500–505, Jun 2023. ISSN 1476-4687. doi: 10.1038/s41586-023-06096-3. URL https://doi.org/10.1038/s41586-023-06096-3. [Cited on page(s) 17, 249].

G. Kiršanskas, M. Goldstein, K. Flensberg, L. I. Glazman, and J. Paaske. Yu-Shiba-Rusinov states in phase-biased superconductor–quantum dot–superconductor junctions. *Phys Rev B*, 92, Dec. 2015. doi: 10.1103/PhysRevB.92.235422. [Cited on page(s) 104].

A. A. Kiselev, E. L. Ivchenko, and U. Rössler. Electron *g* factor in one- and zero-dimensional semiconductor nanostructures. *Phys. Rev. B.*, 58(24), Dec. 1998. doi: 10.1103/physrevb.58.16353. [Cited on page(s) 145, 166].

A. Y. Kitaev. Unpaired Majorana fermions in quantum wires. *Physics-Uspekhi*, 44(10S): 131–136, oct 2001. doi: 10.1070/1063-7869/44/10s/s29. [Cited on page(s) 11, 72, 266].

J. Koch, T. M. Yu, J. Gambetta, A. A. Houck, D. I. Schuster, J. Majer, A. Blais, M. H. Devoret, S. M. Girvin, and R. J. Schoelkopf. Charge-insensitive qubit design derived from the Cooper pair box. *Phys. Rev. A*, 76:042319, Oct 2007. doi: 10.1103/PhysRevA.76.042319. [Cited on page(s) 15, 17, 19, 96, 97, 114, 124, 141, 154, 172, 178, 202].

J. Koch, V. Manucharyan, M. H. Devoret, and L. I. Glazman. Charging effects in the inductively shunted Josephson junction. *Phys. Rev. Lett.*, 103:217004, Nov 2009. doi: 10.1103/PhysRevLett.103.217004. [Cited on page(s) 18].

F. H. L. Koppens, J. A. Folk, J. M. Elzerman, R. Hanson, L. H. W. van Beveren, I. T. Vink, H. P. Tranitz, W. Wegscheider, L. P. Kouwenhoven, and L. M. K. Vandersypen. Control and detection of singlet-triplet mixing in a random nuclear field. *Science*, 309(5739): 1346–1350, 2005. doi: 10.1126/science.1113719. URL https://www.science.org/doi/abs/10.1126/science.1113719. [Cited on page(s) 282].

F. H. L. Koppens, C. Buizert, K. J. Tielrooij, I. T. Vink, K. C. Nowack, T. Meunier, L. P. Kouwenhoven, and L. M. K. Vandersypen. Driven coherent oscillations of a single electron spin in a quantum dot. *Nature*, 442(7104):766–771, Aug 2006. ISSN 1476-4687. doi: 10.1038/nature05065. URL https://doi.org/10.1038/nature05065. [Cited on page(s) 15].

F. H. L. Koppens, K. C. Nowack, and L. M. K. Vandersypen. Spin echo of a single electron spin in a quantum dot. *Phys. Rev. Lett.*, 100:236802, Jun 2008. doi: 10.1103/PhysRevLett.100.236802. URL https://link.aps.org/doi/10.1103/PhysRevLett.100.236802. [Cited on page(s) 282].

P. Krantz, M. Kjaergaard, F. Yan, T. P. Orlando, S. Gustavsson, and W. D. Oliver. A quantum engineer's guide to superconducting qubits. *Applied Physics Reviews*, 6(2), 06 2019. ISSN 1931-9401. doi: 10.1063/1.5089550. URL https://doi.org/10.1063/1.5089550. 021318. [Cited on page(s) 15, 22].

A. Kringhøj, L. Casparis, M. Hell, T. W. Larsen, F. Kuemmeth, M. Leijnse, K. Flensberg, P. Krogstrup, J. Nygård, K. D. Petersson, and C. M. Marcus. Anharmonicity of a superconducting qubit with a few-mode Josephson junction. *Phys Rev B*, 97(6), Feb. 2018. ISSN 2469-9969. doi: 10.1103/PhysRevB.97.060508. [Cited on page(s) 117, 156].

A. Kringhøj, B. van Heck, T. W. Larsen, O. Erlandsson, D. Sabonis, P. Krogstrup, L. Casparis, K. D. Petersson, and C. M. Marcus. Suppressed charge dispersion via resonant tunneling in a single-channel transmon. *Phys. Rev. Lett.*, 124:246803, Jun 2020. doi: 10.1103/PhysRevLett.124.246803. [Cited on page(s) 84, 94, 100, 117, 155, 181, 268, 269, 277].

A. Kringhøj, T. W. Larsen, B. van Heck, D. Sabonis, O. Erlandsson, I. Petkovic, D. I. Pikulin, P. Krogstrup, K. D. Petersson, and C. M. Marcus. Controlled DC monitoring of a superconducting qubit. *Phys. Rev. Lett.*, 124:056801, Feb 2020b. doi: 10.1103/PhysRevLett.124.056801. URL https://link.aps.org/doi/10.1103/PhysRevLett.124.056801. [Cited on page(s) 211].

A. Kringhøj, T. W. Larsen, O. Erlandsson, W. Uilhoorn, J. Kroll, M. Hesselberg, R. McNeil, P. Krogstrup, L. Casparis, C. Marcus, and K. Petersson. Magnetic-field-compatible superconducting transmon qubit. *Phys. Rev. Appl.*, 15:054001, May 2021. doi: 10.1103/PhysRevApplied.15.054001. URL https://link.aps.org/doi/10.1103/PhysRevApplied.15.054001. [Cited on page(s) 202, 234].

S. Krinner, S. Storz, P. Kurpiers, P. Magnard, J. Heinsoo, R. Keller, J. Lütolf, C. Eichler, and A. Wallraff. Engineering cryogenic setups for 100-qubit scale superconducting circuit systems. *EPJ Quantum Technology*, 6(1), may 2019. doi: 10.1140/epjqt/s40507-019-0072-0. [Cited on page(s) 45].

S. Krinner, N. Lacroix, A. Remm, A. D. Paolo, E. Genois, C. Leroux, C. Hellings, S. Lazar, F. Swiadek, J. Herrmann, G. J. Norris, C. K. Andersen, M. Müller, A. Blais, C. Eichler, and A. Wallraff. Realizing repeated quantum error correction in a distance-three surface code. *Nature*, 605(7911), May 2022. doi: 10.1038/s41586-022-04566-8. [Cited on page(s) 17, 34, 244].

H. Krishna-murthy, J. Wilkins, and K. Wilson. Renormalization-group approach to the Anderson model of dilute magnetic alloys. I. Static properties for the symmetric case. *Phys Rev B*, 21(3), Feb. 1980. doi: 10.1103/physrevb.21.1003. [Cited on page(s) 112].

P. Krogstrup, N. L. B. Ziino, W. Chang, S. M. Albrecht, M. H. Madsen, E. Johnson, J. Nygård, C. M. Marcus, and T. S. Jespersen. Epitaxy of semiconductor-superconductor nanowires. *Nature Materials*, 14:400 EP –, Jan 2015. [Cited on page(s) 9, 41, 73, 75, 96, 119, 139, 157, 194, 216, 308].

J. G. Kroll, W. Uilhoorn, K. L. van der Enden, D. de Jong, K. Watanabe, T. Taniguchi, S. Goswami, M. C. Cassidy, and L. P. Kouwenhoven. Magnetic field compatible circuit quantum electrodynamics with graphene Josephson junctions. *Nature Communications*, 9(1):4615, 2018. ISSN 2041-1723. doi: 10.1038/s41467-018-07124-x. [Cited on page(s) 67, 72, 202, 268, 284].

J. G. Kroll, F. Borsoi, K. L. van der Enden, W. Uilhoorn, D. de Jong, M. Quintero-Pérez, D. J. van Woerkom, A. Bruno, S. R. Plissard, D. Car, E. P. A. M. Bakkers, M. C. Cassidy, and L. P. Kouwenhoven. Magnetic-field-resilient superconducting coplanar-waveguide resonators for hybrid circuit quantum electrodynamics experiments. *Phys. Rev. Applied*, 11:064053, Jun 2019. doi: 10.1103/PhysRevApplied.11.064053. [Cited on page(s) 40, 63, 64, 66, 67, 97, 202, 256].

I. Kulik. Macroscopic quantization and the proximity effect in SNS junctions. *Soviet Journal of Experimental and Theoretical Physics*, 30:944, 1969. URL `http://www.jetp.ras.ru/cgi-bin/dn/e_030_05_0944.pdf`. [Cited on page(s) 138].

A. Kumar, M. Gaim, D. Steininger, A. Levy Yeyati, A. Martín-Rodero, A. K. Hüttel, and C. Strunk. Temperature dependence of Andreev spectra in a superconducting carbon nanotube quantum dot. *Phys Rev B*, 89, Feb. 2014. doi: 10.1103/PhysRevB.89.075428. [Cited on page(s) 94].

P. D. Kurilovich, V. D. Kurilovich, V. Fatemi, M. H. Devoret, and L. I. Glazman. Microwave response of an Andreev bound state. *Phys Rev B*, 104, Nov. 2021. doi: 10.1103/PhysRevB.104.174517. [Cited on page(s) 94, 99].

A. J. Landig, J. V. Koski, P. Scarlino, U. C. Mendes, A. Blais, C. Reichl, W. Wegscheider, A. Wallraff, K. Ensslin, and T. Ihn. Coherent spin–photon coupling using a resonant exchange qubit. *Nature*, 560(7717), Aug. 2018. ISSN 1476-4687. doi: 10.1038/s41586-018-0365-y. [Cited on page(s) 172, 200].

A. J. Landig, J. V. Koski, P. Scarlino, C. Müller, J. C. Abadillo-Uriel, B. Kratochwil, C. Reichl, W. Wegscheider, S. N. Coppersmith, M. Friesen, A. Wallraff, T. Ihn, and K. Ensslin. Virtual-photon-mediated spin-qubit–transmon coupling. *Nat Commun*, 10(1), Nov. 2019. ISSN 2041-1723. doi: 10.1038/s41467-019-13000-z. [Cited on page(s) 178, 197, 285].

T. W. Larsen. Mesoscopic Superconductivity towards Protected Qubits. 2018. PhD thesis. University of Copenhagen. [Cited on page(s) 275].

T. W. Larsen, K. D. Petersson, F. Kuemmeth, T. S. Jespersen, P. Krogstrup, J. Nygård, and C. M. Marcus. Semiconductor-nanowire-based superconducting qubit. *Phys. Rev. Lett.*, 115:127001, Sep 2015. doi: 10.1103/PhysRevLett.115.127001. [Cited on page(s) 11, 72, 77, 94, 202, 234].

T. W. Larsen, M. E. Gershenson, L. Casparis, A. Kringhøj, N. J. Pearson, R. P. G. McNeil, F. Kuemmeth, P. Krogstrup, K. D. Petersson, and C. M. Marcus. Parity-protected superconductor-semiconductor qubit. *Phys Rev Lett*, 125, July 2020. doi: 10.1103/PhysRevLett.125.056801. [Cited on page(s) 109, 275, 277].

K. Laubscher, J. D. Sau, and S. Das Sarma. Majorana zero modes in gate-defined germanium hole nanowires. *arXiv e-prints*, art. arXiv:2305.14313, May 2023. doi: 10.48550/arXiv.2305.14313. [Cited on page(s) 268].

N. Lauk, N. Sinclair, S. Barzanjeh, J. P. Covey, M. Saffman, M. Spiropulu, and C. Simon. Perspectives on quantum transduction. *Quantum Sci. Technol.*, 5(2), Mar. 2020. doi: 10.1088/2058-9565/ab788a. [Cited on page(s) 138].

P. C. Lauterbur. Image formation by induced local interactions: Examples employing nuclear magnetic resonance. *Nature*, 242(5394):190–191, Mar 1973. ISSN 1476-4687. doi: 10.1038/242190a0. URL https://doi.org/10.1038/242190a0. [Cited on page(s) 2].

W. Lawrie. Spin qubits in silicon and germanium. *PhD Thesis*, 2022. doi: 10.4233/UUID:9CD36947-5E27-4436-9BBB-D7FC5DAA6047. [Cited on page(s) 281, 284, 285].

W. I. L. Lawrie, N. W. Hendrickx, F. van Riggelen, M. Russ, L. Petit, A. Sammak, G. Scappucci, and M. Veldhorst. Spin relaxation benchmarks and individual qubit addressability for holes in quantum dots. *Nano Letters*, 20(10):7237–7242, Oct 2020. ISSN 1530-6984. doi: 10.1021/acs.nanolett.0c02589. URL https://doi.org/10.1021/acs.nanolett.0c02589. [Cited on page(s) 282].

N. H. Le, M. Cykiert, and E. Ginossar. Scalable and robust quantum computing on qubit arrays with fixed coupling. *npj Quantum Information*, 9(1):1, Jan 2023. ISSN 2056-6387. doi: 10.1038/s41534-022-00668-3. URL https://doi.org/10.1038/s41534-022-00668-3. [Cited on page(s) 26].

E. J. Lee, X. Jiang, M. Houzet, R. Aguado, C. M. Lieber, and S. De Franceschi. Spin-resolved Andreev levels and parity crossings in hybrid superconductor-semiconductor nanostructures. *Nat Nanotechnol*, 9(1), Dec. 2014. ISSN 1748-3395. doi: 10.1038/nnano.2013.267. URL http://www.nature.com/naturenanotechnology. [Cited on page(s) 13, 94, 103, 105].

E. J. H. Lee, X. Jiang, R. Aguado, G. Katsaros, C. M. Lieber, and S. De Franceschi. Zero-bias anomaly in a nanowire quantum dot coupled to superconductors. *Phys Rev Lett*, 109, Oct. 2012. doi: 10.1103/PhysRevLett.109.186802. [Cited on page(s) 94].

E. J. H. Lee, X. Jiang, R. Žitko, R. Aguado, C. M. Lieber, and S. De Franceschi. Scaling of subgap excitations in a superconductor-semiconductor nanowire quantum dot. *Phys. Rev. B*, 95:180502, May 2017. doi: 10.1103/PhysRevB.95.180502. URL https://link.aps.org/doi/10.1103/PhysRevB.95.180502. [Cited on page(s) 13, 94, 103].

C. Leroux and A. Blais. Cat-qubit-inspired gate on $\cos(2\theta)$ qubits, 2023. [Cited on page(s) 277].

R. Li, L. Petit, D. P. Franke, J. P. Dehollain, J. Helsen, M. Steudtner, N. K. Thomas, Z. R. Yoscovits, K. J. Singh, S. Wehner, L. M. K. Vandersypen, J. S. Clarke, and M. Veldhorst. A crossbar network for silicon quantum dot qubits. *Science Advances*, 4(7):eaar3960, 2018. doi: 10.1126/sciadv.aar3960. URL https://www.science.org/doi/abs/10.1126/sciadv.aar3960. [Cited on page(s) 244].

S. Li, N. Kang, P. Caroff, and H. Q. Xu. $0-\pi$ phase transition in hybrid superconductor–InSb nanowire quantum dot devices. *Phys Rev B*, 95, Jan. 2017. doi: 10.1103/PhysRevB.95.014515. [Cited on page(s) 94].

Y. X. Li, P. J. French, and R. F. Wolffenbuttel. Effects of plasma etching chemistry and post-processing on the mechanical adhesion and electrical contact of double polysilicon layer structures. *IEEE TRANSACTIONS ON ELECTRON DEVICES*, 42, January 1995. [Cited on page(s) 57].

D. Liang and X. Gao. Strong tuning of Rashba spin–orbit interaction in single InAs nanowires. *Nano Lett.*, 12(6), May 2012. doi: 10.1021/nl301325h. [Cited on page(s) 140].

N. Linden, H. Barjat, and R. Freeman. An implementation of the Deutsch–Jozsa algorithm on a three-qubit NMR quantum computer. *Chemical Physics Letters*, 296(1):61–67, 1998. ISSN 0009-2614. doi: https://doi.org/10.1016/S0009-2614(98)01015-X. URL https://www.sciencedirect.com/science/article/pii/S000926149801015X. [Cited on page(s) 26, 286].

J. Linder and J. W. A. Robinson. Superconducting spintronics. *Nature Physics*, 11(4):307–315, apr 2015. doi: 10.1038/nphys3242. [Cited on page(s) 145].

X. Liu, Z. Hao, E. Khalaf, J. Y. Lee, Y. Ronen, H. Yoo, D. Haei Najafabadi, K. Watanabe, T. Taniguchi, A. Vishwanath, and P. Kim. Tunable spin-polarized correlated states in twisted double bilayer graphene. *Nature*, 583(7815):221–225, Jul 2020. ISSN 1476-4687. doi: 10.1038/s41586-020-2458-7. URL https://doi.org/10.1038/s41586-020-2458-7. [Cited on page(s) 83].

J. Long, T. Zhao, M. Bal, R. Zhao, G. S. Barron, H.-s. Ku, J. A. Howard, X. Wu, C. R. H. McRae, X.-H. Deng, G. J. Ribeill, M. Singh, T. A. Ohki, E. Barnes, S. E. Economou, and D. P. Pappas. A universal quantum gate set for transmon qubits with strong ZZ interactions. *arXiv e-prints*, art. arXiv:2103.12305, Mar. 2021. doi: 10.48550/arXiv.2103.12305. [Cited on page(s) 26].

D. Loss and D. P. DiVincenzo. Quantum computation with quantum dots. *Phys Rev A*, 57, Jan. 1998. doi: 10.1103/PhysRevA.57.120. [Cited on page(s) 15, 172, 200, 206].

M. Luethi, K. Laubscher, S. Bosco, D. Loss, and J. Klinovaja. Planar Josephson junctions in germanium: Effect of cubic spin-orbit interaction. *Phys. Rev. B*, 107:035435, Jan 2023. doi: 10.1103/PhysRevB.107.035435. URL https://link.aps.org/doi/10.1103/PhysRevB.107.035435. [Cited on page(s) 268].

M. Luethi, H. F. Legg, K. Laubscher, D. Loss, and J. Klinovaja. Majorana bound states in germanium Josephson junctions via phase control. *arXiv e-prints*, art. arXiv:2304.12689, Apr. 2023b. doi: 10.48550/arXiv.2304.12689. [Cited on page(s) 268].

D. J. Luitz, F. F. Assaad, T. Novotný, C. Karrasch, and V. Meden. Understanding the Josephson current through a Kondo-correlated quantum dot. *Phys Rev Lett*, 108, May 2012. doi: 10.1103/PhysRevLett.108.227001. [Cited on page(s) 94, 140].

R. M. Lutchyn, E. P. A. M. Bakkers, L. P. Kouwenhoven, P. Krogstrup, C. M. Marcus, and Y. Oreg. Majorana zero modes in superconductor-semiconductor heterostructures. *Nature Reviews Materials*, 3(5):52–68, 2018. doi: 10.1038/s41578-018-0003-1. [Cited on page(s) 72].

F. Lüthi. Circuit Quantum Electrodynamics in a Magnetic Field. 2019. doi: 10.4233/uuid:5986ee2b-e9e6-42ed-a932-bddd5e78648e. PhD thesis. TU Delft. [Cited on page(s) 275].

F. Luthi, T. Stavenga, O. W. Enzing, A. Bruno, C. Dickel, N. K. Langford, M. A. Rol, T. S. Jespersen, J. Nygård, P. Krogstrup, and L. DiCarlo. Evolution of nanowire transmon qubits and their coherence in a magnetic field. *Phys. Rev. Lett.*, 120:100502, Mar 2018. doi: 10.1103/PhysRevLett.120.100502. [Cited on page(s) 72, 77, 97, 123, 124, 234].

X. Ma, G. Zhang, F. Wu, F. Bao, X. Chang, J. Chen, H. Deng, R. Gao, X. Gao, L. Hu, H. Ji, H.-S. Ku, K. Lu, L. Ma, L. Mao, Z. Song, H. Sun, C. Tang, F. Wang, H. Wang, T. Wang, T. Xia, M. Ying, H. Zhan, T. Zhou, M. Zhu, Q. Zhu, Y. Shi, H.-H. Zhao, and C. Deng. Native approach to controlled-Z gates in inductively coupled fluxonium qubits. *arXiv e-prints*, art. arXiv:2308.16040, Aug. 2023. doi: 10.48550/arXiv.2308.16040. [Cited on page(s) 26, 248, 249, 282].

M. T. Mądzik, S. Asaad, A. Youssry, B. Joecker, K. M. Rudinger, E. Nielsen, K. C. Young, T. J. Proctor, A. D. Baczewski, A. Laucht, V. Schmitt, F. E. Hudson, K. M. Itoh, A. M. Jakob, B. C. Johnson, D. N. Jamieson, A. S. Dzurak, C. Ferrie, R. Blume-Kohout, and A. Morello. Precision tomography of a three-qubit donor quantum processor in silicon. *Nature*, 601(7893):348–353, Jan 2022. ISSN 1476-4687. doi: 10.1038/s41586-021-04292-7. URL https://doi.org/10.1038/s41586-021-04292-7. [Cited on page(s) 244].

T. H. Mainan. Stimulated optical radiation in ruby. *Nature*, 187(4736):493–494, Aug 1960. ISSN 1476-4687. doi: 10.1038/187493a0. URL https://doi.org/10.1038/187493a0. [Cited on page(s) 2].

J. Majer, J. M. Chow, J. M. Gambetta, J. Koch, B. R. Johnson, J. A. Schreier, L. Frunzio, D. I. Schuster, A. A. Houck, A. Wallraff, A. Blais, M. H. Devoret, S. M. Girvin, and R. J. Schoelkopf. Coupling superconducting qubits via a cavity bus. *Nature*, 449:443 EP –, Sep 2007. doi: 10.1038/nature06184. [Cited on page(s) 17, 23, 24].

N. Maleeva, L. Grünhaupt, T. Klein, F. Levy-Bertrand, O. Dupre, M. Calvo, F. Valenti, P. Winkel, F. Friedrich, W. Wernsdorfer, A. V. Ustinov, H. Rotzinger, A. Monfardini, M. V. Fistul, and I. M. Pop. Circuit quantum electrodynamics of granular aluminum resonators. *Nature Communications*, 9(1):3889, 2018. doi: 10.1038/s41467-018-06386-9. [Cited on page(s) 73, 278].

F. K. Malinowski, F. Martins, P. D. Nissen, S. Fallahi, G. C. Gardner, M. J. Manfra, C. M. Marcus, and F. Kuemmeth. Symmetric operation of the resonant exchange qubit. *Phys Rev B*, 96, July 2017. doi: 10.1103/PhysRevB.96.045443. [Cited on page(s) 177, 195].

F. K. Malinowski, F. Martins, L. Cywiński, M. S. Rudner, P. D. Nissen, S. Fallahi, G. C. Gardner, M. J. Manfra, C. M. Marcus, and F. Kuemmeth. Spectrum of the nuclear environment for GaAs spin qubits. *Phys Rev Lett*, 118, Apr. 2017b. doi: 10.1103/PhysRevLett.118.177702. [Cited on page(s) 178, 280].

F. K. Malinowski, F. Martins, P. D. Nissen, E. Barnes, Ł. Cywiński, M. S. Rudner, S. Fallahi, G. C. Gardner, M. J. Manfra, C. M. Marcus, and F. Kuemmeth. Notch filtering the nuclear environment of a spin qubit. *Nature Nanotechnology*, 12(1):16–20, Jan 2017c. ISSN 1748-3395. doi: 10.1038/nnano.2016.170. URL https://doi.org/10.1038/nnano.2016.170. [Cited on page(s) 280, 283].

P. Mansfield and A. A. Maudsley. Medical imaging by NMR. *The British Journal of Radiology*, 50(591):188–194, 1977. doi: 10.1259/0007-1285-50-591-188. URL https://doi.org/10.1259/0007-1285-50-591-188. PMID: 849520. [Cited on page(s) 2].

V. E. Manucharyan. Superinductance. *PhD Thesis*, 2012. Yale University. [Cited on page(s) 73, 269].

V. E. Manucharyan, J. Koch, L. I. Glazman, and M. H. Devoret. Fluxonium: Single Cooper-pair circuit free of charge offsets. *Science*, 326(5949):113–116, 2009. doi: 10.1126/science.1175552. [Cited on page(s) 15, 17, 21, 73, 87, 264, 269, 270].

V. E. Manucharyan, N. A. Masluk, A. Kamal, J. Koch, L. I. Glazman, and M. H. Devoret. Evidence for coherent quantum phase slips across a Josephson junction array. *Phys. Rev. B*, 85:024521, Jan 2012. doi: 10.1103/PhysRevB.85.024521. [Cited on page(s) 269].

A. Martín-Rodero and A. Levy Yeyati. Josephson and Andreev transport through quantum dots. *Adv Phys*, 60(6), Dec. 2011. ISSN 0001-8732. doi: 10.1080/00018732.2011.624266. [Cited on page(s) 12, 94, 140].

J. M. Martinis. Saving superconducting quantum processors from decay and correlated errors generated by gamma and cosmic rays. *npj Quantum Information*, 7(1):90, Jun 2021. ISSN 2056-6387. doi: 10.1038/s41534-021-00431-0. URL https://doi.org/10.1038/s41534-021-00431-0. [Cited on page(s) 63].

J. M. Martinis and K. Osborne. Superconducting Qubits and the Physics of Josephson Junctions. *arXiv e-prints*, art. cond-mat/0402415, Feb. 2004. doi: 10.48550/arXiv.cond-mat/0402415. [Cited on page(s) 8].

J. M. Martinis, S. Nam, J. Aumentado, and C. Urbina. Rabi oscillations in a large Josephson-junction qubit. *Phys. Rev. Lett.*, 89:117901, Aug 2002. doi: 10.1103/PhysRevLett.89.117901. [Cited on page(s) 17].

J. M. Martinis, K. B. Cooper, R. McDermott, M. Steffen, M. Ansmann, K. D. Osborn, K. Cicak, S. Oh, D. P. Pappas, R. W. Simmonds, and C. C. Yu. Decoherence in Josephson qubits from dielectric loss. *Phys. Rev. Lett.*, 95:210503, Nov 2005. doi: 10.1103/PhysRevLett.95.210503. URL https://link.aps.org/doi/10.1103/PhysRevLett.95.210503. [Cited on page(s) 61].

F. J. Matute-Cañadas, C. Metzger, S. Park, L. Tosi, P. Krogstrup, J. Nygård, M. F. Goffman, C. Urbina, H. Pothier, and A. L. Yeyati. Signatures of interactions in the Andreev spectrum of nanowire Josephson junctions. *Phys. Rev. Lett.*, 128:197702, May 2022. doi: 10.1103/PhysRevLett.128.197702. URL https://link.aps.org/doi/10.1103/PhysRevLett.128.197702. [Cited on page(s) 94, 109].

K. A. Matveev, A. I. Larkin, and L. I. Glazman. Persistent current in superconducting nanorings. *Phys. Rev. Lett.*, 89:096802, Aug 2002. doi: 10.1103/PhysRevLett.89.096802. [Cited on page(s) 268].

R. Maurand, T. Meng, E. Bonet, S. Florens, L. Marty, and W. Wernsdorfer. First-order 0–π quantum phase transition in the Kondo regime of a superconducting carbon-nanotube quantum dot. *Phys. Rev. X*, 2, Feb. 2012. doi: 10.1103/PhysRevX.2.011009. [Cited on page(s) 94].

D. C. McKay, C. J. Wood, S. Sheldon, J. M. Chow, and J. M. Gambetta. Efficient z gates for quantum computing. *Phys. Rev. A*, 96:022330, Aug 2017. doi: 10.1103/PhysRevA.96.022330. URL https://link.aps.org/doi/10.1103/PhysRevA.96.022330. [Cited on page(s) 286].

V. Meden. The Anderson–Josephson quantum dot—a theory perspective. *J. Phys.: Condens. Matter*, 31(16), Feb. 2019. doi: 10.1088/1361-648x/aafd6a. [Cited on page(s) 94, 111, 140, 146].

J. Medford, L. Cywiński, C. Barthel, C. M. Marcus, M. P. Hanson, and A. C. Gossard. Scaling of dynamical decoupling for spin qubits. *Phys Rev Lett*, 108, Feb. 2012. doi: 10.1103/PhysRevLett.108.086802. [Cited on page(s) 177].

T. Meng, S. Florens, and P. Simon. Self-consistent description of Andreev bound states in Josephson quantum dot devices. *Phys. Rev. B*, 79:224521, Jun 2009. doi: 10.1103/PhysRevB.79.224521. URL https://link.aps.org/doi/10.1103/PhysRevB.79.224521. [Cited on page(s) 12, 147].

C. Metzger, S. Park, L. Tosi, C. Janvier, A. A. Reynoso, M. F. Goffman, C. Urbina, A. L. Yeyati, and H. Pothier. Circuit-QED with phase-biased Josephson weak links. *Phys. Rev. Research*, 3(1), Jan. 2021. doi: 10.1103/physrevresearch.3.013036. [Cited on page(s) 138, 144, 172, 174, 203].

X. Mi, J. V. Cady, D. M. Zajac, P. W. Deelman, and J. R. Petta. Strong coupling of a single electron in silicon to a microwave photon. *Science*, 355(6321):156–158, 2017. ISSN 0036-8075. doi: 10.1126/science.aal2469. [Cited on page(s) 33, 72].

X. Mi, M. Benito, S. Putz, D. M. Zajac, J. M. Taylor, G. Burkard, and J. R. Petta. A coherent spin–photon interface in silicon. *Nature*, 555(7698), Mar. 2018. ISSN 1476-4687. doi: 10.1038/nature25769. [Cited on page(s) 172, 200].

A. R. Mills, C. R. Guinn, M. J. Gullans, A. J. Sigillito, M. M. Feldman, E. Nielsen, and J. R. Petta. Two-qubit silicon quantum processor with operation fidelity exceeding 99%. *Science Advances*, 8(14):eabn5130, 2022. doi: 10.1126/sciadv.abn5130. URL https://www.science.org/doi/abs/10.1126/sciadv.abn5130. [Cited on page(s) 244].

R. Mizokuchi, R. Maurand, F. Vigneau, M. Myronov, and S. De Franceschi. Ballistic one-dimensional holes with strong g-factor anisotropy in germanium. *Nano Letters*, 18 (8):4861–4865, Aug 2018. ISSN 1530-6984. doi: 10.1021/acs.nanolett.8b01457. URL https://doi.org/10.1021/acs.nanolett.8b01457. [Cited on page(s) 268].

J. E. Mooij and C. J. P. M. Harmans. Phase-slip flux qubits. *New Journal of Physics*, 7: 219–219, oct 2005. doi: 10.1088/1367-2630/7/1/219. [Cited on page(s) 268].

J. E. Mooij and Y. V. Nazarov. Superconducting nanowires as quantum phase-slip junctions. *Nature Physics*, 2(3):169–172, Mar 2006. doi: 10.1038/nphys234. [Cited on page(s) 268].

M. Müller, T. Luschmann, A. Faltermeier, S. Weichselbaumer, L. Koch, G. B. P. Huber, H. W. Schumacher, N. Ubbelohde, D. Reifert, T. Scheller, F. Deppe, A. Marx, S. Filipp, M. Althammer, R. Gross, and H. Huebl. Magnetic field robust high quality factor NbTiN superconducting microwave resonators. *Materials for Quantum Technology*, 2(1):015002, feb 2022. doi: 10.1088/2633-4356/ac50f8. URL https://dx.doi.org/10.1088/2633-4356/ac50f8. [Cited on page(s) 63, 64].

S. Nadj-Perge, S. M. Frolov, E. P. A. M. Bakkers, and L. P. Kouwenhoven. Spin–orbit qubit in a semiconductor nanowire. *Nature*, 468(7327), Dec. 2010. doi: 10.1038/nature09682. [Cited on page(s) 138, 144, 145, 172, 173, 174, 177, 178, 180, 196, 204, 208, 282].

Y. Nakamura, Y. A. Pashkin, and J. S. Tsai. Coherent control of macroscopic quantum states in a single-Cooper-pair box. *Nature*, 398:786 EP –, Apr 1999. doi: 10.1038/19718. [Cited on page(s) 17, 19].

L. B. Nguyen, Y.-H. Lin, A. Somoroff, R. Mencia, N. Grabon, and V. E. Manucharyan. High-coherence fluxonium qubit. *Phys. Rev. X*, 9:041041, Nov 2019. doi: 10.1103/PhysRevX.9.041041. URL https://link.aps.org/doi/10.1103/PhysRevX.9.041041. [Cited on page(s) 282].

T. Niemczyk, F. Deppe, H. Huebl, E. P. Menzel, F. Hocke, M. J. Schwarz, J. J. Garcia-Ripoll, D. Zueco, T. Hümmer, E. Solano, A. Marx, and R. Gross. Circuit quantum electrodynamics in the ultrastrong-coupling regime. *Nature Physics*, 6(10):772–776, Oct 2010. ISSN 1745-2481. doi: 10.1038/nphys1730. URL https://doi.org/10.1038/nphys1730. [Cited on page(s) 285].

A. Noiri, K. Takeda, T. Nakajima, T. Kobayashi, A. Sammak, G. Scappucci, and S. Tarucha. Fast universal quantum gate above the fault-tolerance threshold in silicon. *Nature*, 601(7893):338–342, Jan 2022. ISSN 1476-4687. doi: 10.1038/s41586-021-04182-y. URL https://doi.org/10.1038/s41586-021-04182-y. [Cited on page(s) 244].

K. C. Nowack, F. H. L. Koppens, Y. V. Nazarov, and L. M. K. Vandersypen. Coherent control of a single electron spin with electric fields. *Science*, 318(5855), 2007. doi: 10.1126/science.1148092. [Cited on page(s) 138, 144, 172, 173, 174, 177, 246, 281].

A. Oguri, Y. Tanaka, and A. C. Hewson. Quantum phase transition in a minimal model for the Kondo effect in a Josephson junction. *J. Phys. Soc. Jpn.*, 73, Nov. 2004. ISSN 0031-9015. doi: 10.1143/JPSJ.73.2494. [Cited on page(s) 94, 102, 103, 140, 147].

W. D. Oliver and P. B. Welander. Materials in superconducting quantum bits. *MRS Bulletin*, 38(10):816–825, Oct 2013. ISSN 1938-1425. doi: 10.1557/mrs.2013.229. URL https://doi.org/10.1557/mrs.2013.229. [Cited on page(s) 61].

J.-L. Orgiazzi, C. Deng, D. Layden, R. Marchildon, F. Kitapli, F. Shen, M. Bal, F. R. Ong, and A. Lupascu. Flux qubits in a planar circuit quantum electrodynamics architecture: Quantum control and decoherence. *Phys. Rev. B*, 93:104518, Mar 2016. doi: 10.1103/PhysRevB.93.104518. URL https://link.aps.org/doi/10.1103/PhysRevB.93.104518. [Cited on page(s) 282].

T. P. Orlando, J. E. Mooij, L. Tian, C. H. van der Wal, L. S. Levitov, S. Lloyd, and J. J. Mazo. Superconducting persistent-current qubit. *Phys. Rev. B*, 60:15398–15413, Dec 1999. doi: 10.1103/PhysRevB.60.15398. URL https://link.aps.org/doi/10.1103/PhysRevB.60.15398. [Cited on page(s) 26, 286].

C. Ortega-Taberner, A.-P. Jauho, and J. Paaske. Anomalous Josephson current through a driven double quantum dot. *Phys. Rev. B*, 107:115165, Mar 2023. doi: 10.1103/PhysRevB.107.115165. URL https://link.aps.org/doi/10.1103/PhysRevB.107.115165. [Cited on page(s) 271].

A. D. O'Connell, M. Ansmann, R. C. Bialczak, M. Hofheinz, N. Katz, E. Lucero, C. McKenney, M. Neeley, H. Wang, E. M. Weig, A. N. Cleland, and J. M. Martinis. Microwave dielectric loss at single photon energies and millikelvin temperatures. *Applied Physics Letters*, 92(11):112903, 03 2008. ISSN 0003-6951. doi: 10.1063/1.2898887. URL https://doi.org/10.1063/1.2898887. [Cited on page(s) 61].

J. Paajaste, M. Amado, S. Roddaro, F. S. Bergeret, D. Ercolani, L. Sorba, and F. Giazotto. Pb/InAs nanowire Josephson junction with high critical current and magnetic flux focusing. *Nano Letters*, 15(3):1803–1808, Mar 2015. doi: 10.1021/nl504544s. [Cited on page(s) 72].

C. Padurariu and Y. V. Nazarov. Theoretical proposal for superconducting spin qubits. *Phys Rev B*, 81, Apr. 2010. doi: 10.1103/PhysRevB.81.144519. [Cited on page(s) 13, 14, 15, 16, 25, 26, 94, 109, 138, 139, 140, 142, 144, 145, 164, 172, 173, 180, 187, 199, 200, 204, 205, 207, 209, 210, 211, 212, 223, 244, 247].

S. Park and A. L. Yeyati. Andreev spin qubits in multichannel Rashba nanowires. *Phys Rev B*, 96(12), Sept. 2017. doi: 10.1103/physrevb.96.125416. [Cited on page(s) 138, 172].

L. Pavešić and R. Žitko. Qubit based on spin-singlet Yu-Shiba-Rusinov states. *Phys Rev B*, 105, Feb. 2022. doi: 10.1103/PhysRevB.105.075129. [Cited on page(s) 94].

L. Pavešič, R. Aguado, and R. Žitko. Strong-coupling theory of quantum dot Josephson junctions: the role of a residual quasiparticle. *arXiv e-prints*, art. arXiv:2304.12456, Apr. 2023. doi: 10.48550/arXiv.2304.12456. [Cited on page(s) 271, 272].

L. Pavešić, M. Pita-Vidal, A. Bargerbos, and R. Žitko. Impurity Knight shift in quantum dot Josephson junctions. *SciPost Phys.*, 15:070, 2023b. doi: 10.21468/SciPostPhys.15.2.070. URL https://scipost.org/10.21468/SciPostPhys.15.2.070. [Cited on page(s) 142, 175, 204, 271, 272, 274, 284].

I. V. Pechenezhskiy, R. A. Mencia, L. B. Nguyen, Y.-H. Lin, and V. E. Manucharyan. The superconducting quasicharge qubit. *Nature*, 585(7825):368–371, Sep 2020. ISSN 1476-4687. doi: 10.1038/s41586-020-2687-9. URL https://doi.org/10.1038/s41586-020-2687-9. [Cited on page(s) 277, 278].

D. Pekker, C.-Y. Hou, V. E. Manucharyan, and E. Demler. Proposal for coherent coupling of Majorana zero modes and superconducting qubits using the 4π Josephson effect. *Phys. Rev. Lett.*, 111:107007, Sep 2013. doi: 10.1103/PhysRevLett.111.107007. [Cited on page(s) 72, 73, 83, 263, 264, 265].

J. R. Petta, A. C. Johnson, J. M. Taylor, E. A. Laird, A. Yacoby, M. D. Lukin, C. M. Marcus, M. P. Hanson, and A. C. Gossard. Coherent manipulation of coupled electron spins in semiconductor quantum dots. *Science*, 309(5744):2180–2184, 2005. doi: 10.1126/science.1116955. URL https://www.science.org/doi/abs/10.1126/science.1116955. [Cited on page(s) 282].

D. Phan, J. Senior, A. Ghazaryan, M. Hatefipour, W. M. Strickland, J. Shabani, M. Serbyn, and A. P. Higginbotham. Detecting induced $p \pm ip$ pairing at the Al-InAs interface with a quantum microwave circuit. *Phys. Rev. Lett.*, 128:107701, Mar 2022. doi: 10.1103/PhysRevLett.128.107701. URL https://link.aps.org/doi/10.1103/PhysRevLett.128.107701. [Cited on page(s) 263].

S. G. J. Philips, M. T. Mądzik, S. V. Amitonov, S. L. de Snoo, M. Russ, N. Kalhor, C. Volk, W. I. L. Lawrie, D. Brousse, L. Tryputen, B. P. Wuetz, A. Sammak, M. Veldhorst, G. Scappucci, and L. M. K. Vandersypen. Universal control of a six-qubit quantum processor in silicon. *Nature*, 609(7929):919–924, Sep 2022. ISSN 1476-4687. doi: 10.1038/s41586-022-05117-x. URL https://doi.org/10.1038/s41586-022-05117-x. [Cited on page(s) 244].

D. Pikulin, K. Flensberg, L. I. Glazman, M. Houzet, and R. M. Lutchyn. Coulomb blockade of a nearly open Majorana island. *Phys Rev Lett*, 122(1), Jan. 2019. ISSN 1079-7114. doi: 10.1103/PhysRevLett.122.016801. [Cited on page(s) 13].

D. I. Pikulin, B. van Heck, T. Karzig, E. A. Martinez, B. Nijholt, T. Laeven, G. W. Winkler, J. D. Watson, S. Heedt, M. Temurhan, V. Svidenko, R. M. Lutchyn, M. Thomas, G. de Lange, L. Casparis, and C. Nayak. Protocol to identify a topological superconducting phase in a three-terminal device. *arXiv e-prints*, Mar. 2021. [Cited on page(s) 109].

J. D. Pillet, C. H. L. Quay, P. Morfin, C. Bena, A. Levy Yeyati, and P. Joyez. Andreev bound states in supercurrent-carrying carbon nanotubes revealed. *Nat Phys*, 6(12), Nov.

2010. ISSN 1745-2481. doi: 10.1038/nphys1811. URL http://www.nature.com/naturephysics. [Cited on page(s) 94].

J.-D. Pillet, P. Joyez, R. Žitko, and M. F. Goffman. Tunneling spectroscopy of a single quantum dot coupled to a superconductor: From Kondo ridge to Andreev bound states. *Phys Rev B*, 88, 2013. ISSN 1098-0121. doi: 10.1103/physrevb.88.045101. [Cited on page(s) 94].

D. M. Pino, R. Seoane Souto, and R. Aguado. Minimal Kitaev-transmon qubit based on double quantum dots. *arXiv e-prints*, art. arXiv:2309.12313, Sept. 2023. doi: 10.48550/arXiv.2309.12313. [Cited on page(s) 267].

M. Pita-Vidal, A. Bargerbos, J. J. Wesdorp, and C. K. de Andersen. A gradiometric device and an array of such gradiometric devices, 2023. Patent pending. [Cited on page(s) 50].

J. H. Plantenberg, P. C. de Groot, C. J. P. M. Harmans, and J. E. Mooij. Demonstration of controlled-NOT quantum gates on a pair of superconducting quantum bits. *Nature*, 447(7146):836–839, Jun 2007. ISSN 1476-4687. doi: 10.1038/nature05896. URL https://doi.org/10.1038/nature05896. [Cited on page(s) 25, 26, 286].

S. Plugge, A. Rasmussen, R. Egger, and K. Flensberg. Majorana box qubits. *New J Phys*, 19(1), Jan. 2017. doi: 10.1088/1367-2630/aa54e1. [Cited on page(s) 94].

I. M. Pop, I. Protopopov, F. Lecocq, Z. Peng, B. Pannetier, O. Buisson, and W. Guichard. Measurement of the effect of quantum phase slips in a Josephson junction chain. *Nature Physics*, 6(8):589–592, Aug 2010. ISSN 1745-2481. doi: 10.1038/nphys1697. [Cited on page(s) 268].

I. M. Pop, K. Geerlings, G. Catelani, R. J. Schoelkopf, L. I. Glazman, and M. H. Devoret. Coherent suppression of electromagnetic dissipation due to superconducting quasiparticles. *Nature*, 508:369 EP –, Apr 2014. doi: 10.1038/nature13017. [Cited on page(s) 133].

D. M. Pozar. *Microwave Engineering*. John Wiley & Sons, Inc, Hoboken, NJ, fourth edition edition, 2012. ISBN 978-0-470-63155-3. [Cited on page(s) 32].

E. Prada, P. San-Jose, M. W. A. de Moor, A. Geresdi, E. J. H. Lee, J. Klinovaja, D. Loss, J. Nygård, R. Aguado, and L. P. Kouwenhoven. From Andreev to Majorana bound states in hybrid superconductor–semiconductor nanowires. *Nature Reviews Physics*, 2(10):575–594, Oct 2020. doi: 10.1038/s42254-020-0228-y. URL https://doi.org/10.1038/s42254-020-0228-y. [Cited on page(s) 11, 109].

E. I. Rashba and A. L. Efros. Orbital mechanisms of electron-spin manipulation by an electric field. *Phys Rev Lett*, 91(12), Sept. 2003. doi: 10.1103/physrevlett.91.126405. [Cited on page(s) 138].

S. Richer and D. DiVincenzo. Circuit design implementing longitudinal coupling: A scalable scheme for superconducting qubits. *Phys. Rev. B*, 93:134501, Apr 2016. doi: 10.1103/PhysRevB.93.134501. URL https://link.aps.org/doi/10.1103/PhysRevB.93.134501. [Cited on page(s) 22].

S. Richer, N. Maleeva, S. T. Skacel, I. M. Pop, and D. DiVincenzo. Inductively shunted transmon qubit with tunable transverse and longitudinal coupling. *Phys. Rev. B*, 96: 174520, Nov 2017. doi: 10.1103/PhysRevB.96.174520. URL https://link.aps.org/doi/10.1103/PhysRevB.96.174520. [Cited on page(s) 22, 26].

M. Rol, F. Battistel, F. Malinowski, C. Bultink, B. Tarasinski, R. Vollmer, N. Haider, N. Muthusubramanian, A. Bruno, B. Terhal, and L. DiCarlo. Fast, high-fidelity conditional-phase gate exploiting leakage interference in weakly anharmonic superconducting qubits. *Phys Rev Lett*, 123(12):120502, sep 2019. doi: 10.1103/physrevlett.123.120502. [Cited on page(s) 206].

M. A. Rol, L. Ciorciaro, F. K. Malinowski, B. M. Tarasinski, R. E. Sagastizabal, C. C. Bultink, Y. Salathe, N. Haandbaek, J. Sedivy, and L. DiCarlo. Time-domain characterization and correction of on-chip distortion of control pulses in a quantum processor. *Applied Physics Letters*, 116(5):054001, 02 2020. ISSN 0003-6951. doi: 10.1063/1.5133894. URL https://doi.org/10.1063/1.5133894. [Cited on page(s) 206].

P. Rot. Microwave Spectroscopy of InSb-Al Shadow-Wall Nanowire Josephson Junctions. *Master Thesis, TU Delft*, 2022. [Cited on page(s) 216, 297].

H. Rotzinger, S. T. Skacel, M. Pfirrmann, J. N. Voss, J. Münzberg, S. Probst, P. Bushev, M. P. Weides, A. V. Ustinov, and J. E. Mooij. Aluminium-oxide wires for superconducting high kinetic inductance circuits. *Superconductor Science and Technology*, 30(2): 025002, nov 2016. doi: 10.1088/0953-2048/30/2/025002. [Cited on page(s) 73].

A. Rozhkov and D. Arovas. Interacting-impurity Josephson junction: Variational wave functions and slave-boson mean-field theory. *Phys Rev B*, 62, Sept. 2000. ISSN 0163-1829. doi: 10.1103/physrevb.62.6687. [Cited on page(s) 147].

A. V. Rozhkov, D. P. Arovas, and F. Guinea. Josephson coupling through a quantum dot. *Phys. Rev. B*, 64:233301, Nov 2001. doi: 10.1103/PhysRevB.64.233301. URL https://link.aps.org/doi/10.1103/PhysRevB.64.233301. [Cited on page(s) 271].

E. Sajadi, T. Palomaki, Z. Fei, W. Zhao, P. Bement, C. Olsen, S. Luescher, X. Xu, J. A. Folk, and D. H. Cobden. Gate-induced superconductivity in a monolayer topological insulator. *Science*, 362(6417):922–925, 2018. doi: 10.1126/science.aar4426. URL https://www.science.org/doi/abs/10.1126/science.aar4426. [Cited on page(s) 263].

J. E. Saldaña, A. Vekris, G. Steffensen, R. Žitko, P. Krogstrup, J. Paaske, K. Grove-Rasmussen, and J. Nygård. Supercurrent in a double quantum dot. *Phys Rev Lett*, 121 (25):257701, dec 2018. doi: 10.1103/physrevlett.121.257701. [Cited on page(s) 271].

N. Samkharadze, A. Bruno, P. Scarlino, G. Zheng, D. P. DiVincenzo, L. DiCarlo, and L. M. K. Vandersypen. High-kinetic-inductance superconducting nanowire resonators for circuit QED in a magnetic field. *Phys. Rev. Applied*, 5:044004, Apr 2016. doi: 10.1103/PhysRevApplied.5.044004. [Cited on page(s) 63, 64, 65, 66, 67, 73, 75, 98, 202, 256].

N. Samkharadze, G. Zheng, N. Kalhor, D. Brousse, A. Sammak, U. C. Mendes, A. Blais, G. Scappucci, and L. M. K. Vandersypen. Strong spin-photon coupling in silicon. *Science*, 359(6380):1123–1127, 2018. ISSN 0036-8075. doi: 10.1126/science.aar4054. [Cited on page(s) 172, 200].

S. D. Sarma, M. Freedman, and C. Nayak. Majorana zero modes and topological quantum computation. *Npj Quantum Information*, 1:15001 EP –, Oct 2015. doi: 10.1038/npjqi.2015.1. [Cited on page(s) 72].

M. Sato and Y. Ando. Topological superconductors: a review. *Reports on Progress in Physics*, 80(7):076501, may 2017. doi: 10.1088/1361-6633/aa6ac7. [Cited on page(s) 72].

K. Satori, H. Shiba, O. Sakai, and Y. Shimizu. Numerical renormalization group study of magnetic impurities in superconductors. *J. Phys. Soc. Jpn.*, 61, 1992. ISSN 0031-9015. doi: 10.1143/jpsj.61.3239. [Cited on page(s) 96, 112].

J. D. Sau and S. D. Sarma. Realizing a robust practical Majorana chain in a quantum-dot-superconductor linear array. *Nat Commun*, 3, July 2012. ISSN 2041-1723. doi: 10.1038/ncomms1966. URL https://www.nature.com/articles/ncomms1966. [Cited on page(s) 109].

J. A. Sauls. Andreev bound states and their signatures. *Philos. Trans. Royal Soc. A*, 376 (2125), June 2018. doi: 10.1098/rsta.2018.0140. [Cited on page(s) 138].

G. Scappucci, C. Kloeffel, F. A. Zwanenburg, D. Loss, M. Myronov, J.-J. Zhang, S. De Franceschi, G. Katsaros, and M. Veldhorst. The germanium quantum information route. *Nat. Rev. Mater.*, 6(10), Oct. 2021. ISSN 2058-8437. doi: 10.1038/s41578-020-00262-z. [Cited on page(s) 180, 209, 283].

P. Scarlino, D. J. van Woerkom, U. C. Mendes, J. V. Koski, A. J. Landig, C. K. Andersen, S. Gasparinetti, C. Reichl, W. Wegscheider, K. Ensslin, T. Ihn, A. Blais, and A. Wallraff. Coherent microwave-photon-mediated coupling between a semiconductor and a superconducting qubit. *Nature Communications*, 10(1):3011, Jul 2019. ISSN 2041-1723. doi: 10.1038/s41467-019-10798-6. URL https://doi.org/10.1038/s41467-019-10798-6. [Cited on page(s) 285].

P. Scarlino, J. Ungerer, D. van Woerkom, M. Mancini, P. Stano, C. Müller, A. Landig, J. Koski, C. Reichl, W. Wegscheider, T. Ihn, K. Ensslin, and A. Wallraff. In-situ tuning of the electric-dipole strength of a double-dot charge qubit: Charge-noise protection and ultrastrong coupling. *Phys. Rev. X*, 12(3):031004, jul 2022. doi: 10.1103/physrevx.12.031004. [Cited on page(s) 179, 285].

C. Schrade, C. M. Marcus, and A. Gyenis. Protected hybrid superconducting qubit in an array of gate-tunable Josephson interferometers. *PRX Quantum*, 3(030303), June 2022. [Cited on page(s) 275, 277].

J. A. Schreier, A. A. Houck, J. Koch, D. I. Schuster, B. R. Johnson, J. M. Chow, J. M. Gambetta, J. Majer, L. Frunzio, M. H. Devoret, S. M. Girvin, and R. J. Schoelkopf. Suppressing charge noise decoherence in superconducting charge qubits. *Phys Rev B*, May 2008. ISSN 1098-0121. doi: 10.1103/PhysRevB.77.180502. [Cited on page(s) 177].

M. D. Schroer, K. D. Petersson, M. Jung, and J. R. Petta. Field tuning the g factor in InAs nanowire double quantum dots. *Phys Rev Lett*, 107(17), Oct. 2011. doi: 10.1103/physrevlett.107.176811. [Cited on page(s) 114, 145, 166, 167].

J. Schulenborg and K. Flensberg. Absence of supercurrent sign reversal in a topological junction with a quantum dot. *Phys Rev B*, 101(1), Jan. 2020. ISSN 2469-9969. doi: 10.1103/PhysRevB.101.014512. [Cited on page(s) 109].

K. Serniak, M. Hays, G. de Lange, S. Diamond, S. Shankar, L. Burkhart, L. Frunzio, M. Houzet, and M. Devoret. Hot nonequilibrium quasiparticles in transmon qubits. *Phys Rev Lett*, 121(15), Oct. 2018. doi: 10.1103/physrevlett.121.157701. [Cited on page(s) 108].

K. Serniak, S. Diamond, M. Hays, V. Fatemi, S. Shankar, L. Frunzio, R. J. Schoelkopf, and M. H. Devoret. Direct dispersive monitoring of charge parity in offset-charge-sensitive transmons. *Phys. Rev. Applied*, 12(1), July 2019. ISSN 2331-7019. doi: 10.1103/PhysRevApplied.12.014052. [Cited on page(s) 106, 169].

S. V. Sharov and A. D. Zaikin. Parity effect and spontaneous currents in superconducting nanorings. *Physica E: Low-dimensional Systems and Nanostructures*, 29(1):360–368, 2005. ISSN 1386-9477. doi: https://doi.org/10.1016/j.physe.2005.05.034. URL https://www.sciencedirect.com/science/article/pii/S1386947705001827. Frontiers of Quantum. [Cited on page(s) 143].

A. Shearrow, G. Koolstra, S. J. Whiteley, N. Earnest, P. S. Barry, F. J. Heremans, D. D. Awschalom, E. Shirokoff, and D. I. Schuster. Atomic layer deposition of titanium nitride for quantum circuits featured. *Appl. Phys. Lett.*, 113:212601, 2018. doi: 10.1063/1.5053461. [Cited on page(s) 61, 278].

S. Sheldon, E. Magesan, J. M. Chow, and J. M. Gambetta. Procedure for systematically tuning up cross-talk in the cross-resonance gate. *Phys. Rev. A*, 93:060302, Jun 2016. doi: 10.1103/PhysRevA.93.060302. URL https://link.aps.org/doi/10.1103/PhysRevA.93.060302. [Cited on page(s) 244].

A. Shnirman, G. Schön, and Z. Hermon. Quantum manipulations of small Josephson junctions. *Phys. Rev. Lett.*, 79:2371–2374, Sep 1997. doi: 10.1103/PhysRevLett.79.2371. [Cited on page(s) 18, 19].

Y. M. Shukrinov. Anomalous Josephson effect. *Physics-Uspekhi*, 65(4):317–354, apr 2022. doi: 10.3367/ufne.2020.11.038894. [Cited on page(s) 145].

M. Sidorova, A. D. Semenov, H.-W. Hübers, S. Gyger, S. Steinhauer, X. Zhang, and A. Schilling. Magnetoconductance and photoresponse properties of disordered NbTiN films. *Phys. Rev. B*, 104:184514, Nov. 2021. doi: 10.1103/PhysRevB.104.184514. URL https://link.aps.org/doi/10.1103/PhysRevB.104.184514. [Cited on page(s) 66].

M. A. Sillanpää, J. I. Park, and R. W. Simmonds. Coherent quantum state storage and transfer between two phase qubits via a resonant cavity. *Nature*, 449(7161):438–442, Sep 2007. ISSN 1476-4687. doi: 10.1038/nature06124. URL https://doi.org/10.1038/nature06124. [Cited on page(s) 17].

W. C. Smith, A. Kou, U. Vool, I. M. Pop, L. Frunzio, R. J. Schoelkopf, and M. H. Devoret. Quantization of inductively shunted superconducting circuits. *Phys. Rev. B*, 94:144507, Oct 2016. doi: 10.1103/PhysRevB.94.144507. [Cited on page(s) 68, 76, 86, 87].

W. C. Smith, A. Kou, X. Xiao, U. Vool, and M. H. Devoret. Superconducting circuit protected by two-Cooper-pair tunneling. *npj Quantum Information*, 6(1):8, Jan 2020. doi: 10.1038/s41534-019-0231-2. [Cited on page(s) 94, 275, 276].

R. D. Somma, D. Nagaj, and M. Kieferová. Quantum speedup by quantum annealing. *Phys. Rev. Lett.*, 109:050501, Jul 2012. doi: 10.1103/PhysRevLett.109.050501. URL https://link.aps.org/doi/10.1103/PhysRevLett.109.050501. [Cited on page(s) 249].

E. M. Spanton, M. Deng, S. Vaitiekėnas, P. Krogstrup, J. Nygård, C. M. Marcus, and K. A. Moler. Current–phase relations of few-mode InAs nanowire Josephson junctions. *Nature Physics*, 13(12):1177–1181, Dec 2017. doi: 10.1038/nphys4224. [Cited on page(s) 10, 11, 123, 161].

M. Spethmann, X.-P. Zhang, J. Klinovaja, and D. Loss. Coupled superconducting spin qubits with spin-orbit interaction. *Phys. Rev. B*, 106:115411, Sep 2022. doi: 10.1103/PhysRevB.106.115411. URL https://link.aps.org/doi/10.1103/PhysRevB.106.115411. [Cited on page(s) 138, 140, 146, 180, 204, 244].

B. I. Spivak and S. A. Kivelson. Negative local superfluid densities: The difference between dirty superconductors and dirty Bose liquids. *Phys Rev B*, 43, Feb. 1991. doi: 10.1103/PhysRevB.43.3740. [Cited on page(s) 95, 99, 139, 150].

L. J. Splitthoff, A. Bargerbos, L. Grünhaupt, M. Pita-Vidal, J. J. Wesdorp, Y. Liu, A. Kou, C. K. Andersen, and B. van Heck. Gate-tunable kinetic inductance in proximitized nanowires. *Phys. Rev. Appl.*, 18:024074, Aug 2022. doi: 10.1103/PhysRevApplied.18.024074. URL https://link.aps.org/doi/10.1103/PhysRevApplied.18.024074. [Cited on page(s) 58, 124, 263, 297].

G. Stan, S. B. Field, and J. M. Martinis. Critical field for complete vortex expulsion from narrow superconducting strips. *Phys. Rev. Lett.*, 92:097003, Mar 2004. doi: 10.1103/PhysRevLett.92.097003. [Cited on page(s) 75].

T. Stavenga, S. A. Khan, Y. Liu, P. Krogstrup, and L. DiCarlo. Lower-temperature fabrication of airbridges by grayscale lithography to increase yield of nanowire transmons in circuit QED quantum processors. *Applied Physics Letters*, 123(2):024004, July 2023. ISSN 0003-6951. doi: 10.1063/5.0146814. [Cited on page(s) 35].

G. O. Steffensen, J. C. E. Saldaña, A. Vekris, P. Krogstrup, K. Grove-Rasmussen, J. Nygård, A. L. Yeyati, and J. Paaske. Direct transport between superconducting subgap states in a double quantum dot. *Phys. Rev. B*, 105:L161302, Apr 2022. doi: 10.1103/PhysRevB.105.L161302. URL https://link.aps.org/doi/10.1103/PhysRevB.105.L161302. [Cited on page(s) 271].

L. E. A. Stehouwer, A. Tosato, D. Degli Esposti, D. Costa, M. Veldhorst, A. Sammak, and G. Scappucci. Germanium wafers for strained quantum wells with low disorder. *Applied Physics Letters*, 123(9):092101, 08 2023. ISSN 0003-6951. doi: 10.1063/5.0158262. URL https://doi.org/10.1063/5.0158262. [Cited on page(s) 268, 284].

J. P. T. Stenger, B. D. Woods, S. M. Frolov, and T. D. Stanescu. Control and detection of Majorana bound states in quantum dot arrays. *Phys Rev B*, 98, Aug. 2018. doi: 10.1103/PhysRevB.98.085407. [Cited on page(s) 109].

J. P. T. Stenger, M. Hatridge, S. M. Frolov, and D. Pekker. Braiding quantum circuit based on the 4π Josephson effect. *Phys. Rev. B*, 99:035307, Jan 2019. doi: 10.1103/PhysRevB.99.035307. [Cited on page(s) 72, 73].

R. Stockill, C. L. Gall, C. Matthiesen, L. Huthmacher, E. Clarke, M. Hugues, and M. Atatüre. Quantum dot spin coherence governed by a strained nuclear environment. *Nat Commun*, 7, Sept. 2016. doi: 10.1038/ncomms12745. [Cited on page(s) 176, 192, 194, 281].

G. M. Stojanović, L. Zivanov, and M. Damjanovic. Compact form of expressions for inductance calculation of meander inductors. *Serbian Journal of Electrical Engineering*, 1:57–68, 01 2004. doi: 10.2298/SJEE0403057S. [Cited on page(s) 59].

E. Strambini, A. Iorio, O. Durante, R. Citro, C. Sanz-Fernández, C. Guarcello, I. V. Tokatly, A. Braggio, M. Rocci, N. Ligato, V. Zannier, L. Sorba, F. S. Bergeret, and F. Giazotto. A Josephson phase battery. *Nat Nanotechnol*, 15(8), June 2020. doi: 10.1038/s41565-020-0712-7. [Cited on page(s) 144].

D. B. Szombati, S. Nadj-Perge, D. Car, S. R. Plissard, E. P. A. M. Bakkers, and L. P. Kouwenhoven. Josephson ϕ_0-junction in nanowire quantum dots. *Nature Physics*, 12:568 EP –, May 2016. doi: 10.1038/nphys3742. [Cited on page(s) 11, 81, 94, 103, 138, 143, 144, 276].

M. Tadokoro, T. Nakajima, T. Kobayashi, K. Takeda, A. Noiri, K. Tomari, J. Yoneda, S. Tarucha, and T. Kodera. Designs for a two-dimensional Si quantum dot array with spin qubit addressability. *Scientific Reports*, 11(1):19406, Sep 2021. ISSN 2045-2322. doi: 10.1038/s41598-021-98212-4. URL https://doi.org/10.1038/s41598-021-98212-4. [Cited on page(s) 244].

Y. Tanaka, A. Oguri, and A. C. Hewson. Kondo effect in asymmetric Josephson couplings through a quantum dot. *New Journal of Physics*, 9(5):115, may 2007. doi: 10.1088/1367-2630/9/5/115. URL https://dx.doi.org/10.1088/1367-2630/9/5/115. [Cited on page(s) 12, 94, 140, 147, 271].

M. Tinkham and M. Gordon. Introduction to superconductivity. Second edition. *McGraw-Hill New York.*, 1996. [Cited on page(s) 11].

H. Topsøe. Geometric Factors in Four Point Resistivity Measurement. 13(476), May. 1966. [Cited on page(s) 296].

A. Tosato, V. Levajac, J.-Y. Wang, C. J. Boor, F. Borsoi, M. Botifoll, C. N. Borja, S. Martí-Sánchez, J. Arbiol, A. Sammak, M. Veldhorst, and G. Scappucci. Hard superconducting gap in germanium. *Communications Materials*, 4(1):23, Apr 2023. ISSN 2662-4443. doi: 10.1038/s43246-023-00351-w. URL https://doi.org/10.1038/s43246-023-00351-w. [Cited on page(s) 180, 209, 268, 283, 284].

L. Tosi, C. Metzger, M. F. Goffman, C. Urbina, H. Pothier, S. Park, A. L. Yeyati, J. Nygård, and P. Krogstrup. Spin-orbit splitting of Andreev states revealed by microwave spectroscopy. *Phys. Rev. X*, 9(1), Oct. 2018. ISSN 2160-3308. doi: 10.1103/PhysRevX.9.011010. [Cited on page(s) 11, 16, 72, 94, 109, 138, 144, 200].

A. M. Tyryshkin, S. Tojo, J. J. L. Morton, H. Riemann, N. V. Abrosimov, P. Becker, H.-J. Pohl, T. Schenkel, M. L. W. Thewalt, K. M. Itoh, and S. A. Lyon. Electron spin coherence exceeding seconds in high-purity silicon. *Nature Materials*, 11(2):143–147, Feb 2012. ISSN 1476-4660. doi: 10.1038/nmat3182. URL https://doi.org/10.1038/nmat3182. [Cited on page(s) 283].

W. Uilhoorn, J. G. Kroll, A. Bargerbos, S. D. Nabi, C.-K. Yang, P. Krogstrup, L. P. Kouwenhoven, A. Kou, and G. de Lange. Quasiparticle trapping by orbital effect in a hybrid superconducting-semiconducting circuit. *arXiv e-prints*, art. arXiv:2105.11038, May 2021. doi: 10.48550/arXiv.2105.11038. [Cited on page(s) 67, 94, 98, 106, 169, 202, 230].

S. Vaitiekėnas, M.-T. Deng, J. Nygård, P. Krogstrup, and C. M. Marcus. Effective g factor of subgap states in hybrid nanowires. *Phys. Rev. Lett.*, 121:037703, Jul 2018. doi: 10.1103/PhysRevLett.121.037703. URL https://link.aps.org/doi/10.1103/PhysRevLett.121.037703. [Cited on page(s) 204].

T. Vakhtel and *et al*. Resonant Josephson tunneling in a fluxonium circuit. *In preparation*, 2023b. [Cited on page(s) 269, 270, 271, 275, 277].

T. Vakhtel and B. van Heck. Quantum phase slips in a resonant Josephson junction. *Phys. Rev. B*, 107:195405, May 2023. doi: 10.1103/PhysRevB.107.195405. URL https://link.aps.org/doi/10.1103/PhysRevB.107.195405. [Cited on page(s) 268, 269].

M. Valentini, F. Peñaranda, A. Hofmann, M. Brauns, R. Hauschild, P. Krogstrup, P. San-Jose, E. Prada, R. Aguado, and G. Katsaros. Nontopological zero-bias peaks in full-shell nanowires induced by flux-tunable Andreev states. *Science*, 373, July 2021. ISSN 0036-8075. doi: 10.1126/science.abf1513. [Cited on page(s) 13, 94, 105].

M. Valentini, O. Sagi, L. Baghumyan, T. de Gijsel, J. Jung, S. Calcaterra, A. Ballabio, J. Aguilera Servin, K. Aggarwal, M. Janik, T. Adletzberger, R. Seoane Souto, M. Leijnse, J. Danon, C. Schrade, E. Bakkers, D. Chrastina, G. Isella, and G. Katsaros. Radio frequency driven superconducting diode and parity conserving Cooper pair transport in a two-dimensional germanium hole gas. *arXiv e-prints*, art. arXiv:2306.07109, June 2023. doi: 10.48550/arXiv.2306.07109. [Cited on page(s) 209, 268, 284].

J. A. van Dam, Y. V. Nazarov, E. P. A. M. Bakkers, S. De Franceschi, and L. P. Kouwenhoven. Supercurrent reversal in quantum dots. *Nature*, 442(7103):667–670, Aug 2006. doi: 10.1038/nature05018. [Cited on page(s) 13, 94, 99, 103, 140, 276].

J. W. G. van den Berg, S. Nadj-Perge, V. S. Pribiag, S. R. Plissard, E. P. A. M. Bakkers, S. M. Frolov, and L. P. Kouwenhoven. Fast spin-orbit qubit in an indium antimonide nanowire. *Phys Rev Lett*, 110(6), Feb. 2013. doi: 10.1103/physrevlett.110.066806. [Cited on page(s) 138, 145, 173, 175, 177, 178, 180, 196, 282].

C. H. van der Wal, A. C. J. ter Haar, F. K. Wilhelm, R. N. Schouten, C. J. P. M. Harmans, T. P. Orlando, S. Lloyd, and J. E. Mooij. Quantum superposition of macroscopic persistent-current states. *Science*, 290(5492):773–777, 2000. doi: 10.1126/science.290.5492.773. [Cited on page(s) 17].

B. van Heck, J. I. Väyrynen, and L. I. Glazman. Zeeman and spin-orbit effects in the Andreev spectra of nanowire junctions. *Phys. Rev. B*, 96:075404, Aug 2017. doi: 10.1103/PhysRevB.96.075404. [Cited on page(s) 72].

J. van Veen, D. de Jong, L. Han, C. Prosko, P. Krogstrup, J. D. Watson, L. P. Kouwenhoven, and W. Pfaff. Revealing charge-tunneling processes between a quantum dot and a superconducting island through gate sensing. *Phys Rev B*, 100(17), Nov. 2019. doi: 10.1103/physrevb.100.174508. [Cited on page(s) 140, 263].

D. J. van Woerkom, A. Proutski, B. van Heck, D. Bouman, J. I. Väyrynen, L. I. Glazman, P. Krogstrup, J. Nygård, L. P. Kouwenhoven, and A. Geresdi. Microwave spectroscopy of spinful Andreev bound states in ballistic semiconductor Josephson junctions. *Nature Physics*, 13, Jun 2017. doi: 10.1038/nphys4150. [Cited on page(s) 11, 72, 77, 81].

L. M. K. Vandersypen and I. L. Chuang. NMR techniques for quantum control and computation. *Rev. Mod. Phys.*, 76:1037–1069, Jan 2005. doi: 10.1103/RevModPhys.76.1037. URL https://link.aps.org/doi/10.1103/RevModPhys.76.1037. [Cited on page(s) 25].

L. M. K. Vandersypen, M. Steffen, G. Breyta, C. S. Yannoni, M. H. Sherwood, and I. L. Chuang. Experimental realization of Shor's quantum factoring algorithm using nuclear magnetic resonance. *Nature*, 414(6866):883–887, Dec 2001. ISSN 1476-4687. doi: 10.1038/414883a. URL https://doi.org/10.1038/414883a. [Cited on page(s) 26].

L. M. K. Vandersypen, H. Bluhm, J. S. Clarke, A. S. Dzurak, R. Ishihara, A. Morello, D. J. Reilly, L. R. Schreiber, and M. Veldhorst. Interfacing spin qubits in quantum dots and donors—hot, dense, and coherent. *npj Quantum Information*, 3(1):34, Sep 2017. ISSN 2056-6387. doi: 10.1038/s41534-017-0038-y. URL https://doi.org/10.1038/s41534-017-0038-y. [Cited on page(s) 200, 244].

J. I. Väyrynen, G. Rastelli, W. Belzig, and L. I. Glazman. Microwave signatures of Majorana states in a topological Josephson junction. *Phys. Rev. B*, 92:134508, Oct 2015. doi: 10.1103/PhysRevB.92.134508. [Cited on page(s) 72].

E. Vecino, A. Martín-Rodero, and L. Yeyati. Josephson current through a correlated quantum level: Andreev states and π junction behavior. *Phys Rev B*, 68(11), July 2003. ISSN 1550-235X. doi: 10.1103/PhysRevB.68.035105. [Cited on page(s) 147].

M. Veldhorst, J. C. C. Hwang, C. H. Yang, A. W. Leenstra, B. de Ronde, J. P. Dehollain, J. T. Muhonen, F. E. Hudson, K. M. Itoh, A. Morello, and A. S. Dzurak. An addressable quantum dot qubit with fault-tolerant control-fidelity. *Nature Nanotechnology*, 9(12):981–985, Dec 2014. ISSN 1748-3395. doi: 10.1038/nnano.2014.216. URL https://doi.org/10.1038/nnano.2014.216. [Cited on page(s) 284].

M. Veldhorst, C. H. Yang, J. C. C. Hwang, W. Huang, J. P. Dehollain, J. T. Muhonen, S. Simmons, A. Laucht, F. E. Hudson, K. M. Itoh, A. Morello, and A. S. Dzurak. A two-qubit logic gate in silicon. *Nature*, 526(7573):410–414, Oct 2015. ISSN 1476-4687. doi: 10.1038/nature15263. URL https://doi.org/10.1038/nature15263. [Cited on page(s) 284].

R. Versluis, S. Poletto, N. Khammassi, B. Tarasinski, N. Haider, D. J. Michalak, A. Bruno, K. Bertels, and L. DiCarlo. Scalable quantum circuit and control for a superconducting surface code. *Phys. Rev. Appl.*, 8:034021, Sep 2017. doi: 10.1103/PhysRevApplied.8.034021. URL https://link.aps.org/doi/10.1103/PhysRevApplied.8.034021. [Cited on page(s) 244].

F. Vigneau, R. Mizokuchi, D. C. Zanuz, X. Huang, S. Tan, R. Maurand, S. Frolov, A. Sammak, G. Scappucci, F. Lefloch, and S. De Franceschi. Germanium quantum-well Josephson field-effect transistors and interferometers. *Nano Letters*, 19(2):1023–1027, Feb 2019. ISSN 1530-6984. doi: 10.1021/acs.nanolett.8b04275. URL https://doi.org/10.1021/acs.nanolett.8b04275. [Cited on page(s) 268].

F. Vigneau, F. Fedele, A. Chatterjee, D. Reilly, F. Kuemmeth, M. F. Gonzalez-Zalba, E. Laird, and N. Ares. Probing quantum devices with radio-frequency reflectometry. *Applied Physics Reviews*, 10(2):021305, 02 2023. ISSN 1931-9401. doi: 10.1063/5.0088229. URL https://doi.org/10.1063/5.0088229. [Cited on page(s) 263].

L. Viola and S. Lloyd. Dynamical suppression of decoherence in two-state quantum systems. *Phys. Rev. A*, 58:2733–2744, Oct 1998. doi: 10.1103/PhysRevA.58.2733. URL https://link.aps.org/doi/10.1103/PhysRevA.58.2733. [Cited on page(s) 281].

A. Vuik, B. Nijholt, A. R. Akhmerov, and M. Wimmer. Reproducing topological properties with quasi-Majorana states. *SciPost Phys.*, 7:061, 2019. doi: 10.21468/SciPostPhys.7.5.061. URL https://scipost.org/10.21468/SciPostPhys.7.5.061. [Cited on page(s) 266].

R. Žitko and T. Pruschke. Energy resolution and discretization artefacts in the numerical renormalization group. *Phys Rev B*, 79, 2009. [Cited on page(s) 99, 112].

A. Wallraff, D. I. Schuster, A. Blais, L. Frunzio, R.-S. Huang, J. Majer, S. Kumar, S. M. Girvin, and R. J. Schoelkopf. Strong coupling of a single photon to a superconducting qubit using circuit quantum electrodynamics. *Nature*, 431(7005):162–167, 2004. doi: 10.1038/nature02851. [Cited on page(s) 17, 24, 72, 172].

G. Wang, T. Dvir, G. P. Mazur, C.-X. Liu, N. van Loo, S. L. D. ten Haaf, A. Bordin, S. Gazibegovic, G. Badawy, E. P. A. M. Bakkers, M. Wimmer, and L. P. Kouwenhoven. Singlet and triplet Cooper pair splitting in hybrid superconducting nanowires. *Nature*, 612(7940):448–453, Dec 2022. ISSN 1476-4687. doi: 10.1038/s41586-022-05352-2. URL https://doi.org/10.1038/s41586-022-05352-2. [Cited on page(s) 266].

J. I.-J. Wang, D. Rodan-Legrain, L. Bretheau, D. L. Campbell, B. Kannan, D. Kim, M. Kjaergaard, P. Krantz, G. O. Samach, F. Yan, J. L. Yoder, K. Watanabe, T. Taniguchi, T. P. Orlando, S. Gustavsson, P. Jarillo-Herrero, and W. D. Oliver. Coherent control of a hybrid

superconducting circuit made with graphene-based van der Waals heterostructures. *Nature Nanotechnology*, 14(2):120–125, 2019. doi: 10.1038/s41565-018-0329-2. [Cited on page(s) 72, 268, 284].

Q. Wang, S. L. D. ten Haaf, I. Kulesh, D. Xiao, C. Thomas, M. J. Manfra, and S. Goswami. Triplet correlations in Cooper pair splitters realized in a two-dimensional electron gas. *Nature Communications*, 14(1):4876, Aug 2023. ISSN 2041-1723. doi: 10.1038/s41467-023-40551-z. URL https://doi.org/10.1038/s41467-023-40551-z. [Cited on page(s) 266, 267].

P. Welch. The use of fast Fourier transform for the estimation of power spectra: A method based on time averaging over short, modified periodograms. *IEEE Transactions on Audio and Electroacoustics*, 15(2), June 1967. doi: 10.1109/tau.1967.1161901. [Cited on page(s) 132].

M. Werninghaus, D. J. Egger, F. Roy, S. Machnes, F. K. Wilhelm, and S. Filipp. Leakage reduction in fast superconducting qubit gates via optimal control. *npj Quantum Inf.*, 7(1), Jan. 2021. ISSN 2056-6387. doi: 10.1038/s41534-020-00346-2. [Cited on page(s) 175].

J. Wesdorp and *et al.* Microwave spectroscopy of Andreev bound states in InSb-Al nanowire Josephson junctions defined using shadow-wall lithography in a circuit-QED architecture. *In preparation*, 2023b. [Cited on page(s) 16, 35, 267, 268, 297].

J. J. Wesdorp and G. de Lange. Superconducting quantum interference devices and uses thereof, 2020. URL https://patents.google.com/patent/WO2022058025A1. Patent pending: WO2022058025A1, EP4214644A1, AU2020467946A1, KR20230069112A. [Cited on page(s) 50].

J. J. Wesdorp, F. J. Matute-Cañadas, A. Vaartjes, L. Grünhaupt, T. Laeven, S. Roelofs, L. J. Splitthoff, M. Pita-Vidal, A. Bargerbos, D. J. van Woerkom, P. Krogstrup, L. P. Kouwenhoven, C. K. Andersen, A. Levy Yeyati, B. van Heck, and G. de Lange. Microwave spectroscopy of interacting Andreev spins. *arXiv e-prints*, aug 2022. [Cited on page(s) 11, 16, 141, 144, 174, 175, 183, 189, 200, 202, 203, 204, 218, 250, 256, 297].

J. J. Wesdorp, L. Grünhaupt, A. Vaartjes, M. Pita-Vidal, A. Bargerbos, L. J. Splitthoff, P. Krogstrup, B. van Heck, and G. de Lange. Dynamical polarization of the fermion parity in a nanowire josephson junction. *Phys. Rev. Lett.*, 131:117001, Sep 2023. doi: 10.1103/PhysRevLett.131.117001. URL https://link.aps.org/doi/10.1103/PhysRevLett.131.117001. [Cited on page(s) 106, 108, 121, 134, 158, 189, 200, 250, 256, 297].

A. M. Whiticar, A. Fornieri, A. Banerjee, A. C. C. Drachmann, S. Gronin, G. C. Gardner, T. Lindemann, M. J. Manfra, and C. M. Marcus. Zeeman-driven parity transitions in an Andreev quantum dot. *Phys. Rev. B*, 103:245308, Jun 2021. doi: 10.1103/PhysRevB.103.245308. URL https://link.aps.org/doi/10.1103/PhysRevB.103.245308. [Cited on page(s) 94, 105].

D. Willsch, D. Rieger, P. Winkel, M. Willsch, C. Dickel, J. Krause, Y. Ando, R. Lescanne, Z. Leghtas, N. T. Bronn, P. Deb, O. Lanes, Z. K. Minev, B. Dennig, S. Geisert, S. Günzler,

S. Ihssen, P. Paluch, T. Reisinger, R. Hanna, J. H. Bae, P. Schüffelgen, D. Grützmacher, L. Buimaga-Iarinca, C. Morari, W. Wernsdorfer, D. P. DiVincenzo, K. Michielsen, G. Catelani, and I. M. Pop. Observation of Josephson Harmonics in Tunnel Junctions. *arXiv e-prints*, art. arXiv:2302.09192, Feb. 2023. doi: 10.48550/arXiv.2302.09192. [Cited on page(s) 8].

K. G. Wilson. The renormalization group: Critical phenomena and the Kondo problem. *Rev Mod Phys*, 47, 1975. ISSN 0034-6861. doi: 10.1103/revmodphys.47.773. [Cited on page(s) 96, 99, 112].

P. Winkel, K. Borisov, L. Grünhaupt, D. Rieger, M. Spiecker, F. Valenti, A. V. Ustinov, W. Wernsdorfer, and I. M. Pop. Implementation of a transmon qubit using superconducting granular aluminum. *Phys. Rev. X*, 10:031032, Aug 2020. doi: 10.1103/PhysRevX.10.031032. [Cited on page(s) 75].

G. W. Winkler, D. Varjas, R. Skolasinski, A. A. Soluyanov, M. Troyer, and M. Wimmer. Orbital contributions to the electron *g* factor in semiconductor nanowires. *Phys. Rev. Lett.*, 119:037701, Jul 2017. doi: 10.1103/PhysRevLett.119.037701. URL https://link.aps.org/doi/10.1103/PhysRevLett.119.037701. [Cited on page(s) 145, 166].

G. W. Winkler, A. E. Antipov, B. van Heck, A. A. Soluyanov, L. I. Glazman, M. Wimmer, and R. M. Lutchyn. Unified numerical approach to topological semiconductor-superconductor heterostructures. *Phys. Rev. B*, 99:245408, Jun 2019. doi: 10.1103/PhysRevB.99.245408. URL https://link.aps.org/doi/10.1103/PhysRevB.99.245408. [Cited on page(s) 117].

S. Wu, V. Fatemi, Q. D. Gibson, K. Watanabe, T. Taniguchi, R. J. Cava, and P. Jarillo-Herrero. Observation of the quantum spin hall effect up to 100 Kelvin in a monolayer crystal. *Science*, 359(6371):76–79, 2018. ISSN 0036-8075. doi: 10.1126/science.aan6003. [Cited on page(s) 83, 268].

Y. Wu, W.-S. Bao, S. Cao, F. Chen, M.-C. Chen, X. Chen, T.-H. Chung, H. Deng, Y. Du, D. Fan, M. Gong, C. Guo, C. Guo, S. Guo, L. Han, L. Hong, H.-L. Huang, Y.-H. Huo, L. Li, N. Li, S. Li, Y. Li, F. Liang, C. Lin, J. Lin, H. Qian, D. Qiao, H. Rong, H. Su, L. Sun, L. Wang, S. Wang, D. Wu, Y. Xu, K. Yan, W. Yang, Y. Yang, Y. Ye, J. Yin, C. Ying, J. Yu, C. Zha, C. Zhang, H. Zhang, K. Zhang, Y. Zhang, H. Zhao, Y. Zhao, L. Zhou, Q. Zhu, C.-Y. Lu, C.-Z. Peng, X. Zhu, and J.-W. Pan. Strong quantum computational advantage using a superconducting quantum processor. *Phys. Rev. Lett.*, 127:180501, Oct 2021. doi: 10.1103/PhysRevLett.127.180501. URL https://link.aps.org/doi/10.1103/PhysRevLett.127.180501. [Cited on page(s) 17].

Y. Xu, J. Chu, J. Yuan, J. Qiu, Y. Zhou, L. Zhang, X. Tan, Y. Yu, S. Liu, J. Li, F. Yan, and D. Yu. High-fidelity, high-scalability two-qubit gate scheme for superconducting qubits. *Phys. Rev. Lett.*, 125:240503, Dec 2020. doi: 10.1103/PhysRevLett.125.240503. URL https://link.aps.org/doi/10.1103/PhysRevLett.125.240503. [Cited on page(s) 25, 26].

X. Xue, M. Russ, N. Samkharadze, B. Undseth, A. Sammak, G. Scappucci, and L. M. K. Vandersypen. Quantum logic with spin qubits crossing the surface code threshold. *Nature*, 601(7893):343–347, Jan 2022. ISSN 1476-4687. doi: 10.1038/s41586-021-04273-w. URL https://doi.org/10.1038/s41586-021-04273-w. [Cited on page(s) 244].

K. Yavilberg, E. Ginossar, and E. Grosfeld. Differentiating Majorana from Andreev bound states in a superconducting circuit. *Phys. Rev. B*, 100:241408, Dec 2019. doi: 10.1103/PhysRevB.100.241408. [Cited on page(s) 72].

Yokogawa. GS610 Source Measure Unit User's manual, Nov. 2021. URL https://cdn.tmi.yokogawa.com/1/6104/files/IM765501-01E.pdf. [Online; accessed 27-September-2023]. [Cited on page(s) 248].

T. Yokoyama, M. Eto, and Y. V. Nazarov. Anomalous Josephson effect induced by spin-orbit interaction and Zeeman effect in semiconductor nanowires. *Phys. Rev. B*, 89:195407, May 2014. doi: 10.1103/PhysRevB.89.195407. [Cited on page(s) 81, 138, 143].

J. Yoneda, K. Takeda, T. Otsuka, T. Nakajima, M. R. Delbecq, G. Allison, T. Honda, T. Kodera, S. Oda, Y. Hoshi, N. Usami, K. M. Itoh, and S. Tarucha. A quantum-dot spin qubit with coherence limited by charge noise and fidelity higher than 99.9%. *Nature Nanotechnology*, 13(2):102–106, Feb 2018. ISSN 1748-3395. doi: 10.1038/s41565-017-0014-x. URL https://doi.org/10.1038/s41565-017-0014-x. [Cited on page(s) 284].

T. Yoshioka and Y. Ohashi. Numerical renormalization group studies on single impurity Anderson model in superconductivity: a unified treatment of magnetic, nonmagnetic impurities, and resonance scattering. *J. Phys. Soc. Jpn.*, 69, 2000. ISSN 0031-9015. doi: 10.1143/jpsj.69.1812. [Cited on page(s) 94, 96, 112, 140].

C. X. Yu, S. Zihlmann, J. C. Abadillo-Uriel, V. P. Michal, N. Rambal, H. Niebojewski, T. Bedecarrats, M. Vinet, É. Dumur, M. Filippone, B. Bertrand, S. De Franceschi, Y.-M. Niquet, and R. Maurand. Strong coupling between a photon and a hole spin in silicon. *Nature Nanotechnology*, Mar 2023. doi: 10.1038/s41565-023-01332-3. URL https://doi.org/10.1038/s41565-023-01332-3. [Cited on page(s) 172, 200].

P. Zalom, V. Pokorný, and T. c. v. Novotný. Spectral and transport properties of a half-filled Anderson impurity coupled to phase-biased superconducting and metallic leads. *Phys Rev B*, 103, Jan. 2021. doi: 10.1103/PhysRevB.103.035419. [Cited on page(s) 104].

A. Zazunov, V. S. Shumeiko, E. N. Bratus', J. Lantz, and G. Wendin. Andreev level qubit. *Phys. Rev. Lett.*, 90:087003, Feb 2003. doi: 10.1103/PhysRevLett.90.087003. [Cited on page(s) 94, 99, 138, 270, 287].

A. Zazunov, V. S. Shumeiko, G. Wendin, and E. N. Bratus'. Dynamics and phonon-induced decoherence of Andreev level qubit. *Phys. Rev. B*, 71:214505, Jun 2005. doi: 10.1103/PhysRevB.71.214505. [Cited on page(s) 270, 287].

A. Zazunov, R. Egger, T. Jonckheere, and T. Martin. Anomalous Josephson current through a spin-orbit coupled quantum dot. *Phys Rev Lett*, 103, Oct. 2009. doi: 10.1103/PhysRevLett.103.147004. [Cited on page(s) 138, 139, 143, 144].

A. Zazunov, A. Brunetti, A. L. Yeyati, and R. Egger. Quasiparticle trapping, Andreev level population dynamics, and charge imbalance in superconducting weak links. *Phys. Rev. B*, 90:104508, Sep 2014. doi: 10.1103/PhysRevB.90.104508. [Cited on page(s) 72].

Y. Zhao, Y. Ye, H.-L. Huang, Y. Zhang, D. Wu, H. Guan, Q. Zhu, Z. Wei, T. He, S. Cao, F. Chen, T.-H. Chung, H. Deng, D. Fan, M. Gong, C. Guo, S. Guo, L. Han, N. Li, S. Li, Y. Li, F. Liang, J. Lin, H. Qian, H. Rong, H. Su, L. Sun, S. Wang, Y. Wu, Y. Xu, C. Ying, J. Yu, C. Zha, K. Zhang, Y.-H. Huo, C.-Y. Lu, C.-Z. Peng, X. Zhu, and J.-W. Pan. Realization of an error-correcting surface code with superconducting qubits. *Phys. Rev. Lett.*, 129: 030501, Jul 2022. doi: 10.1103/PhysRevLett.129.030501. URL https://link.aps.org/doi/10.1103/PhysRevLett.129.030501. [Cited on page(s) 244].

R. Žitko. NRG Ljubljana, 8f90ac4. *Zenodo*, May 2021. doi: 10.5281/zenodo.4841076. [Cited on page(s) 12, 99, 112].

R. Žitko and F. Michele. Non-Fermi-liquid behavior in quantum impurity models with superconducting channels. *Phys Rev B*, 95, Feb. 2017. doi: 10.1103/PhysRevB.95.085121. [Cited on page(s) 104].

C. W. Zollitsch, J. O'Sullivan, O. Kennedy, G. Dold, and J. J. L. Morton. Tuning high-Q superconducting resonators by magnetic field reorientation. *AIP Advances*, 9(12): 125225, Dec. 2019. ISSN 2158-3226. doi: 10.1063/1.5129032. URL https://doi.org/10.1063/1.5129032. [Cited on page(s) 63, 64, 65, 256].

K. Zuo, V. Mourik, D. B. Szombati, B. Nijholt, D. J. van Woerkom, A. Geresdi, J. Chen, V. P. Ostroukh, A. R. Akhmerov, S. R. Plissard, D. Car, E. P. A. M. Bakkers, D. I. Pikulin, L. P. Kouwenhoven, and S. M. Frolov. Supercurrent interference in few-mode nanowire Josephson junctions. *Phys. Rev. Lett.*, 119:187704, Nov 2017. doi: 10.1103/PhysRevLett.119.187704. [Cited on page(s) 11, 72, 81].

A. M. J. Zwerver, T. Krähenmann, T. F. Watson, L. Lampert, H. C. George, R. Pillarisetty, S. A. Bojarski, P. Amin, S. V. Amitonov, J. M. Boter, R. Caudillo, D. Correas-Serrano, J. P. Dehollain, G. Droulers, E. M. Henry, R. Kotlyar, M. Lodari, F. Lüthi, D. J. Michalak, B. K. Mueller, S. Neyens, J. Roberts, N. Samkharadze, G. Zheng, O. K. Zietz, G. Scappucci, M. Veldhorst, L. M. K. Vandersypen, and J. S. Clarke. Qubits made by advanced semiconductor manufacturing. *Nature Electronics*, 5(3), Mar. 2022. ISSN 2520-1131. doi: 10.1038/s41928-022-00727-9. [Cited on page(s) 172].

ACKNOWLEDGEMENTS

¡Pero qué buen maestro es usted, don Roberto!

Elena, in the film *Amanece, que no es poco*, by José Luis Cuerda

The culmination of a PhD thesis is not only a moment to celebrate, but also an opportunity to reflect on the circumstances that made such an achievement possible. Success and accomplishments, whether in academia or any aspect of life, are only minimally determined by individual merit; rather, they are highly correlated with the circumstances we happen to be under. As I stand at the end of my PhD journey, I must acknowledge the favorable factors that have converged to make my path seemingly effortless. Growing up in a stable European nation, belonging to a supportive family, benefiting from a robust public education system, and not having any major responsibilities outside of the lab, I've been granted a series of advantages that have massively facilitated the terrain ahead. Working within a well-equipped institute, surrounded by an exceptional team, and guided by excellent supervisors, I realize how fortunate I've been. Yet, I'm fully aware that these privileged circumstances are far from universal. With this awareness, I embrace the responsibility to work towards a more equitable academic community and I invite all who read this to join me in fostering an inclusive and fair academic realm.

It is with this realization that I embark on the task of recognizing the people who've contributed to the results presented in this thesis, as well as all who make QuTech the supportive and inspiring research environment that I found it to be. Throughout the past few years, I had the opportunity of working together with excellent supervisors: my promotors, **Leo** and **Christian**, as well as my two former supervisors **Bernard** and **Angela**. Your complimentary approaches to research have shaped my own view of science and your varied areas of expertise have been vital for developing the hybrid research discussed in this thesis. I'm glad I've had the chance to learn from all of you. I couldn't have hoped for better supervision.

Leo, it's been amazing to have the opportunity to learn from your experience, you are an encyclopedia of Delft research history. You are impressively efficient and effective at meetings; each ten-minute discussion with you has taught me what would have taken me two days to figure out on my own. Thanks for the freedom to work on the experiments I wanted. It's been an honor to work in your lab. **Christian**, apart from being an excellent supervisor, you are a OneNote and Overleaf ninja with your live comments and replies. I envy your time management skills. Somehow, you manage to supervise like a thousand projects at the same time while teaching, designing courses, staying up to date with the literature and coming up with yet new research ideas. I wonder how you still manage to give instantaneous and constructive feedback on any topic. Your mentorship during the qubit experiments in the second half of my thesis has been price-

less. **Bernard**, having the guidance of a condensed matter theory God during the most physics-heavy part of my PhD was a true gift. Thanks to you, we established collaborations with Ramón, Rok and Tess that led to stimulating discussions about new topics beyond the initially planned. Your love for pure and open knowledge is truly inspiring. Lots of success with your research at Uniroma! **Angela**, I learned a ton of things from you. With your patience and positivity, you introduced me to the world of hybrid cQED when I was still a baby physicist breaking stuff around the lab. I was impressed by your freshly built lab in Urbana-Champaign when we visited. Your students are very lucky to work with you!

I'd also like to thank my committee members for dedicating part of their precious time to reviewing and assessing my thesis. **Ramón**, your vast knowledge of SQDS junctions has been invaluable for the research presented here. Thank you for always seeing the interesting part of every new measurement, for so many scientific discussions and for hosting us in Madrid. Collaborating with you has been a enriching experience! **Pablo**, you triggered my interest in condensed matter, and your advice played an important role in my decision to come to Delft. So this thesis owes much of its existence to you. Thanks for taking the time to answer all of my questions, from science, to career, to life, when I was still a bachelor student. **Pasquale**, it is a great honor having you as a member of my committee. Your hybrid research is truly inspiring! **Barbara**, I keep going back to my "Special Topics" notes to, each time, figure out again how to write down my circuit Hamiltonian. I also recall the in-depth feedback and interesting questions that you posed during my go-no-go evaluation. Thanks for teaching me so much!

Throughout my PhD, I had the fortune to work alongside three brilliant, dedicated and very cool PhD candidates: Arno, Jaap and Lukas. **Arno**, teaming up with you for the SQDS projects was one of the wisest decisions of my PhD. It is not that you have a good balance between intelligence and hard work, you beat the system at both. We went through so many iterations of devices that you even designed an entire new chip assuming that the previous one wasn't going to work. But in the end, it did. And it gave great results! It's been a lot of fun not only to write endless supplementary sections with you, but also to travel around half of the US, to enjoy your amazing homemade negronis and to prove how bad I am at Risk. I look forward to sharing tamales with you and **Maureen** when you come visit in Zurich. **Jaap**, this last year working with you was full of memorable moments, both in the lab and during the many conference trips. Your optimism being 100% sure that one particular day we would measure coupling was very contrasting with my prior experience measuring with Arno. It took us like one more week since that day to take the first coupling measurements, but we did! But this was also a year of hearing you interrogate many taxi drivers in many different languages (from Vienna to Madrid to Las Vegas), of learning that there is no limit to how many random electronics a single person can buy, of receiving overcomplete photo reports of Madrid underground and of realizing that it is possible to overthink even more than I. Thanks for the endless discussions about research and life. I hope you convince many people to do core stability in Helsinki, and lots of luck to you and **Ilse** fitting all your life in a single van! **Lukas S.**, you are always willing to help everyone, even during your busiest times. Thank you for feeding me tons of delicious dry pears and candy (thanks also to **Gerd** actually), for being a trap-filling ninja and, of course, thanks for the tens and tens of nanowires that

you deposited for the SQDS devices!

Over time the cQED team was formed by many more people. **Willemijn**, one of the giants over whose shoulders we stand. You taught me a lot about cleanroom techniques, work-life balance and how not to turn right. Your enthusiasm and positivity are really inspiring. **Lukas G.**, I am fortunate of having shared time with you, your expertise and your amazing organizational skills in the group. I hold great memories of that week being stuck in Denver, thanks for so much fun and team retro's. **Tess**, our in-house WKP expert and the person I know with the greatest genuine interest in every topic. From hardcore altermagnet physics to learning about how to load a fridge, you always show the same passion. Thanks for your WKP masterclasses and the many discussions about high-T and a bunch of other random topics! **David**, you really learn fast, it was a lot of fun to learn about resonators with you. Lots of success at the SQUID lab! Thanks also to **James**, **Tim** (who dedicated precious time at the end of his master project to training me at the e-beam and superAJA), **Jouri**, **Däniel**, **Ruben**, **Arjen**, **Pepijn**, **Duiquan** and **Miguel**.

I'd also like to mention everyone else who made QuRe a division to be proud of. **Guan**, thanks for the insightful discussions about the ASQ-ASQ project and about career paths. It is always great to chat with you! **Ivan**, incredibly hard-working, a great person and, together with **Ting**, part of the SuperAJA monitoring team. You are always willing to help, both inside and outside the lab. It's been great to work with you! **Greg**, thanks for always being open to answering any scientific question and for the fun moments in the lab late in the evening! **Vukan**, it's been great to share the office with you. Good luck to you and **David** in you next steps. **Filip**, thanks for sharing your valuable knowledge about nuclear noise and how to learn about it! **Christian P.**, a super-intelligent person, a great friend and an awesome office mate. **Qing**, thanks for the fun conversations about physics and career. Good luck with the final sprint in your PhD. **Christan M.** and **Damaz**, together with Willemijn and Arno you made the after-Denver trip memorable. **Daan**, I hold great memories of you showing up early every morning at the Denver Airbnb and late in the evening at my old desk in the B wing. **Michael W.** and **Anton**, it's been a great experience to TA for CompPhys. Thanks for the opportunity! **Judi**, we've had endless discussions about physics, painting and life. I'm impressed by your hard work in the lab and by your unique way of expressing feelings through your art. **Siddharth**, I recognize myself in you every time you accept to become part of yet another committee. Keep doing it! The super-heroes **Taryn** and **Figen**, **Martijn**, **Eugene**, **Miguel** and everyone else in the Andersen lab, you've made a lot of progress in the past years. Lots of luck making fluxoniums rule the world! **Natasha**, I have no doubt you'll do great in your freshly started PhD. **Nick**, **Tom**, **David van D.**, **Di**, **Francesco Z.**, **Alberto**, **Cristina**, **Jan Cornelis**, **Jiyin**, **Jie**, **Lin**, **Bas**, **Mathilde**, **Jouri**, **Fokko**, **Michiel**, **Attila**, **Matt**, **Nikolai**, **Alex**, **Dominique**, **Vanessa**, **Nicolò**, **Luca**, **Senja**, **Lieuwe**, **Francesco B.**, **Jasper**, **Srijit**, **Prasanna**, **Nikos**, **Rebecca**, **Delphine**, **Isidora**, and everyone else in QuRe, I am grateful for the shared discussions, dinners and coffees.

During my PhD, I also had the fortune to learn from my colleagues in the Microsoft lab. **David van W.** and **CK**, thanks for your help and for sharing your vast fab knowledge during the fluxonium project. **Kongyi**, you are a nanowire deposition master. Thanks for teaching me how to do InSb deposition. **Kevin**, thank you for your valuable help with the fluxonium simulations. **Wolfgang** and **Gijs**, thanks for the discussions and for

all of your great input for the fluxonium project. **Marina**, you helped me a lot in my attempts to build smart-walls on my cQED chips. Your cleanroom skills are amazing. **Victor**, thanks for filling the K2 traps so many times! **Andrey** and **Roman**, it was an honor to learn from you during my internship in Santa Barbara. **John**, **Elvedin**, **Jonne**, **Amrita**, **Mikhail**, **Emrah**, **Alexandra**, **Sebastian**, and everyone else in the MSFT team, it's been great to work with you.

Apart from the people mentioned above, I had the luck to collaborate and learn from several outstanding scientists throughout my PhD. **Nadia**, thanks for the hard work with the fluxonium simulations. **Thijs**, I appreciate you sharing your vast experience on gatemon physics and nanowire contacting. **Nandini** and **Chris(tos)**, I appreciate our discussions about NbTiN sputtering and your hard work troubleshooting the SuperAJA together. **Rok**, you were essential for understanding the SQDS data. I learned a lot from the discussions with you and Ramón. Thank you for your in-depth replies to my many questions and for all of your fast Overleaf feedback. I'm happy that our long email chain on the Knight shift led to the great work with **Luka**. It's been an honor to collaborate with you two. **Yuli**, thanks for accepting us in your office to discuss the SQDS/ASQ results. Your expert insights are really valuable. **Valla** and the Yale team, I appreciate your insightful comments and questions about the ASQ papers. Also, thank you Valla for hosting us last year at Cornell. It was great to see what you are building. Similarly, I appreciate **Pavel** and **Tom** for showing us around Yale. I learned a lot from the discussions with everyone during the visits and I was really impressed by your research. It's been great to interact with Valla and Pavel once more regarding the high T stories with Tess. I hope to keep learning from your expertise in the future! **Xiao** and **Jurgen** thanks for sharing your distant spin-spin coupling knowledge.

I've also had great discussions with people during different trips and lab visits. **Praveen**, although the Denver March meeting was canceled, showing each other our presentations at a random coffee place in Denver was a lot of fun. It was great to hang out again in Chicago with you and **Connie** and to learn about InAs quantum dots. It's a pity that the West Coast lab tour last year didn't work out in the end. I hope to keep seeing each other every year in March! **Francisco** and **Cyril**, it was great to hang out in Chicago and learn about ABSs from you! Around MM 2022, I had the luck to visit various labs together with the rest of the cQED team. Apart from the hosts already mentioned, I appreciate **Andrés** showing us around **Philip Kim**'s lab and compiling such an interesting discussion schedule. I was impressed by the diversity of research topics and techniques in the lab. It was great to see you again in person after having shared an office seven years ago. Also, thanks to **Joel**, at **Will Oliver**'s lab, for his time and for the fantastic lab tour. I had a memorable day in which I learned a lot about protected qubits and hybrid devices. **Max**, the ASQ discussions with you in Boston and the multi-qubit coupling ones later over Teams were really insightful. Thanks for sharing your knowledge! **Dani**, it was great to see you again in Boston. I appreciate you showing us around Pablo's lab and sharing your graphene JJ expertise with the Delft crew! I also hold great memories of my two visits to Vienna, both thanks to **Giorgos**. Thank you for giving me and Arno the opportunity to visit and meet everyone in your group. The work that they are doing is impressively varied and I learned a lot from all of them. I also appreciate the interesting discussions in Madrid and Delft, I learned a lot about hybrid germanium devices from you and I

hope to keep interacting in the future. Thank you, finally, for organizing an amazing hybrid conference this year. At HQT I met incredible scientists like **Joan** and **Marcelo**, **Federico** and **Natalia** or **Marco**, **Fieke**, **Manuel** and **Daniel** from **Fabrizio**'s group. You guys made the conference an amazing experience, I hope HQT keeps happening in the future! **Manas**, it was fun to hang out in Manchester, thanks for the insightful discussions on singlet-doublet transitions. It was inspiring to discuss new ideas with **Francisco**, **Alfredo**, **Gorm**, everyone else at the UAM, and **Ramón** during our visit this year. **Eduardo**, **Nacho**, **Ángel** and the rest of the group, I appreciate you showing us your lab and the insightful fab discussions. Thanks all for hosting us and for guiding Jaap and me around Madrid nightlife during our visit. The semiconducting junctions research environment in Madrid is truly vibrant! It was great to see Nacho and Ángel again during your visit to Delft a few months later. I'm sure we'll cross paths again in the future. I also appreciate the fantastic scientific environment that I experienced when I visited **Morten**'s lab in Copenhagen. **Svend**, thanks for the insightful discussions and for showing me everything the city of Copenhagen has to offer. I'm sure you'll have a bright career. **David**, **Zhenhai**, **Jacob**, and everyone else, you are building a massive squid over a wooden floor. Keep going! **Patrick**, **Andreas** and everyone at the spin team at IBM Research, thanks for sharing your interesting thoughts on spin qubits and for showing me around. See you soon!

Everyone who ever helped me in the cleanroom, thanks for making the cleanroom a bit more human. **Alessandro**, thanks for showing me the intricacies of TiN ALD. **Ivan**, I had four years to get access to the QT-AJA, but I never did. Thanks for always being willing to deposit palladium with me! **Ewan**, **Charles**, **Eugene**, **Hozanna**, **Mark**, **Marc**, **Arnold**, **Anja** and everyone else, your work is priceless! And outside of the cleanroom, I appreciate **Matvey**, **Alessandro** and **Leo** for letting me use the Vespa so many times. **Jason** and **Olaf**, we are incredibly lucky of having you around. I appreciate that you were there to help me with my questions so many times. **Kees**, thanks for illuminating me about the different manufacturing methods for blind vias, every visit to DEMO throughout my PhD has been a very educational experience. **Raymond**, your electronics knowledge has no limits. I appreciate everything you taught me at the electronics course and all the time and effort you spent helping me troubleshoot PCBs.

I'd also like to acknowledge several people who have made my life much much easier than it could have been over the past few years. **Joachim**, I learned a lot about intellectual property from you. Thank you for dedicating so much of your time to explaining really basic concepts and for the many references. Good luck with your next steps! **Kees**, I appreciate your help in making everything work out smoothly under time pressure. **Lydia**, I can't find enough words to express how helpful it was to have you around the Microsoft lab. You are incredibly understanding and professional and always found an instantaneous solution for every complex problem. Thank you for everything and lots of success in Denmark. **Jenny**, I've passed by your office countless times to ask you countless questions about countless topics and you always knew exactly what the way to proceed was. Working with you around is very easy. **Csilla**, thanks for always being there to answer all of my complicated questions and for always finding a perfect solution for every challenge. **Chantal**, **Marja**, **Simone** and everyone else, I truly appreciate every time you've helped me.

También quiero agradecer a las personas clave que hicieron que desarrollase mi interés por la física mucho antes de empezar mi doctorado. **Socorro Liste**, **Antonio Rivas**, **Carmen Touza** y **Antonio Vidal**, me hicisteis ver lo divertida que puede ser la física. ¡Gracias por todo lo que me enseñasteis!

The support from friends and family outside of the lab gave me the energy and balance that were essential to complete this thesis. **Ivan** and **Alina**, living next to you during the covid times made the isolation much easier. I really value your friendship! **Hélène** and **Christian**, it's been a lot of fun to hang out with you for the past six years. It took you an in-depth investigation of options to choose a country, but you finally did. Good luck in Norway! **Boris**, **Mattias**, **Rasa**, **Chien** and **Eugenio**, you are an awesome group of people, I hope to keep seeing you when we depart paths. **Diego**, con tus llegadas aleatorias a traernos alfajores y tomar café pusiste una pincelada de normalidad en un lugar en que, por algún motivo, la gente planea su vida con semanas de antelación. Lo pasé muy bien en las múltiples cenas contigo en Róterdam. **Iñaki** y **Paulina**, conoceros en Róterdam fue increíble. Gracias por las noches de pizza y juegos de mesa, ayudaron a balancear mi trabajo en el laboratorio. Espero que hagamos muchos más viajes como el de Francia en el futuro. ¡Nos vemos pronto en Polonia! **Óscar**, **Pol**, **Juanjo**, **Eric**, **Iris**, **Antonella**, pese a estar repartidos por el mundo, conseguimos coincidir varias veces estos últimos años. Aunque en la distancia, quiero agradecer también a **Júlia**, **Borja**, **Irene**, **Carlos**, **Gemma** y **Èlia**. Por lo que parece, solamente nos vemos en bodas, ¡pero al menos nos vemos! Finalmente, quiero agradecer a mi familia su interés y su apoyo durante los últimos años. **Reyna**, **Israel**, **Chuchín**, **Jazmín**, **Poncho**, **Teco** y toda la familia, gracias por viajar tanta distancia para vernos en Róterdam, por los buenos momentos y por las risas. **Carmen**, agradezco mucho las múltiples visitas, los viajes juntos y las muchísimas veces que me acojiste en tu casa durante estos años. **María**, **Mon**, **Inés**, **Laura** y **Carmen**, vuestras visitas hicieron de Róterdam un lugar más familiar. Inés, ¡tus complicadas preguntas sobre diferentes tipos de aceleración rotacional o distintas formas de resolver EDO mantienen mi cerebro funcionando! **Juan**, **Lidia**, **Eva** y **Pablo**, me lo pasé muy bien viajando con vosotros por Holanda y Bélgica. ¡Os espero en Suiza! **Belén**, **Alejandro** y **Lucía**, gracias por el apoyo y por siempre estar ahí! Agradezco, Alejandro, que hayas venido tantas veces a Róterdam. El año que viene te visito seguro. Abuela **Carmelina**, abuelo **Ricardo**, **Juani** y abuelo **Alberto**, no creo que pueda imaginar mejores abuelos; vuestro cariño durante el doctorado fue indispensable. ¡Agradezco mucho las visitas a Delft y a Róterdam! **Manuela**, **Alberto** y mis padres, **Beatriz** y **Ricardo**, si estoy aquí es por vosotros. Gracias por escuchar mis interminables explicaciones y por ayudarme tantísimas veces a tomar decisiones. Agradezco el interés constante sobre cómo van las cosas y los buenos días y las buenas noches por Whatsapp. Manuela, gracias por diseñar la portada de mi tesis y Alberto, gracias por los consejos sobre como mejorarla. **Hugo**, me atrevo a decir que no hay nadie en el laboratorio cuya pareja sepa tato como tú sobre su investigación. Gracias por el feedback sobre mi tesis y por atender horas y horas a explicacioes sobre uniones de Josephson, fluxóniums o *Andreev spin qubits*. Que hayas estado siempre conmigo durante estos años fue lo más ipotante. Deseando ver lo que nos deparará el futuro.

Marta

CURRICULUM VITÆ

Marta PITA-VIDAL

17-10-1994 Born in Ferrol, Spain.

EDUCATION

2006–2010 Secondary school
IES Pontepedriña, Santiago de Compostela, Spain

2010–2012 Highschool (science and technology)
IES Rosalía de Castro, Santiago de Compostela, Spain

2010–2012 International Baccalaureate Diploma Programme
IES Rosalía de Castro, Santiago de Compostela, Spain

2012–2017 Bachelor's degree in Mathematics
Centre de Formació Interdisciplinària Superior (CFIS) of the Universitat Politècnica de Catalunya (UPC), Barcelona, Spain

2012–2017 Bachelor's degree in Physics Engineering
Centre de Formació Interdisciplinària Superior (CFIS) of the Universitat Politècnica de Catalunya (UPC), Barcelona, Spain

Thesis:	Viscous regime of electron transport at a graphene constriction
Supervisor:	Prof. dr. Ramón Alcubilla González
Supervisor:	Dr. Qiong Ma
Supervisor:	Prof. dr. Pablo Jarillo-Herrero

2017–2019 Master's degree in Applied Physics
Delft University of Technology, Delft, The Netherlands.

Track:	Physics for Quantum Devices and Quantum Computing
Thesis:	Development of nanowire-based fluxonium devices
Supervisor:	Prof. dr. ir. L. P. Kouwenhoven
Supervisor:	Dr. A. Kou

2019–2023 PhD degree
Delft University of Technology, Delft, The Netherlands.
Thesis: Realizing superconducting spin qubits
Promotor: Prof. dr. ir. L. P. Kouwenhoven
Promotor: Dr. C. K. Andersen

LIST OF PUBLICATIONS

Included as a chapter of this thesis.
Discussed in the outlook of this thesis.
* These authors contributed equally.

PUBLICATIONS AND PREPRINTS

15. *Blueprint for all-to-all connected superconducting spin qubits.*
M. Pita-Vidal, J. J. Wesdorp and C. K. Andersen
In preparation. [Included in chapter 10].

14. *Microwave spectroscopy of Andreev bound states in InSb-Al nanowire Josephson junctions defined using shadow-wall lithography in a circuit-QED architecture.*
J. J. Wesdorp, P. A. Rot, N. van Loo, A. Vaartjes, L. Grünhaupt, L. J. Splitthoff, **M. Pita-Vidal**, A. Bargerbos, J. C. Wolff, G. P. Mazur, L. P. Kouwenhoven, G. de Lange and C. K. Andersen,
In preparation.

13. *Tunneling of fluxons via a Josephson resonant level.*
T. Vakhtel, P. Kurilovich, **M. Pita-Vidal**, A. Bargerbos, V. Fatemi and B. van Heck
arXiv:2310.03102 [Discussed in Sec. 11.1.2].

12. *Gate-tunable kinetic inductance parametric amplifier.*
L. J. Splitthoff, J. J. Wesdorp, **M. Pita-Vidal**, A. Bargerbos and C. K. Andersen
arXiv 2308.06989

11. *Strong tunable coupling between two distant superconducting spin qubits.*
M. Pita-Vidal*, J. J. Wesdorp*, L. J. Splitthoff, A. Bargerbos, Y. Liu, L. P. Kouwenhoven and C. K. Andersen
arXiv 2307.15654 [Included in chapter 9].

10. *Microwave spectroscopy of interacting Andreev spins.*
J. J. Wesdorp, F. J. Matute-Cañadas, A. Vaartjes, L. Grünhaupt, T. Laeven, S. Roelofs, L. J. Splitthoff, **M. Pita-Vidal**, A. Bargerbos, D. J. van Woerkom, P. Krogstrup, L. P. Kouwenhoven, C. K. Andersen, A. Levy Yeyati, B. van Heck and G. de Lange
arXiv 2208.11198

9. *Dynamical polarization of the fermion parity in a nanowire Josephson junction.*
J. J. Wesdorp, L. Grünhaupt, A. Vaartjes, **M. Pita-Vidal**, A. Bargerbos, L. J. Splitthoff, P. Krogstrup, B. van Heck and G. de Lange
Phys. Rev. Lett. 131, 117001 (2023).

8. *Spectroscopy of spin-split Andreev levels in a quantum dot with superconducting leads.*
A. Bargerbos*, **M. Pita-Vidal***, R. Žitko, L. J. Splitthoff, L. Grünhaupt, J. J. Wesdorp, Y. Liu, L. P. Kouwenhoven, R. Aguado, C. K. Andersen, A. Kou and B. van Heck
Phys. Rev. Lett. **131**, 097001 (2023) [Included in chapter 7].

7. *Impurity Knight shift in quantum dot Josephson junctions.*
L. Pavešić, **M. Pita-Vidal**, A. Bargerbos and R. Žitko
SciPost Phys. **15**, 070, (2023) [Discussed in Sec. 11.1.3].

6. *Direct manipulation of a superconducting spin qubit strongly coupled to a transmon qubit.*
M. Pita-Vidal*, A. Bargerbos*, R. Žitko, L. J. Splitthoff, L. Grünhaupt, J. J. Wesdorp, Y. Liu, L. P. Kouwenhoven, R. Aguado, B. van Heck, A. Kou and C. K. Andersen
Nature Physics, DOI: 10.1038/s41567-023-02071-x (2023) [Included in chapter 8].

5. *Mitigation of quasiparticle loss in superconducting qubits by phonon scattering.*
A. Bargerbos, L. J. Splitthoff, **M. Pita-Vidal**, J. J. Wesdorp, Y. Liu, P. Krogstrup, L. P. Kouwenhoven, C. K. Andersen and L. Grünhaupt
Phys. Rev. Applied **19**, 024014 (2023)

4. *Gate-tunable kinetic inductance in proximitized nanowires.*
L. J. Splitthoff, A. Bargerbos, L. Grünhaupt, **M. Pita-Vidal**, J. J. Wesdorp, Y. Liu, A. Kou, C. K. Andersen and B. van Heck
Phys. Rev. Applied **18**, 024074 (2022)

3. *Singlet-Doublet Transitions of a Quantum Dot Josephson Junction Detected in a Transmon Circuit.*
A. Bargerbos*, **M. Pita-Vidal***, R. Žitko, J. Ávila, L. J. Splitthoff, L. Grünhaupt, J. J. Wesdorp, C. K. Andersen, Y. Liu, L. P. Kouwenhoven, R. Aguado, A. Kou, and B. van Heck
PRX Quantum **3**, 030311 (2022) [Included in chapter 6].

2. *Gate-tunable field-compatible fluxonium.*
M. Pita-Vidal, A. Bargerbos, C-K Yang, D. J. van Woerkom, W. Pfaff, N. Haider, P. Krogstrup, L. P. Kouwenhoven, G. de Lange and A. Kou
Phys. Rev. Applied **14**, 064038 (2020) [Included in chapter 5].

1. *Manipulation and steering of hyperbolic surface polaritons in hexagonal boron nitride.*
S. Dai, M. Tymchenko, Y. Yang, Q. Ma, **M. Pita-Vidal**, K. Watanabe, T. Taniguchi, P. Jarillo-Herrero, M. M. Fogler, A. Alù and D. N. Basov
Advanced Materials **30**, 1706358 (2019)

PATENT APPLICATION

1. *A gradiometric device and an array of such gradiometric devices.*
M. Pita-Vidal, A. Bargerbos, J. J. Wesdorp and C. K. Andersen
Patent pending.

2. *Scalable architecture for coupling Andreev spin qubits, and methods of manufacturing and operating such.*
M. Pita-Vidal, J. J. Wesdorp and C. K. Andersen
Patent pending.

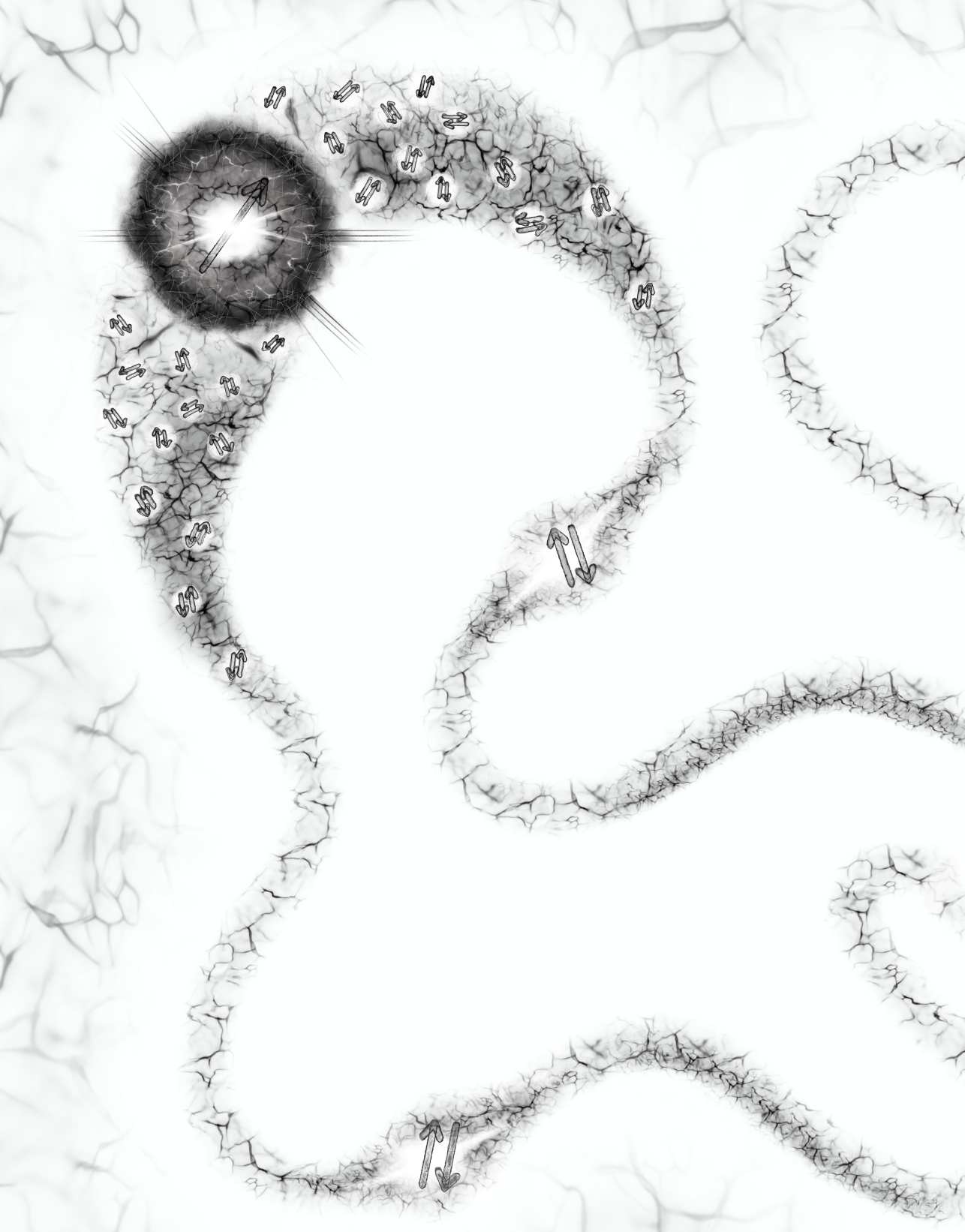

ISBN: 978-90-8593-584-1

Casimir PhD series: 2023-38